



University  
of Glasgow

Chen, Yi (2010) *Dynamical modelling of a flexible motorised momentum exchange tether and hybrid fuzzy sliding mode control for spin-up*. PhD thesis.

<http://theses.gla.ac.uk/1844/>

Copyright and moral rights for this thesis are retained by the Author

A copy can be downloaded for personal non-commercial research or study, without prior permission or charge

This thesis cannot be reproduced or quoted extensively from without first obtaining permission in writing from the Author

The content must not be changed in any way or sold commercially in any format or medium without the formal permission of the Author

When referring to this work, full bibliographic details including the author, title, awarding institution and date of the thesis must be given



University  
of Glasgow

**Dynamical Modelling of a Flexible  
Motorised Momentum Exchange Tether  
and Hybrid Fuzzy Sliding Mode Control  
for Spin-up**

Yi Chen

*Submitted in fulfilment of the requirements for  
the Degree of Doctor of Philosophy*

*Department of Mechanical Engineering  
Faculty of Engineering  
University of Glasgow*

© Yi Chen, September 2009

*To My Family*

[八声甘州.清秋怀古]

遍古今长江水东流，千年风雨稠。  
帝尧部族传，夏商祭幻，烽火二周。  
秦俑汉相玄奘，瘦金河图上。  
古道断西风，史外话万象。

曾经勤学路远，昨夜书万卷，朝田暮殿。  
剑影落叶旋，浅酒菊花粥。  
烟波一伞秋色满，缘浅灯深窗半悬。  
谁如烟，渺渺诗笺，明月正圆。

---

# Abstract

---

A space tether is a long cable used to couple satellites, probes or spacecrafts to each other or to other masses, such as a spent booster rocket, space station, or an asteroid. Space tethers are usually made of thin strands of high-strength fibres or conducting wires, which range from a few hundred metres to several kilometres and have a relatively small diameter. Space tethers can provide a mechanical connection between two space objects that enables a transfer of energy and momentum from one object to the other, and as a result they can be used to provide space propulsion without consuming propellant. Additionally, conductive space tethers can interact with the Earth's magnetic field and ionospheric plasma to generate thrust or drag forces without expending propellant.

The motorised momentum exchange tether (MMET) was first proposed by Cartmell in 1996 and published in 1998. The system comprises a specially designed tether connecting two payload modules, with a central launcher motor. For the purposes of fundamental dynamical modelling the launcher mass can be regarded as a two part assembly, where the rotor is attached to one end of each tether subspan, and the other side is the stator, which is attached to the rotor by means of suitable bearings. Both the launcher and the payload can be attached to the tether by means of suitable clamps or bearing assemblies, dependent on the requirements of the design.

The further chapters in this thesis focus on a series of dynamical models of the symmetrical MMET system, including the dumbbell MMET system, the solid massless MMET system, the flexible massless MMET system, the solid MMET system and the discretised flexible MMET system. The models in this context have shown that including axial, torsional and pendular elasticity, the MMET systems have a significant bearing on overall performance and that this effect should not be ignored in future, particularly for control studies. All subsequent analyses for control applications should henceforth include flexible compliance within the modelling procedure.

Numerical simulations have been given for all types of MMET models, in which, accurate and stable periodic behaviours are observed, including the rigid body motions, the tether

spin-up and the flexible motions, with proper parameter settings. The MMET system's spin-up control methods design and analysis will henceforth be referenced on the results.

For the non-linear dynamics and complex control problem, it was decided to investigate fuzzy logic based controllers to maintain the desired length and length deployment rate of the tether. A standard two input and one output fuzzy logic control (FLC) is investigated with numerical simulations, in which the control effects on the MMET system's spin-up are observed.

Furthermore, to make the necessary enhancement to the fuzzy sliding mode control, a specialised hybrid control law, named  $F\alpha$ SMC is proposed, which combines fuzzy logic control with a SkyhookSMC control law together, then it is applied for the control of motorised space tether spin-up coupled with an flexible oscillation phenomenon. It is easy to switch the control effects between the SkyhookSMC and the FLC modes when a proper value of  $\alpha$  is selected ( $0 < \alpha < 1$ ) to balance the weight of the fuzzy logic control to that of the SkyhookSMC control, and the hybrid fuzzy sliding mode controller is thus generated.

Next, the simulations with the given initial conditions have been devised in a connecting programme between the control code written in MATLAB and the dynamics simulation code constructed within MATHEMATICA. Both the FLC and the hybrid fuzzy sliding mode control methods are designed for the control of spin-up of the discretised flexible MMET system with tether-tube subspans, and the results have shown the validated effects of both these control methods for the MMET system spin-up with included flexible oscillation.

To summarise, the objectives of this thesis are, firstly, **to propose** a series of new dynamical models for the motorised momentum exchange tethers; secondly, **to discuss** two types of control methods for the spin-up behaviour of a flexible motorised momentum exchange tether, which **include** a fuzzy logic control and a hybrid fuzzy sliding mode control. By the weight factor  $\alpha$ , fuzzy logic control and SkyhookSMC controllers can be balanced from one to each other, and there is observed difference for each of the elastic behaviour in the MMET system involving these MMET systems with different controllers - FLC( $\alpha = 1$ ),  $F\alpha$ SMC( $\alpha = 0.5$ ) and SkyhookSMC( $\alpha = 0.0$ ). The results state the control effects for FLC,  $F\alpha$ SMC and FLC, which lead to stable spin-up behaviour with flexible oscillations.

---

# Contents

---

<b>Contents</b>	<b>i</b>
<b>List of Symbols and Abbreviations</b>	<b>vii</b>
<b>List of Figures</b>	<b>xi</b>
<b>List of Tables</b>	<b>xx</b>
<b>1 Introduction to Space Tethers</b>	<b>1</b>
1.1 Introduction . . . . .	1
1.1.1 History of the Tether Concept . . . . .	9
1.1.2 Tether Missions . . . . .	11
1.1.3 Momentum Exchange Tethers . . . . .	17
1.1.4 Electrodynamic Tethers . . . . .	18
1.2 Objectives . . . . .	19
1.3 Contributions . . . . .	20
1.4 Thesis Structure . . . . .	20
<b>2 Literature Review on Space Tethers and Tethered System Control</b>	<b>25</b>
2.1 Introduction . . . . .	25
2.2 Tether Deployment and Retrieval . . . . .	26
2.3 Trajectory Generation and Orbit Control . . . . .	31
2.4 Tether Attitude and Motion Control . . . . .	35
2.5 Tether Vibration Control and Dynamical Simulations . . . . .	44
2.6 Space Tether Dynamical Models . . . . .	49
2.7 Conclusions . . . . .	51
<b>3 The Motorised Momentum Exchange Tether (MMET)</b>	<b>52</b>
3.1 Introduction . . . . .	52

3.2	Dumbbell Tether . . . . .	53
3.2.1	Kinetic Energy . . . . .	56
3.2.2	Potential Energy . . . . .	56
3.2.3	Generalised Coordinates . . . . .	56
3.2.4	Generalised Forces . . . . .	57
3.2.5	Governing Equations of Motion . . . . .	57
3.2.6	Simulations and Discussions . . . . .	58
3.3	The Motorised Momentum Exchange Tether . . . . .	63
3.4	The Dumbbell MMET . . . . .	66
3.4.1	Kinetic Energy . . . . .	68
3.4.2	Potential Energy . . . . .	69
3.4.3	Generalised Coordinates . . . . .	69
3.4.4	Generalised Forces . . . . .	69
3.4.5	Governing Equations of Motion . . . . .	70
3.4.6	Simulations and Discussions . . . . .	70
3.5	The Dumbbell MMET with Cylindrical Payloads and a Motor Facility . . . . .	76
3.5.1	Payload Mass Moment of Inertias . . . . .	78
3.5.2	Motor Facility Mass Moment of Inertias . . . . .	79
3.5.3	Torque Plane . . . . .	80
3.5.4	Generalised Coordinates . . . . .	80
3.5.5	Kinetic Energy . . . . .	81
3.5.6	Potential Energy . . . . .	81
3.5.7	Generalised Forces . . . . .	82
3.5.8	Governing Equations of Motion . . . . .	83
3.5.9	Simulations and Discussions . . . . .	86
3.6	The MMET as a Rigid Body . . . . .	91
3.6.1	Tether-Tube Mass Moments of Inertia . . . . .	92
3.6.2	Tether-Tube Discretisation . . . . .	93
3.6.3	Discrete Mass Point Mass Moments of Inertia . . . . .	95
3.6.4	Potential Energy . . . . .	96
3.6.5	Kinetic Energy . . . . .	97
3.6.6	Generalised Coordinates . . . . .	98
3.6.7	Generalised Forces . . . . .	98
3.6.8	Governing Equations of Motion . . . . .	98
3.6.9	Simulations and Discussions . . . . .	107

3.7	Conclusions . . . . .	110
<b>4</b>	<b>Dynamical Modelling of a Flexible Massless MMET System</b>	<b>113</b>
4.1	Introduction . . . . .	113
4.2	Dynamical Modelling incorporating Axial Elasticity . . . . .	115
4.2.1	Governing Equations of Motion . . . . .	119
4.2.2	Simulations and Discussions . . . . .	123
4.3	Dynamical Modelling including Axial and Torsional Elasticity . . . . .	129
4.3.1	Governing Equations of Motion . . . . .	131
4.3.2	Simulations and Discussions . . . . .	137
4.4	Dynamical Modelling for the Flexible Massless MMET . . . . .	143
4.4.1	Governing Equations of Motion . . . . .	148
4.4.2	Simulations and Discussions . . . . .	154
4.5	Conclusions . . . . .	160
<b>5</b>	<b>Discretised Axially MMET Elastic System</b>	<b>163</b>
5.1	Introduction . . . . .	163
5.2	The Cartesian Coordinates for the Motor Facility and the Payloads . . . . .	165
5.3	The Cartesian Components for the Mass Points $m_1$ to $m_{10}$ . . . . .	166
5.4	Potential Energy . . . . .	167
5.5	Kinetic Energy . . . . .	168
5.6	Generalised Coordinates . . . . .	169
5.7	Generalised Forces . . . . .	171
5.8	Governing Equations of Motion . . . . .	171
5.9	Simulations and Discussions . . . . .	173
5.10	Conclusions . . . . .	182
<b>6</b>	<b>Discretised MMET System involving Axial and Torsional Elasticity</b>	<b>184</b>
6.1	Introduction . . . . .	184
6.2	Potential Energy . . . . .	186
6.3	Kinetic Energy . . . . .	187
6.4	Generalised Coordinates . . . . .	188
6.5	Generalised Forces . . . . .	188
6.6	Governing Equations of Motion . . . . .	188
6.7	Simulations and Discussions . . . . .	188
6.8	Conclusions . . . . .	200

<b>7</b>	<b>Dynamical Modelling for a Discretised Flexible MMET System</b>	<b>201</b>
7.1	Introduction . . . . .	201
7.2	Potential Energy . . . . .	205
7.3	Kinetic Energy . . . . .	206
7.4	Generalised Coordinates . . . . .	207
7.5	Generalised Forces . . . . .	208
7.6	Governing Equations of Motion . . . . .	208
7.7	Simulations and Discussions . . . . .	212
7.8	Conclusions . . . . .	223
<b>8</b>	<b>Fuzzy Logic Control for MMET Spin-up</b>	<b>227</b>
8.1	Introduction . . . . .	227
8.2	Control Objective . . . . .	230
8.3	Linguistic Descriptions . . . . .	231
8.4	Inputs and Outputs . . . . .	231
8.5	Fuzzification . . . . .	233
8.5.1	Normalisation . . . . .	233
8.5.2	Membership functions . . . . .	235
8.6	Rule-base and Inference Mechanisms . . . . .	237
8.7	Defuzzification . . . . .	241
8.8	Simulations and Discussions . . . . .	241
8.9	Conclusions . . . . .	248
<b>9</b>	<b>Hybrid Fuzzy Sliding Mode Control for Spin-up of the MMET</b>	<b>249</b>
9.1	Introduction . . . . .	249
9.2	Ideal Skyhook Damping . . . . .	250
9.3	Skyhook Surface Definition for Sliding Mode Control . . . . .	251
9.4	Hybrid Fuzzy Sliding Mode Control Design . . . . .	255
9.5	Simulations and Discussions . . . . .	255
9.6	Conclusions . . . . .	268
<b>10</b>	<b>Conclusions and Future Work</b>	<b>269</b>
10.1	Work Summary . . . . .	269
10.2	Conclusions . . . . .	274
10.3	Future Work . . . . .	277

<b>References</b>	<b>278</b>
<b>A Partial Derivatives for Equation 3.5.11</b>	<b>299</b>
<b>B Partial Derivatives for Equation 3.5.12</b>	<b>301</b>
<b>C Simulation Parameter Settings</b>	<b>303</b>
<b>D Lagrange Equation Components for Section 4.2</b>	<b>306</b>
D.1 Potential Energy . . . . .	306
D.2 Kinetic Energy . . . . .	307
D.3 Generalised Coordinates . . . . .	307
D.4 Generalised Forces . . . . .	308
<b>E Lagrange Equation Components for Section 4.3</b>	<b>309</b>
E.1 Potential Energy . . . . .	309
E.2 Kinetic Energy . . . . .	310
E.3 Generalised Coordinates . . . . .	311
E.4 Generalised Forces . . . . .	311
<b>F Lagrange Equation Components for Section 4.4</b>	<b>313</b>
F.1 Generalised Coordinates . . . . .	313
F.2 Kinetic Energy . . . . .	313
F.3 Potential Energy . . . . .	314
F.4 Generalised Forces . . . . .	315
<b>G Axial Elastic MMET System with Two Discretised Mass Points</b>	<b>317</b>
G.1 The Cartesian Coordinates for Payloads $M_{P1}$ and $M_{P2}$ . . . . .	317
G.2 The Cartesian Coordinates for Mass Points $m_1$ to $m_2$ . . . . .	319
G.3 Potential Energy . . . . .	319
G.4 Kinetic Energy . . . . .	320
G.5 Governing Equations of Motion . . . . .	320
<b>H Axial and Torsional Elastic MMET System with Two Discretised Mass Points</b>	<b>321</b>
H.1 Potential Energy . . . . .	321
H.2 Kinetic Energy . . . . .	323
H.3 Governing Equations of Motion . . . . .	323
<b>I Flexible MMET System with Two Discretised Mass Points</b>	<b>324</b>

I.1	Potential Energy . . . . .	327
I.2	Kinetic Energy . . . . .	327
I.3	Governing Equations of Motion . . . . .	328
<b>J</b>	<b>Elastic Motion Figures for Chapter 8</b>	<b>329</b>
<b>K</b>	<b>Elastic Motion Figures for Chapter 9</b>	<b>338</b>
<b>L</b>	<b>SMATLINK - How to integrate MATLAB with MATHEMATICA</b>	<b>356</b>
L.1	Introduction . . . . .	356
L.2	Why SMATLINK . . . . .	356
L.3	MMET spin-up control co-simulation . . . . .	357
<b>M</b>	<b>Fuzzy Logic Control Terminology</b>	<b>360</b>

---

# List of Symbols and Abbreviations

---

$\theta$	true anomaly
$R$	radius scalar to the orbiting tether's centre of mass
$e$	eccentricity
$G$	universal gravitational constant
$n$	number of massless points
$N$	number of mass points
$\epsilon$	the factor for the mass point mass moment of inertia
$\mu$	gravitational constant
$m_i$	the discrete mass point $m_i$
$l_i$	the static distance from COM to the discrete mass point $m_i$
$M_P$	propulsion tether payload mass
$M_M$	mass of motor facility
$M_T$	the mass of the tether subspan centre of mass
$r_{\text{Tinner}}$	radius of tether inner tube
$r_{\text{Touter}}$	radius of tether outer tube
$r_M$	radius of motor facility
$r_P$	radius of payload
$r_{\text{per}}$	periapsis distance
$r_{\text{apo}}$	apoapsis distance
$T_n$	the number of cycles of period (NCP)
$L_0$	static length tether sub-span
$U$	potential energy
$T$	kinetic energy
$q_i$	generalised coordinate $q_i$
$Q_i$	generalised force for generalised coordinate $q_i$
$W_{q_i}$	virtual work for generalised coordinate $q_i$

$A$	undeformed tether tube cross-sectional area
$\rho$	tether density
$\psi_0$	initial angular
$\dot{\psi}_0$	initial angular velocity
$\tau$	motor torque
$c_i$	tether sub-span axial damping coefficient
$k_i$	tether sub-span axial stiffness
$c_{ti}$	tether sub-span torsional damping coefficient
$k_{ti}$	tether sub-span torsional stiffness
$c_{eqmi}$	axial equivalent damping coefficient for discretised MMET
$k_{eqmi}$	axial equivalent stiffness coefficient for discretised MMET
$e(t)$	FLC input signal of error
$ec(t)$	FLC input signal of change-in-error
$u(t)$	FLC output signal of control
$E$	fuzzified input of error
$EC$	fuzzified input of change-in-error
$FL$	fuzzified output of length
$K_e$	FLC scaling gains for $e(t)$
$K_{ec}$	FLC scaling gains for $ec(t)$
$K_u$	FLC scaling gains for $u(t)$
$\alpha$	F $\alpha$ SMC switching factor
$c_0$	SkyhookSMC damping coefficient
$\delta$	thickness of the sliding mode boundary layer
$\lambda$	slope of the sliding surface

AERO	The Aerospace Corporation
ANN	Artificial Neural Networks
ASI	The Italian Space Agency
CI	computational intelligence
COM	Centre of Mass
CRC	Communications Research Centre Canada
CSA	Canadian Space Agency
ED	Electrodynamic
ESA	The European Space Agency
EVA	Extravehicular Activities
FIS	Fuzzy Inference System
FLC	Fuzzy Logic Control
FLT	Feedback Linearization Technique
FSMC	Fuzzy Sliding Mode Control
F $\alpha$ SMC	Hybrid Fuzzy Sliding Mode Control with Balance Factor $\alpha$
GA	Genetic Algorithms
GATE	Getaway Tether Experiment
GATV	Gemini Agena Target Vehicle
GEO	Geosynchronous Orbits
GTO	Geosynchronous Transfer Orbit
GSO	Geostationary Orbit
ISAS	The Japanese Institute of Space and Astronautical Science
JAXA	The Japanese Aerospace Exploration Agency
LEO	Low Earth Orbit
LTO	Lunar Transfer Orbit
MACE	Middeck Active Control Experiment
MMET	Motorised Momentum Exchange Tether
MSFC	The George C. Marshall Space Flight Center
MXER	Hybrid of Momentum eXchange/Electrodynamic Reboost
MX	Momentum Exchange

NASA	The National Aeronautics and Space Administration
NCP	The number of cycles of period
NDRE	The Norwegian Defence Research Establishment
NRC	The National Research Council
NRO	The National reconnaissance Office
NRL	The Naval Research Laboratory
NTG	Nonlinear Trajectory Generation
PID	Proportional Integral Derivative
PMG	Plasma Motor Generator
PO	Polar Orbits
ProSEDS	Propulsive Small Expendable Deployer system
RLV	Reusable Launch Vehicle
SE	Space Elevator
SEDS	Small Expendable-tether Deployer System
SkyhookSMC	Skyhook Surface Sliding Mode Control
SPECS	Submillimeter Probe of the Evolution of Cosmic Structure
SSO	Sun Synchronous Orbits
SMC	Sliding Mode Control
TAG	Tethered Artificial Gravity
TPE	Tethered Payload Experiment
TSS	Tethered Satellite Systems
TSS-1R	Tethered Satellite System Reflight
VSC	Variable Structure Control
VSS	Variable Structure System
*	Normalisation Operation

---

# List of Figures

---

1.1	Elliptical orbit . . . . .	3
1.2	Geocentric inertial coordinate system . . . . .	5
1.3	Heliocentric ecliptic coordinate system defining vernal equinox direction . . . . .	6
1.4	Momentum exchange tether system . . . . .	17
1.5	Electrodynamic tether system . . . . .	19
1.6	Thesis structure by chapters . . . . .	23
1.7	Thesis structure by models . . . . .	24
3.1	Mathematical components for Lagrange equation . . . . .	53
3.2	The dumbbell tether dynamical model . . . . .	54
3.3	<b>The dumbbell tether dynamical model - top view</b> . . . . .	55
3.4	Dumbbell tether angular displacement $\psi$ ( $T_n = 400.01$ ) . . . . .	58
3.5	Dumbbell tether angular displacement $\psi$ ( $T_n = 40.01$ ) . . . . .	59
3.6	Dumbbell tether angular displacement $\psi$ ( $T_n = 4.01$ ) . . . . .	59
3.7	Dumbbell tether true anomaly $\theta$ ( $T_n = 400.01$ ) . . . . .	60
3.8	Dumbbell tether true anomaly $\theta$ ( $T_n = 4.01$ ) . . . . .	60
3.9	<b>Dumbbell tether distance <math>R</math> (<math>T_n = 400.01</math>)</b> . . . . .	61
3.10	<b>Dumbbell tether distance <math>R</math> (<math>T_n = 4.01</math>)</b> . . . . .	61
3.11	<b>Dumbbell tether out-of-plane angle <math>\alpha</math> (<math>T_n = 4.01</math>)</b> . . . . .	62
3.12	The conceptual schematic of the motorised momentum exchange tether . . . . .	64
3.13	The scale model of the MMET experiment on ice [68] [69] . . . . .	64
3.14	<b>The conceptual schematic of the dumbbell motorised momentum exchange tether</b> . . . . .	66
3.15	<b>The model for dumbbell MMET system</b> . . . . .	67
3.16	<b>The model for the dumbbell MMET system - top view</b> . . . . .	68
3.17	Dumbbell MMET tether angular displacement $\psi$ ( $T_n = 400.01$ ) . . . . .	71
3.18	Dumbbell MMET tether angular displacement $\psi$ ( $T_n = 4.01$ ) . . . . .	72
3.19	Dumbbell MMET tether elliptical $\theta$ ( $T_n = 400.01$ ) . . . . .	72

3.20	Dumbbell MMET tether elliptical $\theta$ ( $T_n = 4.01$ ) . . . . .	73
3.21	Dumbbell MMET tether out-of-plane angle $\alpha$ ( $T_n = 4.01$ ) . . . . .	73
3.22	Dumbbell MMET distance R ( $T_n = 400.01$ ) . . . . .	74
3.23	Dumbbell MMET distance R ( $T_n = 40.01$ ) . . . . .	74
3.24	Dumbbell MMET distance R ( $T_n = 4.01$ ) . . . . .	75
3.25	The MMET system with cylindrical payloads and a motor facility . . . . .	76
3.26	The MMET system with cylindrical payloads and a motor facility - top view . . . . .	77
3.27	The definition of local axes for two cylindrical payloads . . . . .	78
3.28	The definition of local axes for the cylindrical motor facility . . . . .	79
3.29	The $x_0, y_0, z_0$ components of the ‘torque-plane’ . . . . .	80
3.30	The dumbbell MMET with cylindrical payloads spin-up $\psi$ ( $T_n = 400.01$ ) . . . . .	86
3.31	The dumbbell MMET with cylindrical payloads spin-up $\psi$ ( $T_n = 4.01$ ) . . . . .	87
3.32	The dumbbell MMET with cylindrical payloads distance R ( $T_n = 400.01$ ) . . . . .	87
3.33	The dumbbell MMET with cylindrical payloads distance R ( $T_n = 4.01$ ) . . . . .	88
3.34	The dumbbell MMET with cylindrical payloads elliptical orbit $\theta$ ( $T_n = 400.01$ ) . . . . .	88
3.35	The dumbbell MMET with cylindrical payloads angular position of $\theta$ ( $T_n = 4.01$ ) . . . . .	89
3.36	The dumbbell MMET with cylindrical payloads out-of-plane angle $\alpha$ ( $T_n = 4.01$ ) . . . . .	89
3.37	The dumbbell MMET with cylindrical payloads rolling angle $\gamma$ ( $T_n = 4.01$ ) . . . . .	90
3.38	The MMET with solid tether-tube generalised coordinates and defined on orbit . . . . .	91
3.39	The definition of local axes for tether mass components . . . . .	92
3.40	The definition of local axes for the tether subspan . . . . .	92
3.41	$\ln(\theta)$ function singularity when $\theta \in [0, \pi]$ . . . . .	94
3.42	$\ln(\theta)$ function singularity when $\theta \in [0, 20\pi]$ . . . . .	95
3.43	The discretisation for axial elasticity for motorised momentum exchange tether . . . . .	103
3.44	The point mass location scheme . . . . .	104
3.45	The point mass locations as percentage . . . . .	105
3.46	The definition of local axes for mass point $m_i$ . . . . .	105
3.47	The discrete and full tether potential energies . . . . .	106
3.48	The potential energy error of discrete and full tether . . . . .	106
3.49	The rigid body MMET spin-up displacement $\psi$ ( $T_n = 400.01$ ) . . . . .	107
3.50	The rigid body MMET spin-up displacement $\psi$ ( $T_n = 4.01$ ) . . . . .	107
3.51	The rigid body MMET elliptical orbit angular position of $\theta$ ( $T_n = 400.01$ ) . . . . .	108
3.52	The rigid body MMET elliptical orbit angular position of $\theta$ ( $T_n = 4.01$ ) . . . . .	108
3.53	The rigid body MMET out-of-plane angle $\alpha$ ( $T_n = 4.01$ ) . . . . .	109
3.54	The rigid body MMET base point distance of R ( $T_n = 400.01$ ) . . . . .	109

3.55	The rigid body MMET base point distance of R ( $T_n = 4.01$ )	110
3.56	The rigid body MMET rolling angle $\gamma$ ( $T_n = 4.01$ )	110
4.1	The MMET pendular elasticity plane definition	114
4.2	Reference plane definition for MMET torsional and pendular elasticity	115
4.3	The conceptual schematic of the massless MMET with axially elastic tether	116
4.4	The massless MMET system with axial elasticity on orbit	117
4.5	The MMET system with axially elastic massless tether subspan	118
4.6	The massless point at each end of a ‘spring-damper’ group	118
4.7	Massless axial elastic MMET spin-up, $\psi$ ( $T_n = 400.01$ )	123
4.8	Massless axial elastic MMET spin-up, $\psi$ ( $T_n = 4.01$ )	124
4.9	Massless axial elastic MMET elliptical $\theta$ ( $T_n = 400.01$ )	124
4.10	Massless axial elastic MMET elliptical $\theta$ ( $T_n = 4.01$ )	125
4.11	Massless axial elastic MMET $\alpha$ ( $T_n = 4.01$ )	125
4.12	Massless axial elastic MMET base point distance R ( $T_n = 400.01$ )	126
4.13	Massless axial elastic MMET base point distance R ( $T_n = 4.01$ )	126
4.14	Massless axial elastic MMET rolling angle $\gamma$ ( $T_n = 4.01$ )	127
4.15	Axial displacement along tether subspan of $L_x$ ( $T_n = 4.01$ )	127
4.16	Axial elastic length vs. static length ratio along tether subspan of $\frac{L_x}{L_0}$ ( $T_n = 4.01$ )	128
4.17	The MMET model generalised coordinates defined on orbit	130
4.18	The Axial and torsional elasticity model referenced onto plane $x_0 - O - z_0$	131
4.19	Reference onto the plane $x_0 - O - z_0$ for MMET torsional elasticity	131
4.20	Massless axial and torsional elastic MMET spin-up ( $T_n = 400.01$ )	137
4.21	Massless axial and torsional elastic MMET spin-up ( $T_n = 4.01$ )	137
4.22	Massless axial and torsional elastic MMET $\theta$ ( $T_n = 400.01$ )	138
4.23	Massless axial and torsional elastic MMET $\theta$ ( $T_n = 4.01$ )	138
4.24	Massless axial and torsional elastic MMET $\theta$ ( $T_n = 4.01$ )	139
4.25	Massless axial and torsional elastic MMET base point R ( $T_n = 400.01$ )	139
4.26	Massless axial and torsional elastic MMET base point R ( $T_n = 4.01$ )	140
4.27	Massless axial and torsional elastic MMET rolling angle of $\gamma$ ( $T_n = 4.01$ )	140
4.28	Axial displacement along tether subspan of $L_x$ ( $T_n = 4.01$ )	141
4.29	Axial elastic length vs. static length ratio ( $T_n = 4.01$ )	141
4.30	Torsional displacement $\gamma_x$ ( $T_n = 4.01$ )	142
4.31	Reference onto the plane $x_0 - O - y_0$ for MMET pendular elasticity	144
4.32	The MMET pendular elasticity modelling referenced onto the plane $x_0 - O - y_0$	144

4.33	The flexible massless MMET system generalised coordinate definitions on orbit	145
4.34	The MMET pendular elasticity modelling reference on the plane $z_0 - O - y_0$	146
4.35	Reference on the plane $z_0 - O - y_0$ for MMET pendular elasticity	146
4.36	The equivalent axial, torsional and pendular elasticity	147
4.37	Massless flexible MMET spin-up $\psi$ ( $T_n = 400.01$ )	154
4.38	Massless flexible MMET spin-up $\psi$ ( $T_n = 4.01$ )	154
4.39	Massless flexible MMET $\theta$ ( $T_n = 400.01$ )	155
4.40	Massless flexible MMET $\theta$ ( $T_n = 4.01$ )	155
4.41	Massless flexible MMET out-of-plane angle $\alpha$ ( $T_n = 4.01$ )	156
4.42	Massless flexible MMET base point distance R to the Earth ( $T_n = 400.01$ )	156
4.43	Massless flexible MMET base point distance R ( $T_n = 4.01$ )	157
4.44	Massless flexible MMET rolling angle $\gamma$ ( $T_n = 400.01$ )	157
4.45	Massless flexible MMET axial displacement $L_x$ ( $T_n = 4.01$ )	158
4.46	Massless flexible MMET axial elastic length vs. static length ratio $\frac{L_x}{L_0}$ ( $T_n = 4.01$ )	158
4.47	Massless flexible MMET torsional displacement $\gamma_x$ ( $T_n = 4.01$ )	159
4.48	Massless flexible MMET, on plane $x_0 - O - y_0$ , $\psi_x$ ( $T_n = 4.01$ )	159
4.49	Massless flexible MMET, on plane $z_0 - O - y_0$ , $\alpha_x$ ( $T_n = 4.01$ )	160
5.1	Axial elastic MMET tether with 10 discrete mass points	164
5.2	The spring-damper groups	165
5.3	The MMET system with axial elasticity definition on orbit	170
5.4	Axial elastic MMET system spin-up, angular displacement $\psi$ ( $T_n = 4.01$ )	173
5.5	Axial elastic MMET system spin-up, angular displacement $\psi$ ( $T_n = 400.01$ )	174
5.6	Axial elastic MMET system base point distance R ( $T_n = 4.01$ )	174
5.7	Axial elastic MMET system base point distance R ( $T_n = 400.01$ )	175
5.8	Axial elastic MMET system elliptical orbit angular position of $\theta$ ( $T_n = 4.01$ )	175
5.9	Axial elastic MMET system elliptical orbit angular position of $\theta$ ( $T_n = 400.01$ )	176
5.10	Axial elastic MMET system out-of-plane angle $\alpha$ ( $T_n = 4.01$ )	176
5.11	Axial elastic MMET system out-of-plane angle $\alpha$ ( $T_n = 400.01$ )	177
5.12	Axial elastic MMET system rolling angle $\gamma$ ( $T_n = 4.01$ )	177
5.13	Axial displacement responses $\eta_1$ and $\eta_{p1}$ ( $T_n = 4.01$ )	178
5.14	Axial displacement responses $\eta_1$ and $\eta_{p1}$ ( $T_n = 400.01$ )	178
5.15	Axial displacement responses $\eta_1$ and $\eta_{p1}$ , $T_n = 4.01$ vs. 400.01	179
5.16	Axial displacement responses $\eta_2$ and $\eta_{p2}$ ( $T_n = 4.01$ )	180
5.17	Axial displacement responses $\eta_2$ and $\eta_{p2}$ ( $T_n = 400.01$ )	180

5.18	Axial displacement responses $\eta_2$ and $\eta_{p2}$ , $T_n = 4.01$ vs. 400.01 . . . . .	181
6.1	Torsional elastic MMET tether with 10 discrete mass points . . . . .	185
6.2	Reference on the plane $x_0 - O - z_0$ for MMET torsional elasticity . . . . .	186
6.3	Axial and torsional elastic MMET system spin-up ( $T_n = 4.01$ ) . . . . .	190
6.4	Axial and torsional elastic MMET system spin-up ( $T_n = 400.01$ ) . . . . .	190
6.5	Axial and torsional elastic $\theta$ ( $T_n = 4.01$ ) . . . . .	191
6.6	Axial and torsional elastic $\theta$ ( $T_n = 400.01$ ) . . . . .	191
6.7	Axial and torsional elastic base point distance $R$ ( $T_n = 4.01$ ) . . . . .	192
6.8	Axial and torsional elastic base point distance $R$ ( $T_n = 400.01$ ) . . . . .	192
6.9	Axial and torsional elastic out-of-plane angle $\alpha$ ( $T_n = 4.01$ ) . . . . .	193
6.10	Axial and torsional elastic out-of-plane angle $\alpha$ ( $T_n = 400.01$ ) . . . . .	193
6.11	Axial and torsional elastic MMET system rolling angle of $\gamma$ ( $T_n = 4.01$ ) . . . . .	194
6.12	Axial displacement responses $\eta_1$ and $\eta_{p1}$ ( $T_n = 4.01$ ) . . . . .	194
6.13	Axial displacement responses $\eta_1$ and $\eta_{p1}$ ( $T_n = 400.01$ ) . . . . .	195
6.14	Axial displacement responses $\eta_2$ and $\eta_{p2}$ ( $T_n = 4.01$ ) . . . . .	195
6.15	Axial displacement responses $\eta_2$ and $\eta_{p2}$ ( $T_n = 400.01$ ) . . . . .	196
6.16	Torsional displacement response $\varphi_{p1}$ ( $T_n = 400.01$ ) . . . . .	196
6.17	Torsional displacement response $\varphi_1$ ( $T_n = 400.01$ ) . . . . .	197
6.18	Torsional displacement response $\varphi_{p2}$ ( $T_n = 400.01$ ) . . . . .	197
6.19	Torsional displacement response $\varphi_2$ ( $T_n = 400.01$ ) . . . . .	198
7.1	Pendular elastic MMET tether with 10 discrete mass points - $x_0 - O - y_0$ . . . . .	202
7.2	Pendular elastic MMET tether with 10 discrete mass points - $z_0 - O - y_0$ . . . . .	203
7.3	Reference onto the plane $x_0 - O - y_0$ for MMET pendular elasticity . . . . .	204
7.4	Reference onto the plane $z_0 - O - y_0$ for MMET pendular elasticity . . . . .	204
7.5	The flexible MMET system spin-up $\psi$ ( $T_n = 4.01$ ) . . . . .	212
7.6	The flexible MMET system spin-up $\psi$ ( $T_n = 400.01$ ) . . . . .	213
7.7	The flexible MMET system base point distance $R$ ( $T_n = 4.01$ ) . . . . .	213
7.8	The flexible MMET system base point distance of $R$ ( $T_n = 400.01$ ) . . . . .	214
7.9	The flexible MMET system elliptical orbit angular position of $\theta$ ( $T_n = 4.01$ ) . . . . .	214
7.10	The flexible MMET system elliptical orbit angular position of $\theta$ ( $T_n = 400.01$ ) . . . . .	215
7.11	The flexible MMET system out-of-plane angle $\alpha$ ( $T_n = 4.01$ ) . . . . .	215
7.12	The flexible MMET system out-of-plane angle $\alpha$ ( $T_n = 400.01$ ) . . . . .	216
7.13	The flexible MMET system rolling angle $\gamma$ ( $T_n = 4.01$ ) . . . . .	216
7.14	Axial displacement responses $\eta_1$ and $\eta_{p1}$ ( $T_n = 4.01$ ) . . . . .	217

7.15	Axial displacement responses $\eta_1$ and $\eta_{p1}$ ( $T_n = 400.01$ )	217
7.16	Axial displacement responses $\eta_2$ and $\eta_{p2}$ ( $T_n = 4.01$ )	218
7.17	Axial displacement responses $\eta_2$ and $\eta_{p2}$ ( $T_n = 400.01$ )	218
7.18	Pendular displacement response $\chi_{p1}$ ( $T_n = 4.01$ )	219
7.19	Pendular displacement response $\chi_1$ ( $T_n = 4.01$ )	219
7.20	Pendular displacement response $\chi_{p2}$ ( $T_n = 4.01$ )	220
7.21	Pendular displacement response $\chi_2$ ( $T_n = 4.01$ )	220
7.22	Pendular displacement response $\zeta_{p1}$ ( $T_n = 4.01$ )	221
7.23	Pendular displacement response $\zeta_1$ ( $T_n = 4.01$ )	221
7.24	Pendular displacement response $\zeta_{p2}$ ( $T_n = 4.01$ )	222
7.25	Pendular displacement response $\zeta_2$ ( $T_n = 4.01$ )	222
8.1	Fuzzy logic controller architecture	229
8.2	The FLC control loop for the MMET spin-up	230
8.3	The Human control loop for the MMET spin-up	232
8.4	Normalisation step 1: scale factor generation	234
8.5	Normalisation step 2: scale operation	234
8.6	Normalisation step 3: shift operation	234
8.7	Gaussian combination membership function definition	235
8.8	The membership function for E	236
8.9	The membership function for EC	236
8.10	The control surface of the fuzzy controller for MMET spin-up	238
8.11	The fuzzy inference system for MMET system spin-up	239
8.12	The fuzzy logic controller work process	240
8.13	The membership function for U	242
8.14	MMET spin-up control simulation loop	242
8.15	The angular displacement $\psi$ for MMET spin-up response ( $T_n = 4.01$ )	243
8.16	The angular displacement $\psi$ for MMET spin-up response ( $T_n = 400.01$ )	243
8.17	The angular velocity $\dot{\psi}$ for MMET spin-up response ( $T_n = 4.01$ )	244
8.18	The angular velocity $\dot{\psi}$ for MMET spin-up response ( $T_n = 400.01$ )	244
8.19	The angular acceleration $\ddot{\psi}$ for MMET spin-up response ( $T_n = 4.01$ )	245
8.20	The angular acceleration $\ddot{\psi}$ for MMET spin-up response ( $T_n = 400.01$ )	245
8.21	The MMET spin-up phase portrait ( $T_n = 4.01$ )	246
8.22	The MMET spin-up phase portrait ( $T_n = 400.01$ )	246
8.23	The FLC controlled tether subspan length for the MMET spin-up ( $T_n = 4.01$ )	247

8.24	The FLC controlled tether subspan length for the MMET spin-up ( $T_n = 400.01$ )	247
9.1	The ideal skyhook damper definition . . . . .	250
9.2	Sliding surface definition with skyhook surface . . . . .	251
9.3	The sliding skyhook surface generation . . . . .	252
9.4	Tanh function definition . . . . .	253
9.5	The $F\alpha$ SMC control strategy definition . . . . .	254
9.6	$\psi$ , with different values of $\alpha$ ( $T_n = 4.01$ ) . . . . .	256
9.7	$\psi$ ( $T_n = 400.01$ ), FLC vs. SkyhookSMC . . . . .	257
9.8	$\psi$ ( $T_n = 400.01$ ), $F\alpha$ SMC vs. SkyhookSMC . . . . .	258
9.9	Velocity of $\psi$ ( $T_n = 4.01$ ) . . . . .	258
9.10	Velocity of $\psi$ ( $T_n = 400.01$ ), FLC vs. SkyhookSMC . . . . .	259
9.11	Velocity of $\psi$ ( $T_n = 400.01$ ), $F\alpha$ SMC vs. SkyhookSMC . . . . .	260
9.12	The MMET spin-up phase plane portrait ( $T_n = 4.01$ ) . . . . .	261
9.13	The MMET spin-up phase plane portrait ( $T_n = 400.01$ ) . . . . .	262
9.14	The MMET spin-up error phase plane portrait ( $T_n = 4.01$ ) . . . . .	263
9.15	The MMET spin-up error phase plane portrait ( $T_n = 400.01$ ) . . . . .	264
9.16	Tether length with control ( $T_n = 4.01$ ) . . . . .	265
9.17	Tether length with control ( $T_n = 400.01$ ) . . . . .	265
9.18	The Lyapunov function for the MMET spin-up control ( $T_n = 4.01$ ) . . . . .	266
9.19	The Lyapunov function for the MMET spin-up control ( $T_n = 400.01$ ) . . . . .	266
9.20	The time derivative of the Lyapunov function ( $T_n = 4.01$ ) . . . . .	267
9.21	The time derivative of the Lyapunov function ( $T_n = 400.01$ ) . . . . .	267
10.1	Thesis structure for flexible MMET models . . . . .	270
G.1	Axial elastic MMET tether with 2 mass points . . . . .	318
H.1	Axial and torsional elastic MMET tether with 2 mass points . . . . .	322
I.1	Pendular elastic MMET tether with 2 discretised mass points - $x_0 - O - y_0$ . . . . .	325
I.2	Pendular elastic MMET tether with 2 discretised mass points - $z_0 - O - y_0$ . . . . .	326
J.1	Axial elastic behaviour with FLC - $\eta_1$ ( $T_n = 4.01$ ) . . . . .	329
J.2	Axial elastic behaviour with FLC - $\eta_1$ ( $T_n = 400.01$ ) . . . . .	330
J.3	Axial elastic behaviour with FLC - $\eta_{p1}$ ( $T_n = 4.01$ ) . . . . .	330
J.4	Axial elastic behaviour with FLC - $\eta_{p1}$ ( $T_n = 400.01$ ) . . . . .	331
J.5	Axial elastic behaviour with FLC - $\eta_2$ ( $T_n = 4.01$ ) . . . . .	331

J.6	Axial elastic behaviour with FLC - $\eta_2$ ( $T_n = 400.01$ ) . . . . .	332
J.7	Axial elastic behaviour with FLC - $\eta_{P2}$ ( $T_n = 4.01$ ) . . . . .	332
J.8	Axial elastic behaviour with FLC - $\eta_{P2}$ ( $T_n = 400.01$ ) . . . . .	333
J.9	Pendular elastic behaviour with FLC - $\chi_1$ ( $T_n = 4.01$ ) . . . . .	333
J.10	Pendular elastic behaviour with FLC - $\chi_{P1}$ ( $T_n = 4.01$ ) . . . . .	334
J.11	Pendular elastic behaviour with FLC - $\chi_2$ ( $T_n = 400.01$ ) . . . . .	334
J.12	Pendular elastic behaviour with FLC - $\chi_{P2}$ ( $T_n = 4.01$ ) . . . . .	335
J.13	Pendular elastic behaviour with FLC - $\zeta_1$ ( $T_n = 4.01$ ) . . . . .	335
J.14	Pendular elastic behaviour with FLC - $\zeta_{P1}$ ( $T_n = 4.01$ ) . . . . .	336
J.15	Pendular elastic behaviour with FLC - $\zeta_2$ ( $T_n = 400.01$ ) . . . . .	336
J.16	Pendular elastic behaviour with FLC - $\zeta_{P2}$ ( $T_n = 4.01$ ) . . . . .	337
K.1	Axial elastic behaviours with control - $\eta_1$ ( $T_n = 4.01$ ) . . . . .	340
K.2	Axial elastic behaviours with control - $\eta_1$ ( $T_n = 400.01$ ) . . . . .	341
K.3	Axial elastic behaviours with control - $\eta_2$ ( $T_n = 4.01$ ) . . . . .	342
K.4	Axial elastic behaviours with control - $\eta_2$ ( $T_n = 400.01$ ) . . . . .	343
K.5	Axial elastic behaviours with control - $\eta_{P1}$ ( $T_n = 4.01$ ) . . . . .	344
K.6	Axial elastic behaviours with control - $\eta_{P1}$ ( $T_n = 400.01$ ) . . . . .	345
K.7	Axial elastic behaviours with control - $\eta_{P2}$ ( $T_n = 4.01$ ) . . . . .	346
K.8	Axial elastic behaviours with control - $\eta_{P2}$ ( $T_n = 400.01$ ) . . . . .	347
K.9	Torsional elastic behaviours with control - $\chi_1$ ( $T_n = 4.01$ ) . . . . .	348
K.10	Torsional elastic behaviours with control - $\chi_1$ ( $T_n = 4.01$ ) . . . . .	348
K.11	Torsional elastic behaviours with control - $\chi_2$ ( $T_n = 4.01$ ) . . . . .	349
K.12	Torsional elastic behaviours with control - $\chi_2$ ( $T_n = 4.01$ ) . . . . .	349
K.13	Torsional elastic behaviours with control - $\chi_{P1}$ ( $T_n = 4.01$ ) . . . . .	350
K.14	Torsional elastic behaviours with control - $\chi_{P1}$ ( $T_n = 4.01$ ) . . . . .	350
K.15	Torsional elastic behaviours with control - $\chi_{P2}$ ( $T_n = 4.01$ ) . . . . .	351
K.16	Torsional elastic behaviours with control - $\chi_{P2}$ ( $T_n = 4.01$ ) . . . . .	351
K.17	Torsional elastic behaviours with control - $\zeta_1$ ( $T_n = 4.01$ ) . . . . .	352
K.18	Torsional elastic behaviours with control - $\zeta_1$ ( $T_n = 4.01$ ) . . . . .	352
K.19	Torsional elastic behaviours with control - $\zeta_2$ ( $T_n = 4.01$ ) . . . . .	353
K.20	Torsional elastic behaviours with control - $\zeta_2$ ( $T_n = 4.01$ ) . . . . .	353
K.21	Torsional elastic behaviours with control - $\zeta_{P1}$ ( $T_n = 4.01$ ) . . . . .	354
K.22	Torsional elastic behaviours with control - $\zeta_{P1}$ ( $T_n = 4.01$ ) . . . . .	354
K.23	Torsional elastic behaviours with control - $\zeta_{P2}$ ( $T_n = 4.01$ ) . . . . .	355

K.24 Torsional elastic behaviours with control - $\zeta_{p2}$ ( $T_n = 4.01$ ) . . . . .	355
L.1 SMATLINK::matlabcall work loop . . . . .	357
L.2 SMATLINK::mathematicacall work loop . . . . .	357
L.3 The MMET system spin-up control co-simulation via SMATLINK . . . . .	358
L.4 How to call MATHEMATICA function from MATLAB . . . . .	358
L.5 SMATLINK timing control . . . . .	359

---

# List of Tables

---

1.1	Tether mission history . . . . .	12
3.1	The dumbbell tether generalised coordinates and generalised forces . . . . .	57
3.2	The components of the basic conceptual schematic of the MMET system . . . . .	63
3.3	The dumbbell tether generalised coordinates and generalised forces . . . . .	69
3.4	The dumbbell MMET with cylindrical payload generalised coordinates . . . . .	83
3.5	The MMET with discrete tether-tube subspan generalised coordinates . . . . .	98
3.6	Figures for spin-up $\psi$ in Chapter 3 . . . . .	111
3.7	Figures for $R$ in Chapter 3 . . . . .	111
3.8	Figures for $\theta$ in Chapter 3 . . . . .	111
4.1	The axial elastic massless MMET generalised coordinates . . . . .	120
4.2	The axial and torsional elastic massless MMET generalised coordinates . . . . .	132
4.3	The flexible massless MMET generalised coordinates and generalised forces . . . . .	148
4.4	Figures for spin-up $\psi$ in Chapter 4 . . . . .	161
4.5	Figures for $R$ in Chapter 4 . . . . .	161
4.6	Figures for $\alpha$ in Chapter 4 . . . . .	161
4.7	Figures for $\theta$ in Chapter 4 . . . . .	161
4.8	Figures for $\gamma$ in Chapter 4 . . . . .	161
4.9	Figures for $L_x$ in Chapter 4 . . . . .	161
4.10	Figures for $\gamma_x$ in Chapter 4 . . . . .	161
4.11	Figures for $\psi_x$ in Chapter 4 . . . . .	162
4.12	Figures for $\alpha_x$ in Chapter 4 . . . . .	162
5.1	The axial elastic MMET generalised coordinates . . . . .	171
5.2	The axial elastic MMET generalised coordinates . . . . .	172
6.1	The axial and torsional elastic MMET generalised coordinates . . . . .	189
6.2	The axial and torsional elastic MMET generalised coordinates . . . . .	189

7.1	The axial, torsional and pendular elastic MMET generalised coordinates . . . .	209
7.2	The axial, torsional and pendular elastic MMET generalised coordinates (continue)	210
7.3	The axial, torsional and pendular elastic MMET generalised coordinates . . . .	211
7.4	Figures for spin-up $\psi$ in Chapters 5,6 and 7 . . . . .	223
7.5	Figures for R in Chapters 5,6 and 7 . . . . .	224
7.6	Figures for $\theta$ in Chapters 5,6 and 7 . . . . .	224
7.7	Figures for $\alpha$ in Chapters 5,6 and 7 . . . . .	224
7.8	Figures for $\gamma$ in Chapters 5,6 and 7 . . . . .	224
7.9	Figures for $\eta_1$ and $\eta_{p1}$ in Chapters 5,6 and 7 . . . . .	224
7.10	Figures for $\eta_2$ and $\eta_{p2}$ Chapters 5,6 and 7 . . . . .	224
7.11	Torsional elastic motions figures for Chapters 6 and 7 . . . . .	224
7.12	Figures for pendular elasticity in Chapter 7 - plane $x_0 - O - y_0$ . . . . .	225
7.13	Figures for pendular elasticity in Chapter 7 - plane $z_0 - O - y_0$ . . . . .	225
8.1	Inputs and output linguistic description . . . . .	231
8.2	<a href="#">The '2-in-1-out' FLC rule table for MMET system</a> . . . . .	237
C.1	MMET system parameters . . . . .	303
C.2	MMET system parameters - (Continued) . . . . .	304
C.3	MMET system parameters - (Continued) . . . . .	305
M.1	<a href="#">Fuzzy Linguistic Values</a> . . . . .	360

---

# Acknowledgements

---

I would like to gratefully acknowledge the enthusiastic supervision of Professor Matthew Cartmell in every aspect during my PhD studies.

I also would like to thank my secondary supervisor Professor Margaret Lucas for the assistance in each step of my PhD progress.

And, I would like to thank Dr. Ekaterina Pavlovskaja and Dr. Henrik Gollee for their comments on this thesis.

I am forever indebted to my family for the support they provided me through my entire life, without whose love, understanding and encouragement, I would not have finished my PhD process with the thesis.

Finally, I would like to acknowledge the support provided by the Overseas Research Students Awards Scheme (ORSAS) awarded by the University of Glasgow and the scholarship awarded by the Faculty of Engineering, University of Glasgow.

# Chapter 1

---

## Introduction to Space Tethers

---

### 1.1 Introduction

A space tether is a long cable, constructed from thin strands of high-strength fibre used to couple spacecraft to each other or to other masses, and it provides a mechanical connection which enables the transfer of energy and momentum from one object to the other. Tethers are typically very long structures ranging from a few hundred metres to many kilometres, and have a relatively small diameter. Basically, there are two general categories of tethers [1] [2]:

- ⟨1⟩ momentum exchange tethers, which allow momentum and energy to be transferred between objects in space;
- ⟨2⟩ electrodynamic tethers, which interact with the Earth's magnetosphere to generate power or provide propulsion.

Space tethers can be used in a diverse range of applications, which include the study of plasma physics and electrical generation in the upper atmosphere, the orbiting or deorbiting of space vehicles and payloads, for inter-planetary propulsion, and potentially for specialised missions, such as asteroid rendezvous, or in extreme form as the well publicised space elevator. In the century since their conception, space tethers have not yet been fully utilised. As the convergence of materials and technology continues, however, there should be numerous opportunities to use tethers in space [2].

An orbiting satellite follows an elliptical path around the body being orbited, frequently called the primary, and located at one of the two foci. As shown in Figure 1.1, which is adopted from Curtis 2004 [3], an elliptical orbit is defined as a curve with the property that for each point on an ellipse, the sum of its distances from the two fixed foci is constant. The

longest and shortest lines which can be drawn through the centre of an ellipse are the major axis and the minor axis, respectively. The semi-major axis is one-half of the major axis and represents a satellite's mean distance from its primary. Eccentricity ( $e$ ) is the distance between the foci divided by the length of the major axis, and is a number between zero and one, as defined in equation (1.1.1), an zero eccentricity indicates a circle orbit.

Periapsis is the point on an orbit closest to the primary. The opposite of periapsis, the furthest point on an orbit, is called the apoapsis. Periapsis and apoapsis are usually modified to apply to the body being orbited, such as the perihelion and the aphelion for the Sun, the perigee and the apogee for Earth, the perijove and the apojove for Jupiter, and perilune and apolune for the Moon. The argument of periapsis is the angular distance between the ascending node and the point of periapsis. The time of periapsis passage is the time in which a satellite moves through its point of periapsis.

$$e = \frac{r_{\text{apo}} - r_{\text{per}}}{r_{\text{apo}} + r_{\text{per}}} \quad (1.1.1)$$

$$a = \frac{r_{\text{apo}} + r_{\text{per}}}{2} = \frac{h^2}{\mu} \frac{1}{1 - e^2} \quad (1.1.2)$$

$$r_{\text{apo}} = a(1 + e) = \frac{h^2}{\mu} \frac{1}{1 - e} \quad (1.1.3)$$

$$r_{\text{per}} = a(1 - e) \quad (1.1.4)$$

$$\frac{r_{\text{per}}}{r_{\text{apo}}} = \frac{1 - e}{1 + e} \quad (1.1.5)$$

As shown in Figure 1.1,  $\theta$  is the true anomaly, which is the angle between the eccentricity vector and the position vector  $R$ .  $a$  is the semimajor axis of the ellipse in equation (1.1.2).  $r_{\text{apo}}$  is the apogee radius in equation (1.1.3),  $r_{\text{per}}$  is the perigee radius in equation (1.1.4). Given  $e = 0.2$  and  $r_{\text{per}} = 6.89 \times 10^6$ , then  $r_{\text{apo}} = 1.0335 \times 10^7$ , as shown in equation (1.1.5).

$p$  is the semilatus rectum in equation (1.1.6).  $\beta$  is the true anomaly of point B, the radial coordinate  $r_B$  is given in equation (1.1.7). The projection of  $r_B$  onto the apseline is  $ae$ , as given in equation (1.1.8).

$$p = a(1 - e^2) = b^2/a = r_{\text{per}}(1 + e) = r_{\text{apo}}(1 - e) \quad (1.1.6)$$

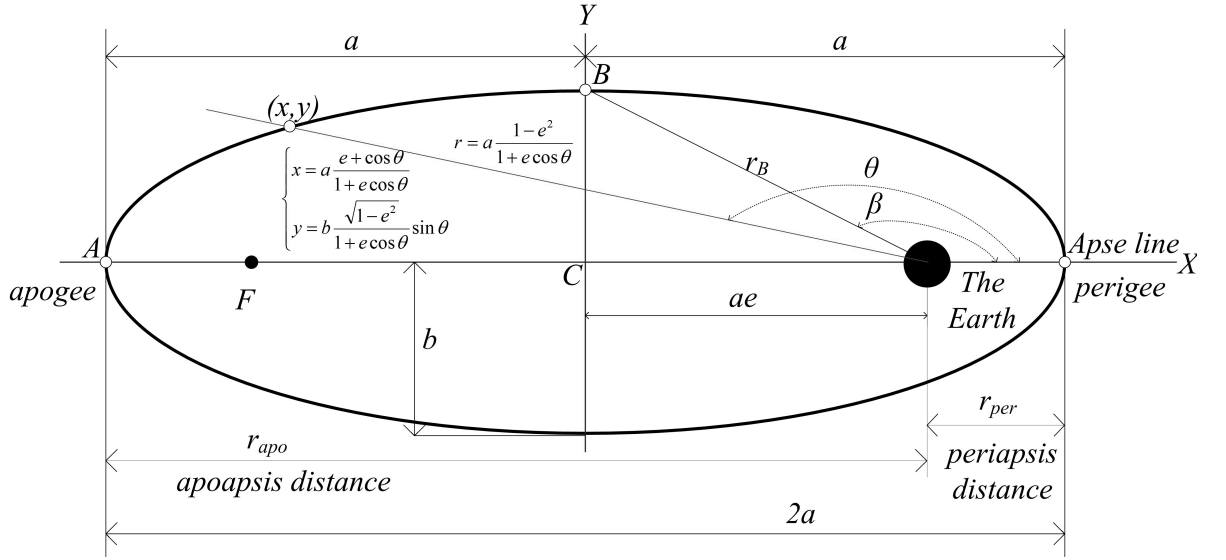


Figure 1.1: Elliptical orbit [3] [4]

$$r_B = a \frac{1 - e^2}{1 + e \cos \beta} \quad (1.1.7)$$

$$ae = r_B \cos(180 - \beta) = - \left( a \frac{1 - e^2}{1 + e \cos \beta} \right) \cos \beta \quad (1.1.8)$$

$$T = \frac{2\pi ab}{h} = \frac{2\pi}{\mu^2} \left( \frac{h}{\sqrt{1 - e^2}} \right)^3 = \frac{2\pi}{\sqrt{\mu}} a^{\frac{3}{2}} \quad (1.1.9)$$

$$h = \sqrt{\mu a (1 - e^2)} \quad (1.1.10)$$

As defined in equation (1.1.9),  $T$  is the orbital period of a space tether travelling along an elliptic orbit,  $h$  is an orbital parameter, as defined in equation (1.1.10),  $\mu$  is the product of the universal gravitational constant  $G = 6.6742 \times 10^{11} \text{ m}^3/\text{kg}\cdot\text{s}^2$  with the Earth's mass [3] [4] [5] [6]. When  $T = 1$ , it means that the space tether goes around the Earth on the elliptical orbit for one cycle.

$$t = T_n \times T \quad (1.1.11)$$

As defined in equation (1.1.11), the space tether's simulation time  $t$  can be expressed as a gain factor  $T_n$  times a specific orbital period  $T$  on an elliptical orbit with a specific eccentricity  $e$ , in which  $T_n$  is the number of cycles of period (NCP, or for short, cycle number) and will be taken as the timing index for the simulations in this thesis. As listed in Appendix C, when  $e = 0.2$  and  $r_{per} = 6.890 \times 10^6 \text{ m}$ ,

- if  $T_n = 4.01$ , the simulation time  $t$  is  $3.1899 \times 10^4$  seconds;

- if  $T_n = 40.01$ , the simulation time  $t$  is  $3.18183 \times 10^5$  seconds;
- if  $T_n = 400.01$ , the simulation time  $t$  is  $3.1811 \times 10^6$  seconds.

As shown in Figures 1.1 and 1.2, according to the orbital theory [3] [4], in the orbital plane,  $R$  represents the radius vector to the orbiting tether's centre of mass. The true anomaly,  $\theta$ , defines the angle in the direction of motion from the perigee to the tether's centre of mass. These parameters, together with the orbit eccentricity,  $e$ , and the mean anomaly, are sufficient to define completely the position of the tether's centre of mass in space. The mean anomaly is defined as the orbital mean motion multiplied by the time elapsed since passing the perigee.

Again, as seen in Figures 1.1 and 1.2,  $a$  is the semimajor axis (or  $b$  is the semiminor axis), which specifies the size of the orbit;  $e$  is the eccentricity, specifying the shape of the elliptical orbit;  $i$  is the inclination, which is the angle between the orbital plane and the Earth's equatorial plane.  $\omega$  is the argument of periapsis, an angle of an orbiting body's periapsis relative to its ascending node.  $\theta$  is the true anomaly, and is an angular parameter which defines the position of a body moving along a Keplerian orbit and is the angle between the direction of periapsis and the current position of the body, as seen from the main focus of the ellipse (the point around which the object orbits).  $\Omega$  is the longitude of the ascending node, the angle from the origin of longitude to the direction of the ascending node [3] [4].

To describe an orbit mathematically, one needs to define a minimum of six quantities. Traditionally, the set of orbital elements commonly used is called the set of Keplerian elements. This comprises [7] [8]:

- $a$  the semimajor axis
- $e$  the eccentricity
- $i$  the inclination
- $\omega$  the argument of periapsis
- $\theta$  the true anomaly
- $\Omega$  the longitude of the ascending node

As shown in Figure 1.2, the nodes are the points where an orbit crosses on orbital plane, such as are shown here, where a satellite is crossing the Earth's equatorial plane. If the satellite crosses the plane going from south to north, the node is defined as the ascending node; if moving from north to south, it is called the descending node. The longitude of the ascending node is the node's celestial longitude. Celestial longitude is analogous to longitude on Earth and is measured in degrees counter-clockwise from zero, with zero longitude being

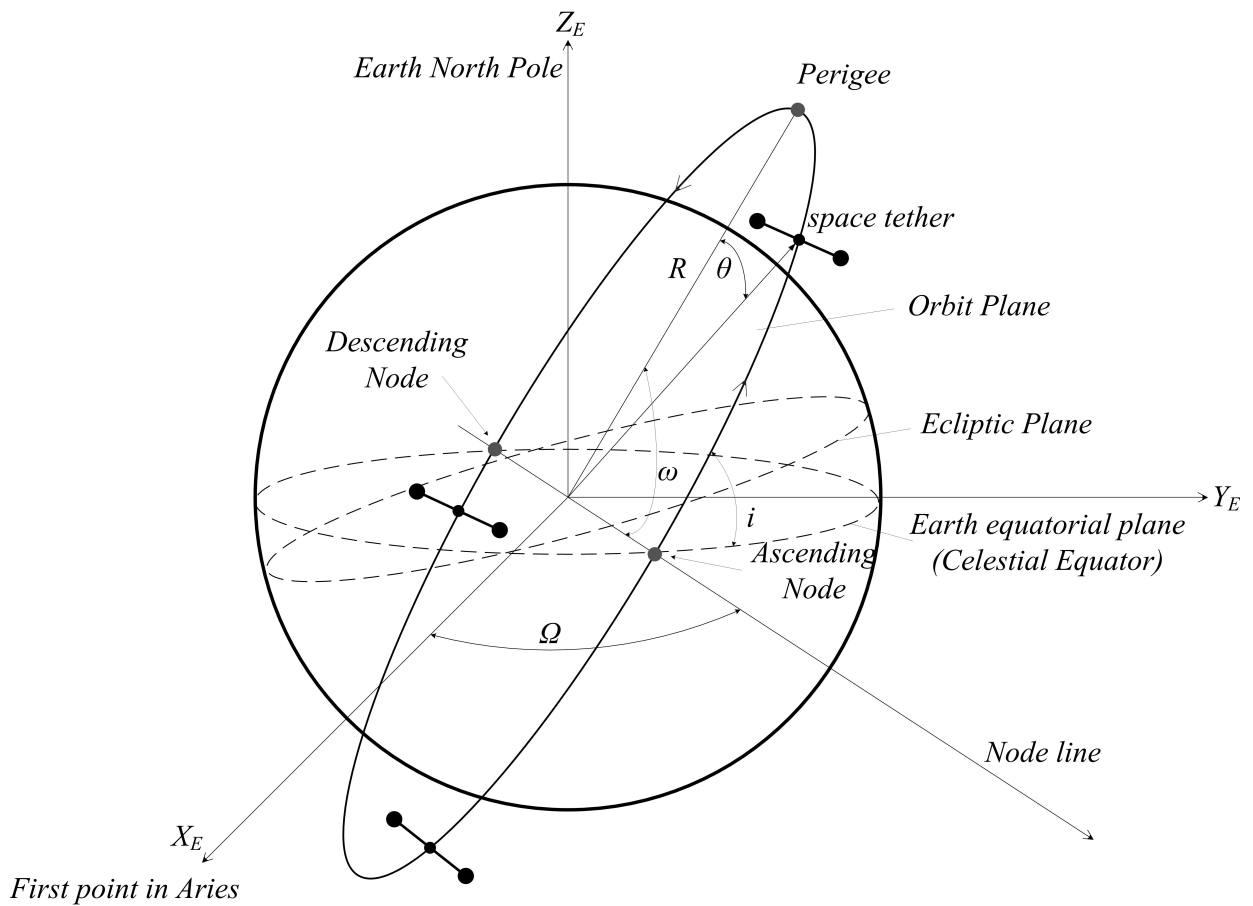


Figure 1.2: **Geocentric inertial coordinate system** [3] [4] [5]

in the direction of the vernal equinox [3] [4] [5].

The plane of the tether's orbit about the Earth can be inclined to the Earth's equatorial plane by the angle  $i$ , the inclination of the orbit, defined where the intersection of the two planes occurs at the node line. An inclination of zero degrees indicates an orbit about the primary's equator in the same direction as the primary's rotation, a direction called prograde. An inclination of 90 degrees indicates a polar orbit. An inclination of 180 degrees indicates a retrograde equatorial orbit. A retrograde orbit is one in which a satellite moves in a direction opposite to the rotation of its primary. The right ascension of  $\Omega$  measures the angle in the plane of the equator from the vernal equinox eastward to the ascending node. The angle formed in the orbit plane in the direction of motion from the ascending node to the perigee is the argument of perigee,  $\omega$  [5] [6] [7].

The coordinate system used to describe Earth orbits in three dimensions is defined in terms of the Earth's equatorial plane - the ecliptic plane, and the Earth's axis of rotation. The ecliptic is the plane of the Earth's orbit around the sun, and is illustrated in Figures 1.1 and 1.2. The Earth's axis of rotation, passing through the North and South Poles, is not perpendicular to the ecliptic. It is tilted away by an angle known as the obliquity of

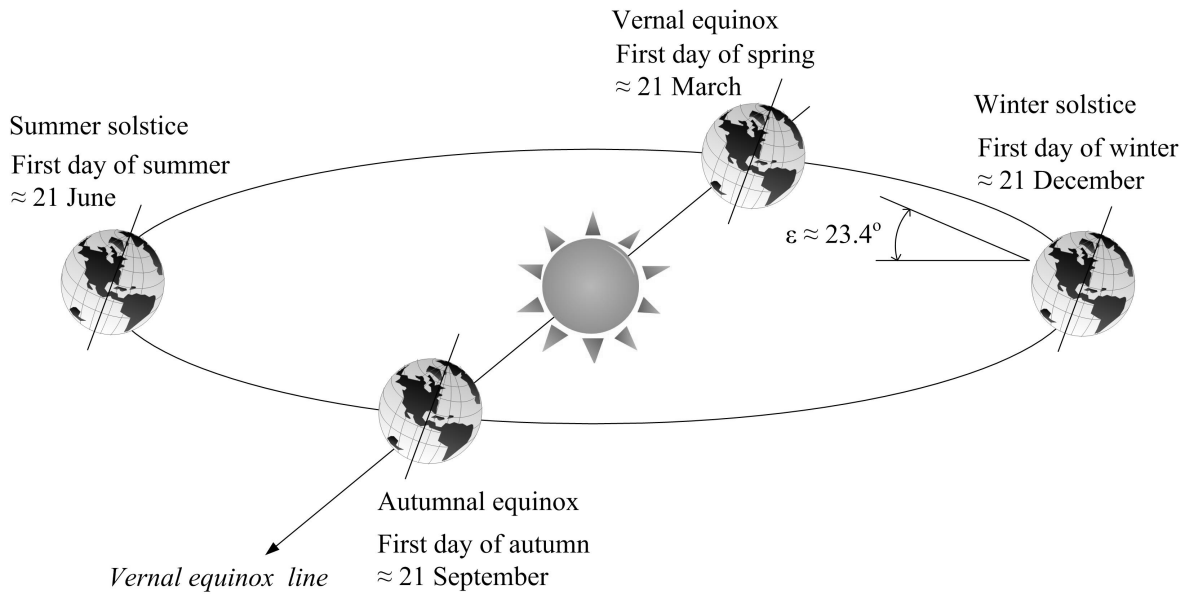


Figure 1.3: **Heliocentric ecliptic coordinate system defining vernal equinox direction [7] [8]**

the ecliptic -  $\epsilon$ . For the Earth  $\epsilon$  is approximately 23.4 degrees, as shown in Figure 1.3. Therefore, the Earth's equatorial plane and the ecliptic intersect along a line, known as the vernal equinox line. On the calendar, the 'vernal equinox' is the first day of spring in the northern hemisphere, when the noontime Sun crosses the equator from South to North. The position of the Sun at that instant defines the location of a point in the sky called the vernal equinox. On the day of the vernal equinox, the number of hours of daylight and darkness is equal - hence the word 'equinox'. The other equinox occurs precisely one-half year later, when the Sun crosses back over the equator from North to South, thereby defining the first day of autumn [7] [8] [9].

The geocentric coordinate system, where the Earth's centre of mass is treated as the origin, is used to provide an inertial system in space. In this system the governing equations of motion can be derived for a tether orbiting the Earth. As shown in Figure 1.2, the  $Z_E$  axis points in the direction of the Earth's north pole and represents the Earth's axis of rotation in a positive direction. The  $X_E - Y_E - Z_E$  system is non-rotating with respect to the stars, and the Earth rotates relative to that coordinate system. The  $X_E - Y_E$  plane is coplanar within the Earth's equator, which is inclined by about 23.4 degrees to the ecliptic plane of the Earth's orbit about the Sun, as in Figure 1.3. On the first day of the northern hemisphere's spring the ecliptic and the  $X_E - Y_E$  plane intersect along a line, which is coincidental with the  $X_E$  axis, pointing to the first point of the Aries constellation, or the vernal equinox direction [11].

In reality, the geocentric system is not a true inertial system, the Earth orbits the Sun on an almost circular orbit and in turn the Sun orbits the centre of the Milky Way on an approximately circular orbit. The geocentric system is continuously experiencing an acceleration

and, therefore, cannot be considered as a proper inertial reference frame. Furthermore, the direction of the Earth's axis of rotation does not remain constant, because of the precessional motion due to the Sun with a period of 25,800 years together with a nutational motion due to the Moon with a period of 18.6 years. Both the equatorial and ecliptic plane move with respect to the stars, since the planets affect the orientation of the ecliptic plane in the slow rotational motion of planetary precession. Consequently, the geocentric system moves slowly relative to the stars, and when extreme precision is required, the coordinates of an object based on the vernal equinox direction of a particular year or epoch have to be specified. However, the accelerations are relatively small and for practical purposes the geocentric system can be accepted as being inertial [7] [8] [9] [10] [11] [14] [15].

For a spacecraft to achieve Earth orbit, it must be launched to an elevation above the Earth's atmosphere and accelerated to orbital velocity. The most energy efficient orbit, which requires the least amount of propellant, is a direct low inclination orbit. To achieve such an orbit, a spacecraft is launched in an eastward direction from a site near the Earth's equator. High inclination orbits are less able to take advantage of the initial speed provided by the Earth's rotation, thus the launch vehicle can provide a greater part, or all, of the energy required to attain orbital velocity. Although high inclination orbits are less energy efficient, they do have advantages over equatorial orbits for certain applications. Below we describe several types of orbits and the advantages of each: [3] [4] [5] [7] [8] [9] [10] [11]:

- ◇ A Low Earth Orbit (LEO) is generally defined as an orbit within the locus extending from the Earth's surface up to an altitude of 2000 km. Given the rapid orbital decay of objects below approximately 200 km, the commonly accepted definition for LEO is between 160 - 2000 km above the Earth's surface.

- ◇ Geosynchronous orbit (GEO) is circular orbit around the Earth and has a period of 24 hours. A GEO with an inclination of zero degrees is called a geostationary orbit. A spacecraft in a geostationary orbit (GSO) appears to hang motionless above one position on the Earth's equator. For this reason, it is ideal for some types of communication or meteorological satellites. A spacecraft in an inclined geosynchronous orbit appears to follow a regular pattern in the sky, once every orbit. To attain geosynchronous orbit, a spacecraft is first launched into an elliptical orbit with an apogee of 35,786 km, called a geosynchronous transfer orbit (GTO). The orbit is then circularised by firing the spacecraft's engine at apogee.

- ◇ A polar orbit (PO) is an orbit in which a satellite passes above or nearly above both poles of the body, such as the Earth, or the Sun, which is orbited on each revolution.

Usually it has an inclination of 90 degrees. The PO is useful for satellites which carry out mapping or surveillance operations, because as the planet rotates the spacecraft is able to access virtually every point on the planet's surface.

◇ A walking orbit of an orbiting satellite is subjected to a great many gravitational influences. First, planets are not perfectly spherical, and they have slightly uneven mass distribution. These fluctuations have an effect on a spacecraft's trajectory. Also, the Sun, the Moon, and the planets contribute a gravitational influence on an orbiting satellite. With proper planning, it is possible to design an orbit which takes advantage of these influences to induce a precession in the satellite's orbital plane. The resulting orbit is called a walking orbit, or precessing orbit.

◇ A Sun synchronous orbit (SSO) is a walking orbit whose orbital plane precesses with the same period as the planet's solar orbit period. In such an orbit, a satellite crosses periapsis at about the same local time every orbit. This is useful if a satellite is carrying instruments which depend on a certain angle of solar illumination on the planet's surface. In order to maintain an exact synchronous timing, it may be necessary to conduct occasional propulsive maneuvers in order to adjust the orbit.

◇ Molniya orbits were named after a series of Soviet/Russian Molniya (Russian: "Lightning") communications satellites, which have been using this type of orbit since the mid 1960s. A Molniya orbit is a type of highly elliptical orbit with an orbital period of about 12 hours (2 revolutions per day). The orbital inclination is chosen so the rate of change of perigee is zero, thus both apogee and perigee can be maintained over fixed latitudes. This condition occurs at inclinations of 63.4 degrees and 116.6 degrees. For these orbits the argument of perigee is typically placed in the southern hemisphere, so the satellite remains above the northern hemisphere near apogee for approximately 11 hours per orbit. This orientation can provide good ground coverage at high northern latitudes.

◇ Hohmann transfer orbits are interplanetary trajectories. Their advantage is that they consume the least possible amount of propellant. A Hohmann transfer orbit to an outer planet, such as Mars, is achieved by launching a spacecraft and accelerating it in the direction of Earth's revolution around the Sun, until it breaks free of the Earth's gravity and reaches a velocity which places it in a Sun orbit with an aphelion equal to the orbit of the outer planet. Upon reaching its destination, the spacecraft must decelerate so that the planet's gravity can capture it into a planetary orbit.

### 1.1.1 History of the Tether Concept

The idea of an orbital tower was first originally conceived by Konstantin Tsiolkovsky in 1895 [12] [13]. He looked at the Eiffel Tower in Paris and imagined a giant tower reaching into space with a “celestial castle” at the top, and the free-floating spindle-shaped tower - “Tsiolkovsky” tower - reaching from the surface of Earth to GSO. His proposal of a ‘Shuttle-borne Skyhook’ for low orbital altitude research marked the advent of tethered satellite systems (TSS). It would be supported in tension by excess centrifugal force on the part of the tower beyond geosynchronous altitude. These were the first of a series of “space elevator” or “beanstalk” concepts having a tether in a synchronous orbit reaching all the way down to the ground. Payloads would be transported up and down the tether without the use of any propellant. This structure would be held in tension between Earth and the counterweight in space, like a guitar string held taut. Space elevators have also sometimes been referred to as beanstalks, space bridges, space lifts, space ladders, skyhook, orbital towers, or orbital elevators [16] [17] [18].

Yuri Artsutanov, another Russian scientist, wrote on some of the first modern concepts about space elevators as a non-technical story in 1960 [19]. Artsutanov suggested using a geostationary satellite as the base from which to deploy the structure downward. By using a counterweight, a cable would be lowered from geostationary orbit to the surface of Earth, while the counterweight was extended from the satellite away from Earth, keeping the centre of gravity of the cable motionless relative to Earth. Artsutanov’s idea was introduced to the Russian-speaking public in an interview published in the Sunday supplement of *Komsomolskaya Pravda* (usually translated as *Komsomol Truth* in English) in 1960, but was not available in English until much later. He also proposed tapering the cable thickness so that the tension in the cable was constant, this gives a thin cable at ground level, thickening up towards GSO [20] [21] [22].

In 1966, Isaacs, Vine, Bradner and Bachus, four American engineers, reinvented the concept, naming it a “Sky-hook”, and published their analysis in the journal *Science* [23]. They decided to determine what type of material would be required to build a space elevator, assuming it would be a straight cable with no variations in its cross section, and found that the strength required would be twice that of any existing material including graphite, quartz, and diamond [22] [24].

Colombo et al. provided an idea for a shuttle-borne skyhook for low-orbital altitude research in 1974 [25]. The concept finally came to the attention of the space flight engineering community through a technical paper written in 1975 by Jerome Pearson [26] of the air

force research laboratory. He designed a tapered cross section which would be better suited to building the elevator. The completed cable would be thickest at the geostationary orbit, where the tension was greatest, and would be narrowest at the tips so as to reduce the amount of weight per unit area of cross section that any point on the cable would have to bear. He suggested using a counterweight that would be slowly extended out to 144,000 kilometres as the lower section of the elevator was built. Without a large counterweight, the upper portion of the cable would have to be longer than the lower, due to the way in which gravitational and centrifugal forces change with distance from Earth. His analysis included disturbances such as the gravitation of the Moon, wind and moving payloads up and down the cable. The weight of the material needed to build the elevator would have required thousands of space Shuttle trips, although part of the material could be transported up the elevator when a minimum strength strand reached the ground, or it could be manufactured in space from asteroids [13].

In 1977, Hans Moravec published an article called “A Non-Synchronous Orbital Skyhook” [27], in which he proposed an alternative space elevator concept, using a rotating cable, in which the rotation speed exactly matches the orbital speed in such a way that the instantaneous velocity, at the point where the cable was at the closest point to the Earth, was zero. This concept was an early version of a space tether transportation system.

In 1979, Jerome Pearson discussed the concept of anchored lunar satellites in *The Journal of the Astronautical Sciences*, in which it was observed of anchored lunar satellites that they balanced about the collinear libration points of the Earth-moon system and attached to the lunar surface [28].

Also in 1979, space elevators were introduced to a broader audience with the simultaneous publication of Arthur C. Clarke’s novel, “The Fountains of Paradise”, in which engineers constructed a space elevator on top of a mountain peak in the fictional island country of Taprobane.

In 1984, Georg von Tiesenhausen wrote a history of these concepts and their more modest derivatives [29]. Joseph A. Carroll conducted some studies on the advantages of swinging and barely spinning systems [30] [31].

Since then, a series of interesting space tether applications have been proposed and analysed. In the last decade, the study of space tether has received significant attention from researchers covering a broad range of applications. Some examples of applications which have considerable promise include: the deployment and retrieval of subsatellites, aerobraking, electrodynamic boost, deorbit of satellites and momentum-transfer with libration and rotation analysis. Control research on space tether applications was one of the most impor-

tant aspects of space tether study, and each control method suited each application or mission requirement, such as: liberation, oscillation, attitude, motion and deployment [1].

### 1.1.2 Tether Missions

Over the past forty years, a series of missions have been delivered for aerospace application using tethered satellite systems. These proposals include scientific experiments in the micro-gravity environment, upper atmospheric research, the generation of electricity, cargo transfer between orbiting bodies, collections of planetary dust, and the expansion of the geostationary orbit resource by tethered chain satellites. For example, NASA has been developing tether technology for space applications since the 1960s, and these include electrodynamic tether propulsion, the Propulsive Small Expendable Deployer system (ProSEDS) flight experiment, “Hanging” momentum exchange tethers, rotating momentum exchange tethers, and tethers supporting scientific space research. A number of such tethers have already been flown on missions, these include: the Small Expendable-tether Deployer System (SEDS), the Tether Satellite System (TSS), the Tether Physics and Survivability experiment (TiPS), and the Space Technology Experiments (STEX). Table 1.1 gives a brief tether mission history and shows the status of each one [2] [13] [17] [30] [32] [33] [34] [35] [36] [37] [38] [39] [40].

The Gemini XI was a manned spaceflight in NASA’s Gemini program, launched on September 12, 1966 [36]. It was the 9th manned Gemini flight, the 17th manned American flight, and the 25th spaceflight of all time, including X-15 flights, at altitudes of over 100 km. The Gemini XI mission’s main objectives were: (1) rendezvous with the Gemini Agena Target Vehicle (GATV); (2) to conduct docking practice and extravehicular activity (EVA); (3) to conduct the eight scientific experiments: the synergistic effect of zero-g and radiation on white blood cells, the synoptic terrain photography, the synoptic weather photography, the nuclear emulsions, the airglow horizon photography, the UV astronomical photography, the Gemini ion wake measurement, and the dim sky photography; (4) synoptic terrain photography and a tethered vehicle test; (5) demonstrating automatic re-entry and parking the GATV. All the Gemini XI mission’s objectives were achieved, except the evaluation of the minimum reaction power tool, which was not performed, because the umbilical EVA was terminated prematurely.

The Gemini XII was a manned spaceflight in NASA’s Gemini program launched on November 11, 1966. The major objectives were: (1) rendezvous, docking and evaluation for the EVA; (2) tethered vehicle evaluation and experiments; (3) revolution rendezvous,

Table 1.1: Tether mission history [2] [13] [17] [30] [32] [33] [34] [36] [37]

Mission	Year	Sponsor	Orbit	Length	Status
Gemini XI	1967	NASA	LEO	50 m	Launched
Gemini XII	1967	NASA	LEO	30 m	Launched
TPE-1	1980	NASA/ISAS	suborbital	400 m	Launched
TPE-2	1981	NASA/ISAS	suborbital	500 m	Launched
TPE-3(CHARGE-1)	1983	NASA/ISAS	suborbital	500 m	Launched
CHARGE-2	1985	NASA/ISAS	suborbital	500 m	Launched
MAIMIK	1986	NASA/NDRE	LEO	400 m	Launched
ECHO-7	1988	USAF	suborbital	-	Launched
OEDIPUS-A	1989	NRC/NASA/CRC/CSA	suborbital	958 m	Launched
CHARGE-2B	1992	NASA/ISAS	suborbital	500 m	Launched
TSS-1(STS-46)	1992	NASA/ASI	LEO	267 m	Launched
SEDS-1	1993	NASA	LEO	20 m	Launched
PMG	1993	NASA	LEO	500 m	Launched
SEDS-2	1994	NASA	LEO	20 m	Launched
OEDIPUS-C	1995	NASA/NRC/CRC/CSA	suborbital	1 km	Launched
TSS-1R(STS-75)	1996	NASA/ASI	LEO	19.6 km	Launched
TSS-2(STS-75)	1996	NASA	LEO	100 m	Cancelled
TiPS	1996	NRO/NRL	LEO	4 km	Launched
YES	1997	ESA/Delta-Utec	LEO	35 m	Launched
ATE <sub>x</sub>	1999	NRO/NRL	LEO	22 m	Launched
PICOSATs	2000	Aerospace Corporation	LEO	30 m	Launched
MEPSI	2002	Aerospace Corporation	LEO	15.2 m	Launched
ProSEDS	2003	NASA	LEO	15 m	Cancelled
MAST	2007	NASA/TUI/Stanford	LEO	1 km	Launched
YES2	2007	ESA/Delta-Utec	LEO	31.7 m	Launched

docking and automatic re-entry demonstration; (4) docked maneuvering for a high-apogee excursion, docking practice, system tests and GATV parking. All the other objectives were achieved except the high-apogee excursion, because an anomaly was noted in the GATV primary propulsion system during insertion, and then the GATV's parking was not attempted because its attitude control gas was depleted [35] [37].

After the Gemini experiments, the first two experiments of the early 1980s were in 1980 and 1981, which were part of a joint program involving the Institute of Space and Astronautical Science (ISAS) in Japan and the Centre for Atmospheric and Space Science of Utah State University. The project was called the Tethered Payload Experiment (TPE); the missions TPE-1 and TPE-2 were launched using two types of Japanese rocket, Kappa 9M (flight H-9M-69) and S-520 (flight S-520-2). From the Japanese Kagoshima Space Centre, the TPE-1 mission was launched via Kappa 9M rocket on January 16, 1980. Its plan was to deploy 400 metres of cable, but its deployed cable was about 38 metres. The TPE-2 mission was launched on 29 January, 1981, and its tether was deployed to a distance about 65 metres [13] [34].

In 1983, the TPE-3 was planned by ISAS and Utah State University, which was also called CHARGE-1, and the tether length was about 500 m. As the deployment system was improved, the tether deployed to its full length of 418 meters, and the tether was also found to act as a radio antenna for the electrical current through the cable. After that, CHARGE-2 was carried out as an international program between Japan and the USA using a NASA sounding rocket at White Sands Missile Range, in December 1985, its tether deployed to a length of 426 metres [13] [38].

The MAIMIK experiment was a joint mission by NASA and NDRE in 1986, for which the tether length was about 400 m. This mission was designed to study the charging of an electron-beam emitting payload using a tethered mother-daughter payload configuration [39] [40].

In 1988, the U.S. Air Force Geophysics Laboratory launched the Echo-7, which was designed to study the artificial electron beam propagation along magnetic field lines in space. The mission was designed to study how the artificial electron beam propagates along magnetic field lines in space [13] [41].

In 1989, the mission OEDIPUS-A was organised by the National Research Council of Canada(NRC), NASA and some other partners, in which a conducting tether was deployed over 958 metres during the flight of a Black Brant sounding rocket into the auroral ionosphere. [42] [13].

With similar equipment to that on CHARGE-2, the CHARGE-2B tethered rocket mission was launched in 1992 by NASA with a Black Brant V rocket. The mission was to generate electromagnetic waves by modulating the electron beam. The tether was fully deployed over 400 metres and the experiments all worked as planned [43] [13].

The following OEDIPUS mission was the OEDIPUS-C tethered payload mission, which was launched in 1995 with an 1174 metres deployed tether, and a Tether Dynamics Experiment (TDE) was also included as a part of the OEDIPUS-C [13] [44].

The first orbital flight experiment with a long tether was the Tethered Satellite System (TSS) mission, launched on the Space Shuttle in July 1992. The Tethered Satellite System-1 (TSS-1) was flown during STS-46, aboard the Space Shuttle Atlantis, from July 31 to August 8, 1992. The TSS-1 mission discovered a lot about the dynamics of the tethered system. Although the satellite was deployed only 260 metres, it was able to show that the tether could be deployed, controlled, and retrieved, and that the TSS was easy to control, and even more stable than predicted. The TSS was an electrodynamic tether, its deployment mechanism jammed resulting in tether sever and less than 1000 metres of deployment. The objectives of TSS-1 were: (1) to verify the performance of the TSS equipment; (2) to study

the electromagnetic interaction between the tether and the ambient space plasma; (3) to investigate the dynamical forces acting on a tethered satellite. In the first tether deployment, when the satellite was moving excessively side to side, the deployment was aborted. The second trial of deployment was unreeled to a length of 260 metres [45] [46] [47] [48] [49] [13].

The Shuttle Electrodynamic Tether System (SETS) experiment formed part of the scientific experiments comprising the first flight of the NASA/ASI Tethered-Satellite System flown at an altitude of 300 km and at an orbital inclination of 28.5 degrees in July/August 1992. The SETS experiment was designed to study the electrodynamic behaviour of the Orbiter-Tether-Satellite system, as well as to provide background measurements of the ionospheric environment near the Orbiter. The SETS experiment was able to operate continuously during the mission thereby providing a large data set. Details of the SETS objectives, its instrumentation, and initial results from the mission highlighting voltage, current, and charging measurements were presented [50].

The Small Expendable Deployer System-1 (SEDS-1) was launched from Cape Canaveral Air Force Station as a Delta/GPS secondary payload in 1993. As a secondary payload on a Delta II launch vehicle, SEDS-1 was the first successful 20-kilometre space-tether experiment. When 1 km of tether remained, active braking was applied by wrapping the tether around a 'barber pole' brake. Finally, the braking system and sensors did not work as predicted, resulting in hard stop/endmass recoil at deployment completion [1].

In 1996, the Plasma Motor Generator (PMG) was launched by NASA. This was an electrodynamic tether, which could assess the effectiveness of using hollow cathode assemblies to deploy an ionised gas, and to 'ground' electrical currents by discharging the energy to space. An early experiment used a 500 metre conducting tether. When the tether was fully deployed during this test, it generated a potential of 3,500 volts. This conducting single-line tether was severed after five hours of deployment. It was believed that the failure was caused by an electric arc generated by the conductive tether's movement through the Earth's magnetic field. The PMG flight demonstration proved the ability of the proposed Space Station plasma grounding techniques in maintaining the electrostatic potential between the Space Station and the surrounding plasma medium. The PMG also demonstrated the ability to use electrostatic tethers to provide thrust to offset drag in LEO space systems, and it demonstrated the use of direct magnetic (non-rocket) propulsion for orbital maneuvering [1].

The Small Expendable Deployer System-2 (SEDS-2) was launched on the last GPS Block 2 satellite in 1994. The SEDS-2 used feedback braking, which started early in deployment. This limited the residual swing after deployment to 4 degrees. Mission success

was defined as deployment of at least 18 km, plus a residual swing angle of less than 15 degrees. The SEDS-2 had an improved braking system compared to SEDS-1, which was a feed-back control system and applied braking force as a function of the measured speed of the unrolling tether. This was to ensure the satellite stopped flying out just when the whole tether was deployed, and to prevent the bounces experienced during the previous mission [13].

In 1996, the Tethered Satellite System Reflight (TSS-1R) was carried by using U.S space shuttle STS-75 successfully. The primary objective of STS-75 was to carry the Tethered Satellite System Reflight (TSS-1R) into orbit and to deploy it spacewards on a conducting tether. The mission also flew the United States Microgravity Payload (USMP-3), designed to investigate materials science and condensed matter physics. **The TSS1-R mission objectives were: (1) to characterise the current-voltage response of the TSS-orbiter system; (2) to characterise the satellite's high-voltage sheath structure and current collection process; (3) to demonstrate electric power generation; (4) to verify tether control laws and basic tether dynamics; (5) to demonstrate the effect of neutral gas on the plasma sheath and current collection; (6) to characterise the TSS radio frequency and plasma wave emissions; (7) to characterise the TSS dynamic-electrodynamic coupling [51] [52].**

The Tether Physics and Survivability Experiment (TiPS) was deployed on 20 June 1996 at an altitude of 1,022 kilometres as a project of the US Naval Research Laboratory. The satellite was a tether physics experiment consisting of two end masses connected by a 4 km non-conducting tether, for which the two tethered objects were called “Ralph” and “Norton”. This experiment was designed to increase knowledge about gravity-gradient tether dynamics and the survivability of tethers in space [53].

The first Young Engineers' Satellite (YES-1) programme was completed on 3rd November 1997. It was designed to operate with a 35 km tether deployment, but the mission was cancelled before the flight when the launch authority changed the nominal Ariane orbit. In the new orbit configuration a deployed 35 km tether would have constituted a hazard to satellites in LEO [54].

The Advanced Tether Experiment (ATEX) was launched into orbit aboard the National Reconnaissance Office (NRO) sponsored Space Technology Experiment spacecraft (STEX) on October 3, 1998. ATEX was intended to demonstrate the deployment and survivability of a novel tether design, as well being used for controlled libration manoeuvres. On January 16, 1999, after a deployment of only 22 m of tether, ATEX was jettisoned from STEX due to an out-of-limit condition sent by the experiment's tether angle sensor. The ATEX lower end mass was jettisoned from the host spacecraft and the tethered upper and lower end masses

freely orbited the Earth in a demonstration of long term tether survivability. The ATE<sub>x</sub> was a tethered satellite experiment with the following mission objectives: (1) deployment of a novel, nonconductive polyethylene tape tether; (2) verification of dynamical models of deployment and orbital libration; (3) ejection of the ATE<sub>x</sub> lower end mass from the host spacecraft [55].

The PICOSAT mission was launched on September 30, 2001. It was a real time tracking satellite of the miniaturised picosatellite satellite series. The name “PICO” combined the first letters of all four of its experiments, which were the Polymer Battery Experiment (PBEX), the Ionospheric Occultation Experiment (IOX), the Coherent Electromagnetic Radio Tomography (CERTO), and the On Orbit Mission Control (OOMC) [56]. A pair of 0.25 kg MEMS picosatellites with an intersatellite communications experiment were included in this mission, and were connected by a 30 metre tether [56].

The MEPSI series (Micro Electro-Mechanical Systems-based PicoSat Inspector) was a pair of tethered picosatellites, based on the CubeSat design, launched by a custom deployer aboard the STS-113 Endeavour mission on 2nd December 2002. The spacecraft were manufactured for the Defense Advanced Research Projects Agency (DARPA) by the Aerospace corporation in collaboration with NASA’s Jet Propulsion Laboratory (JPL). The two spacecraft were cubic in shape, of mass 1 kg each, and were connected via a 15.2 m tether in order to facilitate detection and tracking via ground-based radar [56].

The Propulsive Small Expendable Deployer System (ProSEDS) was a NASA space tether propulsion experiment intended to be a follow-up to SEDS. It was originally intended to be flown along with a launch of a Global Positioning System (GPS) satellite in the spring of 2003, but was cancelled at the last moment, due to concerns that the tether might collide with the international space station [57].

The Multi-Application Survivable Tether (MAST) experiment was launched into LEO on 17th April 2007, in which the 1 km multi-strand interconnected tether (Hoytether) was intended to test and prove the long-term survivability of tethers in space, but the tether failed to deploy. The experiment hardware was designed under a NASA Small Business Technology Transfer (STTR) collaboration between Tethers Unlimited Inc (TUI) and Stanford University, with TUI developing the tether, the tether deployer, the tether inspection subsystem, the satellite avionics, and the software system, and Stanford students developing the satellite structures and assisting with the avionics design [58].

The second Young Engineers Satellite (YES2) was launched on 14th September 2007. It was a technology demonstration project designed to test and produce data for the “Space Mail” concept, wherein a tether was used to return material from space to Earth, instead of

by conventional chemical propulsion. YES2 aimed to demonstrate a tether-assisted re-entry concept, whereby the payload would be returned to Earth using momentum provided from a swinging tether. Deployment was intended to take place in two phases: (1) deployment of 3.5 km of tether to the local vertical and hold, and (2) deployment to 30 km for a swinging cut. The measured altitude gain of the Fonton-M3 corresponded with what simulations showed would happen if 31.7 km of tether were extended, another strong indication that the YES-2 tether had in fact been fully deployed.

The YES-2 mission was very nearly a complete success: (1) the entire record-breaking length of tether has been deployed; (2) Fotino rocket seemed to have been de-orbited by using momentum exchange; (3) plentiful data has been gathered on tether deployment, dynamics and de-orbiting, which may lead to an operational way of returning capsules without any form of propulsion. [13] [59] [60].

The Fortissimo is a developing space tether experiment which is proposed to be used for deploying a 300 m bare electrodynamic tether tape, with a width of 25 mm, and a thickness of 0.05 mm, in order to conduct two scientific experiments, as the first ever attempt in the world by an international team consisting of Japanese, European, American, and Australian tether enthusiasts. A S-520 sounding rocket will be prepared by ISAS/JAXA and has been intended to be launched in the summer of 2009 [61].

### 1.1.3 Momentum Exchange Tethers

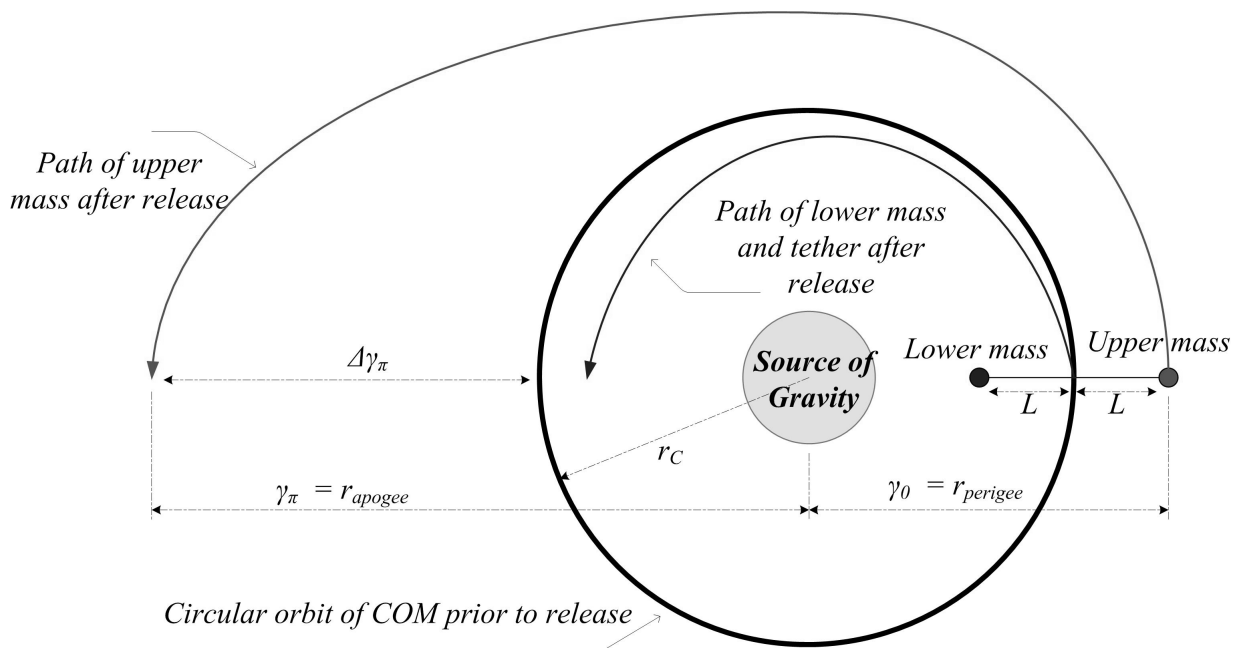


Figure 1.4: Momentum exchange tether system for payload transfer [13] [62] [65]

A momentum exchange (MX) tether is a long thin cable used to couple or connect two

space objects in space, so that the tether can provide a mechanical connection between two space objects, which enables the transfer of energy and momentum from one object to the other, and as a result they can be used to provide space propulsion without consuming propellant.

As shown in Figure 1.4, a pure momentum exchange tether does not create orbital energy by itself, but rather exchanges momentum and energy with others. The exchange of momentum can take place quickly, and increase the orbital energy of the payload dramatically. As it catches and throws a payload, its orbital energy is reduced, and it assumes a lower orbit. Without reboost, it will soon lose enough orbital energy to burn up in the atmosphere. Hence, without reboost, the momentum exchange tether would soon be useless. Any type of propulsion system, in theory, could be used to reboost a momentum exchange tether - chemical, physical and nuclear are all options - but if rocket reboost is used, the momentum exchange tether station will need to be refuelled regularly, and the entire tether system will be no more efficient than the reboost rocket [2] [13] [66] [67].

#### 1.1.4 Electrodynamic Tethers

The electrodynamic tethers can work as the generators, by converting their kinetic energy to electrical energy. Electric energy is generated across a conductive tether when moving through the Earth's magnetic field. The choice of the metal conductor to be used in an electrodynamic tether is determined by a variety of factors, which include high electrical conductivity, low density, cost, strength, and melting point [13] [73] [74].

Typically, as shown in Figure 1.5, an electric field of about 0.2 V/m develops as a consequence of the motion in the Earth's magnetic field. For most satellites and structures this field has little effect, but for an electrodynamic (ED) tether with length  $L$  crossing the magnetic field lines at velocity  $\vec{v}_0$ , the potential difference is defined in equation (1.1.12) [75] [76], the tether acts as a unipolar generator depending on the relative geometry of the three intervening vectors of  $\vec{v}_0$ ,  $\vec{B}$  and  $\vec{L}$ , assuming a rectilinear tether, the potential difference may amount to several kilovolt for lengths of the order of 10-20 km, and what matters is the relative velocity between the orbiting conductor and the magnetic field lines [77] [78] [79] [80].

$$\Delta V = \int_0^L (\vec{v}_0 \times \vec{B}) \cdot d\vec{l} \quad (1.1.12)$$

$$\vec{F}_{ED} = \int_0^L i(l) (d\vec{l} \times \vec{B}) \quad (1.1.13)$$

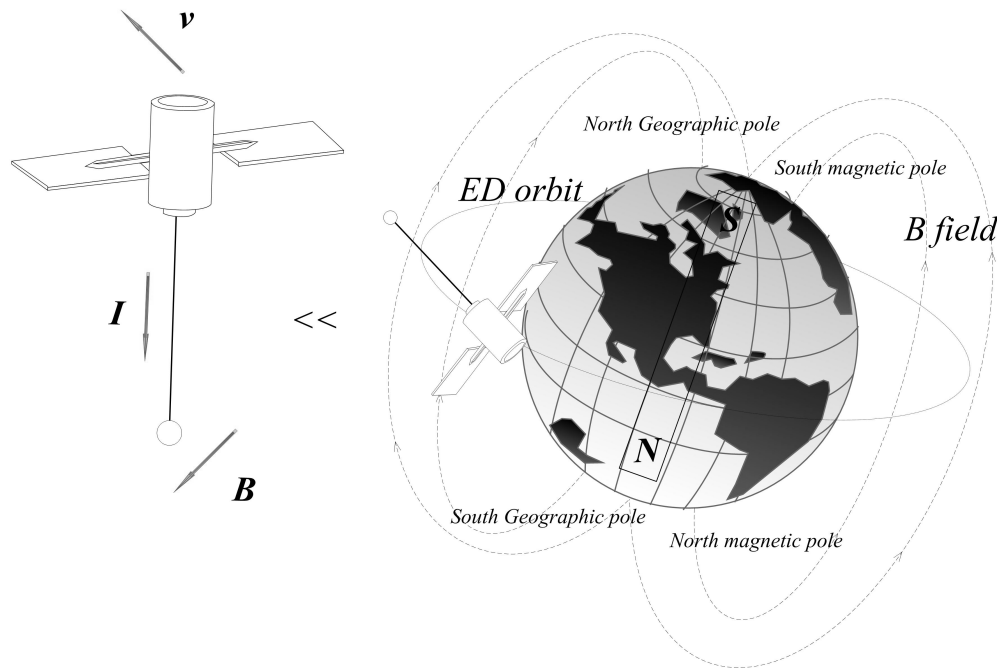


Figure 1.5: **Electrodynamic tether system** [13] [76] [82]

where  $\vec{F}_{ED}$  is the force,  $i$  a scalar current value,  $d\vec{l}$  is the tether vector,  $L$  is the length of tether, and  $\vec{B}$  is the magnetic field vector [82].

Most of the technological interest in electrodynamic tethers arises from their possible utilisation for space propulsion. The interaction of the current with the Earth's magnetic field results in the ED force given in equation (1.1.13) [76] [82]. Propulsion and drag by means of electrodynamic tethers were generated by the interaction of the conductive wire with the Earth's magnetic field.

If the tether is moving across electrical fields with the surrounding ionised medium, charge is collected and an electrical current flows along the tether. As already pointed out in the introduction, the effectiveness of tethers for propulsion and de-orbiting depends crucially on the magnitude of this current. The thrust or drag is generated by the interaction of the current with the local magnetic field, according to the Lorentz law [81] [82].

As this ED force is continuous, its action can result in large momentum transfer and significant changes in the orbital elements. To be effective, however, the magnetic field must not be parallel either to  $\vec{v}_0$  or  $\vec{B}$ , a condition which makes such tethers much less efficient in polar orbits [83] [84].

## 1.2 Objectives

There are two primary objectives for this thesis,

- ▷ To propose a series of dynamical models for motorised momentum exchange tethers;
- ▷ To discuss two control methods for a flexible motorised momentum exchange tether's spin-up behaviour, which include a fuzzy logic control method and a hybrid fuzzy sliding mode control method.

## 1.3 Contributions

The primary contributions of this thesis are listed below,

- ▷ a series of new dynamical models for motorised momentum exchange tethers were obtained, which include the rigid body models, the massless tether subspan models, and the flexible body motorised momentum exchange tethers;
- ▷ a fuzzy logic control method for a flexible motorised momentum exchange tether spin-up was proposed;
- ▷ a hybrid fuzzy sliding mode control method for a flexible motorised momentum exchange tether spin-up was proposed based on the fuzzy logic control method mentioned above;
- ▷ SMATLINK - a co-simulation toolbox, which allows easy data exchange and manipulation, implementation of existing MATLAB or MATHEMATICA codes, was developed. This toolbox can connect the controllers in MATLAB with the dynamical models of space tethers in MATHEMATICA.

## 1.4 Thesis Structure

There are 10 chapters in this dissertation. In order to demonstrate the structure in a quick and clear way, Figure 1.6 lists the structure of this dissertation by chapter order, showing how the chapters are organised one by one. Figure 1.7 plots the dissertation's structure by MMET models order, indicating how the chapters are laid out by the types of dynamical models; then two control methods are discussed.

- Chapter 1 - Introduction to space tethers - this chapter gives an introduction to space tether history, missions related to space tethers, and basic concepts for the electrodynamic tethers .

- Chapter 2 - Literature review on space tethers and tethered system control - this is a literature review regarding the control of space tethers; this chapter highlights relevant control research and its related application to space tethers from a series of reference papers.
- Chapter 3 - The motorised momentum exchange tether - this chapter addresses background information on the momentum exchange tether and the motorised momentum exchange tether.
- Chapter 4 - Dynamical modelling of a flexible massless MMET system - this chapter provides a modelling process for the motorised momentum exchange tether system with axial, torsional and pendular elasticity, using Lagrangian dynamics.
- Chapter 5 - Discretised Axially MMET Elastic System - this chapter discusses the dynamical modelling of the motorised momentum exchange tether system with axial elasticity by discretising the tether subspans into a series of mass points, and then connected these mass points by groups of 'spring-dampers' along each tether subspan.
- Chapter 6 - Discretised MMET system involving axial and torsional elasticity - based on Chapter 5, this chapter summarises the dynamical modelling for the motorised momentum exchange tether system with axial and torsional elasticity by means of a similar modelling process.
- Chapter 7 - Dynamical modelling for a discretised flexible MMET system - based on Chapter 6, this chapter explains the dynamical modelling for the motorised momentum exchange tether system with axial, torsional and pendular elasticity, using a consistent process.
- Chapter 8 - Fuzzy logic control for MMET spin-up - this chapter discusses the design process for a fuzzy logic controller with two inputs and one output as used for the spin-up of the flexible MMET system, and as defined in Chapter 7.

- Chapter 9 - Hybrid fuzzy sliding mode control for the MMET spin-up - a hybrid fuzzy sliding mode control method is proposed in this chapter, combining together the fuzzy logic control method and the skyhook surface sliding mode control method, and balanced by a switching factor. Then, this hybrid control method is applied to the spin-up control for the flexible MMET system in Chapter 7.
- Chapter 10 - Conclusions and future work - this chapter lists the conclusions to all previous chapters and suggests a few future research targets for the control of space tethers.

In particular here, as will be discussed in chapter 4, the dynamical modelling for the flexible massless MMET is discussed by the following steps, which helps to show the flexible massless MMET system modelling process clearly.

- Section 4.2 the massless MMET system: axial elasticity modelling
- Section 4.3 the massless MMET system: axial and torsional elasticity modelling
- Section 4.4 the flexible massless MMET system: axial, torsional and pendular elasticity modelling

In order to distinguish the third modelling from the previous two models, the term ‘flexible’ in this dissertation only means that this MMET system incorporates the axial, torsional and pendular elasticity. Similarly, this modelling process is also applied to the models of discretised MMET systems in the further chapters, that is,

- Chapter 5 the discretised MMET system: axial elasticity modelling
- Chapter 6 the discretised MMET system: axial and torsional elasticity modelling
- Chapter 7 the flexible discretised MMET system: axial, torsional and pendular elasticity modelling

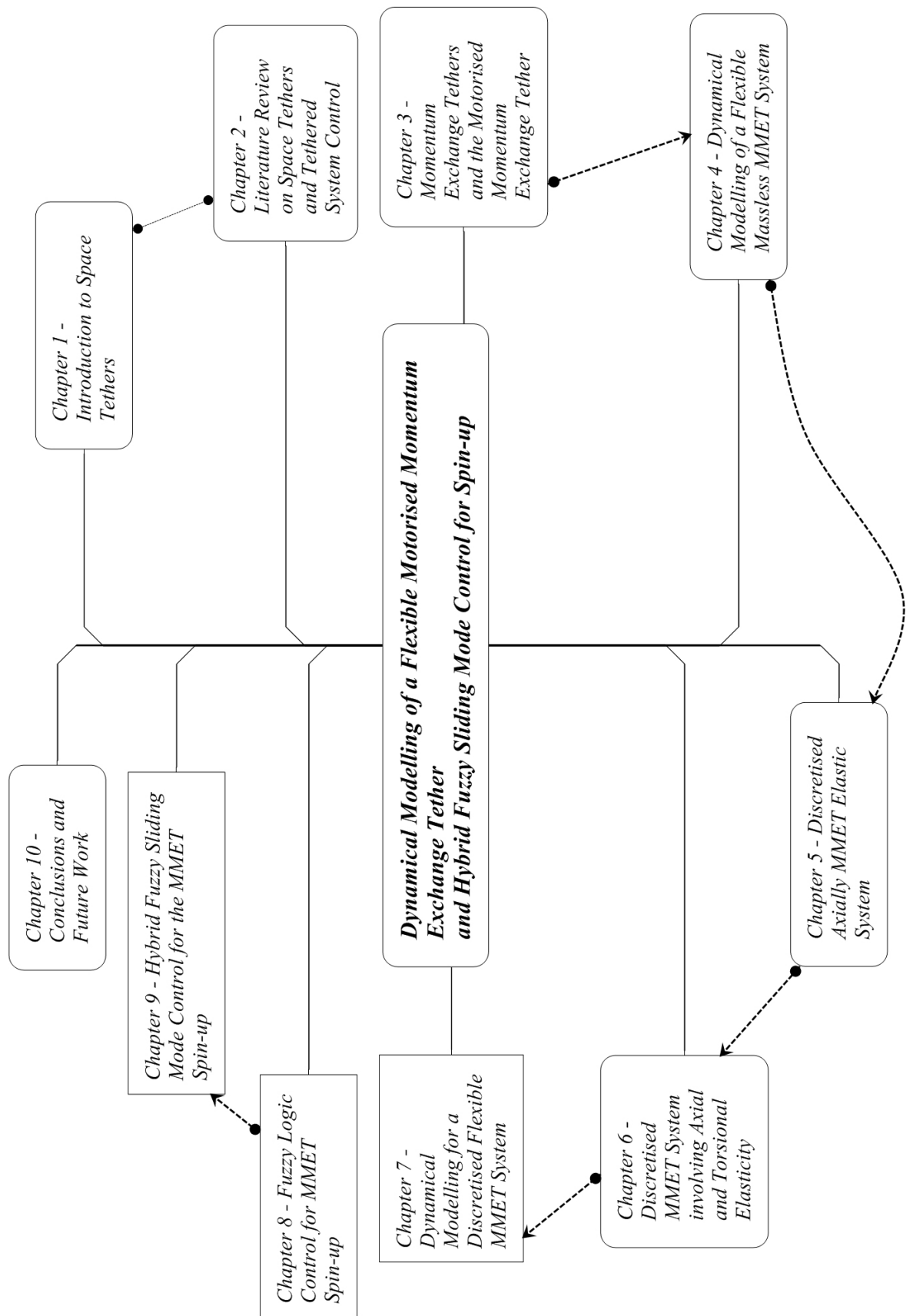


Figure 1.6: Thesis structure by chapters

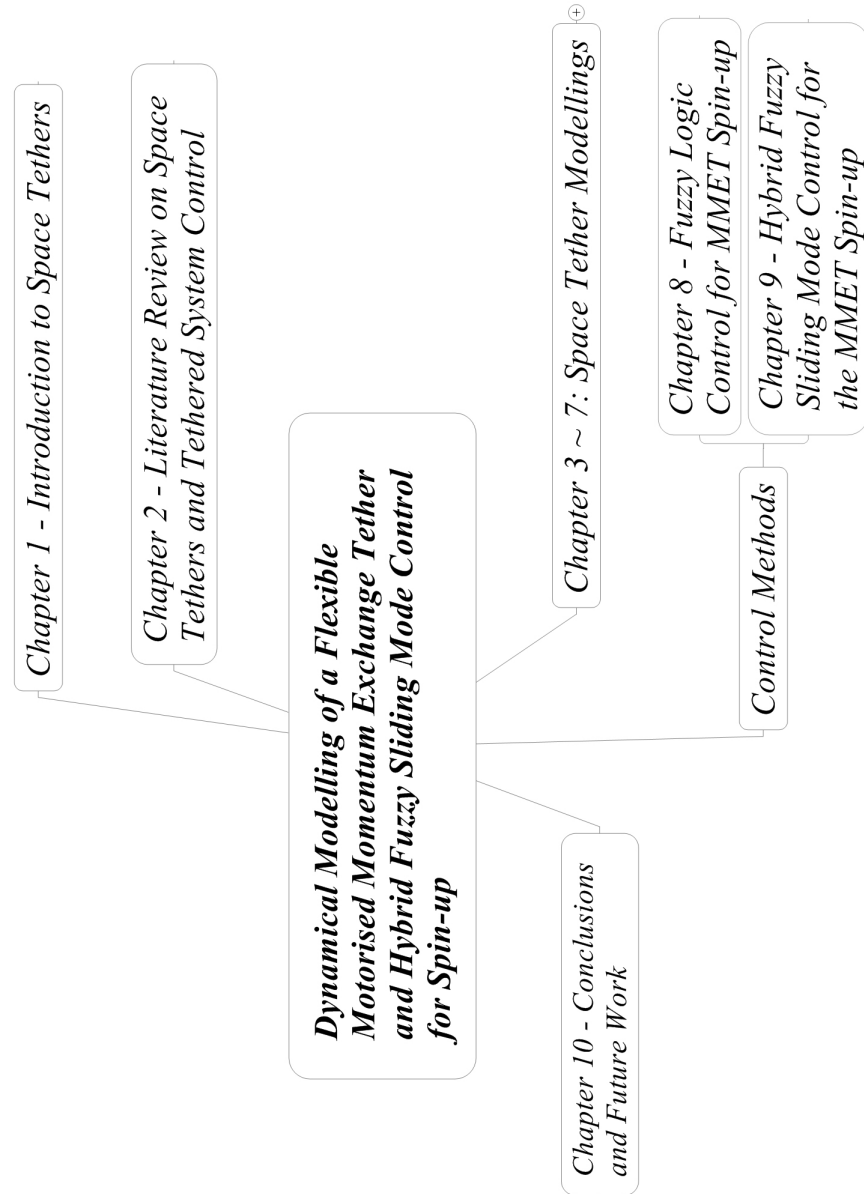


Figure 1.7: Thesis structure by models

## Chapter 2

---

# Literature Review on Space Tethers and Tethered System Control

---

### 2.1 Introduction

A typical tether system related mission always involves tether deployment and payload transfer, tether retrieval, trajectory navigation, attitude control, and motion and vibration control. This may involve three dimensional rigid or flexible dynamics, swinging in-plane or out-of-plane vibrational motion of the space tether system, and longitudinal and transverse vibrations of the space tether system.

Space tether system dynamics are quite complex because they are governed by a set of ordinary or partial nonlinear equations and coupled differential equations, aspects of which can affect space tether system behaviour, and can possibly cause control problems, which could be coupled with others problems.

Generally, Momentum exchange (MX) tethers and Electrodynamic (ED) tethers are the two principal categories of a practical tether system. There are many kinds of tether applications, such as: Hybrid of Momentum eXchange/Electrodynamic Reboost (MXER) tethers; and Electrostatic Tethers [85]. The research on dynamics and control are the two fundamentally important aspects of all tether concepts, designs, and mission architectures [2] [86] [87] [64] [88].

This literature review chapter focuses mainly on five topics regarding the control of space tether:

- tether deployment and retrieval;
- trajectory generation and orbit control;

- tether attitude and motion control;
- tether vibration control and dynamical simulations;
- space tether dynamical models.

With the basic aim of establishing useful sources of fundamental theory in the literature, as well as highlighting the previous control methods developed, this chapter attempts to provide a useful contextualised source of references for further space tether control studies.

## 2.2 Tether Deployment and Retrieval

A typical TSS mission launch involves both deployment and retrieval, besides other operational phases. Tether deployment and retrieval are two of the most important steps in space tether applications [89] - [101].

A general formulation of the deployment dynamics of tether-connected two-body systems was introduced by Modi and Misra in 1979 [102]. It took into account three-dimensional librational motion, and longitudinal and transverse vibrations. Three simple deployment procedures were considered, in the beginning analytical solutions were obtained for the degenerate case of negligible vibrations on a circular orbit, which helped to establish trends for the more general situation.

In 1994, Bergamaschi et al. published a research paper, comparing the results of mathematical models implemented in two different general purpose computer codes in the analysis of the spectra of an accelerometric package mounted onboard TSS-1. The main characteristics of the codes were presented, and a test case outlined the cross-check activity performed for simulator validation. The simulated reconstruction of the dynamics during the on-station period at 256 m was depicted and discussed, then a short review was made of instrument performance and data quality, after which computed and experimental spectra, along with data from a station-keeping phase during tether deployment, were compared and discussed [103].

The motion of a tethered system during the retrieval process was investigated, using a simple nonlinear model, by Chernousko in 1995 [104]. The unique motion was described for the system at a constant tether retrieval rate in which the angle of deviation of the tether vanished at the end of the retrieval. A method of controlling the retrieval process was proposed, which prevented the amplitude of oscillation increasing.

An analysis of the exponential deployment of a tether was carried out by Pelaez in 1995 [105] [106]. It was shown that it was possible to dispense with tether alignment along the

vertical without later libration. There was a two-stage deployment process: the first stage in which the tension was controlled indirectly in order to get a constant radial velocity of the end mass; and the second stage in which the tension was controlled indirectly in order to achieve a constant ratio. In both phases the tether unwound from a reel whose angular velocity could be controlled. The essentially stable character of deployment gave robustness to this open loop strategy, resulting in a residual, negligible libration. Moreover, the proposed deployment scheme could be taken as a starting point for more elaborate strategies.

Koss described the tether deployment mechanism development for the ATEX mission in 1997, giving some design iterations. These included: energetic(spring) deployment, a DC brush motor driven deployment mechanism and a stepper motor driven deployment mechanism [55].

In 1997, a tethered system deployment control by fuzzy logic feedback was proposed by Licata [107]. The feedback control was based on a simple fuzzy-logic rule and minimal measurements for in-plane tether deployment control problems; tethered end-mass terminal deployment position and phasing time constraints, such as tether initiated waste-disposal and capsule re-entry applications, were all illustrated. The fuzzy logic law, for the proposed rate feedback control solution to the in-plane deployed tether terminal position-only problem, has been associated with the tether length-angle state plane, instead of its full state space, or the physical deployment trajectory plane. Simulation results showed the robust characteristics for the numerically implemented terminal angle-length control solution to main system parameter changes, and uncertainty for a nominal tethered system model with a specified deployer configuration design. Solutions to the more complex space-time tether deployment control problem with terminal deployment angle-length-time constraints, associated with a tether initiated capsule re-entry application, have also been formulated and were presented as extensions of the previously stated deployment terminal position control, together with numerical simulation results for the nominal tethered system model and deployer configuration.

Carter and Greene studied the simulation of the retrieval and deployment characteristics for the Getaway Tether Experiment (GATE) in 1998 [108]. The GATE was a single-tether satellite system for the study of tether dynamics and electrodynamic technology. One goal of GATE was to measure and control tether disturbances, such as those induced by micro meteorite impact, using an active reel type deployer which was able to retrieve and deploy the tether. A close-loop controller for the tethered system was given. This allowed the tether to be actively reeled in (retrieval) or passively reeled out (deployment), to and from the mother subsatellite. Their simulation results were presented and showed the effects of retrieval and

deployment on the system. Three cases were considered: an exponential retrieval rate; a constant retrieval rate; and a pulsed deployment.

A linear tension control law was provided by Kumar and Pradeep in 1998 [109]. In this paper they provided a procedure used for determining a control law which could be used to solve new problems. The approach was applied to the problem of three-dimensional tether deployment considering both in-plane and out-of-plane librations.

An adaptive neural control concept for the deployment of a tethered re-entry capsule was provided by Glabe et al. in 2004 [110]. The control concept applied an indirect neural controller, which combined two neural networks, a controller network and a plant model network. While the controller network was initialised by means of multiple conventional linear quadratic regulator designs, the plant model network was trained to predict future states, and thus deviated from an optimised reference path. System inputs were found by means of an online optimisation process, which minimised a user-defined cost function. That was shown to influence the performance of the neural controller. Due to the special structure of the controller network, stability investigations of the closed control loop were possible. After introducing the tether deployment scenario, assumptions and simplifications were applied to the mathematical system model. The numerical simulations focused on the effects of perturbations concerning the initial states and the plant model. The simulation results allowed a performance comparison of the linear quadratic regulator and the neural control concept.

The dynamical behaviour of tether-connected satellite systems during the deployment and retrieval process was considered by Djebli et al. [111] [112] in 1999 and 2002. The system consisted of a space-station connected to a subsatellite by means of a tether of variable length. A simplified model was given in which the space-station and the subsatellite were reduced to material points and the system mass centre moved along a circular orbit with three-dimensional transverse and longitudinal oscillations. Strategies for retrieval were obtained in order to increase the tension in the tether at the final stage of retrieval. These laws of retrieval were deduced from the laws obtained in a previous paper for the particular case of a massless tether. Some particular laws of deployment retrieval, leading to analytical solutions for the small in-plane and out-of-plane motions of the system, were obtained. Another application of the method was the so-called "crawler system" in which the subsatellite crawls towards the space-station along a tether of fixed length, previously deployed.

An in-depth analysis was presented by Campbell [113] regarding the closed-loop results and insights from the on-orbit control experiments of the Mid-deck Active Control Experiment (MACE). MACE was flown in the Shuttle mid-deck on STS-67 in March 1995 to

investigate issues associated with a change in operational environment from ground to space for a payload pointing spacecraft. This cannot be tested in a realistic ground simulation. These closed-loop results provided insight into how future on-orbit closed-loop experiments could be improved, and they also helped to build confidence in the on-orbit capabilities of future multi-payload spacecraft. This practical control design for flexible systems involved many issues, such as the selection of effective control topologies, the validation of robust control designs and techniques, the development of robust control design methodologies for both finite element and identified models, and the development of effective tools for system analysis. The MACE was designed to be a reusable dynamics and control laboratory which could be used to investigate many of these issues during both ground- and space-based operations. The paper presented an in-depth analysis of the extensive set of modelling and closed-loop control experiments performed on the MACE test during 14 days of on-orbit operations on STS-67.

In 2003 and 2005, Barkow et al. published three papers on various methods used for controlling the deployment of tethered satellites [114] [115] [116]. The deployment of a tethered satellite system is one of the most critical phases in a tether mission, due to its complicated dynamics. High amplitude oscillations are likely to arise in such systems, and it can take a long time to reach the desired stable radial equilibrium state. Based on a viscoelastic space billiard model [115], a targeting strategy was developed which made use of the system's chaotic nature and allowed the system to be steered into its equilibrium faster and more efficiently, when compared to conventional strategies. Also, the deployment of a subsatellite from a mother spaceship moving on a circular orbit would be a delicate operation for a tethered satellite system, because this process could lead to unstable motion with respect to the stable radial relative equilibrium of such a system if the tether length was constant. An optimal control strategy to simulate the force controlled deployment of a tethered satellite from a spaceship was proposed. The authors compared this strategy with free deployment, deployment controlled by Kissel's law [117] and an approach which made use of the concept of targeting which is used in the controlling chaos approach. Both deployment time and energy input were computed and compared to other deployment strategies.

In 2003, Steindl and Troger proposed their thesis that the optimal control of deployment of a tethered subsatellite moving on a circular orbit around the Earth. An optimal control of deployment and retrieval of a tethered subsatellite from a main satellite was treated by Steindl in [118] and [119]. Therefore, they introduced an optimal control strategy, using the Maximum Principle [120] to achieve a force controlled deployment of the tethered subsatellite from the radial relative equilibrium position close to the spacecraft to the radial relative

equilibrium position far away from the spacecraft. Since a straightforward application of the mathematical methods of optimal control theory could be easily formulated only for a finite dimensional system, they considered a simplified system model in which the tether was assumed to be massless. Meanwhile, the main problem during retrieval was that it resulted in an unstable motion concerning the radial relative equilibrium which was stable for a tether of constant length. The uncontrolled retrieval resulted in a strong oscillatory motion.

In 2006, Williams published a paper on the optimal deployment and retrieval for a tethered formation with spinning in the orbital plane [121]. The tethered formation was modelled by point mass satellites, which were connected via inelastic tethers. The optimal deployment and retrieval trajectories using tension control were determined for different spinning conditions. Deployment and retrieval trajectories were obtained which could maintain the tether spin at the desired rate and keep the system in a desired physical arrangement at the end of deployment and retrieval. The parametric studies of the effect of system spin-rate and maneuver time were performed, and it was necessary to constrain the relative tether geometry to prevent any two tethers crossing each other. The results also showed that the tether spin rate tended to decrease during deployment but could be restored to the desired value by over-deploying the tethers and then reeling in rapidly.

In 2007, Mantri's research [122] aimed to model and understand the deployment of space systems with long and short tethers. This research was divided into two parts. In the first part, a model for short and medium length tether systems was developed and simulated by solving equations of motion. A detailed parametric study was conducted after identifying important parameters affecting the deployment, and after studying the effect of each parameter for the deployment performance. A simulation tool was developed to assist mission planners in predicting the deployment performance of a space tether system with a given set of parameters. The second part of the research was motivated by Space Elevator (SE). SE was a futuristic and highly challenging technology which was based on the idea of connecting Earth and Space by an approximately 100,000 km long tether, which would be deployed from GEO. With this motivation, the short tether analysis from the previous section was extended to the analysis of long tethers. A model for the long tether deployment was developed and governing equations of motion were formulated. The critical parameters were identified, and then the problems involved in SE deployment were investigated. Tether mass was initially included in the model, but it was found that the mass of the tether has little effect on the overall qualitative dynamics of the system. Hence, for further analysis, a massless tether model was adopted. Upon simulating the system, it was found that the long tether could be highly unstable during deployment, and it could crash onto the Earth. However, a con-

siderable fraction of the tether could be deployed successfully without any external control mechanism before the instability manifested itself.

## 2.3 Trajectory Generation and Orbit Control

In 1995, Modi's paper reviewed the attitude dynamics and trajectory mechanics of spacecraft in the environmental forces, with particular emphasis on the solar radiation induced pressure and thermal effects on attitude dynamics [144]. Several semi-passive controllers were proposed which could use the environmental forces to advantage in stabilizing the system. The solar radiation-induced forces could be put to advantage for propulsion and trajectory transfer. The examples given of contemporary interest illustrated the effectiveness of the concepts in achieving the desired attitude and trajectory. [The results suggested that the gravity gradient torque could be put to advantage in stabilising spacecraft by the appropriate distribution of inertias.](#)

[In 1996, Nohmi et al. proposed a "tethered robot system", in which a robot attached through a tether to the spacecraft \[123\]. For its position control of the centre of mass of the robot, tether tension was used to control the position, by taking into account the gravity gradient and the centrifugal force. The motion of the tethered robot system was simulated on the trajectories planned, in which the feedforward control strategy was applied. The results from the trajectory planning procedure suggested that the shape of the path depends both on the direction to the destination point, and the time taken to accomplish the mission, but did not depend on the distance. The motion of the robot centre of mass could be controlled on trajectories away from the equilibrium point. Translation on planned trajectories would be possible in case the destination point was close to the initial point or in case the time of accomplishment of the mission was longer.](#)

A research paper which focused on a novel ground-based prototype manipulator was proposed by Cao et al. in 2003 [124]. The system had two identical modules connected in a chain topology. Each module consisted of two links: one free to slew, while the other was permitted to deploy. Construction and integration of the manipulator were explained, and this was followed by the development of a mathematical model for the manipulator using the Lagrangian procedure. Finally, a series of trajectories were tracked, using the proportional integral derivative (PID) control and feedback linearisation technique (FLT). The objective was the real-time implementation of the control algorithms, developed for the unique space manipulator on an Earth-based prototype system.

In 2003, Milam developed a computationally efficient Nonlinear Trajectory Generation

(NTG) algorithm, and also described its software implementation in order to solve real-time nonlinear optimal trajectory generation problems for constrained systems [125]. NTG was a nonlinear trajectory generation software package which combined nonlinear control theory, B-spline basis functions, and nonlinear programming. This paper compared NTG with other numerical optimal control problem solution techniques, such as direct collocation, shooting, adjoints, and differential inclusions, and then demonstrated the performance of NTG on the Caltech Ducted Fan test-bed. Aggressively, the constrained optimal control problems were solved in real-time for hover-to-hover, forward flight, and terrain avoidance test cases. Then, the real-time trajectory generation results were shown for both the two degrees of freedom and the receding horizon control designs. Further experimental demonstration was provided with the station-keeping, reconfiguration, and de-configuration of micro-satellite formation, with complex nonlinear constraints. Successful applications of NTG in these cases demonstrated the reliable real-time trajectory generation, both for highly nonlinear and non-convex systems. The results were among the first to apply receding horizon control techniques for agile flight in an experimental setting, using representative dynamics and computation.

In 2006, Padgett proposed a tethered satellite system for many space mission applications, due to the useful dynamics that could be generated in null-cline analysis systems [126]. For instance, tethered satellite systems could be used to increase the orbital radius of LEO payloads, using angular momentum transfer. Another tethered satellite system proposal involved the use of a variable length, spinning tethered system to produce specific levels of artificial gravity in LEO. An analytic method of qualitatively describing the possible dynamics of a tethered satellite system was presented. This analysis centred on the study of the sets of states in which at least one of the non-dimensional time derivatives of the state variables was zero, and these sets were known as the null-clines of a system, and they bound regions of the phase plane, in which tethered satellite behaviour was similar. The qualitative analysis of the null-clines provided an explanation, and suggested the controllability of many types of tethered satellite behaviour. A Tethered Artificial Gravity (TAG) satellite system was used as a canonical tethered system, and the derived results were applied to this system. The utility of the described analytical method was demonstrated by using the method to characterise two different tethered satellite missions.

In 2007 Sharma et al. presented a study on global path planning algorithms for the Titan aerobot, based on user defined way points in 2D and 3D space [127]. The algorithms were implemented using information obtained through a planner user interface, and the trajectory planning algorithms were designed to accurately represent the Titan aerobot's characteris-

tics, such as its minimum turning radius. Additionally, trajectory planning techniques were implemented so as to allow for the surveying of a planar area based solely on camera fields of view, airship altitude and the location of the planar area's perimeter. The developed paths allowed for planar navigation and three dimensional path planning. These calculated trajectories were optimised to produce the shortest possible path, while still remaining within realistic bounds of airship dynamics.

In 2005, Kim proposed a low-thrust system operated for significant periods of the mission time [128], and as a result the solution approached requires continuous optimisation, and the associated optimal control problems were in general numerically ill-conditioned. The objective was to design an efficient optimal control algorithm and then apply it to the minimum time transfer problem of low-thrust spacecraft. It devised a cascaded computational scheme based on numerical and analytical methods. Whereas other conventional optimisation packages relied on numerical solution approaches, it employed analytical and semi-analytical techniques, such as symmetry and homotopy methods, to assist in the solution-finding process. The first objective was to obtain a single optimised trajectory which satisfied some given boundary conditions. The initialisation phase for this first trajectory included a global, stochastic search based on an adaptive simulated annealing algorithm, and the fine tuning of optimisation parameters - the local search - was accomplished via Quasi-Newtonian and Newtonian methods. Once an optimised trajectory was obtained, then, the author could use system symmetry and homotopy techniques in order to generate additional optimal control solutions efficiently. It obtained optimal trajectories for several interrelated problem families that were described as multi-point boundary value problems. It presented and proved two theorems by describing system symmetries for solar sail spacecraft, and then discussed symmetry properties and symmetry breaking for electric spacecraft system models. It demonstrated how these symmetry properties could be used to significantly simplify the solution-finding process.

A balloon trajectory control system was discussed that was under development for use on NASA's Ultra Long Duration Balloon Project [129]. The trajectory control system exploited the natural wind field variation with altitude to generate passive pendular control forces on a balloon, using a tether-deployed aerodynamic surface below the balloon. The model confirmed many aspects of trajectory control system performance.

In 2003, Sakamoto and Yasaka addressed the motion of orbital objects, which followed Kepler's law, and then an orbit determination system in ground stations algorithm for analysing the Kepler's motion was derived [130]. A tethered satellite system was the representative future space system, and did not follow the conventional space dynamics. The following three

problems were considered: first, the sensitivity of the length of tether and the librational motion influence observations, which were range, range rate, and direction. Secondly, the filtering algorithm was proposed for the orbit determination of a TSS. Thirdly, the initial orbit determination of a TSS was discussed - the observations of range and range rate could reflect the motion of a TSS, whilst on the other hand observations of direction were not effective for the detection of a TSS motion.

In 2004, Takeichi studied the periodic solution of the librational motion of a tethered system in elliptic orbit, and clarified its mechanical characteristics [131]. The basic libration control toward the periodic solution was also presented, and a tethered system was modelled as a rigid body, and in addition a set of nonlinear equations of motion for the librational and the orbital motions was formulated. An approximated analytical solution was obtained through the Lindstedt perturbation method. The total mechanical energy was formulated, and it showed the minimum value when the librational and orbital motions coincide with the periodic solution. The periodic solution was the minimum energy solution, and the periodic solution in an elliptic orbit had the same significance as the equilibrium state in a circular orbit from the mechanical point of view. A libration control towards the periodic solution was also investigated, and the effectiveness of this control strategy was demonstrated by using the periodic on-off control through a thruster installed on the subsatellite.

In 2005, a survivability analysis was carried out to support the design of a tether system by Anselmo [132]. [Various tether configurations were analysed, and a numerical simulation was obtained to assess the survival probability of an electrodynamic tether system for end-of-life de-orbiting. In addition, the collision risk with large, intact space objects was analysed as well in its implications, in order to guarantee a sufficiently short de-orbiting time for relatively massive payloads.](#)

In 2009, Williams put forward his work which discussed a control system for the YES-2 mission [60]. This mission was intended to demonstrate the ability to deploy a payload via a tether, so that it could return the payload to the Earth using momentum-transfer. By deploying the tether in an appropriate manner, the tether could gain sufficient swing velocity, so that when the tether passed through the local vertical it could be severed. This effectively removed momentum from the payload and allowed it to re-enter the atmosphere. Optimal trajectories were determined for both phases after comparing the effect of different cost functions on the deployment dynamics. The controllers were tested in a flexible tether model with large disturbances to the hardware model and environmental variables. Closed-loop simulations showed that the system could be controlled quite well using only feedback of length and length rate.

## 2.4 Tether Attitude and Motion Control

In 1975, a paper on the flexural-rotational coupled motion of three identical flexible cylindrical cantilevers was written by Modi and Misra [133]; it joined symmetrically to a central head. The effects of the tensile follower forces and inertia parameters on the natural frequencies of the system were studied. The analysis suggested two types of in-plane motion and three sets of eigenvalues govern the out-of-plane motion. For in-plane motion, one corresponding to the oscillation of the cantilevers without any rotation of the central body, while the other involves coupled motion of the array. The repeated eigenvalues were identical to those of a single cantilever having the same axial tension parameter. Three sets of eigenvalues govern the out-of-plane motion: (a) the central head remaining stationary with no rolling motion of the array; (b) vertical motion of the central body without any rolling motion of the array; and (c) rigid body rolling motion without any vertical motion of the central head. There was a possibility of dynamic instability for small inertia parameters and large axial tension.

An alternative control law based on the linear regulator problem was developed by Bainum et al in 1980 [134], which could be used in the operation of the Shuttle Tethered Subsatellite system. This control law was assumed to be provided only by modulating the tension level in the tether as a function of the difference between actual and commanded tether line length, length rate, in orbital plane swing angle, and swing angle rate. Necessary and sufficient conditions for stability of the linear system motion in the vicinity of its nominal local vertical orientation were also developed. By proper selection of the state and control penalty matrices, it was possible to obtain faster responses with no increase in maximum power levels for use in station keeping, when compared with alternate control strategies. The weighting matrices were adjusted in a piecewise adaptive manner to provide control law gains in order to achieve a smooth deployment history.

A spatial dynamics of the space shuttle based tethered satellite system was investigated [135], by using a nonlinear model which accounted for the aerodynamic drag in a rotating oblate atmosphere, by Modi. The result showed that the normally unstable retrieval manoeuvre could be stabilised satisfactorily using a nonlinear tether tension control strategy, which depends on the tether length, its variation with time, and pitch rate. Effectiveness of the control was illustrated through an example involving a 100 km tether supporting a proposed satellite for charting the Earth's magnetic field.

The dynamics of a tether-connected three-body system was investigated by Misra, Amier

and Modi in 1988 [136]. The system was treated as a double-pendulum, and the motion in the orbital plane was considered for the two cases of fixed-length tethers and variable-length tethers. For the fixed-length tethers, there were four possible equilibrium configurations: both tethers aligned along the local vertical; both tethers horizontal; and for certain combinations of parameters, two other configurations where one tether was along the local vertical, while the other was inclined to the local vertical. Only the vertical equilibrium configuration was stable. Frequencies of oscillations around the stable configuration and corresponding modes were given, the dynamic response of the system during deployment of the three-body constellation was obtained. Dynamical behaviour during transportation of a cargo from one end-body to the other was also studied.

In 1990, Modi published a paper which provided brief reviews on complex interactions, between flexibility, deployment, environmental forces and attitude dynamics, during both steady state and transient phases. Parametric studies suggested that critical combinations of system variables could drive the spacecraft to be unstable, and if provided with suitable control strategies, it could be available to restore equilibrium. The paper's emphasis was on the methodology of an approach to complex dynamical systems and analysis of results, which helped to gain better physical appreciation as to their response behaviours [137].

In 1992, Lea et al. developed a fuzzy logic based tether length controller into the TSS-1 simulation, which investigated the usefulness and robustness that could be achieved with fuzzy control. They reported the performance of the controller with the bead dynamics model, also known as the finite element model. The tether mass was represented as a lumped mass in a head and the entire tether length was divided into several segments, thus making several beads with three degrees of freedom motion in the orbital environment. The control algorithm based on fuzzy logic for controlling tether length was described, and details were provided of the membership functions and rule-base. The results comparing the performance in terms of length error, tension error, and librational oscillations were presented [138].

In 1992, Modi and Lakshmanan proposed a mathematical model for the study of the dynamics of the tethered satellite system consisting of a plate-type space station, from which a tether supported subsatellite was deployed or retrieved [139]. The rigid body dynamics of the tether, subsatellite and space station were analysed, by accounting for the mass of the tether as well as a three-dimensional offset of its point of attachment. Controllability of the linearised equations was established numerically, and a comparative study of three different control strategies was conducted. The strategies employed the thrusters, the tension in the tether line, or the offset motion of the attachment, which helped to achieve control for the system subjected to relatively large initial disturbances. The offset control proved to be the

most efficient in terms of energy consumption, but the response to disturbance persisted over a longer duration. In addition, the performance of the thruster control, tension control, and offset control strategies, as well as their combinations, were analysed during retrieval of the tether.

A mathematical model of a platform based flexible tethered satellite system in an arbitrary orbit, undergoing planar motion, was obtained using the Lagrangian procedure by Modia and Pidgeon in 1994 [140]. The governing equations of motion accounted for the platform and tether pitch, longitudinal tether oscillations, offset of the tether attachment point, as well as deployment and retrieval of the tether. The **models** of the interactions, involving system librations, tether flexibility, eccentricity and retrieval maneuvers **were modelled**. The simulation response showed high frequency modulations corresponding to the longitudinal tether oscillations, and the system was found to be unstable during retrieval. The Linear Quadratic Regulator based offset control strategy, in conjunction with the platform mounted momentum gyros, was proposed to alleviate the situation. The results showed that a strategy involving independent parallel control of low and high frequency responses could damp rather severe disturbances in a fraction of an orbit.

A three-axis attitude control system based on the integration of a reaction wheel, and a mobile tether attachment point on board of each platform of a two-mass tethered system, was analysed by Grassi et al. in 1994 [141]. An abrupt stop of the mobile attachment point of one platform was simulated, and a control law to limit the two-platform angular differences was derived considering the other platform mobile attachment point. The control laws were derived by making use of analytical attitude models, and were then implemented in a three-dimensional numerical code, which simultaneously integrated the system orbital and attitude dynamics. Final results showed that the proposed control laws allowed to limit the angular differences between the two platforms within values adequate for microwave remote sensing applications. Moreover, the attitude high frequency oscillations were effectively damped.

In 1995, Grassi and Cosmo's studies were conducted on SEDS attitude dynamics and stability [142]. The SEDS system provided a low-cost facility for deploying tethered payloads in space. Among various objectives, the SEDS mission's first flight would assess the capability of tethered platforms to carry out measurements in the upper atmosphere. The performance of onboard instruments was seriously affected by the payload's attitude dynamics. This mission's attitude dynamics and stability were analytically and numerically analysed for the nominal mission. It was shown that although a passive damper could be used to reduce the amplitudes of the attitude angles, appropriate control techniques were required for scientific instrumented platforms.

Furthermore, another mathematical model was developed for studying the dynamics and control of the tethered satellite systems undergoing planar motion in a Keplerian orbit, by Modi, Pradhan and Misra in 1995 [143]. The system consisted of a rigid platform, from which a point mass subsatellite was deployed or retrieved by a flexible tether. The model incorporated the offset of the tether attachment point from the platform centre of mass and its time-dependent variation. The governing equations of motion were obtained by using the Lagrangian formulation. The offset control strategy, which involves movement of the attachment point, was used to regulate the tether swing, and the platform dynamics were controlled by a momentum gyro. The offset control was implemented using a manipulator, which moves the tether attachment point as required. Their simulation results showed that the control procedure regulated the system dynamics, and the state feedback controller for the system was designed using graph theoretic approach, which had computational advantage particularly for higher order systems.

In 1996, Modi et al. [145] proposed a paper on ground based experiments of the OEDIPUS-C sounding rocket mission. The ground based experiments were conducted as a part of the OEDIPUS-C. The OEDIPUS-C configuration consisted of two spinning bodies connected by a long tether, the spin axis was nominally along the tether line. The objective was to assess the dynamic behaviour of the tether and the payload. The test configuration consisted of an end-body supported by a tether. The test procedure involved slow spin-up of the system and identifying the speeds corresponding to onset of the tether modes or the large amplitude end-body coning. Experimental results were obtained for four different bodies to study the system stability over a wide range of mass and geometric parameters. Effect of offset of the tether attachment from the end-body centre of mass was also investigated. The observed critical speeds were compared with those given by the linear theory. The several transient phenomena observed during the test suggest that system nonlinearities could not be ignored when modelling such a complex system.

In 1997, Pascal's paper [146] studied a tethered satellite system in a relatively dense atmosphere. The relevant dynamic problem was characterised by strong nonlinearities, mainly due to aerodynamic effects. Two mechanical models with different degrees of fidelity were developed to analyse the static equilibrium of the system. A rigid tether model and a flexible tether model were discussed. Both of the models for the tether were taken as an elastic continuum with mass, and aerodynamic forces were distributed along the system. The results of the rigid tether model, with an approximation of the system behaviour, were used as a starting point for the numerical procedure, which adopted for computing more accurately the tether shape with the flexible model.

In 1999, Pradhan, Modi and Misra [147] presented a paper which studied several applications of the offset scheme in controlling the tethered systems, in which planar equations of motion of a space platform based TSS were derived by the Lagrangian procedure. Simulation results aimed at the offset control of platform pitch, tether attitude and vibration motions. The offset scheme was used for the simultaneous control of platform and tether pitch motion. Finally attention was directed towards the simultaneous regulation of the platform pitch and longitudinal tether vibration. The numerical results showed considerable promise for the offset control scheme in regulating tether, platform and combined tether-platform dynamics.

The equations of motion for a class of TSS undergoing planar motion in a Keplerian orbit were derived using the Lagrangian procedure by Modi et al. in 1997 [148]. The system consisted of a rigid platform from which a point mass subsatellite could be deployed or retrieved by a flexible tether. The model incorporated an offset of the tethered attachment point from the platform centre of mass and its time dependent variation. The feedback linearisation technique was used to design the attitude regulator. A hybrid strategy, using thruster and offset schemes, was used for regulating the tether swing, and momentum gyros were employed for the platform control. The offset strategy was also used for active control of the tether flexibility during station-keeping, in conjunction with the thruster-based attitude controller. Finally, the effectiveness of the offset-based attitude controller was demonstrated through ground-based experiments, thus substantiating the trends predicted by the numerical simulations.

In 2000, Yu's paper discussed a TSS with two-dimensional motion, in which the tether was assumed to be massless [149]. The equations of motion were given in a spherical coordinate system to describe the magnitude (tether length) and direction angle of the position vector between the satellites. A length rate control algorithm was adopted and the controlled motion of the directional angle by the algorithm would have a stable equilibrium state. The equilibrium state was a fixed point if the orbit of the base-satellite was circular and a limit cycle if the orbit was elliptic. According to the results, the stability of the equilibrium state was determined by the parameters of the control algorithm, and the bifurcation analysis was also given.

An advantage of combining a crisp algorithmic controller and a soft knowledge-based controller was introduced by Goulet et al. in 2001 [150], which was in the specific context of controlling a space-based manipulator with flexible deployable and slewing links. A hierarchical control structure with a high-speed conventional controller at the bottom layer, and an intelligent tuner at an upper layer, was developed. The top-level intelligent tuner used a valid set of linguistic rules for adjusting proportional-derivative servos based on fuzzy sys-

tem concepts. The performance of the hierarchical control system was evaluated on the basis of the space-based simulation results. Based on the analysis, it could be concluded that initial tuning of the parameters of a conventional low-level controller together with tuning during operation could improve the positioning accuracy of the manipulator. The hierarchical control structure permitted desirable combination of a conventional high-bandwidth and knowledge-based low-bandwidth controllers.

A paper on the use of dual satellite platforms connected through a tether was proposed by Kumar et al. in 2001 [151]. The feasibility of suitably varying tether offsets for achieving desired maneuvers of both the platforms was explored. The Lagrangian formulation approach was utilised to develop the governing system of nonlinear ordinary differential equations for the constrained system. A simple open-loop strategy was developed for the tether offset variations, which ensured judiciously controlled changes in the orientation of satellite platforms. The numerical simulation of the nonlinear governing equations of motion for these tether offset variations established the feasibility of achieving desired attitude maneuvers. The nearly passive nature of the proposed orientation control strategy could make it particularly attractive for future space missions.

In 2004, Kim and Hall [152] investigated a mathematical model for a tether system, in which the effects of the smoothness and non-smoothness of desired mission trajectories on control performance was discussed. The equations of motion were derived by the use of Lagrange equations, and several mission scenarios for a proposed NASA mission which consider the operation of an infrared telescope were introduced. Techniques were developed to control the motion of a tethered satellite system comprising  $N$  point masses and interconnected arbitrarily by  $m$  idealised tethers; specifically, the control problem of a triangular and symmetrical TSS with 3 point masses and 3 tethers was discussed. Asymptotic tracking laws based on input-state feedback linearisation were developed, and the effects of the smoothness and non-smoothness of desired mission trajectories on control performance were discussed. It was asserted that required thrust levels could be decreased by the use of additional tether length control, to keep the TSS in a state corresponding to an instantaneous relative equilibrium, at any point in time during the mission.

In 2004, Williams and his colleagues [95] [96] presented their research on deployment of a payload on a spinning tether in a hyperbolic orbit with a sufficient velocity change, while it was captured in an elliptical orbit at the destination planet. Due to conservation of momentum, the main spacecraft gained a “momentum-enhanced gravity-assist”, which used tethers for planetary capture. In planetary exploration and payload transfer, it was investigated by conducting numerical simulations of a simplified tether system, the tether mass required to

prevent rupture of the tether was optimised using numerical and iterative techniques for each of the major planets in the solar system. It was demonstrated that mass savings could be achieved when compared to the requirements for chemical propulsion. Finally, it was shown that controlling the tether length during the maneuver could be done in order to correct errors in the system trajectory for both spinning and non-spinning capture cases. Meanwhile, another paper proposed utilising the distributed Lorentz forces that were induced in an electromagnetic tether as a control actuator for controlling the tether motion [97]. The control input governing the magnitude of the applied actuator force was the current being conducted within the tether. A wave-absorbing controller was also proposed to suppress the unstable high-order modes which tended to be initiated by electromagnetic forces. The absorption of travelling waves along the tether could be achieved by proper movement of the tether attachment point on the main satellite. A mission function control law was presented for controlling the tether length and in- and out-of-plane librations, derived from a model that treats the tether as an inextensible rigid rod.

In 2004, Lovera and Astolfi [153] discussed the problem of inertial attitude regulation for a small spacecraft using only magnetic coils as actuators, and a global solution to the problem was proposed based on static attitude and rate feedback. A local solution based on dynamic attitude feedback was also presented, that attitude regulation could be achieved even in the absence of additional active or passive attitude control actuators such as momentum wheels or gravity gradient booms.

In 2005, Modi et al. presented their studies on the development and implementation of an intelligent hierarchical controller for the vibration control of a deployable manipulator [154]. The emphasis was on the use of knowledge-based tuning of the low-level controller to improve the performance of the system. To this end, a fuzzy inference system (FIS) was developed. The FIS was then combined with a conventional modal controller to construct a hierarchical control system. Specifically, a knowledge-based fuzzy system was used to tune the parameters of the modal controller. The effectiveness of the hierarchical control system was investigated through numerical simulation. Realistic examples were considered where the system experiences vibrations due to initial disturbances at the flexible revolute joint or due to maneuvers of a deployable manipulator.

An adaptive fuzzy sliding mode control was applied onto the attitude stabilization control of a flexible satellite by Guan in 2005 [155], in which the detailed design procedure of the fuzzy sliding mode control system was presented. The adaptive fuzzy control was utilised to approach an equivalent [method](#) of sliding mode control, and then the adaptive law was derived. A hitting control, which guaranteed the stability of the control system, was devel-

oped. In order to attenuate the chattering phenomena, fuzzy rules were employed to smooth the hitting control. Simulation results showed that precise attitude control was accomplished based on the proposed method.

In 2006, Zhou's paper discussed the stability control of equilibrium positions, and a complete model of a tethered satellite system was considered [156], in which a main satellite and a subsatellite were connected by a conductive tether, with mass distributed along it. To regulate both the in-plane and out-of-plane motions of the tether, the current and the rate of change in tether length were employed as two control parameters. A feedback control law was proposed to maintain the radial equilibrium position of the system. It was found that this control law was not applicable for the equatorial plane because no out-of-plane force was available there. For each inclined orbit, it was shown that there were two singularity points. To avoid these points, and by considering some other practical restrictions, the proposed control law was divided into four conditional parts. Numerical cases were provided and the results validated the applicability of the control law.

The dynamics and control of spinning tethers in elliptical orbits for payload rendezvous were studied by Williams in 2006 [100]. The required rendezvous conditions for the tether tip were derived for the case where the tether system centre of mass and payloads were in coplanar elliptic orbits. It was proposed that rendezvous control could be achieved by tracking the unique tip trajectory, which was generated by propagating the rendezvous conditions backwards in time. The range of suitable combinations of tether system orbit eccentricity, tether length, and payload orbit eccentricity, were studied numerically. It was proved that certain combinations of parameters led to non-spinning capture requirements and slack tethers. Control of the tether motion through tether reeling was examined by using a nonlinear model predictive control strategy.

The control problems of two different configurations of tethered satellite systems for NASA's Submillimetre Probe of the Evolution of Cosmic Structure (SPECS) mission were studied by Kim in 2007 [157]. The configuration of the main focus was the TetraStar model, which was composed of three controlled spacecraft and three uncontrolled counterweights. This system was compared with a triangular tethered satellite system consisting of three controlled spacecraft. The equations of motion were derived using Lagrange equation. Several mission scenarios for the SPECS mission considering the operation of an infrared telescope were introduced and asymptotic tracking laws based on Lyapunov control were developed.

In 2007, a tethered satellite cluster system, which consisted of a cluster of satellites connected by tethers, was discussed by Mori and Matunaga [158]. An active control law, which could maintain and change formation of the tether tension and length, was introduced, with

the aim of saving thruster fuel and improving control accuracy. This concept could be applied to tethered multisatellites for in-orbit servicing, which could perform various missions, including inspection, casting, capture, recovery, moorage, and deorbiting of an uncontrolled satellite. The rotational motions of such a system, in which the satellites were in formation flying, were required to rotate about the centre of mass of the system on the same desired plane. The equilibrium conditions that the tether tension imposes on the rotational motion were given, and a coordinated control method for the thrusters, the reaction wheels, and the tether tension or torque was proposed. Numerical simulations and ground experiments showed that the control of the tether tension and torque could not only save thruster fuel, but also improves the position and attitude accuracy of formation flying.

In 2007, Chung, Slotine and Miller [159] published a paper which aimed to investigate a fully decentralised nonlinear control law for spinning tethered formation flight, which was based on exploiting geometric symmetries to reduce the original nonlinear dynamics into simpler stable dynamics. Motivated by oscillation synchronization in biological systems, they used contraction theory to prove that a control law stabilising a single-tethered spacecraft could also stabilise arbitrary large circular arrays of spacecraft, as well as the three inline configuration.

In 2008, Chung, Slotine and Miller also introduced a decentralised attitude control strategy which could dramatically reduce the usage of propellant, by taking full advantage of the physical coupling of the tether [160] [161]. In the first paper [160], they reported propellant-free underactuated control results for tethered formation flying spacecraft, and also described the hardware development and experimental validation of the proposed method using the synchronised position hold, engage and reorient experimental satellites test bed. In particular, a new relative sensing mechanism that uses six-degree-of-freedom force-torque sensors and rate gyroscopes was introduced, which was validated in the closed-loop control experiments. In the second paper [161], they exploited the physical coupling of tethered spacecraft to derive a propellant-free spin-up and attitude control strategy, and then took a nonlinear control approach to under-actuated tethered formation flying spacecraft, whose lack of full state feedback linearisability, along with their complex nonholonomic behaviour, characterises the difficult nonlinear control problem. This article also illustrated the potential of the proposed strategy, by providing a new momentum dumping method that did not use torque-generating thrusters.

Misra presented a paper on dynamics and control of two-body and n-body tethered satellites in 2008 [162]. The multi-tethered systems were initially related to the deployment of multiple probes from a spacecraft to the upper atmosphere and for microgravity applica-

tions, which were modeled as an open chain of tether-connected bodies. At first, nonlinear roll and pitch motions of two-body systems were examined, then the effects of aerodynamic and electrodynamic forces on the stability of a tethered satellite were discussed. Various control schemes to stabilise the dynamics during retrieval of the subsatellite were described, and some dynamics and stability results for n-body tethered satellites were proposed.

## **2.5 Tether Vibration Control and Dynamical Simulations**

In 1971, Tschann's paper on the stability of planar librational motion of an undamped rigid satellite in eccentric orbit was studied through an analog simulation of the governing, nonlinear, non-autonomous equations of motion. The method was extended to investigate the effect of damping on stability and the response of such a system in circular orbit [163].

In 1978, Lips [164] presented a paper on a general formulation for librational dynamics of satellites with an arbitrary number, types, and orientation of deploying flexible appendages. The generalised force term was incorporated making the formulation applicable to a wide variety of situations, where aerodynamic forces, solar radiation, Earth's magnetic field, etc. became significant. In particular, the case of a beam-type flexible appendage deploying from a satellite in an arbitrary orbit was considered. The corresponding nonlinear, non-autonomous equations for in-plane and out-of-plane vibrations were derived, allowing for the variation of mass density, and flexural rigidity along the length with time dependent deployment velocity and spin rate. The linearised analysis of the in-plane vibrational equation using the assumed-mode method and its substantiation through numerical integration were also considered. Simulations for both steady-state and transient attitude behaviour for a representative gravity gradient configuration for a range of initial conditions and system parameters were performed. The results showed the combined effect of flexibility and deployment on the dynamics of the system to be substantial. Disturbance of the appendage could excite large amplitude librations, furthermore, coriolis loading, induced by the extending appendages could become a limiting factor in arriving at a deployment strategy.

A research paper on vibrations of orbiting tethers was proposed by Misra, Xu and Modi in 1986 [165]. It considered three dimensional transverse and longitudinal oscillations of a tether connecting a subsatellite to the shuttle, and also, it focused on the dynamics during the terminal phase of retrieval of the subsatellite. Nonlinearity in the strain-displacement relation was taken into account, since it was important and helpful during this phase. Retrieval schemes that could assist in arresting the growth of vibrations were obtained by simplified analysis and validated through numerical solution of the original equations.

A simulation of an orbiting single tether system composed of two subsatellites and a connecting tether was developed by Carter and Greene in 1992 [166]. The dynamics of the tethered system was modelled by using a series of mass beads inter-connected by springs and dash pots. The bead model allowed the tether to become slack (no tension) and to deform to an arbitrary shape. Simulation results were presented and discussed for two types of motion: (1) tether vibrations and (2) end mass retrieval.

In 1997, Pasca and Monica [72] investigated a tethered satellite system to be flown in the relatively dense atmosphere, which is characterised by strong nonlinearities due to aerodynamic effects. Two mechanical models with different degrees of fidelity, were developed for analysing the systems' static equilibrium. The first model was assumed as a straight tether, and the second tether model was treats a perfectly flexible continuum, and in both of the models, the aerodynamic forces distributed along the system. Simulation results of the first model were used as a starting point for the numerical procedure adopted for computing. The flexible tether model gave a more detailed description of the system mechanics, which was able to deal with an elastic tether with variable diameter and provided amore accurate solution of the static problem. The effectiveness of the proposed control laws was shown by means of both analytical arguments and simulation runs.

The equations of motion for a multi-body tethered satellite system in a three dimensional Keplerian orbit were derived by Kalantzis, Modi, Pradhan and Misra in 1998 [167], which considered a multi-satellite systems, which were connected in series by flexible tethers, both tethers and subsatellites were free to undergo three dimensional attitude motion together with longitudinal and transverse vibration for the tether. The elastic deformations of the tethers were discretised using the assumed-mode method. In addition, the tether attachment points to the subsatellites were kept arbitrary, and time varying with deployment and retrieval degrees of freedom. The governing equations of motion were derived using an order-N Lagrangian formulation. Two independent controllers, an attitude and vibration controller, were designed to regulate the rigid and flexible motion present in the system, which excited from various manoeuvres performed during the course of a mission.

In 2000, a tethered satellite system was modelled by the method of multi-body systems using symbolic equations of motion, and a method of damping structural vibrations using optimisation techniques was presented, and then applied to a tethered satellite system by Dignath and Schiehlen [168]. The system showed large displacements and require active and passive damping mechanisms. Active damping was provided by an actuator between the main body and the tether. The control parameters were optimised, the energy decay of the system was used as the performance criterion. The complex dynamics of the motion of this

system were demonstrated in simulations with different initial conditions including structural vibrations. It was concluded that an optimisation process enables the control parameters could be improved with respect to the dissipation of energy of longitudinal structural vibrations.

Dynamic simulations were performed by Leamy et al. in 2001 [169] for the NASA planned ProSEDS space tether mission using two finite element analysis codes. The first was a specialised code for simulating tethered space systems. The second was an in-house flexible multi-body dynamics code adapted herein for modelling tethered satellites. The simulation of the ProSEDS mission was divided into two operations: a tether deployment operation and an electrodynamic operation. The specialised code used a fixed number of nodes and finite elements in simulating the deployment operation, while the in-house code used a variable number of nodes and elements. A fuzzy-set technique was used in conjunction with the two codes to assess the effect of parameter variations on the deployment and electrodynamic operation of the ProSEDS tether. Detailed numerical simulations revealed that the deployment operation was not sensitive to variations in material parameters, but was sensitive to variations in the initial tether ejection momentum and to controller parameters. The electrodynamic operation was found to be highly sensitive to variations in Earth's magnetic field, and variations in material and plasma parameters.

A tether-mediated rendezvous between a noncooperative payload and a maneuverable tether was considered by Williams in 2005 [170]. The practical scenarios were derived, in which the tether system orbit and payload were inclined relative to each other, and it meant that capture was no longer limited to the orbital plane. The necessary conditions for achieving a zero position and zero velocity rendezvous when the tether system and payload in arbitrary orbits were derived. Three case studies were given, in which, the payload was inclined relative to the tether system by 0.5, 1.0, and 1.5 degree. Two direct transcription methods were used to obtain minimum reel acceleration trajectories for the system. It was inferred that significant manipulation of the three-dimensional dynamics could be achieved under two orbits, using only tension control with smooth variations in tether length. A non-linear receding horizon feedback controller was used to simulate numerically the control of the system with large disturbances to the initial conditions and with changes to the system mass distribution.

In 2006, Krupa et al. [171] presented a paper on tethered satellite systems, which posed quite challenging problems concerning the modelling. Equations of motion and numerical simulations were derived on stability of relative equilibria, provided the system moves on a circular orbit around the Earth and the occurrence of chaotic dynamics. Moreover, for the

processes of deployment, and the retrieval of one satellite from or to another satellite, certain control strategies were studied, which included time and energy optimal control.

A control of an aerial-towed flexible cable system for precision rendezvous and snatch pickup of payloads was considered by Williams et al. in 2006 [172]. Optimal trajectories were determined assuming that the cable remained straight. However, aerodynamic drag and deployment forces could cause bowing of the cable, that could significantly alter the position of the cable tip relative to the aircraft. To account for this, the cable was modelled using lumped masses, connected via rigid links. Multiple rendezvous sequences using only cable winch control and including features, such as collision avoidance and variable winds, were obtained by multiple-phase direct transcription methods. Numerical results showed that for some multiple rendezvous scenarios, it was necessary to use the cable pendular dynamics and swing motion to avoid impact with elevated terrain. The effect of different wind speeds and directions were also studied.

In 2006, Williams [173] discussed a strategy for the control of the librations for a tethered satellite system in elliptic orbits, which using tether length control. For simplicity, only the in-plane motion of the system was considered. The results were obtained with the controlled periodic libration trajectories. He proposed that there was a range of eccentricities up to about 0.4453, for which no length variations were needed for the system to follow the periodic trajectory. Above this eccentricity, it was necessary to vary the length of tether to maintain a periodic trajectory. The method for finding these trajectories to minimise the control input utilised a collocation solution, in which the closed-loop stability was observed by a linear feedback control law, whose feedback gains were also periodic.

A novel concept for the remote delivery of payloads from a fixed wing aircraft was investigated by Williams and Trivailo in 2006 [101]. The concept used taut cable deployed from a circling aircraft as a support structure for sliding payloads from high altitude to the ground. Anchoring the cable tip guaranteed accurate positioning of the cable tip on the ground. Simulations of the cable dynamics suggested that it was necessary to use some form of braking to slow the descent of the payload. If the payload speed was too excessive, then the cable dynamics could become unstable and the peak tension could reach high levels.

A detailed geometrically exact bifurcation analysis was performed by Valverde et al. in 2006 [174], for a model of a power-generating tethered device of interest to the space industries. The structure, a short electrodynamic tether, comprised of a thin, long rod that was spun in a horizontal configuration from a satellite in low Earth orbit with a massive electrically conducting disk at its free end. The system was modelled by using a Cosserat formulation, leading to a system of Kirchhoff equations for the rod's shape as a function of

position and time. Moving to a rotating frame, incorporating the effects of internal damping, intrinsic curvature due to the deployment method and novel force and moment boundary conditions at the contactor, the problem for steady rotating solutions was formulated as a two-point boundary value problem. Using numerical continuation methods, a bifurcation analysis was carried out varying rotation speeds up to many times the critical resonance frequency. Spatial finite differences were used to formulate the stability problem for each steady state and the corresponding eigenvalues were computed. The results showed excellent agreement with earlier multi-body dynamics simulations of the same problem.

In 2007, Williams and Trivailo proposed two papers for the study of the dynamics of circularly towed cable systems [175] [176]. In the paper [175], when a long cable was towed in a circular flight path, the system could exhibit quasi-stationary solutions, for which the cable tip appeared to remain stationary relative to the orbiting aircraft. For applications involving pickup and delivery of payloads, tighter turns at high speeds, which led to nearly stationary motion of the cable tip in an inertial frame. This work studied the dynamics of the cable system, and focused on the stability and equilibria of solutions. A numerical analysis of the system was carried out by using a discretised lumped mass model of the cable. With constrained numerical optimisation, practical towing solutions that achieve small motion of the towed body were obtained. In the second paper [176], when the tow point of an aerial cable system moving in a tight circular path, the drogue at the cable tip would move towards the centre of the circle, and its altitude decreased relative to its equilibrium position in forward flight. Such a system would have both military and civilian applications, including remote pickup and delivery of payloads. This work studied the transitional dynamics of such a system as the aircraft changed from straight flight to circular flight. The system dynamics were modelled using a discretised cable model, allowing the cable to take on zero tension values. Numerical simulation results showed that the cable became slack during the transition if the aircraft turns too rapidly. Parametric studies of the towpath were performed for both tow-in and tow-out maneuvers. Tension waves could be reduced by appropriate control of the tow point. Simulated annealing method was used to optimise some parameters used to specify the tow-in maneuver. Alternatively, a deployment controller was developed using fuzzy logic, that avoided some of these problems by deploying the cable, while the aircraft orbiting. Instability of deployment for certain combinations of cable length and length rate were observed.

## 2.6 Space Tether Dynamical Models

Dumbbell tether is one of the most important tether systems, and a lot of tether systems can be considered as some form of dumb-bell system, in which two massive bodies, not necessarily of the same mass or size, are coupled together by a low-mass tether by which momentum is exchanged between them [1] [2] [177] [178]. In the implication of the general dumb-bell model, the tether is treated as a rigid body. The rigid dumb-bell tether can provide not only for gaining an understanding of general global motions of a tether in space, but also as a fundamental tool for mission conceptualisation. In practice, the elastic tether models will be needed, particularly when very high accuracies are required, both in predicting the tether location and orientation, but also in properly understanding the deformation of a tether in cases where the application is particularly demanding.

In 1989, DeCou [179] discussed the case of the orbiting stellar interferometer with planar deformation of a spinning system comprising three collimating telescopes. The tethers were broken down into segments and an iterative procedure was used to calculate the static shape, in which, axial stretch was mentioned as a parameter. The tether's static shape with finite mass density was determined under the influence of the centrifugal forces, which caused by the rotation, and in the absence of any disturbing dynamic forces, such as gravity gradients, solar radiation pressure, and thermal expansion forces. **These forces' dynamic effects were addressed next as perturbations from the static shape.** The static problem was solved by first deriving nonlinear differential equations relating the position of each tether point to the tension at each point. A numerical solution to these equations was then outlined, and the results of a computer program based on this method were summarised.

In 1992, Kumar, Kumar and Misra [180] presented their work on the effect of deployment rate and librations on tethered payload raising. A special rule for planar librations and circular pre-release orbits was introduced, it showed clear general relationships between apogee altitude gain as a function of deployment rate and explains how suitable deployment rates could be selected for optimising altitude gain, for a given system.

In 1997, Vigneron et al. [181] discussed a dumb-bell tether (up to 1 km) for the OEDI-PUS ionospheric plasma test mission. A mathematical model of the laboratory system was derived, including the terrestrial effects as well as the in-flight phenomena. It was shown that the model was able to reduce to a linear, vibratory, damped, and gyroscopic system, for which an eigenfunction analysis was used to obtain the damped gyroscopic modes shapes, stability, and natural frequencies for various physical configurations. Meanwhile, this work

also showed that linear modelling could be used to represent modal frequencies and payload attitude stability quite well, however, it obviously did not cover all the possible dynamical phenomena in the system, and would overlook certain regions of convergent attitude motion and limit cycle behaviour.

In 1998, Cartmell [67] presented a motorised momentum exchange tether system, which showed that forced, motor driven spin could be generated for a large symmetrical dumb-bell tether, and that complicated non-planar motions of the tether could also be initiated. Based on this preliminary model, in this thesis, a series of new motorised momentum exchange tether models will be discussed.

A general stability and control problem which exists with long tethers in space was examined in 2000 by Kumar and Kumar [182]. A stability criterion was evolved for a simplified situation using first order perturbation equations around the nominal equilibrium configuration. The set of complicated ordinary nonlinear differential equations was non-dimensionalised and the reduced parameter space was numerically explored.

Mazzoleni and Hoffman investigated the non-planar spin-up dynamics of the advanced safety tether operation and reliability (ASTOR) satellite in [183] and showed that this spin-up manoeuvre was an example of artificial gravity, which could perhaps be harnessed within human-based missions in the future. If tethers were to be used successfully for artificial gravity generation then attitude control of the end bodies was also required during spin-up.

Tether retrieval is the opposite of deployment and is equally important in dynamical terms. Retrieval of a sub-satellite to a larger vehicle, specifically a space station, was examined by Djebli et al. [112] in 2002, which concentrated on laws for retrieval and also deployment, specifically combining ‘simple’ linear or exponential retrieval and ‘fast’ laws, and specific acceleration profiles were also proposed. This would be applicable to passive momentum exchange tethers and potentially to ED tethers.

An artificial gravity system was discussed by Mazzoleni and Hoffman in 2003 [184], which comprised two tethered satellites and included tether elasticity within the so-called tethered artificial gravity satellite. The so-called ‘g-force’ was generated by the tether, which could maximise the  $r$  and minimise the  $\omega$  within the  $r\omega^2$ . The spin-up phase was also examined in particular and it was found that an initial out-of-plane angle of the system and the location of the tether attachment point could both significantly affect the dynamics of the end-body motion of a tethered satellite system during spin-up.

As one objective and new idea for this thesis, it will discuss the spin-up performance for the motorised momentum exchange tether system, which incorporating axial, torsional and pendular elastic effects.

## 2.7 Conclusions

In this chapter, the literature review work focuses on five topics which are related to the space tether control researches: ⟨1⟩ tether deployment and retrieval; ⟨2⟩ trajectory generation and orbit control; ⟨3⟩ tether attitude and motion control; ⟨4⟩ tether vibration control and dynamical simulations; ⟨5⟩ space tether dynamical models. With the basic aim of establishing useful sources of fundamental researches in the literature, and highlighting the previous control methods developed, this chapter attempts to provide a useful contextualised source of references for the further space tether control studies.

The momentum exchange tether is a one of the most important key technology offering major potential applications for reductions in space transportation costs, and a wide potential range of space missions. An indepth review of mechanical tether system performance was conducted by Ziegler and Cartmell [62], who showed conclusively that motorised spinning momentum exchange tethers demonstrate the best performance and also potentially the most efficient performance. The motorised momentum exchange tether (MMET) has received extensive modelling effort, both for circular and elliptical orbital contexts [62][67], since then, the MMET has been one of the most important subjects of momentum exchange tether development, and in this thesis a series of new MMET systems will be investigated in Chapter 3 to Chapter 7.

In 2004, Mouterde, Cartmell and Wang [185] presented a paper to investigate the general problem of unexpected changes to two example system parameters in the motorised momentum exchange tether context with spin-up control applied specifically by means of conventional feedback linearisation with adaptive gains. To compare the feedback linearised control for a rigid body motorised momentum exchange tether on an elliptical Earth orbit, two control methods for a flexible motorised momentum exchange tether spin-up behaviour, which include a fuzzy logic control method and a hybrid fuzzy sliding mode control method, will be discussed in this thesis, and the control objective of MMET's spin-up is one of the last potential applications.

## Chapter 3

---

# The Motorised Momentum Exchange Tether

---

### 3.1 Introduction

This chapter introduces the basic concepts in momentum exchange modelling and the conceptual modelling of the symmetrical motorised momentum exchange tether (MMET), which includes dumbbell tether systems, a rigid massless MMET system, and a solid tether-tube subspan MMET system, all using the Lagrangian procedure. The Lagrange equation is given in the form of equation (3.1.1) [186].

$$\frac{d}{dt} \left[ \frac{\partial T}{\partial \dot{q}_i} \right] - \frac{\partial T}{\partial q_i} + \frac{\partial U}{\partial q_i} = Q_i \quad (3.1.1)$$

$$i = 1, 2, \dots, N$$

Where the  $Q_i$  is the generalised force for the corresponding generalised coordinate  $q_i$ ,  $U$  is the potential energy, and  $T$  is the kinetic energy.

The Lagrange equation is taken as the modelling tool for all the MMET systems, as shown in Figure 3.1, which includes generalised coordinates, generalised forces and energy components [187]; this also helps to organise the chapters.

Environmental effects such as solar radiation, aerodynamic drag and electrodynamic forces, which can influence the tether modelling, are all assumed to be negligible in the space tether modelling context. In addition to the assumptions made in deriving the equations of motion for all types of the MMET modelling, the bearing connecting the motor's rotor and stator is assumed to be perfect and to cause no significant frictional losses. This assumption implies that the outrigger will behave qualitatively identically to the propulsion side but will

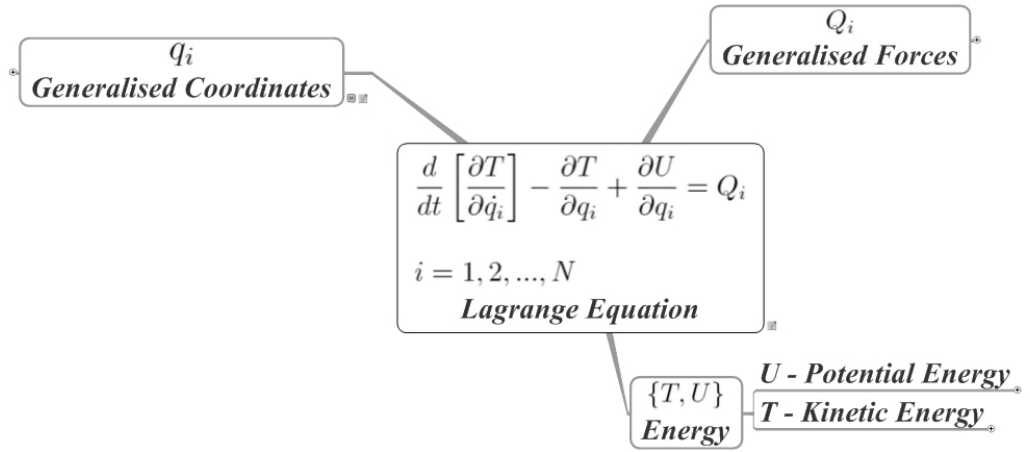


Figure 3.1: [Mathematical components for Lagrange equation \[187\]](#)

rotate in the opposite direction and, thus, this potentially requires only the propulsion side to be modelled. The power supplies, control systems, and communication equipment are assumed to be fitted within the surrounding stator assembly in a practical installation. The stator provides the necessary reaction, through coupling across the motor, which is required for the rotor to spin-up in a friction-free environment. Unless stated otherwise, all of the modelling is based on the conditions stated above. All the dynamical [models](#) for MMET systems are processed under these environmental conditions without further declaration.

Because of the similarity of the tether and the outrigger in the system, only the modelling and simulations of the tether will be discussed in the following chapters. The outrigger modelling can be discussed in a similar way and will not be described in full detail in this context.

## 3.2 Dumbbell Tether

A dumbbell tether system is a type of momentum exchange tether system, as shown in Figure 3.2, in which there are two generalised coordinate systems. One is an Earth centred global coordinate system -  $\{X, Y, Z\}$ , and the other is the relative rotating coordinate system -  $\{x_0, y_0, z_0\}$ . The centre of the Earth is denoted by  $E(E_x, E_y, E_z)$ , which is defined as the origin of the  $\{X, Y, Z\}$  system, where,  $E_x, E_y, E_z$  are set to  $(0, 0, 0)$ , that is,  $E(0, 0, 0)$  [3] [65].

The dumbbell tether system consists of two end masses,  $M_1$  and  $M_2$ , connected by the tether subspans, where the distance from the dumbbell tether's base point to each end mass is denoted by  $L_1$  and  $L_2$ . The dumbbell tether subspans are assumed to be massless relative to the masses of the two end bodies. These are treated as point masses with no mass moments of inertia.  $R$  is the distance from  $E(0, 0, 0)$  to the dumbbell tether's base point  $P_0$ , which is

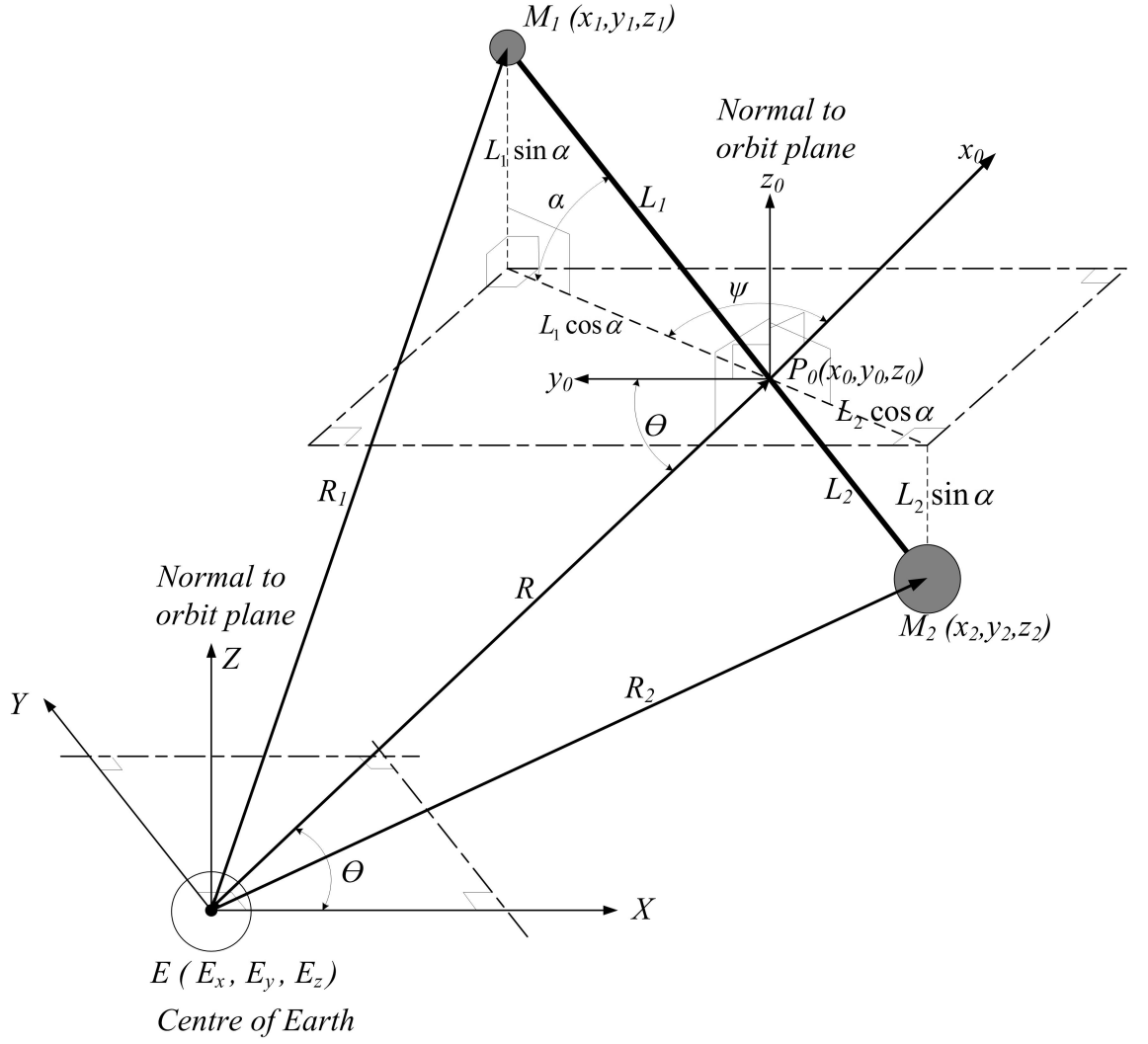


Figure 3.2: The dumbbell tether dynamical model [3] [65]

shown in equation (3.2.1) [3].  $R_1$  and  $R_2$  are the distances from  $E(0,0,0)$  to mass points  $M_1(x_1, y_1, z_1)$  and  $M_2(x_2, y_2, z_2)$ , respectively, which are shown in equations (3.2.2) and (3.2.3). Equations (3.2.4), (3.2.5) and (3.2.6) define the location for the base point and two payloads at each end of the tether [65].

$$R = \frac{r_p (1 + e)}{1 + e \cos \theta} \quad (3.2.1)$$

where,  $r_p$  is the radius at periapsis,  $e$  is the eccentricity,  $\theta$  is the true anomaly.

$$R_1 = \sqrt{x_1^2 + y_1^2 + z_1^2} = \sqrt{L_1^2 + R^2 + 2L_1 R \cos \alpha \cos \psi} \quad (3.2.2)$$

$$R_2 = \sqrt{x_2^2 + y_2^2 + z_2^2} = \sqrt{L_2^2 + R^2 - 2L_2 R \cos \alpha \cos \psi} \quad (3.2.3)$$

Figure 3.3 is the counter-Z-direction view of Figure 3.2. The  $X, Y$  plane and the  $x_0, y_0$  plane lie coplanar to the orbit plane, where the  $Z$  and  $z_0$  axes are perpendicular to the orbit

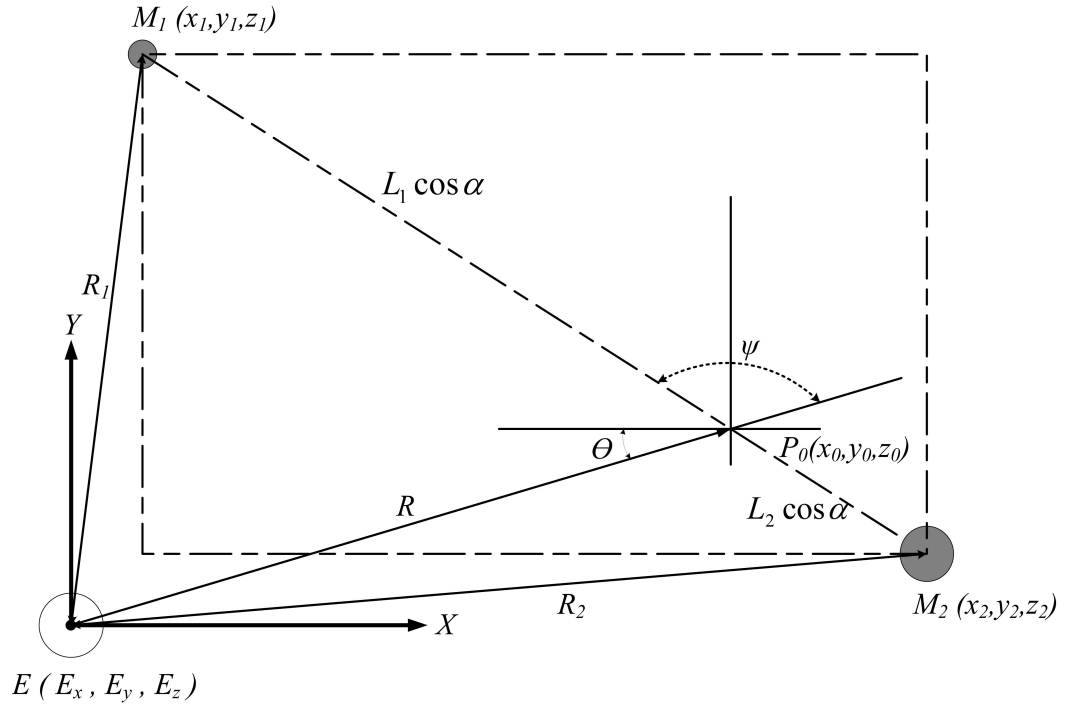


Figure 3.3: **The dumbbell tether dynamical model - top view**

plane. The  $X$  axis is aligned along the direction of the perigee of the orbit, and the  $x_0$  axis is an extension of  $R$ .  $\psi$  is the in-plane pitch angle, and this denotes the angle from the  $x_0$  axis to the projection of the tether onto the orbit plane.  $\alpha$  is the out-of-plane angle, from the projection of the tether onto the orbit plane to the tether, and is always within a plane normal to the orbit plane.  $\theta$  is the circular or elliptical orbit angular position, effectively the true anomaly.  $R$ ,  $\theta$ ,  $\alpha$ ,  $\psi$  are independent generalised coordinates and are functions of time. In the case of a planar circular orbit, the  $R$  and  $\dot{\theta}$  are constants.

As shown in in Figures 3.2 and 3.3, the Cartesian components of the base point  $P_0$  and the end masses of  $M_1$  and  $M_2$  are given in equations (3.2.4), (3.2.5) and (3.2.6) [65].

$$\begin{cases} x_0 = R \cos \theta \\ y_0 = R \sin \theta \\ z_0 = 0 \end{cases} \quad (3.2.4)$$

$$\begin{cases} x_1 = x_0 + L_1 \cos \alpha \cos (\theta + \psi) \\ y_1 = y_0 + L_1 \cos \alpha \sin (\theta + \psi) \\ z_1 = z_0 + L_1 \sin \alpha \end{cases} \quad (3.2.5)$$

$$\begin{cases} x_2 = x_0 - L_2 \cos \alpha \cos (\theta + \psi) \\ y_2 = y_0 - L_2 \cos \alpha \sin (\theta + \psi) \\ z_2 = z_0 - L_2 \sin \alpha \end{cases} \quad (3.2.6)$$

### 3.2.1 Kinetic Energy

As the end masses are treated as point masses without mass moment of inertia measurements, the kinetic energy of the system comprises solely the translation of the end payloads, and is given in equation (3.2.7). The prime denotes differentiation with respect to time.

$$T = \frac{1}{2}M_1 (\dot{x}_1^2 + \dot{y}_1^2 + \dot{z}_1^2) + \frac{1}{2}M_2 (\dot{x}_2^2 + \dot{y}_2^2 + \dot{z}_2^2) \quad (3.2.7)$$

where, assuming the moment equilibrium in equation 3.2.8 [3] [65].

$$M_1 L_1 = M_2 L_2 \quad (3.2.8)$$

### 3.2.2 Potential Energy

The gravitational potential energy is obtained by implementing Newton's gravitational law [3] and by convention defining one of the states of the evaluated integral to be zero at infinity. Thus, the tether's potential energy is given in equation (3.2.9),  $\mu$  is the product of the universal gravitational constant  $G$  with the Earth's mass,  $L_1$  and  $L_2$  are the two tether subspan lengths.

$$\begin{aligned} U &= -\frac{\mu M_1}{R_1} - \frac{\mu M_2}{R_2} \\ &= -\frac{\mu M_1}{\sqrt{L_1^2 + R^2 + 2L_1 R \cos \alpha \cos \psi}} - \frac{\mu M_2}{\sqrt{L_2^2 + R^2 - 2L_2 R \cos \alpha \cos \psi}} \end{aligned} \quad (3.2.9)$$

### 3.2.3 Generalised Coordinates

The preferred choice of generalised coordinates depends on what is required of the analysis as well as on algebraic considerations. It is known that in orbital system there can be tendencies for unwanted singularities if the choice of coordinates is not optimal. Based on this basic requirement, in the case of dumbbell modelling, it is decided to represent the system dynamics by means of three angular coordinates ( $\psi, \theta, \alpha$ ) and one translational coordinate ( $R$ ).

Table 3.1: The dumbbell tether generalised coordinates and generalised forces

$i$	$q_i$	$Q_i$	$T$	$U$	Equations of Motion
1	$\psi$	0	(3.2.7)	(3.2.9)	(3.2.10)
2	$\theta$	0			(3.2.11)
3	$\alpha$	0			(3.2.12)
4	$R$	0			(3.2.13)

As given in Table 3.1, the selection of the generalised coordinates  $q_i$  are as following:

- 1)  $\psi$  is the in-plane pitch angle, and this denotes the angle from the  $x_0$  axis to the projection of the tether onto the orbit plane.
- 2)  $\theta$  is the elliptical orbit angular position, effectively, the true anomaly.
- 3)  $\alpha$  is the out-of-plane angle, from the projection of the tether onto the orbit plane to the tether, and it is always within a plane normal to the orbit plane.
- 4)  $R$  is the space tether's position generalised coordinate, which indicates the distance from the Earth  $E(0, 0, 0)$  to the base point  $P_0(x_0, y_0, z_0)$ .

### 3.2.4 Generalised Forces

The generalised forces  $Q_i$ ,  $i = 1$  to 4, are all zeros, since no non-conservative forces are acting on this system, in which the generalised coordinates are  $q_1 = \psi$ ,  $q_2 = \theta$ ,  $q_3 = \alpha$ ,  $q_4 = R$ .

### 3.2.5 Governing Equations of Motion

According to the Lagrange equation (3.1.1), the following motion equations for generalised coordinates  $q_i$  are derived and stated in equations (3.2.10) to (3.2.13).

$$\begin{aligned}
 & -\frac{\mu M_1 L_1 R \cos \alpha \sin \psi}{(R^2 + 2RL_1 \cos \alpha \cos \psi + L_1^2)^{3/2}} + \frac{\mu M_2 L_2 R \cos \alpha \sin \psi}{(R^2 - 2RL_2 \cos \alpha \cos \psi + L_2^2)^{3/2}} \\
 & + (M_1 L_1^2 + M_2 L_2^2) (\cos^2 \alpha (\ddot{\theta} + \ddot{\psi}) - \dot{\alpha} \sin 2\alpha (\dot{\theta} + \dot{\psi})) \\
 & + 2 \cos^2 \alpha (\dot{\theta} + \dot{\psi}) (M_1 L_1 \dot{L}_1 + M_2 L_2 \dot{L}_2) = Q_\psi
 \end{aligned} \tag{3.2.10}$$

$$\begin{aligned}
 & (R^2 \ddot{\theta} + 2R\dot{R}\dot{\theta}) (M_1 + M_2) + (M_1 L_1^2 + M_2 L_2^2) (\cos^2 \alpha (\ddot{\theta} + \ddot{\psi}) - \dot{\alpha} \sin 2\alpha (\dot{\theta} + \dot{\psi})) \\
 & + 2 \cos^2 \alpha (\dot{\theta} + \dot{\psi}) (M_1 L_1 \dot{L}_1 + M_2 L_2 \dot{L}_2) = Q_\theta
 \end{aligned} \tag{3.2.11}$$

$$\begin{aligned}
& -\frac{\mu M_1 L_1 R \cos \psi \sin \alpha}{(R^2 + 2RL_1 \cos \alpha \cos \psi + L_1^2)^{3/2}} + \frac{\mu M_2 L_2 R \cos \psi \sin \alpha}{(R^2 - 2RL_2 \cos \alpha \cos \psi + L_2^2)^{3/2}} \\
& + (M_1 L_1^2 + M_2 L_2^2) \left( \ddot{\alpha} + \frac{1}{2} \sin 2\alpha (\dot{\theta} + \dot{\psi})^2 \right) \\
& + 2\dot{\alpha} (M_1 L_1 \dot{L}_1 + M_2 L_2 \dot{L}_2) = Q_\alpha
\end{aligned} \tag{3.2.12}$$

$$\begin{aligned}
& \frac{\mu M_1 (R + L_1 \cos \alpha \cos \psi)}{(R^2 + 2RL_1 \cos \alpha \cos \psi + L_1^2)^{3/2}} + \frac{\mu M_2 (R - L_2 \cos \alpha \cos \psi)}{(R^2 - 2RL_2 \cos \alpha \cos \psi + L_2^2)^{3/2}} \\
& + (M_1 + M_2) (\ddot{R} - R\dot{\theta}^2) = Q_R
\end{aligned} \tag{3.2.13}$$

### 3.2.6 Simulations and Discussions

Numerical results are obtained using MATHEMATICA for the selected generalised coordinates  $\psi$ ,  $\theta$ ,  $\alpha$  and  $R$ , as listed in Table 3.1. The parameters for the dumbbell tether system simulations are given in Appendix C. Unless stated, all the MMET simulation results in the following chapters are generated by the parameters in Appendix C.  $T_n$  is the number of cycles of period, as defined in Chapter 1 equation (1.1.11), in this case of  $e = 0.2$ , when  $T_n = 4.01$ , the simulation time  $t$  is 0 to  $3.1899 \times 10^4$  seconds; when  $T_n = 400.01$ , the simulation time  $t$  is 0 to  $3.1811 \times 10^6$  seconds.

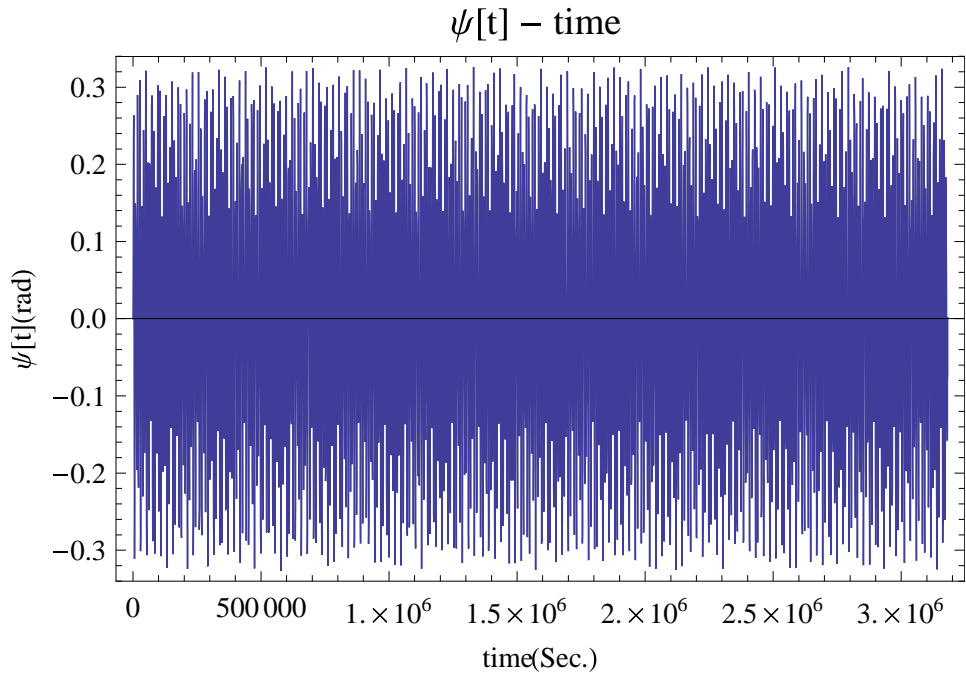


Figure 3.4: Dumbbell tether spin-up, angular displacement  $\psi$  ( $T_n = 400.01$ )

▷ The spin-up generalised coordinate is  $\psi$ , which denotes the angle from the  $x_0$  axis to the projection of the tether onto the orbit plane, as shown in Figure 3.2. With the given

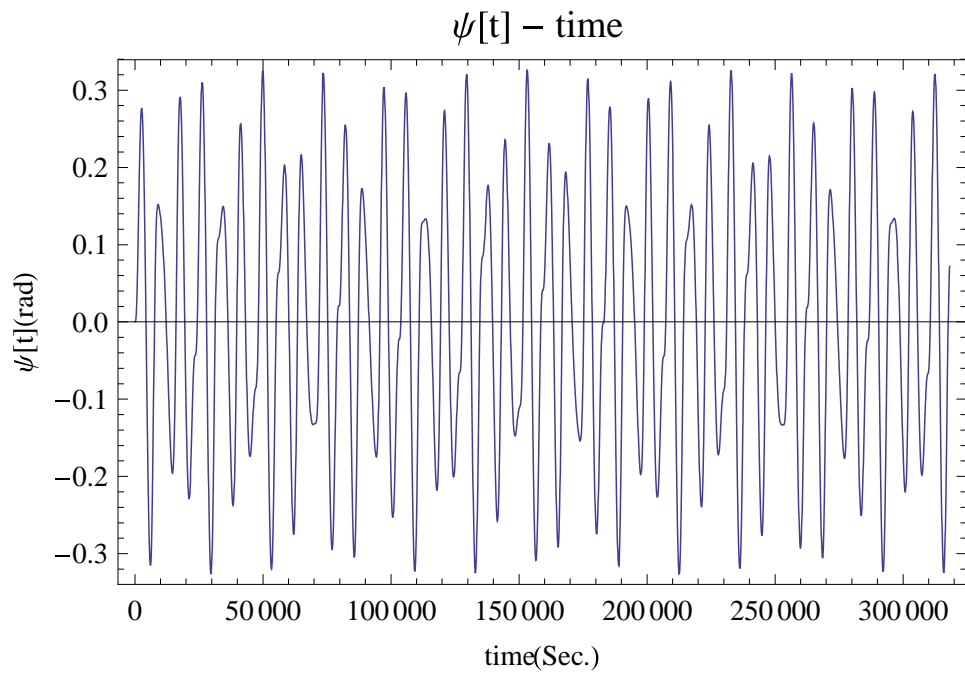


Figure 3.5: Dumbbell tether spin-up, angular displacement  $\psi$  ( $T_n = 40.01$ )

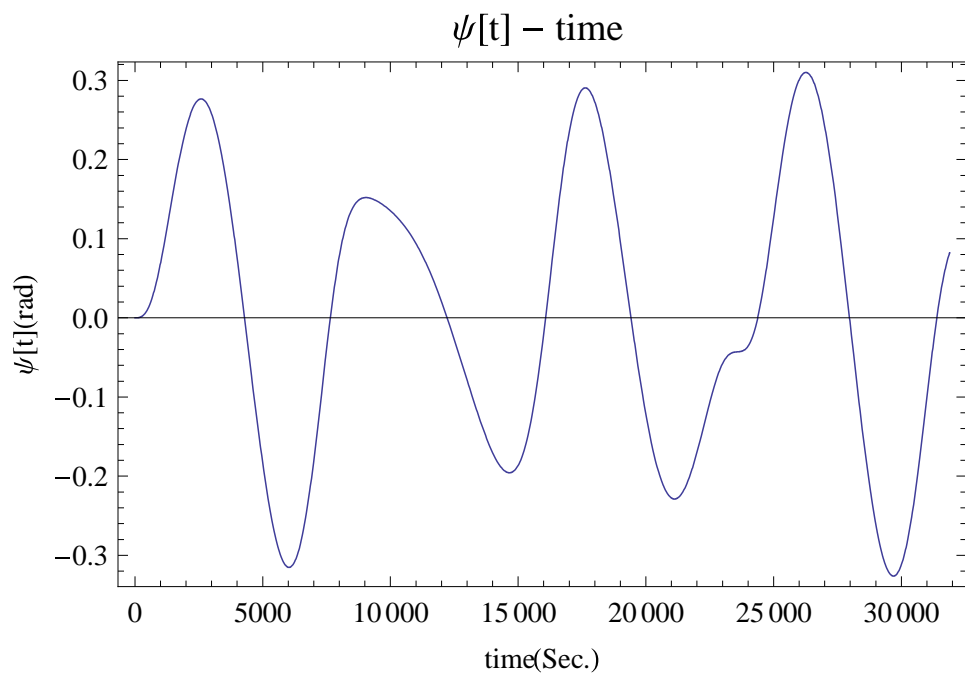


Figure 3.6: Dumbbell tether spin-up, angular displacement  $\psi$  ( $T_n = 4.01$ )

parameters in Appendix C, the  $\psi$  response's amplitude goes between -0.325 to 0.325 rad, periodically, as shown in Figures 3.4, 3.5 and 3.6, which describe the dumbbell tether's periodic spin-up (the period is about 180,000 seconds) behaviour during the simulation time with the number of cycles of period  $T_n = 400.01$ , 40.01 and 4.01. Figure 3.6 states the dumbbell tether's periodic spin-up behaviour during NCP  $T_n = 4.01$ , which is the first 10 percent of Figure 3.4 with  $T_n = 400.01$ .

▷ Figures 3.7 and 3.8 describe the stable increasing  $\theta$  angle of orbit position with slight

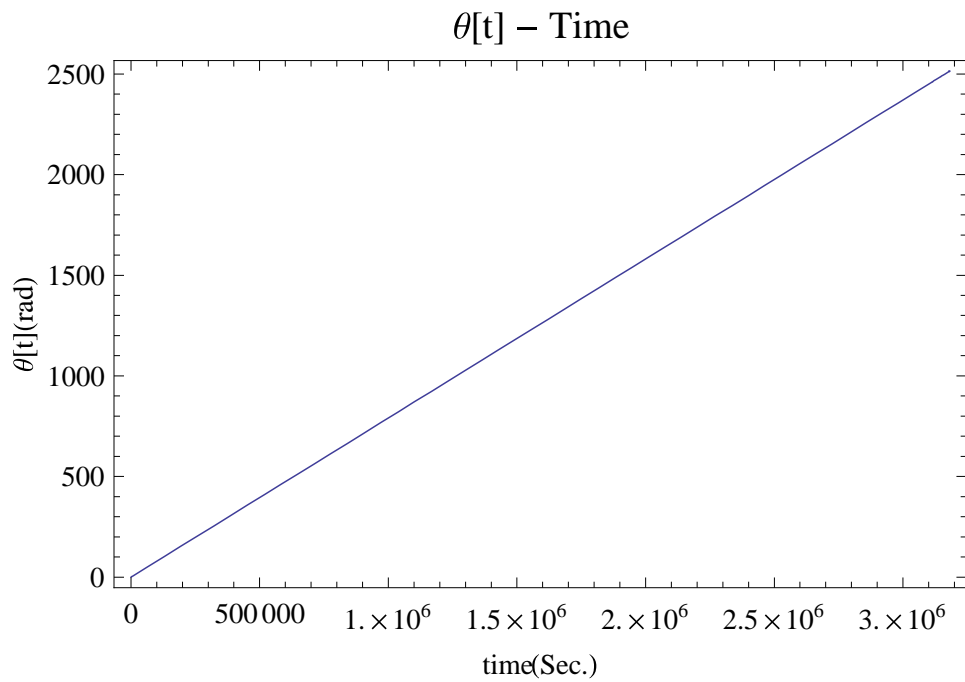


Figure 3.7: Dumbbell tether true anomaly on elliptical orbit, angle  $\theta$  ( $T_n = 400.01$ )

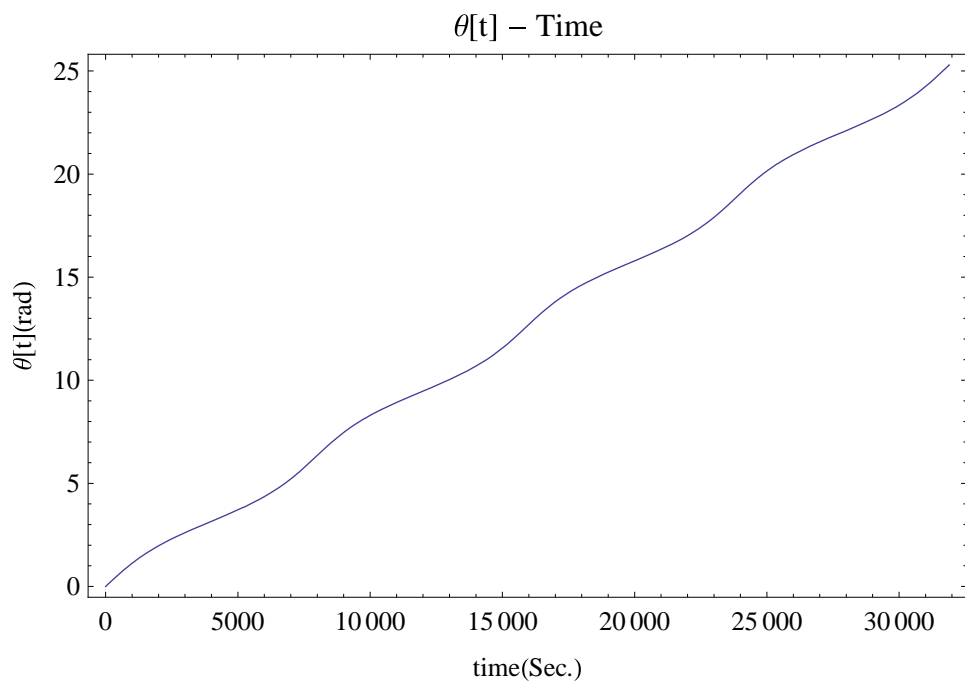


Figure 3.8: Dumbbell tether true anomaly on elliptical orbit, angle  $\theta$  ( $T_n = 4.01$ )

fluctuation around the Earth during  $T_n = 4.01$  and  $T_n = 400.01$  simulation time.

▷ Figures 3.9 and 3.10 state the dumbbell tether’s position changing around the Earth periodically, together with Figures 3.4 and 3.8, they can express the specific trajectory and position for the dumbbell tether during the full simulation time for the NCP  $T_n = 400.01$  and  $T_n = 4.01$ , within the amplitude range from  $r_p$  to  $r_a$ .

▷ The out-of-plane angle  $\alpha$  for the dumbbell tether is staying in a planar status, whose

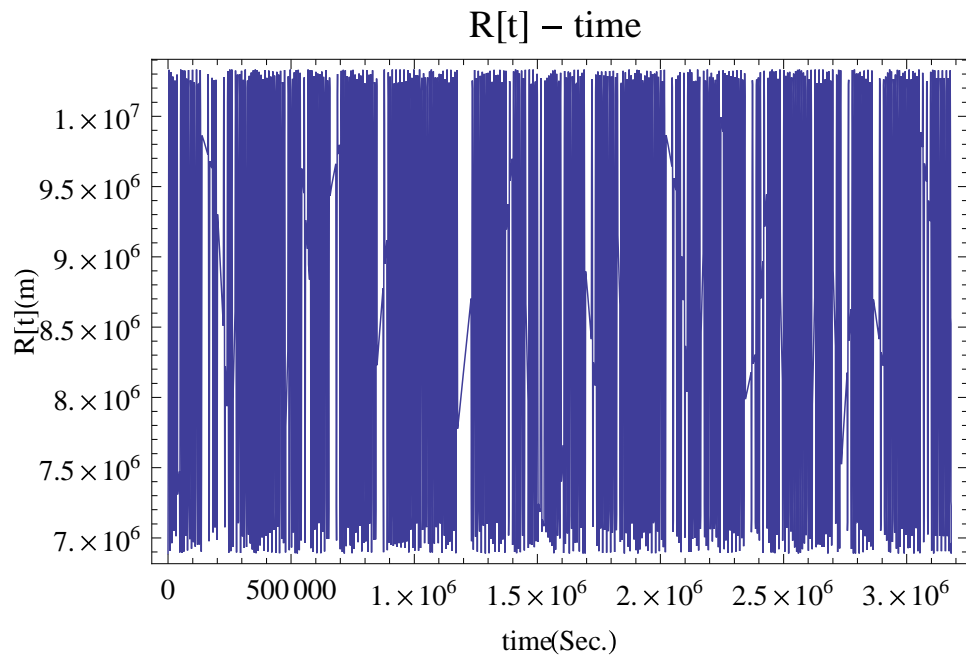


Figure 3.9: Dumbbell tether distance  $R$  ( $T_n = 400.01$ )

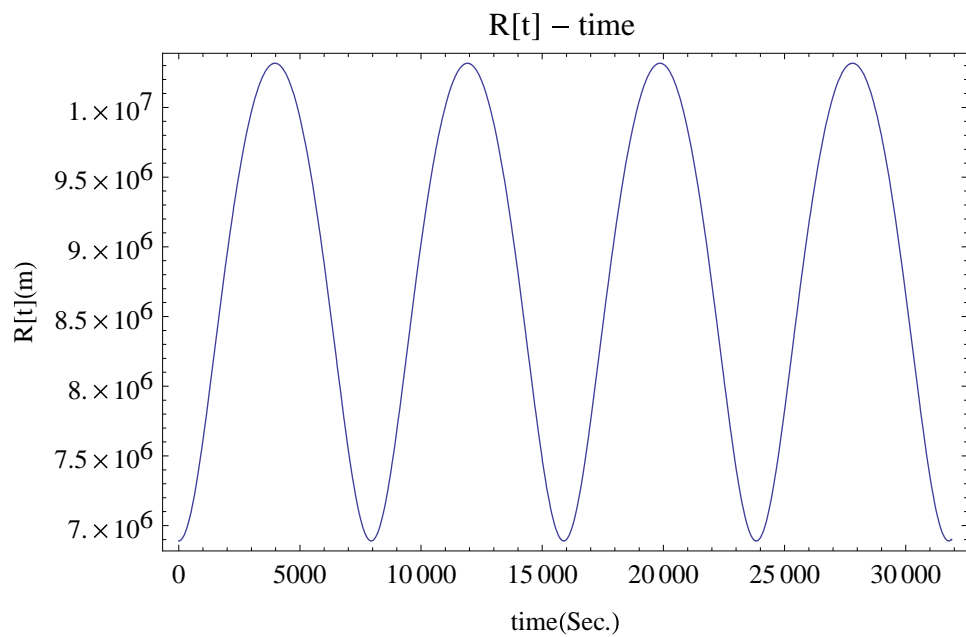


Figure 3.10: Dumbbell tether distance  $R$  ( $T_n = 4.01$ )

response is zero over simulation time, with zero initial conditions ( $\alpha(0) = 0$  rad and  $\dot{\alpha}(0) = 0$  rad/s). With the non-zero initial values, as shown in Figure 3.11,  $\alpha(0) = 0.001$  rad and  $\dot{\alpha}(0) = 0.001$  rad/s, the out-of-plane angle  $\alpha$  is acting periodically around the reference plane.

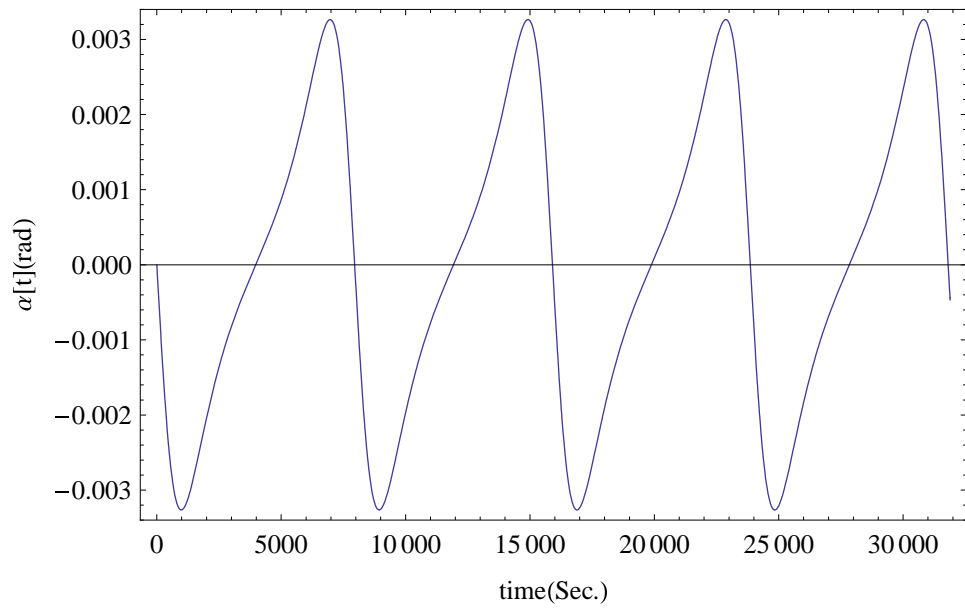


Figure 3.11: Dumbbell tether out-of-plane angle  $\alpha$  ( $T_n = 4.01$ )

### 3.3 The Motorised Momentum Exchange Tether

The concept of the motorised momentum exchange tether (MMET) was first proposed by Cartmell [67], and its modelling and conceptual design were developed further, in particular the modelling of the MMET system as a rigid body was developed by Ziegler and Cartmell [62], and the modelling of the MMET system with axial elasticity was developed by Chen and Cartmell [71].

The basic conceptual schematic of the MMET system is shown in Figure 3.12. The system is composed of the following parts: a pair of propulsion tether subspans (#A and #B in Figure 3.12), a corresponding pair of outrigger tether subspans (#C and #D in Figure 3.12), the launcher motor mass within the rotor and the launcher motor mass within the stator (#J and #I in Figure 3.12), the outrigger masses (#H and #G in Figure 3.12), and the two payload masses (#E and #F in Figure 3.12), as also shown in Table 3.2. The MMET system is excited by means of a motor, and the dynamical model using angular generalised coordinates to represent spin and tilt, together with the true anomaly for circular orbital motion, or the true anomaly and a variable radius coordinate for elliptical orbits. Another angular coordinate defines the backspin of the propulsion motor's stator components. The payload masses are fitted to each end of the tether subspans, and the system orbits a source of gravity in space, in this case the Earth. The use of a tether generally means that all constituent parts of the system have the same angular velocity as the overall centre of mass (COM). As implied in Figure 3.12, the symmetrical double-ended motorised spinning tether can be applied as an orbital transfer system, in order to exploit momentum exchange for propelling and transferring payloads in space. A series of terrestrial scale model tests of the MMET system were carried out on ice by Cartmell and Ziegler in 2001 [68] and 2003 [69], as shown in Figure 3.13.

Table 3.2: The components of the basic conceptual schematic of the MMET system

Position	Component
# A	Braided propulsion tether subspan
# B	Braided propulsion tether subspan
# C	Braided outrigger tether subspan
# D	Braided outrigger tether subspan
# E	Payload mass
# F	Payload mass
# G	Outrigger mass
# H	Outrigger mass
# I	Launcher mass (stator)
# J	Launcher mass (rotor)

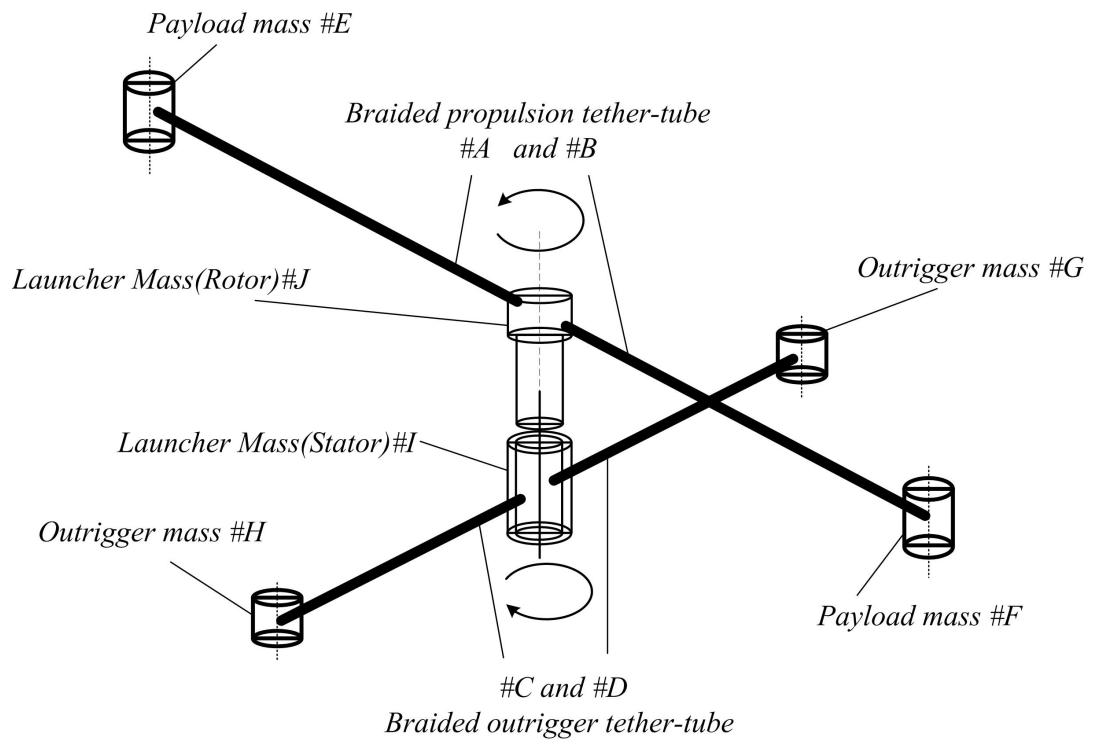


Figure 3.12: The conceptual schematic of the motorised momentum exchange tether [67]

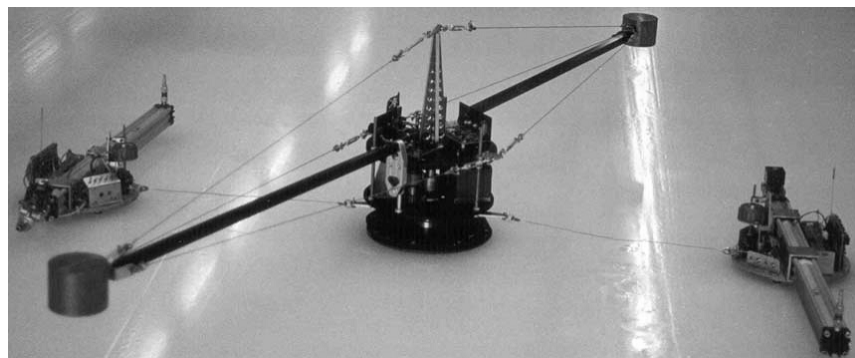


Figure 3.13: The scale model of the MMET experiment on ice [68] [69]

This novel concept is of a long tethered system with a mass at each end, where one mass can be regarded as a launcher, essentially consisting of an electric motor, and the other as the payload. The tether is a long line of appropriate cross section and material properties. The principle of operation is that once the tether is deployed the launcher motor is energised with the result that the whole system starts to spin in a circle about its overall centre of mass. The system is then allowed to accelerate until the tangential velocity of the payload reaches the required level. The main aims of these studies for MMET system are as follows [2] [67] :

- ⟨1⟩ To limit the use of electrical (solar) power in order to build up rotational energy over time;
- ⟨2⟩ To achieve velocity increments (tangential to the payload spin-circle) necessary for inter-planetary launch of sizeable payloads;

⟨3⟩ To build in as much system re-use as possible;

⟨4⟩ To exploit new tether technologies for long-term, reliable deployment.

The basic capabilities of mechanical tethers for space transportation could be related to scenarios, which involve transport from ground to Earth orbit, transfer from low Earth orbit to geostationary orbit, and injection into interplanetary trajectories. Additionally, with these basic lift capabilities, they offered also propulsionless de-orbiting of satellites, de-orbiting of re-entry capsules, and orbit injection and descent initiation at other planetary bodies. The mechanical tethers all exploited the concept of momentum exchange in one way or another and tend to fall into one of three operational categories based on hanging orientations, systems exhibiting librating motions, and spinning systems. Librating mechanical and electrodynamic tethers and their possible technical feasibility have received the most attention so far.

In 2001, Ziegler and Cartmell's paper [62] demonstrated a symmetrically laid out system, in which the driving motor facility is attached half way along a tether. It has two identical payloads at either end, it could be made to spin-up by means of a controlled counter-inertia attached to the motor stator. An in-depth treatment of the rigid body dynamics of tethers in space was given, in which the dumb-bell tether was modelled at various levels of accuracy, and approximate analytical solutions were obtained by means of the method of multiple scales for periodic solutions. Comprehensive dynamical systems analyses were summarised for different configurations and models, and global stability criteria for a rigid body dumb-bell tether, in both passive and motorised forms, were also defined and investigated. Further treatment of the spin-up criterion was also provided.

Gravity gradient stabilisation is an important underpinning phenomenon when considering spacecraft stability, and this is particularly the case for long momentum exchange tethers. The work in 2003 by Cartmell et al. [69] considered dumb-bell models for momentum exchange tethers. Offshoots and developments made after this work had shown conclusively that hanging, librating, and spinning tether motions were intimately connected to this fundamental phenomenon.

In 2003, Eiden and Cartmell discussed the tether systems roadmap for space transportation applications [64], in which some potential applications for continuation of the staged MMET system research were discussed, as shown below:

⟨1⟩ There will be colonisation of the Moon in the future and regular two-way freight transportation will then be a necessity;

⟨2⟩ Staged MMET based systems will provide extremely low cost regular payload exchange between two planetary bodies;

⟨3⟩ Staged MMET transportation offers reusable environmentally acceptable transportation of bulk material on the basis that computers and sensors, plus the necessary orbital maintenance, are considerably cheaper and cleaner than burning large quantities of toxic rocket fuel;

From this section on, all the MMET models are based on the motorised momentum exchange tether conceptual schematic. Figure 3.13 is the scale MMET model experiment on ice in 2001 and 2003 [68] [69].

### 3.4 The Dumbbell MMET

As shown in Figure 3.14, the dumbbell MMET system consists of two end payload masses  $M_P$  at each end, are connected by a massless tether with the same length of subspans from the tether's centre of mass  $M_M$ , denoted by  $L$ .  $R$  is the distance from  $E(0,0,0)$  to  $M_M(x_0, y_0, z_0)$ , which is the same as introduced in section 3.2.

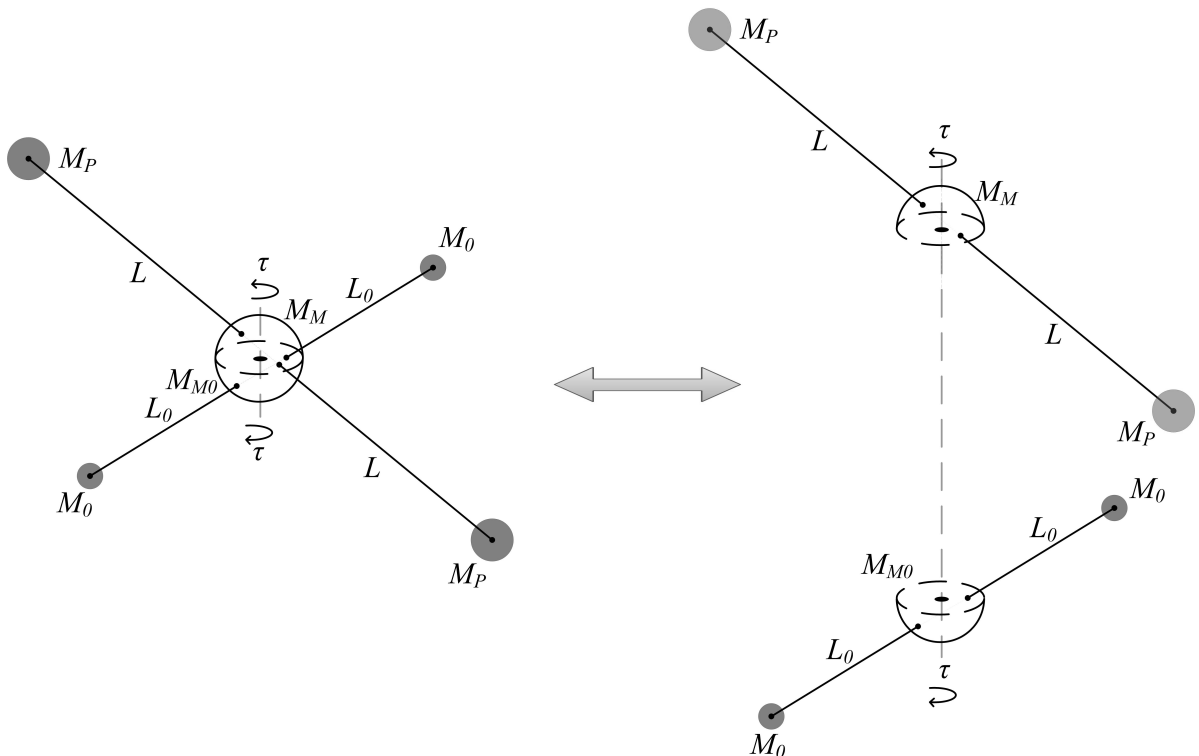


Figure 3.14: **The conceptual schematic of the dumbbell motorised momentum exchange tether**

$$R_1 = \sqrt{x_1^2 + y_1^2 + z_1^2} = \sqrt{L^2 + R^2 + 2LR \cos \alpha \cos \psi} \quad (3.4.1)$$



$$\begin{cases} x_1 = x_0 + L \cos \alpha \cos (\theta + \psi) \\ y_1 = y_0 + L \cos \alpha \sin (\theta + \psi) \\ z_1 = z_0 + L \sin \alpha \end{cases} \quad (3.4.3)$$

$$\begin{cases} x_2 = x_0 - L \cos \alpha \cos (\theta + \psi) \\ y_2 = y_0 - L \cos \alpha \sin (\theta + \psi) \\ z_2 = z_0 - L \sin \alpha \end{cases} \quad (3.4.4)$$

### 3.4.1 Kinetic Energy

The equations of the dumbbell MMET system with massless subspans are obtained via the Lagrangian formulation. Figure 3.16 is the z-oriented view which is looking to the origin of Figure 3.15. As the end masses are treated as point masses, the kinetic energy of the system comprises solely the translation of the end bodies in equation (3.4.5), with  $M_0 = M_M$ .

$$T = \frac{1}{2}M_1 (\dot{x}_1^2 + \dot{y}_1^2 + \dot{z}_1^2) + \frac{1}{2}M_2 (\dot{x}_2^2 + \dot{y}_2^2 + \dot{z}_2^2) + \frac{1}{2}M_0 (\dot{x}_0^2 + \dot{y}_0^2 + \dot{z}_0^2) \quad (3.4.5)$$

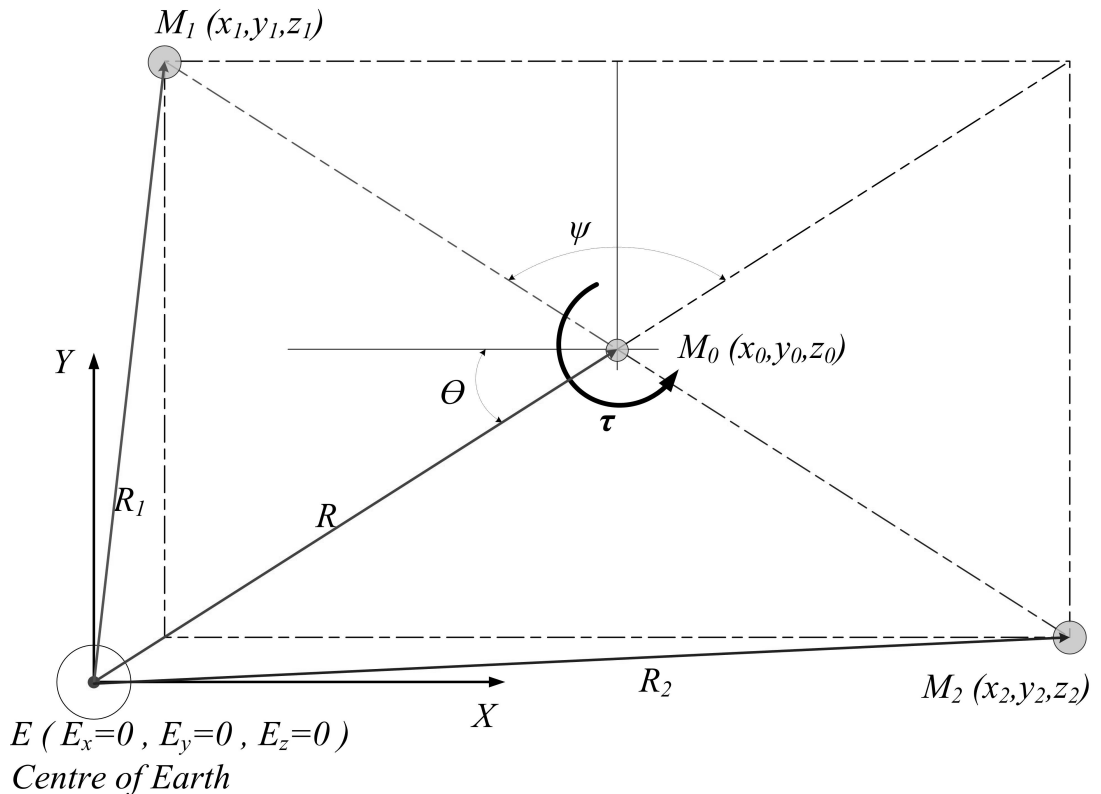


Figure 3.16: The model for the dumbbell MMET system - top view

### 3.4.2 Potential Energy

The gravitational potential energy is obtained by implementing Newton's gravitational law. Thus, the tether's potential energy is given in equation (3.4.6),  $\mu$  is the product of the universal gravitational constant  $G$  with the Earth's Mass,  $L$  is the symmetrical tether subspan length.

$$\begin{aligned} U &= -\frac{\mu M_1}{R_1} - \frac{\mu M_2}{R_2} - \frac{\mu M_0}{R} \\ &= -\frac{\mu M_1}{\sqrt{L^2 + R^2 + 2LR \cos \alpha \cos \psi}} - \frac{\mu M_2}{\sqrt{L^2 + R^2 - 2LR \cos \alpha \cos \psi}} - \frac{\mu M_0}{R} \end{aligned} \quad (3.4.6)$$

### 3.4.3 Generalised Coordinates

In the case of the dumbbell MMET system with massless subspans, it has been decided upon to represent the system dynamics by means of three angular coordinates ( $\psi$ ,  $\theta$ ,  $\alpha$ ) and one translational coordinate ( $R$ ), in which the  $\psi$ ,  $\theta$ ,  $\alpha$  and  $R$  are the same generalised coordinates as in section 3.2.3, as shown in Table 3.3.

Table 3.3: The dumbbell tether generalised coordinates and generalised forces

$i$	$q_i$	$Q_i$	$T$	$U$	Equations of Motion
1	$\psi$	(3.4.7)	(3.4.5)	(3.4.6)	(3.4.8)
2	$\theta$	0			(3.4.9)
3	$\alpha$	0			(3.4.10)
4	$R$	0			(3.4.11)

### 3.4.4 Generalised Forces

The generalised force  $Q_1$  is for the generalised coordinate  $\psi$ , which is given in equation (3.4.7), and the rest of the generalised forces in  $Q_i$  ( $i = 2, 3, 4$ ) are all zeros since no other non-conservative forces are acting on this system, in which the generalised coordinates are  $q_1 = \psi$ ,  $q_2 = \theta$ ,  $q_3 = \alpha$ ,  $q_4 = R$ .

$$Q_\psi = \tau \quad (3.4.7)$$

where,  $\tau$  is the driving torque generated by the motor installed in the COM of the dumbbell MMET.

### 3.4.5 Governing Equations of Motion

According to the Lagrange equation (3.1.1), the following governing equations are derived and stated in equations (3.4.8) to (3.4.11).

$$\begin{aligned} & -\frac{\mu M_p L R \cos \alpha \sin \psi}{(R^2 + 2RL \cos \alpha \cos \psi + L^2)^{3/2}} + \frac{\mu M_p L R \cos \alpha \sin \psi}{(R^2 - 2RL \cos \alpha \cos \psi + L^2)^{3/2}} \\ & + 2M_p L^2 \cos^2 \alpha (\ddot{\theta} + \ddot{\psi}) + 2M_p L (2\dot{L} \cos^2 \alpha - L \sin 2\alpha \dot{\alpha}) (\dot{\theta} + \dot{\psi}) \\ & = Q_\psi \end{aligned} \quad (3.4.8)$$

$$\begin{aligned} & (R^2 \ddot{\theta} + 2R\dot{R}\dot{\theta}) (2M_p + M_0) + 2M_p L^2 \cos^2 \alpha (\ddot{\theta} + \ddot{\psi}) \\ & + 2M_p L (2\dot{L} \cos^2 \alpha - L \sin 2\alpha \dot{\alpha}) (\dot{\theta} + \dot{\psi}) = Q_\theta \end{aligned} \quad (3.4.9)$$

$$\begin{aligned} & -\frac{\mu M_p L R \cos \psi \sin \alpha}{(R^2 + 2RL \cos \alpha \cos \psi + L^2)^{3/2}} + \frac{\mu M_p L R \cos \psi \sin \alpha}{(R^2 - 2RL \cos \alpha \cos \psi + L^2)^{3/2}} \\ & + 2M_p L^2 \left( \ddot{\alpha} + \frac{1}{2} \sin 2\alpha (\dot{\theta} + \dot{\psi})^2 \right) \\ & + 4M_p L \dot{L} \dot{\alpha} = Q_\alpha \end{aligned} \quad (3.4.10)$$

$$\begin{aligned} & \frac{\mu M_p (R + L \cos \alpha \cos \psi)}{(R^2 + 2RL \cos \alpha \cos \psi + L^2)^{3/2}} + \frac{\mu M_p (R - L \cos \alpha \cos \psi)}{(R^2 - 2RL \cos \alpha \cos \psi + L^2)^{3/2}} + \frac{\mu M_0}{R^2} \\ & + (2M_p + M_0) (\ddot{R} - R\dot{\theta}^2) = Q_R \end{aligned} \quad (3.4.11)$$

### 3.4.6 Simulations and Discussions

Figures 3.17 to 3.24 are the numerical results obtained by MATHEMATICA for the selected generalised coordinates  $\psi$ ,  $\theta$ ,  $\alpha$  and  $R$ , as listed in Table 3.3. The parameters for the dumbbell tether system simulations are given in Appendix C,  $T_n$  is the number of cycles of period, and is the same as is discussed in section 3.2.6.

▷ Figures 3.17 and 3.18 express the dumbbell MMET tether's steady spin-up behaviour, which is every close to the spin-up behaviour of dumbbell tether in Figures 3.4 and 3.6; they show the dumbbell MMET tether's periodic spin-up behaviour around the Earth in  $T_n = 4.01$  and  $T_n = 400.01$  simulation time, with the range of -0.325 to 0.325 rad.

▷ Figures 3.19 and 3.20 give the true anomaly for the dumbbell MMET system in  $T_n = 4.01$  and  $T_n = 400.01$  simulation time with slight ups and downs along the  $\theta$  curve's rising process.

- ▷ With zero initial conditions,  $\alpha(0) = 0$  rad and  $\dot{\alpha}(0) = 0$  rad/s, the the out-of-plane angle  $\alpha$  performs a stable zero response, as listed in Appendix C. Figure 3.21 shows the simulation response with non-zero initial conditions  $\alpha(0) = 0.001$  rad and  $\dot{\alpha}(0) = 0.001$  rad/s, which is with similar behaviour as the dumbbell tether in the previous section.
- ▷ Figures 3.22, 3.23 and 3.24 give the position generalised coordinate R, which measure the distance from the Earth E to the dumbbell MMET system's COM  $P_0$ , within the range  $r_p$  to  $r_a$ , in this case, given  $e = 0.2$  and  $r_p = 6.89 \times 10^6$  metre, then  $r_a = 1.0335 \times 10^7$  metre.

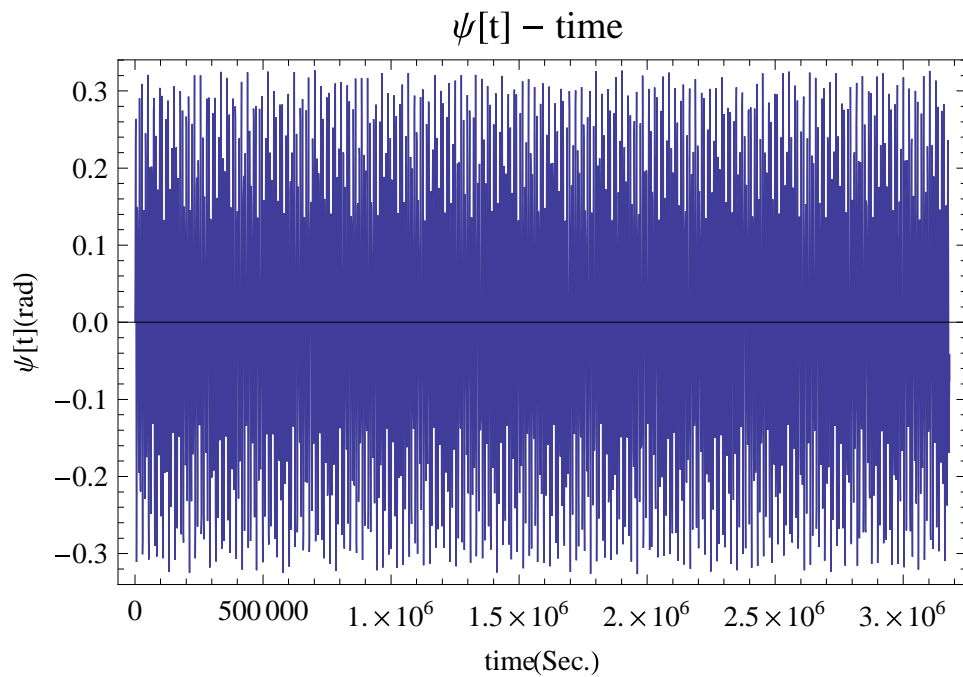


Figure 3.17: Dumbbell MMET tether spin-up, angular displacement  $\psi$  ( $T_n = 400.01$ )

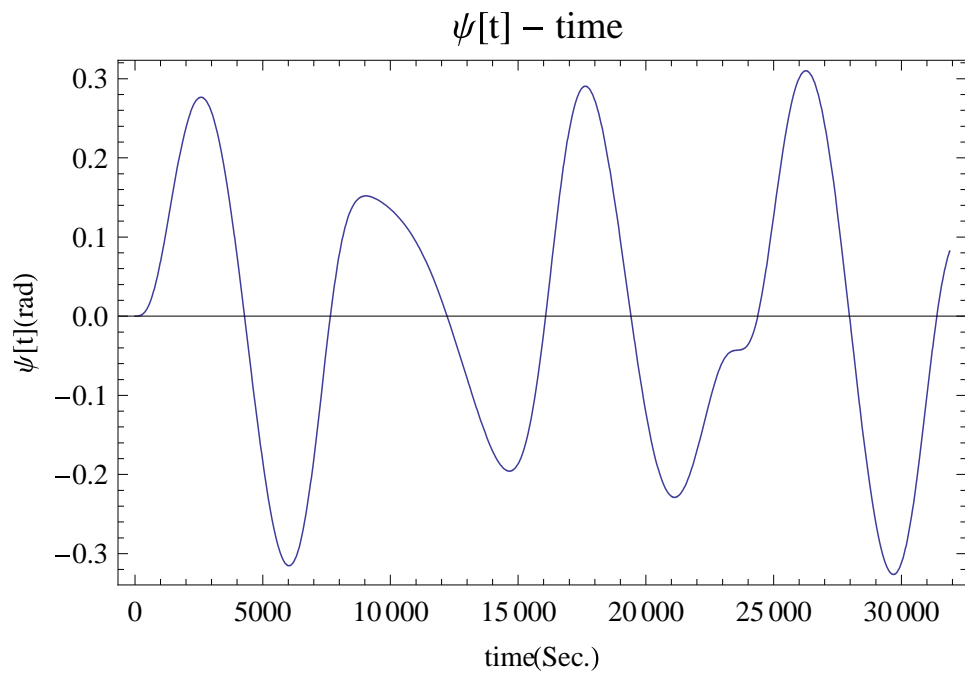


Figure 3.18: Dumbbell MMET tether spin-up, angular displacement  $\psi$  ( $T_n = 4.01$ )

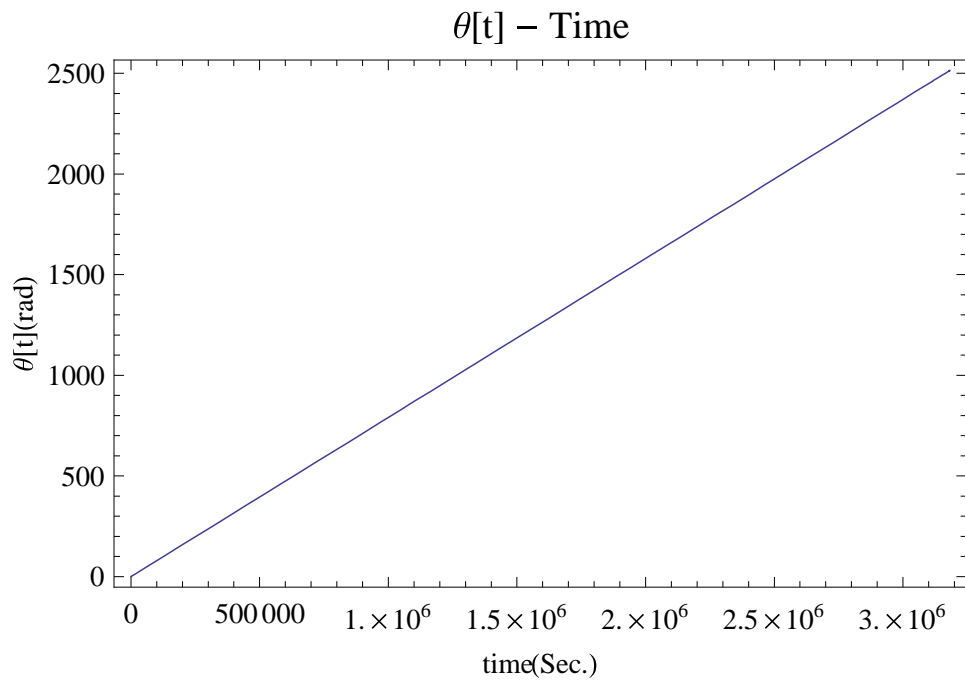


Figure 3.19: Dumbbell MMET tether elliptical orbit angular position  $\theta$  ( $T_n = 400.01$ )

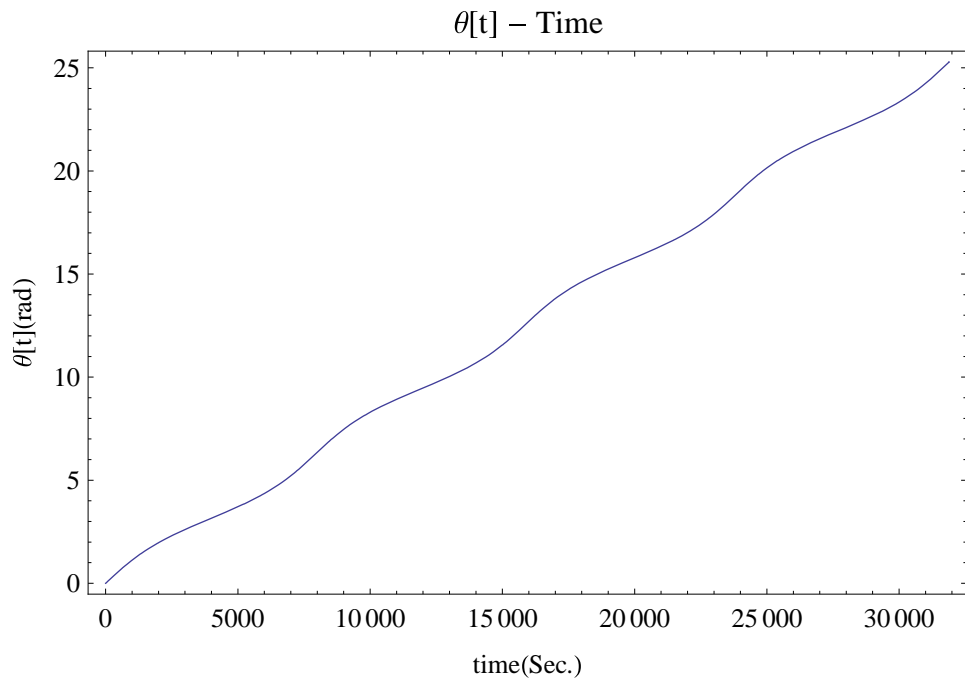


Figure 3.20: Dumbbell MMET tether elliptical orbit angular position  $\theta$  ( $T_n = 4.01$ )

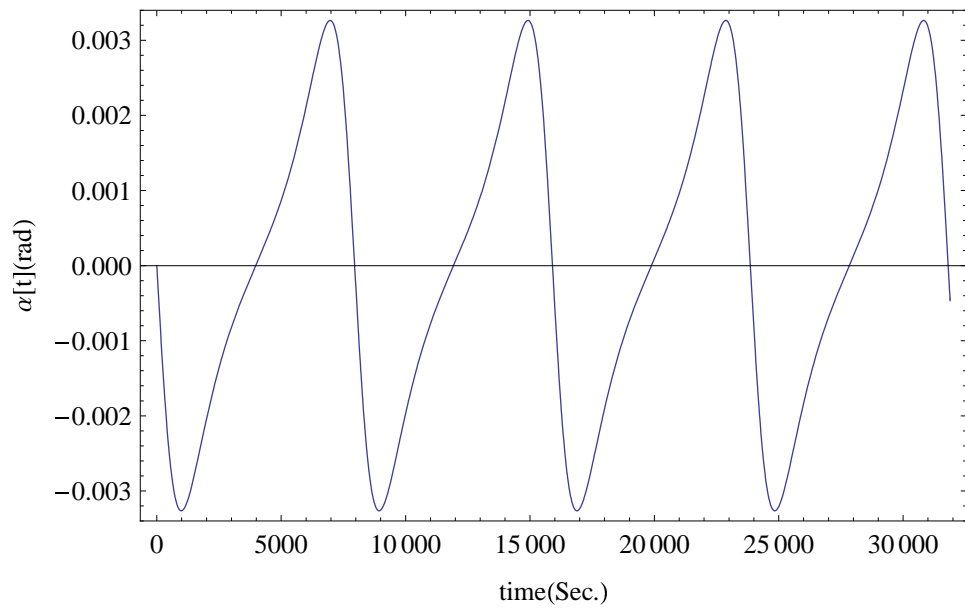


Figure 3.21: Dumbbell MMET tether out-of-plane angle  $\alpha$  ( $T_n = 4.01$ )

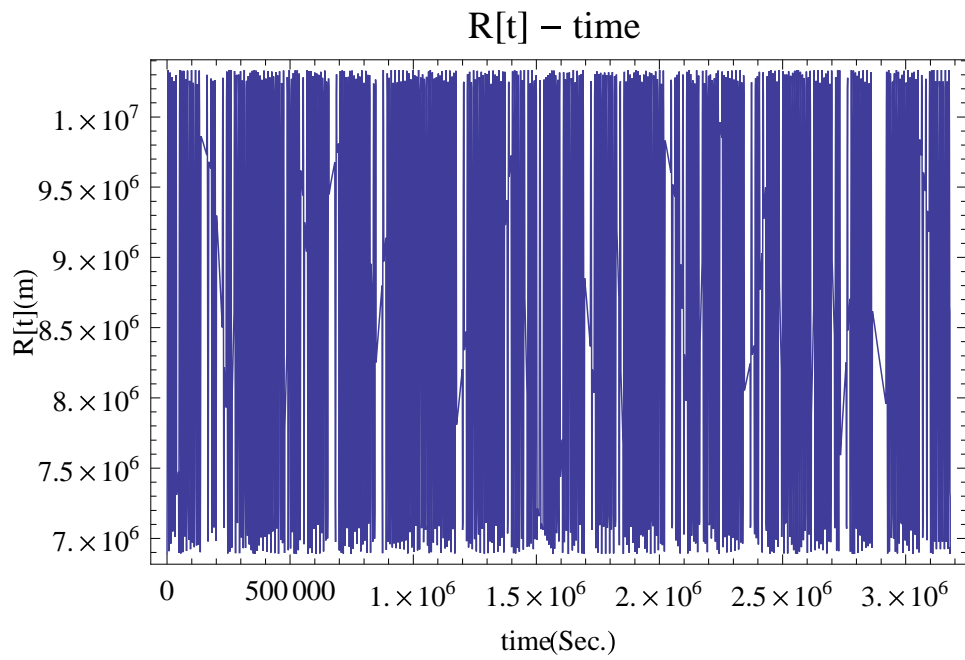


Figure 3.22: Dumbbell MMET distance  $R$  ( $T_n = 400.01$ )

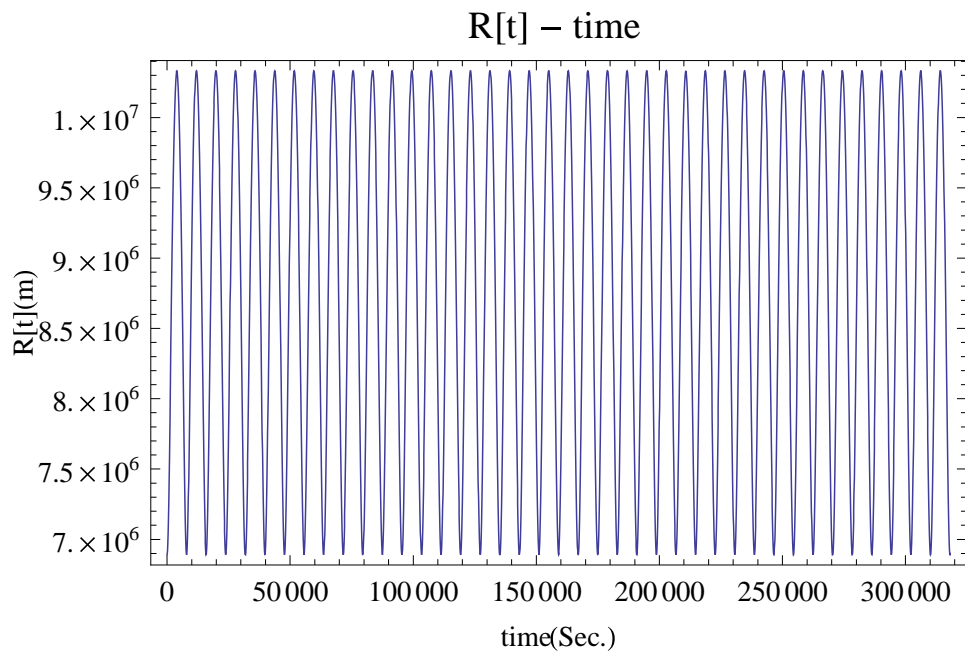


Figure 3.23: Dumbbell MMET distance  $R$  ( $T_n = 40.01$ )

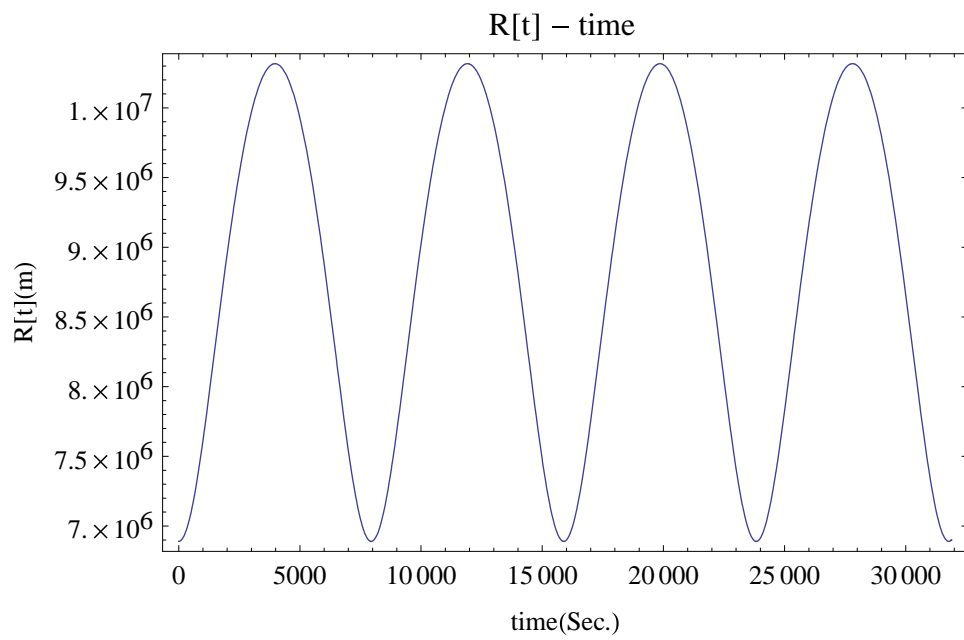


Figure 3.24: Dumbbell MMET distance  $R$  ( $T_n = 4.01$ )

### 3.5 The Dumbbell MMET with Cylindrical Payloads and a Motor Facility

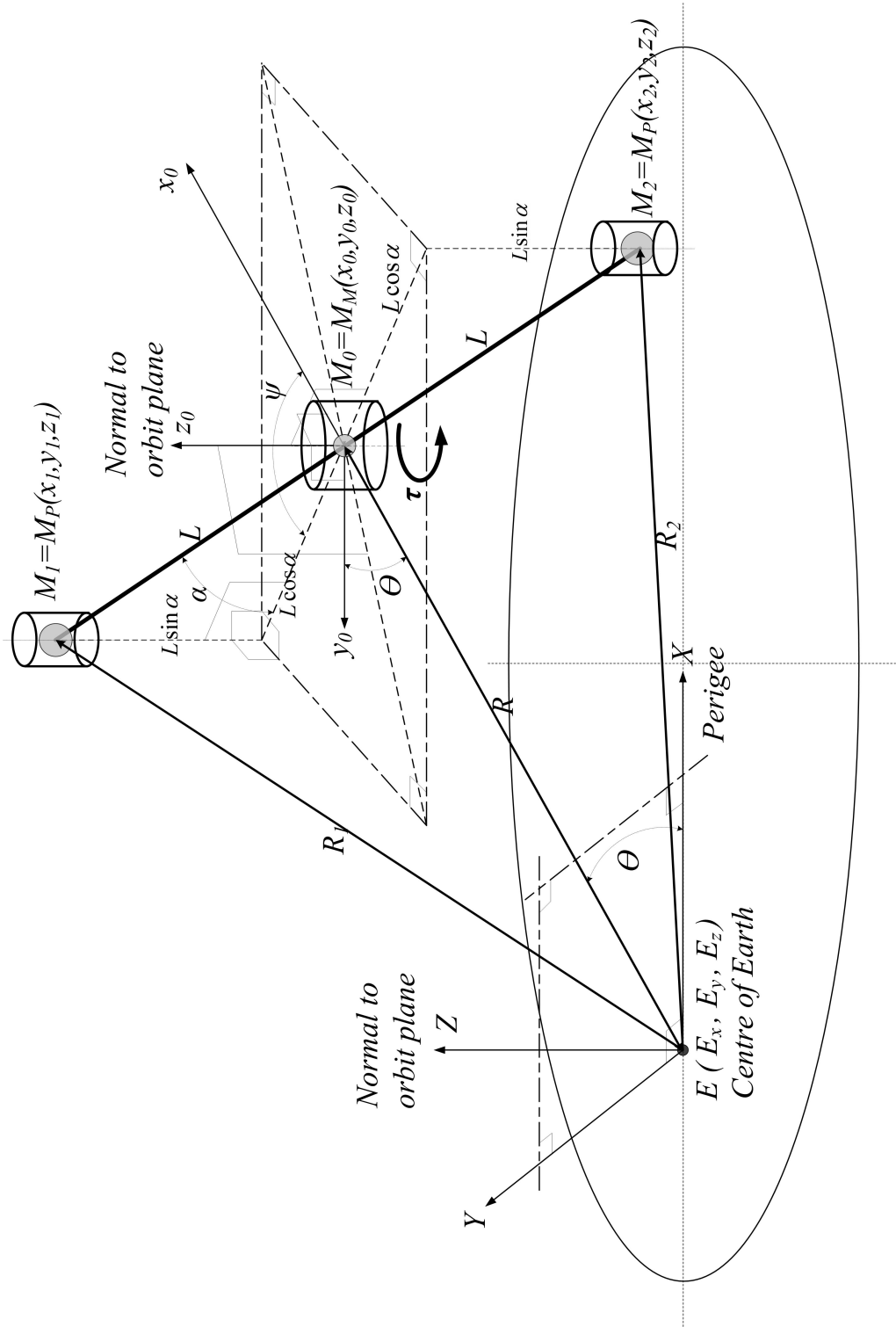


Figure 3.25: The MMET system with cylindrical payloads and a motor facility

Based on the massless dumbbell MMET modelling in section 3.4, and as shown in Figure 3.25, there are two generalised coordinate systems. One is an Earth centred global coordinate

system -  $\{X, Y, Z\}$ , and the other is the relative rotating coordinate system -  $\{x_0, y_0, z_0\}$ .

The tether system consists of two end masses,  $M_1$  and  $M_2$ , connected by a tether with the same distance from the tether's centre of mass  $M_0$  to each end mass, denoted by  $L$ .  $R$  is the distance from  $E(0, 0, 0)$  to  $M_M(x_0, y_0, z_0)$ , which is shown in equation (3.2.1).  $R_1$  and  $R_2$  are the distances from  $E(0, 0, 0)$  to  $M_1(x_1, y_1, z_1)$  and  $M_2(x_2, y_2, z_2)$ , respectively, with  $M_1 = M_2 = M_P$ , and  $M_0 = M_M$ , which are shown in equations (3.4.1), (3.4.2). Equations (3.2.4), (3.4.3) and (3.4.4) define the location of the base point and two payloads in each end of the tether.

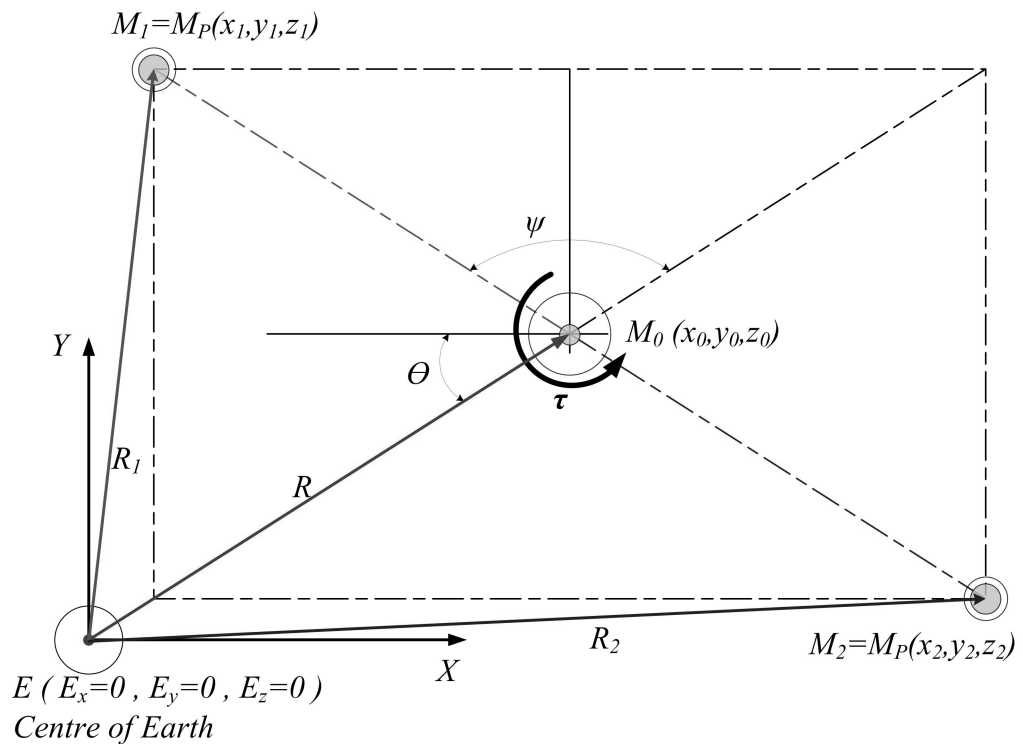


Figure 3.26: **The MMET system with cylindrical payloads and a motor facility - top view**

The MMET tether with massless subspans is assumed to be rigid, and also is not able to longitudinally extend or twist in any direction, in Figure 3.25, and its counter-Z-direction view is presented in Figure 3.26.

The main mass components of the motor consist of a central rotor attached to the propulsion tethers, and a stator which locates the rotor by means of a suitable bearing. The motor torque in the MMET tether with massless subspans acts about the motor drive axis, and it is assumed that the motor drive axis stays normal to the spin plane of the propulsive tethers and payloads. The connection between the tether and the motor will be regarded as a rigid connection, hence when the tether moves out of the orbital plane the motor will similarly rotate about its centre of mass.

### 3.5.1 Payload Mass Moment of Inertias

The definition of the local axes for the two cylindrical payloads is shown in Figure 3.27, and the payloads are denoted by  $M_{P1}$  and  $M_{P2}$ . Equations (3.5.1) and (3.5.2) are the mass moments of inertia for payloads  $M_{P1}$  and  $M_{P2}$ .

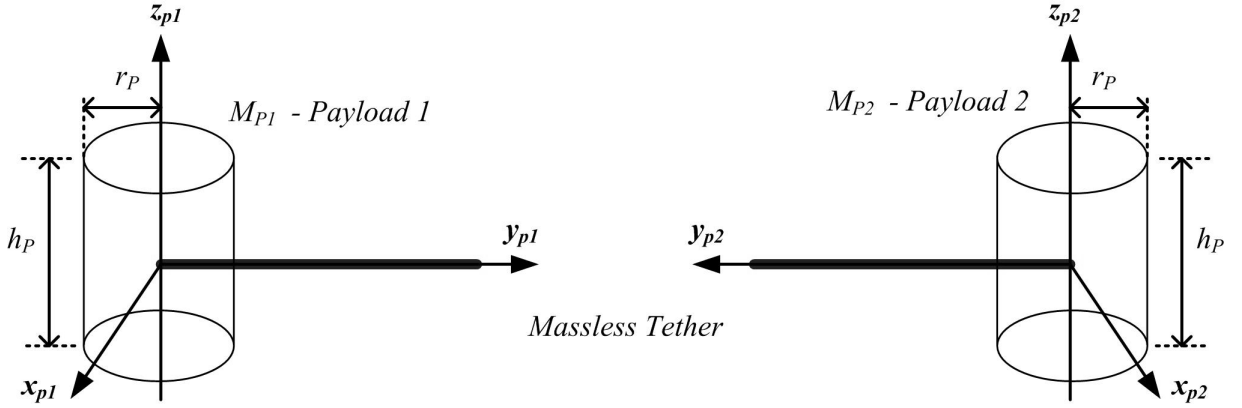


Figure 3.27: The definition of local axes for two cylindrical payloads

$$\left\{ \begin{array}{l} I_{x_{p1}} = \frac{1}{12} M_{P1} (3r_p^2 + h_p^2) \\ I_{y_{p1}} = \frac{1}{12} M_{P1} (3r_p^2 + h_p^2) \\ I_{z_{p1}} = \frac{1}{2} M_{P1} r_p^2 \end{array} \right. \quad (3.5.1)$$

$$\left\{ \begin{array}{l} I_{x_{p2}} = \frac{1}{12} M_{P2} (3r_p^2 + h_p^2) \\ I_{y_{p2}} = \frac{1}{12} M_{P2} (3r_p^2 + h_p^2) \\ I_{z_{p2}} = \frac{1}{2} M_{P2} r_p^2 \end{array} \right. \quad (3.5.2)$$

As shown in Figure 3.27,

$r_p$  is the radius of the payload,  $h_p$  is the height of the cylindrical payload,

$I_{x_{p1}}$  is the  $M_1$  mass moment of inertia about the local axis  $x_{p1}$ ,

$I_{y_{p1}}$  is the  $M_1$  mass moment of inertia about the local axis  $y_{p1}$ ,

$I_{z_{p1}}$  is the  $M_1$  mass moment of inertia about the local axis  $z_{p1}$ ,

$I_{x_{P2}}$  is the  $M_2$  mass moment of inertia about the local axis  $x_{P2}$ ,

$I_{y_{P2}}$  is the  $M_2$  mass moment of inertia about the local axis  $y_{P2}$ ,

$I_{z_{P2}}$  is the  $M_2$  mass moment of inertia about the local axis  $z_{P2}$ .

### 3.5.2 Motor Facility Mass Moment of Inertias

The cylindrical motor facility local axis definition is in Figure 3.28, and equation (3.5.3) is the mass moment of inertia for the cylindrical motor facility  $M_M$ .

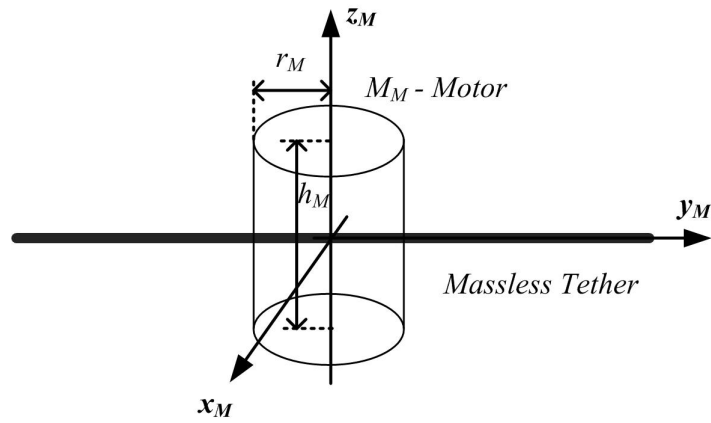


Figure 3.28: The definition of local axes for the cylindrical motor facility

$$\left\{ \begin{array}{l} I_{x_M} = \frac{1}{12} M_M (3r_M^2 + h_M^2) \\ I_{y_M} = \frac{1}{12} M_M (3r_M^2 + h_M^2) \\ I_{z_M} = \frac{1}{2} M_M r_M^2 \end{array} \right. \quad (3.5.3)$$

With definitions as in Figure 3.28,

$r_M$  is the radius of the motor,

$h_M$  is the height of the cylindrical facility of motor,

$I_{x_M}$  is the mass moment of inertia about the local axis  $x_M$ ,

$I_{y_M}$  is the mass moment of inertia about the local axis  $y_M$ ,

$I_{z_M}$  is the mass moment of inertia about the local axis  $z_M$ .

### 3.5.3 Torque Plane

The components of the propulsive force  $F$  is given in equations (3.5.4), and the  $x_0, y_0, z_0$  components of the torque plane are shown in Figure 3.29, adopted from Ziegler's work in 2003 [65].

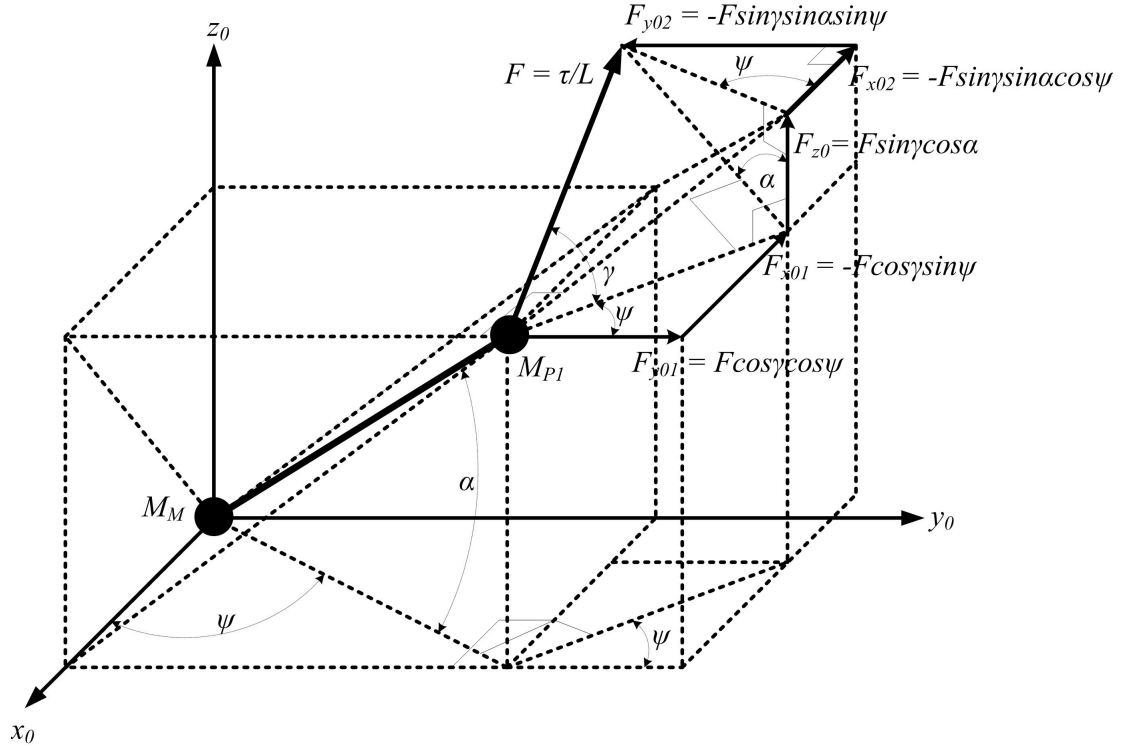


Figure 3.29: The  $x_0, y_0, z_0$  components of the 'torque-plane' (plane O – Q – B) - not parallel to the 'tether-spin-plane' (plane  $x_0 - Q - F_{x1}$ ) and adapted from [65]

$$\vec{F} = \vec{F}_x + \vec{F}_y + \vec{F}_z = \frac{\vec{\tau}}{L} \quad (3.5.4)$$

where,  $\vec{F}_x, \vec{F}_y$  and  $\vec{F}_z$  are the Cartesian components of the force  $F$ , which are given in equation (3.5.5). As shown in Figure 3.29, the components of  $F_x$  and  $F_y$  are  $F_x = F_{x1} + F_{x2}$ ,  $F_y = F_{y1} + F_{y2}$ .

$$\begin{cases} F_x = -F \cos \gamma \sin \psi - F \sin \gamma \sin \alpha \cos \psi \\ F_y = F \cos \gamma \cos \psi - F \sin \gamma \sin \alpha \sin \psi \\ F_z = F \sin \gamma \cos \alpha \end{cases} \quad (3.5.5)$$

### 3.5.4 Generalised Coordinates

In the dumbbell MMET system with cylindrical payloads and centralised motor facility, there are six generalised coordinates, in which four rotational coordinates ( $\psi, \theta, \alpha, \gamma$ ) and two translational coordinates ( $L, R$ ) are selected as the generalised coordinates.

The  $\psi$ ,  $\theta$ ,  $\alpha$ ,  $L$  and  $R$  are the same generalised coordinates as in section 3.4.5.  $\gamma$  is the rolling angle, which is an angle between the torque-plane (where the torque is generated by the motor) and the ‘tether-spin-plane’, Figure 3.29 shows the definition of this angle  $\gamma$ . When the torque-plane [65] is not parallel to the ‘tether-spin-plane’,  $\gamma \neq 0$ . And, if the torque-plane is parallel to the ‘tether-spin-plane’,  $\gamma = 0$ . The rolling angle  $\gamma$  needs to be included, because the torque axis is free to rotate about the longitudinal axis of the tethers. Note that,  $\gamma$  does not alter the location of the end masses’ COM, and the generalised coordinates are independent functions of time.

### 3.5.5 Kinetic Energy

The kinetic energy of the dumbbell MMET system is composed of its translational motion in the inertial frame and its rotation about its centre of mass, as shown in Figure 3.25. As the payload and motor facility masses are connected by massless solid tether subspans, the kinetic energy of the system is given in equation (3.5.6).

$$\begin{aligned}
T = & \frac{1}{2}M_{P1} (\dot{x}_{P1}^2 + \dot{y}_{P1}^2 + \dot{z}_{P1}^2) + \frac{1}{2}M_{P2} (\dot{x}_{P2}^2 + \dot{y}_{P2}^2 + \dot{z}_{P2}^2) + \frac{1}{2}M_M (\dot{x}_0^2 + \dot{y}_0^2 + \dot{z}_0^2) + \\
& \frac{1}{2} [I_{z_{P1}} + I_{z_{P2}} + I_{z_M}] (\dot{\psi} + \dot{\theta})^2 + \\
& \frac{1}{2} [I_{x_{P1}} + I_{x_{P2}} + I_{x_M}] \dot{\alpha}^2 + \\
& \frac{1}{2} [I_{y_{P1}} + I_{y_{P2}} + I_{y_M}] \dot{\gamma}^2
\end{aligned} \tag{3.5.6}$$

### 3.5.6 Potential Energy

The gravitational potential energy is defined by equation (3.5.7) using Newton’s gravitational law, in which  $\mu$  is the product of the universal gravitational constant  $G$  with the Earth’s Mass.

$$\begin{aligned}
u = & -\frac{\mu M_1}{R_1} - \frac{\mu M_2}{R_2} - \frac{\mu M_M}{R} \\
= & -\frac{\mu M_1}{\sqrt{L^2 + R^2 + 2LR \cos \alpha \cos \psi}} - \frac{\mu M_2}{\sqrt{L^2 + R^2 - 2LR \cos \alpha \cos \psi}} - \frac{\mu M_M}{R}
\end{aligned} \tag{3.5.7}$$

### 3.5.7 Generalised Forces

According to the theory of virtual work, the generalised torque exerted by the motor for the MMET system is as defined in equation (3.5.8). Considering the virtual work done by all non-conservative forces through a virtual displacement, leads to equations (3.5.8) and (3.5.9), in which  $Q_{q_i}$  is the generalised force for the generalised coordinate  $q_i$ , as defined in equation (3.5.10).

$$\delta W = F_x \delta x + F_y \delta y + F_z \delta z \quad (3.5.8)$$

$$\delta W_{q_i} = Q_{q_i} \delta q_i \quad (3.5.9)$$

$$Q_{q_i} = F_x \frac{\partial x}{\partial q_i} + F_y \frac{\partial y}{\partial q_i} + F_z \frac{\partial z}{\partial q_i} \quad (3.5.10)$$

where,  $F_x$ ,  $F_y$  and  $F_z$  are obtained in equation (3.5.5). The Cartesian components  $x$ ,  $y$  and  $z$  are shown in equation (3.5.11).

$$\begin{cases} x = L \cos \alpha \cos (\theta + \psi) \\ y = L \cos \alpha \sin (\theta + \psi) \\ z = L \sin \alpha \end{cases} \quad (3.5.11)$$

- The partial derivatives of equation (3.5.11) with respect to each generalised coordinates  $\psi$ ,  $\theta$ ,  $\alpha$ ,  $\gamma$ ,  $R$  and  $L$  are given in [Appendix A](#).

Note that the true anomaly  $\theta$  does not affect the generalised force, so the principle of virtual work, as used here, only considers the virtual displacements relating to the applied non-conservative forces, then equation (3.5.11) for the Cartesian components  $x$ ,  $y$  and  $z$  can be re-formed as equation (3.5.12) [62].

- The partial derivatives of equation (3.5.12) with respect to each generalised coordinates  $\psi$ ,  $\theta$ ,  $\alpha$ ,  $\gamma$ ,  $R$  and  $L$  are given in [Appendix B](#).

$$\begin{cases} x = L \cos \alpha \cos \psi \\ y = L \cos \alpha \sin \psi \\ z = L \sin \alpha \end{cases} \quad (3.5.12)$$

Subsequently, the generalised forces for this solid massless MMET system, as expressed in equations (A.0.7) to equation (A.0.11), can also be transformed as in equations (3.5.13) to (3.5.16).

$$Q_\psi = FL \cos \gamma \cos \alpha = \tau \cos \gamma \cos \alpha \quad (3.5.13)$$

$$Q_\theta = 0 \quad (3.5.14)$$

$$Q_\alpha = \tau \sin \gamma \quad (3.5.15)$$

$$Q_R = 0 \quad (3.5.16)$$

$$Q_\gamma = 0 \quad (3.5.17)$$

### 3.5.8 Governing Equations of Motion

Since no non-conservative forces are acting on the generalised coordinates  $q_i$   $\{i = 2, 4, 5\}$ , their generalised forces  $Q_i$   $\{i = 2, 4, 5\}$  are all zeros, that is,  $Q_2 = Q_\theta = 0$ ,  $Q_4 = Q_R = 0$  and  $Q_5 = Q_\gamma = 0$ . The generalised forces  $Q_1 = Q_\psi$  and  $Q_3 = Q_\alpha$  are given in equations (3.5.13) and (3.5.15). The following governing equations for generalised coordinates  $q_i$  are given in equations (3.5.18) to (3.5.22), for  $q_1 = \psi$ ,  $q_2 = \theta$ ,  $q_3 = \alpha$ ,  $q_4 = R$  and  $q_5 = \gamma$ , and are also as listed in Table 3.4.

Table 3.4: The dumbbell MMET with cylindrical payload and motor facility generalised coordinates and generalised forces

$i$	$q_i$	$Q_i$	T	U	Equations of Motion
1	$\psi$	(3.5.13)	(3.5.6)	(3.5.7)	(3.5.18)
2	$\theta$	(3.5.14)			(3.5.19)
3	$\alpha$	(3.5.15)			(3.5.20)
4	R	(3.5.16)			(3.5.21)
5	$\gamma$	(3.5.17)			(3.5.22)

$$\begin{aligned}
& -\frac{\mu M_p L R \cos \alpha \sin \psi}{(R^2 + 2RL \cos \alpha \cos \psi + L^2)^{3/2}} + \frac{\mu M_p L R \cos \alpha \sin \psi}{(R^2 - 2R \cos \alpha \cos \psi + L^2)^{3/2}} \\
& - (M_{P2} - M_{P1}) \left( \begin{array}{c} \cos \alpha \dot{L} (\sin \psi \dot{R} - \cos \psi R(t)\dot{\theta}) + \\ L \left( \begin{array}{c} \sin \alpha \dot{\alpha} (\cos \psi R\dot{\theta} - \sin \psi \dot{R}) + \\ \cos \alpha (\cos \psi \dot{R} + R \sin \psi \dot{\theta}) (\dot{\theta} + \dot{\psi}) \end{array} \right) \end{array} \right) \\
& + \frac{1}{2} \left( \begin{array}{c} M_M (\ddot{\theta} + \ddot{\psi}) r_M^2 + \\ M_{P1} \left( \begin{array}{c} 2 (\cos^2 \alpha (\ddot{\theta} + \ddot{\psi}) - \sin 2\alpha \dot{\alpha} (\dot{\theta} + \dot{\psi})) L^2 + \\ 2 \left( \begin{array}{c} \sin \alpha \dot{\alpha} (\sin \psi \dot{R} - \cos \psi R\dot{\theta}) + \\ \cos \alpha (\cos \psi (\dot{R} (\dot{\theta} - \dot{\psi}) + R\ddot{\theta}) - \sin \psi (R\dot{\theta}\dot{\psi} + \ddot{R})) \end{array} \right) L \\ + 2 \cos \alpha \dot{L} (-\sin \psi \dot{R} + \cos \psi R\dot{\theta} + 2 \cos \alpha L (\dot{\theta} + \dot{\psi})) + r_p^2 (\ddot{\theta} + \ddot{\psi}) \end{array} \right) \\ + M_{P2} \left( \begin{array}{c} 2 (\cos^2 \alpha (\ddot{\theta} + \ddot{\psi}) - \sin 2\alpha \dot{\alpha} (\dot{\theta} + \dot{\psi})) L^2 - \\ 2 \left( \begin{array}{c} \sin \alpha \dot{\alpha} (\sin \psi \dot{R} - \cos \psi R\dot{\theta}) + \\ \cos \alpha (\cos \psi (\dot{R} (\dot{\theta} - \dot{\psi}) + R\ddot{\theta}) - \sin \psi (R\dot{\theta}\dot{\psi} + \ddot{R})) \end{array} \right) L + \\ 2 \cos \alpha \dot{L} (\sin \psi \dot{R} - \cos \psi R\dot{\theta} + 2 \cos \alpha L (\dot{\theta} + \dot{\psi})) + r_p^2 (\ddot{\theta} + \ddot{\psi}) \end{array} \right) \end{array} \right) \\
& = Q_\psi
\end{aligned} \tag{3.5.18}$$

$$\begin{aligned}
& \frac{1}{2} \left( \begin{array}{c} -2 \cos \alpha (M_{P1} + M_{P2}) (2 \sin \alpha \dot{\alpha} (\dot{\theta} + \dot{\psi}) - \cos \alpha (\ddot{\theta} + \ddot{\psi})) L^2 + \\ 2 \cos \alpha (2 \cos \alpha (M_{P1} + M_{P2}) \dot{L} (\dot{\theta} + \dot{\psi}) + (M_{P1} - M_{P2}) (2 \cos \psi R\dot{\theta} - \sin \psi \dot{R})) L \\ + 2R^2 (M_M + M_{P1} + M_{P2}) \ddot{\theta} + (M_M r_M^2 + (M_{P1} + M_{P2}) r_p^2) (\ddot{\theta} + \ddot{\psi}) + \\ 2R \left( \begin{array}{c} 2 (M_M + M_{P1} + M_{P2}) \dot{R}\dot{\theta} - \\ \sin \psi (M_{P1} - M_{P2}) \left( \begin{array}{c} \cos \alpha (L (\dot{\alpha}^2 + \dot{\psi} (2\dot{\theta} + \dot{\psi})) - \dot{L}) + \\ \sin \alpha (2\dot{L}\dot{\alpha} + L\ddot{\alpha}) \end{array} \right) \\ + \cos \psi (M_{P1} - M_{P2}) \left( \begin{array}{c} 2 \cos \alpha \dot{L} (\dot{\theta} + \dot{\psi}) + \\ L (\cos \alpha (2\ddot{\theta} + \ddot{\psi}) - 2 \sin \alpha \dot{\alpha} (\dot{\theta} + \dot{\psi})) \end{array} \right) \end{array} \right) \end{array} \right) \\
& = Q_\theta
\end{aligned} \tag{3.5.19}$$

$$\begin{aligned}
& -\frac{\mu M_P L R \cos \psi \sin \alpha}{(R^2 + 2RL \cos \alpha \cos \psi + L^2)^{3/2}} + \frac{\mu M_P L R \cos \psi \sin \alpha}{(R^2 - 2RL \cos \alpha \cos \psi + L^2)^{3/2}} \\
& -\frac{1}{2} \left( \begin{aligned} & -L^2 \sin 2\alpha (M_{P1} + M_{P2}) (\dot{\theta} + \dot{\psi})^2 - \\ & 2 \cos \alpha L (M_{P1} - M_{P2}) \dot{\alpha} (\cos \psi \dot{R} + R \sin \psi \dot{\theta}) - \\ & 2 \sin \alpha (M_{P1} - M_{P2}) (\dot{L} (\cos \psi \dot{R} + R \sin \psi \dot{\theta}) - L (\sin \psi \dot{R} - \cos \psi R \dot{\theta}) (\dot{\theta} + \dot{\psi})) \end{aligned} \right) \\
& +\frac{1}{12} \left( \begin{aligned} & 24M_{P1} \dot{L} \dot{\alpha} L + 24M_{P2} \dot{L} \dot{\alpha} L - 12 \cos \alpha (M_{P1} - M_{P2}) \dot{\alpha} (\cos \psi \dot{R} + R \sin \psi \dot{\theta}) L + \\ & \ddot{\alpha} \left( 12M_{P1} L^2 + 12M_{P2} L^2 + 3M_M r_M^2 + 3M_{P1} r_P^2 + 3M_{P2} r_P^2 \right) - \\ & \quad + h_M^2 M_M + h_P^2 M_{P1} + h_P^2 M_{P2} \\ & 12 \sin \alpha (M_{P1} - M_{P2}) \left( \begin{aligned} & \dot{L} (\cos \psi \dot{R} + R \sin \psi \dot{\theta}) + \\ & L (\sin \psi \dot{R} (\dot{\theta} - \dot{\psi}) + \cos \psi (R \dot{\theta} \dot{\psi} + \ddot{R}) + R \sin \psi \ddot{\theta}) \end{aligned} \right) \end{aligned} \right) \\
& = Q_\alpha
\end{aligned} \tag{3.5.20}$$

$$\begin{aligned}
& \frac{\mu M_P (R + L \cos \alpha \cos \psi)}{(R^2 + 2RL \cos \alpha \cos \psi + L^2)^{3/2}} + \frac{\mu M_P (R - L \cos \alpha \cos \psi)}{(R^2 - 2RL \cos \alpha \cos \psi + L^2)^{3/2}} + \frac{2\mu M_2}{R^2} \\
& -\dot{\theta} \left( \begin{aligned} & \sin \psi (M_{P1} - M_{P2}) (\cos \alpha \dot{L} - L \sin \alpha \dot{\alpha}) + R (M_M + M_{P1} + M_{P2}) \dot{\theta} + \\ & \cos \alpha \cos \psi L (M_{P1} - M_{P2}) (\dot{\theta} + \dot{\psi}) \end{aligned} \right) \\
& + \left( \begin{aligned} & (M_M + M_{P1} + M_{P2}) \ddot{R} - \\ & \sin \alpha (M_{P1} - M_{P2}) (\cos \psi (2\dot{L} \dot{\alpha} + L \ddot{\alpha}) - L \sin \psi \dot{\alpha} (\dot{\theta} + 2\dot{\psi})) - \\ & \cos \alpha (M_{P1} - M_{P2}) \left( \begin{aligned} & \cos \psi (L (\dot{\alpha}^2 + \dot{\psi} (\dot{\theta} + \dot{\psi})) - \ddot{L}) + \\ & \sin \psi (\dot{L} (\dot{\theta} + 2\dot{\psi}) + L (\ddot{\theta} + \ddot{\psi})) \end{aligned} \right) \end{aligned} \right) \\
& = Q_R
\end{aligned} \tag{3.5.21}$$

$$\frac{1}{12} (M_M (h_M^2 + 3r_M^2) + (M_{P1} + M_{P2}) (h_P^2 + 3r_P^2)) \ddot{\gamma} = Q_\gamma \tag{3.5.22}$$

### 3.5.9 Simulations and Discussions

Figures 3.30 to 3.35 are the numerical results obtained by MATHEMATICA for the selected generalised coordinates  $\psi$ ,  $\theta$ ,  $\alpha$ ,  $R$  and  $\gamma$ , as listed in Table 3.4. The results show the dumbbell MMET with cylindrical payloads' periodic behaviour on elliptical orbit during  $T_n = 4.01$  and  $T_n = 400.01$  simulation time with zero initial conditions.

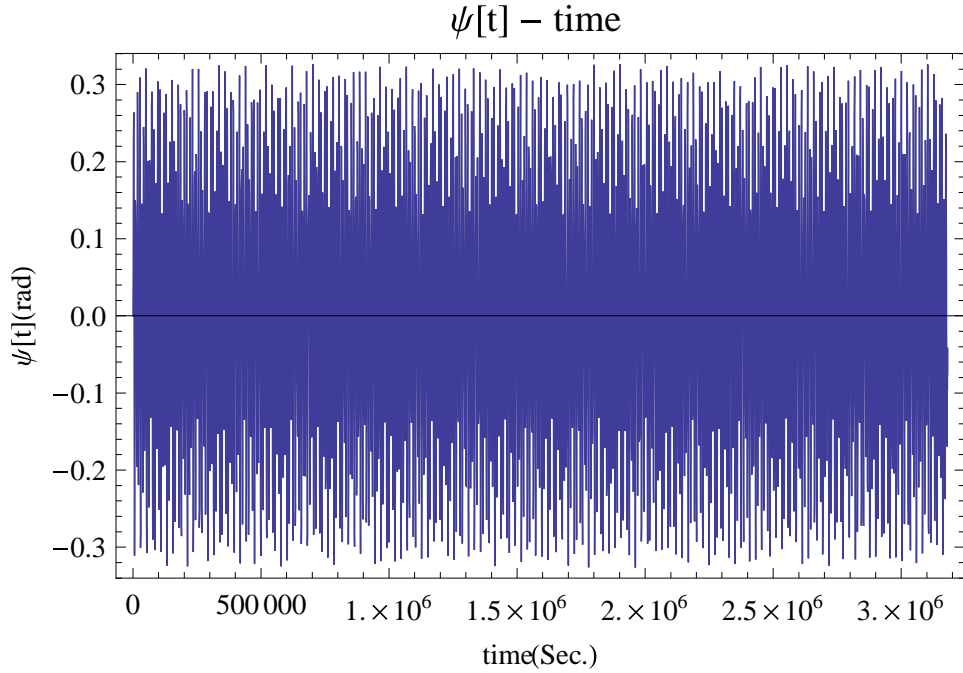


Figure 3.30: The dumbbell MMET with cylindrical payloads spin-up, angular displacement  $\psi$  ( $T_n = 400.01$ )

- ▷ In simulation time  $T_n = 4.01$  and  $T_n = 400.01$ , Figures 3.30 and 3.31 describe the tether's steady spin-up behaviour, which show the MMET tether's periodic performance around the Earth with the range of  $-0.325$  to  $0.325$  rad.
- ▷ In this case, when given  $e = 0.2$  and  $r_p = 6.89 \times 10^6$  metre, then  $r_a = 1.0335 \times 10^7$  metre, the position generalised coordinate  $R$  is stated in Figures 3.32 and 3.33, which indicate the distance from the Earth  $E$  to the MMET system's COM  $M_0$  with the range of  $r_p$  to  $r_a$ , as shown in Figures 3.32 and 3.33.
- ▷ Figures 3.34 and 3.35 give the true anomaly  $\theta$  for the MMET system in  $T_n = 4.01$  and  $T_n = 400.01$  simulation time with slight ups and downs along the data rising responses.
- ▷ As mentioned in sections 3.2.6 and 3.4.5, with zero initial conditions  $\alpha(0) = 0$  rad and  $\dot{\alpha}(0) = 0$  rad/s, the out-of-plane angle  $\alpha$  response is staying in zero over simulation process. The  $\alpha$  response with non-zero initial conditions  $\alpha(0) = 0.001$  rad and  $\dot{\alpha}(0) = 0.001$  rad/s is shown in Figure 3.36, whose periodic range is  $[-0.0032, 0.0032]$  rad.

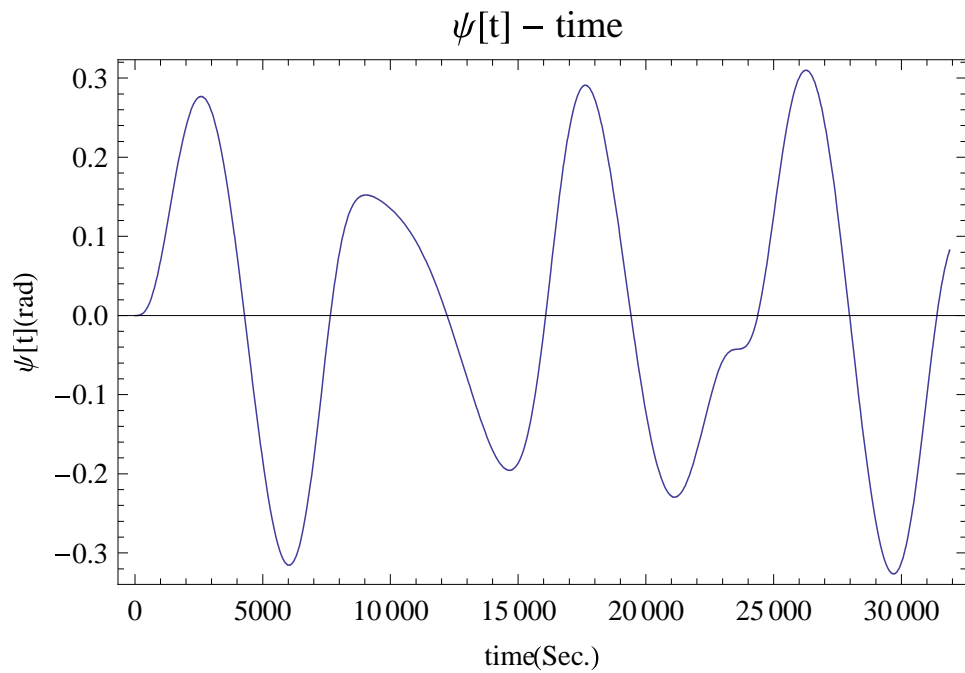


Figure 3.31: The dumbbell MMET with cylindrical payloads spin-up, displacement  $\psi$  ( $T_n = 4.01$ )

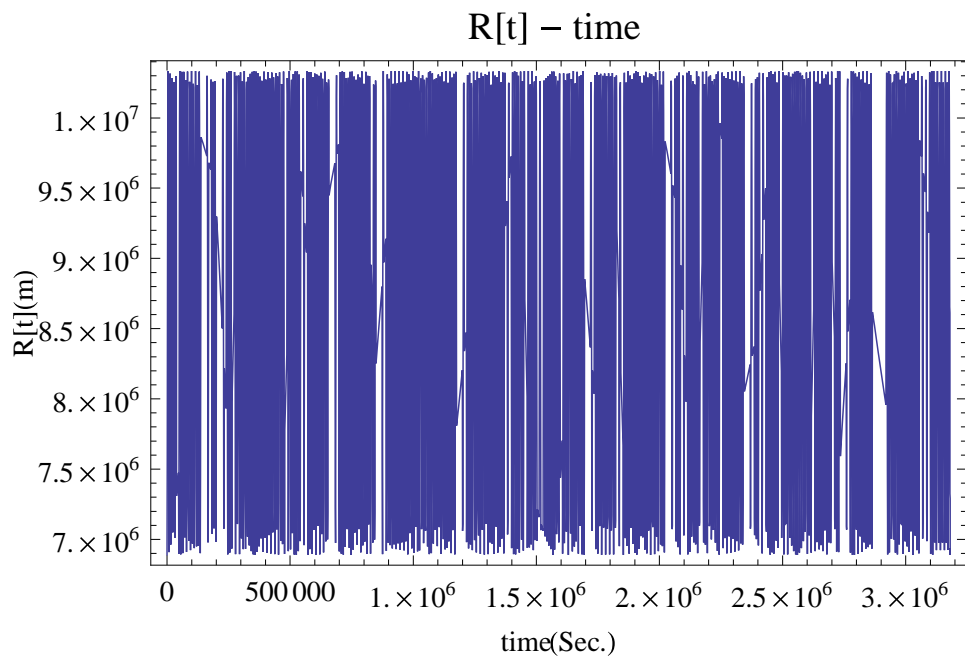


Figure 3.32: The dumbbell MMET with cylindrical payloads distance  $R$  ( $T_n = 400.01$ )

▷  $\gamma$  is the rolling angle, which is an angle between the torque-plane, with zero initial conditions  $\gamma(0) = 0$  rad and  $\dot{\gamma}(0) = 0$  rad/s, the response for the tether's rigid rolling angle shows the steady zero rolling angle output for the tether system. With  $\gamma(0) = 0.001$  rad and  $\dot{\gamma}(0) = 0.001$  rad/s, Figure 3.37 expresses the periodic activities about the balanced position.

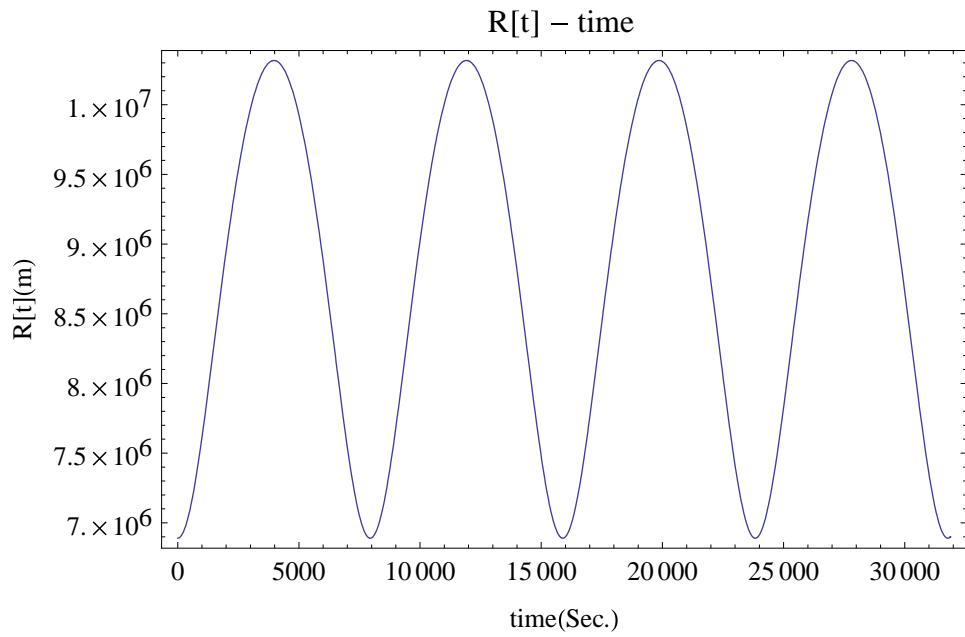


Figure 3.33: The dumbbell MMET with cylindrical payloads distance  $R$  ( $T_n = 4.01$ )

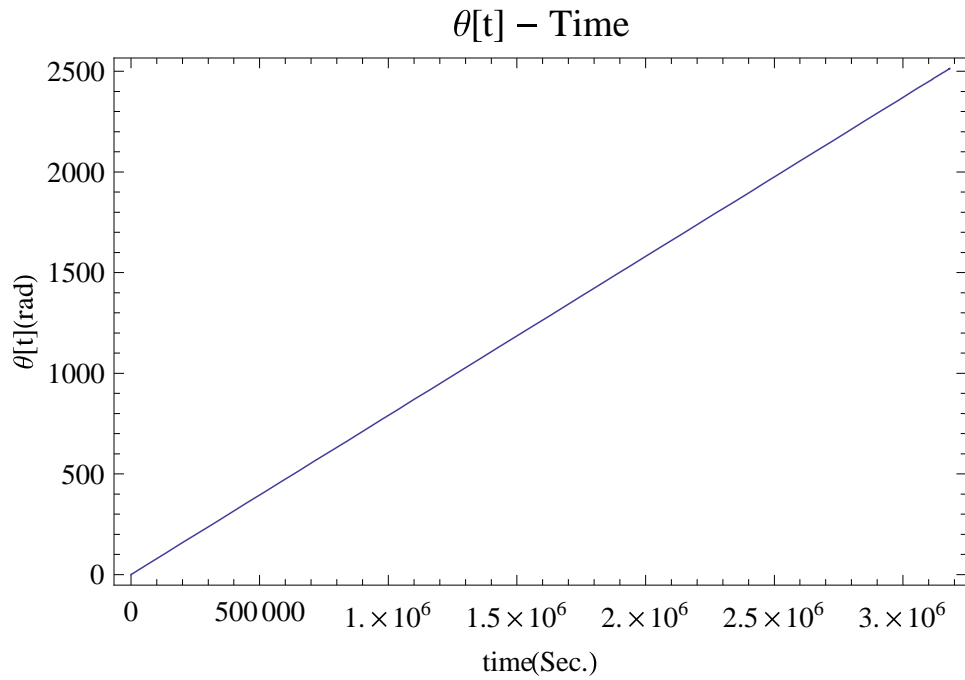


Figure 3.34: The dumbbell MMET with cylindrical payloads elliptical orbit angular position  $\theta$  ( $T_n = 400.01$ )

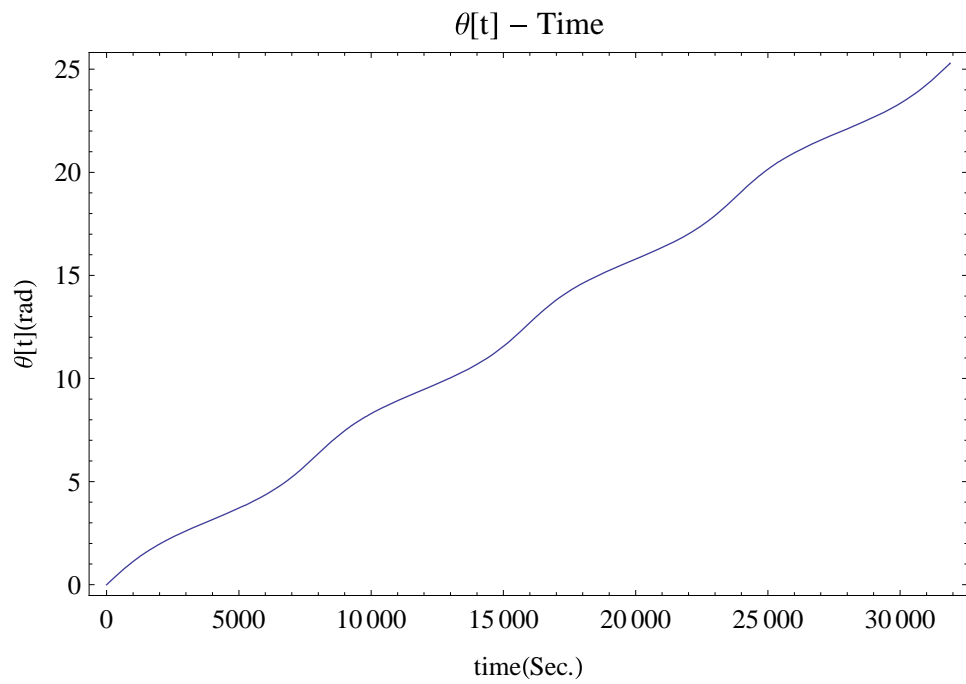


Figure 3.35: The dumbbell MMET with cylindrical payloads elliptical orbit angular position of  $\theta$  ( $T_n = 4.01$ )

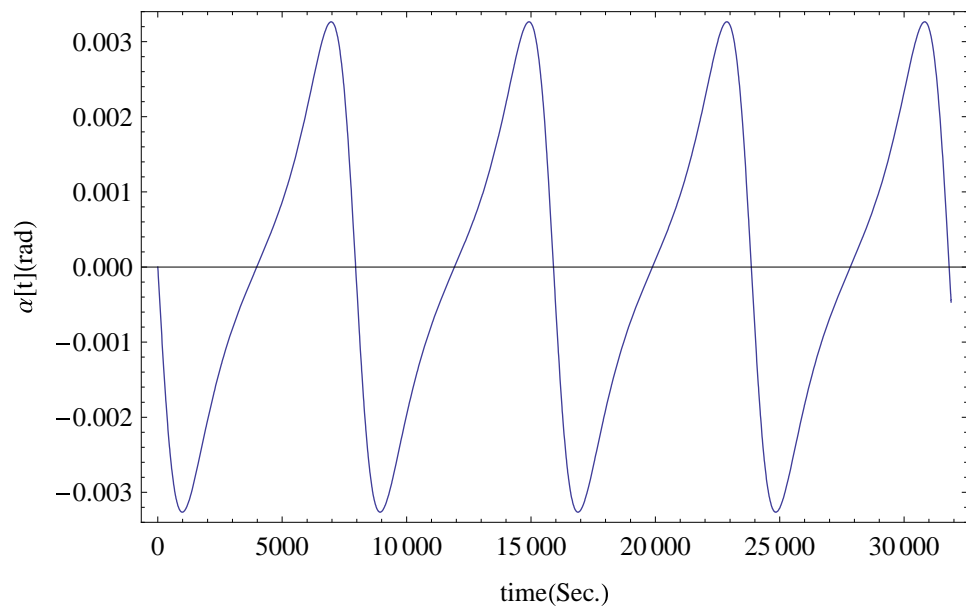


Figure 3.36: The dumbbell MMET with cylindrical payloads, out-of-plane angle  $\alpha$  ( $T_n = 4.01$ )

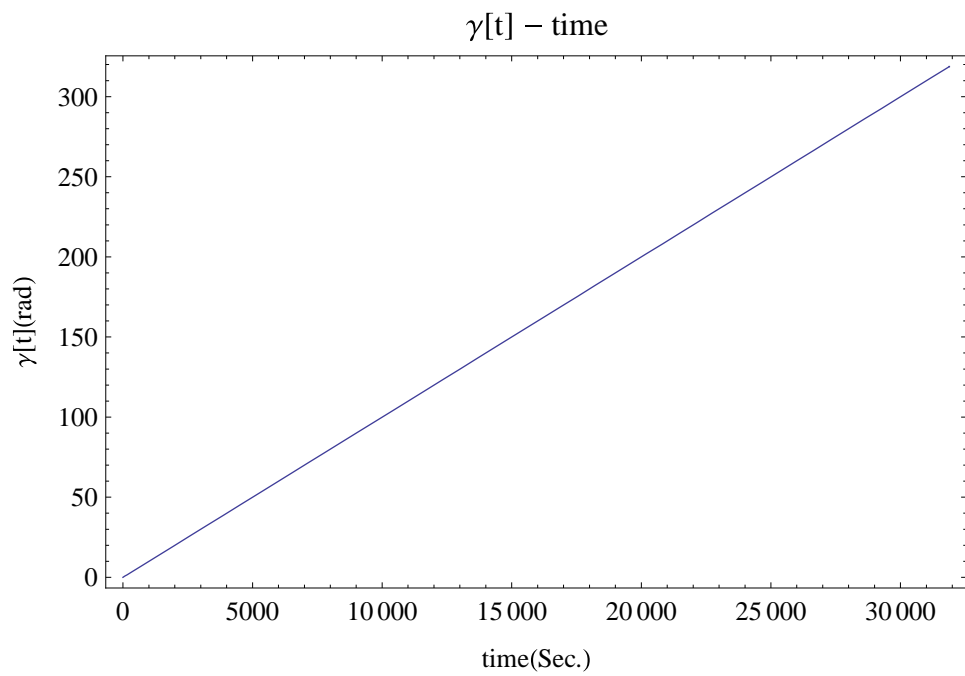


Figure 3.37: The dumbbell MMET with cylindrical payloads, rolling angle  $\gamma$  ( $T_n = 4.01$ )

### 3.6 The MMET as a Rigid Body

To obtain accurate quantitative statements, a rigid body MMET system is investigated in this section, which incorporates the tether's mass and mass moment of inertia. The environmental conditions are the same as in section 3.2. Figure 3.38 describes the conceptual model of this MMET with solid tether-tube subspans. This MMET system comprises a symmetrical double cylindrical payload configuration,  $M_1$  and  $M_2$ , a cylindrical motor facility  $M_M$ , and two tubular tether subspans with the length  $L$ .

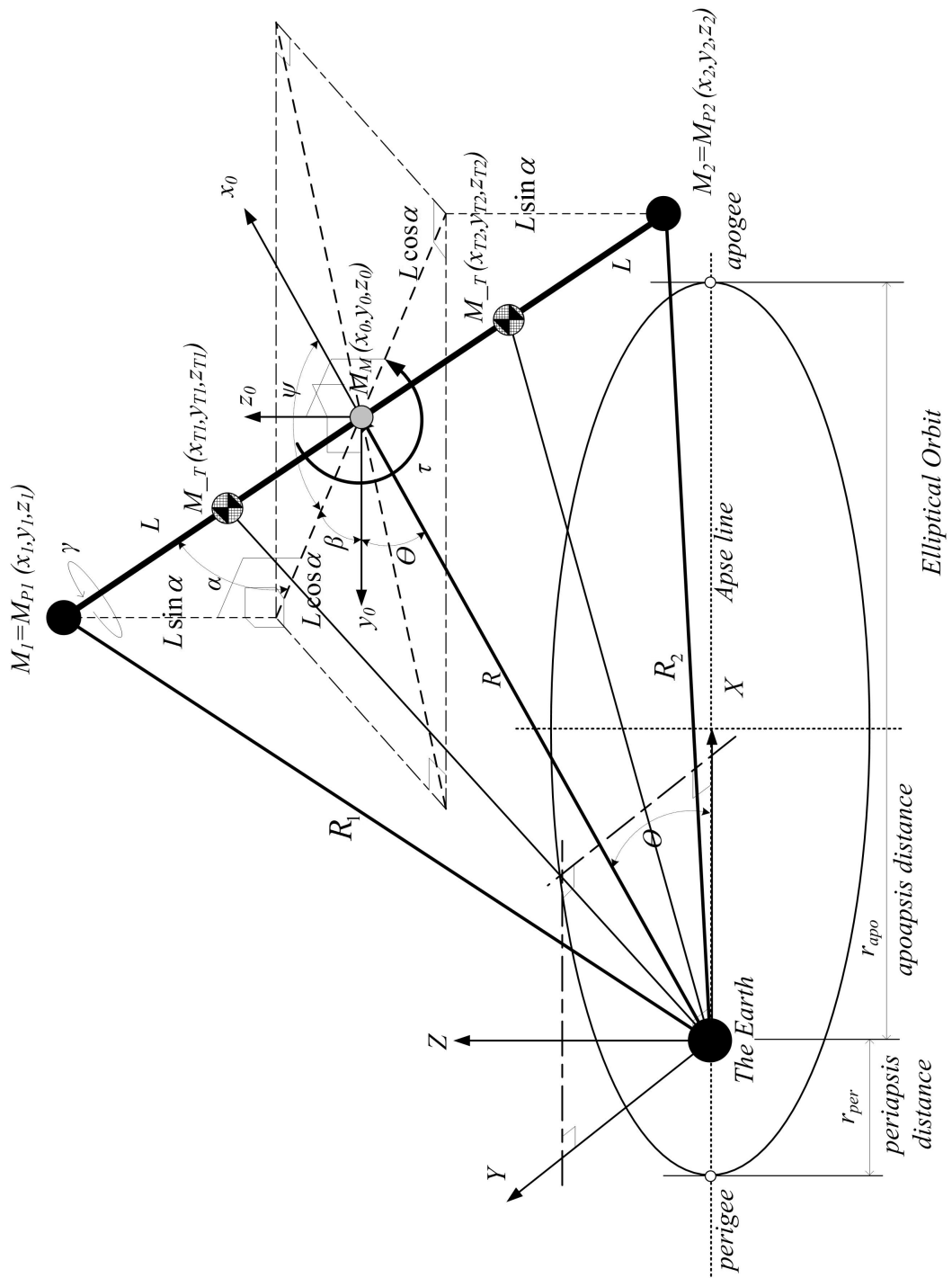


Figure 3.38: The MMET with solid tether-tube generalised coordinates and defined on orbit

### 3.6.1 Tether-Tube Mass Moments of Inertia

The local axis definitions for the tether-tube subspans are demonstrated in Figures 3.39 and 3.40, which state the mass component of  $M_T$  for the MMET dynamical modelling. Equation (3.6.1) is the mass moment of inertia for each tether-tube subspan, equation (3.6.2) states the cross-sectional-area of the tether tube, and equation (3.6.3) provides the mass for each tether-tube subspan.

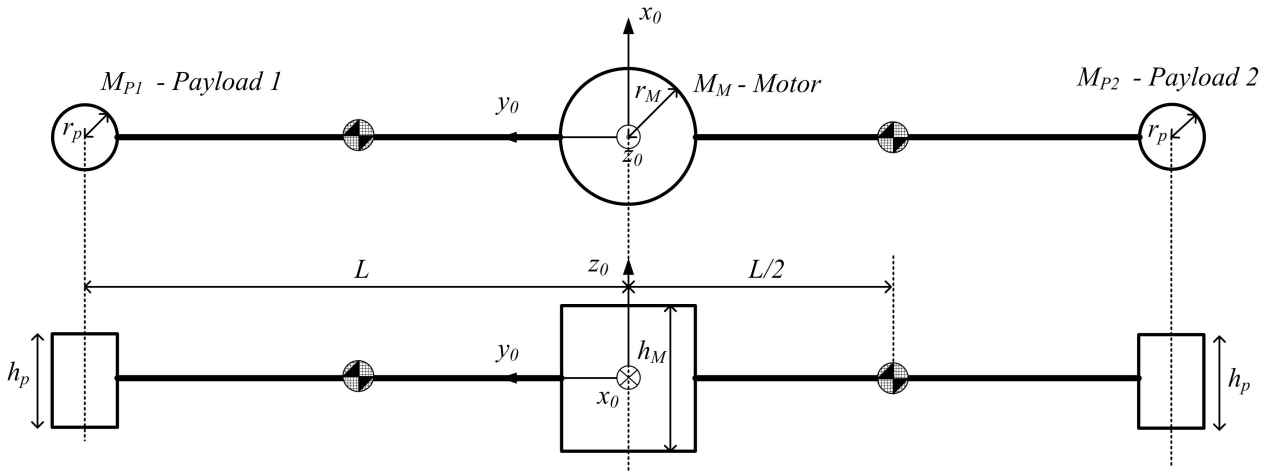


Figure 3.39: The definition of local axes for tether mass components

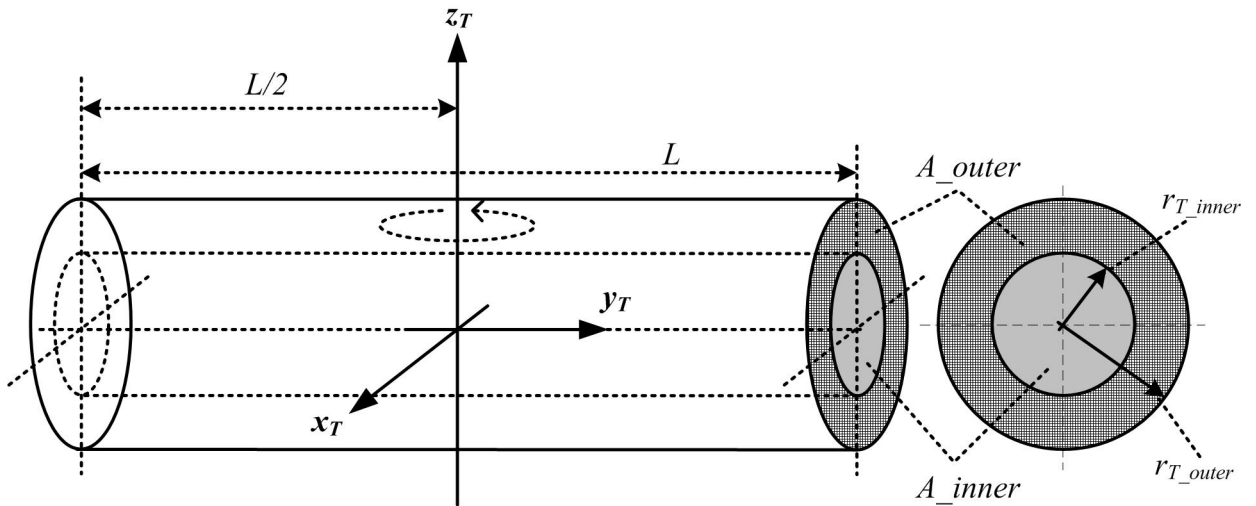


Figure 3.40: The definition of local axes for the tether subspan

$$\begin{cases} I_{x_T} = \frac{1}{12} M_T [3 (r_{T\_inner}^2 + r_{T\_outer}^2) + L^2] \\ I_{y_T} = \frac{1}{2} M_T (r_{T\_inner}^2 + r_{T\_outer}^2) \\ I_{z_T} = \frac{1}{12} M_T [3 (r_{T\_inner}^2 + r_{T\_outer}^2) + L^2] \end{cases} \quad (3.6.1)$$

$$A = A_{\text{outer}} - A_{\text{inner}} = \pi (r_{\text{T,outer}}^2 - r_{\text{T,inner}}^2) \quad (3.6.2)$$

$$M_{\text{T}} = (A_{\text{outer}} - A_{\text{inner}}) L\rho = \pi (r_{\text{T,outer}}^2 - r_{\text{T,inner}}^2) L\rho \quad (3.6.3)$$

where,

$A$  is the tether-tube's cross-sectional area,

$r_{\text{T,outer}}$  is the outer radius of the tether-tube,

$r_{\text{T,inner}}$  is the inner radius of the tether-tube,

$I_{x_{\text{T}}}$  is the mass moment of inertia about the local axis  $x_{\text{T}}$ ,

$I_{y_{\text{T}}}$  is the mass moment of inertia about the local axis  $y_{\text{T}}$ ,

$I_{z_{\text{T}}}$  is the mass moment of inertia about the local axis  $z_{\text{T}}$ , as in Figure 3.40.

### 3.6.2 Tether-Tube Discretisation

The validation of the feasibility of the tether-tube discretisation is obtained by Ziegler [65], considering the MMET system's potential energy, the main advantage for the discretisation process is to avoid the singularity in the MMET numerical simulation. The potential energy of the solid tether-tube subspan is given in equation (3.6.4), in which the function  $\ln()$  appears in the equation, showing a numerical singularity at  $\psi = \pi$  in Figure 3.41, and also in Figure 3.42, at  $\psi = \Omega\pi$ , where  $\Omega$  is an integer. The numerical singularity will be encountered when the MMET system is numerically integrated. To avoid this singularity due to the calculation for  $\ln()$ , an alternative description of the potential energy of the tether-tube was derived, which discretised the tether mass into point masses, in equation (3.6.5) [65].

$$\begin{aligned} U_{\text{T}} &= -\mu\rho A \int_{-L}^L (R^2 + l^2 + 2lR \cos \psi)^{-\frac{1}{2}} dl \\ &= \mu\rho A \ln \left( \frac{R \cos \psi - L + \sqrt{R^2 + L^2 - 2LR \cos \psi}}{R \cos \psi + L + \sqrt{R^2 + L^2 + 2LR \cos \psi}} \right) \end{aligned} \quad (3.6.4)$$

$$U_T = - \sum_{i=1}^N \frac{\mu \rho A L}{N \sqrt{R^2 + \left( \frac{(2i-1)L}{2N} \right)^2 + \frac{2(2i-1)RL}{2N} \cos \psi}} \quad (3.6.5)$$

$$- \sum_{i=1}^N \frac{\mu \rho A L}{N \sqrt{R^2 + \left( \frac{(2i-1)L}{2N} \right)^2 - \frac{2(2i-1)RL}{2N} \cos \psi}}$$

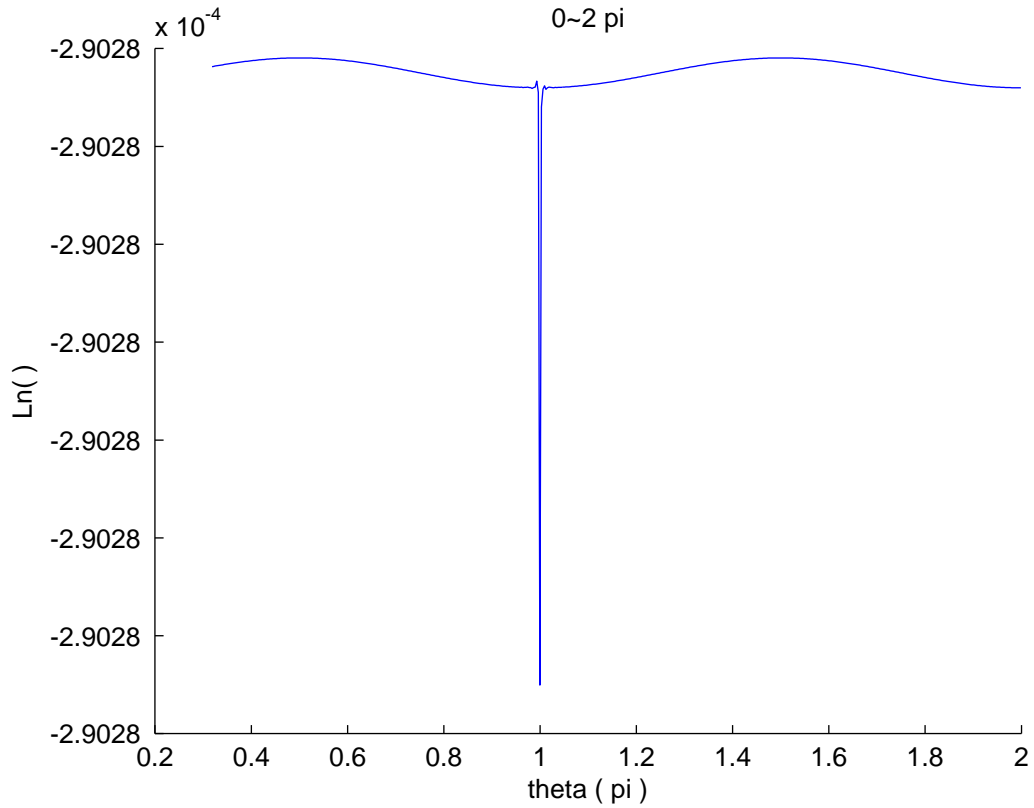


Figure 3.41:  $\ln(\theta)$  function singularity when  $\theta \in [0, \pi]$

The full length of the two tether subspans is  $L_T$  in Figure 3.43, which is given in equation (3.6.6).  $L_0$  is the original length of each subspan of the tether when balanced symmetrically.

Figure 3.43 shows the mass point locations within the full-length  $L_T$ , and the values of  $N$  in the mass points scheme are the scaled locations of the point masses along the full length  $L_T$ . An example for  $N = 2$  is given in Figure 3.44, where  $N = 2$  means there are 2 point masses in the tether, which are located at  $0.25L_T$  and  $0.75L_T$ , respectively. Figure 3.45 lists a 1 to 20 point mass location scheme.

Equation (3.6.7) defines the discrete mass points' location scheme along the tether tube subspans. For example, in a case of mass points  $N = 2$ , the  $l_1 = 0.5$  and  $l_2 = 0.5$ , respectively.

$$L_T = 2L_0 \quad (3.6.6)$$

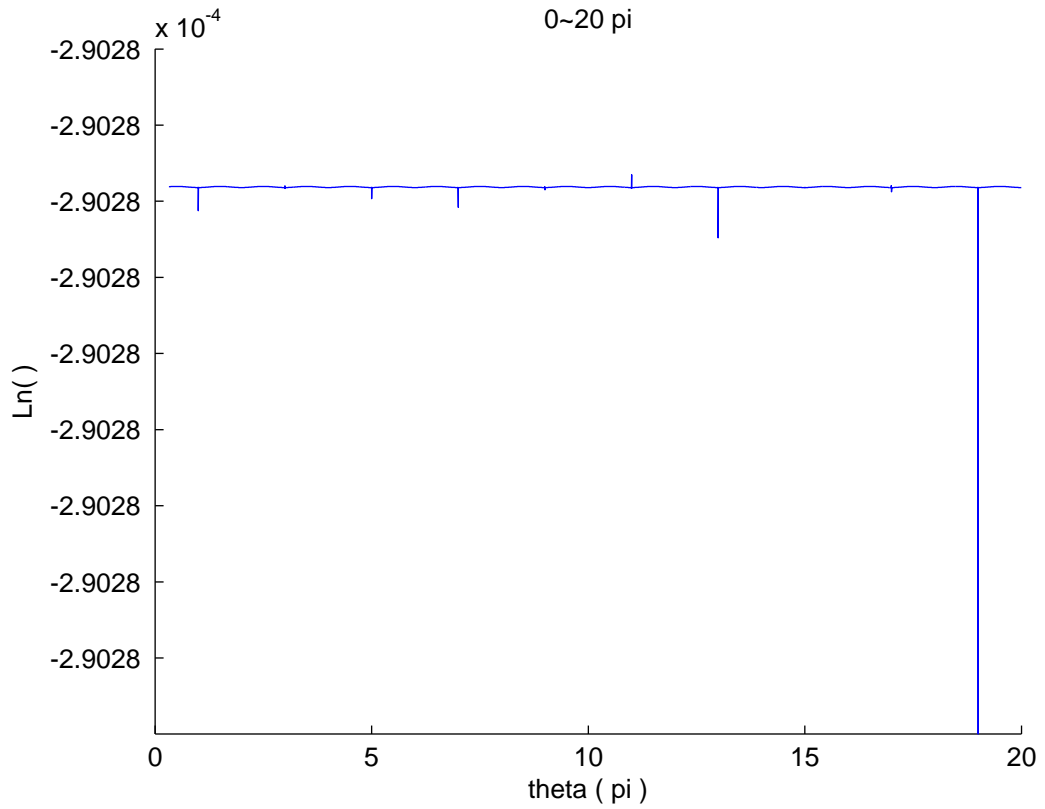


Figure 3.42:  $\ln(\theta)$  function singularity when  $\theta \in [0, 20\pi]$

$$l_i = L_0 - \frac{(2i - 1)L_0}{2N} \quad (3.6.7)$$

### 3.6.3 Discrete Mass Point Mass Moments of Inertia

As shown in Figure 3.46, the mass points are notionally very small, and by taking the same definition of the local axes as for the motor facility in Figure 3.40, it is assumed that there is no significant mass moment of inertia in the mass points  $m_i$  ( $i = 1, 2, \dots, N$ ),  $N$  is the number of the mass points.

In order to study the torsional elastic behaviours, the mass moment of inertia  $I_{y_{m_i}}$  for each mass point  $m_i$  is derived from the tether-tube's mass moments of inertia in this modelling context. Numerically, the mass moment of inertia of the mass points are defined in equation (3.6.8), which can connect the torsional elastic motions of each mass point with the tether subspan's rigid body rolling motion.  $\epsilon$  is the factor for the mass moment of inertia of each mass point,  $\epsilon \geq N$ .

$$\left\{ \begin{array}{l} I_{x_{m_i}} = \frac{I_{x_T}}{\epsilon} \\ I_{y_{m_i}} = \frac{I_{y_T}}{\epsilon} \\ I_{z_{m_i}} = \frac{I_{z_T}}{\epsilon} \end{array} \right. \quad (3.6.8)$$

### 3.6.4 Potential Energy

This solid tether-tube MMET system's potential energy is given in equation (3.6.9), and  $\mu$  is the product of the universal gravitational constant  $G$  with the Earth's Mass. According to the solid tether-tube subspan's discrete equations (3.6.4) and (3.6.5), equation (3.6.9) can be re-stated as equation (3.6.10) [65].

$$\begin{aligned} u &= -\frac{\mu M_p}{\sqrt{L^2 + R^2 + 2LR \cos \psi}} - \frac{\mu M_p}{\sqrt{L^2 + R^2 - 2LR \cos \psi}} - \frac{\mu M_M}{R} \\ &\quad - \mu \rho A \int_{-L}^L (R^2 + l^2 + 2lR \cos \psi)^{-\frac{1}{2}} dl \end{aligned} \quad (3.6.9)$$

$$\begin{aligned} &= -\frac{\mu M_p}{\sqrt{L^2 + R^2 + 2LR \cos \psi}} - \frac{\mu M_p}{\sqrt{L^2 + R^2 - 2LR \cos \psi}} - \frac{\mu M_M}{R} \\ &\quad + \mu \rho A \ln \left( \frac{R \cos \psi - L + \sqrt{R^2 + L^2 - 2LR \cos \psi}}{R \cos \psi + L + \sqrt{R^2 + L^2 + 2LR \cos \psi}} \right) \\ u &= -\frac{\mu M_p}{\sqrt{L^2 + R^2 + 2LR \cos \psi}} - \frac{\mu M_p}{\sqrt{L^2 + R^2 - 2LR \cos \psi}} - \frac{\mu M_M}{R} \\ &\quad - \sum_{i=1}^N \frac{\mu \rho A L}{N \sqrt{R^2 + \left( \frac{(2i-1)L}{2N} \right)^2 + \frac{2(2i-1)RL}{2N} \cos \psi}} \\ &\quad - \sum_{i=1}^N \frac{\mu \rho A L}{N \sqrt{R^2 + \left( \frac{(2i-1)L}{2N} \right)^2 - \frac{2(2i-1)RL}{2N} \cos \psi}} \end{aligned} \quad (3.6.10)$$

Figure 3.47 is a comparison of the potential energy for a full solid tether subspan and a discrete tether subspan, with given initial conditions. Figure 3.48 compares the error of

the potential energy for the full tether subspan and the discrete tether subspan energies, with the same initial conditions. Both Figures prove how many discrete masses are needed to approximate the full tether's potential energy satisfactorily, and it may be seen that there should be at least 15 masses to approximate adequately the full tether-tube subspan.

### 3.6.5 Kinetic Energy

Taking into account the translation and rotation of each component, the kinetic energy of this MMET system is addressed in equation (3.6.11), in which,  $M_{T1}(x_1, y_1, z_1)$  and  $M_{T2}(x_2, y_2, z_2)$  in equations (3.6.12) and (3.6.13) are the tether subspans' centre of mass, as also declared in Figure 3.38.

$$\begin{aligned}
T = & \frac{1}{2}M_{P1} (\dot{x}_{P1}^2 + \dot{y}_{P1}^2 + \dot{z}_{P1}^2) + \frac{1}{2}M_{P2} (\dot{x}_{P2}^2 + \dot{y}_{P2}^2 + \dot{z}_{P2}^2) + \frac{1}{2}M_M (\dot{x}_M^2 + \dot{y}_M^2 + \dot{z}_M^2) \\
& + \frac{1}{2}A\rho L (\dot{x}_{T1}^2 + \dot{y}_{T1}^2 + \dot{z}_{T1}^2) + \frac{1}{2}A\rho L (\dot{x}_{T2}^2 + \dot{y}_{T2}^2 + \dot{z}_{T2}^2) \\
& + \left[ \frac{1}{2}I_{zP1} + \frac{1}{2}I_{zP2} + I_{zT} + \frac{1}{2}I_{zM} \right] (\dot{\psi} + \dot{\theta})^2 \\
& + \left[ \frac{1}{2}I_{xP1} + \frac{1}{2}I_{xP2} + I_{xT} + \frac{1}{2}I_{xM} \right] \dot{\alpha}^2 \\
& + \left[ \frac{1}{2}I_{yP1} + \frac{1}{2}I_{yP2} + I_{yT} + \frac{1}{2}I_{yM} \right] \dot{\gamma}^2
\end{aligned} \tag{3.6.11}$$

where,

$$\begin{cases} x_{T1} = x_0 + \frac{1}{2}L\cos\alpha\cos(\theta + \psi) \\ y_{T1} = y_0 + \frac{1}{2}L\cos\alpha\sin(\theta + \psi) \\ z_{T1} = z_0 + \frac{1}{2}L\sin\alpha \end{cases} \tag{3.6.12}$$

$$\begin{cases} x_{\Pi} = x_0 - \frac{1}{2}L\cos\alpha\cos(\theta + \psi) \\ y_{\Pi} = y_0 - \frac{1}{2}L\cos\alpha\sin(\theta + \psi) \\ z_{\Pi} = z_0 - \frac{1}{2}L\sin\alpha \end{cases} \quad (3.6.13)$$

### 3.6.6 Generalised Coordinates

In the case of this solid MMET modelling, it has been decided to represent the system dynamics by means of four angular coordinates ( $\psi$ ,  $\theta$ ,  $\alpha$ ,  $\gamma$ ) and one translational coordinate ( $R$ ), in which,  $q_1 = \psi$ ,  $q_2 = \theta$ ,  $q_3 = \alpha$ ,  $q_4 = R$ ,  $q_5 = \gamma$ , which are the same generalised coordinates as used in section 3.5.4.

### 3.6.7 Generalised Forces

The generalised forces are same as which stated in section 3.5.7.

### 3.6.8 Governing Equations of Motion

The following motion governing equations for the generalised coordinates  $q_i$  are given in equations (3.6.14) to (3.6.18) by the Lagrange equation, which are also listed in Table 3.5.

Table 3.5: MMET with discrete tether-tube subspans generalised coordinates and generalised forces

$i$	$q_i$	$Q_i$	$T$	$U$	Motion Governing Equation
1	$\psi$	(3.5.13)	(3.6.11)	(3.6.10)	(3.6.14)
2	$\theta$	(3.5.14)			(3.6.15)
3	$\alpha$	(3.5.15)			(3.6.16)
4	$R$	(3.5.16)			(3.6.17)
5	$\gamma$	(3.5.17)			(3.6.18)

$$\begin{aligned}
& \frac{-\mu M_{P1} L R \cos \alpha \sin \psi}{(R^2 + L^2 + 2LR \cos \alpha \cos \psi)^{3/2}} + \frac{\mu M_{P2} L R \cos \alpha \sin \psi}{(R^2 + L^2 - 2LR \cos \alpha \cos \psi)^{3/2}} + \\
& \sum_{i=1}^n \frac{\text{Across}(2i-1) \mu \rho \cos \alpha L^2 R \sin \psi}{2n^2 \left( \frac{(2i-1)^2 L^2}{4n^2} - \frac{(2i-1) \cos \alpha \cos \psi R L}{n} + R^2 \right)^{3/2}} - \\
& \sum_{i=1}^n \frac{\text{Across}(2i-1) \mu \rho \cos \alpha L^2 R \sin \psi}{2n^2 \left( \frac{(2i-1)^2 L^2}{4n^2} + \frac{(2i-1) \cos \alpha \cos \psi R L}{n} + R^2 \right)^{3/2}} + \\
& (M_{P1} - M_{P2}) \left( \begin{array}{l} \cos \alpha \dot{L} (\sin \psi \dot{R} - \cos \psi R \dot{\theta}) + \\ L \left( \begin{array}{l} \sin \alpha \dot{\alpha} (\cos \psi R \dot{\theta} - \sin \psi \dot{R}) + \\ \cos \alpha (\cos \psi \dot{R} + R \sin \psi \dot{\theta}) (\dot{\theta} + \dot{\psi}) \end{array} \right) \end{array} \right) + \\
& \left( \begin{array}{l} A \rho ((3 \cos 2\alpha + 5) (\ddot{\theta} + \ddot{\psi}) - 6 \sin(2\alpha) \dot{\alpha} (\dot{\theta} + \dot{\psi})) L^3 + \\ 3A \rho (3 \cos 2\alpha + 5) \dot{L} (\dot{\theta} + \dot{\psi}) L^2 + \\ 6A \rho (r_{\text{inner}}^2 + r_{\text{outer}}^2) (\ddot{\theta} + \ddot{\psi}) L + \\ 6 (M_M (\ddot{\theta} + \ddot{\psi}) r_M^2 + A \rho (r_{\text{inner}}^2 + r_{\text{outer}}^2) \dot{L} (\dot{\theta} + \dot{\psi})) + \\ \left( \begin{array}{l} 2 \cos \alpha (\cos \alpha (\ddot{\theta} + \ddot{\psi}) - 2 \sin \alpha \dot{\alpha} (\dot{\theta} + \dot{\psi})) L^2 + \\ 6M_{P1} \left( 2L \left( \begin{array}{l} \sin \alpha \dot{\alpha} (\sin \psi \dot{R} - \cos \psi R \dot{\theta}) + \\ \cos \alpha (\cos \psi (\dot{R} (\dot{\theta} - \dot{\psi}) + R \ddot{\theta}) - \sin \psi (R \dot{\theta} \dot{\psi} + \ddot{R})) \end{array} \right) + \right) + \\ \left( \begin{array}{l} 2 \cos \alpha \dot{L} (-\sin \psi \dot{R} + \cos \psi R \dot{\theta} + 2 \cos \alpha L (\dot{\theta} + \dot{\psi})) + r_p^2 (\ddot{\theta} + \ddot{\psi}) \end{array} \right) \end{array} \right) + \\ \\ \left( \begin{array}{l} 2 (\cos^2 \alpha (\ddot{\theta} + \ddot{\psi}) - \sin 2\alpha \dot{\alpha} (\dot{\theta} + \dot{\psi})) L^2 + \\ 6 M_{P2} \left( 2L \left( \begin{array}{l} R \dot{\alpha} \dot{\theta} \cos \psi \sin \alpha - \dot{R} (\sin \alpha \sin \psi \dot{\alpha} + \cos \alpha \cos \psi (\dot{\theta} - \dot{\psi})) + \\ \cos \alpha (\sin \psi (R \dot{\theta} \dot{\psi} + \ddot{R}) - \cos \psi R \ddot{\theta}) \end{array} \right) + \right) + \\ \left( \begin{array}{l} 2 \cos \alpha \dot{L} (\sin \psi \dot{R} - \cos \psi R \dot{\theta} + 2 \cos \alpha L (\dot{\theta} + \dot{\psi})) + r_p^2 (\ddot{\theta} + \ddot{\psi}) \end{array} \right) \end{array} \right) \end{array} \right) \\
& = Q_\psi
\end{aligned}$$

(3.6.14)

$$\begin{aligned}
& (2A\rho\dot{L}\dot{\theta} + (2A\rho L + M_M + M_{P1} + M_{P2})\ddot{\theta}) R^2 + \\
& \left( \begin{aligned}
& 2(2A\rho L + M_M + M_{P1} + M_{P2})\dot{R}\dot{\theta} - \sin\psi(M_{P1} - M_{P2}) \\
& (\cos\alpha(L(\dot{\alpha}^2 + \dot{\psi}(2\dot{\theta} + \dot{\psi})) - \ddot{L}) + \sin(\alpha(t))(2\dot{L}\dot{\alpha} + L\ddot{\alpha})) + \\
& \cos\psi(M_{P1} - M_{P2})\left(2\cos\alpha\dot{L}(\dot{\theta} + \dot{\psi}) + L(\cos\alpha(2\ddot{\theta} + \ddot{\psi}) - 2\sin\alpha\dot{\alpha}(\dot{\theta} + \dot{\psi}))\right)
\end{aligned} \right) R + \\
& \frac{1}{12} \left( \begin{aligned}
& A\rho L^3((3\cos 2\alpha + 5)(\ddot{\theta} + \ddot{\psi}) - 6\sin 2\alpha\dot{\alpha}(\dot{\theta} + \dot{\psi})) + \\
& 3L^2 \left( A\rho(3\cos 2\alpha + 5)\dot{L}(\dot{\theta} + \dot{\psi}) + \right. \\
& \left. 4\cos\alpha(M_{P1} + M_{P2})(\cos\alpha(\ddot{\theta} + \ddot{\psi}) - 2\sin\alpha\dot{\alpha}(\dot{\theta} + \dot{\psi})) \right) + \\
& 6L \left( \begin{aligned}
& 2\cos\alpha \left( \begin{aligned}
& 2\cos\alpha(M_{P1} + M_{P2})\dot{L}(\dot{\theta} + \dot{\psi}) + \\
& (M_{P1} - M_{P2})(2\cos\psi\dot{R}\dot{\theta} - \sin\psi\ddot{R})
\end{aligned} \right) \\
& + A\rho(r_{\text{inner}}^2 + r_{\text{outer}}^2)(\ddot{\theta} + \ddot{\psi})
\end{aligned} \right) \\
& + 6(A\rho(r_{\text{inner}}^2 + r_{\text{outer}}^2)\dot{L}(\dot{\theta} + \dot{\psi}) + (M_M r_M^2 + (M_{P1} + M_{P2})r_P^2)(\ddot{\theta} + \ddot{\psi}))
\end{aligned} \right) \\
& = Q_{\theta}
\end{aligned}$$

(3.6.15)

$$\begin{aligned}
& \frac{-\mu M_{p1} L R \sin \alpha \cos \psi}{(R^2 + L^2 + 2LR \cos \alpha \cos \psi)^{3/2}} + \frac{\mu M_{p2} L R \sin \alpha \cos \psi}{(R^2 + L^2 - 2LR \cos \alpha \cos \psi)^{3/2}} + \\
& \sum_{i=1}^N \frac{A(2i-1)\mu \rho \sin \alpha \cos \psi L^2 R}{2N^2 \left( \frac{(2i-1)^2 L^2}{4N^2} - \frac{(2i-1) \cos \alpha \cos \psi R L}{N} + R^2 \right)^{3/2}} - \\
& \sum_{i=1}^N \frac{A(2i-1)\mu \rho \sin \alpha \cos \psi L^2 R}{2n^2 \left( \frac{(2i-1)^2 L^2}{4n^2} + \frac{(2i-1) \cos \alpha \cos \psi R L}{N} + R^2 \right)^{3/2}} - \\
& \frac{1}{4} \left( \begin{aligned} & -L^2 \sin 2\alpha (A\rho L + 2(M_{p1} + M_{p2})) (\dot{\theta} + \dot{\psi})^2 - \\ & 4 \cos \alpha L (M_{p1} - M_{p2}) \dot{\alpha} (\cos(\psi) \dot{R} + R \sin(\psi) \dot{\theta}) - \\ & 4 \sin \alpha (M_{p1} - M_{p2}) \left( \begin{aligned} & \dot{L} (\cos(\psi) \dot{R} + R \sin(\psi) \dot{\theta}) - \\ & L (\sin(\psi) \dot{R} - \cos(\psi) R \dot{\theta}) (\dot{\theta} + \dot{\psi}) \end{aligned} \right) \end{aligned} \right) + \\
& \frac{1}{12} \left( \begin{aligned} & 8A\rho \ddot{\alpha} L^3 + 24A\rho \dot{L} \dot{\alpha} L^2 + 12 M_{p1} \ddot{\alpha} L^2 + 12 M_{p2} \ddot{\alpha} L^2 + 24 M_{p1} \dot{L} \dot{\alpha} L + \\ & 24 M_{p2} \dot{L} \dot{\alpha} L - 12 \cos \alpha (M_{p1} - M_{p2}) \dot{\alpha} (\cos(\psi) \dot{R} + R \sin(\psi) \dot{\theta}) L + \\ & 6A\rho r_{einner}^2 \ddot{\alpha} L + 6A\rho r_{eouter}^2 \ddot{\alpha} L + 6A\rho r_{einner}^2 \dot{L} \dot{\alpha} + 6A\rho r_{eouter}^2 \dot{L} \dot{\alpha} + \\ & 3M_M r_M^2 \ddot{\alpha} + 3M_{p1} r_p^2 \ddot{\alpha} + 3M_{p2} r_p^2 \ddot{\alpha} + h_M^2 M_M \ddot{\alpha} + h_p^2 M_{p1} \ddot{\alpha} + h_p^2 M_{p2} \ddot{\alpha} - \\ & 12 \sin \alpha (M_{p1} - M_{p2}) \left( \begin{aligned} & \dot{L} (\cos(\psi) \dot{R} + R \sin(\psi) \dot{\theta}) + \\ & L (\sin(\psi) \dot{R} (\dot{\theta} - \dot{\psi}) + \cos(\psi) (R \dot{\theta} \dot{\psi} + \ddot{R}) + R \sin(\psi) \ddot{\theta}) \end{aligned} \right) \end{aligned} \right) \\
& = Q_\alpha
\end{aligned} \tag{3.6.16}$$

$$\begin{aligned}
& \frac{\mu M_M}{R^2} + \frac{\mu M_{P1} (R + L \cos \alpha \cos \psi)}{(R^2 + L^2 + 2LR \cos \alpha \cos \psi)^{3/2}} + \frac{\mu M_{P2} (R - L \cos \alpha \cos \psi)}{(R^2 + L^2 - 2LR \cos \alpha \cos \psi)^{3/2}} + \\
& \sum_{i=1}^N \frac{A \mu \rho L \left( 2R - \frac{(2i-1) \cos \alpha \cos \psi L}{N} \right)}{2N \left( \frac{(2i-1)^2 L^2}{4N^2} - \frac{(2i-1) \cos \alpha \cos \psi RL}{N} + R^2 \right)^{3/2}} + \\
& \sum_{i=1}^N \frac{A \mu \rho L \left( 2R + \frac{(2i-1) \cos \alpha \cos \psi L}{N} \right)}{2N \left( \frac{(2i-1)^2 L^2}{4N^2} + \frac{(2i-1) \cos \alpha \cos \psi RL}{N} + R^2 \right)^{3/2}} - \\
& \dot{\theta} \left( \frac{\sin \psi (M_{P1} - M_{P2}) (\cos \alpha \dot{L} - L \sin \alpha \dot{\alpha}) + R (2A \rho L + M_M + M_{P1} + M_{P2}) \dot{\theta}}{\cos \alpha \cos \psi L (M_{P1} - M_{P2}) (\dot{\theta} + \dot{\psi})} \right) + \\
& \left( \begin{aligned}
& \dot{L} (2A \cos \psi \dot{R} - (M_{P1} - M_{P2}) (2 \cos \psi \sin \alpha \dot{\alpha} + \cos \alpha \sin \psi (\dot{\theta} + 2\dot{\psi}))) \\
& + (2A \rho L + M_M + M_{P1} + M_{P2}) \ddot{R} - \\
& \cos \psi (M_{P1} - M_{P2}) (\cos \alpha (L (\dot{\alpha}^2 + \dot{\psi} (\dot{\theta} + \dot{\psi})) - \ddot{L}) + L \sin \alpha \dot{\alpha}) + \\
& L \sin \psi (M_{P1} - M_{P2}) (\sin \alpha \dot{\alpha} (\dot{\theta} + 2\dot{\psi}) - \cos \alpha (\ddot{\theta} + \ddot{\psi}))
\end{aligned} \right) \\
& = Q_R
\end{aligned} \tag{3.6.17}$$

$$\begin{aligned}
& \frac{1}{12} \ddot{\gamma} [M_M (3r_M^2 + h_M^2) + (M_{P1} + M_{P2}) (3r_p^2 + h_p^2) + 12A \rho (r_{T\_inner}^2 + r_{T\_outer}^2) L] + \\
& \dot{\gamma} \dot{L} A \rho (r_{T\_inner}^2 + r_{T\_outer}^2) = Q_\gamma
\end{aligned} \tag{3.6.18}$$

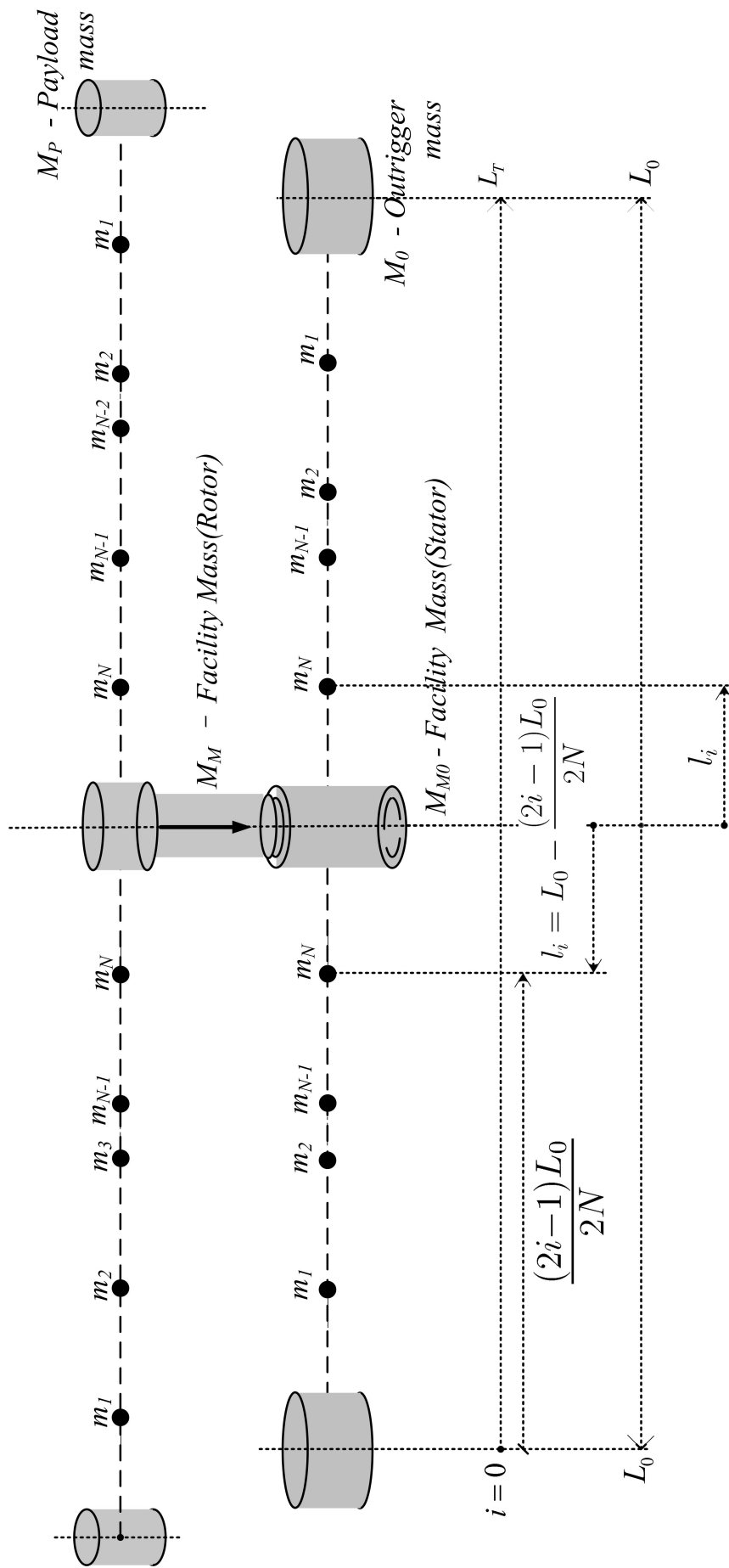


Figure 3.43: The discretisation for axial elasticity for motorised momentum exchange tether

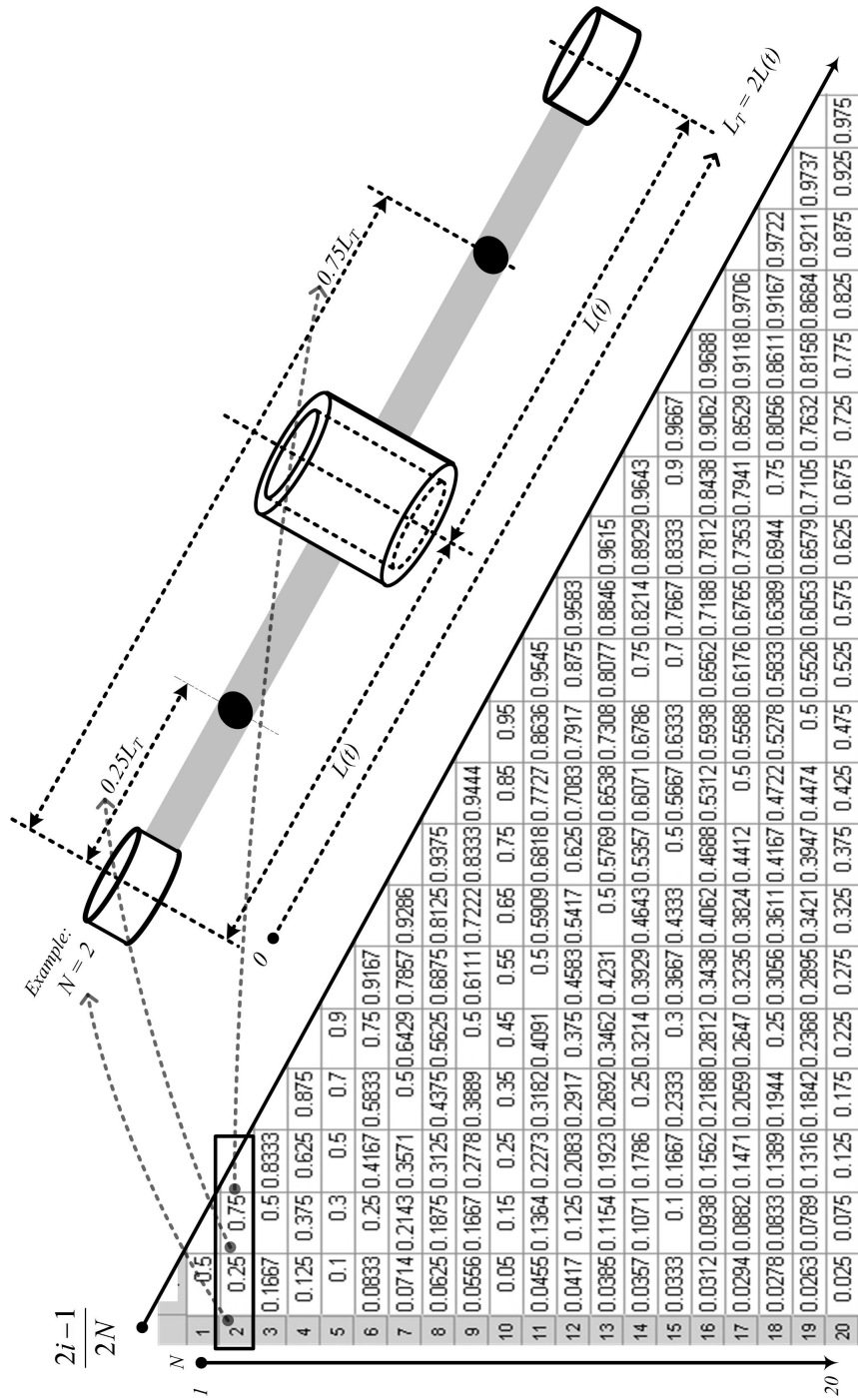


Figure 3.44: The point mass location scheme

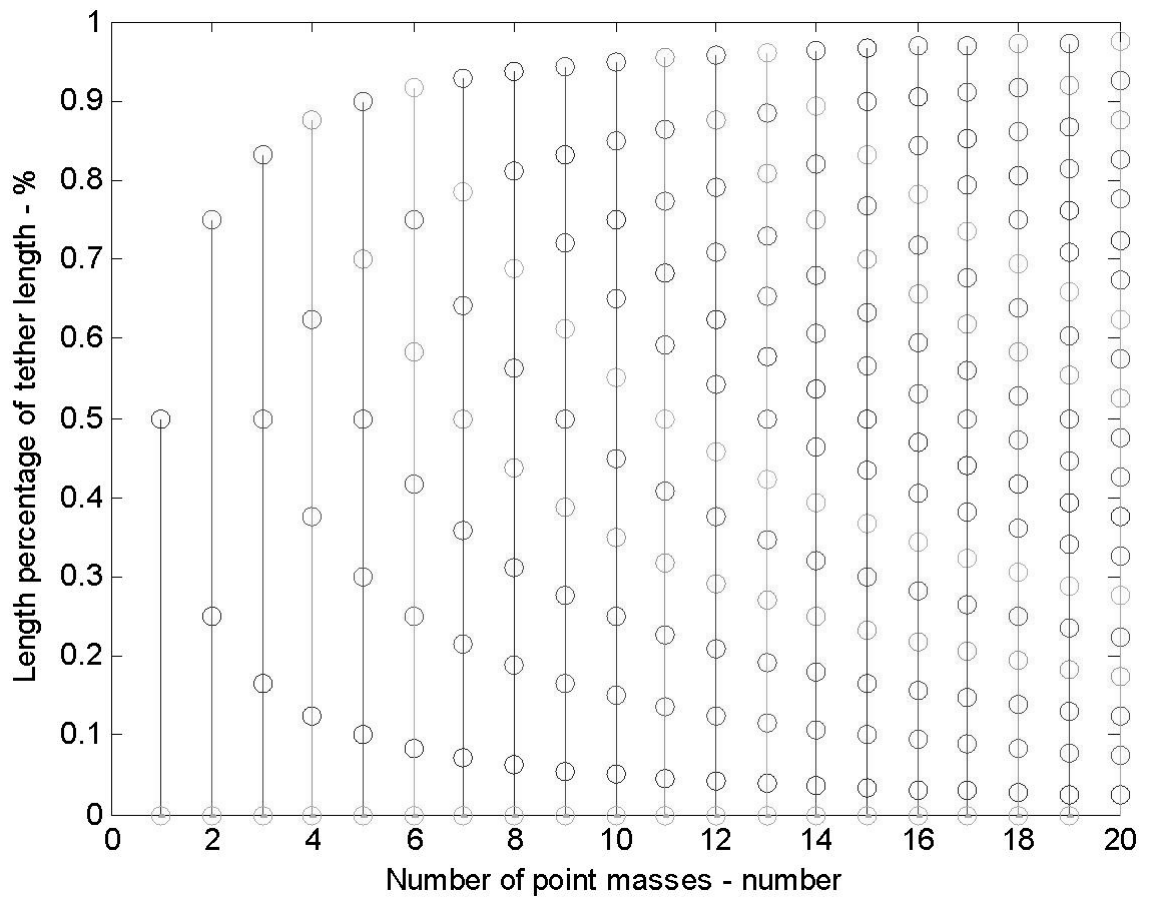


Figure 3.45: The point mass locations as percentage

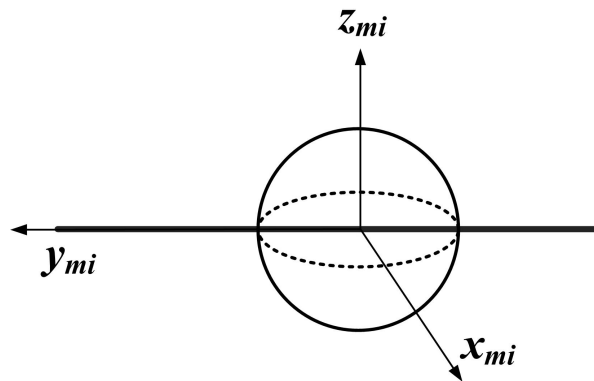


Figure 3.46: The definition of local axes for mass point  $m_i$

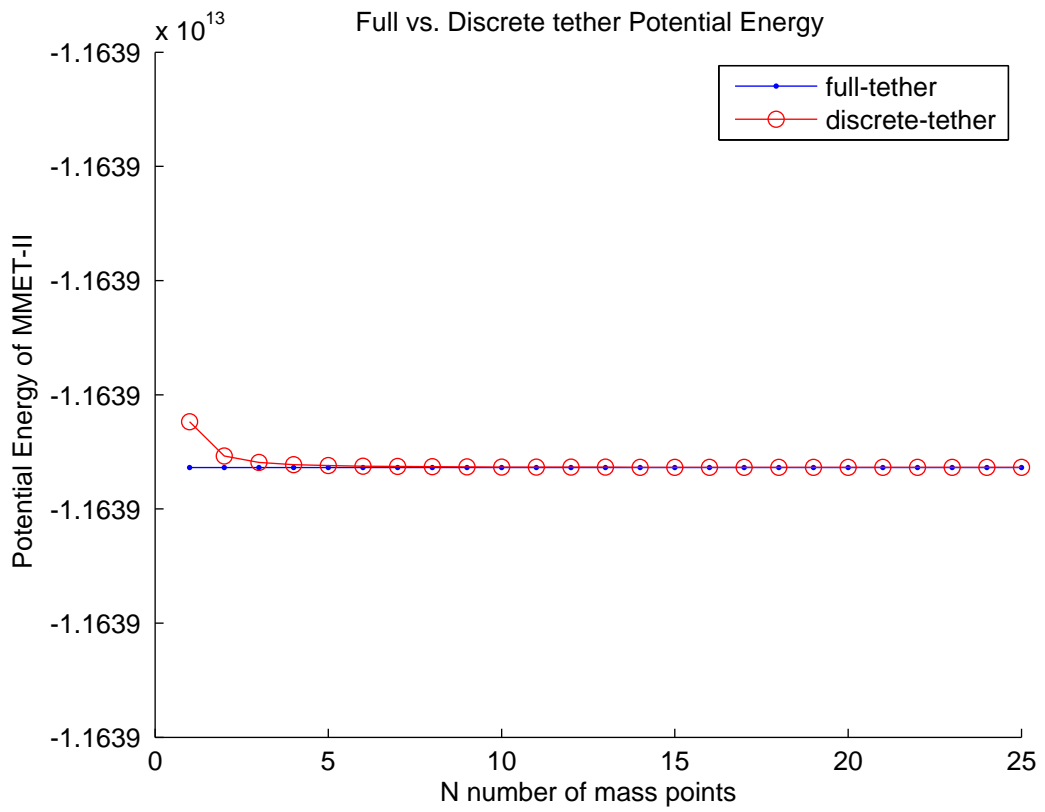


Figure 3.47: The discrete and full tether potential energies [65]

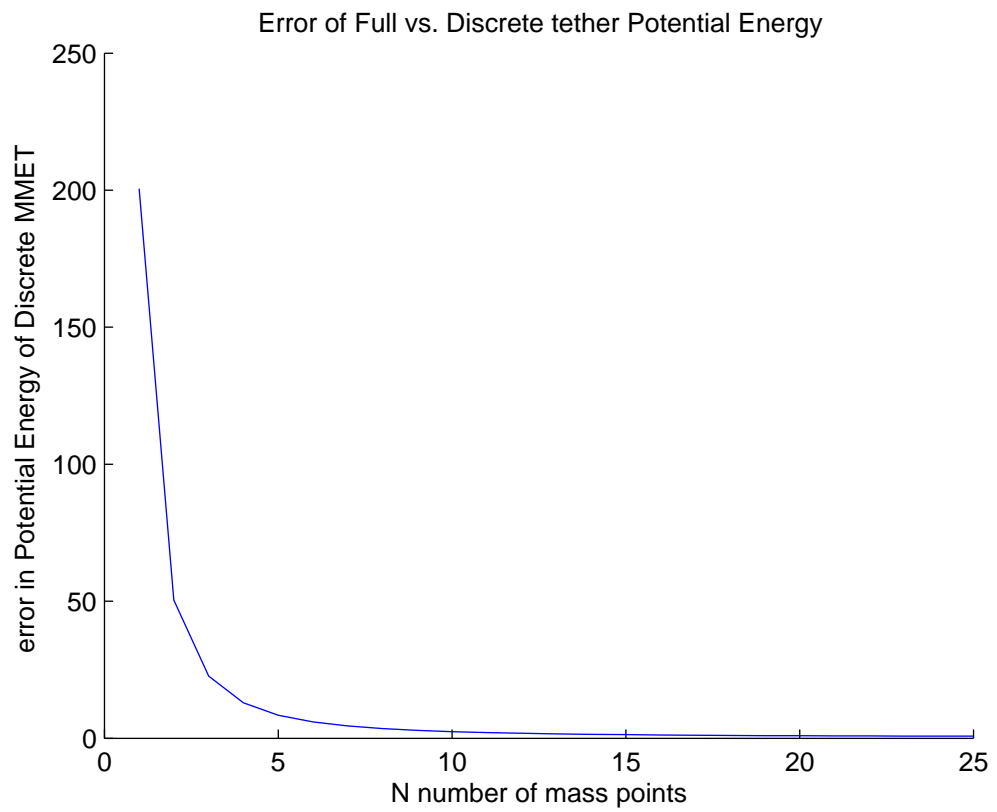


Figure 3.48: The potential energy error of discrete and full tether

### 3.6.9 Simulations and Discussions

Figures 3.49 to 3.55 are the numerical results obtained by MATHEMATICA for the selected generalised coordinates  $\psi$ ,  $\theta$ ,  $\alpha$ ,  $R$  and  $\gamma$ , as listed in Table 3.5. The results show the rigid body MMET's periodic behaviour on orbit, with zero initial conditions as listed in Appendix C.

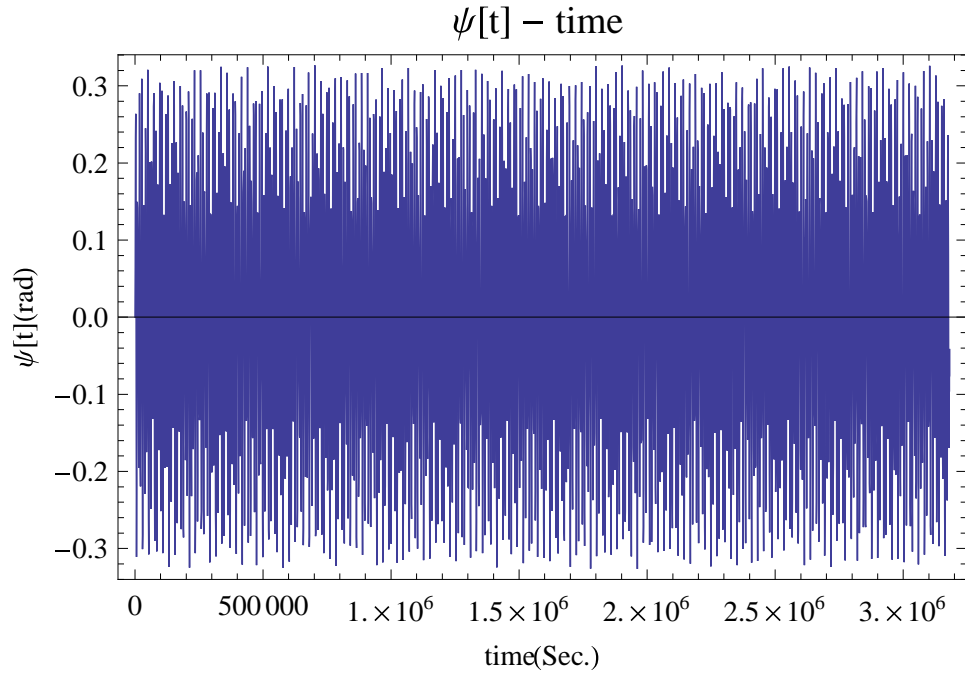


Figure 3.49: The rigid body MMET spin-up displacement  $\psi$  ( $T_n = 400.01$ )

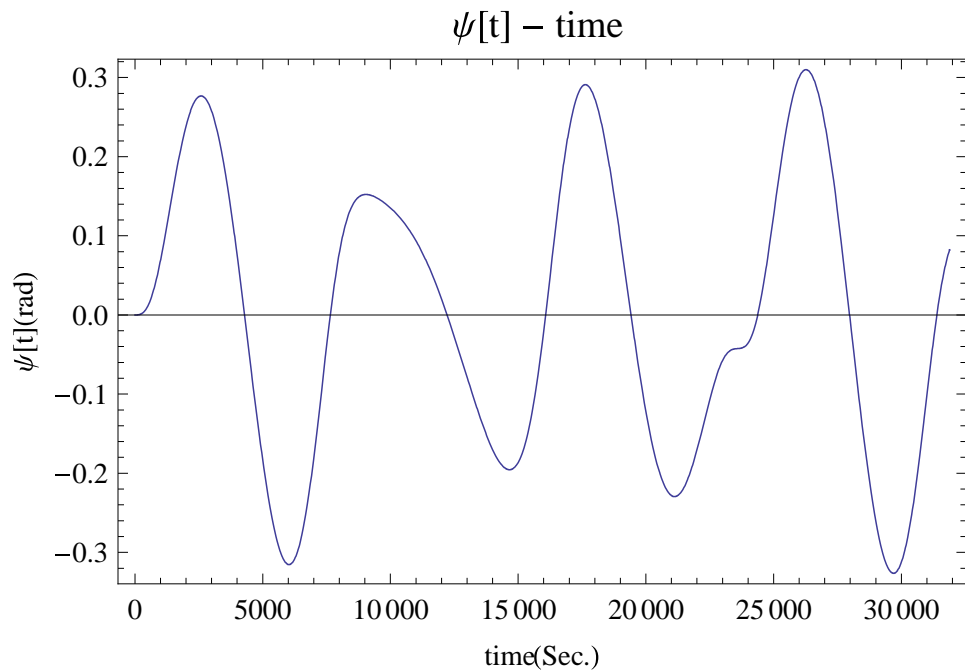


Figure 3.50: The rigid body MMET spin-up displacement  $\psi$  ( $T_n = 4.01$ )

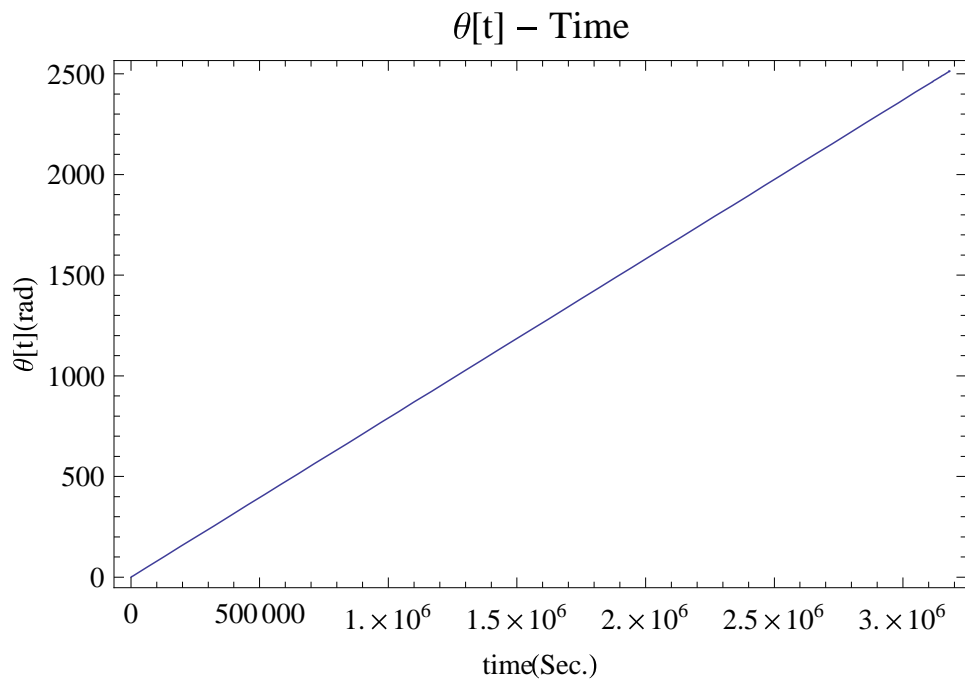


Figure 3.51: The rigid body MMET elliptical orbit angular position of  $\theta$  ( $T_n = 400.01$ )

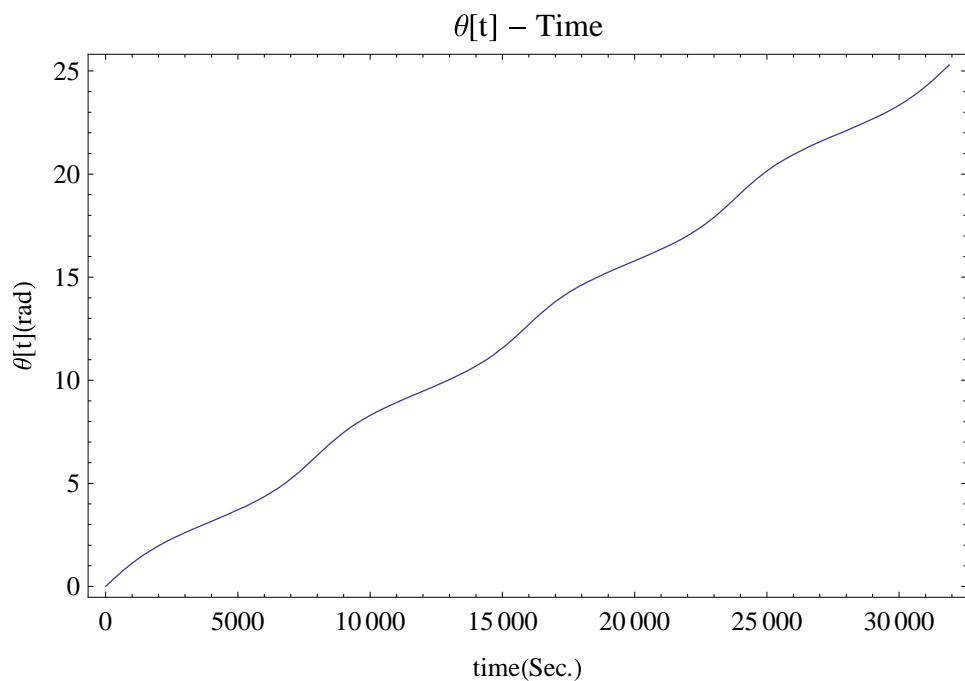


Figure 3.52: The rigid body MMET elliptical orbit angular position of  $\theta$  ( $T_n = 4.01$ )

- ▷ The tether system's spin-up performance is expressed by Figures 3.49 and 3.50, over the the number of cycles of period  $T_n = 4.01$  and  $400.01$ , respectively, with the angular displacement range of  $-0.325$  to  $0.325$  rad,
- ▷  $\theta$  is the true anomaly, as shown in Figure 3.51, the curve is in a linear rising trend from 0 to 2500 rad with small fluctuation spread (0 to 0.5 rad), which can be seen in Figure 3.52.

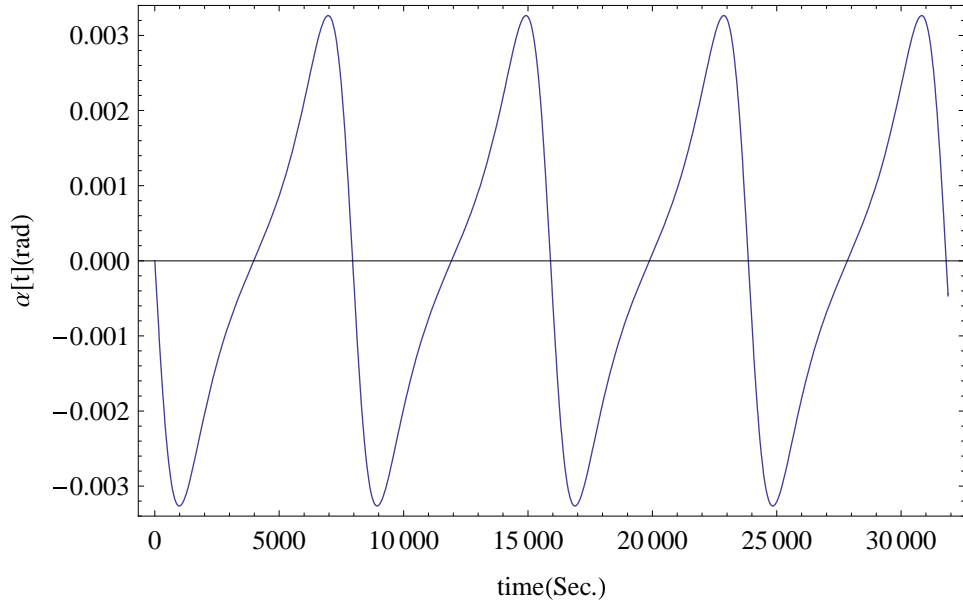


Figure 3.53: The rigid body MMET out-of-plane angle  $\alpha$  ( $T_n = 4.01$ )

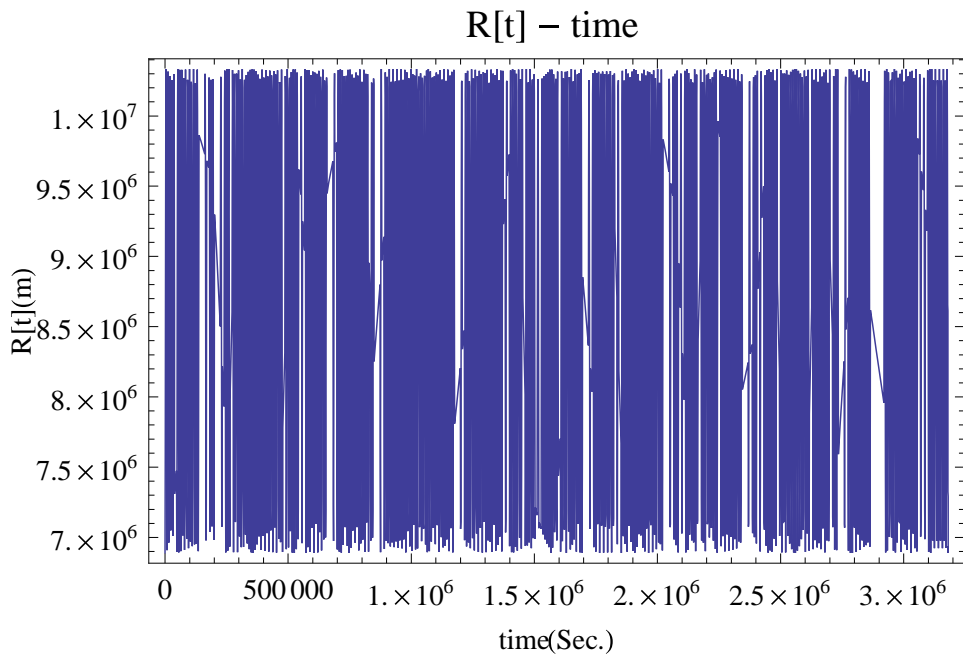


Figure 3.54: The rigid body MMET base point distance of  $R$  ( $T_n = 400.01$ )

▷  $R$  is the distance from the Earth to the tether COM, whose numerical responses go periodically within the range  $r_p$  to  $r_a$ . In this case,  $e = 0.2$ ,  $r_p = 6.89 \times 10^6$  metre and  $r_a = 1.0335 \times 10^7$  metre, as shown in Figures 3.54 and 3.55.

▷ Figure 3.53 is the response for the out-of-plane angle  $\alpha$  with initial conditions  $\alpha(0) = 0.001$  rad and  $\dot{\alpha}(0) = 0.001$  rad/s, which is the projection of the tether onto the orbit plane. If given the zero initial conditions  $\alpha(0) = 0$  rad and  $\dot{\alpha}(0) = 0$  rad/s,  $\alpha$  stays in zero over the full simulation time.

▷ With zero initial conditions  $\gamma(0) = 0$  rad and  $\dot{\gamma}(0) = 0$  rad/s, the rigid rolling angle  $\gamma$

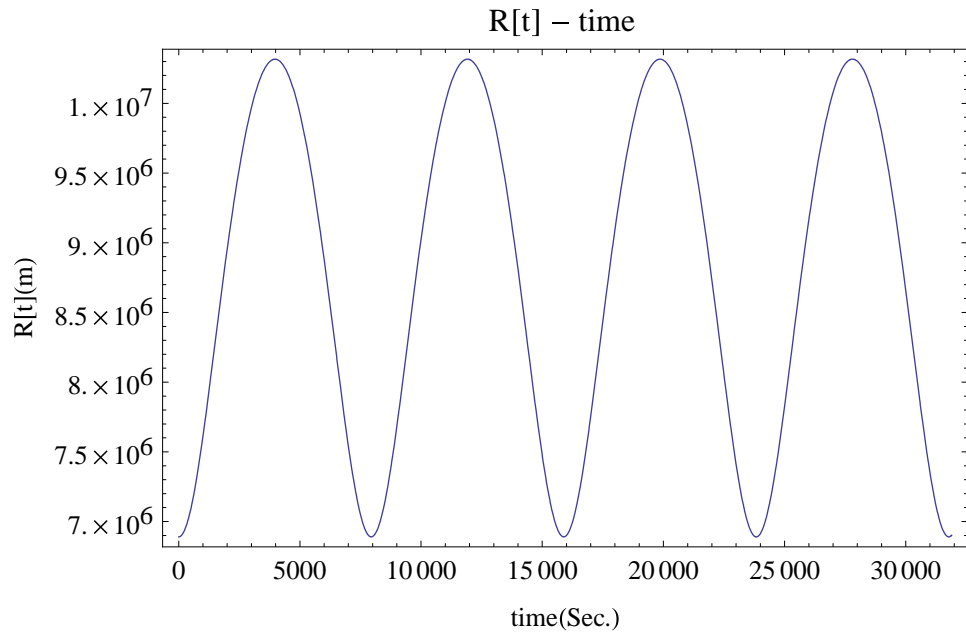


Figure 3.55: The rigid body MMET base point distance of  $R$  ( $T_n = 4.01$ )

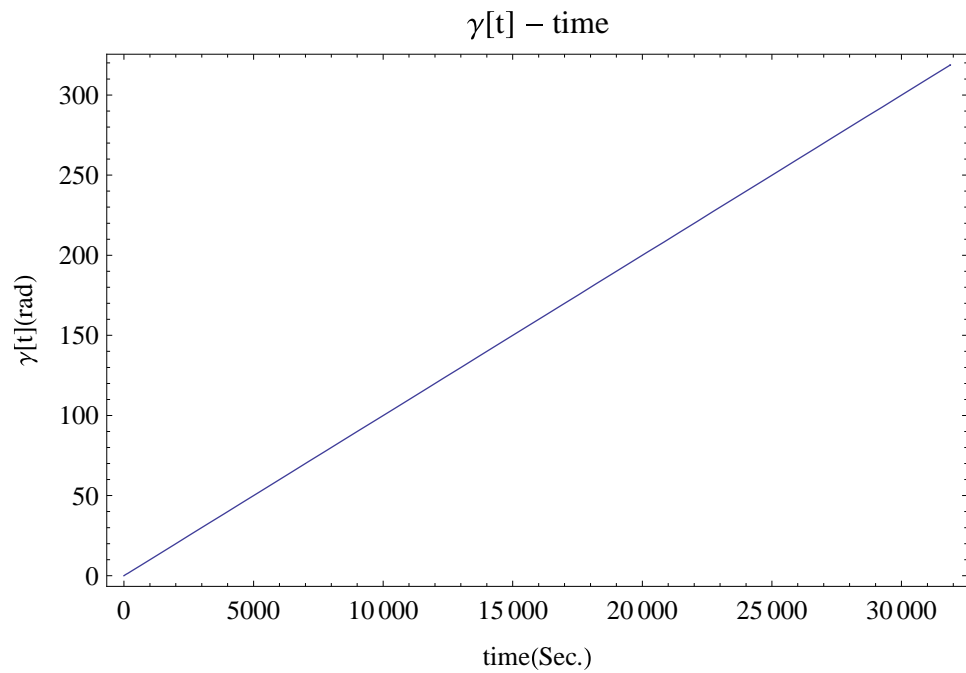


Figure 3.56: The rigid body MMET rolling angle  $\gamma$  ( $T_n = 4.01$ )

keep staying in zero over the full simulation time. Given  $\gamma(0) = 0.001$  rad and  $\dot{\gamma}(0) = 0.001$  rad/s, Figure 3.56 states a rising response for the rolling angle.

### 3.7 Conclusions

Firstly, the dumbbell tether is discussed, then, this chapter has given an introduction to the concept of the motorised momentum exchange tether. A series of MMET concept based Lagrangian dynamical models are proposed, which include the dumbbell tether, the dumbbell

MMET, the dumbbell MMET with cylindrical payloads and centralised motor facility, and the rigid body MMET with discrete tether-tube subspans.

A discretisation methodology has been proposed and validated for the MMET system with discrete tether-tube subspans, and this will also be applied to each of the further stages of MMET systems.

Numerical results are given in sections 3.2.6, 3.4.6, 3.5.9 and 3.6.9 for a series of the MMET concept based tether systems. These results show that the dynamical models can provide stable, accurate and periodic outputs with similar behavioural shapes but tiny differences generated by their similar components in the governing equations, which include the spin-up performance for each MMET model and indications of their connections to each other. Furthermore, the numerical results will also be taken as the reference for the MMET systems in following chapters.

Table 3.6: Figures for spin-up  $\psi$  in Chapter 3

Tether Type	Figure No. ( $T_n = 400.01$ )	Figure No. ( $T_n = 4.01$ )
Dumbbell tether	3.4	3.6
Dumbbell MMET	3.17	3.18
Dumbbell MMET (Cylindrical Payloads)	3.30	3.31
Rigid MMET	3.49	3.50

Table 3.7: Figures for R in Chapter 3

Tether Type	Figure No. ( $T_n = 400.01$ )	Figure No. ( $T_n = 4.01$ )
Dumbbell tether	3.9	3.10
Dumbbell MMET	3.22	3.24
Dumbbell MMET (Cylindrical Payloads)	3.32	3.33
Rigid MMET	3.54	3.55

Table 3.8: Figures for  $\theta$  in Chapter 3

Tether Type	Figure No. ( $T_n = 400.01$ )	Figure No. ( $T_n = 4.01$ )
Dumbbell tether	3.7	3.8
Dumbbell MMET	3.19	3.20
Dumbbell MMET (Cylindrical Payloads)	3.34	3.35
Rigid MMET	3.51	3.52

Table 3.6 gives the  $\psi$  plots for the tether systems,  $\psi$  is the generalised coordinate for the tether's spin-up, which is the angle from the  $x_0$  axis to the projection of the tether onto the orbit plane. With the given parameters in Appendix C, the spin-up responses are changing periodically between -0.325 to 0.325 rad over the the number of cycles of period  $T_n = 400.01$  and 4.01.

Table 3.7 lists the  $R$ , which is the tether's position generalised coordinate and measures the distance from the Earth  $E$  to the dumbbell MMET system's COM. In this case, given  $e = 0.2$ ,  $r_p = 6.89 \times 10^6$  metre and  $r_a = 1.0335 \times 10^7$  metre, it goes within the range of  $r_p$  to  $r_a$ .

The out-of-plane angle  $\alpha$  with zero initial conditions are also discussed, all the numerical responses are staying in zero, which indicate the stable response for  $\alpha$  during simulation NCP  $T_n = 400.01$ .

Table 3.8 is for the true anomaly  $\theta$ , which is in a linear up-changing trend from 0 to 2500 rad coupling range of 0 to 0.5 rad fluctuation spread, over the the number of cycles of period  $T_n = 400.01$ , which indicate the tether systems go around the Earth in an elliptical orbit.

There are two types of tether systems incorporated with the rigid rolling angle  $\gamma$ , which keep staying in zero output with zero initial conditions  $\gamma(0) = 0$  rad and  $\dot{\gamma}(0) = 0$  rad/s. Their responses are sensitive to their initial conditions, which can have direct effects on the tether system's outputs of  $\alpha$  and  $\gamma$ .

## Chapter 4

---

# Dynamical Modelling of a Flexible Massless MMET System

---

### 4.1 Introduction

A dynamical modelling analysis for a flexible massless MMET system, which implies that there is no mass for the tether subspans, is given in this chapter. The use of the word ‘flexible’ means that this MMET system model only contains axial, torsional and pendular elasticity. The modelling process is based on the dumbbell MMET with cylindrical payloads and motor facility, as discussed in section 3.5, because the environmental assumptions are the same as were discussed in chapter 3.

On the supporting assumption that tether mass can be neglected at this level of modelling, with the potential for inclusion later, this flexible massless MMET system is henceforth considered to possess significant elasticity in the axial, torsional and pendular motions, and these will all be referred to ‘elasticity’ from this point onwards.

The tether subspan is assumed as a continuum but is also considered to be massless in the current approach to modelling, and is made up of homogeneous, isotropic elastic material - linear elastic material. The axial, torsional and pendular elasticity of the massless MMET tether system are assumed to be independent of each other, so that a motion, or a compression, or a dissipation, in one element for one of the discretisations, will not affect a motion, or a compression, or a dissipation in another element corresponding to either of the other discretisations. This discretisation methodology is the same as that used in section 3.6.2. This is clearly hypothetical but serves as a starting point.

The assumptions for the massless elasticity modelling process are listed below, and seven

assumptions are numbered as A1 to A6.

- A1 - The tether is massless;
- A2 - The tether is made of homogeneous isotropic material;
- A3 - The MMET system's dissipation function is assumed to be based on the Rayleigh damping theory;
- A4 - The MMET system is in a friction free environment;
- A5 - Every axial 'spring-damper' group is connected to another, in series;
- A6 - Every torsional 'spring-damper' group is connected to another, in series;

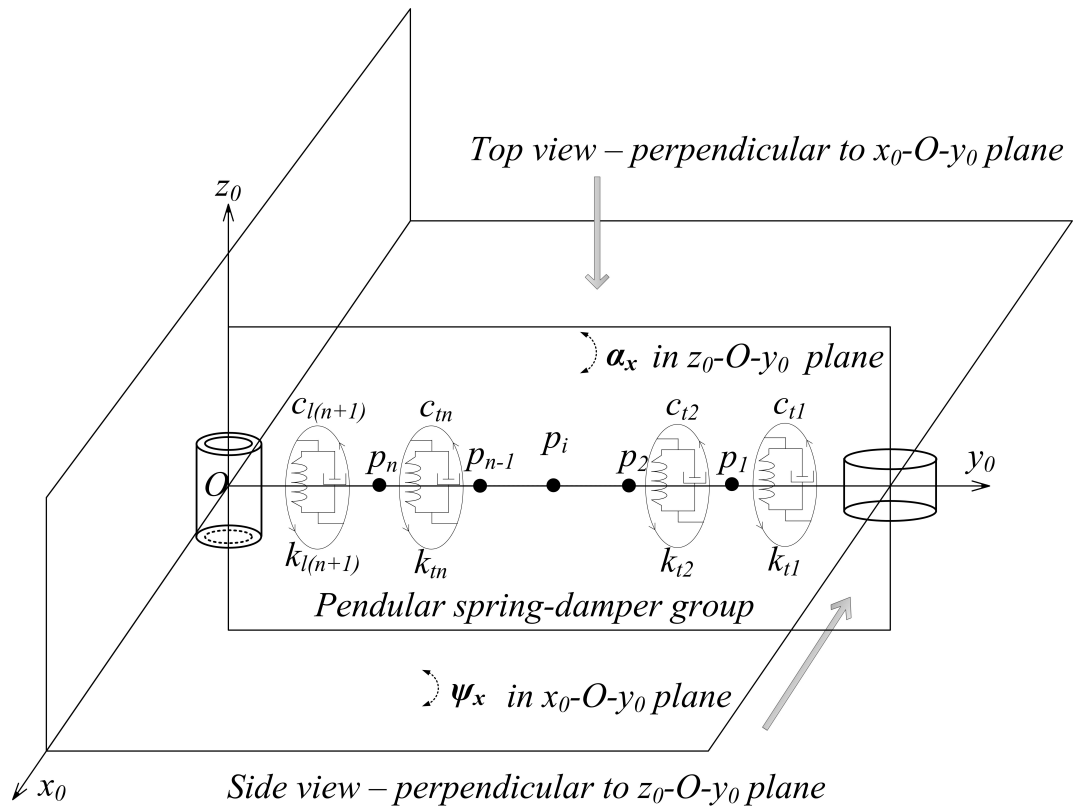


Figure 4.1: The MMET pendular elasticity plane definition

In order to describe the torsional and pendular elasticity more clearly, three 'reference' planes are defined in Figures 4.1 and 4.2. There are three orthogonal reference planes:  $x_0 - O - y_0$ ,  $x_0 - O - z_0$  and  $z_0 - O - y_0$ , which are located at the MMET COM 'O'. The modelling for the torsional elasticity is referenced onto the plane  $x_0 - O - z_0$ , the pendular motion of the tether is referenced onto two orthogonal planes:  $x_0 - O - y_0$  and  $z_0 - O - y_0$ .

Two view points are also defined in Figure 4.1, one is a 'top view', which is a perpendicular point to the plane  $x_0 - O - y_0$ . The other is a 'side view', and it is a perpendicular

point to the plane  $z_0 - O - y_0$ . The two view points, together with the reference planes, help in investigating the modelling for the pendular elasticity later on. In Figure 4.2, three ‘torsional’ planes are defined on the right side, which are associated with three reference planes on the left side, and each of the torsional planes contain a torsional ‘spring-damper’ group, which will be utilised in detail in the following sections.

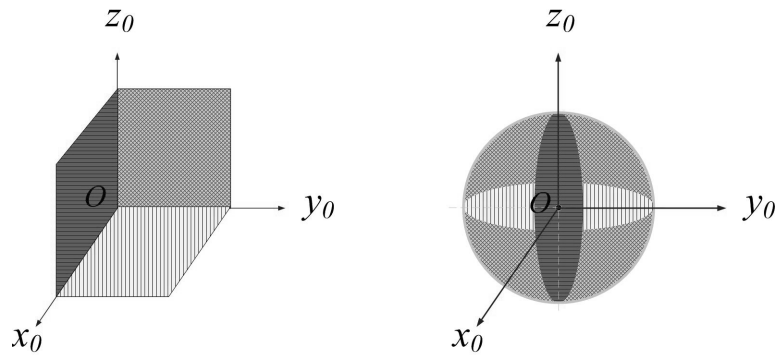


Figure 4.2: Reference plane definition for MMET torsional and pendular elasticity

The models incorporating axial, torsional and pendular elasticity will be discussed in sections 4.2, 4.3 and 4.4 respectively, and then a massless flexible MMET system will be introduced based on the models above.

## 4.2 Dynamical Modelling incorporating Axial Elasticity

The conceptual schematic of a massless MMET system with axial elasticity is shown in Figure 4.3, and its generalised coordinates are shown in Figure 4.4. As implied in Figure 4.4, the symmetrical double-ended motorised spinning tether is applied as an orbital transfer system. In order to exploit momentum exchange for propelling and transferring payloads in space, the Cartesian components of the masses of  $M_M$ ,  $M_1$  and  $M_2$  are given in equations (3.2.4), (3.2.5) and (3.2.6).

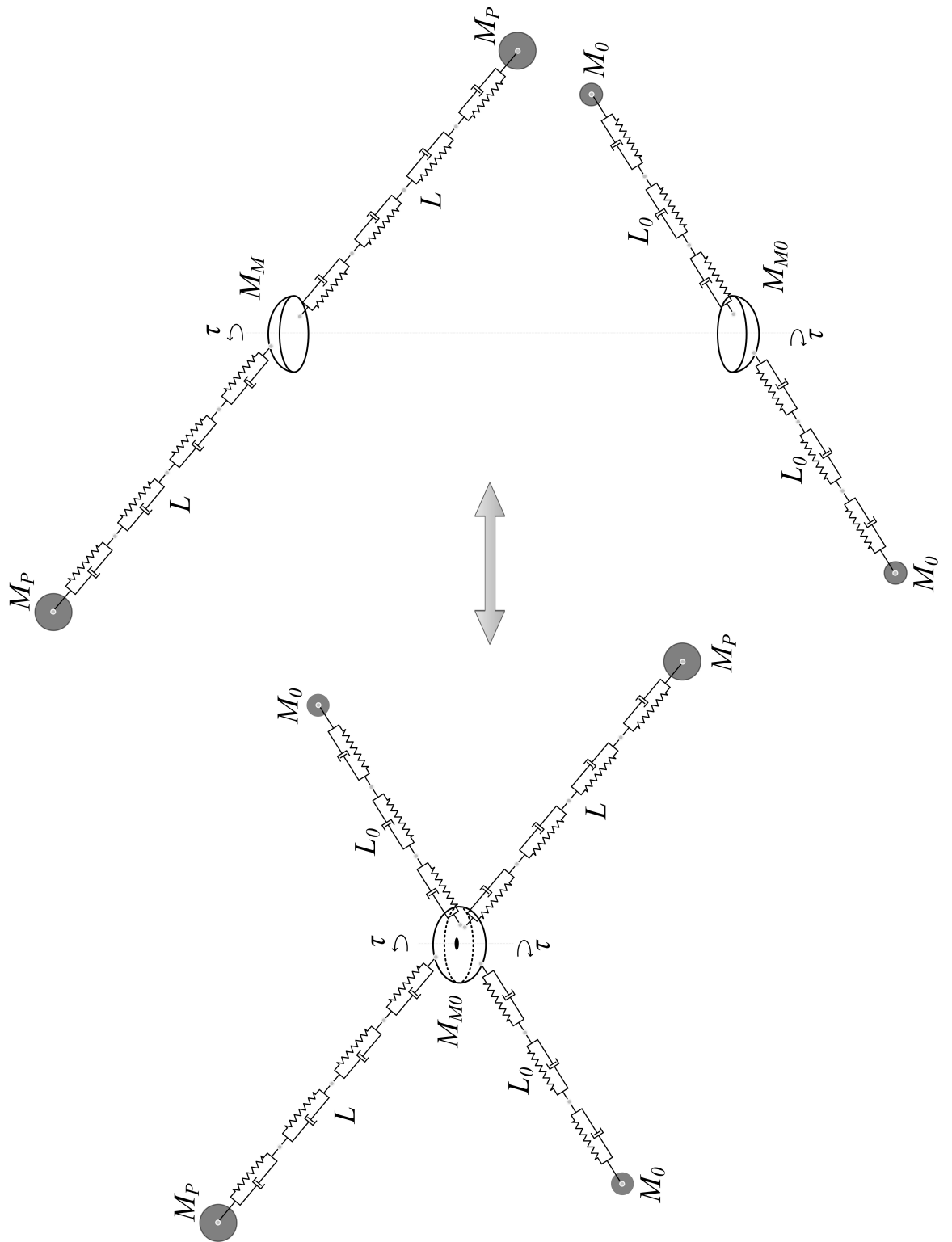


Figure 4.3: **The conceptual schematic of the massless MMET with axially elastic tether**



The discretisation methodology is proposed for the following approach, as given in Figure 4.5, in which the basic idea is to discretise the massless tether subspan into massless points  $p_i$  ( $i = 1, 2, \dots, n$ ),  $n$  is the number of the massless points  $p_i$ , as shown in Figure 4.6, connected by an idealised and hypothetical series of axial ‘spring-damper’ groups along the tether subspans.

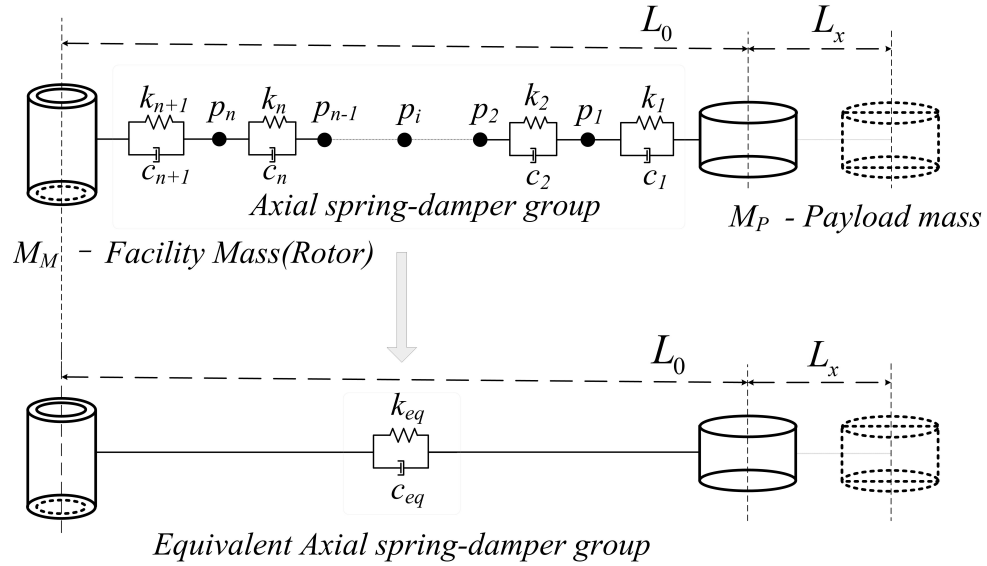


Figure 4.5: The MMET system with axially elastic massless tether subspan

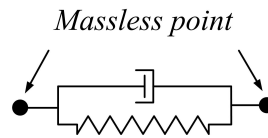


Figure 4.6: The massless point at each end of a ‘spring-damper’ group

In Figure 4.5, the motor mass  $M_M$  and payload mass  $M_P$  are connected by a series of ‘spring-damper’ groups, as given in Figure 4.6, thus the axial elasticity is described by a series of ‘spring-damper’ groups with an axial deformation of  $L_x$ , in equation (4.2.1), where  $L_0$  is the static tether length, and  $L_x$  is the axially elastic deformation along the tether subspans.

$$L = L_0 + L_x \quad (4.2.1)$$

Compared with the rigid massless MMET system in section 3.6, the massless tether subspan was replaced by a few ‘spring-damper’ groups which are connected in series;  $k_i$  and  $c_i$  ( $i = 1, 2, \dots, n + 1$ ) are the spring stiffness and damping coefficients in every ‘spring-damper’ group, respectively.

In summary, the axial elasticity is expressed by a string of ‘spring-damper’ groups ( $k_i, c_i$ ), which connect the massless points  $p_i$  in series with  $k_1 = \dots = k_{n+1}, c_1 = \dots = c_{n+1}$ , where  $i = 1, 2, \dots, n+1$ . They are attached in series along the tether subspans, which can be expressed as an equivalent spring stiffness  $k_{eq}$  and an equivalent damping coefficient  $c_{eq}$  in equations (4.2.2) and (4.2.3). The generalised coordinate  $L_x$  represents the equivalent motion for the axial elasticity in equation (4.2.1), which is additional to the rigid body generalised coordinate  $L$ .

Thus, the equivalent spring stiffness  $k_{eq}$  and damping coefficient  $c_{eq}$  of the series of ‘spring-damper’ groups are given in equations (4.2.2) and (4.2.3). The generalised coordinate  $L_x$  represents the equivalent axial elasticity.

$$\frac{1}{k_{eq}} = \frac{1}{k_1} + \frac{1}{k_2} + \dots + \frac{1}{k_{n+1}} \quad (4.2.2)$$

$$\frac{1}{c_{eq}} = \frac{1}{c_1} + \frac{1}{c_2} + \dots + \frac{1}{c_{n+1}} \quad (4.2.3)$$

Primarily, it must be pointed out that the MMET modelling for axial, torsional and pendular elasticity, including massless tether discretisation and ‘spring-damper’ group connections for each of the massless points, is a mathematical modelling process, the axial and torsional ‘spring-damper’ groups and massless points do not really exist as such physically.

The massless MMET model with axial, torsional and pendular elasticity, using such mathematical elements, potentially leads to enhanced accuracy of the prediction performance, and a useful departure from the usual rigid body MMET modelling, particularly for accurate payload positioning at strategic points, therefore, unless further notice is given, all the modelling processes are under these assumptions and mathematical elements.

► The detail modelling process is attached in Appendix D.

### 4.2.1 Governing Equations of Motion

The generalised forces  $Q_i$   $\{i = 2, 4, 5\}$  are all zeros, that is,  $Q_2 = Q_\theta = 0$ ,  $Q_4 = Q_R = 0$  and  $Q_5 = Q_\gamma = 0$ , and the generalised forces  $Q_1 = Q_\psi$ ,  $Q_3 = Q_\alpha$  and  $Q_6 = Q_{L_x}$  are stated in equations (3.5.13), (3.5.15) and (D.4.5). The following governing equations for generalised coordinates  $q_i$  ( $i = 1, 2, \dots, n$ ) are given in equations (4.2.4) to (4.2.9) for  $q_1 = \psi$ ,  $q_2 = \theta$ ,  $q_3 = \alpha$ ,  $q_4 = R$ ,  $q_5 = \gamma$  and  $q_6 = L_x$ , as summarised in Table 4.1.

Table 4.1: The axial elastic massless MMET generalised coordinates and generalised forces

i	q <sub>i</sub>	Q <sub>i</sub>	T	U	Equations of Motion
1	ψ	(3.5.13)	(D.2.1)	(D.1.1)	(4.2.4)
2	θ	(3.5.14)			(4.2.5)
3	α	(3.5.15)			(4.2.6)
4	R	(3.5.16)			(4.2.7)
5	γ	(3.5.17)			(4.2.8)
6	L <sub>x</sub>	(D.4.5)			(4.2.9)

$$\begin{aligned}
 & \left( \frac{\mu \cos \alpha R \sin \psi M_{P2} (L_0 + L_x)}{\left( R^2 - 2 \cos \alpha \cos \psi (L_0 + L_x) R + (L_0 + L_x)^2 \right)^{3/2}} \right) - (M_{P1} - M_{P2}) \\
 & \left( \frac{\mu \cos \alpha R \sin \psi M_{P1} (L_0 + L_x)}{\left( R^2 + 2 \cos \alpha \cos \psi (L_0 + L_x) R + (L_0 + L_x)^2 \right)^{3/2}} \right) + \\
 & \left( (L_0 + L_x) \left( \begin{array}{l} \sin \alpha \dot{\alpha} (\sin \psi \dot{R} - \cos \psi R \dot{\theta}) - \\ \cos \alpha (\cos \psi \dot{R} + R \sin \psi \dot{\theta}) (\dot{\theta} + \dot{\psi}) \end{array} \right) + \right. \\
 & \left. \cos \alpha (\cos \psi R \dot{\theta} - \sin \psi \dot{R}) \dot{L}_x \right) + \\
 & \left( \begin{array}{l} M_M (\ddot{\theta} + \ddot{\psi}) r_M^2 + \\ 2 \sin \alpha (M_{P1} - M_{P2}) (L_0 + L_x) \dot{\alpha} (\sin \psi \dot{R} - \cos \psi R \dot{\theta}) - \\ 2 \sin 2\alpha (M_{P1} + M_{P2}) (L_0 + L_x)^2 \dot{\alpha} (\dot{\theta} + \dot{\psi}) - \\ 2 \cos \alpha (M_{P1} - M_{P2}) (\sin \psi \dot{R} - \cos \psi R \dot{\theta}) \dot{L}_x + \\ 2 \cos 2\alpha (M_{P1} + M_{P2}) (L_0 + L_x) (\dot{\theta} + \dot{\psi}) \dot{L}_x + \\ 2 \cos \alpha (M_{P1} - M_{P2}) (L_0 + L_x) (\cos \psi (\dot{R} (\dot{\theta} - \dot{\psi}) + R \ddot{\theta}) - \sin \psi (R \dot{\theta} \dot{\psi} + \ddot{R})) + \\ \cos 2\alpha (M_{P1} + M_{P2}) (L_0 + L_x)^2 (\ddot{\theta} + \ddot{\psi}) + \\ (M_{P1} + M_{P2}) \left( 2 (L_0 + L_x) \dot{L}_x (\dot{\theta} + \dot{\psi}) + r_p^2 (\ddot{\theta} + \ddot{\psi}) + (L_0 + L_x)^2 (\ddot{\theta} + \ddot{\psi}) \right) \end{array} \right) \\
 & = Q_\psi
 \end{aligned} \tag{4.2.4}$$

$$\begin{aligned}
& \left( \begin{array}{l} 2(M_M + M_{P1} + M_{P2}) \ddot{\theta} R^2 + \\ 2 \left( \begin{array}{l} 2(M_M + M_{P1} + M_{P2}) \dot{R} \dot{\theta} + \\ \cos \psi (M_{P1} - M_{P2}) \left( \begin{array}{l} \cos \alpha (2(\dot{\theta} + \dot{\psi}) \dot{L}_x + (L_0 + L_x) (2\ddot{\theta} + \ddot{\psi})) \\ -2 \sin \alpha (L_0 + L_x) \dot{\alpha} (\dot{\theta} + \dot{\psi}) \end{array} \right) + \\ \sin \psi (M_{P1} - M_{P2}) \left( \begin{array}{l} \cos \alpha (\ddot{L}_x - (L_0 + L_x) (\dot{\alpha}^2 + \dot{\psi} (2\dot{\theta} + \dot{\psi}))) - \\ \sin(\alpha) (2\dot{\alpha} \dot{L}_x + (L_0 + L_x) \ddot{\alpha}) \end{array} \right) \end{array} \right) R \\ +4 \cos \alpha \cos \psi (M_{P1} - M_{P2}) L_x \dot{R} \dot{\theta} + 2 \cos \alpha \sin \psi (M_{P2} - M_{P1}) L_x \ddot{R} + \\ \frac{1}{2} M_M r_M^2 (\ddot{\theta} + \ddot{\psi}) - \\ 2 \cos \alpha L_0^2 (M_{P1} + M_{P2}) (2 \sin \alpha \dot{\alpha} (\dot{\theta} + \dot{\psi}) - \cos \alpha (\ddot{\theta} + \ddot{\psi})) + \\ 2 \cos \alpha L_0 \left( \begin{array}{l} -4 \sin \alpha (M_{P1} + M_{P2}) L_x \dot{\alpha} (\dot{\theta} + \dot{\psi}) + \\ (M_{P1} - M_{P2}) (2 \cos \psi \dot{R} \dot{\theta} - \sin \psi \ddot{R}) + \\ 2 \cos \alpha (M_{P1} + M_{P2}) ((\dot{\theta} + \dot{\psi}) \dot{L}_x + L_x (\ddot{\theta} + \ddot{\psi})) \end{array} \right) + \\ (M_{P1} + M_{P2}) \left( \begin{array}{l} (\ddot{\theta} + \ddot{\psi}) r_p^2 + \\ 2 \cos \alpha L_x \left( \begin{array}{l} 2 \cos \alpha (\dot{\theta} + \dot{\psi}) \dot{L}_x + \\ L_x (\cos \alpha (\ddot{\theta} + \ddot{\psi}) - 2 \sin(\alpha) \dot{\alpha} (\dot{\theta} + \dot{\psi})) \end{array} \right) \end{array} \right) \end{array} \right) \\ = Q_{\theta} \tag{4.2.5}
\end{aligned}$$

$$\begin{aligned}
& \left( \frac{\mu \cos \psi R \sin \alpha M_{P2} (L_0 + L_x)}{\left( R^2 - 2 \cos \alpha \cos \psi (L_0 + L_x) R + (L_0 + L_x)^2 \right)^{3/2}} - \right. \\
& \left. \frac{\mu \cos \psi R \sin \alpha M_{P1} (L_0 + L_x)}{\left( R^2 + 2 \cos \alpha \cos \psi (L_0 + L_x) R + (L_0 + L_x)^2 \right)^{3/2}} \right) \\
& - \frac{1}{24} \left( \begin{aligned} & -12 \sin 2\alpha (M_{P1} + M_{P2}) (L_0 + L_x)^2 (\dot{\theta} + \dot{\psi})^2 - \\ & 24 \cos \alpha (M_{P1} - M_{P2}) (L_0 + L_x) \dot{\alpha} (\cos \psi \dot{R} + R \sin \psi \dot{\theta}) - \\ & 24 \sin \alpha (M_{P1} - M_{P2}) \left( \begin{aligned} & (\cos \psi \dot{R} + R \sin \psi \dot{\theta}) \dot{L}_x - \\ & (L_0 + L_x) (\sin \psi \dot{R} - \cos \psi R \dot{\theta}) (\dot{\theta} + \dot{\psi}) \end{aligned} \right) \end{aligned} \right) \\
& + \frac{1}{24} \left( \begin{aligned} & -24 \cos \alpha (M_{P1} - M_{P2}) (L_0 + L_x) \dot{\alpha} (\cos \psi \dot{R} + R \sin \psi \dot{\theta}) - \\ & 24 \sin \alpha (M_{P1} - M_{P2}) \dot{L}_x (\cos \psi \dot{R} + R \sin \psi \dot{\theta}) + \\ & 2M_M (h_M^2 + 3r_M^2) \ddot{\alpha} + \\ & 2(M_{P1} + M_{P2}) \left( 24(L_0 + L_x) \dot{\alpha} \dot{L}_x + (h_P^2 + 3(r_P^2 + 4(L_0 + L_x)^2)) \ddot{\alpha} \right) - \\ & 24 \sin \alpha (M_{P1} - M_{P2}) (L_0 + L_x) (\sin \psi \dot{R} (\dot{\theta} - \dot{\psi}) + \cos \psi (R \dot{\theta} \dot{\psi} + \ddot{R}) + R \sin \psi \ddot{\theta}) \end{aligned} \right) \\
& = Q_\alpha
\end{aligned} \tag{4.2.6}$$

$$\begin{aligned}
& \left( \frac{\mu M_M}{R^2} + \frac{\mu M_{P2} (R - \cos \alpha \cos \psi (L_0 + L_x))}{\left( R^2 - 2 \cos \alpha \cos \psi (L_0 + L_x) R + (L_0 + L_x)^2 \right)^{3/2}} + \right. \\
& \left. \frac{\mu M_{P1} (R + \cos \alpha \cos \psi (L_0 + L_x))}{\left( R^2 + 2 \cos \alpha \cos \psi (L_0 + L_x) R + (L_0 + L_x)^2 \right)^{3/2}} \right) - \\
& \dot{\theta} \left( \begin{aligned} & -\sin \alpha \sin \psi (M_{P1} - M_{P2}) (L_0 + L_x) \dot{\alpha} + R M_M \dot{\theta} + R (M_{P1} + M_{P2}) \dot{\theta} + \\ & \cos \alpha (M_{P1} - M_{P2}) (\cos \psi (L_0 + L_x) (\dot{\theta} + \dot{\psi}) + \sin \psi \dot{L}_x) \end{aligned} \right) + \\
& \left( \begin{aligned} & M_M \ddot{R} + (M_{P1} + M_{P2}) \ddot{R} + \\ & \sin \alpha (M_{P1} - M_{P2}) (\sin \psi (L_0 + L_x) \dot{\alpha} (\dot{\theta} + 2\dot{\psi}) - \cos \psi (2\dot{\alpha} \dot{L}_x + (L_0 + L_x) \ddot{\alpha})) + \\ & \cos \alpha (M_{P1} - M_{P2}) \left( \begin{aligned} & \cos \psi (\ddot{L}_x - (L_0 + L_x) (\dot{\alpha}^2 + \dot{\psi} (\dot{\theta} + \dot{\psi}))) - \\ & \sin \psi ((\dot{\theta} + 2\dot{\psi}) \dot{L}_x + (L_0 + L_x) (\ddot{\theta} + \ddot{\psi})) \end{aligned} \right) \end{aligned} \right) \\
& = Q_R
\end{aligned} \tag{4.2.7}$$

$$\frac{1}{12} (M_M (h_M^2 + 3r_M^2) + (M_{P1} + M_{P2}) (h_P^2 + 3r_P^2)) \ddot{\gamma} = Q_\gamma \tag{4.2.8}$$

$$\begin{aligned}
& \left( \frac{2k_0 L_x}{n+1} + \frac{\mu M_{p2} (-\cos \alpha \cos \psi R + L_0 + L_x)}{(R^2 - 2 \cos \alpha \cos \psi (L_0 + L_x) R + (L_0 + L_x)^2)^{3/2}} \right) - \\
& \left( \frac{\mu M_{p1} (\cos \alpha \cos \psi R + L_0 + L_x)}{(R^2 + 2 \cos \alpha \cos \psi (L_0 + L_x) R + (L_0 + L_x)^2)^{3/2}} \right) - \\
& \frac{1}{8} \left( \begin{aligned} & 4 \cos 2\alpha (M_{p1} + M_{p2}) (L_0 + L_x) (\dot{\theta} + \dot{\psi})^2 - \\ & 8 \cos \alpha (M_{p1} - M_{p2}) (\sin \psi \dot{R} - \cos \psi R \dot{\theta}) (\dot{\theta} + \dot{\psi}) - \\ & 8 \sin \alpha (M_{p1} - M_{p2}) \dot{\alpha} (\cos \psi \dot{R} + R \sin \psi \dot{\theta}) + \\ & 4 (M_{p1} + M_{p2}) (L_0 + L_x) (2\dot{\alpha}^2 + (\dot{\theta} + \dot{\psi})^2) \end{aligned} \right) + \quad (4.2.9) \\
& \left( \begin{aligned} & -\sin \alpha (M_{p1} - M_{p2}) \dot{\alpha} (\cos \psi \dot{R} + R \sin \psi \dot{\theta}) + (M_{p1} + M_{p2}) \ddot{L}_x \\ & \cos \alpha (M_{p1} - M_{p2}) (\sin \psi \dot{R} (\dot{\theta} - \dot{\psi}) + \cos \psi (R \dot{\theta} \dot{\psi} + \ddot{R}) + R \sin \psi \ddot{\theta}) \end{aligned} \right) \\
& = Q_{L_x}
\end{aligned}$$

## 4.2.2 Simulations and Discussions

Figures 4.7 to 4.16 are the numerical results obtained by MATHEMATICA for the selected generalised coordinates  $\psi$ ,  $\theta$ ,  $\alpha$ ,  $R$ ,  $\gamma$  and  $L_x$ , as listed in Table 4.1 with zero initial conditions and other parameters in Appendix C, in  $T_n = 4.01$  and  $T_n = 400.01$  simulation time.

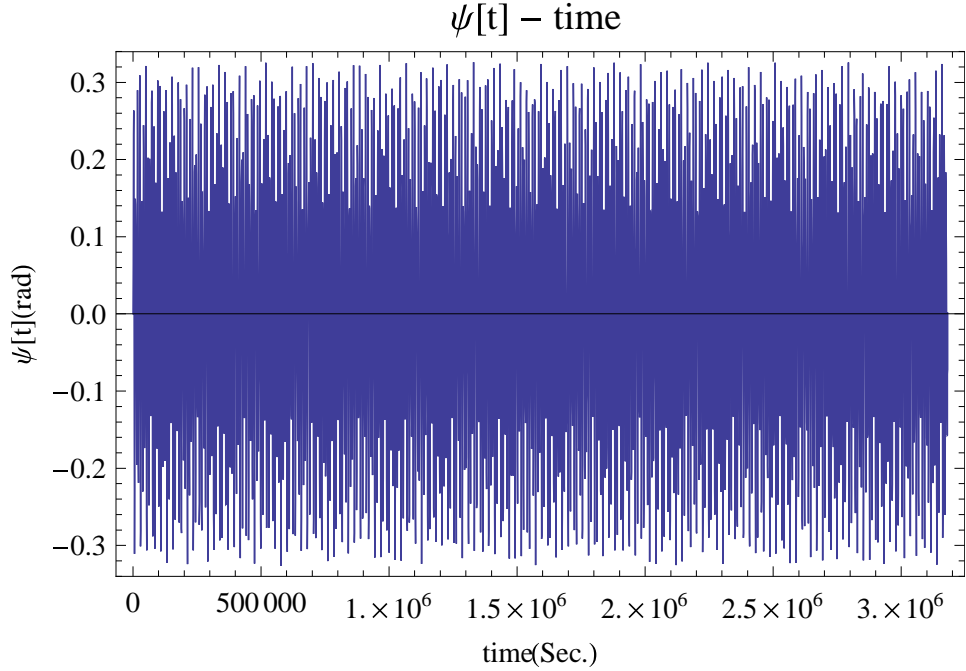


Figure 4.7: Massless axial elastic MMET spin-up, angular displacement  $\psi$  ( $T_n = 400.01$ )

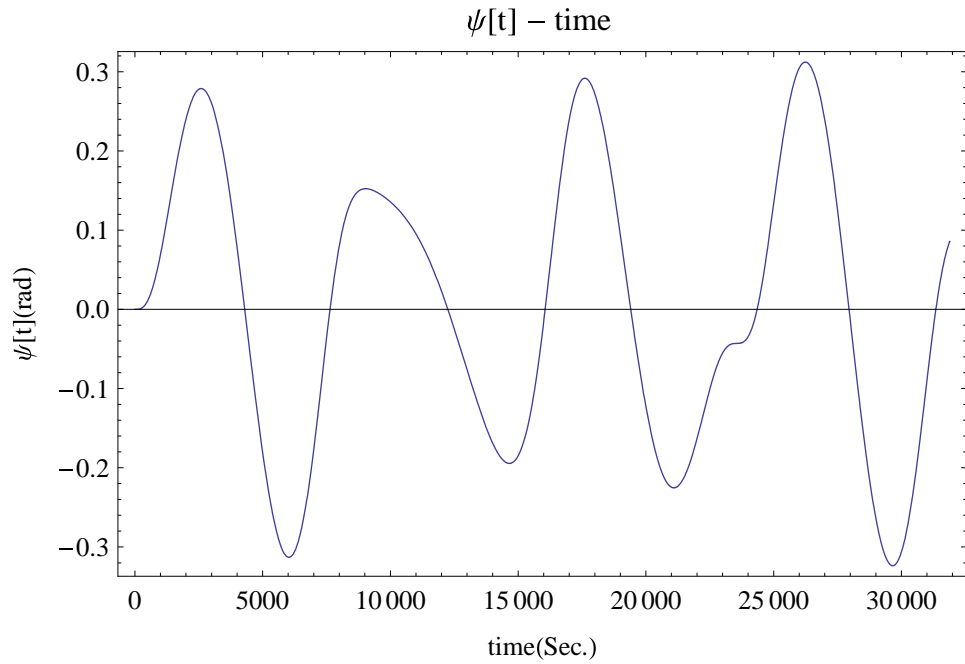


Figure 4.8: Massless axial elastic MMET spin-up, angular displacement  $\psi$  ( $T_n = 4.01$ )

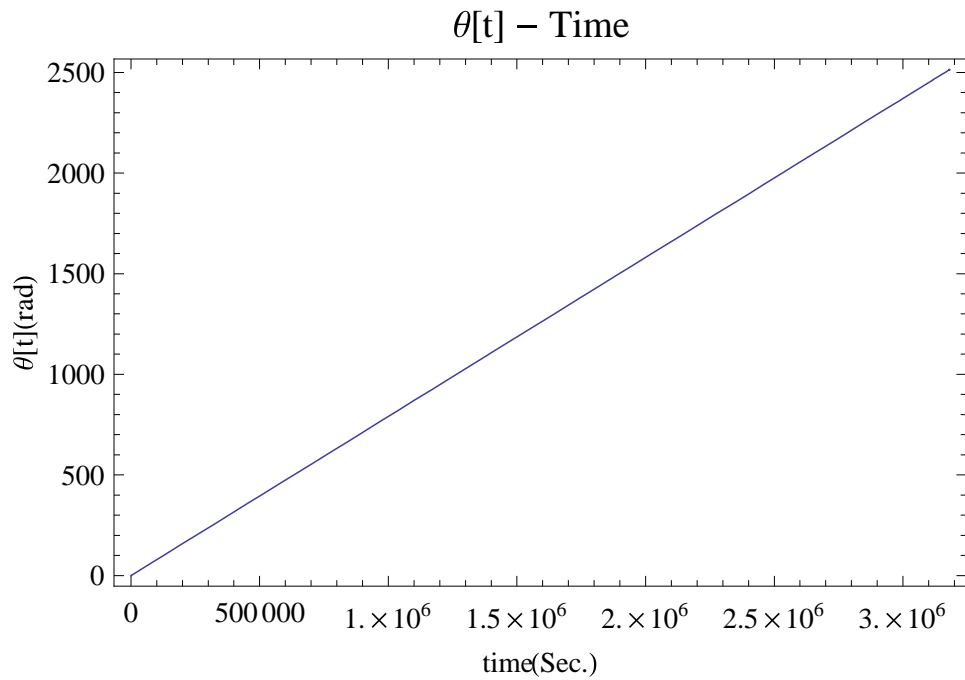


Figure 4.9: Massless axial elastic MMET elliptical orbit angular position of  $\theta$  ( $T_n = 400.01$ )

- ▷ Figures 4.7 and 4.8 show the massless axial elastic MMET system's periodic spin-up behaviour  $\psi$  on an elliptical orbit ( $e = 0.2$ ) around the Earth with the angular displacement range of  $-0.325$  to  $0.325$  rad.
- ▷ The results for the true anomaly  $\theta$  are shown in Figures 4.9 and 4.10 for the number of cycles of period  $T_n = 4.01$  and  $400.01$  simulation time, respectively. The curves are rising in a linear trend from  $0$  to  $25$  ( $T_n = 4.01$ ) or  $2500$  ( $T_n = 400.01$ ) rad with slight fluctuation spread ( $0$  to  $0.5$  rad).

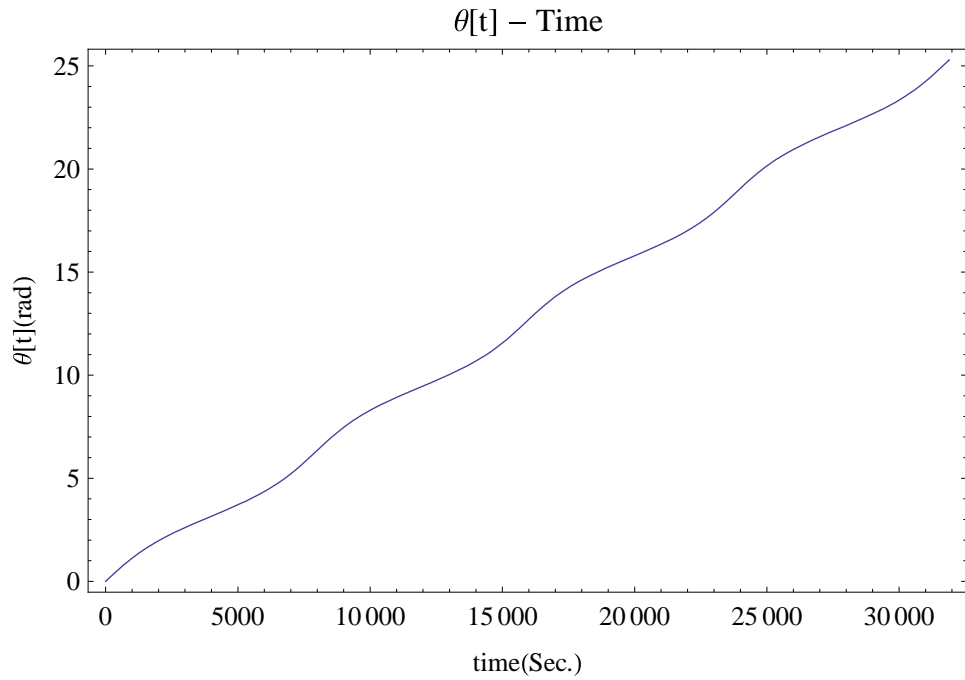


Figure 4.10: Massless axial elastic MMET elliptical orbit angular position of  $\theta$  ( $T_n = 4.01$ )

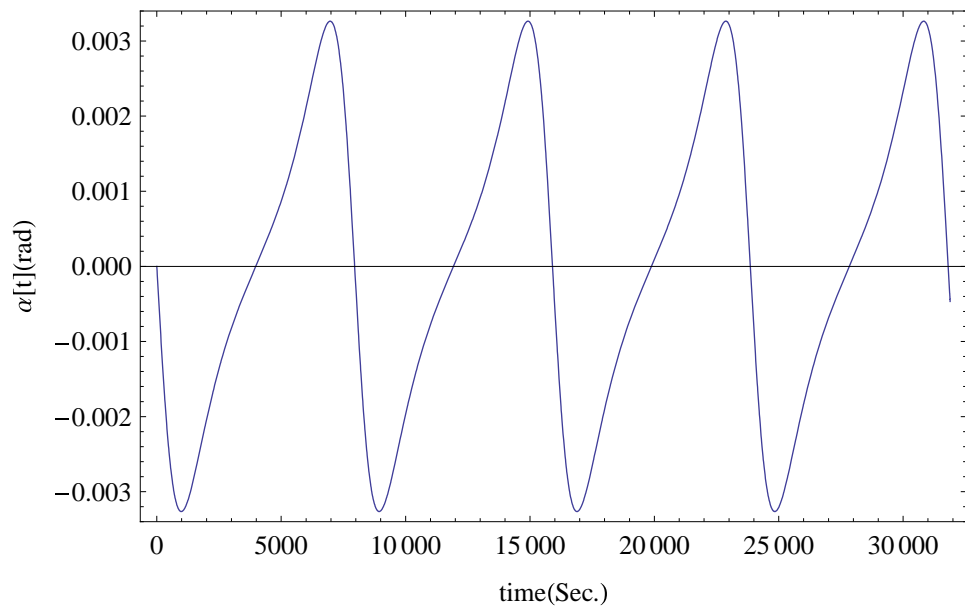


Figure 4.11: Massless axial elastic MMET out-of-plane angle  $\alpha$  ( $T_n = 4.01$ )

▷ With zero initial conditions  $\alpha(0) = 0$  rad and  $\dot{\alpha}(0) = 0$  rad/s, the responses for the out-of-plane angle  $\alpha$  keeps in zero amplitude during the full simulation time. As shown in Figure 4.11, the  $\alpha$  response goes periodically in the range  $[-0.003, 0.003]$  rad.

▷ The distance  $R$  from the Earth to the tether COM is changing periodically, as can be seen in Figures 4.12 and 4.13, which behave within the distance range of  $r_p$  ( $6.89 \times 10^6$  m) to  $r_a$  ( $1.0335 \times 10^7$  m) with given  $e = 0.2$  in this case.

▷ Figure 4.14 is the plot for the rigid rolling angle  $\gamma$  with initial conditions  $\gamma(0) =$

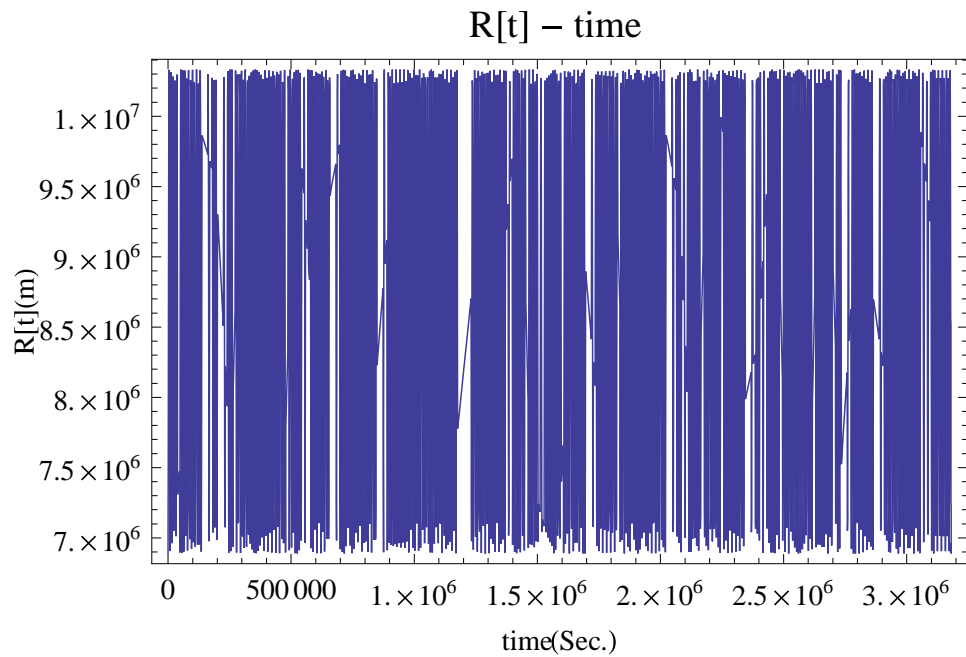


Figure 4.12: Massless axial elastic MMET base point distance  $R$  to the Earth ( $T_n = 400.01$ )

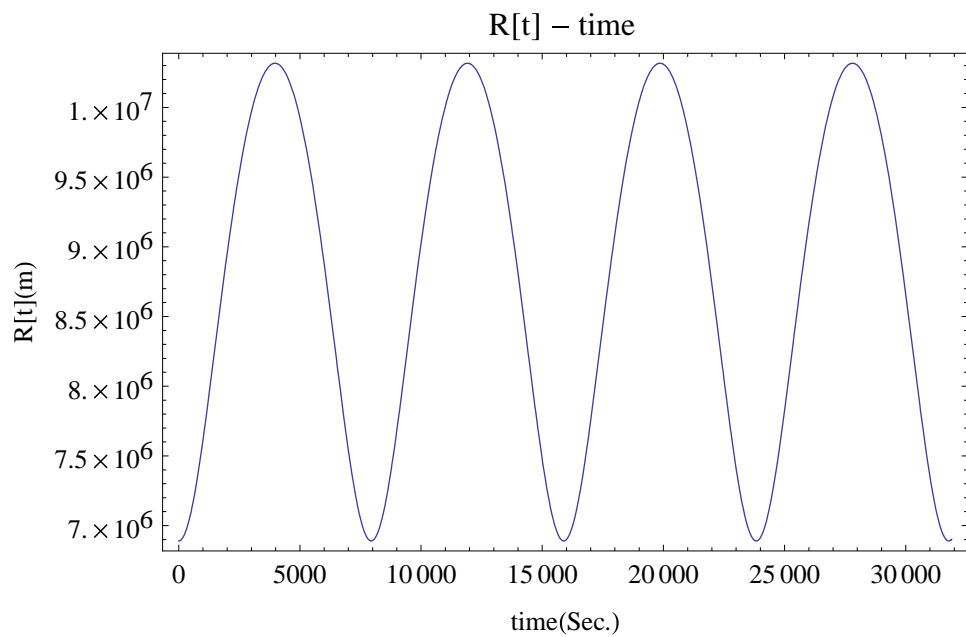


Figure 4.13: Massless axial elastic MMET base point distance  $R$  to the Earth ( $T_n = 4.01$ )

0.001 rad and  $\dot{\gamma}(0) = 0.001$  rad/s. The rigid rolling angle  $\gamma$  stays in zeros output with zero initial conditions  $\gamma(0) = 0$  rad and  $\dot{\gamma}(0) = 0$  rad/s, which indicate that the rigid rolling angle  $\gamma$  is sensitive to its initial values.

▷ Figures 4.15 and 4.16 have shown the periodic axial elastic behaviour along tether subspan in 1 - 31899 seconds simulation time (NCP,  $T_n = 4.01$ ), which are based on the tether system's parameter setting in Appendix C. The tether subspan's axial oscillation  $L_x$  goes within 12.5 to 21.5 m in Figure 4.15, and the ratio of  $L_x$  to  $L_0$  varies 2.25% to

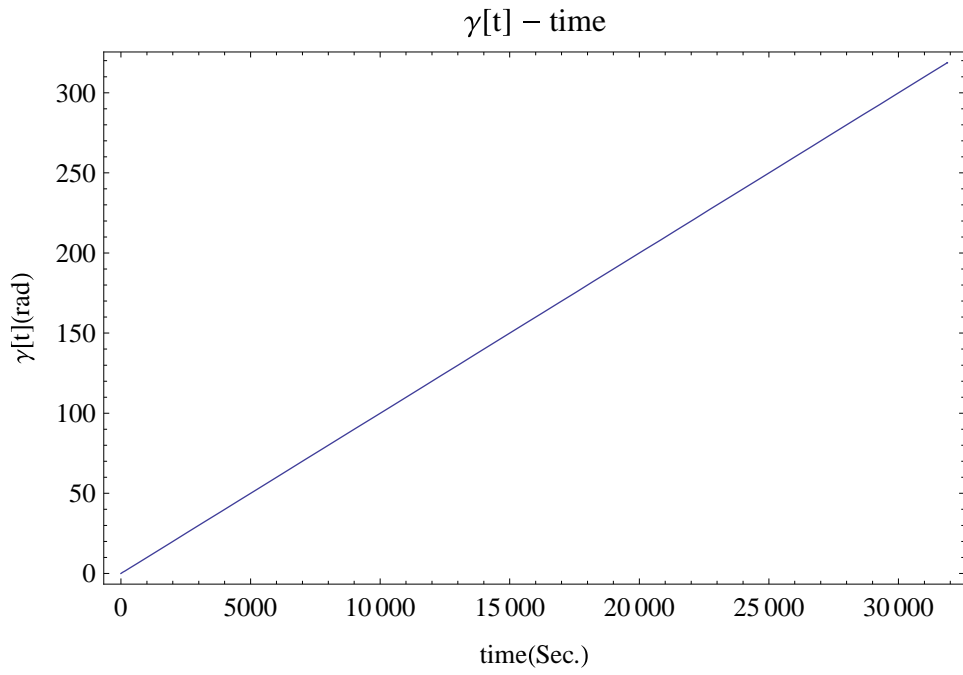


Figure 4.14: Massless axial elastic MMET rolling angle  $\gamma$  ( $T_n = 4.01$ )

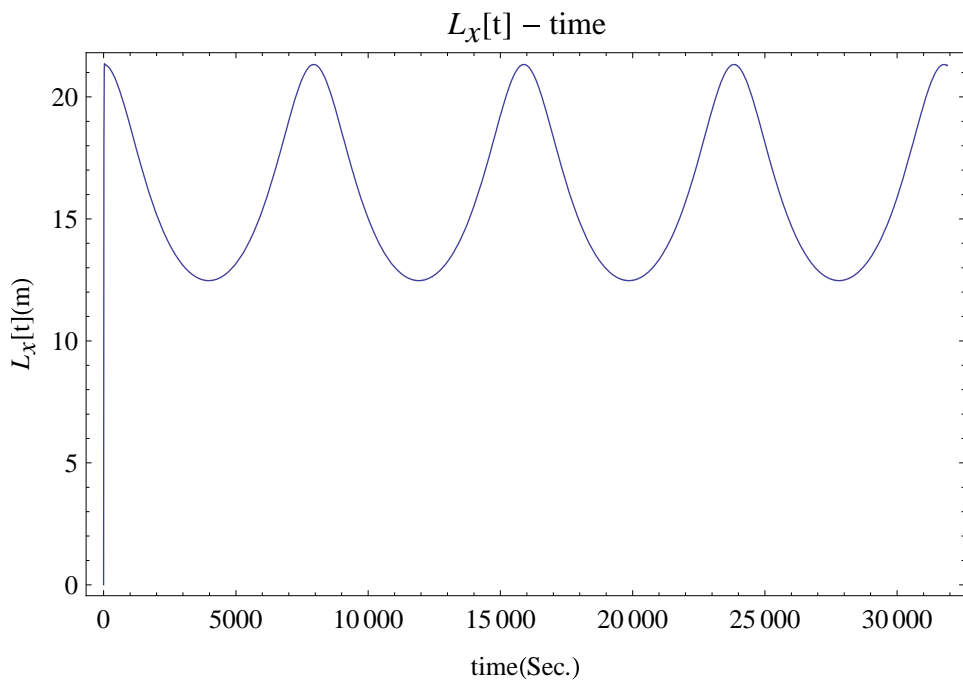


Figure 4.15: Axial displacement along tether subspan of  $L_x$  ( $T_n = 4.01$ )

4.15% in Figure 4.16.

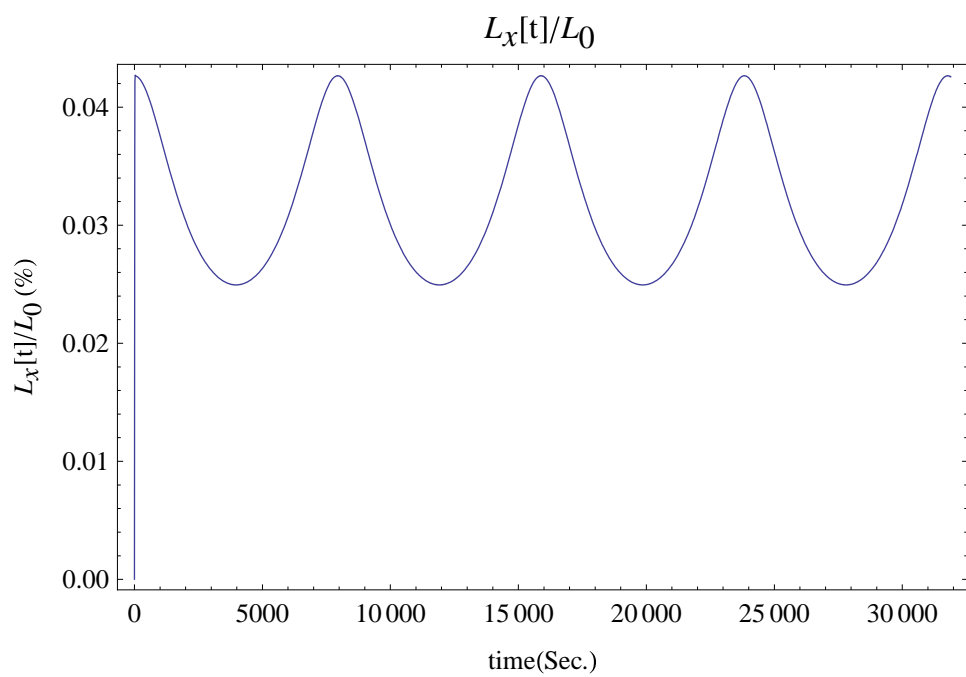


Figure 4.16: Axial elastic length vs. static length ratio along tether subspan of  $\frac{L_x}{L_0}$  ( $T_n = 4.01$ )

### 4.3 Dynamical Modelling including Axial and Torsional Elasticity

Based on the axial massless elastic MMET system in section 4.2, a massless MMET system with axial and torsional elasticity and its generalised coordinate selections are all presented in Figure 4.17.

As implied in Figure 4.17, the symmetrical double-ended motorised spinning tether is applied as an orbital transfer system, in order to exploit momentum exchange for propelling and transferring payloads in space, noting that the Cartesian components of the end masses of  $M_M$ ,  $M_1$  and  $M_2$  are the same as in equations (3.2.4), (3.2.5) and (3.2.6).

As shown in Figure 4.18, besides a few axial ‘spring-damper’ groups for the axial elasticity definition, as discussed in section 4.2, there are a series of torsional ‘spring-damper’ groups ( $k_{ti} - c_{ti}$ ) also attached to the massless points  $p_i$  ( $i = 1, 2, \dots, n$ ) for the torsional elasticity representation. These are referenced onto the plane  $x_0 - O - z_0$  in Figures 4.1 and 4.19 equivalently.

As shown in Figure 4.18, the torsional ‘spring-damper’ groups connect the massless points  $p_i$  in series with  $k_{t1} = \dots = k_{t(n+1)}$ ,  $c_{t1} = \dots = c_{t(n+1)}$ , where  $n$  is the number of massless points.

For the torsional ‘spring-damper’ groups which are attached in series along the tether subspans, stiffness can be expressed as an equivalent spring stiffness  $k_{teq}$  and damping as an equivalent damping coefficient  $c_{teq}$  in equations (4.3.1) and (4.3.2), where  $t$  in the subscript means the torsional elastic parameter, then the generalised coordinate  $\gamma_x$  expresses the equivalent torsional elasticity as shown in Figure 4.18, which is additional to the rigid body rolling generalised coordinate  $\gamma$ .

$$\frac{1}{k_{teq}} = \frac{1}{k_{t1}} + \frac{1}{k_{t2}} + \dots + \frac{1}{k_{t(n+1)}} \quad (4.3.1)$$

$$\frac{1}{c_{teq}} = \frac{1}{c_{t1}} + \frac{1}{c_{t2}} + \dots + \frac{1}{c_{t(n+1)}} \quad (4.3.2)$$

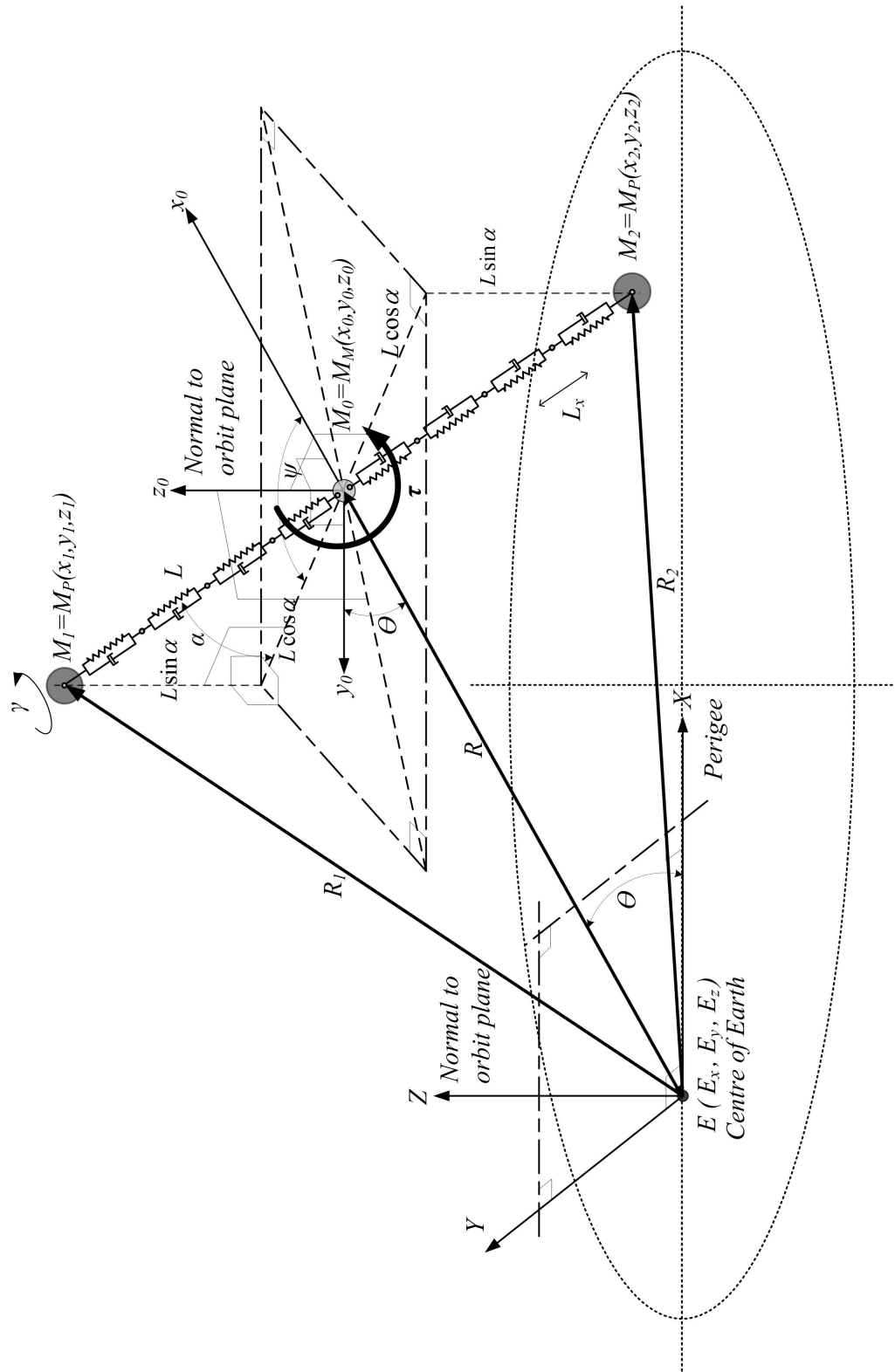


Figure 4.17: The MMET model generalised coordinates defined on orbit

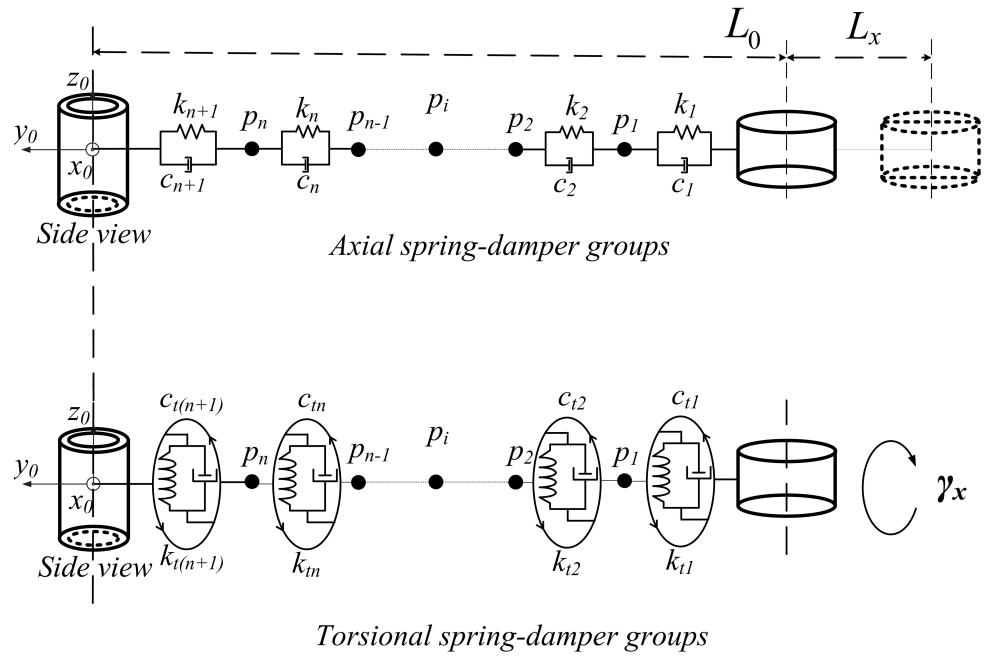


Figure 4.18: **The Axial and torsional elasticity model referenced onto plane  $x_0 - O - z_0$**

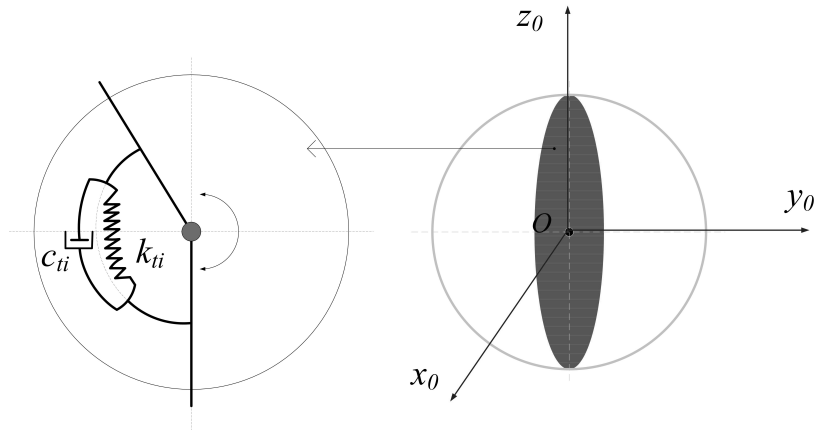


Figure 4.19: Reference onto the plane  $x_0 - O - z_0$  for MMET torsional elasticity

► The detail modelling process is attached in Appendix E.

### 4.3.1 Governing Equations of Motion

The governing equations in terms of generalised coordinates  $q_1 = \psi$ ,  $q_2 = \theta$ ,  $q_3 = \alpha$ ,  $q_4 = R$ ,  $q_5 = L_x$  and  $q_6 = \gamma_x$  are given in equations (4.3.3) to (4.3.8), as shown in Table 4.2, according to the Lagrangian procedure.

Table 4.2: The axial and torsional elastic massless MMET generalised coordinates and generalised Forces

i	q <sub>i</sub>	Q <sub>i</sub>	T	U	Equations of Motion
1	ψ	(3.5.13)	(E.2.1)	(E.1.5)	(4.3.3)
2	θ	(3.5.14)			(4.3.4)
3	α	(3.5.15)			(4.3.5)
4	R	(3.5.16)			(4.3.6)
5	L <sub>x</sub>	(D.4.5)			(4.3.7)
6	γ <sub>x</sub>	(E.4.4)			(4.3.8)

$$\begin{aligned}
 & \left( \frac{\mu M_{P2} \begin{pmatrix} \cos \alpha \sin(\theta + \psi) (L_0 + L_x) (\cos \theta R - \cos \alpha \cos(\theta + \psi) (L_0 + L_x)) - \\ \cos \alpha \cos(\theta + \psi) (L_0 + L_x) (R \sin \theta - \cos \alpha \sin(\theta + \psi) (L_0 + L_x)) \end{pmatrix}}{\left( (\cos \theta R - \cos \alpha \cos(\theta + \psi) (L_0 + L_x))^2 + (-\sin \alpha (L_0 + L_x))^2 + (R \sin \theta - \cos \alpha \sin(\theta + \psi) (L_0 + L_x))^2 \right)^{3/2}} + \right. \\
 & \left. \frac{\mu M_{P1} \begin{pmatrix} \cos \alpha \cos(\theta + \psi) (L_0 + L_x) (R \sin \theta + \cos \alpha \sin(\theta + \psi) (L_0 + L_x)) - \\ \cos \alpha \sin(\theta + \psi) (L_0 + L_x) (\cos \theta R + \cos \alpha \cos(\theta + \psi) (L_0 + L_x)) \end{pmatrix}}{\left( (\cos \theta R + \cos \alpha \cos(\theta + \psi) (L_0 + L_x))^2 + (\sin \alpha (L_0 + L_x))^2 + (R \sin \theta + \cos \alpha \sin(\theta + \psi) (L_0 + L_x))^2 \right)^{3/2}} \right) - \\
 & (M_{P1} - M_{P2}) \begin{pmatrix} (L_0 + L_x) \begin{pmatrix} \sin \alpha \dot{\alpha} (\sin \psi \dot{R} - \cos \psi R \dot{\theta}) - \\ \cos \alpha (\cos \psi \dot{R} + R \sin \psi \dot{\theta}) (\dot{\theta} + \dot{\psi}) \end{pmatrix} \\ + \cos \alpha (\cos \psi R \dot{\theta} - \sin \psi \dot{R}) \dot{L}_x \end{pmatrix} \\
 & \left( -2 \cos \alpha (M_{P1} + M_{P2}) (2 \sin \alpha \dot{\alpha} (\dot{\theta} + \dot{\psi}) - \cos \alpha (\ddot{\theta} + \ddot{\psi})) L_0^2 + \right. \\
 & \left. 2L_0 \begin{pmatrix} \sin \psi (M_{P1} - M_{P2}) (\sin \alpha \dot{R} \dot{\alpha} - \cos \alpha (R \dot{\theta} \dot{\psi} + \ddot{R})) \\ + \cos \psi (M_{P1} - M_{P2}) (\cos \alpha \dot{R} (\dot{\theta} - \dot{\psi}) + R (\cos \alpha \ddot{\theta} - \sin \alpha \dot{\alpha} \dot{\theta})) - \\ 2 \cos \alpha (M_{P1} + M_{P2}) \begin{pmatrix} L_x (2 \sin \alpha \dot{\alpha} (\dot{\theta} + \dot{\psi}) - \cos \alpha (\ddot{\theta} + \ddot{\psi})) - \\ \cos \alpha (\dot{\theta} + \dot{\psi}) \dot{L}_x \end{pmatrix} \end{pmatrix} \right) + \\
 & + \frac{1}{2} 2 \sin \alpha (M_{P1} - M_{P2}) L_x \dot{\alpha} (\sin \psi \dot{R} - \cos \psi R \dot{\theta}) - \\
 & 2 \sin 2\alpha (M_{P1} + M_{P2}) L_x^2 \dot{\alpha} (\dot{\theta} + \dot{\psi}) + \\
 & 2 \cos \alpha (M_{P1} - M_{P2}) \begin{pmatrix} (\cos \psi R \dot{\theta} - \sin \psi \dot{R}) \dot{L}_x + \\ L_x (\cos \psi (\dot{R} (\dot{\theta} - \dot{\psi}) + R \ddot{\theta}) - \sin \psi (R \dot{\theta} \dot{\psi} + \ddot{R})) \end{pmatrix} + \\
 & M_M r_M^2 (\ddot{\theta} + \ddot{\psi}) + \cos 2\alpha (M_{P1} + M_{P2}) L_x (2 (\dot{\theta} + \dot{\psi}) \dot{L}_x + L_x (\ddot{\theta} + \ddot{\psi})) + \\
 & \left. (M_{P1} + M_{P2}) ((\ddot{\theta} + \ddot{\psi}) r_p^2 + 2L_x (\dot{\theta} + \dot{\psi}) \dot{L}_x + L_x^2 (\ddot{\theta} + \ddot{\psi})) \right) \\
 & = Q_\psi
 \end{aligned} \tag{4.3.3}$$

$$\begin{aligned}
& \left( 2(M_M + M_{P1} + M_{P2}) \ddot{R}^2 + \right. \\
& \quad \left. 2R \left( \begin{array}{l} 2(M_M + M_{P1} + M_{P2}) \dot{R}\dot{\theta} + \\ \cos \psi (M_{P1} - M_{P2}) \left( \cos \alpha (2(\dot{\theta} + \dot{\psi}) \dot{L}_x + (L_0 + L_x)(2\ddot{\theta} + \ddot{\psi})) - \right. \\ \left. \left. 2 \sin \alpha (L_0 + L_x) \dot{\alpha} (\dot{\theta} + \dot{\psi}) \right) + \\ \sin \psi (M_{P1} - M_{P2}) \left( \cos \alpha (\ddot{L}_x - (L_0 + L_x)(\dot{\alpha}^2 + \dot{\psi}(2\dot{\theta} + \dot{\psi}))) - \right. \\ \left. \left. \sin \alpha (2\dot{\alpha}\dot{L}_x + (L_0 + L_x)\ddot{\alpha}) \right) \right) \right) + \\
& \quad \frac{1}{2} + 4 \cos \alpha \cos \psi (M_{P1} - M_{P2}) L_x \dot{R}\dot{\theta} + 2 \cos \alpha \sin \psi (M_{P2} - M_{P1}) L_x \ddot{R} + \\
& \quad M_M r_M^2 (\ddot{\theta} + \ddot{\psi}) - 2 \cos \alpha L_0^2 (M_{P1} + M_{P2}) (2 \sin \alpha \dot{\alpha} (\dot{\theta} + \dot{\psi}) - \cos \alpha (\ddot{\theta} + \ddot{\psi})) + \\
& \quad 2 \cos \alpha L_0 \left( \begin{array}{l} -4 \sin \alpha (M_{P1} + M_{P2}) L_x \dot{\alpha} (\dot{\theta} + \dot{\psi}) + \\ (M_{P1} - M_{P2}) (2 \cos \psi \dot{R}\dot{\theta} - \sin \psi \ddot{R}) + \\ 2 \cos \alpha (M_{P1} + M_{P2}) ((\dot{\theta} + \dot{\psi}) \dot{L}_x + L_x (\ddot{\theta} + \ddot{\psi})) \end{array} \right) + \\
& \quad \left. \left. (M_{P1} + M_{P2}) \left( (\ddot{\theta} + \ddot{\psi}) r_p^2 + 2 \cos \alpha L_x \left( \begin{array}{l} 2 \cos \alpha (\dot{\theta} + \dot{\psi}) \dot{L}_x + \\ L_x (\cos \alpha (\ddot{\theta} + \ddot{\psi}) - 2 \sin \alpha \dot{\alpha} (\dot{\theta} + \dot{\psi})) \end{array} \right) \right) \right) \right) \\
& = Q_{\theta}
\end{aligned} \tag{4.3.4}$$

$$\begin{aligned}
& \left( \begin{aligned} & \mu M_{P2} \left( \begin{aligned} & 2 \cos(\theta + \psi) \sin \alpha (L_0 + L_x) (\cos \theta R - \cos \alpha \cos(\theta + \psi) (L_0 + L_x)) - \\ & 2 \cos \alpha (L_0 + L_x) (-\sin \alpha (L_0 + L_x)) + \\ & 2 \sin \alpha \sin(\theta + \psi) (L_0 + L_x) (R \sin \theta - \cos \alpha \sin(\theta + \psi) (L_0 + L_x)) \end{aligned} \right) \\ & \frac{\left( \begin{aligned} & (\cos \theta R - \cos \alpha \cos(\theta + \psi) (L_0 + L_x))^2 + \\ & (-\sin \alpha (L_0 + L_x))^2 + (R \sin \theta - \cos \alpha \sin(\theta + \psi) (L_0 + L_x))^2 \end{aligned} \right)^{3/2}}{2} + \\ & \mu M_{P1} \left( \begin{aligned} & -2 \cos(\theta + \psi) \sin \alpha (L_0 + L_x) (\cos \theta R + \cos \alpha \cos(\theta + \psi) (L_0 + L_x)) + \\ & 2 \cos \alpha (L_0 + L_x) (\sin \alpha (L_0 + L_x)) - \\ & 2 \sin \alpha \sin(\theta + \psi) (L_0 + L_x) (R \sin \theta + \cos \alpha \sin(\theta + \psi) (L_0 + L_x)) \end{aligned} \right) \\ & \frac{\left( \begin{aligned} & (\cos \theta R + \cos \alpha \cos(\theta + \psi) (L_0 + L_x))^2 + \\ & (\sin \alpha (L_0 + L_x))^2 + (R \sin \theta + \cos \alpha \sin(\theta + \psi) (L_0 + L_x))^2 \end{aligned} \right)^{3/2}}{2} \end{aligned} \right) - \\
& \left( \begin{aligned} & -\frac{1}{2} \sin 2\alpha (M_{P1} + M_{P2}) (L_0 + L_x)^2 (\dot{\theta} + \dot{\psi})^2 + \\ & \cos \psi (M_{P1} - M_{P2}) (- (L_0 + L_x) (\cos \alpha \dot{R} \dot{\alpha} + R \sin \alpha \dot{\theta} (\dot{\theta} + \dot{\psi})) - \sin \alpha \dot{R} \dot{L}_x) + \\ & \sin \psi (M_{P1} - M_{P2}) ((L_0 + L_x) (\sin \alpha \dot{R} (\dot{\theta} + \dot{\psi}) - \cos \alpha R \dot{\alpha} \dot{\theta}) - R \sin \alpha \dot{\theta} \dot{L}_x) \end{aligned} \right) + \\
& \left( \begin{aligned} & M_M \ddot{\alpha} h_M^2 - 12 \cos \alpha (M_{P1} - M_{P2}) (L_0 + L_x) \dot{\alpha} (\cos \psi \dot{R} + R \sin \psi \dot{\theta}) + \\ & 24 L_0 M_{P1} \dot{\alpha} \dot{L}_x + 24 L_0 M_{P2} \dot{\alpha} \dot{L}_x + 24 M_{P1} L_x \dot{\alpha} \dot{L}_x + 24 M_{P2} L_x \dot{\alpha} \dot{L}_x + \\ & 3 M_M r_M^2 \ddot{\alpha} + 3 M_{P1} r_P^2 \ddot{\alpha} + 3 M_{P2} r_P^2 \ddot{\alpha} + 12 M_{P1} L_x^2 \ddot{\alpha} + 12 M_{P2} L_x^2 \ddot{\alpha} + \\ & \frac{1}{12} h_P^2 M_{P1} \ddot{\alpha} + 12 L_0^2 M_{P1} \ddot{\alpha} + h_P^2 M_{P2} \ddot{\alpha} + 12 L_0^2 M_{P2} \ddot{\alpha} + 24 L_0 M_{P1} L_x \ddot{\alpha} + 24 L_0 M_{P2} L_x \ddot{\alpha} - \\ & 12 \sin \alpha (M_{P1} - M_{P2}) \left( \begin{aligned} & (\cos \psi \dot{R} + R \sin \psi \dot{\theta}) \dot{L}_x + \\ & L_0 (\sin \psi \dot{R} (\dot{\theta} - \dot{\psi}) + \cos \psi (R \dot{\theta} \dot{\psi} + \ddot{R}) + R \sin \psi \ddot{\theta}) + \\ & L_x (\sin \psi \dot{R} (\dot{\theta} - \dot{\psi}) + \cos(\psi) (R \dot{\theta} \dot{\psi} + \ddot{R}) + R \sin \psi \ddot{\theta}) \end{aligned} \right) \end{aligned} \right) \\
& = Q_\alpha
\end{aligned} \tag{4.3.5}$$

$$\begin{aligned}
& \left( \frac{\mu M_M}{R^2} + \right. \\
& \quad \left. \frac{\mu M_{P2} \left( \begin{array}{l} 2 \cos \theta (\cos \theta R - \cos \alpha \cos(\theta + \psi) (L_0 + L_x)) + \\ 2 \sin \theta (R \sin \theta - \cos \alpha \sin(\theta + \psi) (L_0 + L_x)) \end{array} \right)}{2 \left( \begin{array}{l} (\cos \theta R - \cos \alpha \cos(\theta + \psi) (L_0 + L_x))^2 + (-\sin \alpha (L_0 + L_x))^2 + \\ (R \sin \theta - \cos \alpha \sin(\theta + \psi) (L_0 + L_x))^2 \end{array} \right)^{3/2}} + \right. \\
& \quad \left. \frac{\mu M_{P1} \left( \begin{array}{l} 2 \cos \theta (\cos \theta R + \cos \alpha \cos(\theta + \psi) (L_0 + L_x)) + \\ 2 \sin \theta (R \sin \theta + \cos \alpha \sin(\theta + \psi) (L_0 + L_x)) \end{array} \right)}{2 \left( \begin{array}{l} (\cos \theta R + \cos \alpha \cos(\theta + \psi) (L_0 + L_x))^2 + (\sin \alpha (L_0 + L_x))^2 + \\ (R \sin \theta + \cos \alpha \sin(\theta + \psi) (L_0 + L_x))^2 \end{array} \right)^{3/2}} \right) - \\
& \quad \dot{\theta} \left( \begin{array}{l} R (M_M + M_{P1} + M_{P2}) \dot{\theta} + \cos \alpha \cos \psi (M_{P1} - M_{P2}) (L_0 + L_x) (\dot{\theta} + \dot{\psi}) + \\ \sin \psi (M_{P2} - M_{P1}) (\sin \alpha (L_0 + L_x) \dot{\alpha} - \cos \alpha \dot{L}_x) \end{array} \right) + \\
& \quad \left( \begin{array}{l} (M_M + M_{P1} + M_{P2}) \ddot{R} + \\ \sin \alpha (M_{P1} - M_{P2}) (\sin \psi (L_0 + L_x) \dot{\alpha} (\dot{\theta} + 2\dot{\psi}) - \cos \psi (2\dot{\alpha} \dot{L}_x + (L_0 + L_x) \ddot{\alpha})) + \\ \cos \alpha (M_{P1} - M_{P2}) \left( \begin{array}{l} \cos \psi (\ddot{L}_x - (L_0 + L_x) (\dot{\alpha}^2 + \dot{\psi} (\dot{\theta} + \dot{\psi}))) - \\ \sin \psi ((\dot{\theta} + 2\dot{\psi}) \dot{L}_x + (L_0 + L_x) (\ddot{\theta} + \ddot{\psi})) \end{array} \right) \end{array} \right) \\
& = Q_R
\end{aligned} \tag{4.3.6}$$

$$\begin{aligned}
& \left( \frac{2k_0 L_x}{n+1} + \right. \\
& \left. \mu M_{P2} \left( \begin{array}{l} -2 \cos \alpha \cos(\theta + \psi) (\cos \theta R - \cos \alpha \cos(\theta + \psi) (L_0 + L_x)) - \\ 2 \sin \alpha (-\sin \alpha (L_0 + L_x)) - \\ 2 \cos \alpha \sin(\theta + \psi) (R \sin \theta - \cos \alpha \sin(\theta + \psi) (L_0 + L_x)) \end{array} \right) \right) + \\
& \left. \frac{2 \left( \begin{array}{l} (\cos \theta R - \cos \alpha \cos(\theta + \psi) (L_0 + L_x))^2 + \\ (-\sin \alpha (L_0 + L_x))^2 + \\ (R \sin \theta - \cos \alpha \sin(\theta + \psi) (L_0 + L_x))^2 \end{array} \right)^{3/2}}{\mu M_{P1} \left( \begin{array}{l} 2 \cos \alpha \cos(\theta + \psi) (\cos \theta R + \cos \alpha \cos(\theta + \psi) (L_0 + L_x)) + \\ 2 \sin \alpha (\sin \alpha (L_0 + L_x)) + \\ 2 \cos \alpha \sin(\theta + \psi) (R \sin \theta + \cos \alpha \sin(\theta + \psi) (L_0 + L_x)) \end{array} \right)} \right) + \\
& \left. \frac{2 \left( \begin{array}{l} (\cos \theta R + \cos \alpha \cos(\theta + \psi) (L_0 + L_x))^2 + \\ (\sin \alpha (L_0 + L_x))^2 + (R \sin \theta + \cos \alpha \sin(\theta + \psi) (L_0 + L_x))^2 \end{array} \right)^{3/2}}{\right)} \\
& \left( \begin{array}{l} \frac{1}{2} \cos 2\alpha (M_{P1} + M_{P2}) (L_0 + L_x) (\dot{\theta} + \dot{\psi})^2 + \\ \cos \alpha (M_{P2} - M_{P1}) (\sin \psi \dot{R} - \cos \psi R \dot{\theta}) (\dot{\theta} + \dot{\psi}) + \\ \sin \alpha (M_{P2} - M_{P1}) \dot{\alpha} (\cos \psi \dot{R} + R \sin \psi \dot{\theta}) + \\ \frac{1}{2} (M_{P1} + M_{P2}) (L_0 + L_x) (2\dot{\alpha}^2 + (\dot{\theta} + \dot{\psi})^2) \end{array} \right) + \\
& \left( \begin{array}{l} -\sin \alpha (M_{P1} - M_{P2}) \dot{\alpha} (\cos \psi \dot{R} + R \sin \psi \dot{\theta}) + \\ \cos \alpha (M_{P1} - M_{P2}) (\sin \psi \dot{R} (\dot{\theta} - \dot{\psi}) + \cos \psi (R \dot{\theta} \dot{\psi} + \ddot{R}) + R \sin \psi \ddot{\theta}) \\ + (M_{P1} + M_{P2}) \ddot{L}_x \end{array} \right) \\
& = Q_{L_x}
\end{aligned} \tag{4.3.7}$$

$$\frac{2k_{t0} \gamma_x}{n+1} + \frac{1}{12} (M_{P1} + M_{P2}) (h_p^2 + 3r_p^2) \ddot{\gamma}_x = Q_{\gamma_x} \tag{4.3.8}$$

### 4.3.2 Simulations and Discussions

Figures 4.20 to 4.30 are the numerical results obtained by MATHEMATICA for the selected generalised coordinates  $\psi$ ,  $\theta$ ,  $\alpha$ ,  $R$ ,  $\gamma$ ,  $L_x$  and  $\gamma_x$ , as listed in Table 4.2. The results show the massless axial and torsional elastic MMET system's periodic behaviours on orbit.

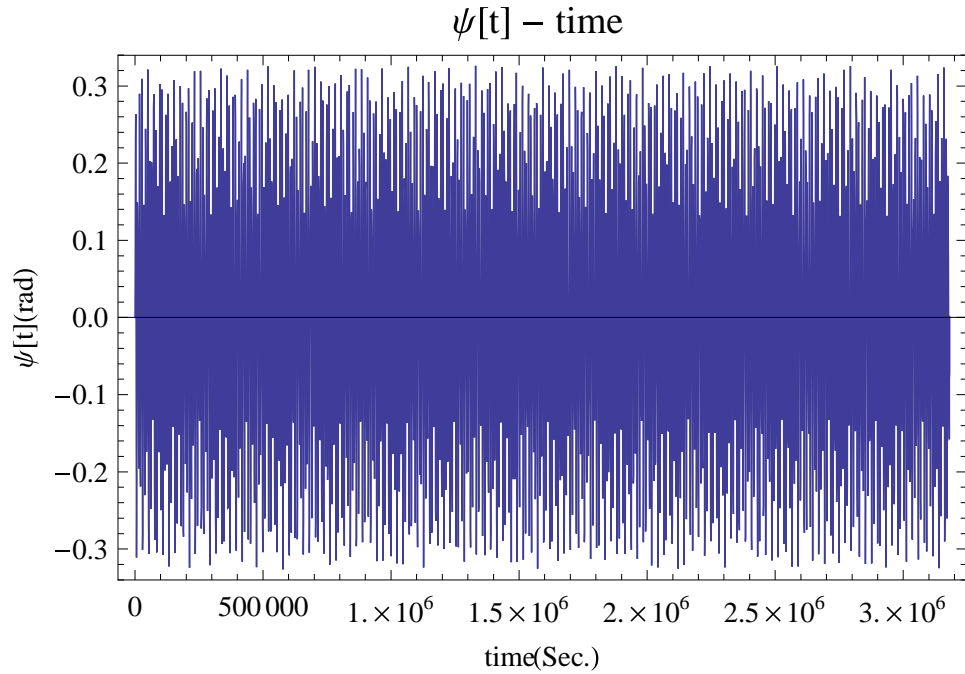


Figure 4.20: Massless axial and torsional elastic MMET spin-up angular displacement  $\psi$  ( $T_n = 400.01$ )

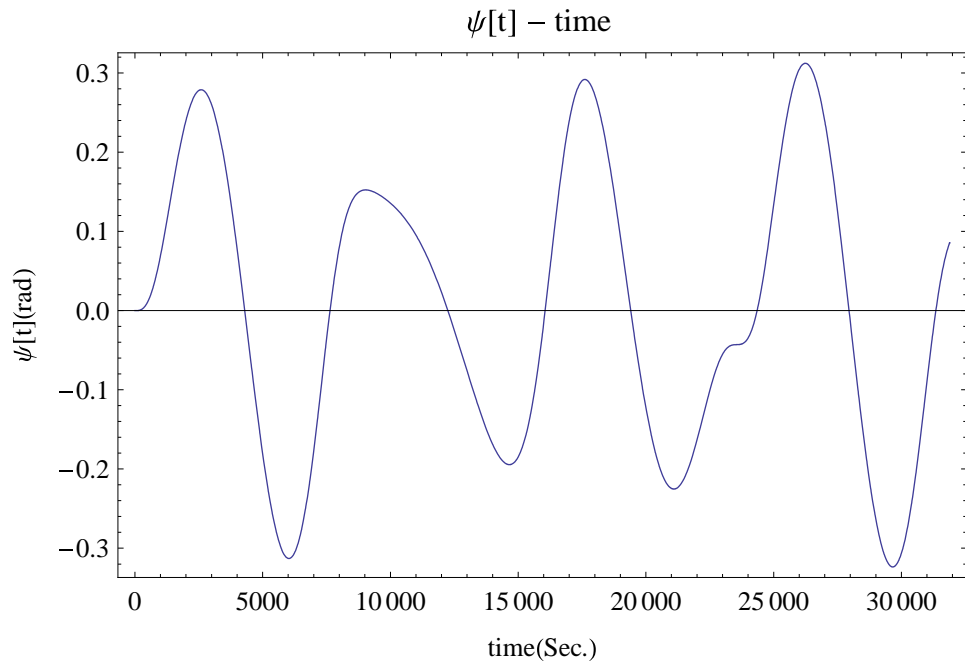


Figure 4.21: Massless axial and torsional elastic MMET spin-up angular displacement  $\psi$  ( $T_n = 4.01$ )

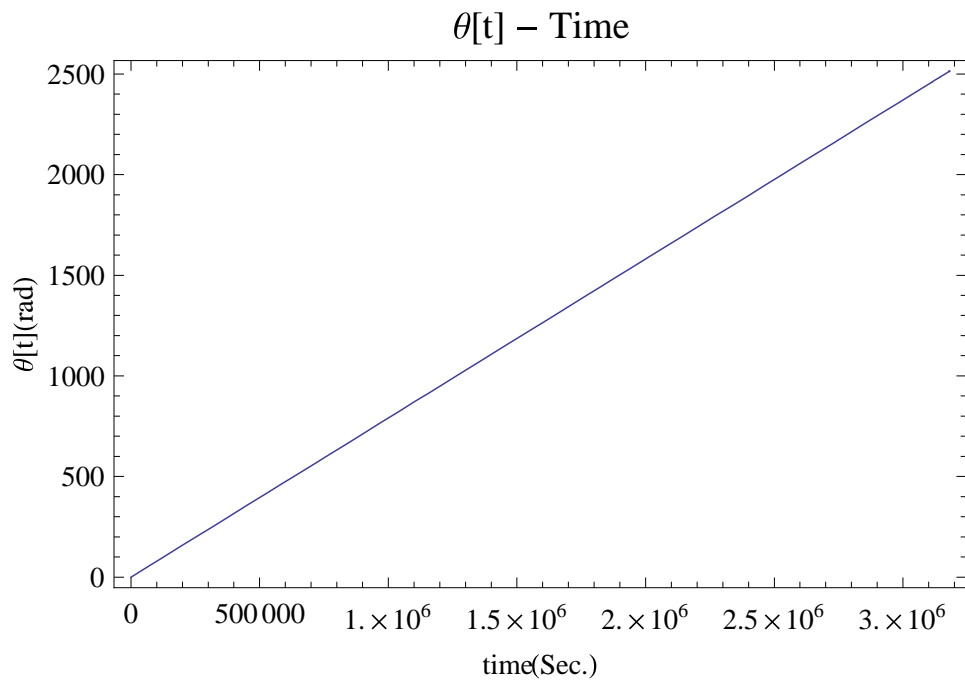


Figure 4.22: Massless axial and torsional elastic MMET elliptical orbit angular position of  $\theta$  ( $T_n = 400.01$ )

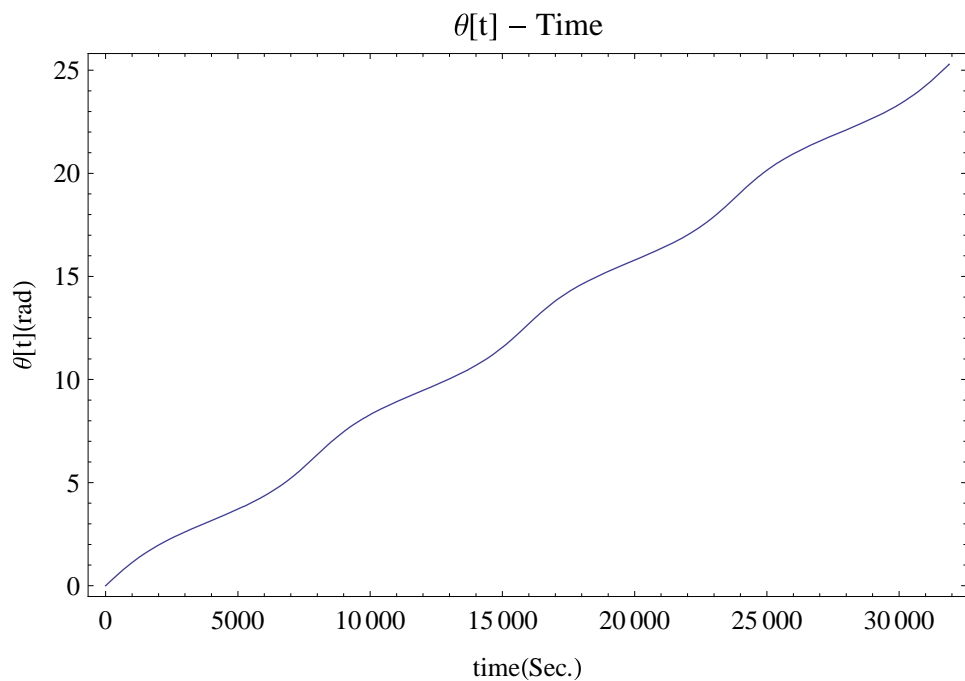


Figure 4.23: Massless axial and torsional elastic MMET elliptical orbit angular position of  $\theta$  ( $T_n = 4.01$ )

▷ Figures 4.20 and 4.21 show the massless axial and torsional elastic MMET system's periodic spin-up behaviour  $\psi$  on an elliptical orbit ( $e = 0.2$ ) with the angular displacement range of  $-0.325$  to  $0.325$  rad.

▷ The results for the true anomaly  $\theta$  are shown in Figures 4.22 and 4.23 for the number of cycles of period  $T_n = 4.01$  and  $400.01$  simulation time, respectively. The curves are

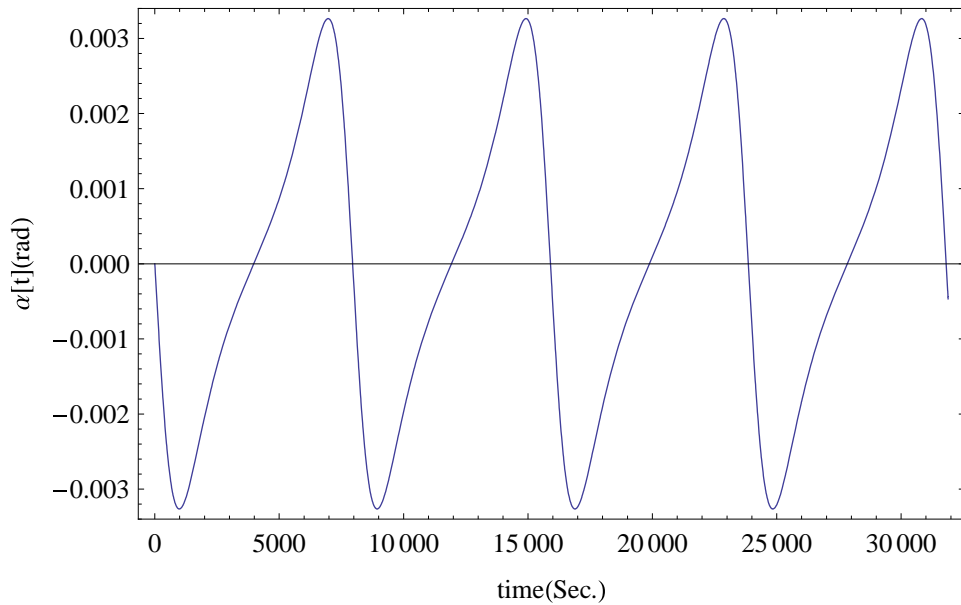


Figure 4.24: Massless axial and torsional elastic MMET out-of-plane angle  $\alpha$  ( $T_n = 4.01$ )

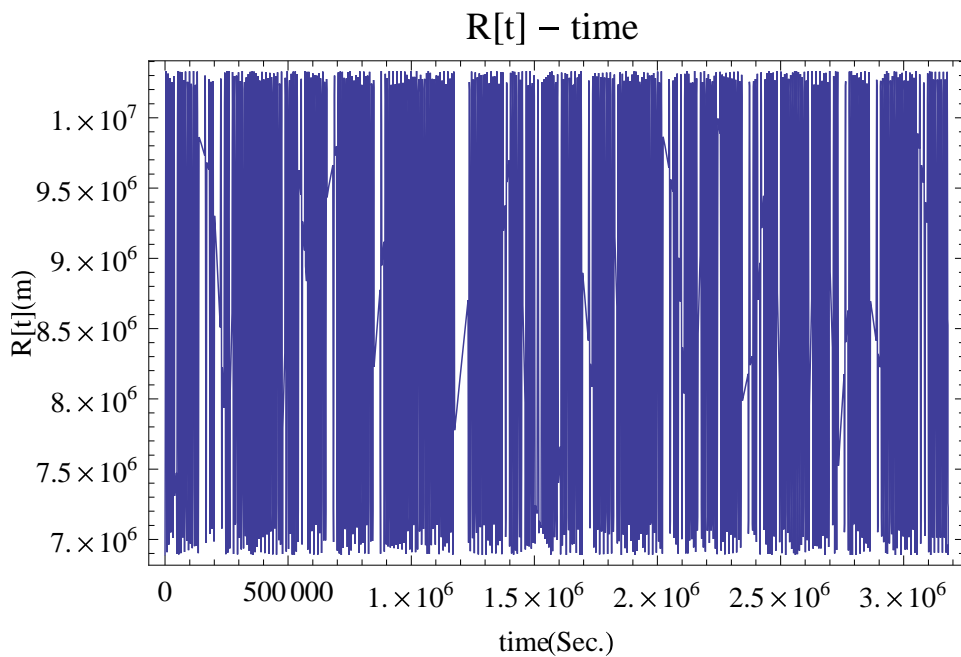


Figure 4.25: Massless axial and torsional elastic MMET base point distance  $R$  to the Earth ( $T_n = 400.01$ )

rising in a linear trend from 0 to 25 ( $T_n = 4.01$ ) or 2500 ( $T_n = 400.01$ ) rad with slight fluctuation spread (0 to 0.5 rad).

▷ With zero initial conditions  $\alpha(0) = 0$  rad and  $\dot{\alpha}(0) = 0$  rad/s, the responses for the out-of-plane angle  $\alpha$  stay in zero amplitude over the full simulation time. Figure 4.24 shows the  $\alpha$ 's response with the period about 8000 seconds if  $\alpha(0) = 0.001$  rad and  $\dot{\alpha}(0) = 0.001$  rad/s are provided.

▷ The distance  $R$  from the Earth to the tether COM is changing periodically, as can

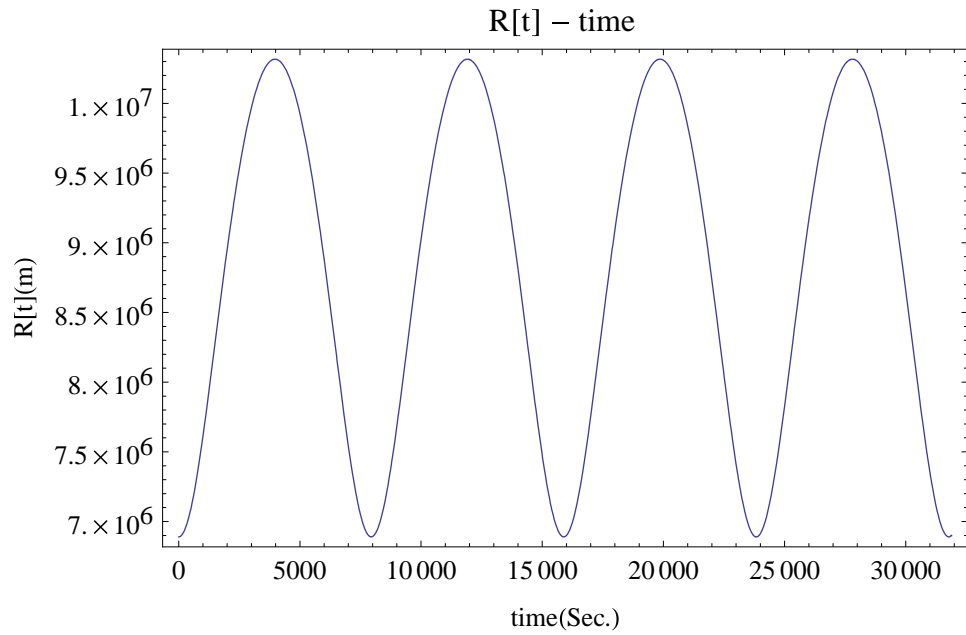


Figure 4.26: Massless axial and torsional elastic MMET base point distance  $R$  to the Earth ( $T_n = 4.01$ )

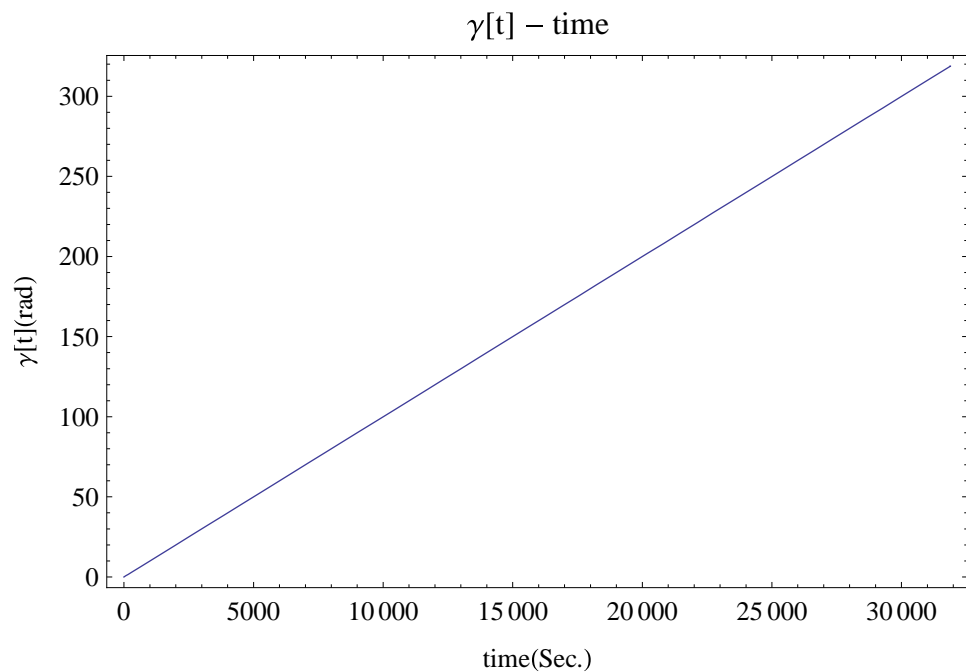


Figure 4.27: Massless axial and torsional elastic MMET rolling angle of  $\gamma$  ( $T_n = 4.01$ )

be seen in the Figures 4.25 and 4.26, which behave within the distance range of  $r_p$  ( $6.89 \times 10^6$  m) to  $r_a$  ( $1.0335 \times 10^7$  m) with given  $e = 0.2$  in this case.

▷ Same as it has been discussed in section 4.2.2, given initial conditions  $\gamma(0) = 0$  rad and  $\dot{\gamma}(0) = 0$  rad/s, the rigid rolling angle  $\gamma$  response stays in zero over full simulation time, which matches the equation (4.2.8).

▷ The tether subspan's axial oscillation  $L_x$  goes within 12.5 to 21.5 m in Figure 4.28,

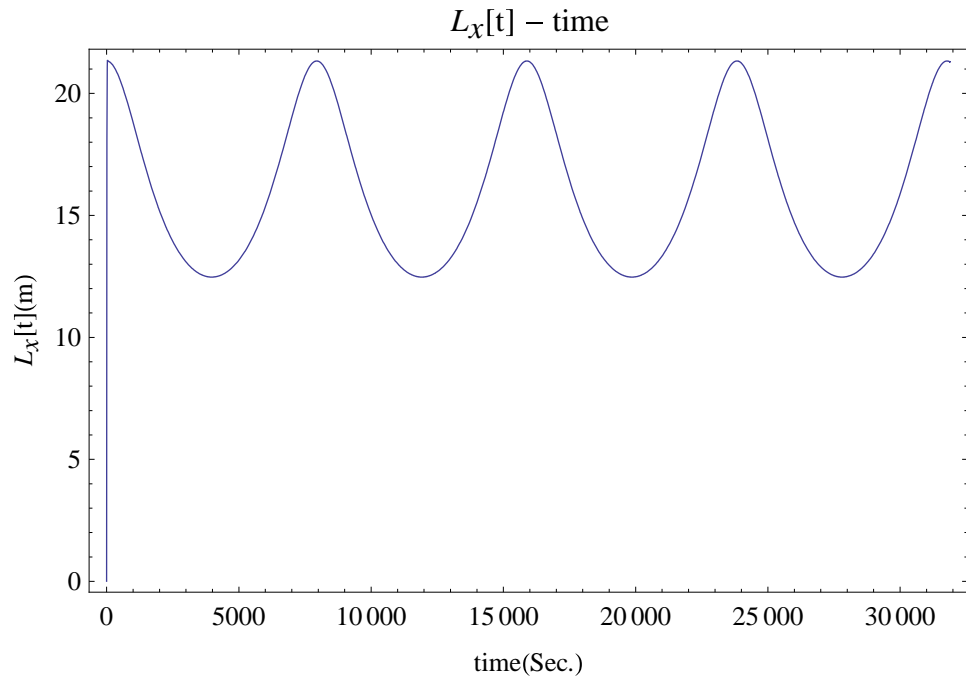


Figure 4.28: Axial displacement along tether subspan of  $L_x$  ( $T_n = 4.01$ )

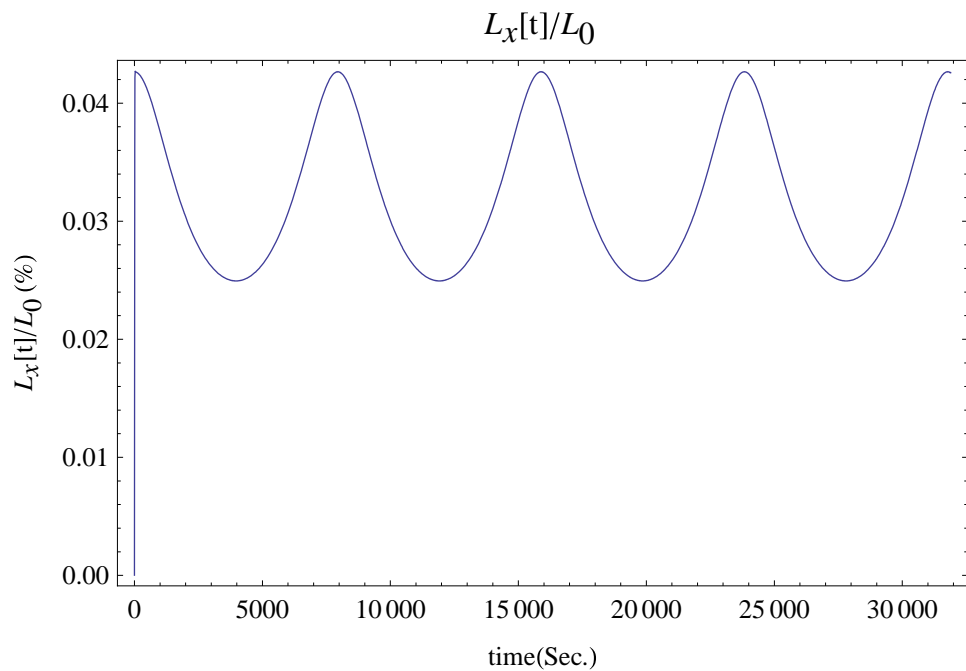


Figure 4.29: Axial elastic length vs. static length ratio along tether subspan of  $\frac{L_x}{L_0}$  ( $T_n = 4.01$ )

and the ratio of  $L_x$  to  $L_0$  varies 2.25% to 4.15% in Figure 4.29.

▷ Figure 4.30 states the torsional elastic angular displacement  $\gamma_x$  for each tether subspan with the range - 0.000075 to 0.000075 rad, which shows that the convergence of the torsional elastic behaviour can be observed clearly at about  $t = 9500$  seconds (with tiny convergent response over  $t$  from 0 to 9500 seconds), and it is approaching to zero status in the end of simulation time.

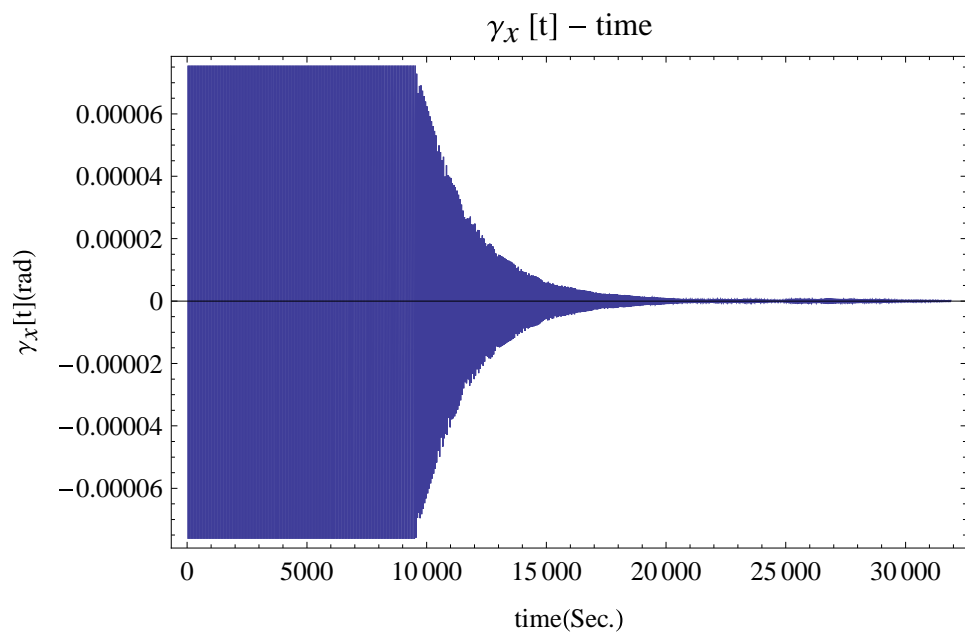


Figure 4.30: Torsional displacement  $\gamma_x$  ( $T_n = 4.01$ )

## 4.4 Dynamical Modelling with the inclusion of Axial, Torsional and Pendular Elasticity

Based on section 4.3, pendular elasticity is also included in the MMET modelling in this section. The modelling of the massless MMET with axial, torsional and pendular elasticity is proposed as in Figure 4.33, and this is also known as the flexible massless MMET system.

As implied in Figure 4.33, the generalised coordinates for the flexible MMET system are defined on orbit, and the Cartesian components of the end masses of  $M_M$ ,  $M_1$  and  $M_2$  are given in equations (3.2.4), (3.2.5) and (3.2.6).

Similar to the previous sections, besides the axial and torsional ‘spring-damper’ groups for the axial elasticity and torsional elasticity in Figure 4.19, another two types of torsional ‘spring-damper’ groups ( $k_{li} - c_{li}$  groups), as shown in Figures 4.31 and 4.35, are added into the modelling for the pendular elasticity. There are two parts of the pendular elasticity, which are stated on the plane  $x_0 - O - y_0$  and the plane  $z_0 - O - y_0$ , respectively,

▷ On the plane  $x_0 - O - y_0$

As shown in Figure 4.31, the  $x_0 - O - y_0$  plane based pendular elasticity is represented by a string of torsional ‘spring-damper’ groups, which connect the massless points of  $p_i$  in series. All the torsional ‘spring-damper’ groups are referenced onto the plane  $x_0 - O - y_0$ , as shown in Figure 4.32. The  $l$  in the subscript means the pendular elastic parameter, so the generalised coordinate  $\psi_x$  states the equivalent behaviour for the pendular elasticity on the plane  $x_0 - O - y_0$ .

▷ On the plane  $z_0 - O - y_0$

As shown in Figure 4.34, the  $z_0 - O - y_0$  plane based pendular elasticity is represented by a string of torsional ‘spring-damper’ groups  $\{k_{li}, c_{li}\}$ , which connect the massless points  $p_i$  in series, and all the torsional ‘spring-damper’ groups are referenced onto the plane  $z_0 - O - y_0$ , as shown in Figure 4.35. The generalised coordinate  $\alpha_x$  states the equivalent behaviour for the pendular elasticity on the plane  $z_0 - O - y_0$ .

$$\frac{1}{k_{leq}} = \frac{1}{k_{l1}} + \frac{1}{k_{l2}} + \dots + \frac{1}{k_{l(n+1)}} \quad (4.4.1)$$

$$\frac{1}{c_{leq}} = \frac{1}{c_{l1}} + \frac{1}{c_{l2}} + \dots + \frac{1}{c_{l(n+1)}} \quad (4.4.2)$$

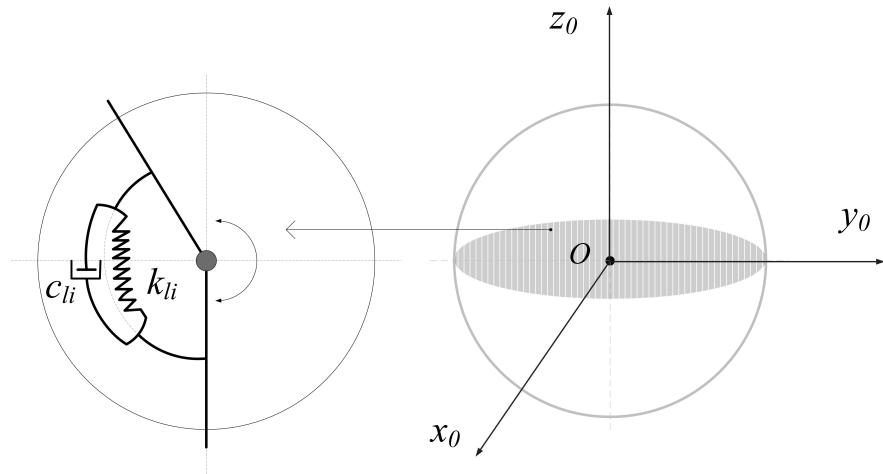


Figure 4.31: Reference onto the plane  $x_0 - O - y_0$  for MMET pendular elasticity

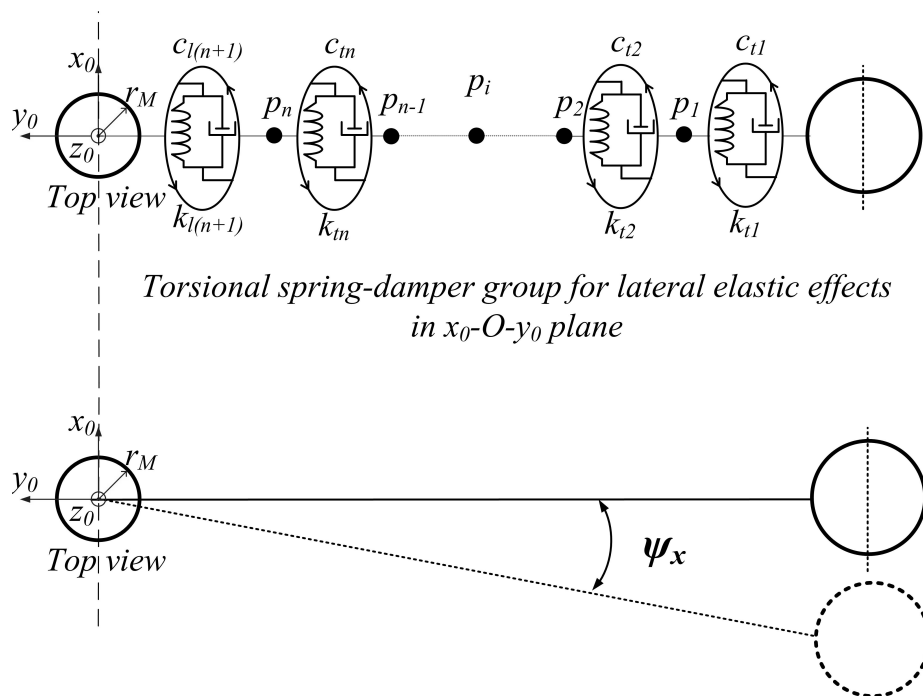


Figure 4.32: The MMET pendular elasticity modelling referenced onto the plane  $x_0 - O - y_0$

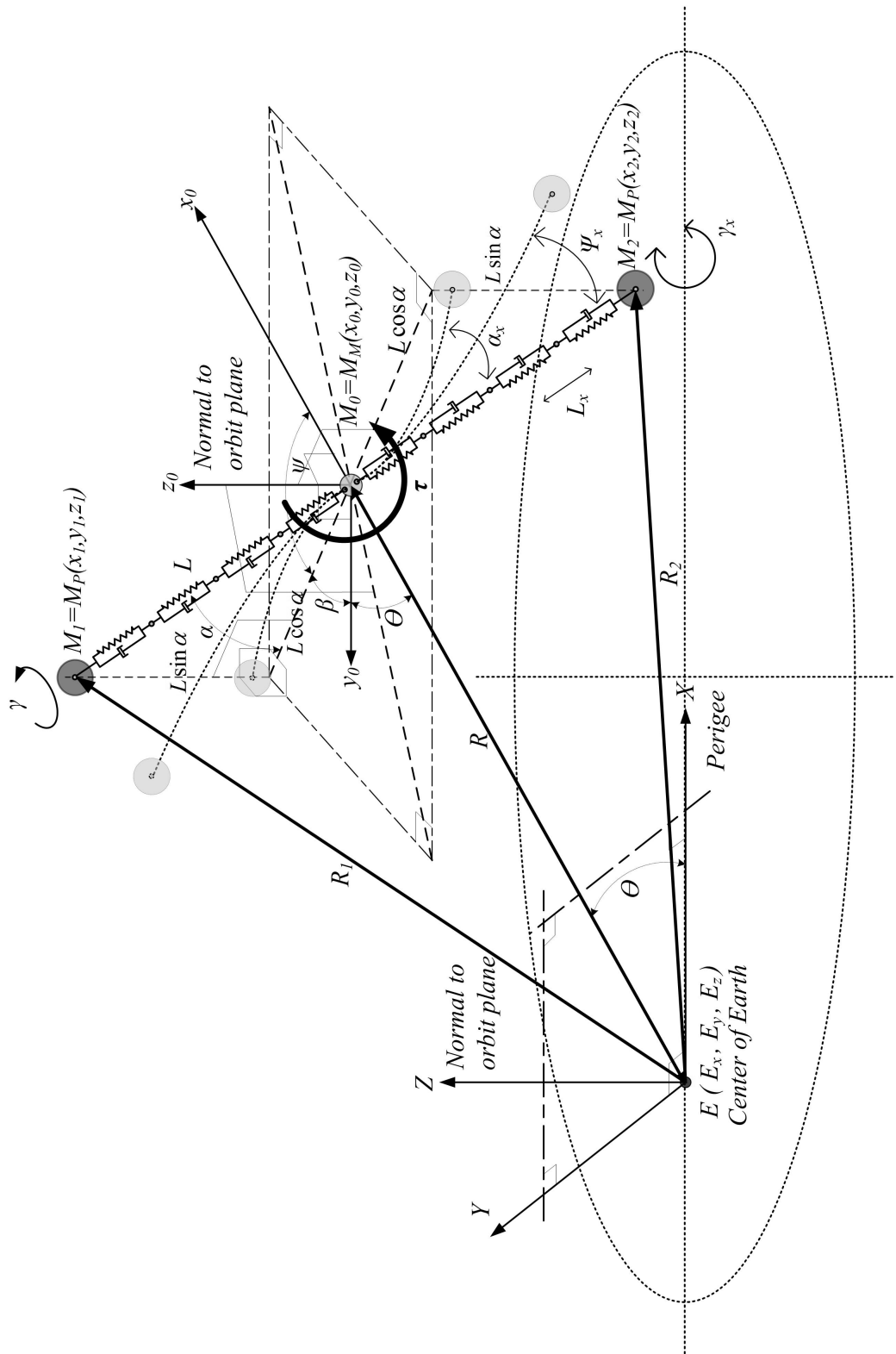


Figure 4.33: The flexible massless MMET system generalised coordinate definitions on orbit

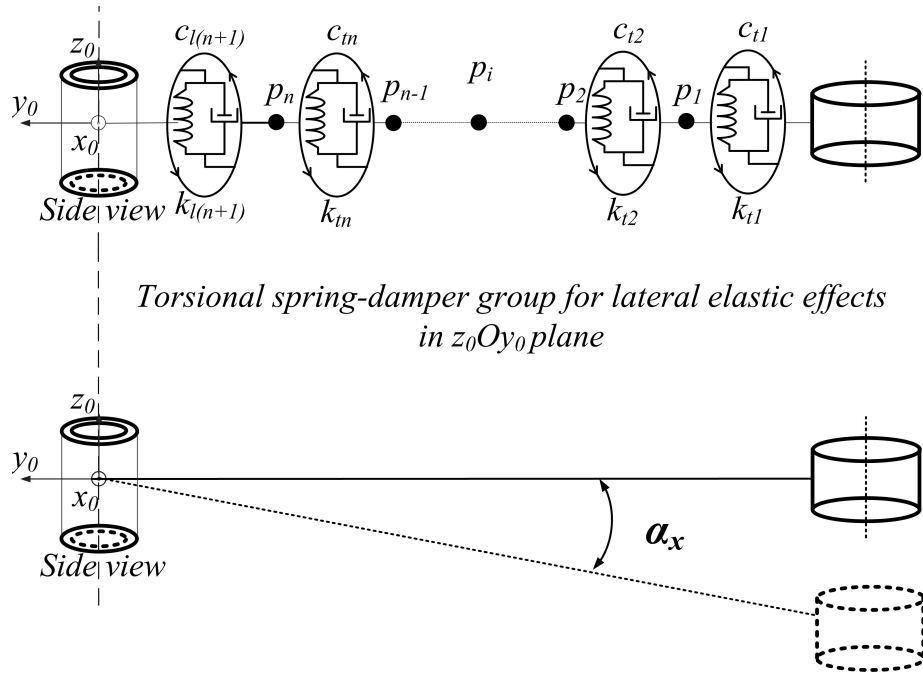


Figure 4.34: **The MMET pendular elasticity modelling reference on the plane  $z_0 - O - y_0$**

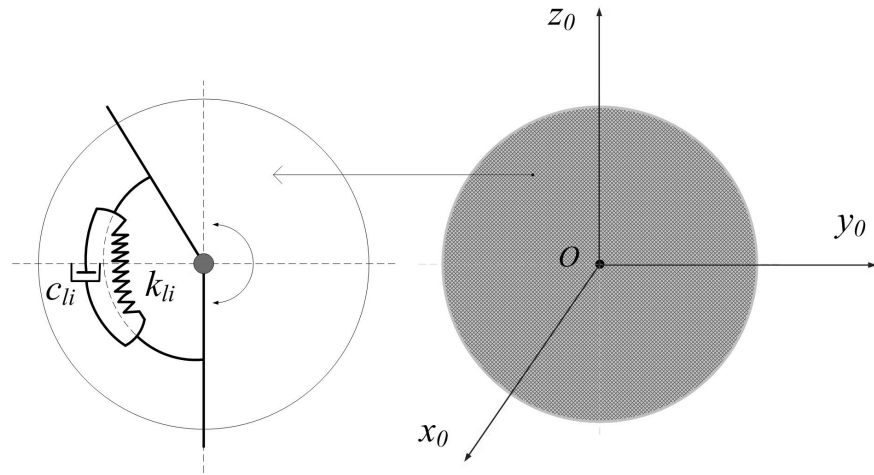


Figure 4.35: Reference on the plane  $z_0 - O - y_0$  for MMET pendular elasticity

Therefore, the pendular elasticity is obtained by a string of torsional ‘spring-damper’ groups  $\{k_{li}, c_{li}\}$ , in which  $k_{l1} = \dots = k_{l(n+1)}$ ,  $c_{l1} = \dots = c_{l(n+1)}$ . They are attached in series along the tether subspans, and can be expressed as equivalent spring stiffness  $k_{leq}$  and equivalent damping coefficient  $c_{leq}$ , which are provided by equations (4.4.1) and (4.4.2).

As shown in Figure 4.36, the axial, torsional and pendular elasticity terms are represented by the generalised coordinates  $L_x$ ,  $\gamma_x$ ,  $\psi_x$  and  $\alpha_x$ , in which the subscript ‘x’ means the elastic generalised coordinate. The equivalent spring stiffness and damping coefficients for axial, torsional and pendular elasticity are expressed as  $\{k_{eq}, c_{eq}\}$ ,  $\{k_{teq}, c_{teq}\}$  and  $\{k_{leq}, c_{leq}\}$ . Based on the serial springs and dampers assumption A5 in section 4.1, it can be summarised that,

⟨1⟩ for accommodating axial elasticity,  $k_0 = k_1 = k_2 = \dots = k_{n+1}$ ,  $c_0 = c_1 = c_2 = \dots = c_{n+1}$ , where the  $k_0$  and  $c_0$  are the default stiffness and damping coefficient values for numerical simulation, the equivalent axial stiffness and damping coefficient are given in equations (D.1.4), (D.1.5);

⟨2⟩ in the case of torsional elasticity,  $k_{t0} = k_{t1} = k_{t2} = \dots = k_{t(n+1)}$ ,  $c_{t0} = c_{t1} = c_{t2} = \dots = c_{t(n+1)}$ , where the  $k_{t0}$  and  $c_{t0}$  are the default stiffness and damping coefficient values for numerical simulation, the equivalent torsional stiffness and damping coefficients are presented by equations (E.1.3), (E.1.4);

⟨3⟩ finally, to include pendular elasticity terms in both the plane  $x_0 - O - y_0$  and the plane  $z_0 - O - y_0$ ,  $k_{l0} = k_{l1} = k_{l2} = \dots = k_{l(n+1)}$ ,  $c_{l0} = c_{l1} = c_{l2} = \dots = c_{l(n+1)}$ , where the  $k_{l0}$  and  $c_{l0}$  are the default stiffness and damping coefficient values, the equivalent torsional stiffness and damping coefficients in equations (4.4.1) and (4.4.2) can be reformed as equations (4.4.3), (4.4.4).

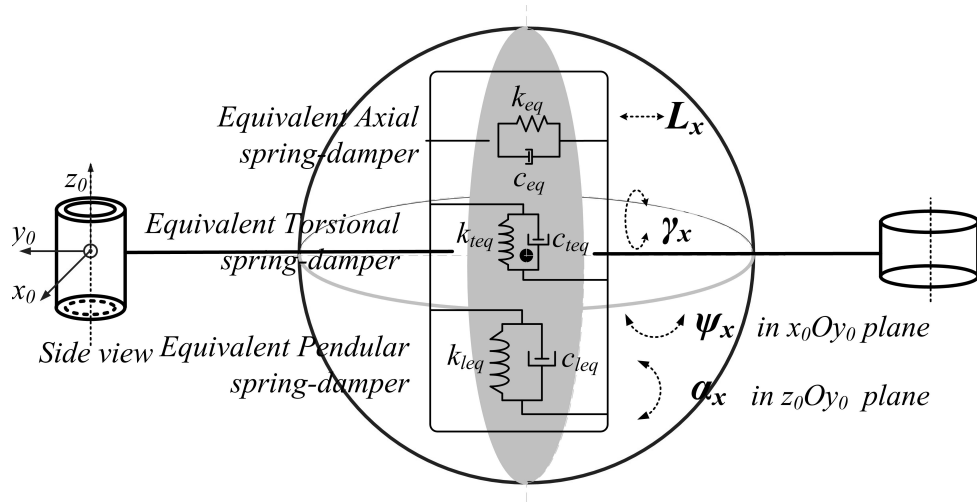


Figure 4.36: **The equivalent axial, torsional and pendular elasticity**

$$k_{teq} = \frac{k_{l0}}{n+1} \quad (4.4.3)$$

$$c_{leq} = \frac{c_{l0}}{n+1} \quad (4.4.4)$$

► The detail modelling process is attached in Appendix F.

### 4.4.1 Governing Equations of Motion

According to the Lagrangian procedure, the following governing equations for the generalised coordinates  $q_i$  are given in equations (4.4.5) to (4.4.13), for  $q_1 = \psi$ ,  $q_2 = \psi_x$ ,  $q_3 = \theta$ ,  $q_4 = \alpha$ ,  $q_5 = \alpha_x$ ,  $q_6 = \gamma$ ,  $q_7 = \gamma_x$ ,  $q_8 = L_x$  and  $q_9 = R$ , respectively, and are also listed in Table 4.3.

Table 4.3: The flexible massless MMET generalised coordinates and generalised forces

$i$	$q_i$	$Q_i$	$T$	$U$	Equations of Motion
1	$\psi$	(3.5.13)	(F.2.1)	(F.3.1)	(4.4.5)
2	$\psi_x$	(F.4.7)			(4.4.6)
3	$\theta$	(3.5.14)			(4.4.7)
4	$\alpha$	(3.5.15)			(4.4.8)
5	$\alpha_x$	(F.4.8)			(4.4.9)
6	$\gamma$	(3.5.17)			(4.4.10)
7	$\gamma_x$	(E.4.4)			(4.4.11)
8	$L_x$	(D.4.5)			(4.4.12)
9	$R$	(3.5.16)			(4.4.13)

$$\begin{aligned}
& \left( \frac{\mu M_{P2} (L_0 + L_x) \cos \alpha \left( \begin{array}{l} \sin(\theta + \psi) (R \cos \theta - \cos \alpha \cos(\theta + \psi) (L_0 + L_x)) - \\ \cos(\theta + \psi) (R \sin \theta - \cos \alpha \sin(\theta + \psi) (L_0 + L_x)) \end{array} \right)}{\left( (\cos \theta R - \cos \alpha \cos(\theta + \psi) (L_0 + L_x))^2 + \right.} \right) + \\
& \left. \left( (-\sin \alpha (L_0 + L_x))^2 + (R \sin \theta - \cos \alpha \sin(\theta + \psi) (L_0 + L_x))^2 \right)^{3/2}} \right) - \\
& \left( \frac{\cos \alpha \mu M_{P1} (L_0 + L_x) \left( \begin{array}{l} \cos(\theta + \psi) (R \sin \theta + \cos \alpha \sin(\theta + \psi) (L_0 + L_x)) - \\ \sin(\theta + \psi) (R \cos \theta + \cos \alpha \cos(\theta + \psi) (L_0 + L_x)) \end{array} \right)}{\left( (R \cos \theta + \cos \alpha \cos(\theta + \psi) (L_0 + L_x))^2 + (\sin \alpha (L_0 + L_x))^2 + \right.} \right) - \\
& \left. \left( (R \sin \theta + \cos \alpha \sin(\theta + \psi) (L_0 + L_x))^2 \right)^{3/2}} \right) \\
& (M_{P1} - M_{P2}) \left( \begin{array}{l} (L_0 + L_x) \left( \begin{array}{l} \sin \alpha \dot{\alpha} (\sin \psi \dot{R} - \cos \psi R \dot{\theta}) - \\ \cos \alpha (\cos \psi \dot{R} + R \sin \psi \dot{\theta}) (\dot{\theta} + \dot{\psi}) \end{array} \right) + \\ \cos \alpha (\cos \psi R \dot{\theta} - \sin \psi \dot{R}) \dot{L}_x \end{array} \right) + \\
& \left( \begin{array}{l} -2 \cos \alpha (M_{P1} + M_{P2}) \left( 2 \sin \alpha \dot{\alpha} (\dot{\theta} + \dot{\psi}) - \cos \alpha (\ddot{\theta} + \ddot{\psi}) \right) L_0^2 \\ \left( \begin{array}{l} \sin \psi (M_{P1} - M_{P2}) (\sin \alpha \dot{R} \dot{\alpha} - \cos \alpha (R \dot{\theta} \dot{\psi} + \ddot{R})) + \\ \cos \psi (M_{P1} - M_{P2}) \left( \begin{array}{l} \cos \alpha \dot{R} (\dot{\theta} - \dot{\psi}) + \\ R (\cos \alpha \ddot{\theta} - \sin \alpha \dot{\alpha} \dot{\theta}) \end{array} \right) \end{array} \right) L_0 \\ -2 \cos \alpha (M_{P1} + M_{P2}) \left( \begin{array}{l} 2 L_x \sin \alpha \dot{\alpha} (\dot{\theta} + \dot{\psi}) - \\ L_x \cos \alpha (\ddot{\theta} + \ddot{\psi}) - \\ \dot{L}_x \cos \alpha (\dot{\theta} + \dot{\psi}) \end{array} \right) \end{array} \right) \\
& \frac{1}{2} + 2 \sin \alpha (M_{P1} - M_{P2}) L_x \dot{\alpha} (\sin \psi \dot{R} - \cos \psi R \dot{\theta}) - \\
& 2 \sin 2\alpha (M_{P1} + M_{P2}) L_x^2 \dot{\alpha} (\dot{\theta} + \dot{\psi}) + L_x^2 (\alpha_x + \varphi_x) \\
& 2 \cos \alpha (M_{P1} - M_{P2}) \left( \begin{array}{l} (\cos \psi R \dot{\theta} - \sin \psi \dot{R}) \dot{L}_x + \\ L_x \left( \begin{array}{l} \cos \psi (\dot{R} (\dot{\theta} - \dot{\psi}) + R \ddot{\theta}) - \\ \sin \psi (R \dot{\theta} \dot{\psi} + \ddot{R}) \end{array} \right) \end{array} \right) \\
& + M_M r_M^2 (\ddot{\theta} + \ddot{\psi}) + \\
& \cos 2\alpha (M_{P1} + M_{P2}) L_x (2 (\dot{\theta} + \dot{\psi}) \dot{L}_x + L_x (\ddot{\theta} + \ddot{\psi})) + \\
& (M_{P1} + M_{P2}) ((\ddot{\theta} + \ddot{\psi}) r_p^2 + 2 L_x (\dot{\theta} + \dot{\psi}) \dot{L}_x + L_x^2 (\ddot{\theta} + \ddot{\psi})) \Big) = Q_\psi
\end{aligned} \tag{4.4.5}$$

$$\begin{aligned}
& \frac{2k_{10} (\alpha_x + \varphi_x)}{n + 1} + \\
& \frac{1}{2} (M_{P1} + M_{P2}) \left( 4 (L_0 + L_x) \dot{L}_x \varphi_x + \left( r_p^2 + 2 (L_0 + L_x)^2 \right) \ddot{\varphi}_x \right) = Q_{\psi_x}
\end{aligned} \tag{4.4.6}$$

$$\begin{aligned}
& \left( 2(M_M + M_{P1} + M_{P2}) \ddot{\theta} R^2 + \right. \\
& \quad \left. 2R \left( \begin{array}{l} 2(M_M + M_{P1} + M_{P2}) \dot{R} \dot{\theta} \\ + \cos \psi (M_{P1} - M_{P2}) \left( \begin{array}{l} \cos \alpha (2(\dot{\theta} + \dot{\psi}) \dot{L}_x + (L_0 + L_x) (2\ddot{\theta} + \ddot{\psi})) - \\ 2 \sin \alpha (L_0 + L_x) \dot{\alpha} (\dot{\theta} + \dot{\psi}) \end{array} \right) \\ + \sin \psi (M_{P1} - M_{P2}) \left( \begin{array}{l} \cos \alpha (\ddot{L}_x - (L_0 + L_x) (\dot{\alpha}^2 + \dot{\psi} (2\ddot{\theta} + \ddot{\psi}))) \\ - \sin \alpha (2\dot{\alpha} \dot{L}_x + (L_0 + L_x) \ddot{\alpha}) \end{array} \right) \end{array} \right) \right) \\
& + 4 \cos \alpha \cos \psi (M_{P1} - M_{P2}) L_x \dot{R} \dot{\theta} + 2 \cos \alpha \sin \psi (M_{P2} - M_{P1}) L_x \ddot{R} \\
& \frac{1}{2} + M_M r_M^2 (\ddot{\theta} + \ddot{\psi}) - 2 \cos \alpha L_0^2 (M_{P1} + M_{P2}) \left( \begin{array}{l} 2 \sin \alpha \dot{\alpha} (\dot{\theta} + \dot{\psi}) \\ - \cos \alpha (\ddot{\theta} + \ddot{\psi}) \end{array} \right) \\
& + 2 \cos \alpha L_0 \left( \begin{array}{l} -4 \sin \alpha (M_{P1} + M_{P2}) L_x \dot{\alpha} (\dot{\theta} + \dot{\psi}) \\ + (M_{P1} - M_{P2}) (2 \cos \psi \dot{R} \dot{\theta} - \sin \psi \ddot{R}) \\ + 2 \cos \alpha (M_{P1} + M_{P2}) ((\dot{\theta} + \dot{\psi}) \dot{L}_x + L_x (\ddot{\theta} + \ddot{\psi})) \end{array} \right) \\
& \quad \left. + (M_{P1} + M_{P2}) \left( \begin{array}{l} (\ddot{\theta} + \ddot{\psi}) r_P^2 \\ + 2 \cos \alpha L_x \left( \begin{array}{l} 2 \cos \alpha (\dot{\theta} + \dot{\psi}) \dot{L}_x \\ + L_x \left( \begin{array}{l} \cos \alpha (\ddot{\theta} + \ddot{\psi}) - \\ 2 \sin \alpha \dot{\alpha} (\dot{\theta} + \dot{\psi}) \end{array} \right) \end{array} \right) \right) \right) \right) = Q_{\theta} \\
\end{aligned} \tag{4.4.7}$$

$$\begin{aligned}
& \left( \frac{\mu M_{P2} \begin{pmatrix} 2 \cos(\theta + \psi) \sin \alpha (L_0 + L_x) (\cos \theta R - \cos \alpha \cos(\theta + \psi) (L_0 + L_x)) \\ -2 \cos \alpha (L_0 + L_x) (-\sin \alpha (L_0 + L_x)) + \\ 2 \sin \alpha \sin(\theta + \psi) (L_0 + L_x) (R \sin \theta - \cos \alpha \sin(\theta + \psi) (L_0 + L_x)) \end{pmatrix}}{2 \begin{pmatrix} (\cos \theta R - \cos \alpha \cos(\theta + \psi) (L_0 + L_x))^2 + \\ (-\sin \alpha (L_0 + L_x))^2 + (R \sin \theta - \cos \alpha \sin(\theta + \psi) (L_0 + L_x))^2 \end{pmatrix}^{3/2}} + \right. \\
& \left. \frac{\mu M_{P1} \begin{pmatrix} -2 \cos(\theta + \psi) \sin \alpha (L_0 + L_x) (\cos \theta R + \cos \alpha \cos(\theta + \psi) (L_0 + L_x)) \\ +2 \cos \alpha (L_0 + L_x) (\sin \alpha (L_0 + L_x)) - \\ 2 \sin \alpha \sin(\theta + \psi) (L_0 + L_x) (R \sin \theta + \cos \alpha \sin(\theta + \psi) (L_0 + L_x)) \end{pmatrix}}{2 \begin{pmatrix} (\cos \theta R + \cos \alpha \cos(\theta + \psi) (L_0 + L_x))^2 + \\ (\sin \alpha (L_0 + L_x))^2 + (R \sin \theta + \cos \alpha \sin(\theta + \psi) (L_0 + L_x))^2 \end{pmatrix}^{3/2}} \right) \\
& - \left( -\frac{1}{2} \sin 2\alpha (M_{P1} + M_{P2}) (L_0 + L_x)^2 (\dot{\theta} + \dot{\psi})^2 + \right. \\
& \left. \cos \psi (M_{P1} - M_{P2}) \left( -(L_0 + L_x) (\cos \alpha \dot{R} \dot{\alpha} + R \sin \alpha \dot{\theta} (\dot{\theta} + \dot{\psi})) - \sin \alpha \dot{R} \dot{L}_x \right) \right. \\
& \left. + \sin \psi (M_{P1} - M_{P2}) \left( (L_0 + L_x) \begin{pmatrix} \sin \alpha \dot{R} (\dot{\theta} + \dot{\psi}) - \\ \cos \alpha R \dot{\alpha} \dot{\theta} \end{pmatrix} - R \sin \alpha \dot{\theta} \dot{L}_x \right) \right) \\
& + \frac{1}{12} \left( M_M \ddot{\alpha} h_M^2 - 12 \cos \alpha (M_{P1} - M_{P2}) (L_0 + L_x) \dot{\alpha} (\cos \psi \dot{R} + R \sin \psi \dot{\theta}) + \right. \\
& 24 L_0 M_{P1} \dot{\alpha} \dot{L}_x + 24 L_0 M_{P2} \dot{\alpha} \dot{L}_x + 24 M_{P1} L_x \dot{\alpha} \dot{L}_x + 24 M_{P2} L_x \dot{\alpha} \dot{L}_x + \\
& 3 M_M r_M^2 \ddot{\alpha} + 3 M_{P1} r_p^2 \ddot{\alpha} + 3 M_{P2} r_p^2 \ddot{\alpha} + 12 M_{P1} L_x^2 \ddot{\alpha} + 12 M_{P2} L_x^2 \ddot{\alpha} + \\
& h_p^2 M_{P1} \ddot{\alpha} + 12 L_0^2 M_{P1} \ddot{\alpha} + h_p^2 M_{P2} \ddot{\alpha} + 12 L_0^2 M_{P2} \ddot{\alpha} + 24 L_0 M_{P1} L_x \ddot{\alpha} + \\
& 24 L_0 M_{P2} L_x \ddot{\alpha} \\
& \left. - 12 \sin \alpha (M_{P1} - M_{P2}) \begin{pmatrix} (\cos \psi \dot{R} + R \sin \psi \dot{\theta}) \dot{L}_x \\ + L_0 \begin{pmatrix} \sin \psi \dot{R} (\dot{\theta} - \dot{\psi}) + \\ \cos \psi (R \dot{\theta} \dot{\psi} + \ddot{R}) + \\ R \sin \psi \ddot{\theta} \end{pmatrix} + \\ L_x \begin{pmatrix} \sin \psi \dot{R} (\dot{\theta} - \dot{\psi}) + \\ \cos \psi (R \dot{\theta} \dot{\psi} + \ddot{R}) + \\ R \sin \psi \ddot{\theta} \end{pmatrix} \end{pmatrix} \right) = Q_\alpha
\end{aligned} \tag{4.4.8}$$

$$\frac{2k_{t0}(\alpha_x + \varphi_x)}{n+1} + \frac{1}{12} (M_{P1} + M_{P2}) \left( 24 (L_0 + L_x) \dot{L}_x \dot{\alpha}_x + \left( h_p^2 + 3 \left( r_p^2 + 4 (L_0 + L_x)^2 \right) \right) \ddot{\alpha}_x \right) = Q_{\alpha_x} \quad (4.4.9)$$

$$\frac{1}{12} (M_M (h_M^2 + 3r_M^2) + (M_{P1} + M_{P2}) (h_p^2 + 3r_p^2)) \ddot{\gamma} = Q_\gamma \quad (4.4.10)$$

$$\frac{2k_{t0}\gamma_x}{n+1} + \frac{1}{12} (M_{P1} + M_{P2}) (h_p^2 + 3r_p^2) \ddot{\gamma}_x = Q_{\gamma_x} \quad (4.4.11)$$

$$\left( \begin{array}{l} \frac{2k_0 L_x}{n+1} + \\ \mu M_{P2} \begin{pmatrix} -2 \cos \alpha \cos(\theta + \psi) (\cos \theta R - \cos \alpha \cos(\theta + \psi) (L_0 + L_x)) \\ -2 \sin \alpha (-\sin \alpha (L_0 + L_x)) \\ -2 \cos \alpha \sin(\theta + \psi) (R \sin \theta - \cos \alpha \sin(\theta + \psi) (L_0 + L_x)) \end{pmatrix} \\ \hline 2 \left( (\cos \theta R - \cos \alpha \cos(\theta + \psi) (L_0 + L_x))^2 + (-\sin \alpha (L_0 + L_x))^2 \right)^{3/2} \\ + (R \sin \theta - \cos \alpha \sin(\theta + \psi) (L_0 + L_x))^2 \\ \mu M_{P1} \begin{pmatrix} 2 \cos \alpha \cos(\theta + \psi) (\cos \theta R + \cos \alpha \cos(\theta + \psi) (L_0 + L_x)) \\ +2 \sin \alpha (\sin \alpha (L_0 + L_x)) \\ +2 \cos \alpha \sin(\theta + \psi) (R \sin \theta + \cos \alpha \sin(\theta + \psi) (L_0 + L_x)) \end{pmatrix} \\ \hline + \frac{\left( (\cos \theta R + \cos \alpha \cos(\theta + \psi) (L_0 + L_x))^2 \right)^{3/2}}{2 \left( (\sin \alpha (L_0 + L_x))^2 \right)} \\ + (R \sin \theta + \cos \alpha \sin(\theta + \psi) (L_0 + L_x))^2 \end{array} \right) \\ - \left( \begin{array}{l} \frac{1}{2} \cos 2\alpha (M_{P1} + M_{P2}) (L_0 + L_x) (\dot{\theta} + \dot{\psi})^2 \\ + \cos \alpha (M_{P2} - M_{P1}) (\sin \psi \dot{R} - \cos \psi R \dot{\theta}) (\dot{\theta} + \dot{\psi}) \\ + \sin \alpha (M_{P2} - M_{P1}) \dot{\alpha} (\cos \psi \dot{R} + R \sin \psi \dot{\theta}) \\ + \frac{1}{2} (M_{P1} + M_{P2}) (L_0 + L_x) \left( 2\dot{\alpha}^2 + (\dot{\theta} + \dot{\psi})^2 + 2(\dot{\alpha}_x^2 + \dot{\varphi}_x^2) \right) \end{array} \right) \\ + \left( \begin{array}{l} -\sin \alpha (M_{P1} - M_{P2}) \dot{\alpha} (\cos \psi \dot{R} + R \sin \psi \dot{\theta}) \\ + \cos \alpha (M_{P1} - M_{P2}) (\sin \psi \dot{R} (\dot{\theta} - \dot{\psi}) + \cos \psi (R \dot{\theta} \dot{\psi} + \ddot{R}) + R \sin \psi \ddot{\theta}) \\ + 2 (M_{P1} + M_{P2}) \ddot{L}_x \end{array} \right) = Q_{L_x} \quad (4.4.12)$$

$$\begin{aligned}
& \left( \frac{\mu M_M}{R^2} + \frac{\mu M_{P2} \left( \begin{array}{l} 2 \cos \theta (\cos \theta R - \cos \alpha \cos(\theta + \psi) (L_0 + L_x)) \\ + 2 \sin \theta (R \sin \theta - \cos \alpha \sin(\theta + \psi) (L_0 + L_x)) \end{array} \right)}{2 \left( \begin{array}{l} (\cos \theta R - \cos \alpha \cos(\theta + \psi) (L_0 + L_x))^2 \\ + (-\sin \alpha (L_0 + L_x))^2 \\ + (R \sin \theta - \cos \alpha \sin(\theta + \psi) (L_0 + L_x))^2 \end{array} \right)^{3/2}} \right) \\
& + \frac{\mu M_{P1} \left( \begin{array}{l} 2 \cos \theta (\cos \theta R + \cos \alpha \cos(\theta + \psi) (L_0 + L_x)) \\ + 2 \sin \theta (R \sin \theta + \cos \alpha \sin(\theta + \psi) (L_0 + L_x)) \end{array} \right)}{2 \left( \begin{array}{l} (\cos \theta R + \cos \alpha \cos(\theta + \psi) (L_0 + L_x))^2 \\ + (\sin \alpha (L_0 + L_x))^2 \\ + (R \sin \theta + \cos \alpha \sin(\theta + \psi) (L_0 + L_x))^2 \end{array} \right)^{3/2}} \\
& - \dot{\theta} \left( \begin{array}{l} R (M_M + M_{P1} + M_{P2}) \dot{\theta} \\ + \cos \alpha \cos \psi (M_{P1} - M_{P2}) (L_0 + L_x) (\dot{\theta} + \dot{\psi}) \\ + \sin \psi (M_{P2} - M_{P1}) (\sin \alpha (L_0 + L_x) \dot{\alpha} - \cos \alpha \dot{L}_x) \end{array} \right) \\
& + \left( \begin{array}{l} (M_M + M_{P1} + M_{P2}) \ddot{R} \\ + \sin \alpha (M_{P1} - M_{P2}) \left( \begin{array}{l} \sin \psi (L_0 + L_x) \dot{\alpha} (\dot{\theta} + 2\dot{\psi}) \\ - \cos \psi (2\dot{\alpha} \dot{L}_x + (L_0 + L_x) \ddot{\alpha}) \end{array} \right) \\ + \cos \alpha (M_{P1} - M_{P2}) \left( \begin{array}{l} \cos \psi (\ddot{L}_x - (L_0 + L_x) (\dot{\alpha}^2 + \dot{\psi} (\dot{\theta} + \dot{\psi}))) \\ - \sin \psi ((\dot{\theta} + 2\dot{\psi}) \dot{L}_x + (L_0 + L_x) (\ddot{\theta} + \ddot{\psi})) \end{array} \right) \end{array} \right) = Q_R
\end{aligned} \tag{4.4.13}$$

## 4.4.2 Simulations and Discussions

Figures 4.37 to 4.49 are the numerical results obtained by MATHEMATICA for the selected generalised coordinates  $\psi$ ,  $\theta$ ,  $\alpha$ ,  $R$ ,  $\gamma$ ,  $L_x$ ,  $\gamma_x$ ,  $\psi_x$  and  $\alpha_x$ , as listed in Table 4.3. The results show the massless flexible elastic MMET system's periodic behaviour on elliptical orbit in simulation time  $T_n = 4.01$  and  $T_n = 400.01$ .

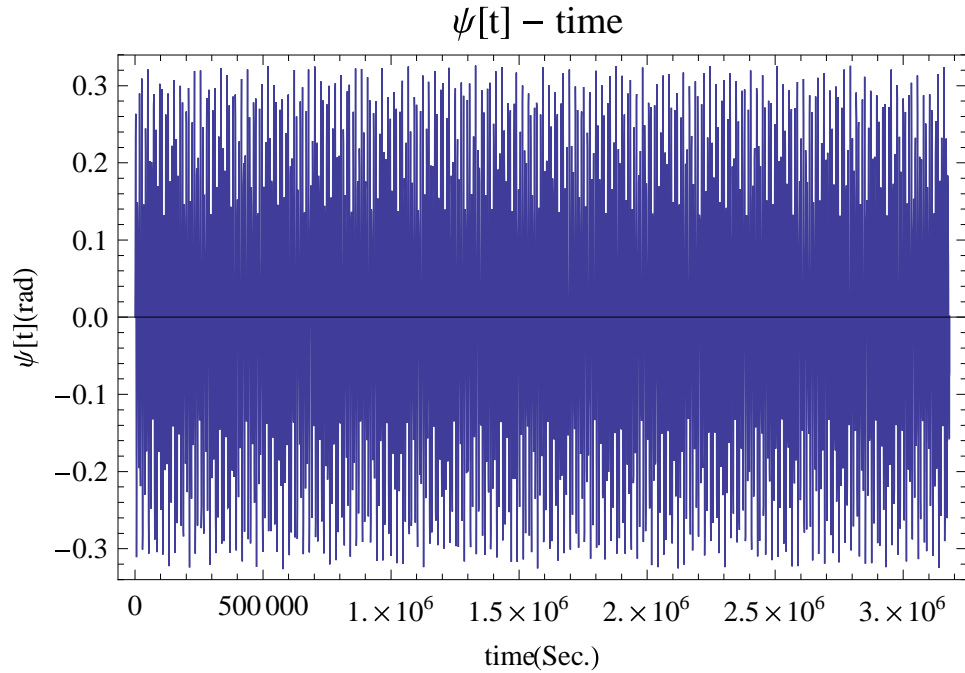


Figure 4.37: Massless flexible MMET spin-up, angular displacement  $\psi$  ( $T_n = 400.01$ )

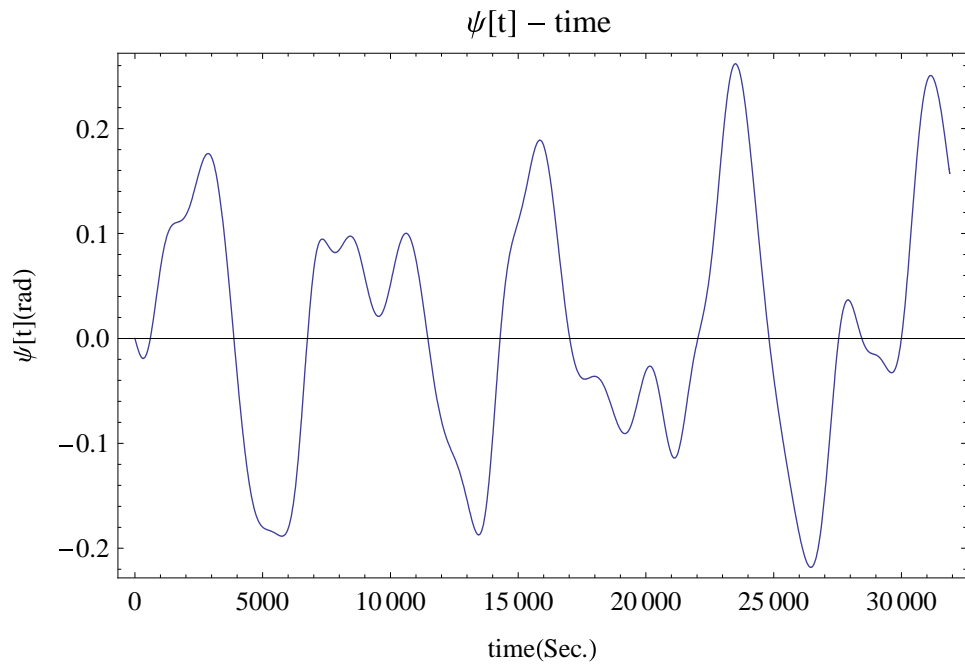


Figure 4.38: Massless flexible MMET spin-up, angular displacement  $\psi$  ( $T_n = 4.01$ )

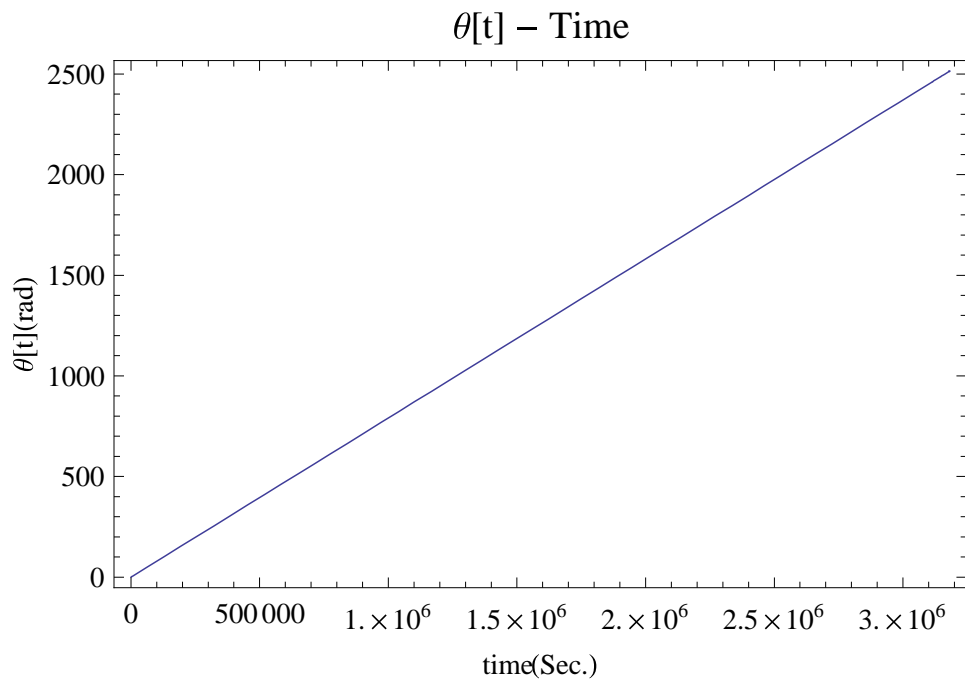


Figure 4.39: Massless flexible MMET elliptical orbit angular position of  $\theta$  ( $T_n = 400.01$ )

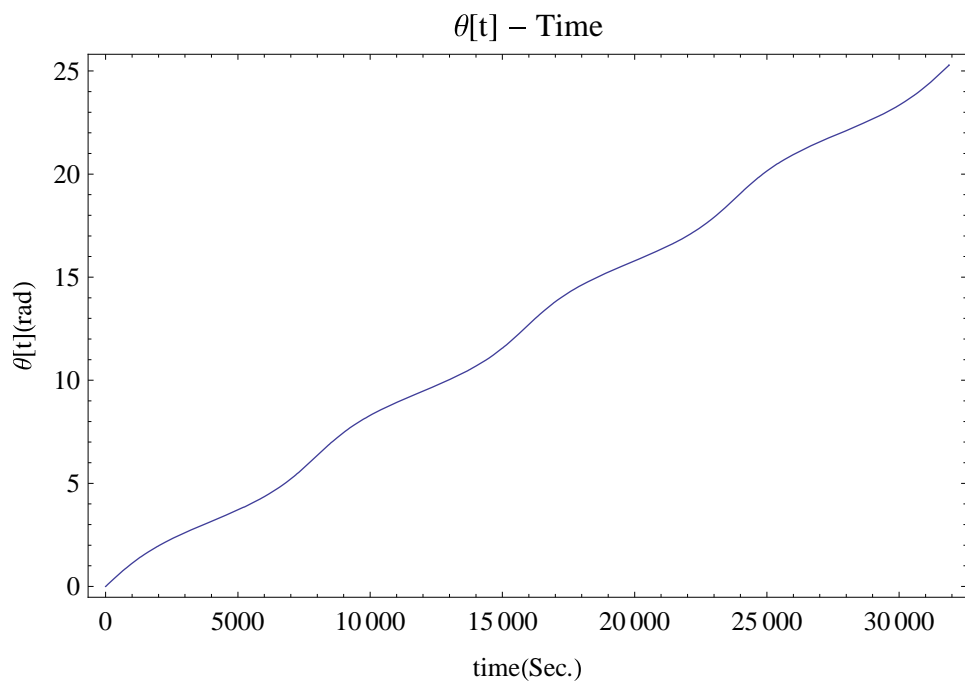


Figure 4.40: Massless flexible MMET elliptical orbit angular position of  $\theta$  ( $T_n = 4.01$ )

▷ Figures 4.37 and 4.38 show the flexible massless MMET system's periodic spin-up behaviour  $\psi$  on an elliptical orbit ( $e = 0.2$ ) with the angular displacement range of  $-0.325$  to  $0.325$  rad. Their shapes contain more ups and downs, which are slightly different from the spin-up output of the axial and torsional elastic massless MMET systems. Its ODE coupled more connections with lateral elastic behaviours ( $\alpha_x$  and  $\varphi_x$ ), as shown in equation (4.4.5).

▷ The results for the true anomaly  $\theta$  are shown in Figures 4.39 and 4.40 for the number

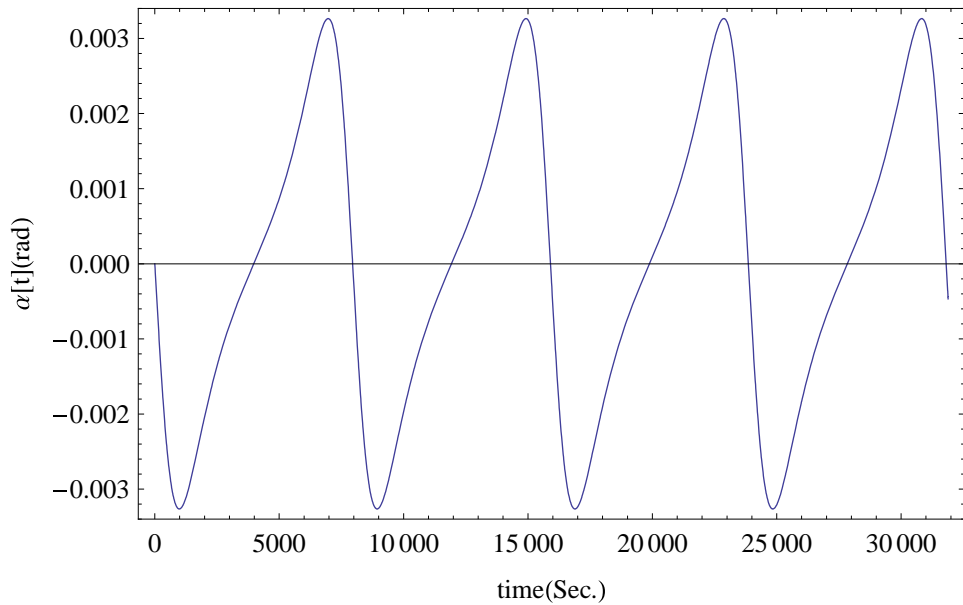


Figure 4.41: Massless flexible MMET out-of-plane angle  $\alpha$  ( $T_n = 4.01$ )

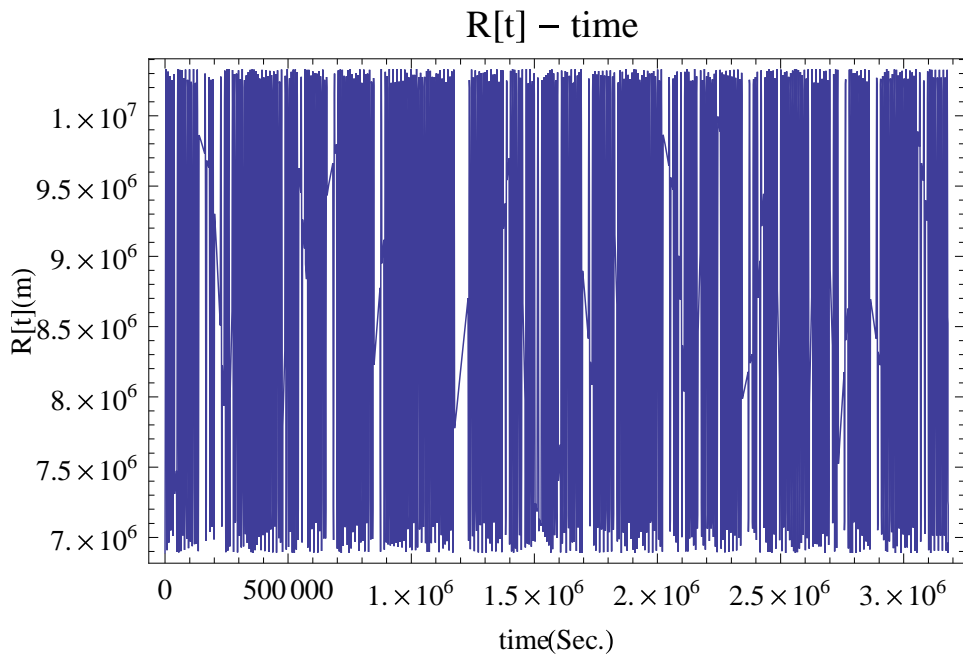


Figure 4.42: Massless flexible MMET base point distance  $R$  to the Earth ( $T_n = 400.01$ )

of cycles of period  $T_n = 4.01$  and  $400.01$  simulation time, respectively. The curves are rising in a linear trend from 0 to 25 ( $T_n = 4.01$ ) or 2500 ( $T_n = 400.01$ ) rad with slight fluctuation spread (0 to 0.5 rad).

▷ Figure 4.41 is the response for  $\alpha$  when  $\alpha(0) = 0.001$  rad and  $\dot{\alpha}(0) = 0.001$  rad/s. If give the initial conditions  $\alpha(0) = 0$  rad and  $\dot{\alpha}(0) = 0$  rad/s, the responses for the out-of-plane angle  $\alpha$  are with zero amplitude over the full simulation time.

▷ The distance  $R$  from the Earth to the tether COM is changing periodically, as can be seen in the Figures 4.42 and 4.43, which behave within the distance range of  $r_p$

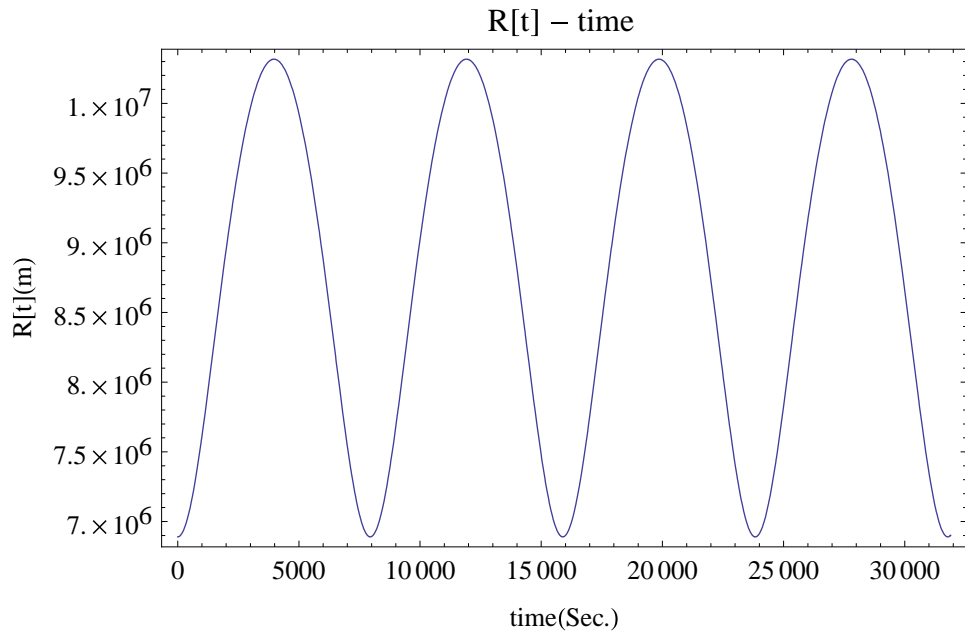


Figure 4.43: Massless flexible MMET base point distance  $R$  to the Earth ( $T_n = 4.01$ )

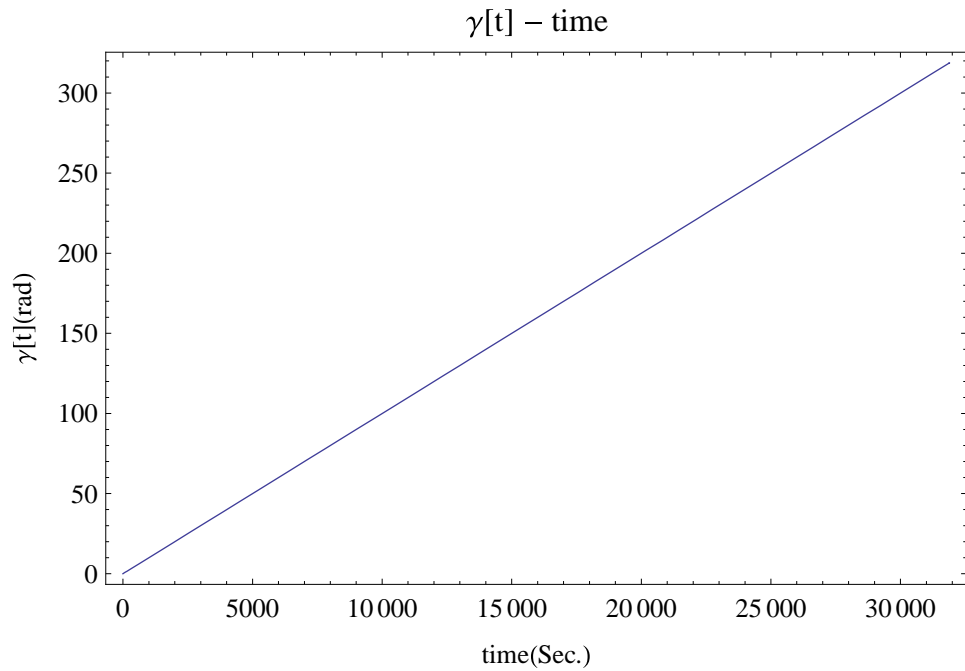


Figure 4.44: Massless flexible MMET rolling angle  $\gamma$  ( $T_n = 400.01$ )

( $6.89 \times 10^6$  m) to  $r_a$  ( $1.0335 \times 10^7$  m) with given  $e = 0.2$  in this case.

▷ The rigid rolling angle  $\gamma$  results stay in zero if given initial conditions  $\gamma(0) = 0$  rad and  $\dot{\gamma}(0) = 0$  rad/s with the same ODE as given in equation (4.2.8). As shown in Figure 4.44, the rigid rolling angle  $\gamma$  is going up over the simulation time with  $\gamma(0) = 0.001$  rad and  $\dot{\gamma}(0) = 0.001$  rad/s.

▷ The tether subspan's axial oscillation  $L_x$  goes 13.5 to 19 m in Figure 4.45, and the ratio of  $L_x$  to  $L_0$  varies 2.8% to 3.8% in Figure 4.46.

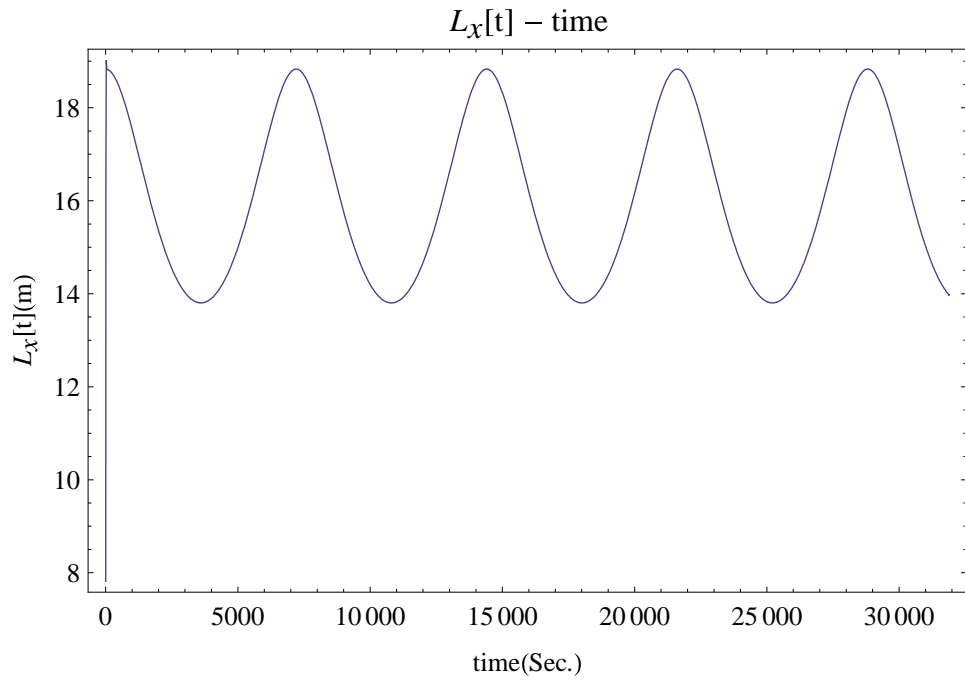


Figure 4.45: Massless flexible MMET axial displacement along tether subspan of  $L_x$  ( $T_n = 4.01$ )

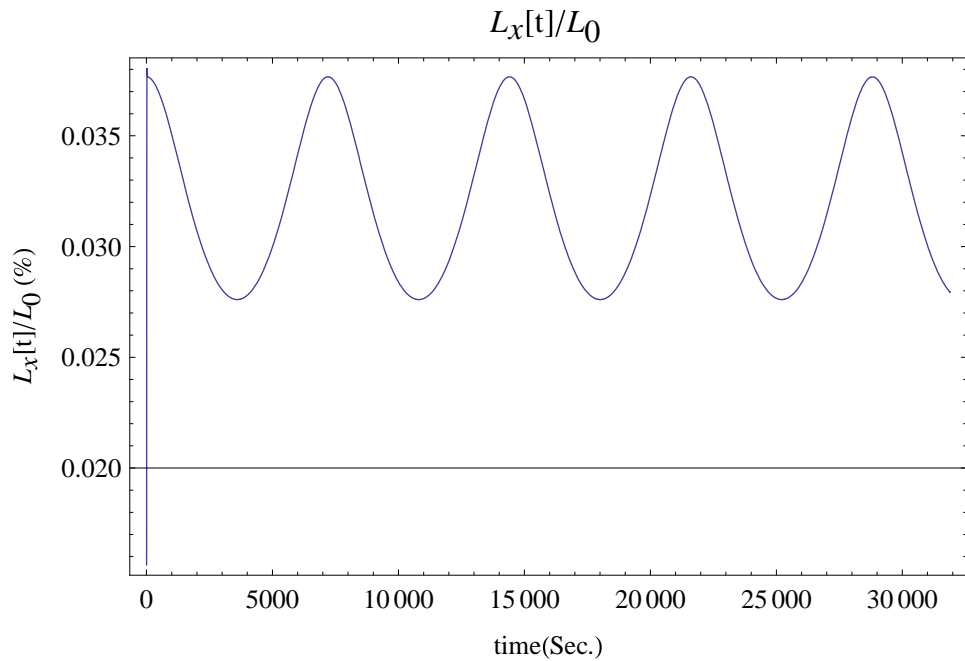


Figure 4.46: Massless flexible MMET axial elastic length vs. static length ratio along tether subspan of  $\frac{L_x}{L_0}$  ( $T_n = 4.01$ )

▷ Figure 4.47 states the torsional elastic angular displacement  $\gamma_x$  for each tether subspan with the range -0.000075 to 0.000075 rad, which shows that the convergence of the torsional elastic behaviour is approaching to zero status in the end of simulation time.

▷ Figures 4.48 and 4.49 are the pendular elastic angular displacements on plane  $x_0$  –

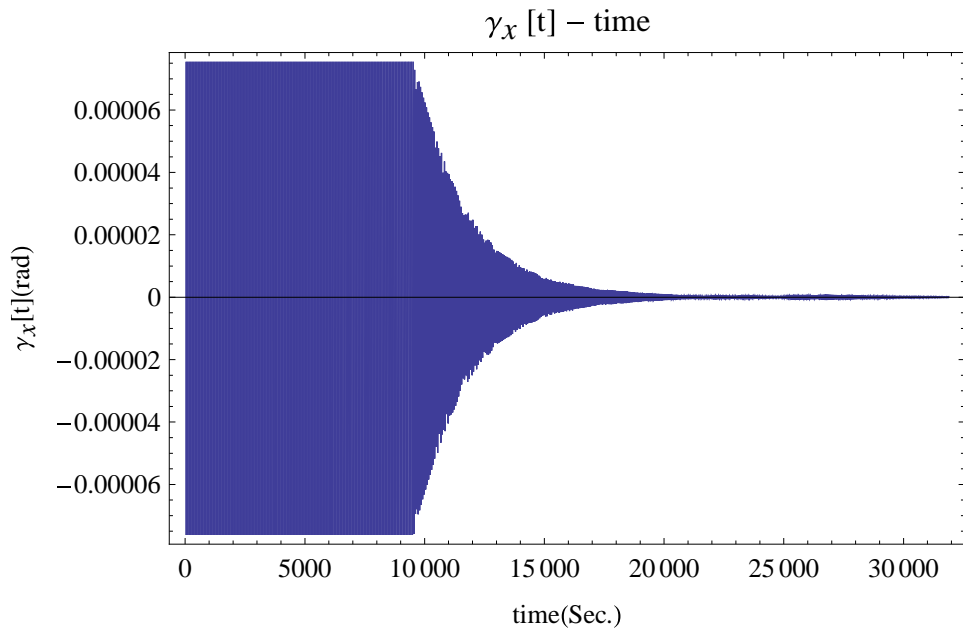


Figure 4.47: Massless flexible MMET torsional displacement  $\gamma_x$  ( $T_n = 4.01$ )

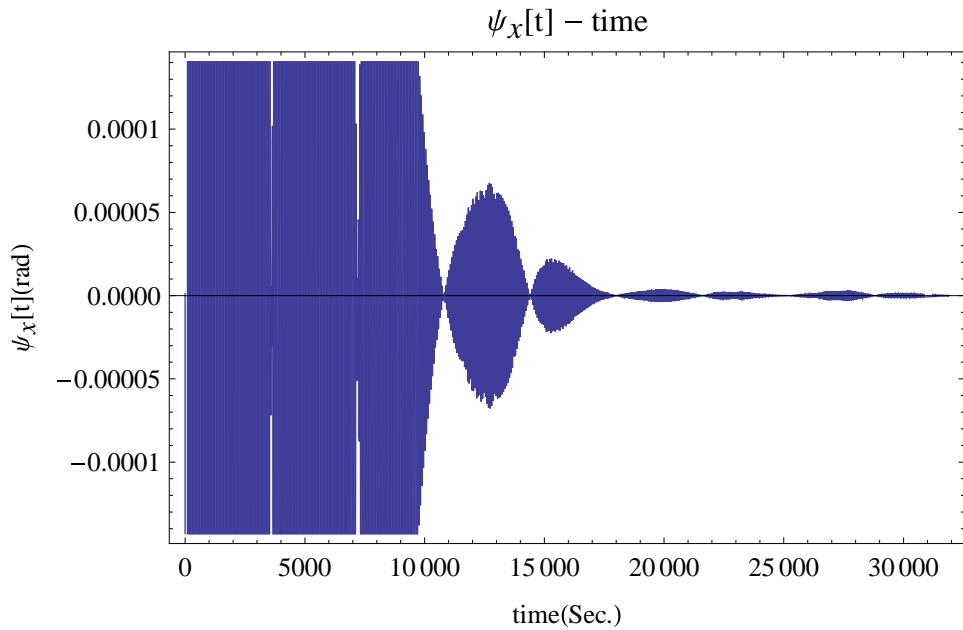


Figure 4.48: Massless flexible MMET, on plane  $x_0 - O - y_0$ , pendular displacement  $\psi_x$  ( $T_n = 4.01$ )

$O - y_0$  and plane  $z_0 - O - y_0$  respectively, and in the beginning their motions are within the range - 0.00014 to 0.00014 rad, and then the curves with convergent pendular elastic behaviours are observed with reducing amplitude of oscillation till to about  $t = 9500$  seconds, and then with obviously approaching to zero. According to the equations (4.4.6) and (4.4.9) for  $\psi_x$  and  $\alpha_x$ , the responses of  $\psi_x$  and  $\alpha_x$  perform alike with slightly different mass moment of inertia.

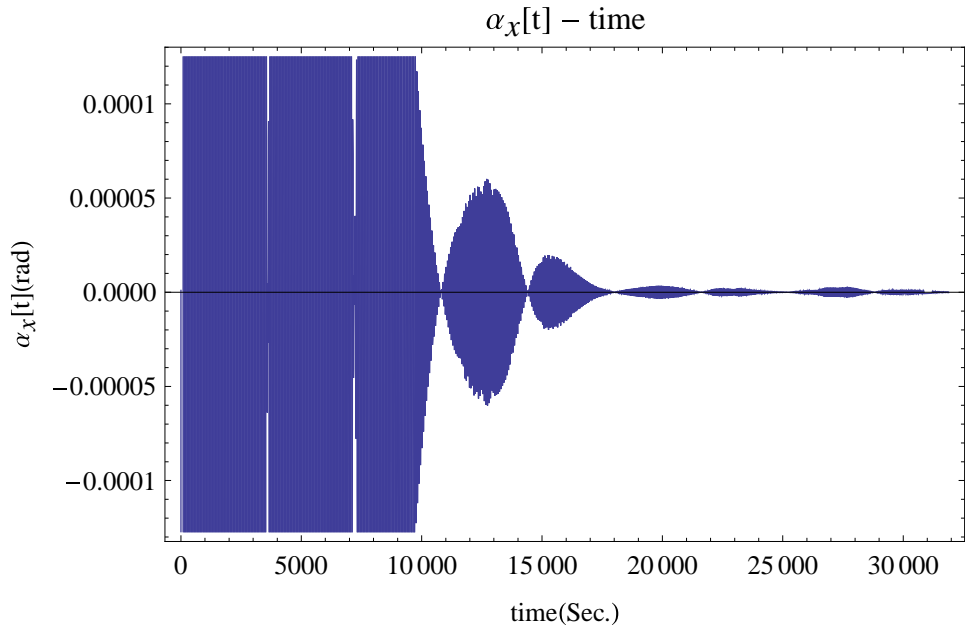


Figure 4.49: Massless flexible MMET, on plane  $z_0 - O - y_0$ , pendular displacement  $\alpha_x$  ( $T_n = 4.01$ )

## 4.5 Conclusions

To address the modelling process for the flexible massless MMET clearly, the axial, torsional and pendular elastic components are investigated simultaneously, and then integrated as one flexible MMET system. There are seven rotational generalised coordinates ( $\psi$ ,  $\psi_x$ ,  $\theta$ ,  $\alpha$ ,  $\alpha_x$ ,  $\gamma$ ,  $\gamma_x$ ) and two translational coordinates ( $L_x$ ,  $R$ ) which were chosen as the generalised coordinates for the flexible massless MMET system, in which the rigid body generalised coordinates ( $\psi$ ,  $\theta$ ,  $\alpha$ ,  $\gamma$ ,  $R$ ) are not duplicating any of the motions of the elastic generalised coordinates ( $\psi_x$ ,  $\alpha_x$ ,  $\gamma_x$ ,  $L_x$ ).

Using the parameters in Appendix C, the numerical results for the selected generalised coordinates in section 4.2.2, section 4.3.2 and section 4.4.2 expressed the periodic motions on orbit, with reducing amplitude of axial, torsional and pendular elastic oscillation for three MMET models in sections 4.2, 4.3 and 4.4 respectively, whose similar spin-up behaviours are also noted.

Meanwhile, this chapter also established a guiding modelling procedure for studies on the discretised flexible MMET system in further chapters, which indicate the models coupled with the flexible behaviours.

Table 4.4 gives the  $\psi$  plots for the massless tether systems, and  $\psi$  is the generalised coordinate for the tether's spin-up, which is the angle from the  $x_0$  axis to the projection of the tether onto the orbit plane. With the given parameters in Appendix C, the spin-up responses change periodically between  $-0.325$  to  $0.325$  rad over the number of cycles of period  $T_n =$

Table 4.4: Figures for spin-up  $\psi$  in Chapter 4

Tether Type	Figure No. ( $T_n = 400.01$ )	Figure No. ( $T_n = 4.01$ )
Axial Elastic	4.7	4.8
Axial and Torsional Elastic	4.20	4.21
Flexible	4.37	4.38

Table 4.5: Figures for R in Chapter 4

Tether Type	Figure No. ( $T_n = 400.01$ )	Figure No. ( $T_n = 4.01$ )
Axial Elastic	4.12	4.13
Axial and Torsional Elastic	4.25	4.26
Flexible	4.42	4.43

Table 4.6: Figures for  $\alpha$  in Chapter 4

Tether Type	Figure No. ( $T_n = 400.01$ )	Figure No. ( $T_n = 4.01$ )
Axial Elastic	-	4.11
Axial and Torsional Elastic	-	4.24
Flexible	-	4.41

Table 4.7: Figures for  $\theta$  in Chapter 4

Tether Type	Figure No. ( $T_n = 400.01$ )	Figure No. ( $T_n = 4.01$ )
Axial Elastic	4.9	4.10
Axial and Torsional Elastic	4.22	4.23
Flexible	4.39	4.40

Table 4.8: Figures for  $\gamma$  in Chapter 4

Tether Type	Figure No. ( $T_n = 400.01$ )	Figure No. ( $T_n = 4.01$ )
Axial Elastic	-	4.14
Axial and Torsional Elastic	-	4.27
Flexible	-	4.44

Table 4.9: Figures for  $L_x$  in Chapter 4

Tether Type	Figure No. ( $T_n = 400.01$ )	Figure No. ( $T_n = 4.01$ )
Axial Elastic	4.15	-
Axial and Torsional Elastic	4.28	-
Flexible	4.45	-

Table 4.10: Figures for  $\gamma_x$  in Chapter 4

Tether Type	Figure No. ( $T_n = 400.01$ )	Figure No. ( $T_n = 4.01$ )
Axial Elastic	-	-
Axial and Torsional Elastic	4.30	-
Flexible	4.47	-

400.01 and 4.01; the spin-up response for the flexible massless tether is slightly different from the other MMET tether systems with more ups and downs during full simulation time, which caused by the pendular behaviours and coupled with tether system's others motions.

Table 4.5 is for the R, which is the tether's position generalised coordinate and determines

Table 4.11: Figures for  $\psi_x$  in Chapter 4

Tether Type	Figure No. ( $T_n = 400.01$ )	Figure No. ( $T_n = 4.01$ )
Axial Elastic	-	-
Axial and Torsional Elastic	-	-
Flexible	-	4.48

Table 4.12: Figures for  $\alpha_x$  in Chapter 4

Tether Type	Figure No. ( $T_n = 400.01$ )	Figure No. ( $T_n = 4.01$ )
Axial Elastic	-	-
Axial and Torsional Elastic	-	-
Flexible	-	4.49

the distance from the Earth E to the dumbbell MMET system's COM. In this case, given  $e = 0.2$ ,  $r_p = 6.89 \times 10^6$  m and  $r_a = 1.0335 \times 10^7$  m, it goes within the range of  $r_p$  to  $r_a$ .

Table 4.6 is for the out-of-plane angle  $\alpha$  with zero initial conditions; all the figures stay at zero, which indicates the stable response for  $\alpha$  over simulation the number of cycles of period  $T_n = 400.01$ .

Table 4.7 is for the true anomaly  $\theta$ , which is in a linear up-changing trend from 0 to 2500 rad coupling range of 0 to 0.5 rad fluctuation spread, over the number of cycles of period  $T_n = 400.01$ , which state that the tether systems go around the Earth in an elliptical orbit.

Table 4.8 is for the rigid rolling angle  $\gamma$ , which keep staying in zeros output with zero initial conditions  $\gamma(0) = 0$  rad and  $\dot{\gamma}(0) = 0$  rad/s.

Table 4.9 is for the axial elastic generalised coordinate along tether subspan with stable axial oscillation during full simulation time.

Table 4.10 is for the torsional elastic generalised coordinate  $\gamma_x$ , which are shown the stable torsional elastic behaviours for massless MMET systems

Table 4.11 is for the pendular elastic generalised coordinate  $\psi_x$  referenced on plane  $x_0 - O - y_0$ . Table 4.12 is for the pendular elastic generalised coordinate  $\alpha_x$  referenced on plane  $z_0 - O - y_0$ , both of them are with convergent pendular elastic behaviours, which are observed with reducing amplitude of oscillation and approaching to zero.

## Chapter 5

---

# Discretised Axially MMET Elastic System

---

### 5.1 Introduction

This chapter presents a discretised MMET system with axial elasticity, based on the rigid MMET system in section 3.6, in which the discrete mass points are connected by elastic elements.

All the environmental conditions, the Earth centred global coordinate system  $\{X, Y, Z\}$ , and the relative rotating coordinate system  $\{x_0, y_0, z_0\}$  are the same as in previous chapters.

As it differs from the assumptions A1 to A6 in section 4.1, the assumptions for the discretised MMET modelling are listed below, as B1 to B6 :

- B1 - The tether is made of homogeneous isotropic material;
- B2 - The MMET system's dissipation function is assumed to be based on Rayleigh damping;
- B3 - The MMET is in a friction free environment;
- B4 - Every axial 'spring-damper' group is connected to another, in series;
- B5 - Every torsional 'spring-damper' group is connected to another, in series;
- B6 - The axial, torsional and pendular elastic oscillations' effects on the rigid body behaviours can be ignored, for the elastic oscillations are much less than the Cartesian coordinates for the mass payloads and the discrete mass points;

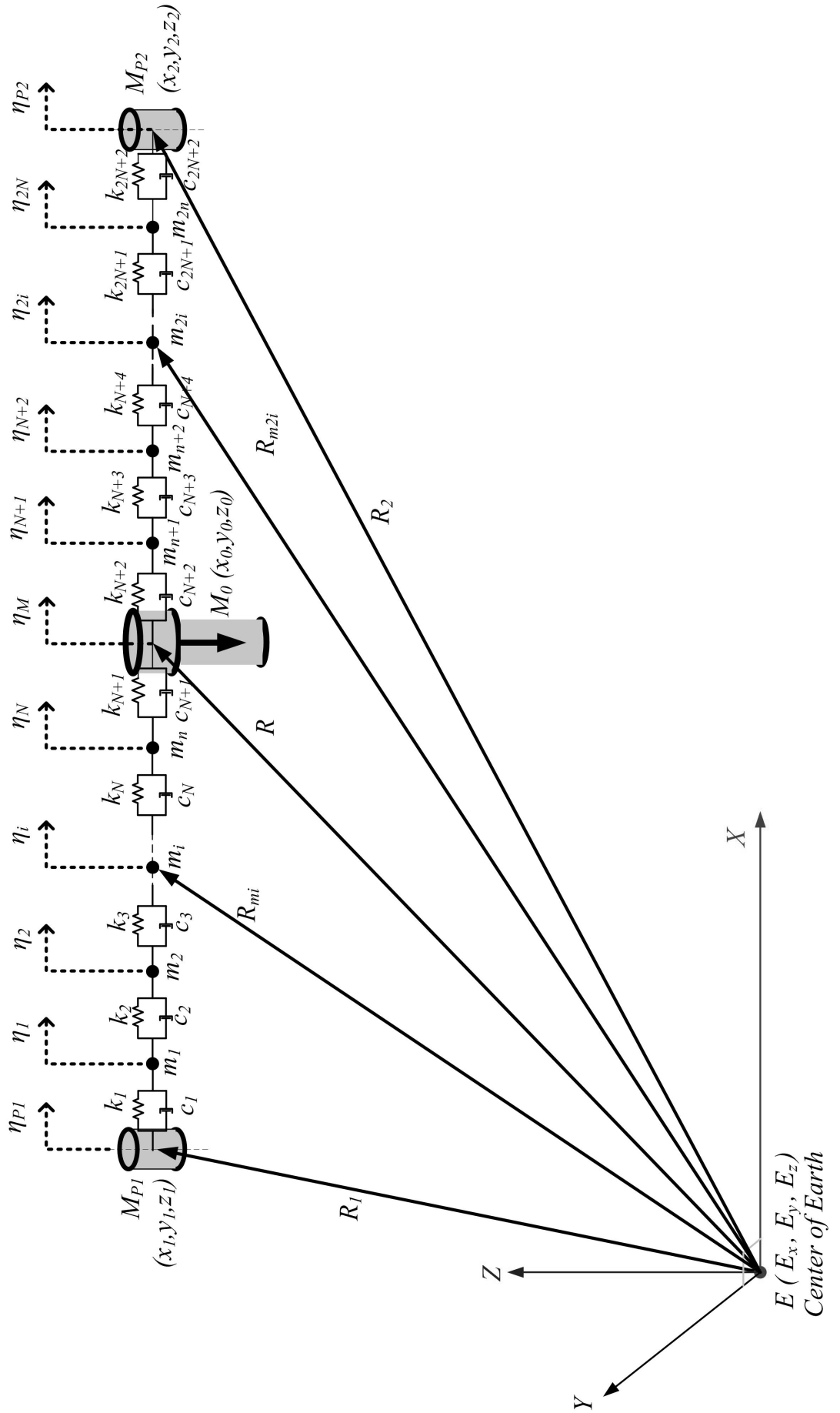


Figure 5.1: Axial elastic MMET tether with 10 discrete mass points

- B7 - The axial and torsional ‘spring-damper’ groups have no masses and mass moments of inertia;

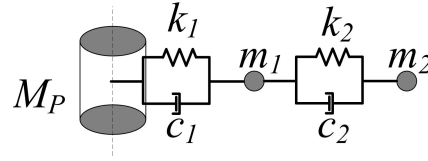


Figure 5.2: The spring-damper groups

As shown in Figure 5.2, axial elasticity is represented by a string of ‘spring-damper’ groups  $(k_i, c_i)$ , which connect the mass points of  $m_i$  in series with  $k_1 = \dots = k_{N+2}$ ,  $c_1 = \dots = c_{N+2}$ , where  $i = 1, 2, \dots, N + 2$ .

As discussed in section (3.6.2), the MMET system’s subspans can be discretised into  $N$  point masses. In this case, the MMET system with an arbitrary choice of  $N = 10$  mass points will be discussed in this chapter. Because it is different from the massless MMET system. From this chapter on the dynamical model for the discretised MMET system includes the tether masses and mass moments of inertia, by using Lagrange’s equations.

An axial elastic MMET system is shown in Figure 5.1 with 10 discrete mass points. That is, there are 5 discrete mass points for each tether subspan, in which the generalised coordinates  $\eta_i$  ( $i = 1$  to 10) define relative axial motions of the 10 discrete mass points,  $\eta_{P1}$  and  $\eta_{P2}$  are the generalised relative axial coordinates for the mass payloads  $M_{P1}$  and  $M_{P2}$ . The positive direction for axial elastic motion is defined as being in the direction from  $M_{P1}$  to  $M_{P2}$ .

## 5.2 The Cartesian Coordinates for the Motor Facility and the Payloads

The Cartesian coordinates for the motor facility  $M_0(x_0, y_0, z_0)$  are given in equation (3.2.4). The Cartesian coordinates for the payloads  $M_{P1}$  and  $M_{P2}$  are given in equations (5.2.1) and (5.2.2).  $L_0$  is the static length from COM of the tether to each payload.

$$\begin{cases} x_1 = x_0 + (\eta_{P1} + \eta_1 + \eta_2 + \eta_3 + \eta_4 + \eta_5 + L_0) \cos \alpha \cos (\theta + \psi) \\ y_1 = y_0 + (\eta_{P1} + \eta_1 + \eta_2 + \eta_3 + \eta_4 + \eta_5 + L_0) \cos \alpha \sin (\theta + \psi) \\ z_1 = (\eta_{P1} + \eta_1 + \eta_2 + \eta_3 + \eta_4 + \eta_5 + L_0) \sin \alpha \end{cases} \quad (5.2.1)$$

$$\begin{cases} x_2 = x_0 - (\eta_6 + \eta_7 + \eta_8 + \eta_9 + \eta_{10} + \eta_{p2} + L_0) \cos \alpha \cos (\theta + \psi) \\ y_2 = y_0 - (\eta_6 + \eta_7 + \eta_8 + \eta_9 + \eta_{10} + \eta_{p2} + L_0) \cos \alpha \sin (\theta + \psi) \\ z_2 = -(\eta_6 + \eta_7 + \eta_8 + \eta_9 + \eta_{10} + \eta_{p2} + L_0) \sin \alpha \end{cases} \quad (5.2.2)$$

### 5.3 The Cartesian Components for the Mass Points $m_1$ to $m_{10}$

The Cartesian components for the discrete mass points  $m_1$  to  $m_{10}$  are given in equations (5.3.1) to (5.3.10). The static length from the tether COM to each mass point  $m_i$  is defined in equation (3.6.7), and for the case of discrete mass points  $N = 10$ , the  $l_i$  ( $i=1, \dots, 10$ ) can be looked-up and transformed from Figure 3.44.

$$\begin{cases} x_{m_1} = x_0 + \left( \eta_1 + \eta_2 + \eta_3 + \eta_4 + \eta_5 + \frac{9L_0}{10} \right) \cos \alpha \cos (\theta + \psi) \\ y_{m_1} = y_0 + \left( \eta_1 + \eta_2 + \eta_3 + \eta_4 + \eta_5 + \frac{9L_0}{10} \right) \cos \alpha \sin (\theta + \psi) \\ z_{m_1} = \left( \eta_1 + \eta_2 + \eta_3 + \eta_4 + \eta_5 + \frac{9L_0}{10} \right) \sin \alpha \end{cases} \quad (5.3.1)$$

$$\begin{cases} x_{m_2} = x_0 + \left( \eta_2 + \eta_3 + \eta_4 + \eta_5 + \frac{7L_0}{10} \right) \cos \alpha \cos (\theta + \psi) \\ y_{m_2} = y_0 + \left( \eta_2 + \eta_3 + \eta_4 + \eta_5 + \frac{7L_0}{10} \right) \cos \alpha \sin (\theta + \psi) \\ z_{m_2} = \left( \eta_2 + \eta_3 + \eta_4 + \eta_5 + \frac{7L_0}{10} \right) \sin \alpha \end{cases} \quad (5.3.2)$$

$$\begin{cases} x_{m_3} = x_0 + \left( \eta_3 + \eta_4 + \eta_5 + \frac{L_0}{2} \right) \cos \alpha \cos (\theta + \psi) \\ y_{m_3} = y_0 + \left( \eta_3 + \eta_4 + \eta_5 + \frac{L_0}{2} \right) \cos \alpha \sin (\theta + \psi) \\ z_{m_3} = \left( \eta_3 + \eta_4 + \eta_5 + \frac{L_0}{2} \right) \sin \alpha \end{cases} \quad (5.3.3)$$

$$\begin{cases} x_{m_4} = x_0 + \left( \eta_4 + \eta_5 + \frac{3L_0}{10} \right) \cos \alpha \cos (\theta + \psi) \\ y_{m_4} = y_0 + \left( \eta_4 + \eta_5 + \frac{3L_0}{10} \right) \cos \alpha \sin (\theta + \psi) \\ z_{m_4} = \left( \eta_4 + \eta_5 + \frac{3L_0}{10} \right) \sin \alpha \end{cases} \quad (5.3.4)$$

$$\begin{cases} x_{m_5} = x_0 + \left( \eta_5 + \frac{L_0}{10} \right) \cos \alpha \cos (\theta + \psi) \\ y_{m_5} = y_0 + \left( \eta_5 + \frac{L_0}{10} \right) \cos \alpha \sin (\theta + \psi) \\ z_{m_5} = \left( \eta_5 + \frac{L_0}{10} \right) \sin \alpha \end{cases} \quad (5.3.5)$$

$$\begin{cases} x_{m_6} = x_0 - \left( \eta_6 + \frac{L_0}{10} \right) \cos \alpha \cos (\theta + \psi) \\ y_{m_6} = y_0 - \left( \eta_6 + \frac{L_0}{10} \right) \cos \alpha \sin (\theta + \psi) \\ z_{m_6} = - \left( \eta_6 + \frac{L_0}{10} \right) \sin \alpha \end{cases} \quad (5.3.6)$$

$$\begin{cases} x_{m_7} = x_0 - \left( \eta_6 + \eta_7 + \frac{3L_0}{10} \right) \cos \alpha \cos (\theta + \psi) \\ y_{m_7} = y_0 - \left( \eta_6 + \eta_7 + \frac{3L_0}{10} \right) \cos \alpha \sin (\theta + \psi) \\ z_{m_7} = - \left( \eta_6 + \eta_7 + \frac{3L_0}{10} \right) \sin \alpha \end{cases} \quad (5.3.7)$$

$$\begin{cases} x_{m_8} = x_0 - \left( \eta_6 + \eta_7 + \eta_8 + \frac{L_0}{2} \right) \cos \alpha \cos (\theta + \psi) \\ y_{m_8} = y_0 - \left( \eta_6 + \eta_7 + \eta_8 + \frac{L_0}{2} \right) \cos \alpha \sin (\theta + \psi) \\ z_{m_8} = - \left( \eta_6 + \eta_7 + \eta_8 + \frac{L_0}{2} \right) \sin \alpha \end{cases} \quad (5.3.8)$$

$$\begin{cases} x_{m_9} = x_0 - \left( \eta_6 + \eta_7 + \eta_8 + \eta_9 + \frac{7L_0}{10} \right) \cos \alpha \cos (\theta + \psi) \\ y_{m_9} = y_0 - \left( \eta_6 + \eta_7 + \eta_8 + \eta_9 + \frac{7L_0}{10} \right) \cos \alpha \sin (\theta + \psi) \\ z_{m_9} = - \left( \eta_6 + \eta_7 + \eta_8 + \eta_9 + \frac{7L_0}{10} \right) \sin \alpha \end{cases} \quad (5.3.9)$$

$$\begin{cases} x_{m_{10}} = x_0 - \left( \eta_6 + \eta_7 + \eta_8 + \eta_9 + \eta_{10} + \frac{9L_0}{10} \right) \cos \alpha \cos (\theta + \psi) \\ y_{m_{10}} = y_0 - \left( \eta_6 + \eta_7 + \eta_8 + \eta_9 + \eta_{10} + \frac{9L_0}{10} \right) \cos \alpha \sin (\theta + \psi) \\ z_{m_{10}} = - \left( \eta_6 + \eta_7 + \eta_8 + \eta_9 + \eta_{10} + \frac{9L_0}{10} \right) \sin \alpha \end{cases} \quad (5.3.10)$$

Similar to the equations (3.2.2) and (3.2.3), the distance from Earth  $E(0,0,0)$  to each of the discrete mass points along each sub-span is represented by  $R_{m_i}$ , as given in equation (5.3.11).

$$R_{m_i} = \sqrt{x_{m_i}^2 + y_{m_i}^2 + z_{m_i}^2} \quad (5.3.11)$$

## 5.4 Potential Energy

The tether's potential energy is given in equation (5.4.1), where  $\mu$  is the product of the universal gravitational constant  $G$  with the Earth's mass.

$$U = -\frac{\mu M_{P1}}{R_1} - \frac{\mu M_{P2}}{R_2} - \frac{\mu M_0}{R} - \frac{\mu m_1}{R_{m_1}} - \frac{\mu m_2}{R_{m_2}} - \dots - \frac{\mu m_{10}}{R_{m_{10}}} \quad (5.4.1)$$

$$+ SE|_{axial}$$

Where, the  $SE|_{axial}$  term is the strain energy of the two tether subspans taking axial elasticity into account, as stated in equation (5.4.2). If it is assumed that  $k_0 = k_1 = \dots = k_{12}$ , and the  $k_0$  is a default stiffness value, then equation (5.4.2) can be re-written as equation (5.4.3).

$$SE|_{axial} = \frac{1}{2}k_1(\eta_{P1} - \eta_1)^2 + \frac{1}{2}k_2(\eta_1 - \eta_2)^2 + \dots + \frac{1}{2}k_6\eta_5^2 \quad (5.4.2)$$

$$+ \frac{1}{2}k_7\eta_6^2 + \dots + \frac{1}{2}k_{12}(\eta_{10} - \eta_{P2})^2$$

$$SE|_{axial} = \frac{1}{2}k_0 ((\eta_{P1} - \eta_1)^2 + (\eta_1 - \eta_2)^2 + \dots + \eta_5^2 + \eta_6^2 + \dots + (\eta_{10} - \eta_{P2})^2) \quad (5.4.3)$$

The  $CE|_{axial}$  quantity is an assumed dissipation function, and the damping coefficient in each group's elastic element is assumed to be in the form of classical linear viscous damping, in which it assumes  $c_0 = c_1 = c_2 = \dots = c_{12}$ , where the  $c_0$  is a default damping coefficient value, so then equation (5.4.4) can be reformed as equation (5.4.5).

$$CE|_{axial} = \frac{1}{2}c_1(\dot{\eta}_{P1} - \dot{\eta}_1)^2 + \frac{1}{2}c_2(\dot{\eta}_1 - \dot{\eta}_2)^2 + \dots + \frac{1}{2}c_6\dot{\eta}_5^2 + \quad (5.4.4)$$

$$\frac{1}{2}c_7\dot{\eta}_6^2 + \dots + \frac{1}{2}c_{12}(\dot{\eta}_{10} - \dot{\eta}_{P2})^2$$

$$CE|_{axial} = \frac{1}{2}c_0 ((\dot{\eta}_{P1} - \dot{\eta}_1)^2 + (\dot{\eta}_1 - \dot{\eta}_2)^2 + \dots + \dot{\eta}_5^2 \dot{\eta}_6^2 \dots + (\dot{\eta}_{10} - \dot{\eta}_{P2})^2) \quad (5.4.5)$$

## 5.5 Kinetic Energy

The kinetic energy of the MMET system is given in equation (5.5.1).

$$\begin{aligned}
T = & \frac{1}{2}M_{P1} (\dot{x}_1^2 + \dot{y}_1^2 + \dot{z}_1^2) + \frac{1}{2}M_{P2} (\dot{x}_2^2 + \dot{y}_2^2 + \dot{z}_2^2) + \frac{1}{2}M_0 (\dot{x}_0^2 + \dot{y}_0^2 + \dot{z}_0^2) + \\
& \left[ \frac{1}{2}m_1 (\dot{x}_{m_1}^2 + \dot{y}_{m_1}^2 + \dot{z}_{m_1}^2) + \frac{1}{2}m_2 (\dot{x}_{m_2}^2 + \dot{y}_{m_2}^2 + \dot{z}_{m_2}^2) + \dots \right] + \\
& \left[ \frac{1}{2}m_{10} (\dot{x}_{m_{10}}^2 + \dot{y}_{m_{10}}^2 + \dot{z}_{m_{10}}^2) \right] + \\
& \left[ \frac{1}{2}I_{z_{P1}} + \frac{1}{2}I_{z_{P2}} + I_{z_T} + \frac{1}{2}I_{z_M} \right] (\dot{\psi} + \dot{\theta})^2 + \\
& \left[ \frac{1}{2}I_{x_{P1}} + \frac{1}{2}I_{x_{P2}} + I_{x_T} + \frac{1}{2}I_{x_M} \right] \dot{\alpha}^2 + \\
& \left[ \frac{1}{2}I_{y_{P1}} + \frac{1}{2}I_{y_{P2}} + I_{y_T} + \frac{1}{2}I_{y_M} \right] \dot{\gamma}^2
\end{aligned} \tag{5.5.1}$$

## 5.6 Generalised Coordinates

[1] As shown in Figure 5.3,  $\psi$  is the generalised coordinate representing the in-plane pitch angle of the overall tether, and this denotes the angle from the  $x_0$  axis to the projection of the tether axis onto the orbit plane.

[2]  $\theta$  is the generalised coordinate representing the orbital angular position, and is the true anomaly, a formal orbital element.

[3]  $\alpha$  is the generalised coordinate denoting the out-of-plane angle of the overall tether, from the projection of the tether axis onto the orbit plane to the tether, and is assumed always to be within a plane normal to the orbit plane.

[4]  $\gamma$  is the generalised coordinate depicting the rolling angle of the overall tether. It does not alter the location of the end masses' centre of mass, and needs to be included because the torque axis is potentially free to rotate about the longitudinal axis of the tether.

[5] The generalised coordinate  $R$  is the distance from the Earth  $E(0, 0, 0)$  to the COM  $M_M(x_0, y_0, z_0)$ .

[6] The generalised coordinate  $\eta_i$  is for each mass point  $m_i$ . For this case, the mass point number is arbitrarily set here to 10, that is,  $m_i$  ( $i = 1, 2, \dots, 10$ ), and  $\eta_{P1}$  and  $\eta_{P2}$  are the generalised coordinates for the  $M_{P1}$  and  $M_{P2}$ , which are listed in Table (5.1).

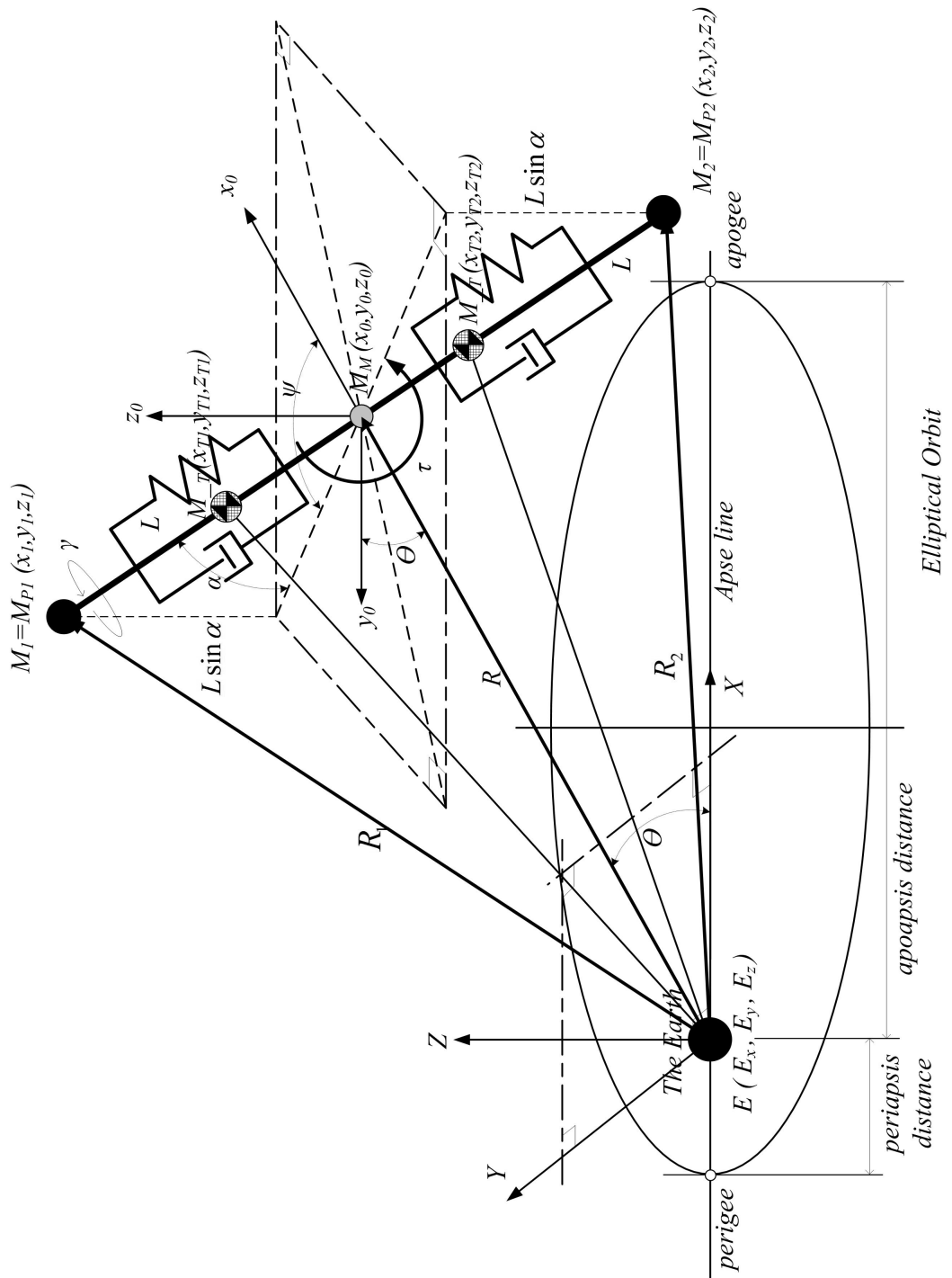


Figure 5.3: The MMET system with axial elasticity definition on orbit

## 5.7 Generalised Forces

The generalised forces  $Q_i$  ( $i = 1$  to  $5$ ) are given in equations (3.5.13) to (3.5.17), and  $Q_{m_i}$  ( $i = 6$  to  $17$ ) are the generalised forces for the mass point  $m_i$ , as listed in Table (5.1), which comes from an assumed dissipation function based on Rayleigh damping.

## 5.8 Governing Equations of Motion

Lagrange's equations are used to generate the governing equations of motion, the full equations are to be found in the path CD-ROM/axial/N10/, as listed in Table 5.1.

Table 5.1: Generalised coordinates and equations of motion (*CD-ROM/axial/N10/*)

$i$	$q_i$	$Q_i$	$T$	$U$	Equations of Motion
1	$\psi$	(3.5.13)	(5.5.1)	(5.4.1)	Chapter5-1-N10-psi.pdf
2	$\theta$	(3.5.14)			Chapter5-2-N10-theta.pdf
3	$\alpha$	(3.5.15)			Chapter5-3-N10-alpha.pdf
4	$\gamma$	(3.5.17)			Chapter5-4-N10-gamma.pdf
5	$R$	(3.5.16)			Chapter5-5-N10-R.pdf
6	$\eta_{P1}$	$-c_0(\dot{\eta}_{P1} - \dot{\eta}_1)$			Chapter5-6-N10-etaP1.pdf
7	$\eta_{P2}$	$-c_0(\dot{\eta}_{10} - \dot{\eta}_{P2})$			Chapter5-7-N10-etaP2.pdf
8	$\eta_1$	$c_0(\dot{\eta}_{P1} - \dot{\eta}_1) - c_0(\dot{\eta}_1 - \dot{\eta}_2)$			Chapter5-8-N10-eta1.pdf
9	$\eta_2$	$c_0(\dot{\eta}_1 - \dot{\eta}_2) - c_0(\dot{\eta}_2 - \dot{\eta}_3)$			Chapter5-9-N10-eta2.pdf
10	$\eta_3$	$c_0(\dot{\eta}_2 - \dot{\eta}_3) - c_0(\dot{\eta}_3 - \dot{\eta}_4)$			Chapter5-10-N10-eta3.pdf
11	$\eta_4$	$c_0(\dot{\eta}_3 - \dot{\eta}_4) - c_0(\dot{\eta}_4 - \dot{\eta}_5)$			Chapter5-11-N10-eta4.pdf
12	$\eta_5$	$c_0(\dot{\eta}_4 - \dot{\eta}_5) - c_0\dot{\eta}_5$			Chapter5-12-N10-eta5.pdf
13	$\eta_6$	$c_0(\dot{\eta}_7 - \dot{\eta}_6) - c_0\dot{\eta}_6$			Chapter5-13-N10-eta6.pdf
14	$\eta_7$	$c_0(\dot{\eta}_6 - \dot{\eta}_7) - c_0(\dot{\eta}_7 - \dot{\eta}_8)$			Chapter5-14-N10-eta7.pdf
15	$\eta_8$	$c_0(\dot{\eta}_7 - \dot{\eta}_8) - c_0(\dot{\eta}_8 - \dot{\eta}_9)$			Chapter5-15-N10-eta8.pdf
16	$\eta_9$	$c_0(\dot{\eta}_8 - \dot{\eta}_9) - c_0(\dot{\eta}_9 - \dot{\eta}_{10})$			Chapter5-16-N10-eta9.pdf
17	$\eta_{10}$	$c_0(\dot{\eta}_9 - \dot{\eta}_{10}) - c_0(\dot{\eta}_{10} - \dot{\eta}_{P2})$			Chapter5-17-N10-eta10.pdf

As shown in Table 5.1, there are 17 nonlinear equations for 17 generalised coordinates with a strong nonlinear coupling, which are listed in the files with hundreds of lines of ODE and lead to the high computationally difficult set of ODEs.

The solution procedure is implemented in code written by the author in MATHEMATICA using the routine NDSolve, the NDSolve function can adapt its step size so that the estimated error in the solution is just within the tolerances.

Practically, it is difficult for the NDSolve to solve the MMET system of coupled differential equations as long as each variable has the appropriate number of conditions by the following simulation trials, in which the number of cycles of period  $T_n$ , as defined in equation (1.1.11), is a concise alternative to determine the simulation time.

(1) The first trial's simulation time is  $T_n = 4.01$  ( $3.1899 \times 10^4$  seconds), and an 'out of memory' error message occurs with the time consumption of about 24 hours, and the NDSolve procedure is terminated automatically without any numerical outputs.

(2) With the  $T_n = 4.01 \times 10^{-4}$  (3.1899 seconds); there is also an 'out of memory' error message occurs with the time consumption of about 24 hours, and the NDSolve procedure can not generate any numerical outputs, either.

To summarise, in the first trial and second trial test the MMET system simulations were in a long ( $3.1899 \times 10^4$  seconds) and short (3.1899 seconds) simulation time respectively, and the 'out of memory' error shows that the ODE equations for the MMET system are too complex for the current computing system to handle. The 'out of memory' error occurs when the nonlinear equations of the MMET system are sent to the NDSolve procedure, which indicates that current computer cluster cannot provide enough hardware support for this MMET system simulation, and the computer is not able to load any additional data into memory during execution, and these will cease to function correctly. This occurs because all available memory including disk swap space has been fully allocated, which is caused by the high computational difficulty of the set of ODEs.

In order to deal with this problem and to explore the interaction of the axial elastic MMET system, we have reduced the discretisation scheme right down to one discrete tether mass point per subspan, that is,  $N = 2$ , and Lagrange's equations have been used to derive a reduced set of nonlinear governing equations of motion for a simplified MMET system, as shown in Appendix G, and the generalised coordinates for the simplified MMET system with two discrete mass points are given in Table 5.2. This decision is based on a compromise between modelling fidelity and likely computational tractability.

► The detail modelling steps for axial elastic MMET system with two discretised mass points is attached in Appendix G.

Table 5.2: Generalised coordinates and equations of motion (*CD-ROM/axial/N2/*)

$i$	$q_i$	$Q_i$	T	U	Equations of Motion
1	$\psi$	(3.5.13)	(G.4.1)	(G.3.1)	Chapter5-1-N2-psi.pdf
2	$\theta$	(3.5.14)			Chapter5-2-N2-theta.pdf
3	$\alpha$	(3.5.15)			Chapter5-3-N2-alpha.pdf
4	$\gamma$	(3.5.17)			Chapter5-4-N2-gamma.pdf
5	R	(3.5.16)			Chapter5-5-N2-R.pdf
6	$\eta_{P1}$	$-c_0(\dot{\eta}_{P1} - \dot{\eta}_1)$			Chapter5-6-N2-etaP1.pdf
7	$\eta_{P2}$	$-c_0(\dot{\eta}_2 - \dot{\eta}_{P2})$			Chapter5-7-N2-etaP2.pdf
8	$\eta_1$	$c_0(\dot{\eta}_{P1} - \dot{\eta}_1) - c_0\dot{\eta}_1$			Chapter5-8-N2-eta1.pdf
9	$\eta_2$	$c_0(\dot{\eta}_{P2} - \dot{\eta}_2) - c_0\dot{\eta}_2$			Chapter5-9-N2-eta2.pdf

## 5.9 Simulations and Discussions

Based on the axial elastic MMET system with two discrete mass points, Figures 5.4 to 5.17 are the numerical results obtained by MATHEMATICA for the selected generalised coordinates  $q_i$  ( $i = 1$  to 9) as listed in Table 5.2. In this case of  $e = 0.2$ , it was decided to evaluate  $T_n = 4.01$  and  $400.01$ , that is, the simulation time  $t$  is 0 to  $3.1899 \times 10^4$  seconds and 0 to  $3.1811 \times 10^6$  seconds, respectively, which can help to describe both of the micro (short simulation time) and the macro (long simulation time) behaviours for every generalised coordinate.

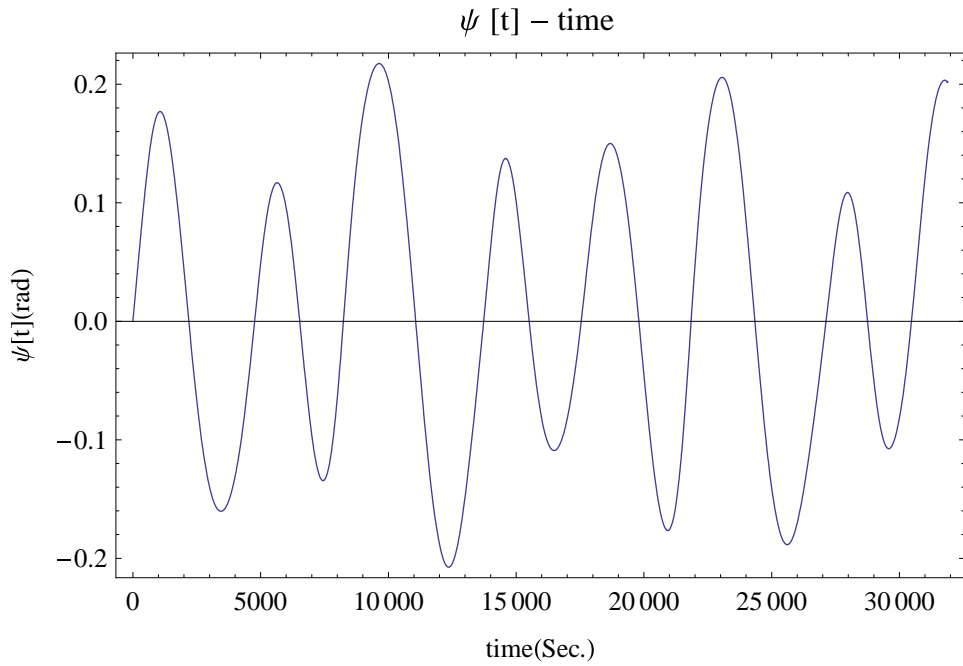


Figure 5.4: Axial elastic MMET system spin-up, angular displacement  $\psi$  ( $T_n = 4.01$ )

- ▷ The results show the discretised axial elastic MMET system's periodic behaviour on an elliptical orbit ( $e = 0.2$ ) with the angular displacement range of  $-0.35$  to  $0.35$  rad, in which Figures 5.4 and 5.5 depict the spin-up behaviour for the axial elastic MMET system over a short simulation time (NCP,  $T_n = 4.01$ ) and for a long simulation time (NCP,  $T_n = 400.01$ ), respectively.
- ▷ The distance  $R$  from the Earth to the tether COM is changing periodically, as can be seen in the Figures 5.6 and 5.7, which behave within the distance range of  $r_p$  ( $6.89 \times 10^6$  metre) to  $r_a$  ( $1.0335 \times 10^7$  metre) with given  $e = 0.2$  in this case.
- ▷ The results for the true anomaly  $\theta$  are shown in Figures 5.8 and 5.9 for the number of cycles of period  $T_n = 4.01$  and  $400.01$  simulation time, respectively. The curves are rising in a linear trend from 0 to 25 ( $T_n = 4.01$ ) or 2500 ( $T_n = 400.01$ ) rad with slight

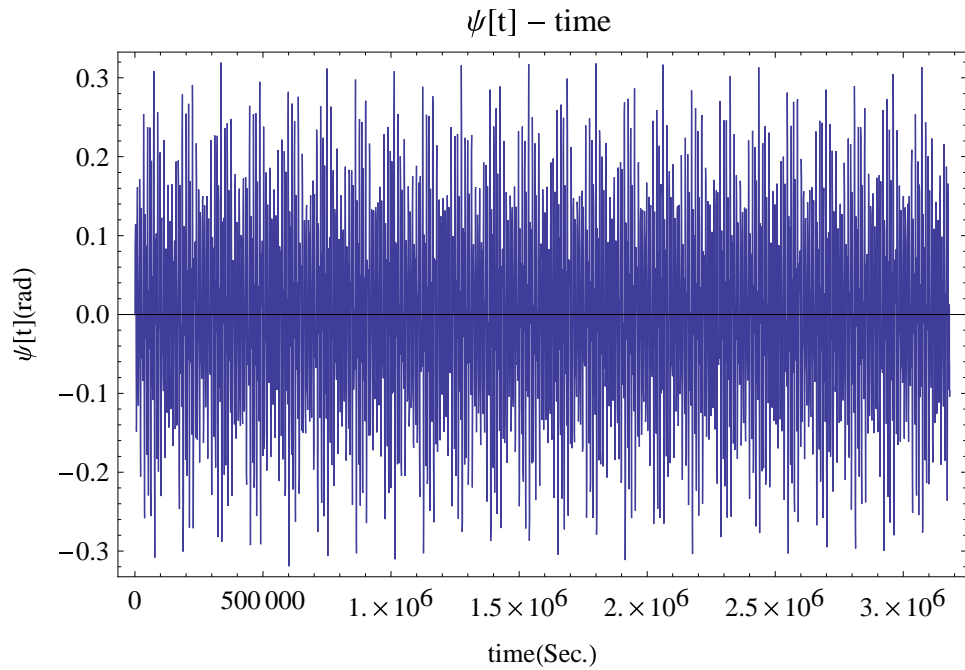


Figure 5.5: Axial elastic MMET system spin-up, angular displacement  $\psi$  ( $T_n = 400.01$ )

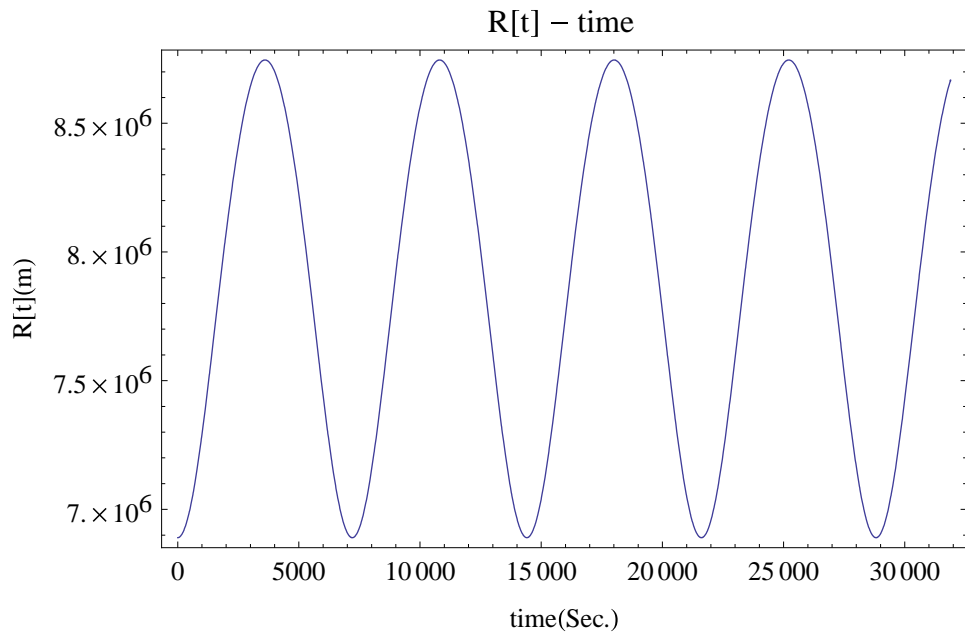


Figure 5.6: Axial elastic MMET system base point distance  $R$  ( $T_n = 4.01$ )

fluctuation spread (0 to 0.5 rad), this angular parameter describes the position of the MMET system moving along the elliptical orbit.

▷ With given non-zero initial conditions  $\alpha(0) = 0.001$  rad and  $\dot{\alpha}(0) = 0.001$  rad/s, the responses for the out-of-plane angle  $\alpha$  are given in Figures 5.10 and 5.11. This shows that, with small initial angular displacement  $\alpha(0)$  and velocity  $\dot{\alpha}(0)$  disturbances, the out-of-plane angle  $\alpha$ 's curve travels steadily within a -0.7 to 0.7 radian periodic fluctuation.

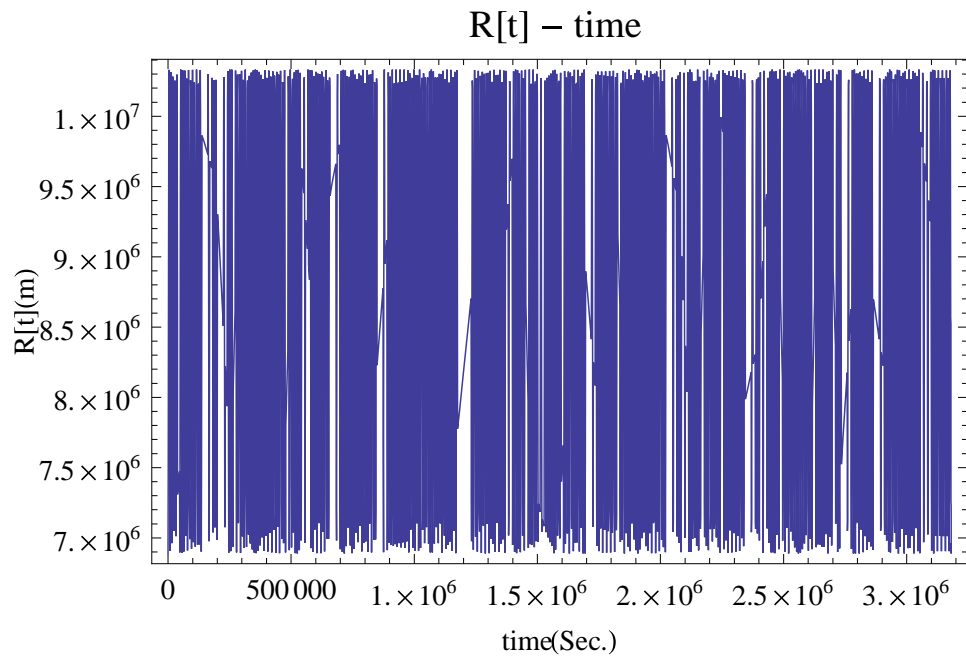


Figure 5.7: Axial elastic MMET system base point distance  $R$  ( $T_n = 400.01$ )

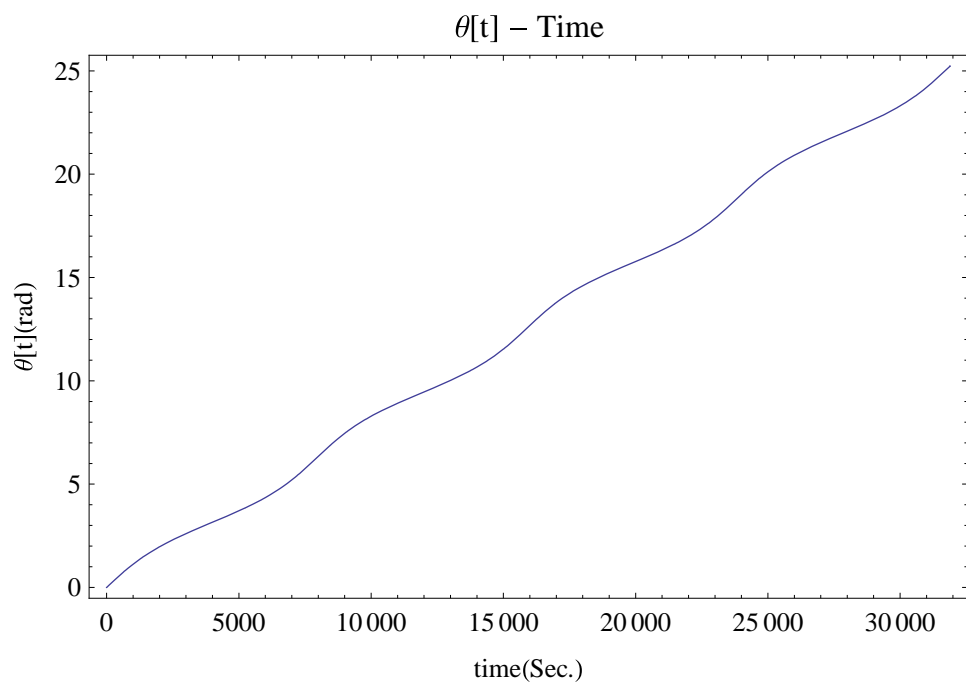


Figure 5.8: Axial elastic MMET system elliptical orbit angular position of  $\theta$  ( $T_n = 4.01$ )

In order to compare the results with different initial values, in Chapters 5, 6 and 7, all the initial values for the  $\alpha(0)$  and  $\dot{\alpha}(0)$  are set to 0.001, as given in Appendix C.

▷ During the full simulation time, the rigid rolling angle  $\gamma$  keeps in linear rising process with given non-zero initial conditions  $\gamma(0) = 0.001$  rad and  $\dot{\gamma}(0) = 0.001$  rad/s, as shown in Figure 5.12. Similar to the initial values setting for  $\alpha$ , in Chapters 5, 6 and 7, all the initial values for the  $\gamma(0)$  and  $\dot{\gamma}(0)$  are set to 0.001 rad, as given in Appendix C. The linear rising phenomenon is caused by its non-zero initial value, the rigid body

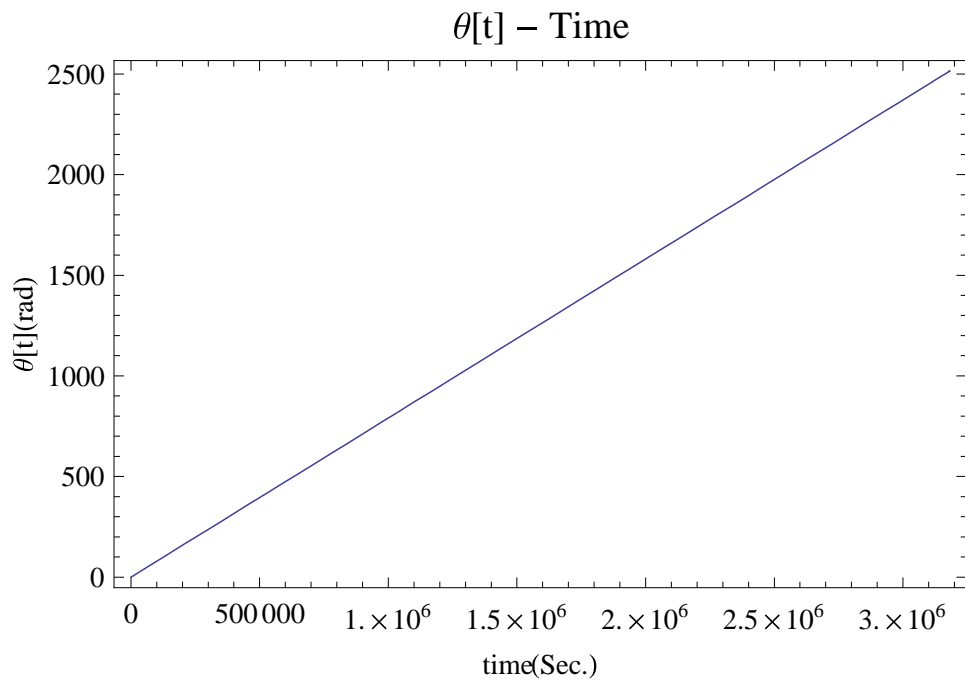


Figure 5.9: Axial elastic MMET system elliptical orbit angular position of  $\theta$  ( $T_n = 400.01$ )

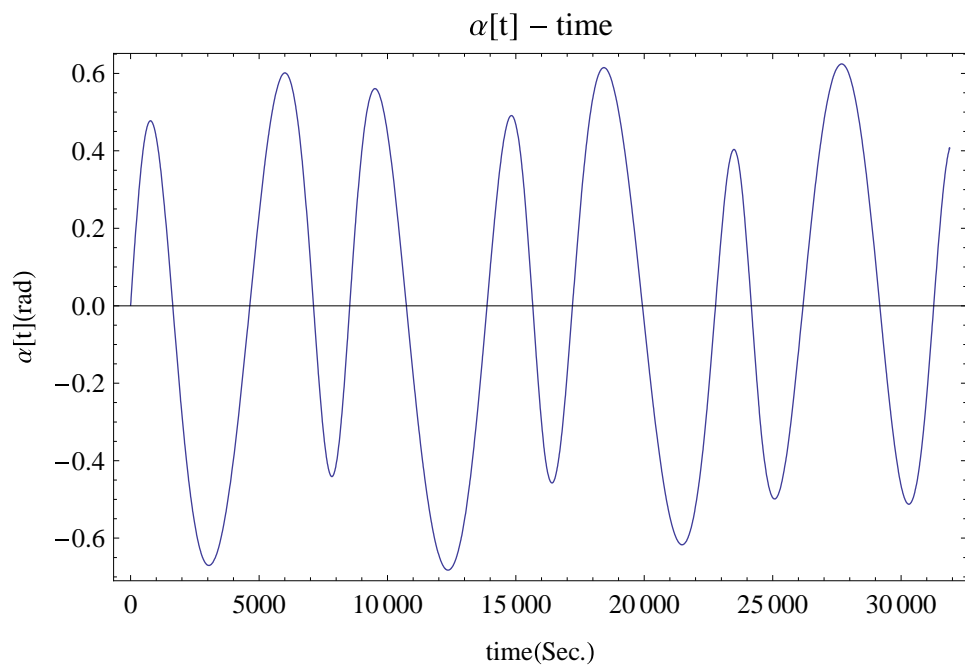


Figure 5.10: Axial elastic MMET system out-of-plane angle  $\alpha$  ( $T_n = 4.01$ )

rolling behaviour can be started or stopped by giving a proper zero or non-zero initial conditions.

▷ Figure 5.13 is a part of Figure 5.14, which shows the axial elastic motions over simulation time  $T_n = 4.01$ , as also shown in Figure 5.15. Figure 5.14 is the response for the axial elastic motions over simulation time  $T_n = 400.01$ . For the simulation time in Figure 5.13 is shorter than Figure 5.14,  $\eta_1$ 's curve in Figure 5.13 seems a monotonic decreasing line, and as can be observed in Figure 5.14, it is also an oscillating curve

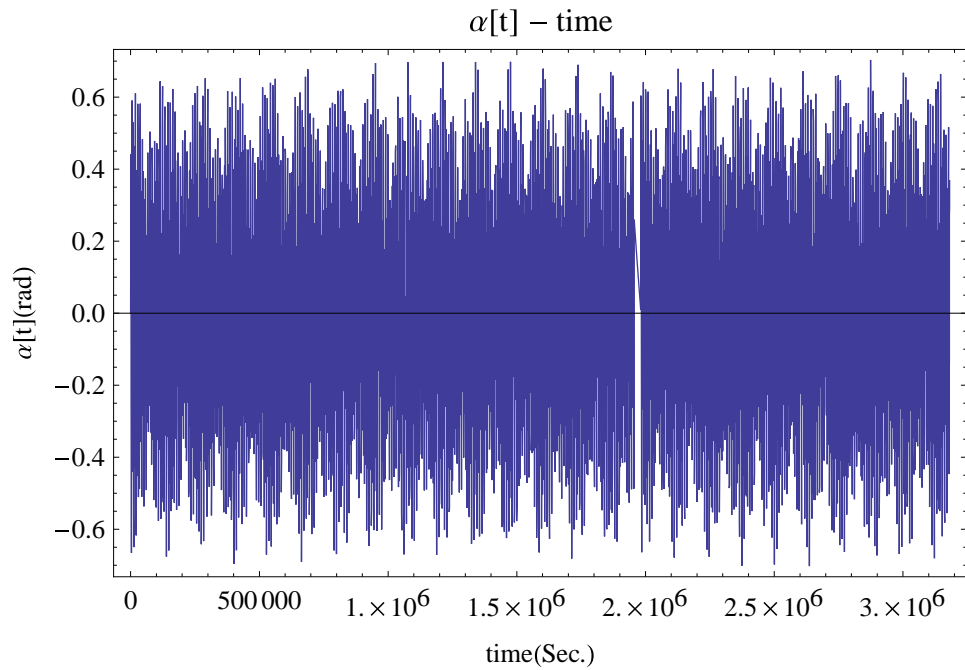


Figure 5.11: Axial elastic MMET system out-of-plane angle  $\alpha$  ( $T_n = 400.01$ )

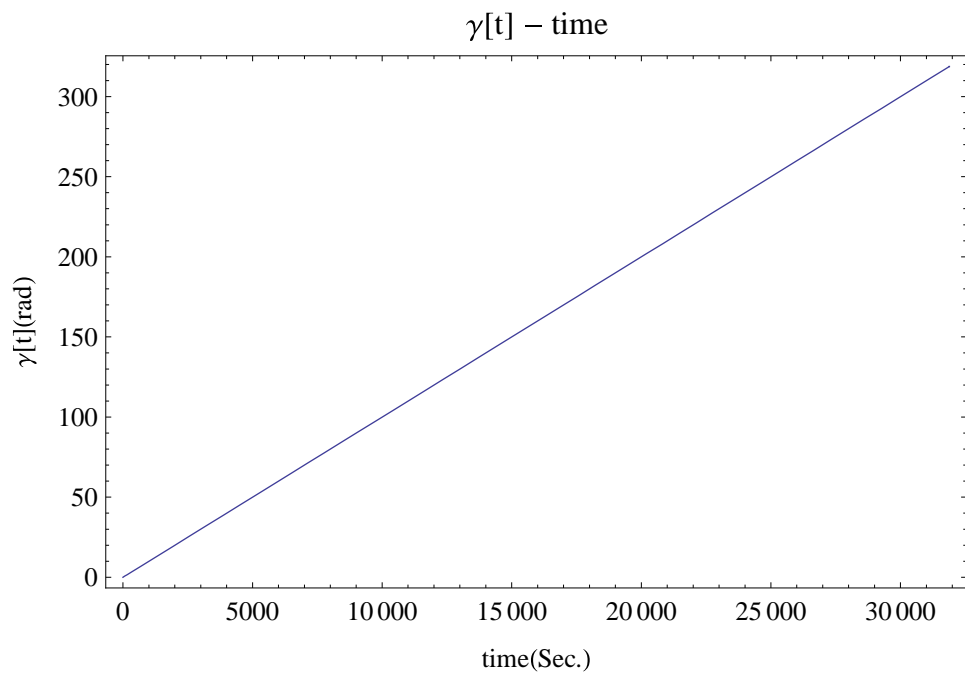


Figure 5.12: Axial elastic MMET system rolling angle  $\gamma$  ( $T_n = 4.01$ )

with larger period than  $\eta_{P1}$ 's response.

Figures 5.13 and 5.14 state the axial elastic motions for  $\eta_1$  and  $\eta_{P1}$  along tether sub-span, in which the period for  $\eta_1$  is larger than the period for  $\eta_{P1}$ , and the  $\eta_1$ 's responses go steadily within the range -3.2 to -4.6 metre and the  $\eta_{P1}$ 's responses are within the range -5 to -11 metre.

▷ Similar to  $\eta_1$  and  $\eta_{P1}$ , Figures 5.16 and 5.17 are the plots for  $\eta_2$  and  $\eta_{P2}$  over the

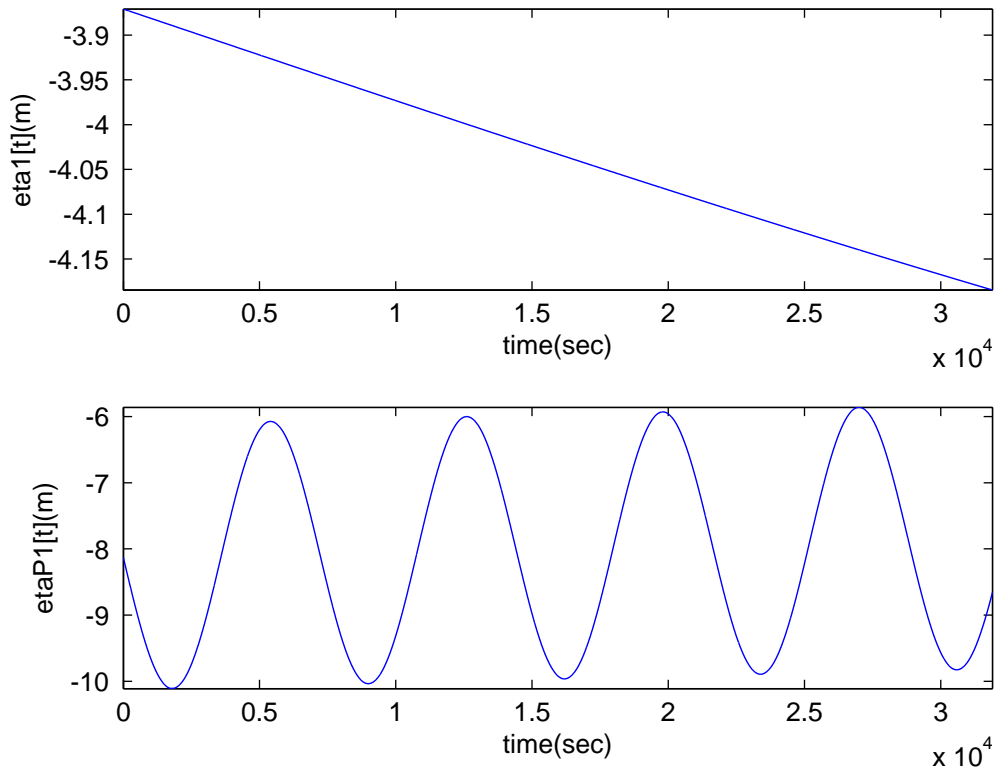


Figure 5.13: Axial displacement responses  $\eta_1$  and  $\eta_{P1}$  ( $T_n = 4.01$ )

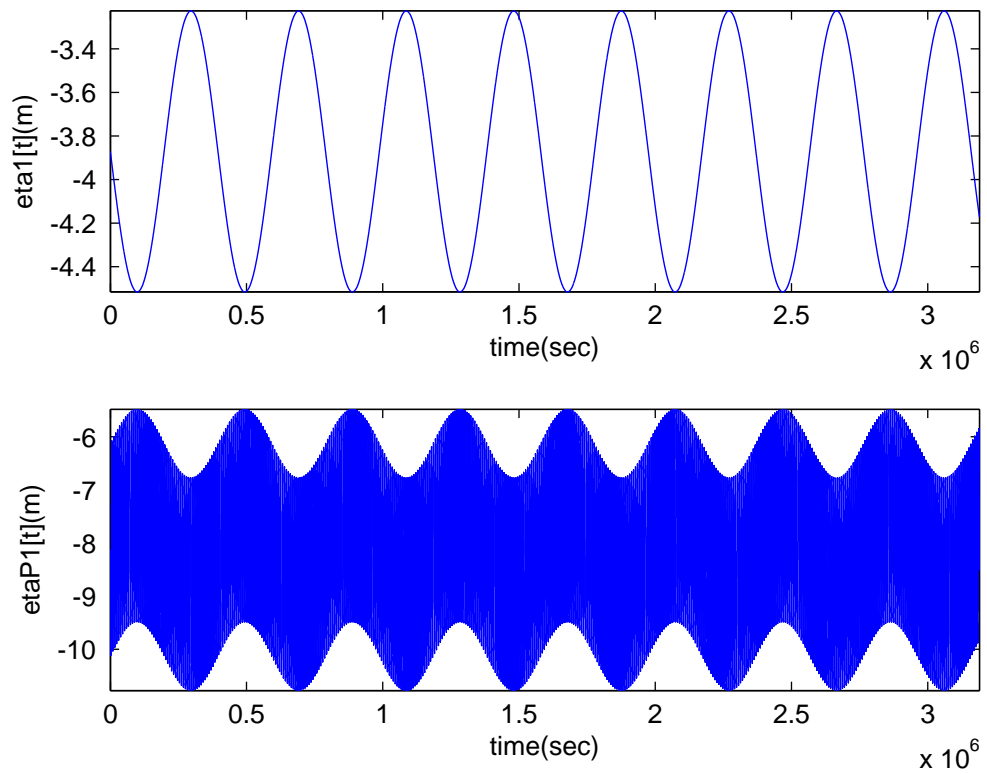


Figure 5.14: Axial displacement responses  $\eta_1$  and  $\eta_{P1}$  ( $T_n = 400.01$ )

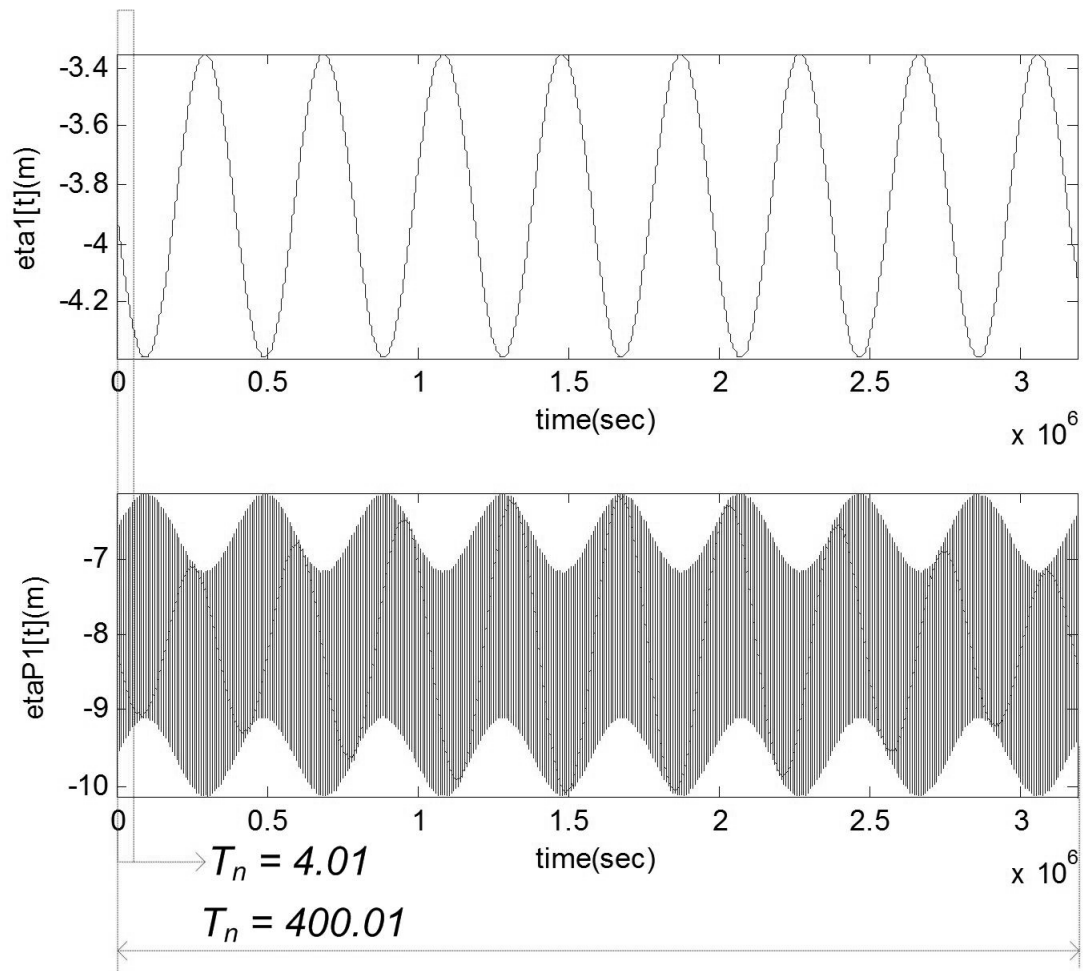


Figure 5.15: Axial displacement responses  $\eta_1$  and  $\eta_{P1}$ ,  $T_n = 4.01$  vs.  $400.01$

simulation time  $T_n = 4.01$  and  $400.01$ , as also shown in Figure 5.18, which show the  $\eta_2$  and  $\eta_{P2}$  curves moving steadily within the range 3.2 to 4.6 metre and 5 to 11 metre, and indicate the  $\eta_2$  and  $\eta_{P2}$ 's behaviours are symmetric to  $\eta_1$  and  $\eta_{P1}$ 's behaviours with respect to the MMET system COM.

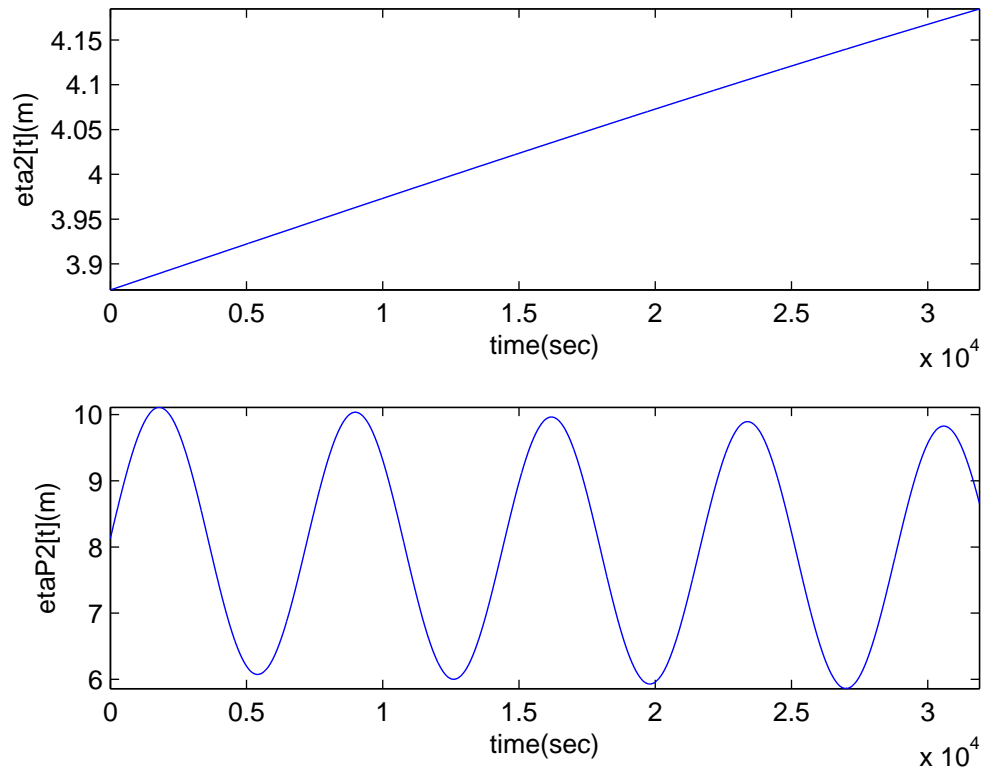


Figure 5.16: Axial displacement responses  $\eta_2$  and  $\eta_{P2}$  ( $T_n = 4.01$ )

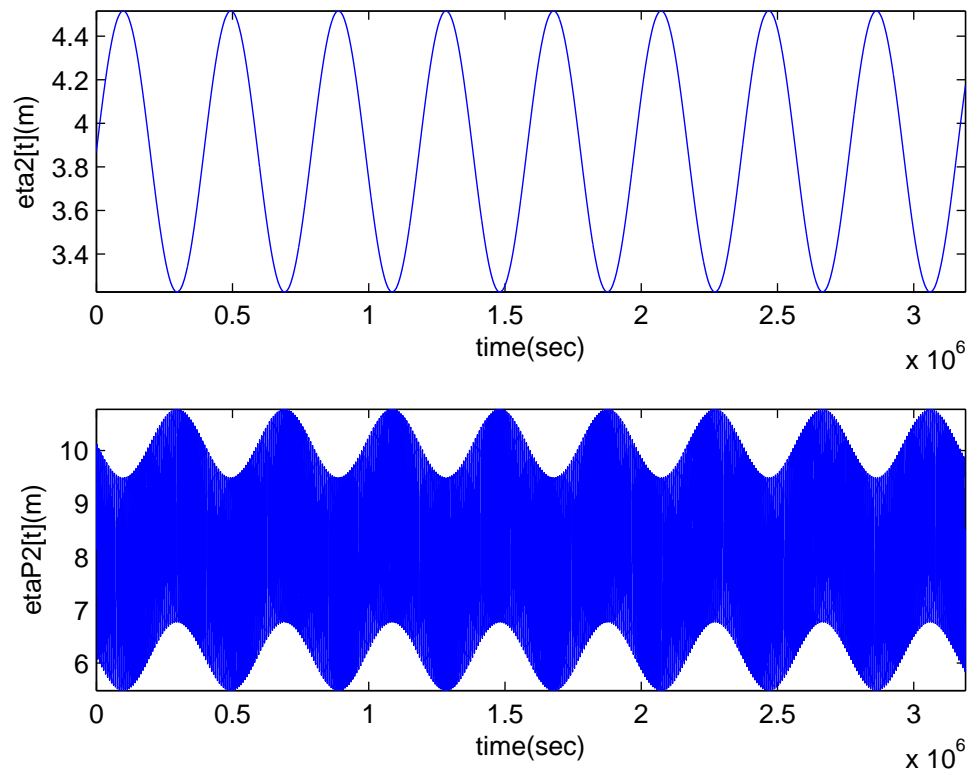


Figure 5.17: Axial displacement responses  $\eta_2$  and  $\eta_{P2}$  ( $T_n = 400.01$ )

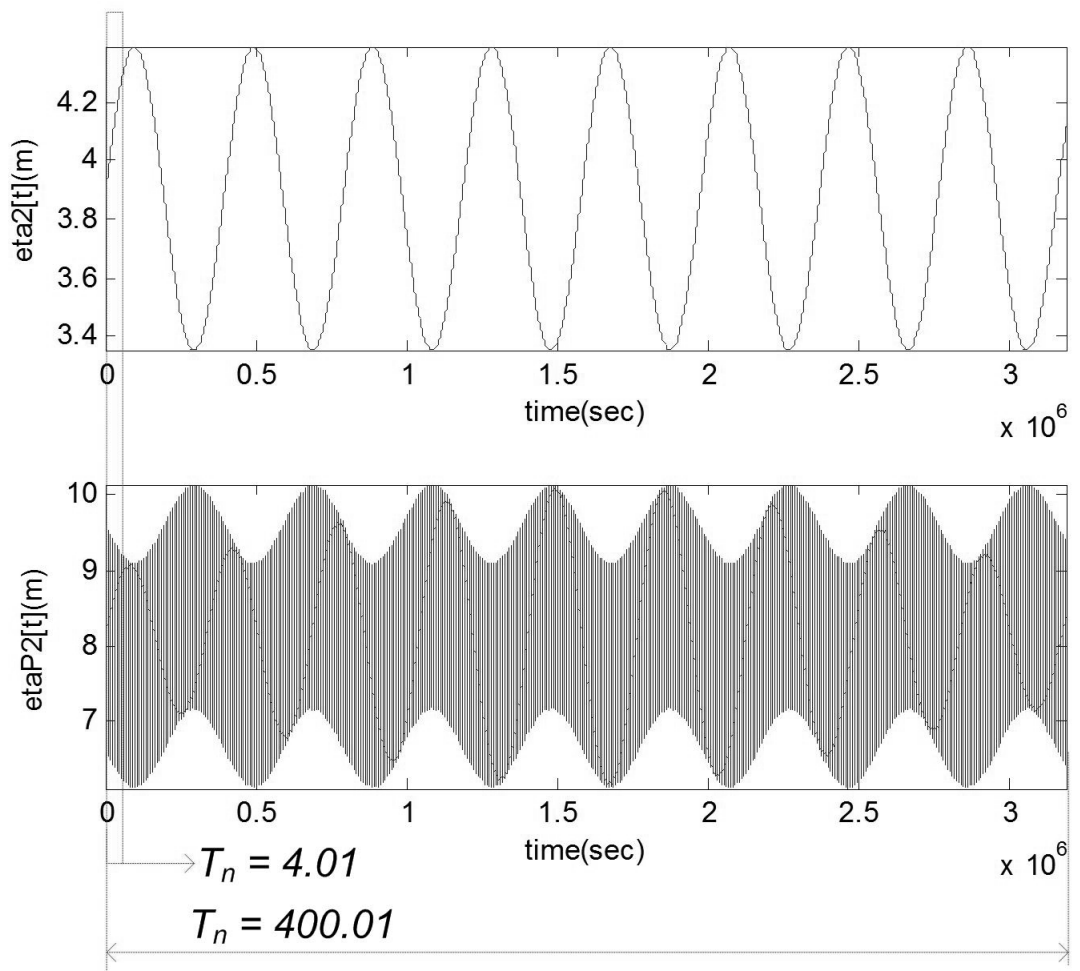


Figure 5.18: Axial displacement responses  $\eta_2$  and  $\eta_{P2}$ ,  $T_n = 4.01$  vs.  $400.01$

## 5.10 Conclusions

The work in this chapter has shown a model of a constantly excited MMET tether on an elliptical Earth orbit with multiple degrees of freedom (MDOF) for axial elastic motions, which can be reformulated into an excited axial elastic oscillation. This analysis represents the tether under the influence of a gravitational field and a directly applied exciting torque from the motor drive.

A MMET system with an arbitrary choice of  $N = 10$  mass points was discussed in this Chapter for the MDOF axial elastic MMET system, which includes the tether masses and mass moments of inertia. Then in order to handle the numerical simulation time-consuming difficulties on the current computational system, an axial elastic MMET system with  $N = 2$  mass points is proposed to reduce the number of the nonlinear ordinary differential equations (ODEs), which can balance the numerical performance and MDOF discretisation scheme for the MMET system.

Numerical results for the MMET system with two discrete mass points are given in section 5.9, in which accurate and periodic behaviour including the spin-up and the axial elastic performance for this MMET model are obtained.

Compared with the spin-up behaviours for the dumbbell MMET systems, the rigid body MMET tethers and the flexible massless MMET systems in Chapters 3 and 4, the spin-up for the discretised axial elastic MMET system are also changing with periodic fluctuations steadily, but with slightly smaller amplitudes and smoother curve shape. When involving the tether's mass and mass moment of inertia, the amplitudes and shapes for the spin-up and the axial elastic behaviours are different with same parameter settings in Appendix C.

The results of the true anomaly  $\theta$  and the distance  $R$  for the tether systems in Chapters 3, 4 and 5 are the position generalised coordinates to locate the tether system's location on the orbit, which are of stability numerical outputs with the other generalised coordinates' different initial values.

The numerical results for the out-of-plane angle  $\alpha$  and the rigid rolling angle  $\gamma$  are sensitive to their initial value settings. In Chapters 3 and 4, their initial value is zero, and their outputs are zero over full simulation time; In this Chapter, by setting to non-zero initial values, they have non-zero outputs over the same simulation time as previous Chapters.

The responses for  $\eta_1$  and  $\eta_{p1}$  are with different periodic motions for the different mass and mass moment of inertia values along each tether subspan.

The numerical results for  $\eta_1$ ,  $\eta_{p1}$ ,  $\eta_2$  and  $\eta_{p2}$  express that the axial motions in the two

tether subspans are moving in an opposite direction with same local relative direction definition, also, this difference validates that the MMET tether system is a symmetrical system with respect to the MMET system COM.

## Chapter 6

---

# Discretised MMET System involving Axial and Torsional Elasticity

---

### 6.1 Introduction

Based on the discretised axial MMET system with an arbitrary choice of  $N = 10$  mass points in Chapter 5, a discretised MMET system involving both axial and torsional elasticity is proposed in this chapter, in which the torsional elasticity modelling process will be discussed, and the axial elasticity modelling process is the same as was discussed in Chapter 5 so it will not be discussed in this chapter.

With the same modelling conditions and assumptions as declared in Chapter 5, the Cartesian coordinates for the motor facility  $M_0$  and the payloads  $M_{P1}$  and  $M_{P2}$  are given in equations (3.2.4), (5.2.1) and (5.2.2). The Cartesian components for the discrete mass points  $m_1$  to  $m_{10}$  are given in equations (5.3.1) to (5.3.10).

As shown in Figure 6.1, with 10 discrete mass points, the generalised relative torsional coordinates  $\varphi_i$  ( $i = 1$  to 10) define the relative torsional motions of the 10 discrete mass points.  $\varphi_{P1}$  and  $\varphi_{P2}$  are the generalised relative torsional coordinates for the mass payloads  $M_{P1}$  and  $M_{P2}$ . The directions for the torsional elastic motions, by following the right-hand rule with the thumb pointing to the  $-y_0$  direction, are defined as positive direction.

All the torsional ‘spring-damper’ groups ( $k_{ti}$ ,  $c_{ti}$ ) are defined on the reference plane  $x_0 - O - z_0$  as shown in Figure 6.2. The ‘t’ in the subscript designates the torsional elastic parameter, and the mass points of  $m_i$  are connected by the torsional ‘spring-damper’ groups in series.

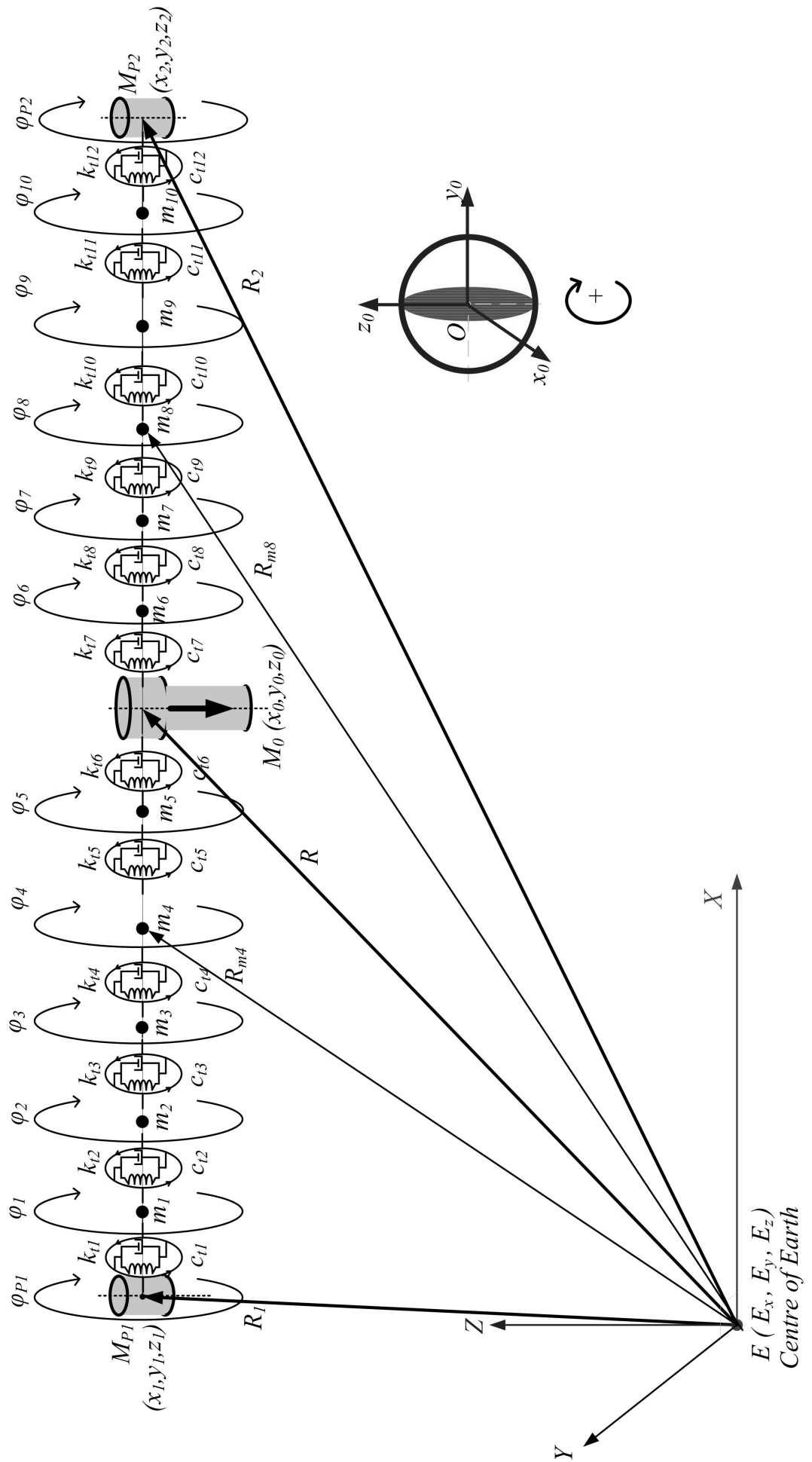


Figure 6.1: Torsional elastic MMET tether with 10 discrete mass points

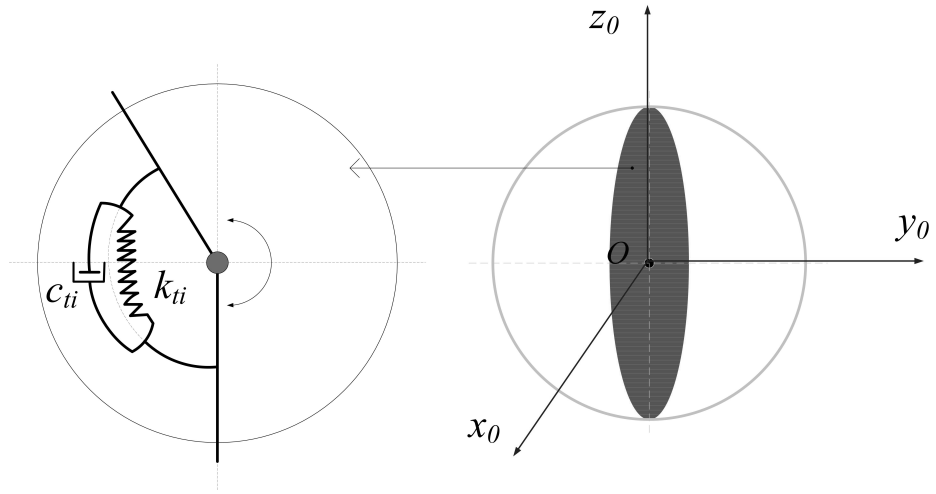


Figure 6.2: Reference on the plane  $x_0 - O - z_0$  for MMET torsional elasticity

## 6.2 Potential Energy

The tether's potential energy is given in equation (6.2.1), where  $\mu$  is the product of the universal gravitational constant  $G$  with the Earth's mass.  $R_1$ ,  $R_2$  and  $R_{m_i}$  ( $i = 1$  to 10) are same as that defined in Chapter 5.

$$\begin{aligned}
 U = & -\frac{\mu M_{P1}}{R_1} - \frac{\mu M_{P2}}{R_2} - \frac{\mu M_0}{R} - \frac{\mu m_1}{R_{m_1}} - \frac{\mu m_2}{R_{m_2}} - \dots - \frac{\mu m_{10}}{R_{m_{10}}} \\
 & + SE|_{axial} + SE|_{torsional}
 \end{aligned} \tag{6.2.1}$$

Where, the  $SE|_{axial}$  term is given in equation (5.4.2),  $SE|_{torsional}$  term is the strain energy of the two tether subspans, taking torsional elasticity into account, as stated in equation (6.2.2).

The  $CE|_{torsional}$  quantity is an assumed dissipation function, and the damping coefficient in each group's elastic element is assumed to be in the form of classical linear viscous damping.

$$\begin{aligned}
 SE|_{torsional} = & \frac{1}{2}k_{t1}(\varphi_{P1} - \varphi_1)^2 + \frac{1}{2}k_{t2}(\varphi_1 - \varphi_2)^2 + \dots + \frac{1}{2}k_{t6}\varphi_5^2 \\
 & + \frac{1}{2}k_{t7}\varphi_6^2 + \dots + \frac{1}{2}k_{t12}(\varphi_{10} - \varphi_{P2})^2
 \end{aligned} \tag{6.2.2}$$

$$\begin{aligned}
CE|_{\text{torsional}} = & \frac{1}{2}c_{t1}(\dot{\varphi}_{P1} - \dot{\varphi}_1)^2 + \frac{1}{2}c_{t2}(\dot{\varphi}_1 - \dot{\varphi}_2)^2 + \cdots + \frac{1}{2}c_{t6}\dot{\varphi}_5^2 + \\
& \frac{1}{2}c_{t7}\dot{\varphi}_6^2 + \cdots + \frac{1}{2}c_{t12}(\dot{\varphi}_{10} - \dot{\varphi}_{P2})^2
\end{aligned} \tag{6.2.3}$$

With  $k_{t0} = k_{t1} = \dots = k_{t(N+2)}$ ,  $c_{t0} = c_{t1} = \dots = c_{t(N+2)}$ , where  $i = 1, 2, \dots, N + 2$ , the  $k_{t0}$  and  $c_{t0}$  are the default stiffness and damping coefficient values,  $N = 10$  is the number of the discrete mass points in this case, then equation (6.2.2) can be re-written as equation (6.2.4), and equation (6.2.3) can be reformed as equation (6.2.5).

$$SE|_{\text{torsional}} = \frac{1}{2}k_{t0} ((\varphi_{P1} - \varphi_1)^2 + (\varphi_1 - \varphi_2)^2 + \cdots + \varphi_5^2 + \varphi_6^2 + \cdots + (\varphi_{10} - \varphi_{P2})^2) \tag{6.2.4}$$

$$CE|_{\text{torsional}} = \frac{1}{2}c_{t0} ((\dot{\varphi}_{P1} - \dot{\varphi}_1)^2 + (\dot{\varphi}_1 - \dot{\varphi}_2)^2 + \cdots + \dot{\varphi}_5^2 \dot{\varphi}_6^2 \cdots + (\dot{\varphi}_{10} - \dot{\varphi}_{P2})^2) \tag{6.2.5}$$

### 6.3 Kinetic Energy

The kinetic energy of the MMET system with  $N = 10$  mass points is given in equation (6.3.1).

$$\begin{aligned}
T = & \frac{1}{2}M_{P1} (\dot{x}_1^2 + \dot{y}_1^2 + \dot{z}_1^2) + \frac{1}{2}M_{P2} (\dot{x}_2^2 + \dot{y}_2^2 + \dot{z}_2^2) + \frac{1}{2}M_0 (\dot{x}_0^2 + \dot{y}_0^2 + \dot{z}_0^2) + \\
& \left[ \frac{1}{2}m_1 (\dot{x}_{m_1}^2 + \dot{y}_{m_1}^2 + \dot{z}_{m_1}^2) + \frac{1}{2}m_2 (\dot{x}_{m_2}^2 + \dot{y}_{m_2}^2 + \dot{z}_{m_2}^2) + \cdots \right. \\
& \quad \left. + \frac{1}{2}m_{10} (\dot{x}_{m_{10}}^2 + \dot{y}_{m_{10}}^2 + \dot{z}_{m_{10}}^2) \right] + \\
& \left[ \frac{1}{2}I_{z_{P1}} + \frac{1}{2}I_{z_{P2}} + I_{z_T} + \frac{1}{2}I_{z_M} \right] (\dot{\psi} + \dot{\theta})^2 + \\
& \left[ \frac{1}{2}I_{x_{P1}} + \frac{1}{2}I_{x_{P2}} + I_{x_T} + \frac{1}{2}I_{x_M} \right] \dot{\alpha}^2 + \left[ \frac{1}{2}I_{y_{P1}} + \frac{1}{2}I_{y_{P2}} + I_{y_T} + \frac{1}{2}I_{y_M} \right] \dot{\gamma}^2 + \\
& \left[ \frac{1}{2}I_{y_{P1}} \dot{\varphi}_{P1}^2 + \frac{1}{2}I_{y_{P2}} \dot{\varphi}_{P2}^2 + \frac{1}{2}I_{y_{m1}} \dot{\varphi}_1^2 + \cdots + \frac{1}{2}I_{y_{m10}} \dot{\varphi}_{10}^2 \right]
\end{aligned} \tag{6.3.1}$$

## 6.4 Generalised Coordinates

Besides the generalised coordinates  $q_1$  to  $q_{17}$  are discussed in section 5.6, the generalised relative torsional coordinates  $\varphi_i$  ( $i = 1, \dots, 10$ ) are for the relative torsional motion of the 10 discrete mass points,  $\varphi_{p1}$  and  $\varphi_{p2}$  are for the relative torsional motion of mass payloads  $M_{p1}$  and  $M_{p2}$ , as given in Table 6.1, which are defined as  $q_{18}$  to  $q_{29}$ .

## 6.5 Generalised Forces

The generalised forces  $Q_1$  to  $Q_{17}$  are the same as in section 5.7, and the generalised forces  $Q_{18}$  to  $Q_{29}$  are the torsional generalised forces for mass points  $m_i$  and payloads  $M_{p1}$  and  $M_{p2}$ , as listed in Table (6.1), which comes from an assumed dissipation function based on Rayleigh damping.

## 6.6 Governing Equations of Motion

Lagrange's equations are used to generate the governing equations of motion, the full equations are to be found in the path CD-ROM/axial-torsional/N10/, as listed in Table 6.1.

Similar to Chapter 5, there are 29 nonlinear equations for 29 generalised coordinates of this MMET system, and it is still difficult in the solution procedure to use the routine NDSolve with the 'out of memory' problem, as discussed in section 5.8.

In order to handle this problem and to explore the interaction of the axial and torsional elastic MMET system, we have reduced the discretisation scheme right down to  $N = 2$ , then used Lagrange's equations to derive a reduced set of nonlinear governing equations of motion for a simplified MMET system, as shown in Appendix H, and the generalised coordinates for the MMET system with two discrete mass points are given in Table 6.2.

- The detail modelling steps for axial and torsional elastic MMET system with two discretised mass points are attached in Appendix H.

## 6.7 Simulations and Discussions

Based on the axial and torsional elastic MMET system with two discrete mass points, Figures 6.3 to 6.19 are the numerical results obtained by MATHEMATICA for the number of cycles of period  $T_n = 4.01$  and 400.01, in which the MMET system's short simulation time and long simulation time behaviours can be observed with the given parameters in Appendix C.

Table 6.1: Generalised coordinates and equations of motion (*CD-ROM/axial-torsional/N10/*)

i	$q_i$	$Q_i$	T	U	Equations of Motion
1	$\psi$	(3.5.13)	(6.3.1)	(6.2.1)	Chapter6-1-N10-psi.pdf
2	$\theta$	(3.5.14)			Chapter6-2-N10-theta.pdf
3	$\alpha$	(3.5.15)			Chapter6-3-N10-alpha.pdf
4	$\gamma$	(3.5.17)			Chapter6-4-N10-gamma.pdf
5	R	(3.5.16)			Chapter6-5-N10-R.pdf
6	$\eta_{P1}$	$-c_0(\dot{\eta}_{P1} - \dot{\eta}_1)$			Chapter6-6-N10-etaP1.pdf
7	$\eta_{P2}$	$-c_0(\dot{\eta}_{10} - \dot{\eta}_{P2})$			Chapter6-7-N10-etaP2.pdf
8	$\eta_1$	$c_0(\dot{\eta}_{P1} - \dot{\eta}_1) - c_0(\dot{\eta}_1 - \dot{\eta}_2)$			Chapter6-8-N10-eta1.pdf
9	$\eta_2$	$c_0(\dot{\eta}_1 - \dot{\eta}_2) - c_0(\dot{\eta}_2 - \dot{\eta}_3)$			Chapter6-9-N10-eta2.pdf
10	$\eta_3$	$c_0(\dot{\eta}_2 - \dot{\eta}_3) - c_0(\dot{\eta}_3 - \dot{\eta}_4)$			Chapter6-10-N10-eta3.pdf
11	$\eta_4$	$c_0(\dot{\eta}_3 - \dot{\eta}_4) - c_0(\dot{\eta}_4 - \dot{\eta}_5)$			Chapter6-11-N10-eta4.pdf
12	$\eta_5$	$c_0(\dot{\eta}_4 - \dot{\eta}_5) - c_0\dot{\eta}_5$			Chapter6-12-N10-eta5.pdf
13	$\eta_6$	$c_0(\dot{\eta}_7 - \dot{\eta}_6) - c_0\dot{\eta}_6$			Chapter6-13-N10-eta6.pdf
14	$\eta_7$	$c_0(\dot{\eta}_6 - \dot{\eta}_7) - c_0(\dot{\eta}_7 - \dot{\eta}_8)$			Chapter6-14-N10-eta7.pdf
15	$\eta_8$	$c_0(\dot{\eta}_7 - \dot{\eta}_8) - c_0(\dot{\eta}_8 - \dot{\eta}_9)$			Chapter6-15-N10-eta8.pdf
16	$\eta_9$	$c_0(\dot{\eta}_8 - \dot{\eta}_9) - c_0(\dot{\eta}_9 - \dot{\eta}_{10})$			Chapter6-16-N10-eta9.pdf
17	$\eta_{10}$	$c_0(\dot{\eta}_9 - \dot{\eta}_{10}) - c_0(\dot{\eta}_{10} - \dot{\eta}_{P2})$			Chapter6-17-N10-eta10.pdf
18	$\varphi_{P1}$	$-c_{t0}(\dot{\varphi}_{P1} - \dot{\varphi}_1)$			Chapter6-18-N10-phiP1.pdf
19	$\varphi_{P2}$	$-c_{t0}(\dot{\varphi}_{10} - \dot{\varphi}_{P2})$			Chapter6-19-N10-phiP2.pdf
20	$\varphi_1$	$c_{t0}(\dot{\varphi}_{P1} - \dot{\varphi}_1) - c_{t0}(\dot{\varphi}_1 - \dot{\varphi}_2)$			Chapter6-20-N10-phi1.pdf
21	$\varphi_2$	$c_{t0}(\dot{\varphi}_1 - \dot{\varphi}_2) - c_{t0}(\dot{\varphi}_2 - \dot{\varphi}_3)$			Chapter6-21-N10-phi2.pdf
22	$\varphi_3$	$c_{t0}(\dot{\varphi}_2 - \dot{\varphi}_3) - c_{t0}(\dot{\varphi}_3 - \dot{\varphi}_4)$			Chapter6-22-N10-phi3.pdf
23	$\varphi_4$	$c_{t0}(\dot{\varphi}_3 - \dot{\varphi}_4) - c_{t0}(\dot{\varphi}_4 - \dot{\varphi}_5)$			Chapter6-23-N10-phi4.pdf
24	$\varphi_5$	$c_{t0}(\dot{\varphi}_4 - \dot{\varphi}_5) - c_{t0}\dot{\varphi}_5$			Chapter6-34-N10-phi5.pdf
25	$\varphi_6$	$c_{t0}(\dot{\varphi}_7 - \dot{\varphi}_6) - c_{t0}\dot{\varphi}_6$			Chapter6-25-N10-phi6.pdf
26	$\varphi_7$	$c_{t0}(\dot{\varphi}_6 - \dot{\varphi}_7) - c_{t0}(\dot{\varphi}_7 - \dot{\varphi}_8)$			Chapter6-26-N10-phi7.pdf
27	$\varphi_8$	$c_{t0}(\dot{\varphi}_7 - \dot{\varphi}_8) - c_{t0}(\dot{\varphi}_8 - \dot{\varphi}_9)$			Chapter6-27-N10-phi8.pdf
28	$\varphi_9$	$c_{t0}(\dot{\varphi}_8 - \dot{\varphi}_9) - c_{t0}(\dot{\varphi}_9 - \dot{\varphi}_{10})$			Chapter6-28-N10-phi9.pdf
29	$\varphi_{10}$	$c_{t0}(\dot{\varphi}_9 - \dot{\varphi}_{10}) - c_{t0}(\dot{\varphi}_{10} - \dot{\varphi}_{P2})$			Chapter6-29-N10-phi10.pdf

Table 6.2: Generalised coordinates and equations of motion (*CD-ROM/axial-torsional/N2/*)

i	$q_i$	$Q_i$	T	U	Equations of Motion
1	$\psi$	(3.5.13)	(H.2.1)	(H.1.1)	Chapter6-1-N2-psi.pdf
2	$\theta$	(3.5.14)			Chapter6-2-N2-theta.pdf
3	$\alpha$	(3.5.15)			Chapter6-3-N2-alpha.pdf
4	$\gamma$	(3.5.17)			Chapter6-4-N2-gamma.pdf
5	R	(3.5.16)			Chapter6-5-N2-R.pdf
6	$\eta_{P1}$	$-c_0(\dot{\eta}_{P1} - \dot{\eta}_1)$			Chapter6-6-N2-etaP1.pdf
7	$\eta_{P2}$	$-c_0(\dot{\eta}_2 - \dot{\eta}_{P2})$			Chapter6-7-N2-etaP2.pdf
8	$\eta_1$	$c_0(\dot{\eta}_{P1} - \dot{\eta}_1) - c_0\dot{\eta}_1$			Chapter6-8-N2-eta1.pdf
9	$\eta_2$	$c_0(\dot{\eta}_{P2} - \dot{\eta}_2) - c_0\dot{\eta}_2$			Chapter6-9-N2-eta2.pdf
10	$\varphi_{P1}$	$-c_{t0}(\dot{\varphi}_{P1} - \dot{\varphi}_1)$			Chapter6-10-N2-phiP1.pdf
11	$\varphi_{P2}$	$-c_{t0}(\dot{\varphi}_2 - \dot{\varphi}_{P2})$			Chapter6-11-N2-phiP2.pdf
12	$\varphi_1$	$c_{t0}(\dot{\varphi}_{P1} - \dot{\varphi}_1) - c_{t0}\dot{\varphi}_1$			Chapter6-12-N2-phi1.pdf
13	$\varphi_2$	$c_{t0}(\dot{\varphi}_{P2} - \dot{\varphi}_2) - c_{t0}\dot{\varphi}_2$			Chapter6-13-N2-phi2.pdf

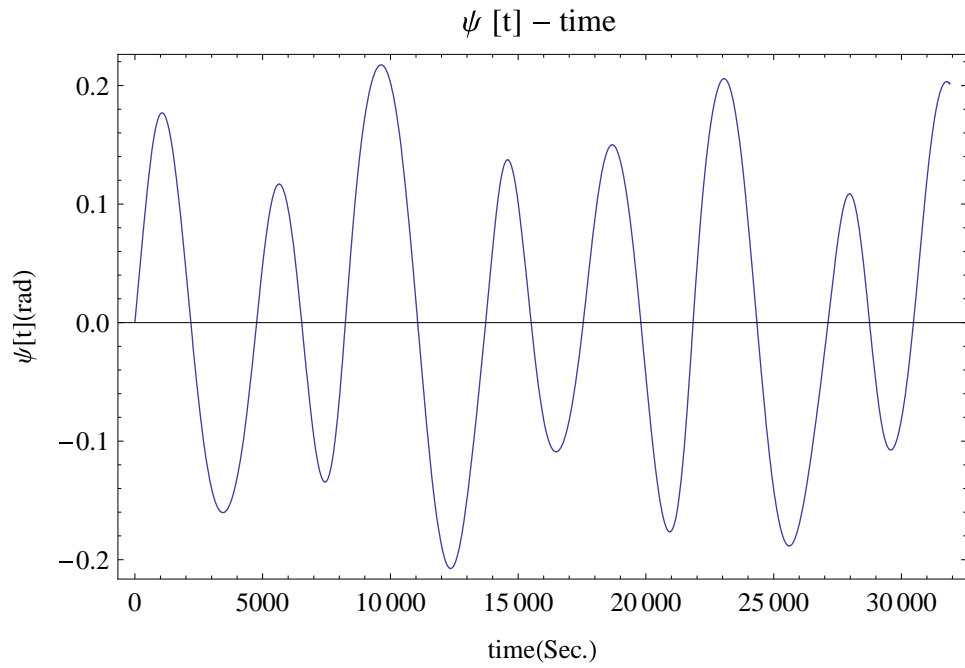


Figure 6.3: Axial and torsional elastic MMET system spin-up, angular displacement of  $\psi$  ( $T_n = 4.01$ )

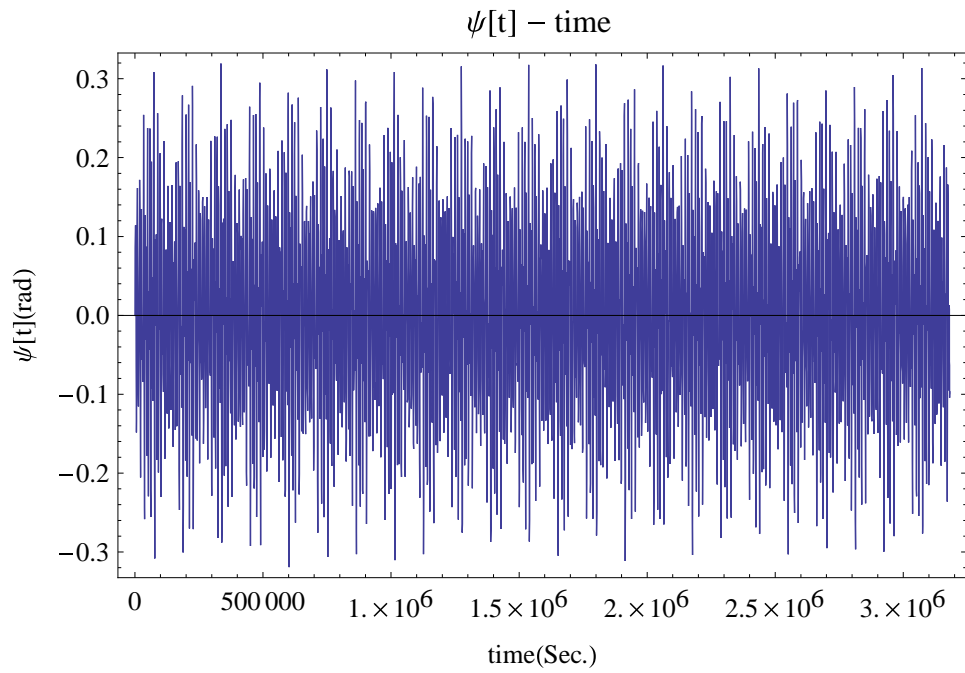


Figure 6.4: Axial and torsional elastic MMET system spin-up displacement of  $\psi$  ( $T_n = 400.01$ )

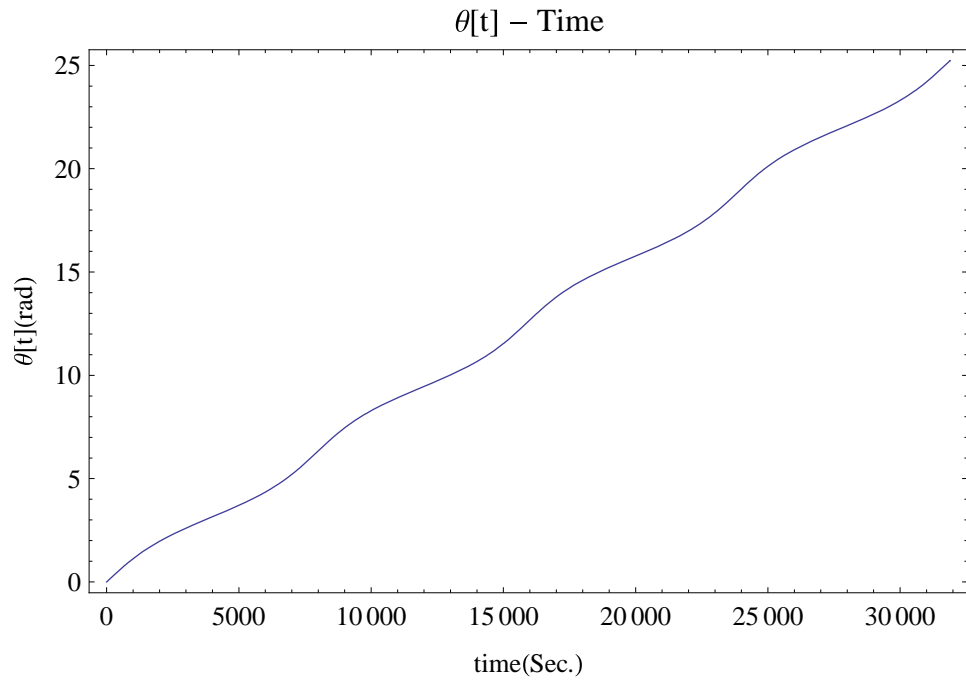


Figure 6.5: Axial and torsional elastic MMET system elliptical orbit angular position of  $\theta$  ( $T_n = 4.01$ )

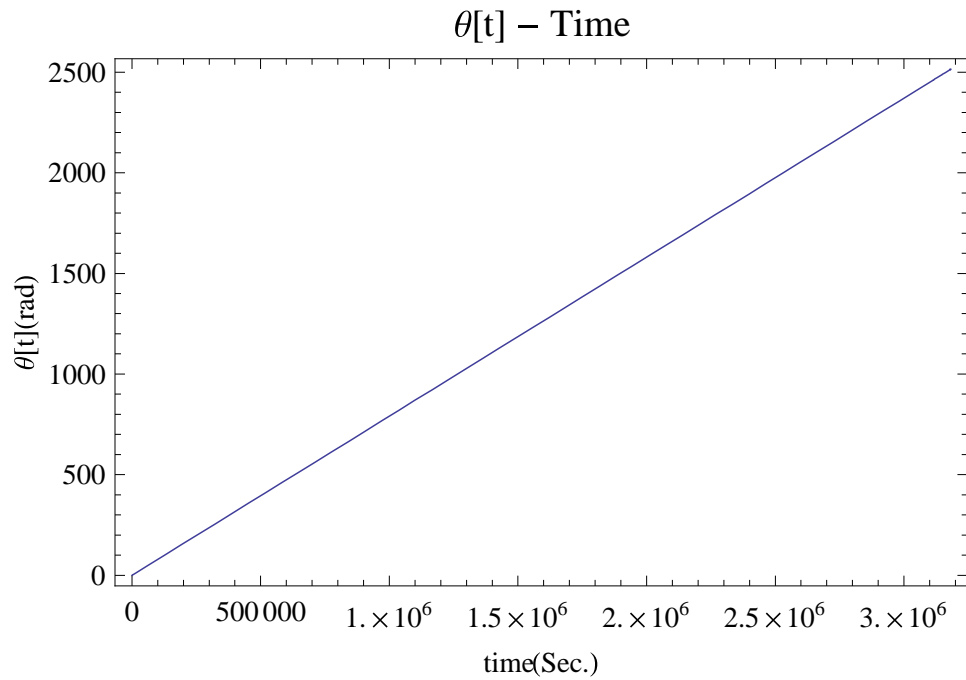


Figure 6.6: Axial and torsional elastic MMET system elliptical orbit angular position of  $\theta$  ( $T_n = 400.01$ )

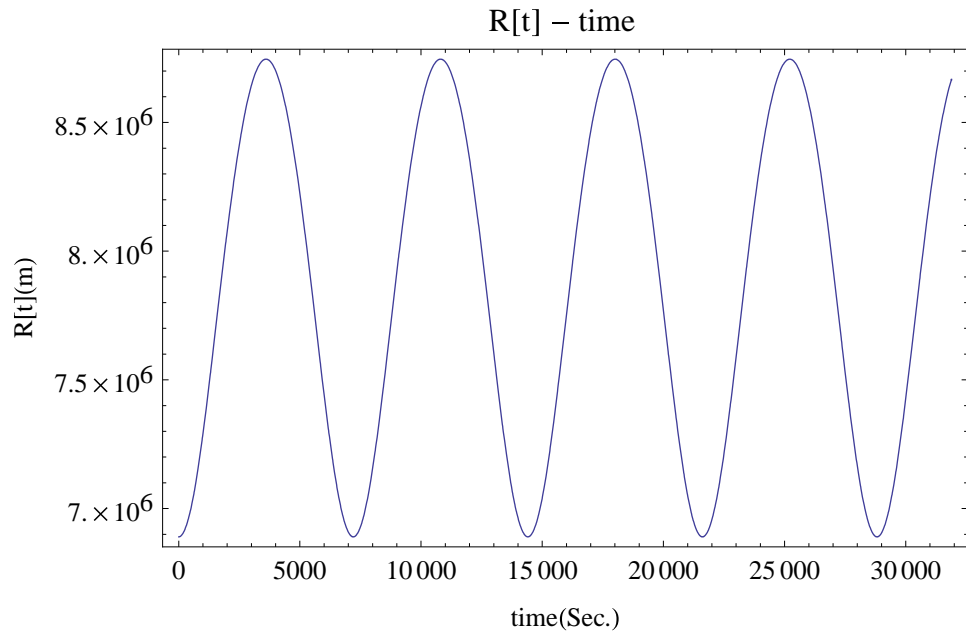


Figure 6.7: Axial and torsional elastic MMET system base point distance  $R$  ( $T_n = 4.01$ )

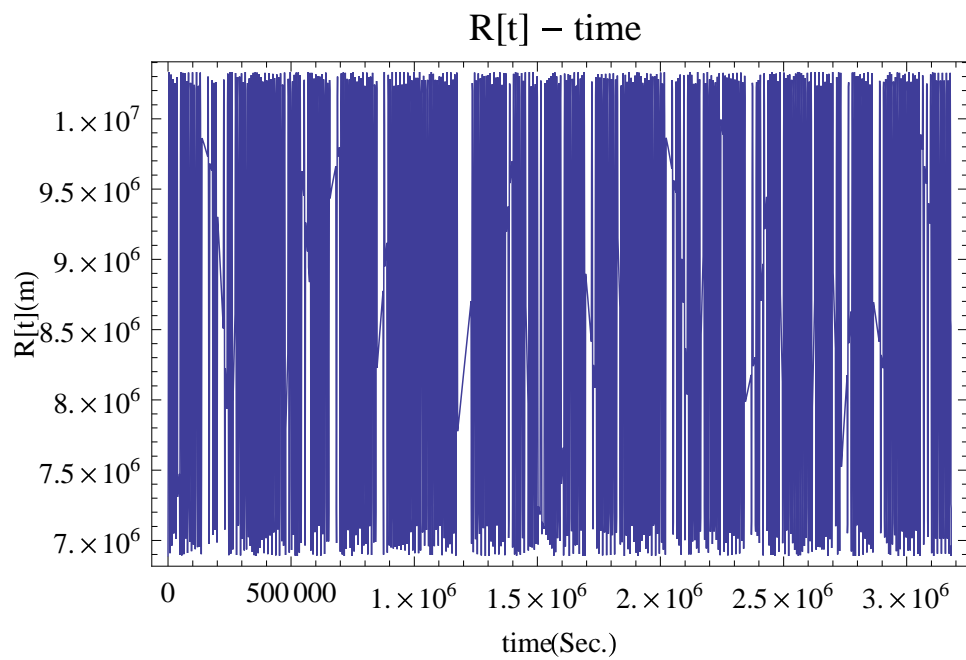


Figure 6.8: Axial and torsional elastic MMET system base point distance  $R$  ( $T_n = 400.01$ )

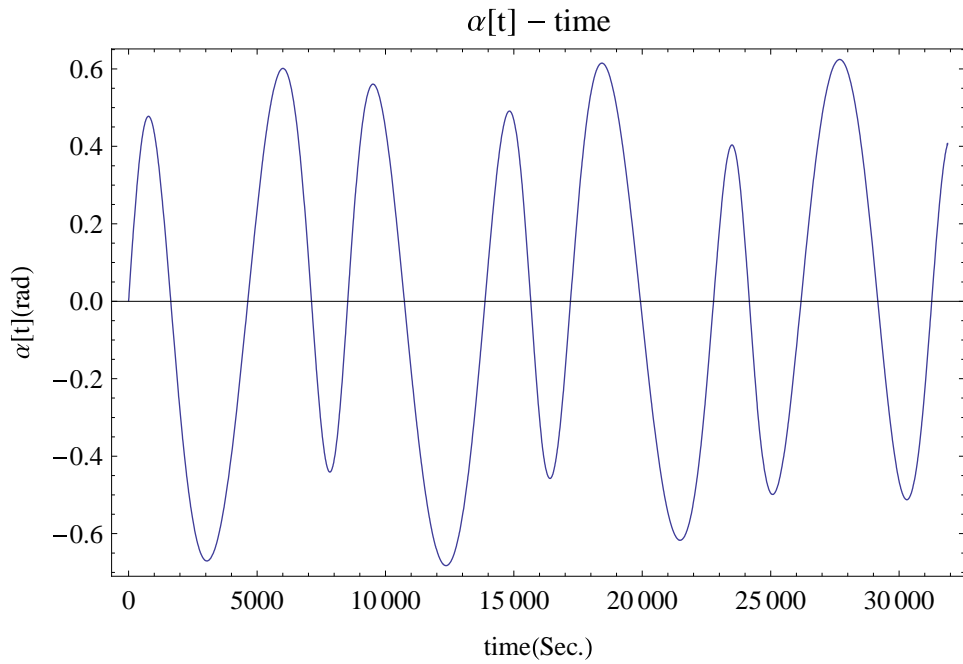


Figure 6.9: Axial and torsional elastic MMET system out-of-plane angle of  $\alpha$  ( $T_n = 4.01$ )

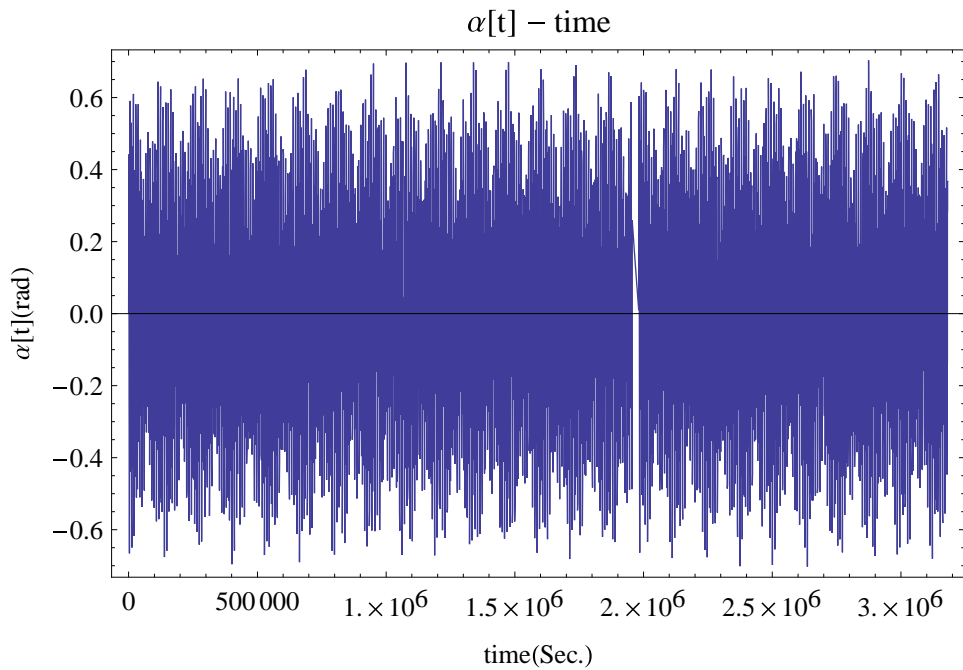


Figure 6.10: Axial and torsional elastic MMET system out-of-plane angle of  $\alpha$  ( $T_n = 400.01$ )

▷ Figures 6.3 to 6.4 are the numerical results for the MMET system's spin-up  $\psi$ . The results show the discretised MMET system with axial and torsional elasticity performance periodically on Earth orbit within the range  $-0.32$  to  $0.32$  rad over the number of cycles of period  $T_n = 4.01$  and  $400.01$ .

▷  $\theta$  and  $R$  are the position generalised coordinates, whose responses are given in Figures 6.5, 6.6 and 6.7, 6.8 for the short ( $T_n = 4.01$ ) and long ( $T_n = 400.01$ ) simulation

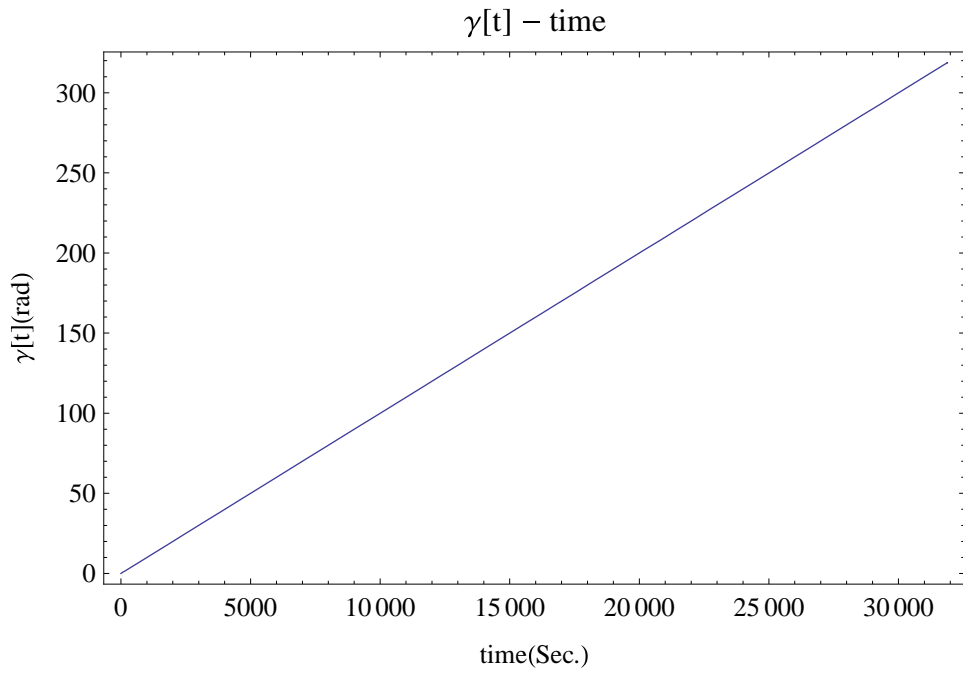


Figure 6.11: Axial and torsional elastic MMET system rolling angle of  $\gamma$  ( $T_n = 4.01$ )

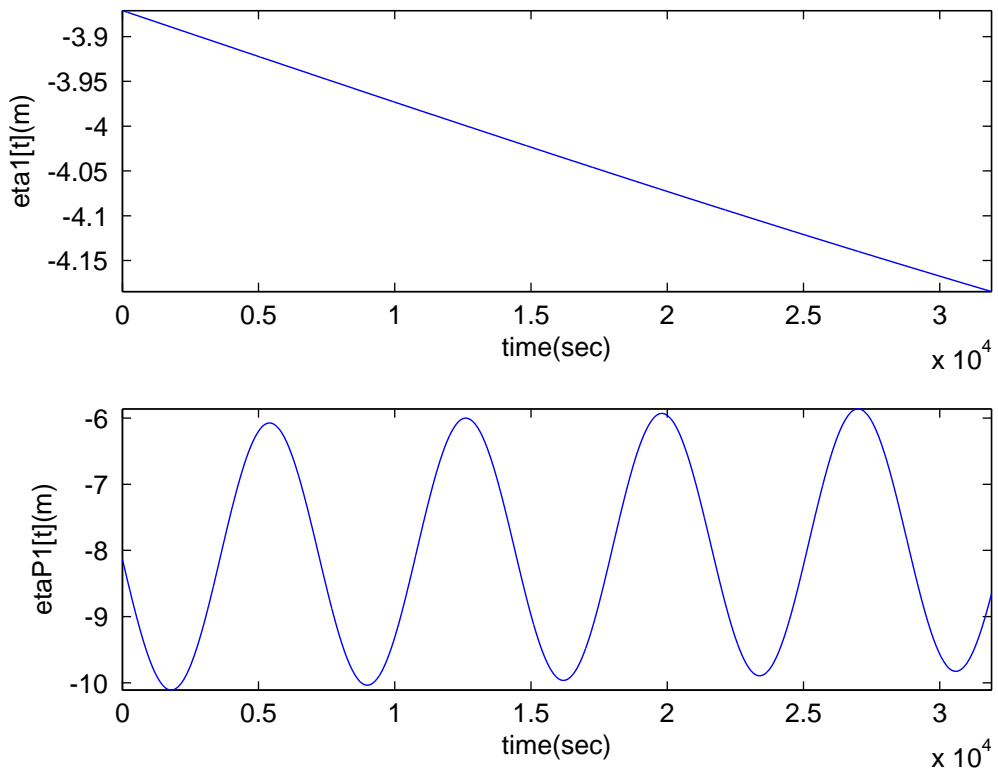


Figure 6.12: Axial displacement responses  $\eta_1$  and  $\eta_{P1}$  ( $T_n = 4.01$ )

times, respectively, and the MMET system can be located via the position coordinates on an elliptical orbit, which are same as they were discussed in Chapter 5.

▷ The out-of-plane angle  $\alpha$ , as shown in Figures 6.9 and 6.10, the fluctuant plots depict the steady motion within - 0.7 to 0.7 rad, with the non-zero initial conditions  $\alpha(0) =$

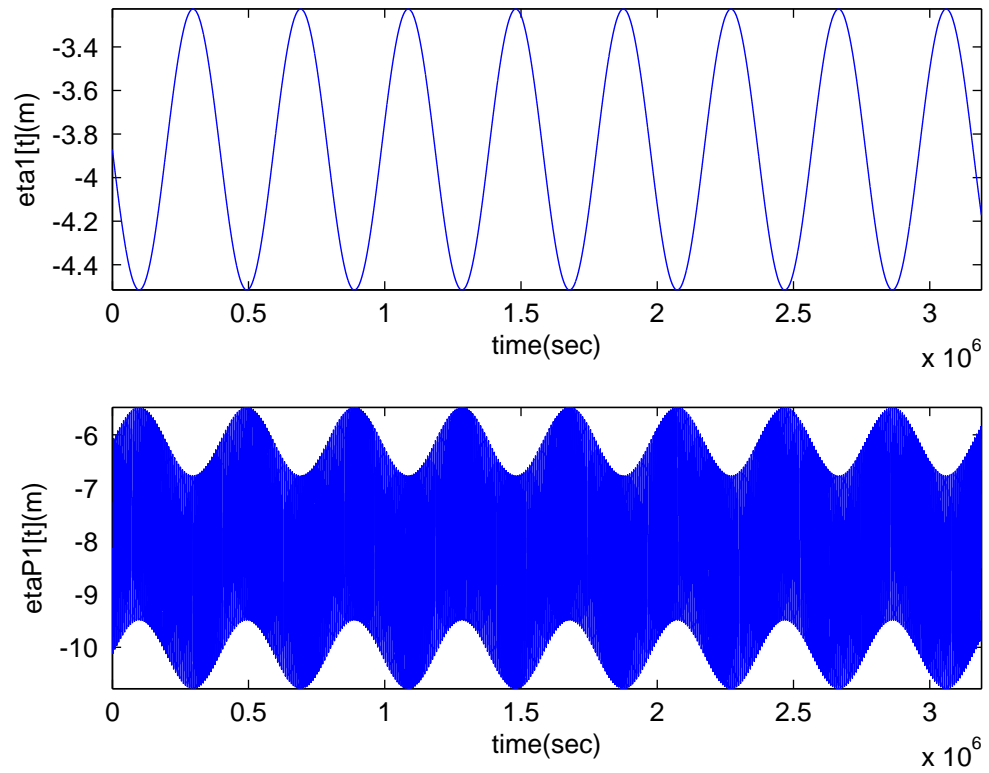


Figure 6.13: Axial displacement responses  $\eta_1$  and  $\eta_{P1}$  ( $T_n = 400.01$ )

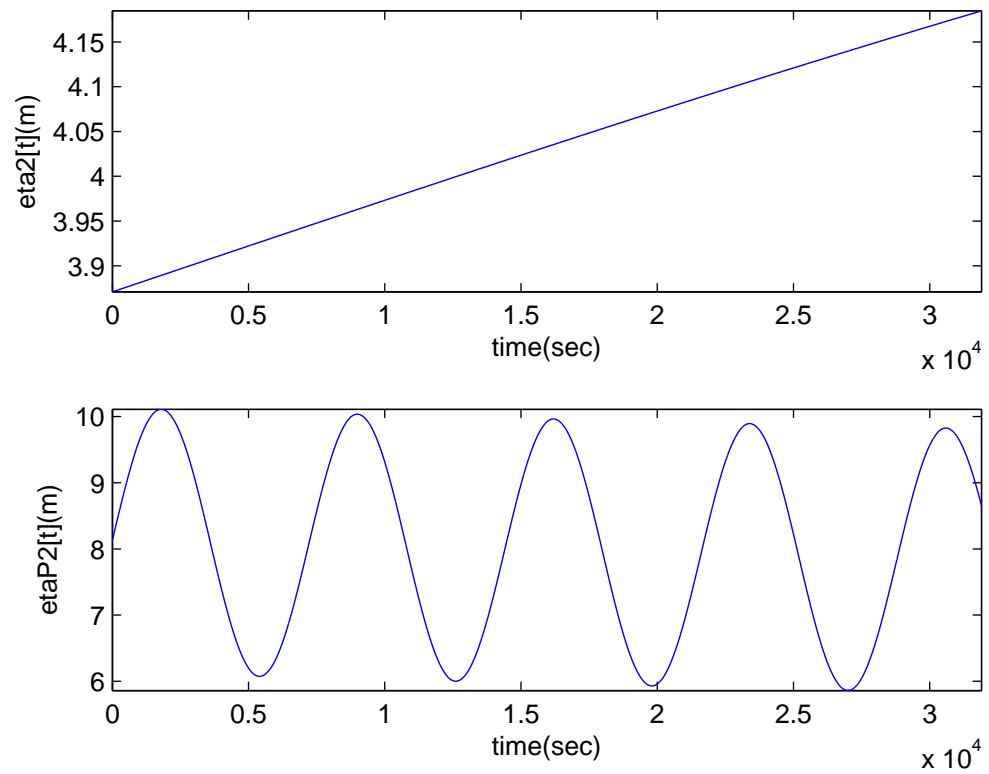


Figure 6.14: Axial displacement responses  $\eta_2$  and  $\eta_{P2}$  ( $T_n = 4.01$ )

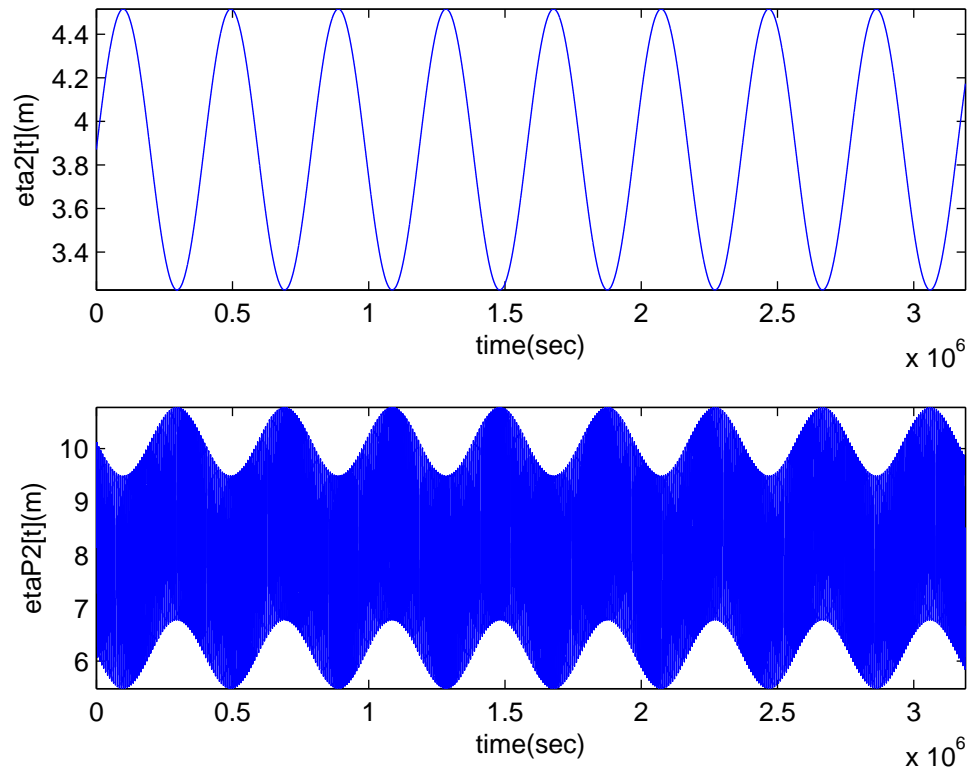


Figure 6.15: Axial displacement responses  $\eta_2$  and  $\eta_{P2}$  ( $T_n = 400.01$ )

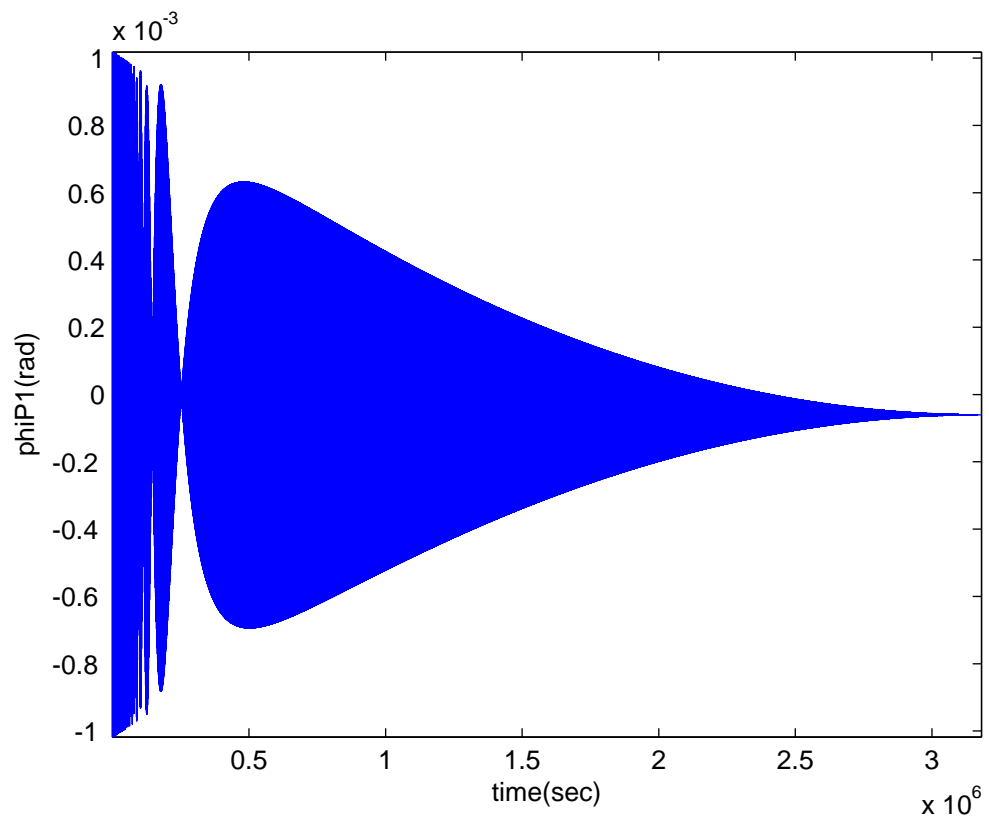


Figure 6.16: Torsional displacement response  $\phi_{P1}$  ( $T_n = 400.01$ )

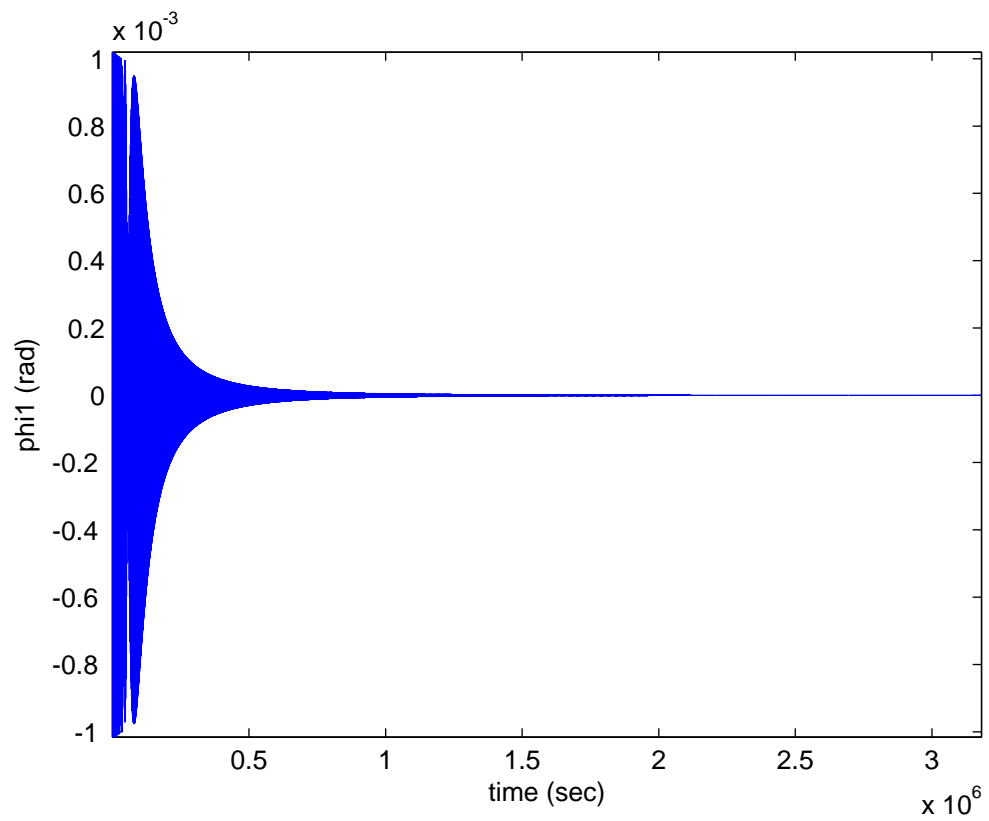


Figure 6.17: Torsional displacement response  $\phi_1$  ( $T_n = 400.01$ )

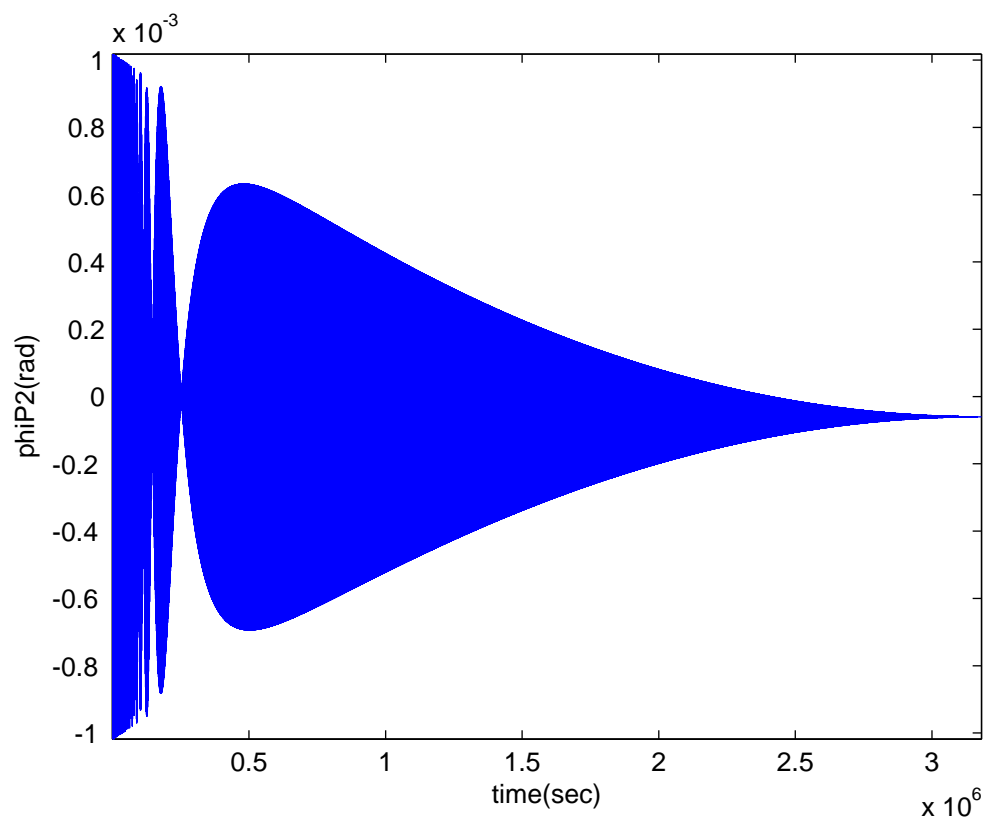


Figure 6.18: Torsional displacement response  $\phi_{P2}$  ( $T_n = 400.01$ )

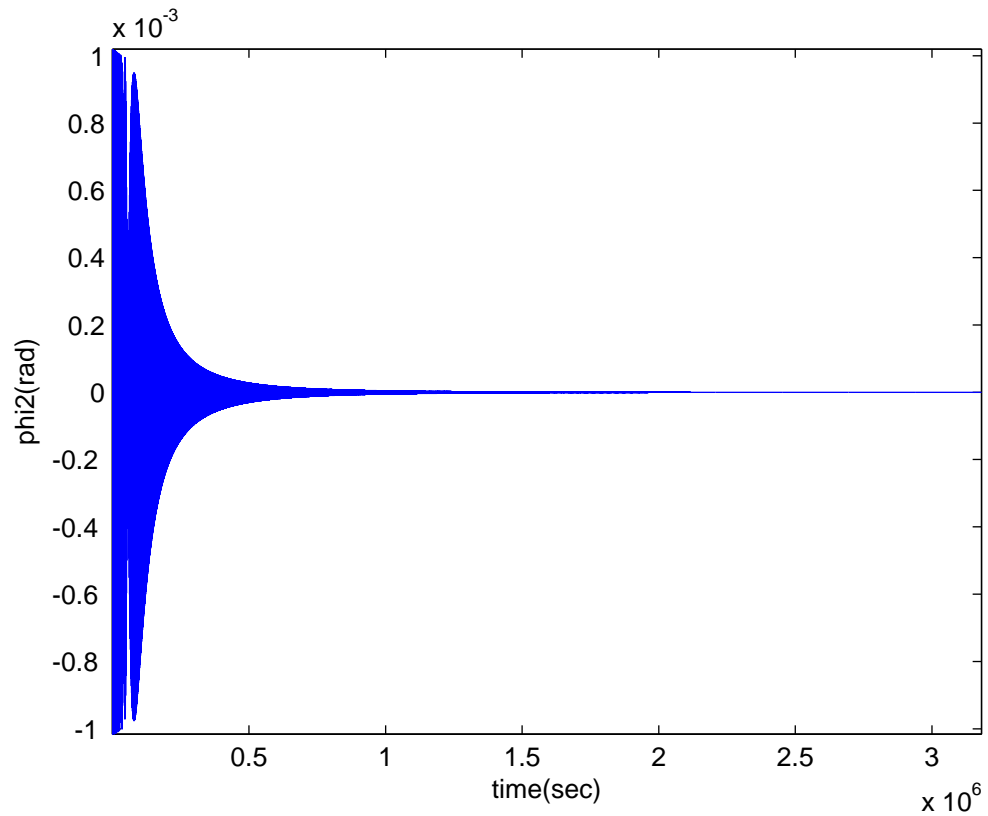


Figure 6.19: Torsional displacement response  $\phi_2$  ( $T_n = 400.01$ )

0.001 rad and  $\dot{\alpha}(0) = 0.001$  rad/s

▷ Figure 6.11 states the tether subspan's rigid rolling angular displacement, with given non-zero initial conditions  $\gamma(0) = 0.001$  rad and  $\dot{\gamma}(0) = 0.001$  rad/s; its response moves up in a linear way over the simulation time.

▷ Figures 6.12 to 6.15 are the MMET system's axial elastic motion over the simulation time  $T_n = 4.01$  and  $400.01$  for the discrete mass points  $M_{P1}$ ,  $m_1$  and  $M_{P2}$ ,  $m_2$ , respectively, which are same as the axial motions in Chapter 5, as it has been discussed in section 5.9.

▷ The torsional motions can be observed in Figures 6.16, 6.17, 6.18 and 6.19 for the payloads and mass points -  $M_{P1}$ ,  $m_1$  and  $M_{P2}$ ,  $m_2$ , which express the convergent torsional behaviours for  $\phi_1$ ,  $\phi_2$ ,  $\phi_{P1}$  and  $\phi_{P2}$ . with their initial values 0.001. On the other hand, with zero initial values, all the torsional motions remain zero valued, which is the one of the most common situations for the MMET system application. For the torsional elastic motions are independent of the other elastic motions, the numerical results should be same in Chapters 6 and 7.

Similar to the rigid body rolling motions, the torsional elastic motion is independent of

the other elastic motions, whose simulation results can be effected by its initial values, if given non-zero initial values, the torsional elastic behaviour can be start or stop by giving a proper zero or non-zero initial conditions, numerically.

## 6.8 Conclusions

With an arbitrary choice of  $N = 10$  mass points, by using the Lagrange's procedure, a discretised MDOF MMET system has been proposed for the axial and torsional elastic behaviours.

To deal with the numerical time-consuming simulation difficulties, this MMET system has been reduced to a  $N = 2$  mass points MMET system with the same discretisation scheme, and a reduced set of nonlinear ODEs and its numerical results have been obtained, which show that the MMET system's torsional elastic motions are decoupling from axial elastic motions and other rigid body motions, and the rigid body and axial elastic behaviours are same as the MMET system in Chapter 5.

The torsional elastic motions are sensitive to the initial values for the torsional generalised coordinates  $\varphi_1$ ,  $\varphi_2$ ,  $\varphi_{P1}$  and  $\varphi_{P2}$ , and are decoupling from the MMET system's other motions.

This chapter is the second stage in the modelling for the discretised MMET system, by using the Lagrangian dynamics, which will be taken as the basic model for the pendular modelling in the chapter which follows.

## Chapter 7

---

# Dynamical Modelling for a Discretised Flexible MMET System

---

### 7.1 Introduction

Based on the MMET model in Chapter 6, a MDOF discretised flexible MMET system with an arbitrary choice of  $N = 10$  mass points is investigated by involving pendular elasticity in this chapter. As mentioned in section 1.4, the word ‘flexible’ means that this MMET system incorporates axial, torsional and pendular elasticity. It must be clear that the ‘pendular’ elasticity in this Chapter means a set of  $N$  coupled pendulums when  $N$  equals the number of elements between each mass element in each of the tether sub-span.

As shown in Figures 7.1 and 7.2, there are two parts of the pendular elasticity, which are expressed on the plane  $x_0 - O - y_0$  and the plane  $z_0 - O - y_0$ , respectively,

⟨1⟩ As shown in Figure 7.1, for the pendular elasticity referenced on the plane  $x_0 - O - y_0$ , it is represented by a string of torsional ‘spring-damper’ groups  $\{k_{li}, c_{li}\}$ , which connect the mass points of  $m_i$  in series. With the assumption of  $k_{l1} = \dots = k_{l12}$ ,  $c_{l1} = \dots = c_{l12}$ , all the torsional ‘spring-damper’ groups are referenced onto the plane  $x_0 - O - y_0$ , as shown in Figure 7.3. The  $l$  in the subscript means the pendular elastic parameter, and the generalised coordinates  $\chi_i$  describe the motions for mass points  $m_i$  ( $i = 1, \dots, 10$ ) of the pendular elasticity on the plane  $x_0 - O - y_0$ .

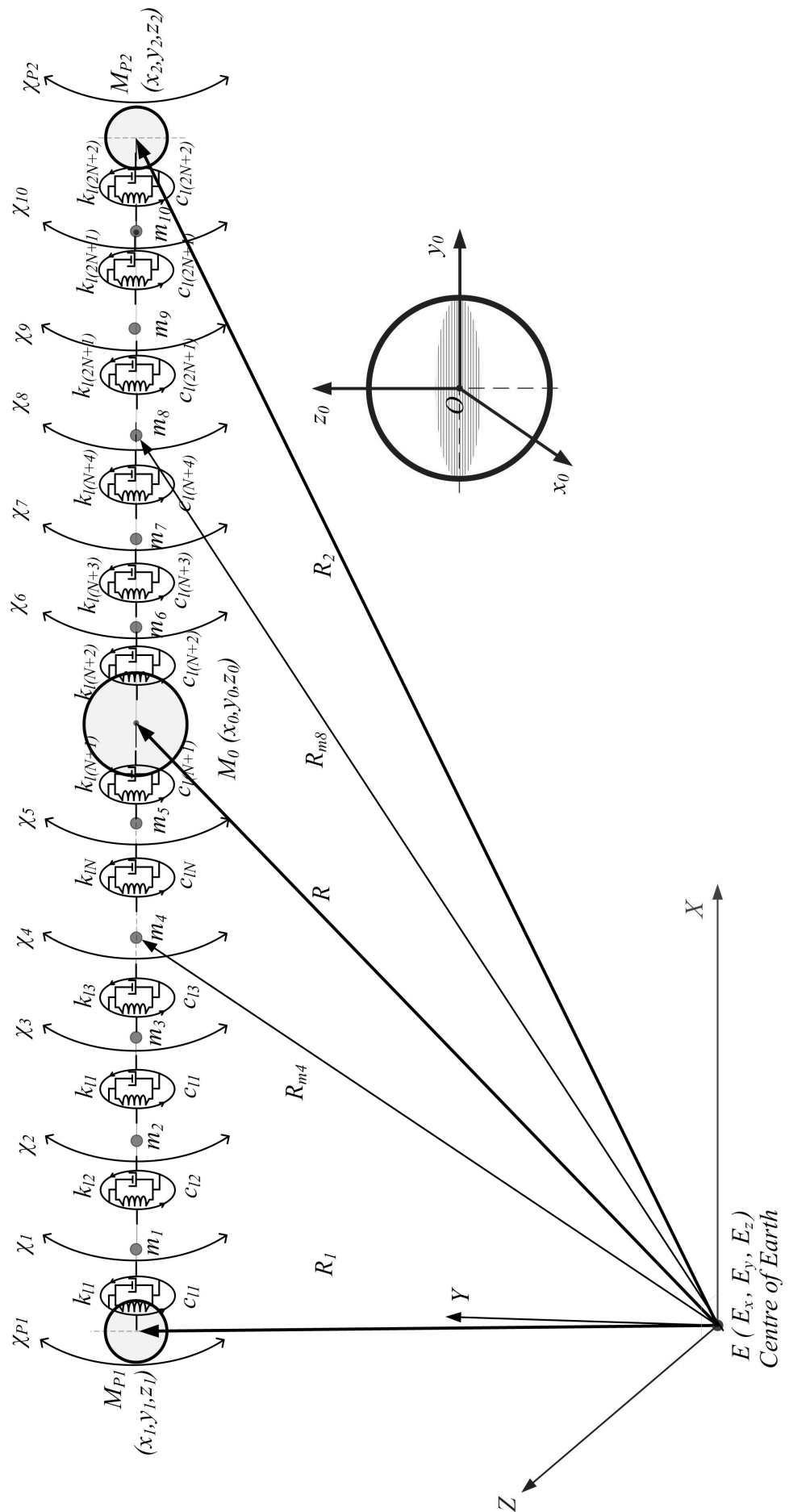


Figure 7.1: Pendular elastic MMET tether with 10 discrete mass points -  $x_0 - O - y_0$

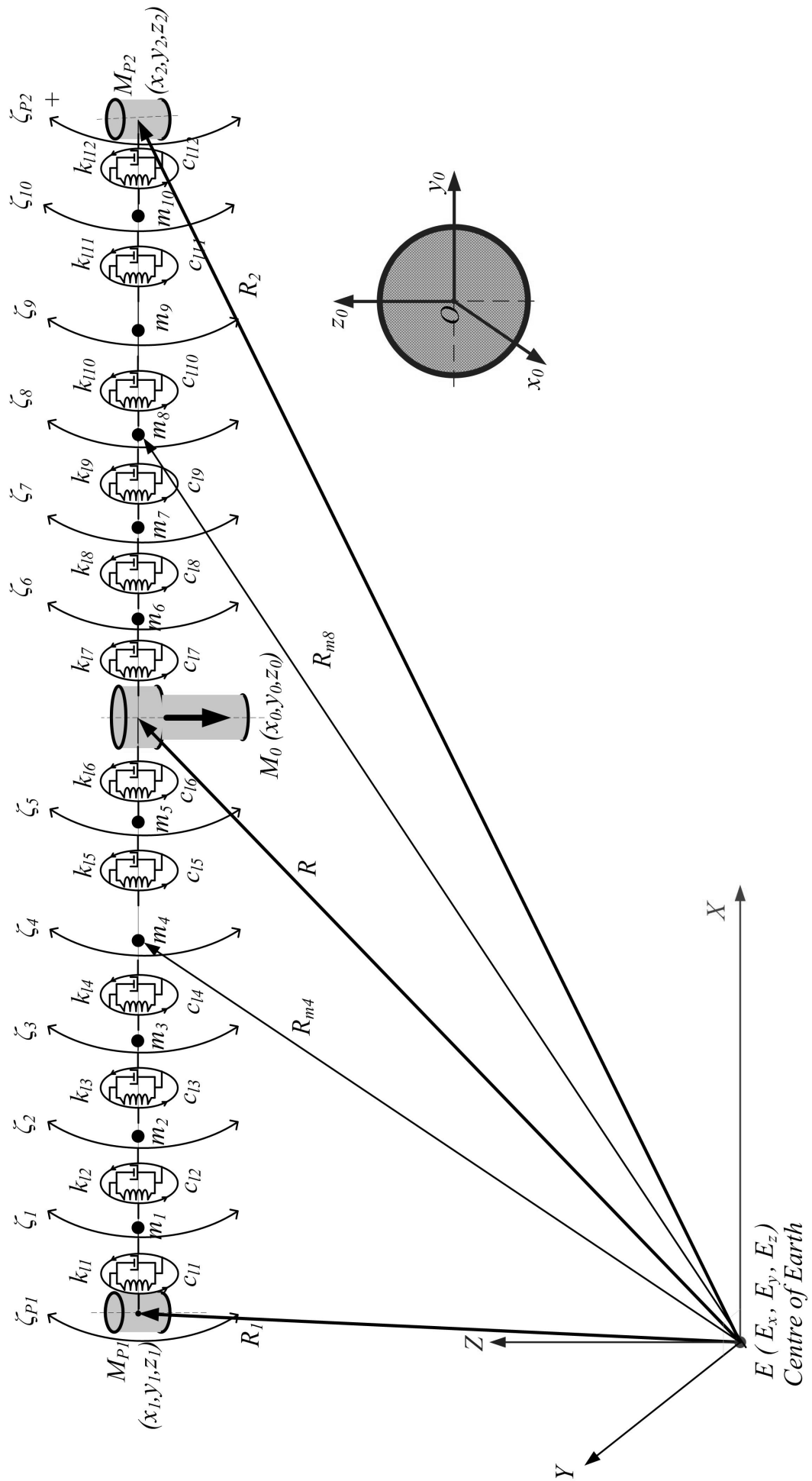


Figure 7.2: Pendular elastic MMET tether with 10 discrete mass points -  $z_0 - O - y_0$

⟨2⟩ Meanwhile, as shown in Figure 7.2, for the pendular elasticity referenced on the plane  $z_0 - O - y_0$ , a string of torsional ‘spring-damper’ groups  $\{k_{li}, c_{li}\}$  connect the discrete mass points  $m_i$ , with the assumption  $k_{l1} = \dots = k_{l12}$ ,  $c_{l1} = \dots = c_{l12}$ , all the torsional ‘spring-damper’ groups are referenced onto the plane  $z_0 - O - y_0$ , as shown in Figure 7.4. The generalised coordinates  $\zeta_i$  describe the behaviours for mass points  $m_i$  ( $i = 1, \dots, 10$ ) of the pendular elasticity on the plane  $z_0 - O - y_0$ .

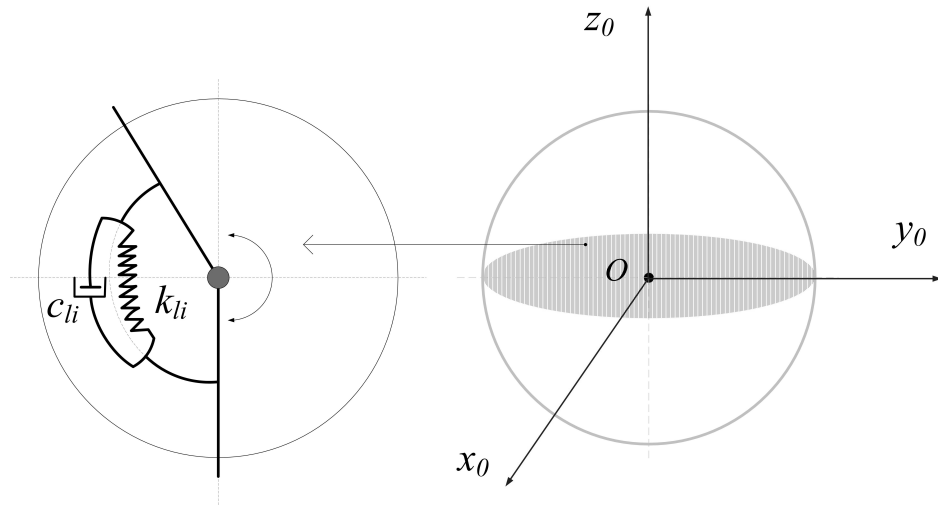


Figure 7.3: Reference onto the plane  $x_0 - O - y_0$  for MMET pendular elasticity

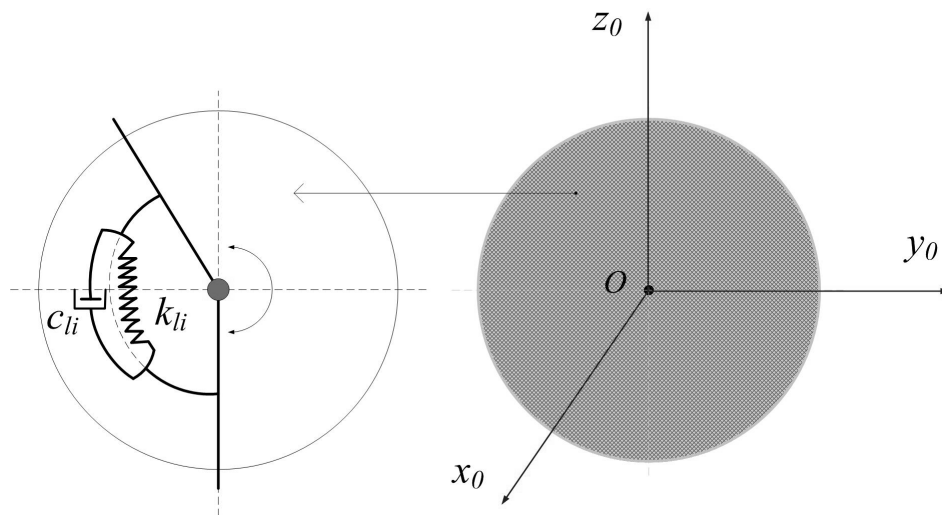


Figure 7.4: Reference onto the plane  $z_0 - O - y_0$  for MMET pendular elasticity

To summarise the flexible MMET modelling process, based on the serial spring and damper assumptions B4 and B5, it can be listed,

⟨1⟩ for axial elasticity,  $k_0 = k_1 = k_2 = \dots = k_{12}$ ,  $c_0 = c_1 = c_2 = \dots = c_{12}$ , where the  $k_0$  and  $c_0$  are the default stiffness and damping coefficient values;

⟨2⟩ for torsional elasticity,  $k_{t0} = k_{t1} = k_{t2} = \dots = k_{t12}$ ,  $c_{t0} = c_{t1} = c_{t2} = \dots = c_{t12}$ , where the  $k_{t0}$  and  $c_{t0}$  are the default stiffness and damping coefficient values;

⟨3⟩ for pendular elasticity both on the plane  $x_0 - O - y_0$  and the plane  $z_0 - O - y_0$ ,  $k_{l0} = k_{l1} = k_{l2} = \dots = k_{l12}$ ,  $c_{l0} = c_{l1} = c_{l2} = \dots = c_{l12}$ , where the  $k_{l0}$  and  $c_{l0}$  are the default stiffness and damping coefficient values. The discretised mass points  $m_0 = m_1 = m_2 = \dots = m_{10}$ , where the  $m_0$  is the default mass value;

## 7.2 Potential Energy

The tether's potential energy is given in equation (7.2.1), where  $\mu$  is the product of the universal gravitational constant  $G$  with the Earth's mass.  $R_1$ ,  $R_2$  and  $R_{m_i}$  ( $i = 1$  to  $10$ ) are the same as that defined in Chapter 5.

$$\begin{aligned}
 U = & -\frac{\mu M_{P1}}{R_1} - \frac{\mu M_{P2}}{R_2} - \frac{\mu M_0}{R} - \frac{\mu m_1}{R_{m_1}} - \frac{\mu m_2}{R_{m_2}} - \dots - \frac{\mu m_{10}}{R_{m_{10}}} \\
 & + SE|_{axial} + SE|_{torsional} + SE|_{pendular}
 \end{aligned} \tag{7.2.1}$$

Where the  $SE|_{axial}$  and  $SE|_{torsional}$  terms are given in equations (5.4.2) and (6.2.2),  $SE|_{pendular}$  term is the strain energy of the two subspans taking pendular elasticity into account, as stated in equation (7.2.2).

The  $CE|_{pendular}$  quantity is an assumed pendular dissipation function, and the damping coefficient in each group's elastic element is assumed to be in the form of classical linear viscous damping.

$$\begin{aligned}
 SE|_{pendular} = & \frac{1}{2}k_{l1}(\chi_{P1} - \chi_1)^2 + \frac{1}{2}k_{l2}(\chi_1 - \chi_2)^2 + \dots + \frac{1}{2}k_{l6}\chi_5^2 \\
 & + \frac{1}{2}k_{l7}\chi_6^2 + \dots + \frac{1}{2}k_{l12}(\chi_{10} - \chi_{P2})^2 + \\
 & \frac{1}{2}k_{l1}(\zeta_{P1} - \zeta_1)^2 + \frac{1}{2}k_{l2}(\zeta_1 - \zeta_2)^2 + \dots + \frac{1}{2}k_{l6}\zeta_5^2 \\
 & + \frac{1}{2}k_{l7}\zeta_6^2 + \dots + \frac{1}{2}k_{l12}(\zeta_{10} - \zeta_{P2})^2
 \end{aligned} \tag{7.2.2}$$

$$\begin{aligned}
CE|_{\text{pendular}} = & \frac{1}{2}c_{11}(\dot{\chi}_{P1} - \dot{\chi}_1)^2 + \frac{1}{2}c_{12}(\dot{\chi}_1 - \dot{\chi}_2)^2 + \cdots + \frac{1}{2}c_{16}\dot{\chi}_5^2 + \\
& \frac{1}{2}c_{17}\dot{\chi}_6^2 + \cdots + \frac{1}{2}c_{112}(\dot{\chi}_{10} - \dot{\chi}_{P2})^2 + \\
& \frac{1}{2}c_{11}(\dot{\zeta}_{P1} - \dot{\zeta}_1)^2 + \frac{1}{2}c_{12}(\dot{\zeta}_1 - \dot{\zeta}_2)^2 + \cdots + \frac{1}{2}c_{16}\dot{\zeta}_5^2 + \\
& \frac{1}{2}c_{17}\dot{\zeta}_6^2 + \cdots + \frac{1}{2}c_{112}(\dot{\zeta}_{10} - \dot{\zeta}_{P2})^2
\end{aligned} \tag{7.2.3}$$

With  $k_{10} = k_{11} = \dots = k_{112}$ ,  $c_{10} = c_{11} = \dots = c_{112}$ , equation (7.2.2) can be re-written as equation (7.2.4), and equation (7.2.3) can be reformed as equation (7.2.5), where  $k_{10}$  and  $c_{10}$  are the default stiffness and damping coefficient values.

$$\begin{aligned}
SE|_{\text{pendular}} = & \frac{1}{2}k_{10} ((\chi_{P1} - \chi_1)^2 + (\chi_1 - \chi_2)^2 + \cdots + \chi_5^2 + \chi_6^2 + \cdots + (\chi_{10} - \chi_{P2})^2) + \\
& \frac{1}{2}k_{10} ((\zeta_{P1} - \zeta_1)^2 + (\zeta_1 - \zeta_2)^2 + \cdots + \zeta_5^2 + \zeta_6^2 + \cdots + (\zeta_{10} - \zeta_{P2})^2)
\end{aligned} \tag{7.2.4}$$

$$\begin{aligned}
CE|_{\text{pendular}} = & \frac{1}{2}c_{10} ((\dot{\chi}_{P1} - \dot{\chi}_1)^2 + (\dot{\chi}_1 - \dot{\chi}_2)^2 + \cdots + \dot{\chi}_5^2 \dot{\chi}_6^2 \cdots + (\dot{\chi}_{10} - \dot{\chi}_{P2})^2) + \\
& \frac{1}{2}c_{10} ((\dot{\zeta}_{P1} - \dot{\zeta}_1)^2 + (\dot{\zeta}_1 - \dot{\zeta}_2)^2 + \cdots + \dot{\zeta}_5^2 \dot{\zeta}_6^2 \cdots + (\dot{\zeta}_{10} - \dot{\zeta}_{P2})^2)
\end{aligned} \tag{7.2.5}$$

## 7.3 Kinetic Energy

The kinetic energy of the MMET system is given in equation (7.3.1).

$$\begin{aligned}
T = & \frac{1}{2}M_{P1} (\dot{x}_1^2 + \dot{y}_1^2 + \dot{z}_1^2) + \frac{1}{2}M_{P2} (\dot{x}_2^2 + \dot{y}_2^2 + \dot{z}_2^2) + \frac{1}{2}M_0 (\dot{x}_0^2 + \dot{y}_0^2 + \dot{z}_0^2) + \\
& \left[ \frac{1}{2}m_1 (\dot{x}_{m_1}^2 + \dot{y}_{m_1}^2 + \dot{z}_{m_1}^2) + \frac{1}{2}m_2 (\dot{x}_{m_2}^2 + \dot{y}_{m_2}^2 + \dot{z}_{m_2}^2) + \dots \right] + \\
& \left[ \frac{1}{2}m_{10} (\dot{x}_{m_{10}}^2 + \dot{y}_{m_{10}}^2 + \dot{z}_{m_{10}}^2) \right] + \\
& \left[ \frac{1}{2}I_{z_{P1}} + \frac{1}{2}I_{z_{P2}} + I_{z_T} + \frac{1}{2}I_{z_M} \right] (\psi + \theta)^2 + \\
& \left[ \frac{1}{2}I_{x_{P1}} + \frac{1}{2}I_{x_{P2}} + I_{x_T} + \frac{1}{2}I_{x_M} \right] \dot{\alpha}^2 + \left[ \frac{1}{2}I_{y_{P1}} + \frac{1}{2}I_{y_{P2}} + I_{y_T} + \frac{1}{2}I_{y_M} \right] \dot{\gamma}^2 + \\
& \left[ \frac{1}{2}I_{y_{P1}} \dot{\phi}_{P1}^2 + \frac{1}{2}I_{y_{P2}} \dot{\phi}_{P2}^2 + \frac{1}{2}I_{y_{m_1}} \dot{\phi}_1^2 + \dots + \frac{1}{2}I_{y_{m_{10}}} \dot{\phi}_{10}^2 \right] + \\
& \left[ \frac{1}{2} (I_{z_{P1}} + M_{P1}x_1^2) \dot{\chi}_{P1}^2 + \frac{1}{2} (I_{z_{m_1}} + m_1x_{m_1}^2) \dot{\chi}_1^2 + \dots + \right. \\
& \left. \frac{1}{2} (I_{z_{m_{10}}} + m_{10}x_{m_{10}}^2) \dot{\chi}_{10}^2 + \frac{1}{2} (I_{z_{P2}} + M_{P2}x_2^2) \dot{\chi}_{P2}^2 \right] + \\
& \left[ \frac{1}{2} (I_{x_{P1}} + M_{P1}x_1^2) \dot{\zeta}_{P1}^2 + \frac{1}{2} (I_{x_{m_1}} + m_1x_1^2) \dot{\zeta}_{m_1}^2 + \dots + \right. \\
& \left. \frac{1}{2} (I_{x_{m_{10}}} + m_{10}x_{m_{10}}^2) \dot{\zeta}_{m_{10}}^2 + \frac{1}{2} (I_{x_{P2}} + M_{P2}x_2^2) \dot{\zeta}_{P2}^2 \right]
\end{aligned} \tag{7.3.1}$$

## 7.4 Generalised Coordinates

Besides the generalised coordinates  $q_1$  to  $q_{29}$ , which are the rigid body, axial and torsional generalised coordinates, as discussed in section 6.4, the relative pendular generalised coordinates  $\chi_i$  and  $\zeta_i$  are included in this chapter, in which

- ▷ The generalised coordinates for the rigid body, axial elastic and torsional elastic motions have been discussed in sections 5.6 and 6.4, in which  $q_1$  to  $q_{29}$ .
- ▷ The generalised relative pendular coordinates  $\chi_i$  are for the relative pendular motions referenced on plane  $x_0 - O - y_0$ ,  $\chi_{P1}$  and  $\chi_{P2}$  are for the pendular motions of mass payloads  $M_{P1}$  and  $M_{P2}$ ,  $\chi_1$  to  $\chi_{10}$  are for the pendular motions of discrete mass points  $m_1$  to  $m_{10}$ , in which  $q_{30}$  to  $q_{41}$ .

▷ The generalised relative pendular coordinates  $\zeta_i$  are for the relative pendular motions referenced on plane  $z_0 - O - y_0$ ,  $\zeta_{P1}$  and  $\zeta_{P2}$  are for the pendular motions of mass payloads  $M_{P1}$  and  $M_{P2}$ ,  $\zeta_1$  to  $\zeta_{10}$  are for the pendular motions of discrete mass points  $m_1$  to  $m_{10}$ , in which  $q_{42}$  to  $q_{53}$ .

## 7.5 Generalised Forces

▷ The generalised forces  $Q_1$  to  $Q_{29}$  are the rigid body, axial and torsional generalised coordinates, as listed in Table 7.1.

▷ The generalised forces  $Q_{30}$  to  $Q_{53}$  are the pendular generalised forces for mass points  $m_i$  and payloads  $M_{P1}$  and  $M_{P2}$ , as listed in Table 7.2, which comes from an assumed dissipation function based on Rayleigh damping.

## 7.6 Governing Equations of Motion

Lagrange's equations are used to generate the governing equations of motion, the full equations are to be found in the path CD-ROM/axial-torsional-pendular/N10/, as listed in Tables 7.1 and 7.2.

Similar to Chapter 5, there are 53 nonlinear equations for 53 generalised coordinates of the flexible MMET system, and it has been found that the 'out of memory' problem solves the MMET system of coupled differential equations, as long as each variable has the appropriate number of conditions, as discussed in section 5.8.

To handle this problem and to speculate the interaction of the flexible MMET system, it has reduced discretisation scheme right down to  $N = 2$ , then we use Lagrange's equations to derive a reduced set of nonlinear governing equations for a simplified flexible MMET system, as shown in Appendix I, and the generalised coordinates for the MMET system with two discrete mass points are given in Table 7.3.

► The detail modelling procedure for a flexible MMET system with two discretised mass points are attached in Appendix I.

Table 7.1: Generalised coordinates and equations of motion (*CD-ROM/axial-torsional/N10/*)

i	$q_i$	$Q_i$	T	U	Equations of Motion
1	$\psi$	(3.5.13)	(7.3.1)	(7.2.1)	Chapter7-1-N10-psi.pdf
2	$\theta$	(3.5.14)			Chapter7-2-N10-theta.pdf
3	$\alpha$	(3.5.15)			Chapter7-3-N10-alpha.pdf
4	$\gamma$	(3.5.17)			Chapter7-4-N10-gamma.pdf
5	R	(3.5.16)			Chapter7-5-N10-R.pdf
6	$\eta_{P1}$	$-c_0(\dot{\eta}_{P1} - \dot{\eta}_1)$			Chapter7-6-N10-etaP1.pdf
7	$\eta_{P2}$	$-c_0(\dot{\eta}_{10} - \dot{\eta}_{P2})$			Chapter7-7-N10-etaP2.pdf
8	$\eta_1$	$c_0(\dot{\eta}_{P1} - \dot{\eta}_1) - c_0(\dot{\eta}_1 - \dot{\eta}_2)$			Chapter7-8-N10-eta1.pdf
9	$\eta_2$	$c_0(\dot{\eta}_1 - \dot{\eta}_2) - c_0(\dot{\eta}_2 - \dot{\eta}_3)$			Chapter7-9-N10-eta2.pdf
10	$\eta_3$	$c_0(\dot{\eta}_2 - \dot{\eta}_3) - c_0(\dot{\eta}_3 - \dot{\eta}_4)$			Chapter7-10-N10-eta3.pdf
11	$\eta_4$	$c_0(\dot{\eta}_3 - \dot{\eta}_4) - c_0(\dot{\eta}_4 - \dot{\eta}_5)$			Chapter7-11-N10-eta4.pdf
12	$\eta_5$	$c_0(\dot{\eta}_4 - \dot{\eta}_5) - c_0\dot{\eta}_5$			Chapter7-12-N10-eta5.pdf
13	$\eta_6$	$c_0(\dot{\eta}_7 - \dot{\eta}_6) - c_0\dot{\eta}_6$			Chapter7-13-N10-eta6.pdf
14	$\eta_7$	$c_0(\dot{\eta}_6 - \dot{\eta}_7) - c_0(\dot{\eta}_7 - \dot{\eta}_8)$			Chapter7-14-N10-eta7.pdf
15	$\eta_8$	$c_0(\dot{\eta}_7 - \dot{\eta}_8) - c_0(\dot{\eta}_8 - \dot{\eta}_9)$			Chapter7-15-N10-eta8.pdf
16	$\eta_9$	$c_0(\dot{\eta}_8 - \dot{\eta}_9) - c_0(\dot{\eta}_9 - \dot{\eta}_{10})$			Chapter7-16-N10-eta9.pdf
17	$\eta_{10}$	$c_0(\dot{\eta}_9 - \dot{\eta}_{10}) - c_0(\dot{\eta}_{10} - \dot{\eta}_{P2})$			Chapter7-17-N10-eta10.pdf
18	$\varphi_{P1}$	$-c_{t0}(\dot{\varphi}_{P1} - \dot{\varphi}_1)$			Chapter7-18-N10-phiP1.pdf
19	$\varphi_{P2}$	$-c_{t0}(\dot{\varphi}_{10} - \dot{\varphi}_{P2})$			Chapter7-19-N10-phiP2.pdf
20	$\varphi_1$	$c_{t0}(\dot{\varphi}_{P1} - \dot{\varphi}_1) - c_{t0}(\dot{\varphi}_1 - \dot{\varphi}_2)$			Chapter7-20-N10-phi1.pdf
21	$\varphi_2$	$c_{t0}(\dot{\varphi}_1 - \dot{\varphi}_2) - c_{t0}(\dot{\varphi}_2 - \dot{\varphi}_3)$			Chapter7-21-N10-phi2.pdf
22	$\varphi_3$	$c_{t0}(\dot{\varphi}_2 - \dot{\varphi}_3) - c_{t0}(\dot{\varphi}_3 - \dot{\varphi}_4)$			Chapter7-22-N10-phi3.pdf
23	$\varphi_4$	$c_{t0}(\dot{\varphi}_3 - \dot{\varphi}_4) - c_{t0}(\dot{\varphi}_4 - \dot{\varphi}_5)$			Chapter7-23-N10-phi4.pdf
24	$\varphi_5$	$c_{t0}(\dot{\varphi}_4 - \dot{\varphi}_5) - c_{t0}\dot{\varphi}_5$			Chapter7-34-N10-phi5.pdf
25	$\varphi_6$	$c_{t0}(\dot{\varphi}_7 - \dot{\varphi}_6) - c_{t0}\dot{\varphi}_6$			Chapter7-25-N10-phi6.pdf
26	$\varphi_7$	$c_{t0}(\dot{\varphi}_6 - \dot{\varphi}_7) - c_{t0}(\dot{\varphi}_7 - \dot{\varphi}_8)$			Chapter7-26-N10-phi7.pdf
27	$\varphi_8$	$c_{t0}(\dot{\varphi}_7 - \dot{\varphi}_8) - c_{t0}(\dot{\varphi}_8 - \dot{\varphi}_9)$			Chapter7-27-N10-phi8.pdf
28	$\varphi_9$	$c_{t0}(\dot{\varphi}_8 - \dot{\varphi}_9) - c_{t0}(\dot{\varphi}_9 - \dot{\varphi}_{10})$			Chapter7-28-N10-phi9.pdf
29	$\varphi_{10}$	$c_{t0}(\dot{\varphi}_9 - \dot{\varphi}_{10}) - c_{t0}(\dot{\varphi}_{10} - \dot{\varphi}_{P2})$			Chapter7-29-N10-phi10.pdf

Table 7.2: Generalised coordinates and equations of motion (*CD-ROM/axial-torsional/N10/*) (continue)

i	$q_i$	$Q_i$	T U	Equations of Motion
30	$\chi_{P1}$	$-c_{10}(\dot{\chi}_{P1} - \dot{\chi}_1)$		Chapter7-30-N10-chiP1.pdf
31	$\chi_{P2}$	$-c_{10}(\dot{\chi}_{10} - \dot{\chi}_{P2})$		Chapter7-31-N10-chiP2.pdf
32	$\chi_1$	$c_{10}(\dot{\chi}_{P1} - \dot{\chi}_1) - c_{10}(\dot{\chi}_1 - \dot{\chi}_2)$		Chapter7-32-N10-chi1.pdf
33	$\chi_2$	$c_{10}(\dot{\chi}_1 - \dot{\chi}_2) - c_{10}(\dot{\chi}_2 - \dot{\chi}_3)$		Chapter7-33-N10-chi2.pdf
34	$\chi_3$	$c_{10}(\dot{\chi}_2 - \dot{\chi}_3) - c_{10}(\dot{\chi}_3 - \dot{\chi}_4)$		Chapter7-34-N10-chi3.pdf
35	$\chi_4$	$c_{10}(\dot{\chi}_3 - \dot{\chi}_4) - c_{10}(\dot{\chi}_4 - \dot{\chi}_5)$		Chapter7-35-N10-chi4.pdf
36	$\chi_5$	$c_{10}(\dot{\chi}_4 - \dot{\chi}_5) - c_{10}\dot{\chi}_5$		Chapter7-36-N10-chi5.pdf
37	$\chi_6$	$c_{10}(\dot{\chi}_7 - \dot{\chi}_6) - c_{10}\dot{\chi}_6$		Chapter7-37-N10-chi6.pdf
38	$\chi_7$	$c_{10}(\dot{\chi}_6 - \dot{\chi}_7) - c_{10}(\dot{\chi}_7 - \dot{\chi}_8)$		Chapter7-38-N10-chi7.pdf
39	$\chi_8$	$c_{10}(\dot{\chi}_7 - \dot{\chi}_8) - c_{10}(\dot{\chi}_8 - \dot{\chi}_9)$		Chapter7-39-N10-chi8.pdf
40	$\chi_9$	$c_{10}(\dot{\chi}_8 - \dot{\chi}_9) - c_{10}(\dot{\chi}_9 - \dot{\chi}_{10})$		Chapter7-40-N10-chi9.pdf
41	$\chi_{10}$	$c_{10}(\dot{\chi}_9 - \dot{\chi}_{10}) - c_{10}(\dot{\chi}_{10} - \dot{\chi}_{P2})$		Chapter7-41-N10-chi10.pdf
42	$\zeta_{P1}$	$-c_{10}(\dot{\zeta}_{P1} - \dot{\zeta}_1)$		Chapter7-42-N10-zetaP1.pdf
43	$\zeta_{P2}$	$-c_{10}(\dot{\zeta}_{10} - \dot{\zeta}_{P2})$		Chapter7-43-N10-zetaP2.pdf
44	$\zeta_1$	$c_{10}(\dot{\zeta}_{P1} - \dot{\zeta}_1) - c_{10}(\dot{\zeta}_1 - \dot{\zeta}_2)$		Chapter7-44-N10-zeta1.pdf
45	$\zeta_2$	$c_{10}(\dot{\zeta}_1 - \dot{\zeta}_2) - c_{10}(\dot{\zeta}_2 - \dot{\zeta}_3)$		Chapter7-45-N10-zeta2.pdf
46	$\zeta_3$	$c_{10}(\dot{\zeta}_2 - \dot{\zeta}_3) - c_{10}(\dot{\zeta}_3 - \dot{\zeta}_4)$		Chapter7-46-N10-zeta3.pdf
47	$\zeta_4$	$c_{10}(\dot{\zeta}_3 - \dot{\zeta}_4) - c_{10}(\dot{\zeta}_4 - \dot{\zeta}_5)$		Chapter7-47-N10-zeta4.pdf
48	$\zeta_5$	$c_{10}(\dot{\zeta}_4 - \dot{\zeta}_5) - c_{10}\dot{\zeta}_5$		Chapter7-48-N10-zeta5.pdf
49	$\zeta_6$	$c_{10}(\dot{\zeta}_7 - \dot{\zeta}_6) - c_{10}\dot{\zeta}_6$		Chapter7-49-N10-zeta6.pdf
50	$\zeta_7$	$c_{10}(\dot{\zeta}_6 - \dot{\zeta}_7) - c_{10}(\dot{\zeta}_7 - \dot{\zeta}_8)$		Chapter7-50-N10-zeta7.pdf
51	$\zeta_8$	$c_{10}(\dot{\zeta}_7 - \dot{\zeta}_8) - c_{10}(\dot{\zeta}_8 - \dot{\zeta}_9)$		Chapter7-51-N10-zeta8.pdf
52	$\zeta_9$	$c_{10}(\dot{\zeta}_8 - \dot{\zeta}_9) - c_{10}(\dot{\zeta}_9 - \dot{\zeta}_{10})$		Chapter7-52-N10-zeta9.pdf
53	$\zeta_{10}$	$c_{10}(\dot{\zeta}_9 - \dot{\zeta}_{10}) - c_{10}(\dot{\zeta}_{10} - \dot{\zeta}_{P2})$		Chapter7-53-N10-zeta10.pdf

Table 7.3: Generalised coordinates and equations of motion (*CD-ROM/axial-torsional/N2/*)

$i$	$q_i$	$Q_i$	T	U	Equations of Motion
1	$\psi$	(3.5.13)	(I.2.1)	(I.1.1)	Chapter7-1-N2-psi.pdf
2	$\theta$	(3.5.14)			Chapter7-2-N2-theta.pdf
3	$\alpha$	(3.5.15)			Chapter7-3-N2-alpha.pdf
4	$\gamma$	(3.5.17)			Chapter7-4-N2-gamma.pdf
5	R	(3.5.16)			Chapter7-5-N2-R.pdf
6	$\eta_{P1}$	$-c_0(\dot{\eta}_{P1} - \dot{\eta}_1)$			Chapter7-6-N2-etaP1.pdf
7	$\eta_{P2}$	$-c_0(\dot{\eta}_2 - \dot{\eta}_{P2})$			Chapter7-7-N2-etaP2.pdf
8	$\eta_1$	$c_0(\dot{\eta}_{P1} - \dot{\eta}_1) - c_0\dot{\eta}_1$			Chapter7-8-N2-eta1.pdf
9	$\eta_2$	$c_0(\dot{\eta}_{P2} - \dot{\eta}_2) - c_0\dot{\eta}_2$			Chapter7-9-N2-eta2.pdf
10	$\varphi_{P1}$	$-c_{t0}(\dot{\varphi}_{P1} - \dot{\varphi}_1)$			Chapter7-10-N2-phiP1.pdf
11	$\varphi_{P2}$	$-c_{t0}(\dot{\varphi}_2 - \dot{\varphi}_{P2})$			Chapter7-11-N2-phiP2.pdf
12	$\varphi_1$	$c_{t0}(\dot{\varphi}_{P1} - \dot{\varphi}_1) - c_{t0}\dot{\varphi}_1$			Chapter7-12-N2-phi1.pdf
13	$\varphi_2$	$c_{t0}(\dot{\varphi}_{P2} - \dot{\varphi}_2) - c_{t0}\dot{\varphi}_2$			Chapter7-13-N2-phi2.pdf
14	$\chi_{P1}$	$-c_{l0}(\dot{\chi}_{P1} - \dot{\chi}_1)$			Chapter7-10-N2-chiP1.pdf
15	$\chi_{P2}$	$-c_{l0}(\dot{\chi}_2 - \dot{\chi}_{P2})$			Chapter7-11-N2-chiP2.pdf
16	$\chi_1$	$c_{l0}(\dot{\chi}_{P1} - \dot{\chi}_1) - c_{l0}\dot{\chi}_1$			Chapter7-12-N2-chi1.pdf
17	$\chi_2$	$c_{l0}(\dot{\chi}_{P2} - \dot{\chi}_2) - c_{l0}\dot{\chi}_2$			Chapter7-13-N2-chi2.pdf
18	$\zeta_{P1}$	$-c_{l0}(\dot{\zeta}_{P1} - \dot{\zeta}_1)$			Chapter7-10-N2-zetaP1.pdf
19	$\zeta_{P2}$	$-c_{l0}(\dot{\zeta}_2 - \dot{\zeta}_{P2})$			Chapter7-11-N2-zetaP2.pdf
20	$\zeta_1$	$c_{l0}(\dot{\zeta}_{P1} - \dot{\zeta}_1) - c_{l0}\dot{\zeta}_1$			Chapter7-12-N2-zeta1.pdf
21	$\zeta_2$	$c_{l0}(\dot{\zeta}_{P2} - \dot{\zeta}_2) - c_{l0}\dot{\zeta}_2$			Chapter7-13-N2-zeta2.pdf

## 7.7 Simulations and Discussions

Figures 7.5 to 7.25 are the numerical results obtained by MATHEMATICA for the flexible MMET system with two discrete mass points, and the motion equations are listed in Table 7.3. The figures in this section are the selected numerical results for the flexible MMET system over a short simulation time (the number of cycles of period,  $T_n = 4.01$ ) and long simulation time (the number of cycles of period,  $T_n = 400.01$ ), respectively, as given in Appendix C.

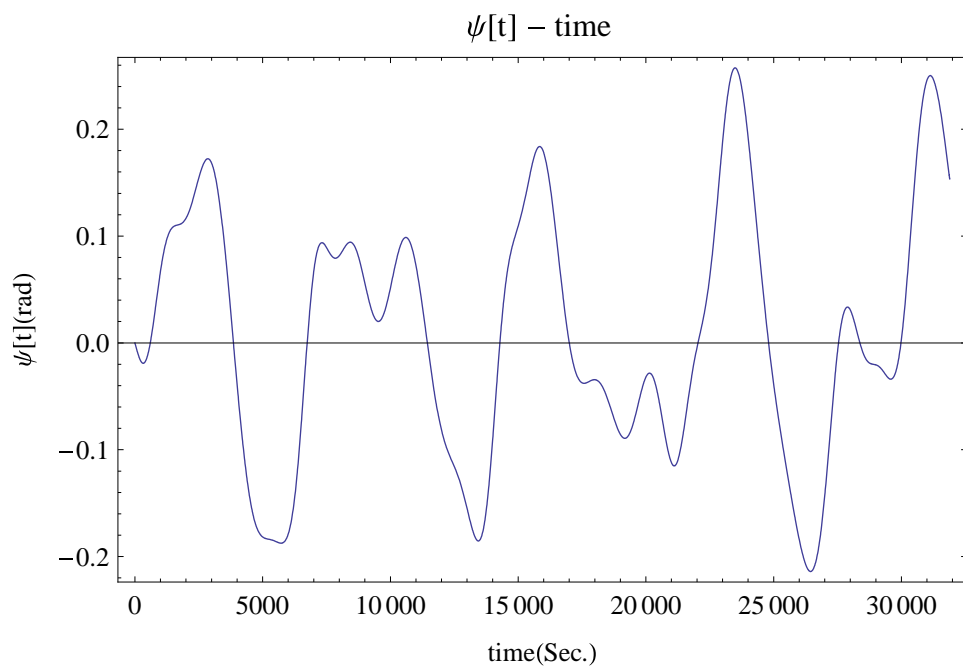


Figure 7.5: The flexible MMET system spin-up  $\psi$  ( $T_n = 4.01$ )

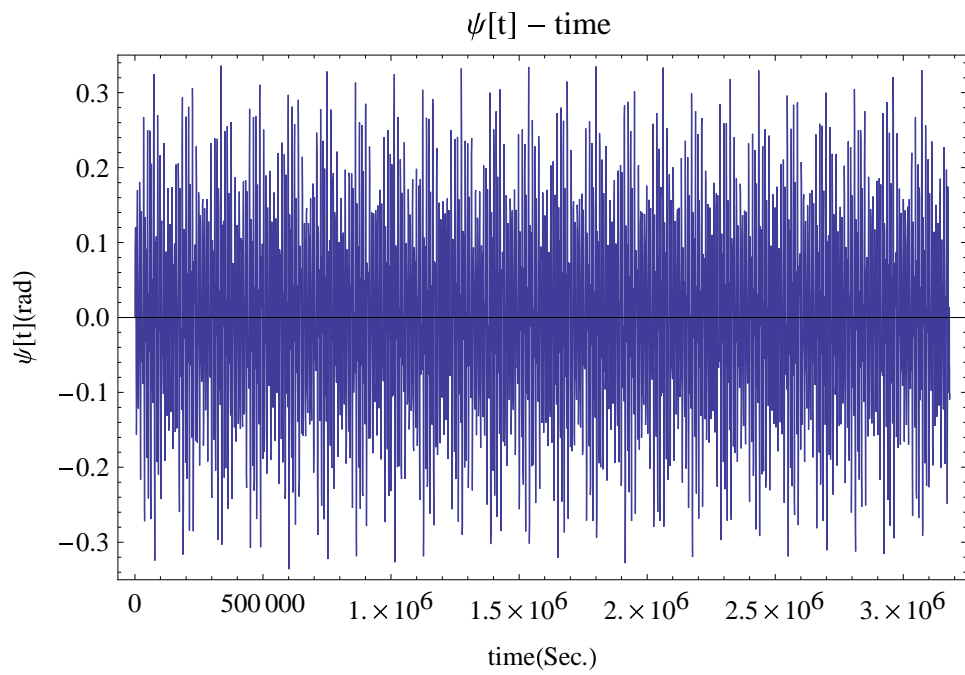


Figure 7.6: The flexible MMET system spin-up  $\psi$  ( $T_n = 400.01$ )

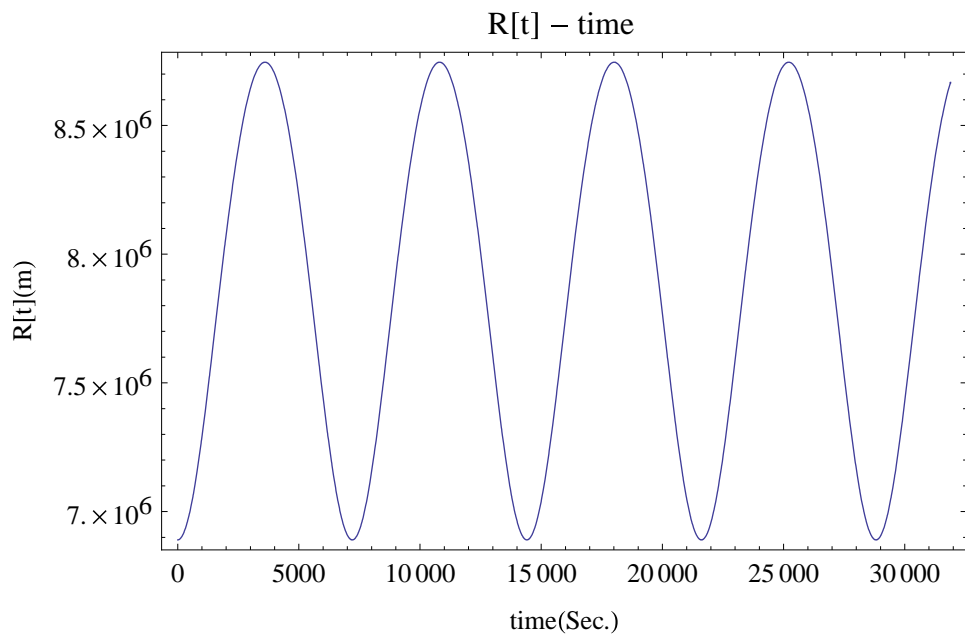


Figure 7.7: The flexible MMET system base point distance  $R$  ( $T_n = 4.01$ )

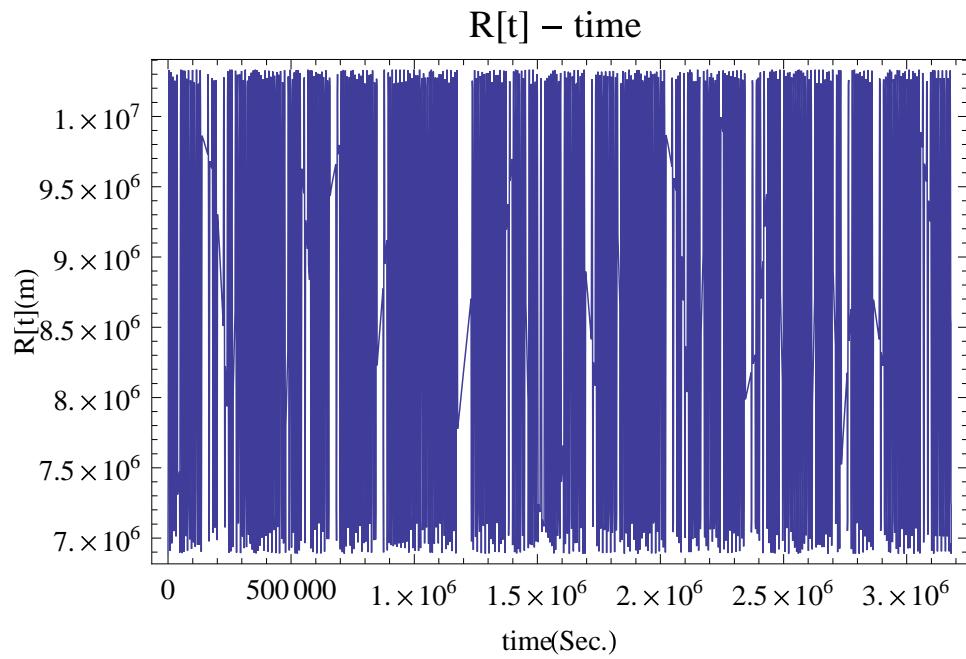


Figure 7.8: The flexible MMET system base point distance of  $R$  ( $T_n = 400.01$ )

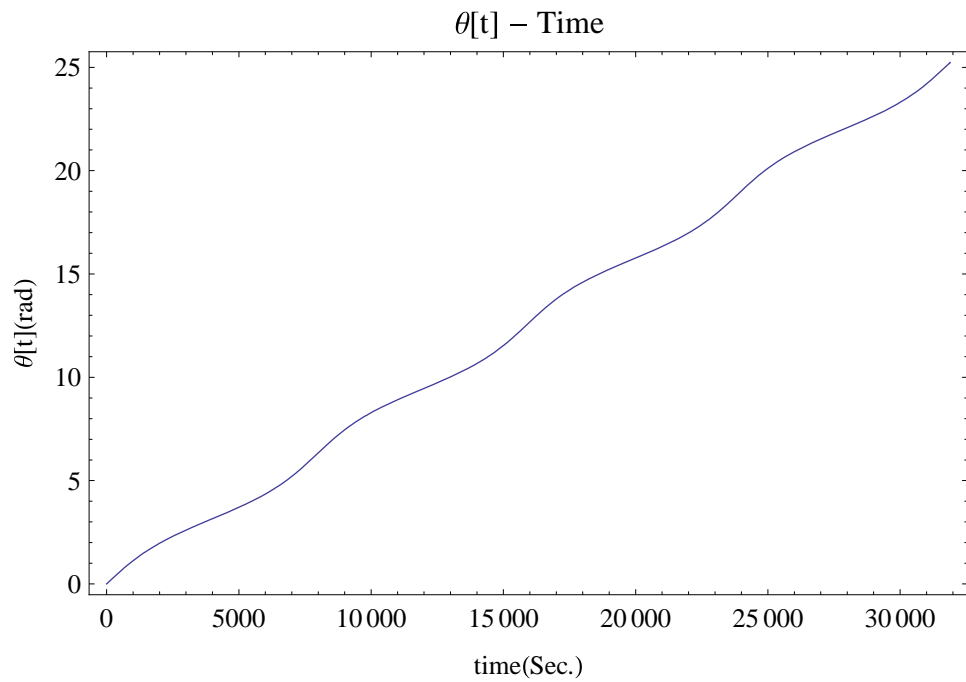


Figure 7.9: The flexible MMET system elliptical orbit angular position of  $\theta$  ( $T_n = 4.01$ )

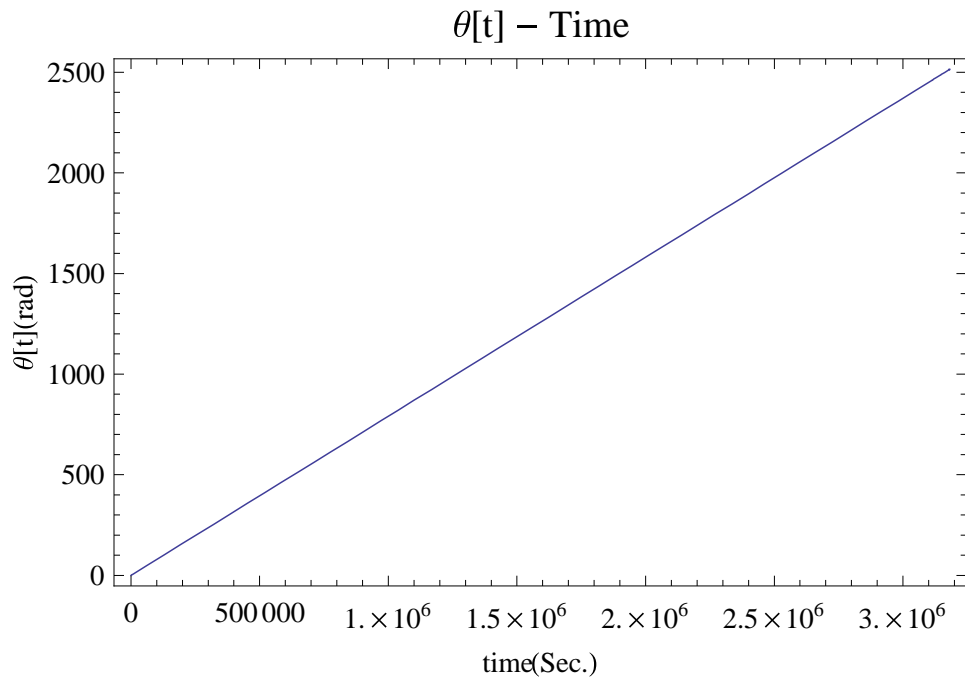


Figure 7.10: The flexible MMET system elliptical orbit angular position of  $\theta$  ( $T_n = 400.01$ )

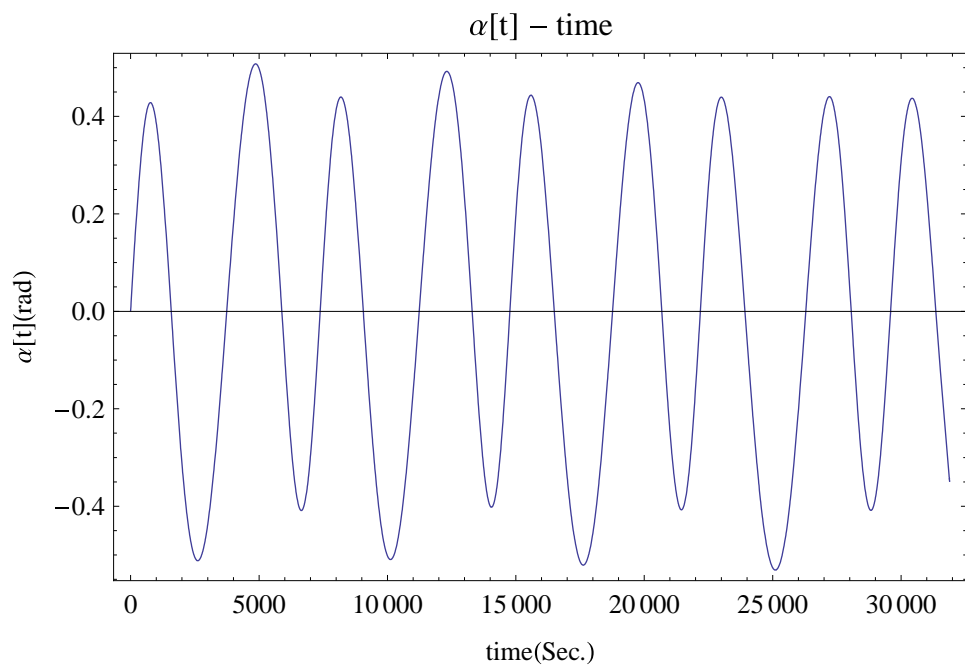


Figure 7.11: The flexible MMET system out-of-plane angle  $\alpha$  ( $T_n = 4.01$ )

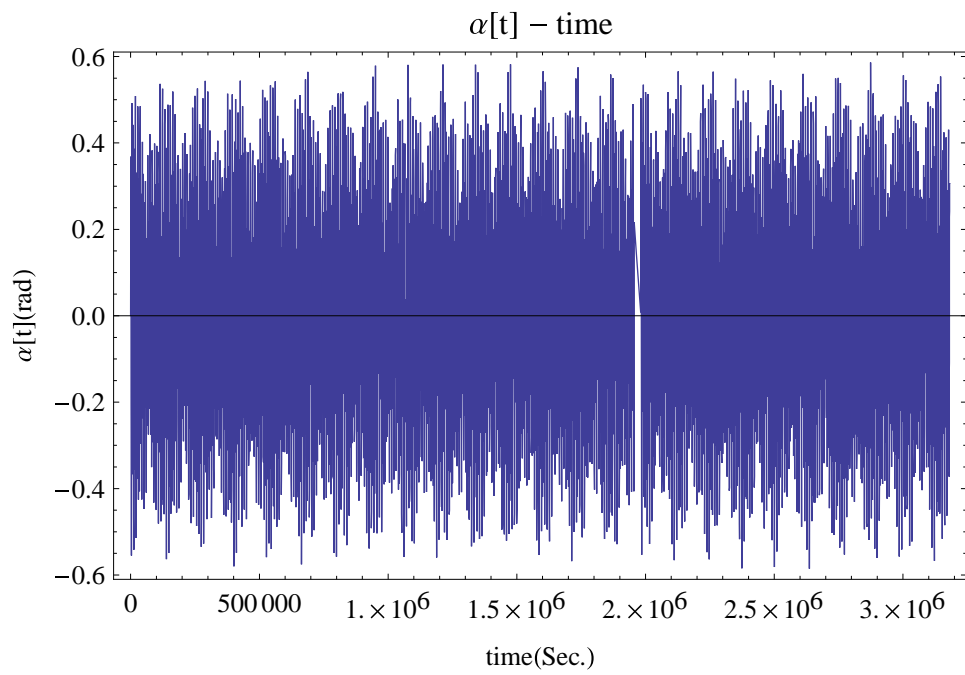


Figure 7.12: The flexible MMET system out-of-plane angle  $\alpha$  ( $T_n = 400.01$ )

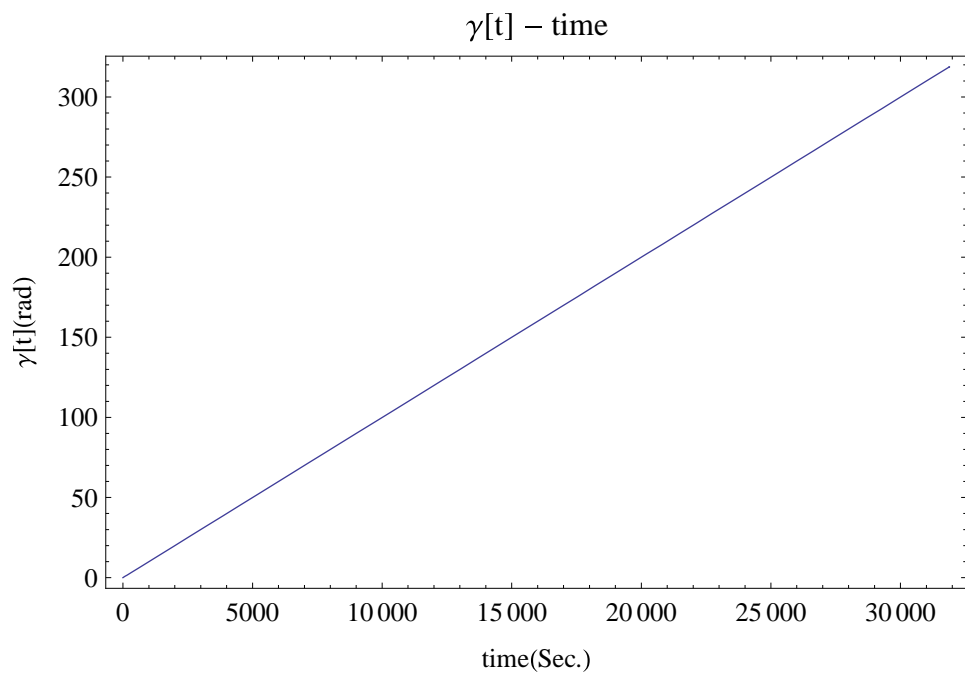


Figure 7.13: The flexible MMET system rolling angle  $\gamma$  ( $T_n = 4.01$ )

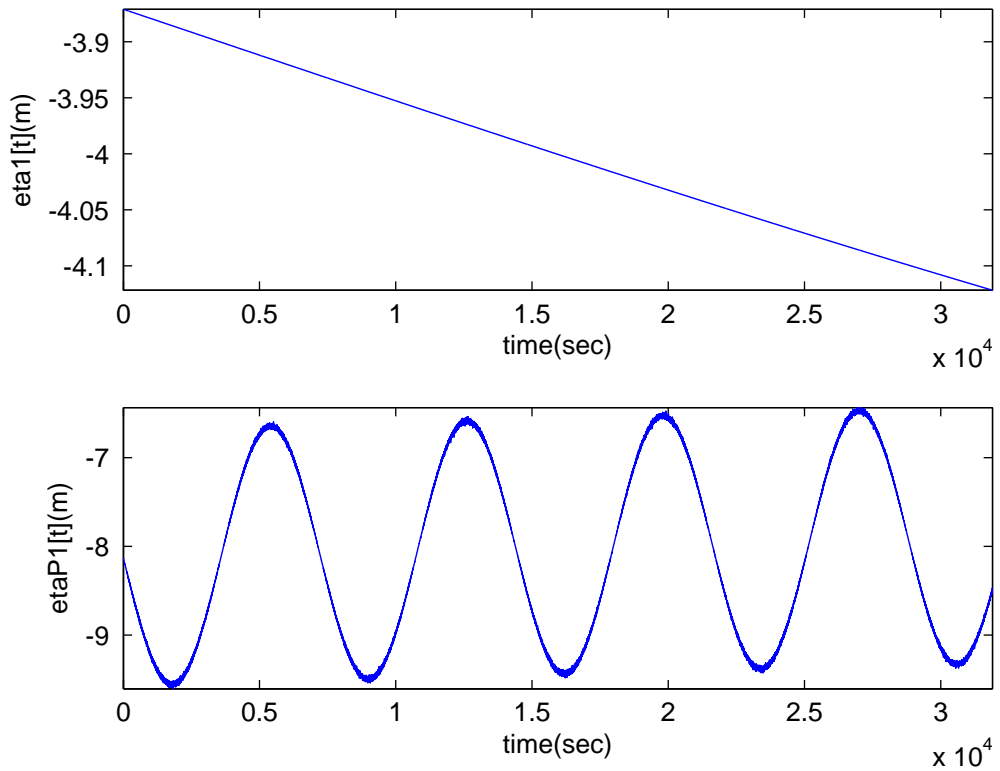


Figure 7.14: Axial displacement responses  $\eta_1$  and  $\eta_{P1}$  ( $T_n = 4.01$ )

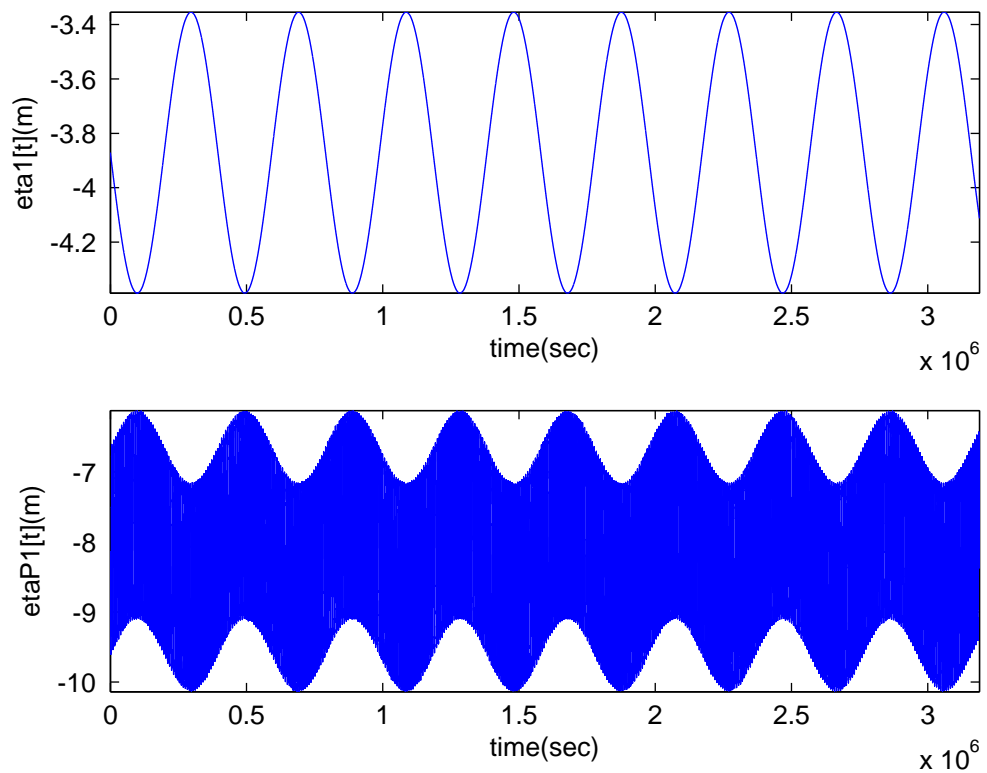


Figure 7.15: Axial displacement responses  $\eta_1$  and  $\eta_{P1}$  ( $T_n = 400.01$ )

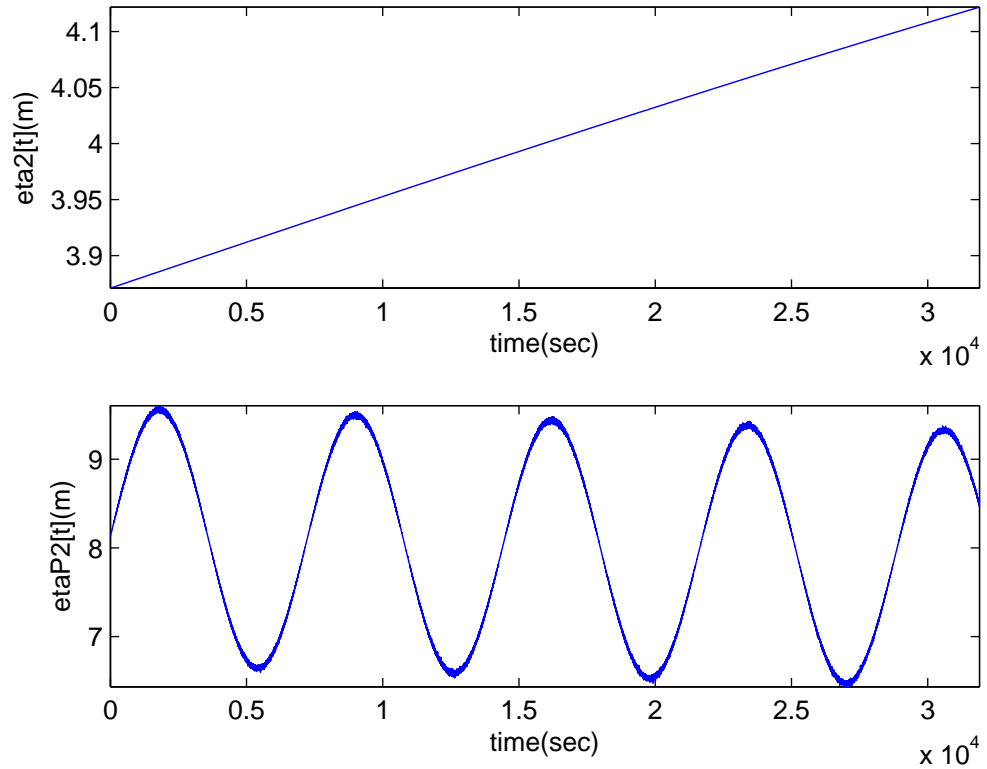


Figure 7.16: Axial displacement responses  $\eta_2$  and  $\eta_{P2}$  ( $T_n = 4.01$ )

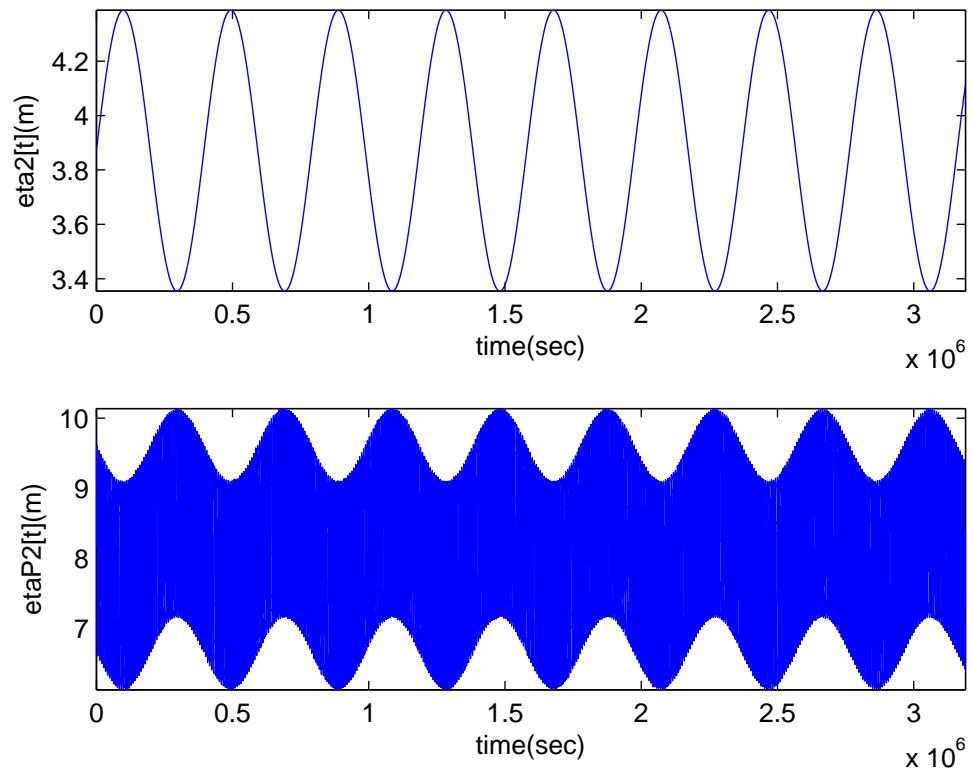


Figure 7.17: Axial displacement responses  $\eta_2$  and  $\eta_{P2}$  ( $T_n = 400.01$ )

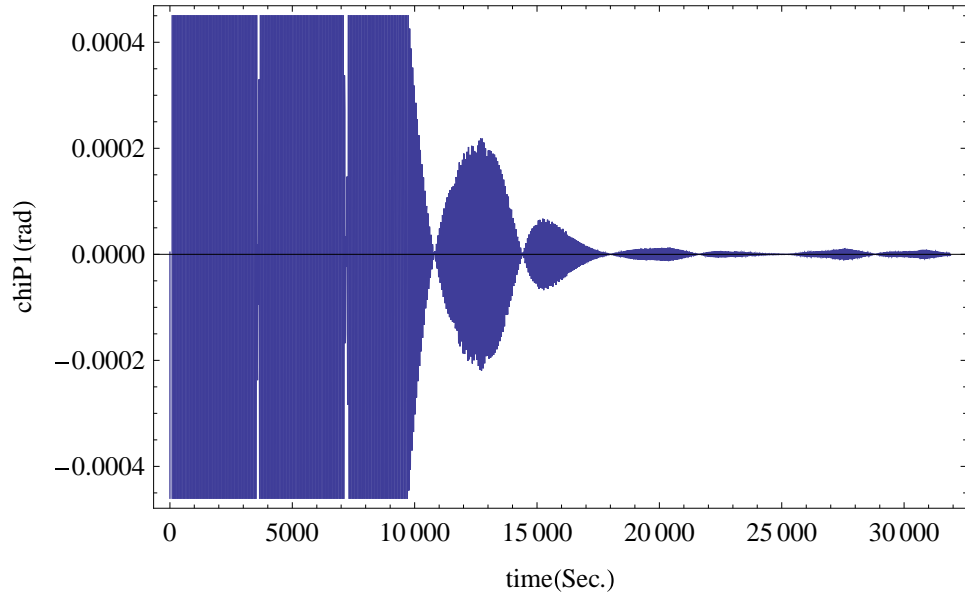


Figure 7.18: Pendular displacement response  $\chi_{P1}$  ( $T_n = 4.01$ )

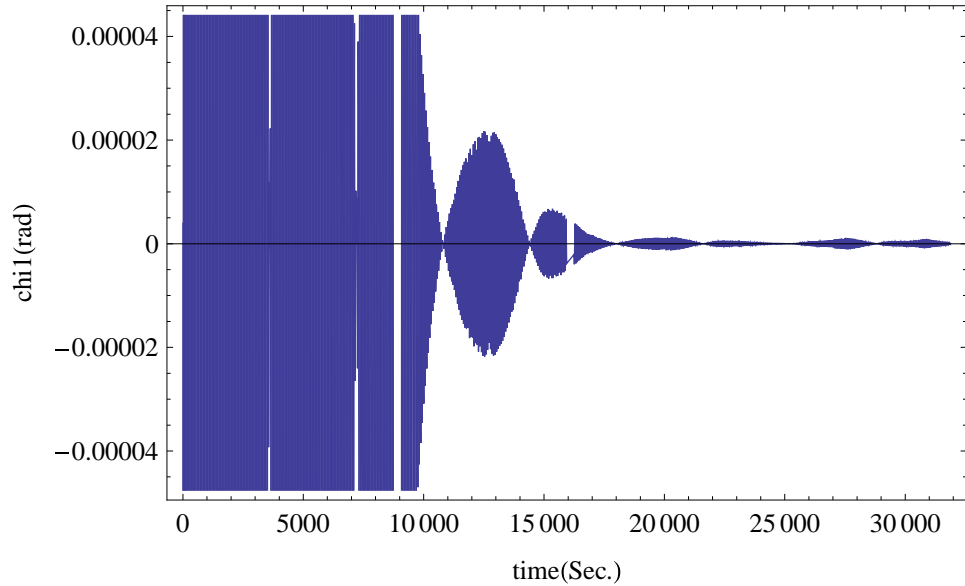


Figure 7.19: Pendular displacement response  $\chi_I$  ( $T_n = 4.01$ )

- ▷ Figures 7.5 and 7.6 are the plots for the flexible MMET system spin-up behaviour, which varies within the range -0.32 to 0.32 rad, and their shapes are different from the responses for the MMET systems with axial or torsional elasticity.
- ▷ As shown in Figures 7.7 and 7.8,  $R$  is the distance from the Earth to the MMET system COM over simulation time  $T_n = 4.01$  and  $400.01$ , which varies within the range of  $r_p$  to  $r_a$ , and together with Figures 7.9 and 7.10 for the true anomaly  $\theta$ , which indicate that the MMET system goes around the Earth periodically on an elliptical orbit.

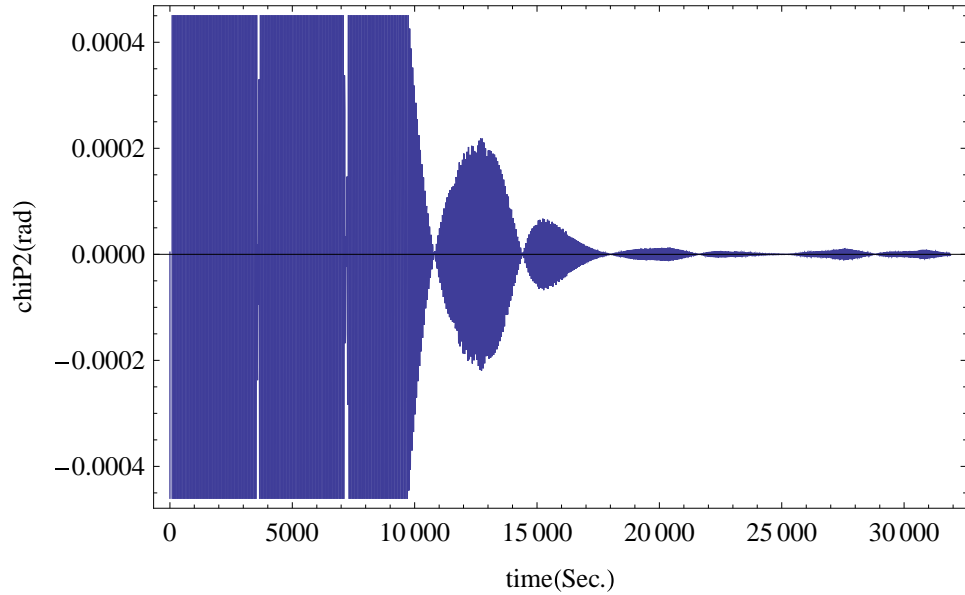


Figure 7.20: Pendular displacement response  $\chi_{P2}$  ( $T_n = 4.01$ )

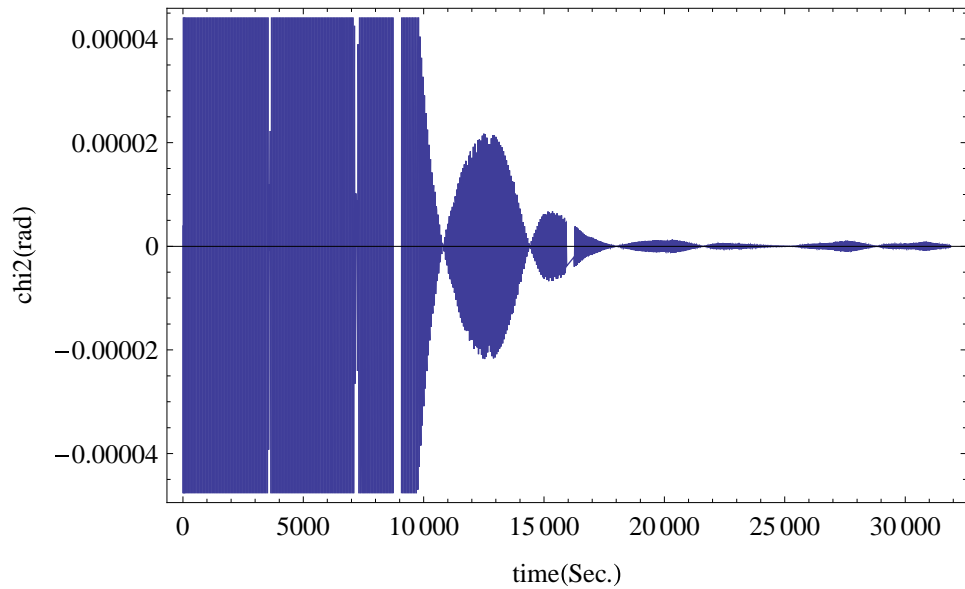


Figure 7.21: Pendular displacement response  $\chi_2$  ( $T_n = 4.01$ )

▷ Figures 7.11 and 7.12 are out-of-plane angle  $\alpha$  responses, which are changing within -0.6 to 0.6 rad fluctuatedly.

▷ As shown in Figure 7.13, the rigid rolling angle  $\gamma$  stays in a steady linear increasing trend, with given non-zero initial conditions  $\gamma(0) = 0.001$  rad and  $\dot{\gamma}(0) = 0.001$  rad/s. As also discussed in sections 6.7 and 5.9, since the motion of  $\gamma$  is independent of the other motions, the zero initial value setting can help to control this rigid body rolling motion.

▷ Figures 7.14 and 7.15 are the axial elastic plots for the discrete mass point  $m_1$  and payload  $M_{P1}$ , Figures 7.16 and 7.17 are the axial elastic plots for the discrete mass

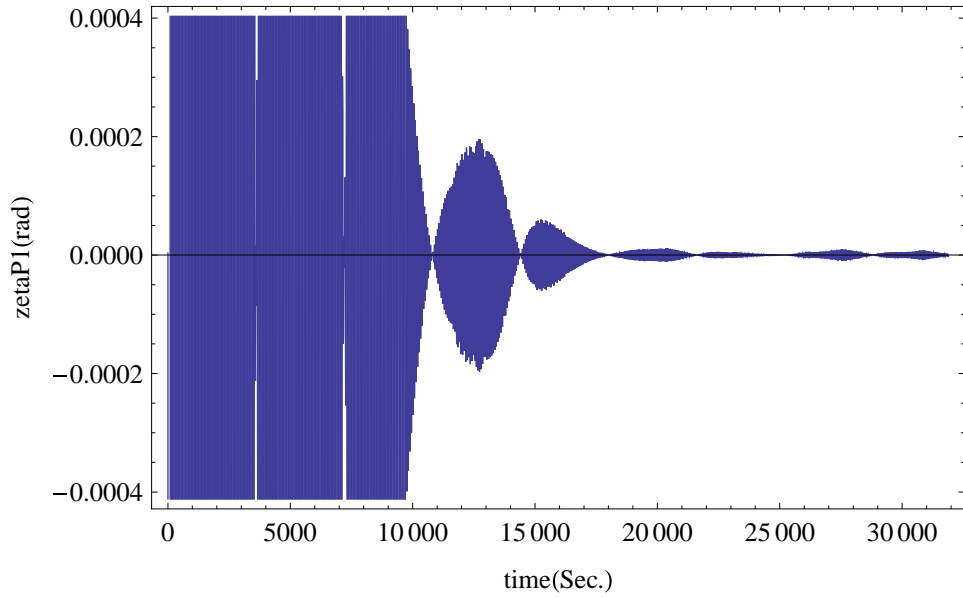


Figure 7.22: Pendular displacement response  $\zeta_{P1}$  ( $T_n = 4.01$ )

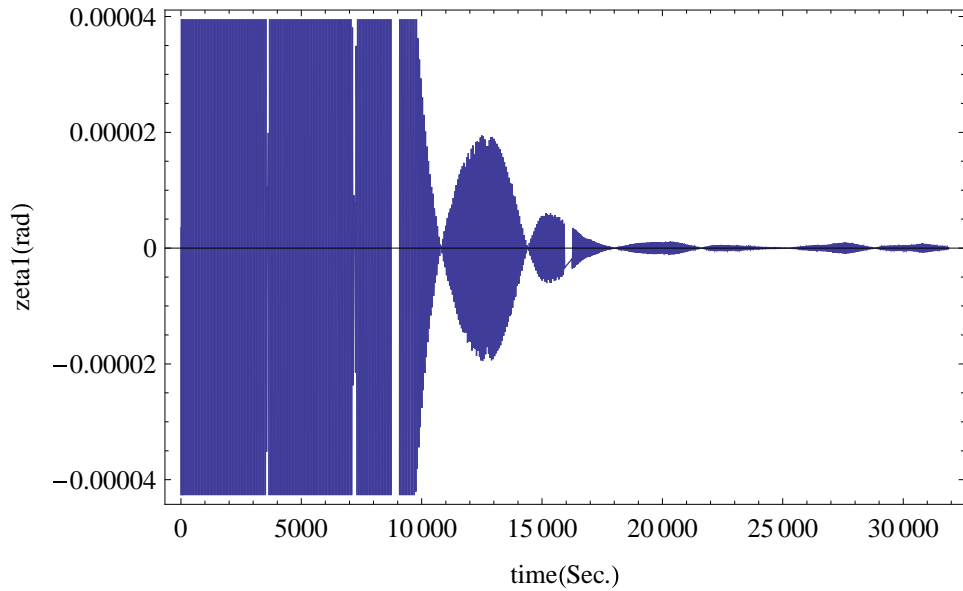


Figure 7.23: Pendular displacement response  $\zeta_I$  ( $T_n = 4.01$ )

point  $m_2$  and payload  $M_{P2}$ , which express the MMET system's axial elastic motions along each of the tether subspans over the simulation time  $T_n = 4.01$  and  $400.01$ , symmetrically.

The  $\eta_1$ 's response keeps steadily within the range  $-3.4$  to  $-4.4$  metre and the  $\eta_{P1}$ 's response are within the range  $-6$  to  $-10.5$  metre, meanwhile,  $\eta_2$  and  $\eta_{P2}$ 's motions are symmetric to  $\eta_1$  and  $\eta_{P1}$ 's motions with respect to the MMET system COM, whose ranges are  $3.4$  to  $4.4$  metre and  $6$  to  $10.5$  metre, respectively.

Similar to sections 5.9 and 6.7, the curves of  $\eta_1$  and  $\eta_2$  are with larger period than  $\eta_{P1}$  and  $\eta_{P2}$ 's responses respectively. Besides, they are also carrying some tiny oscillations

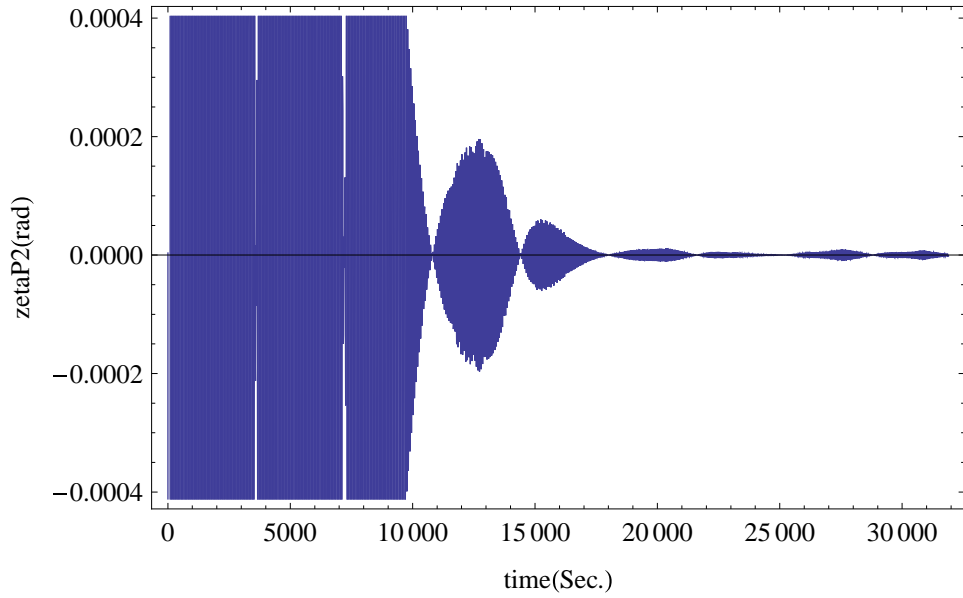


Figure 7.24: Pendular displacement response  $\zeta_{P2}$  ( $T_n = 4.01$ )

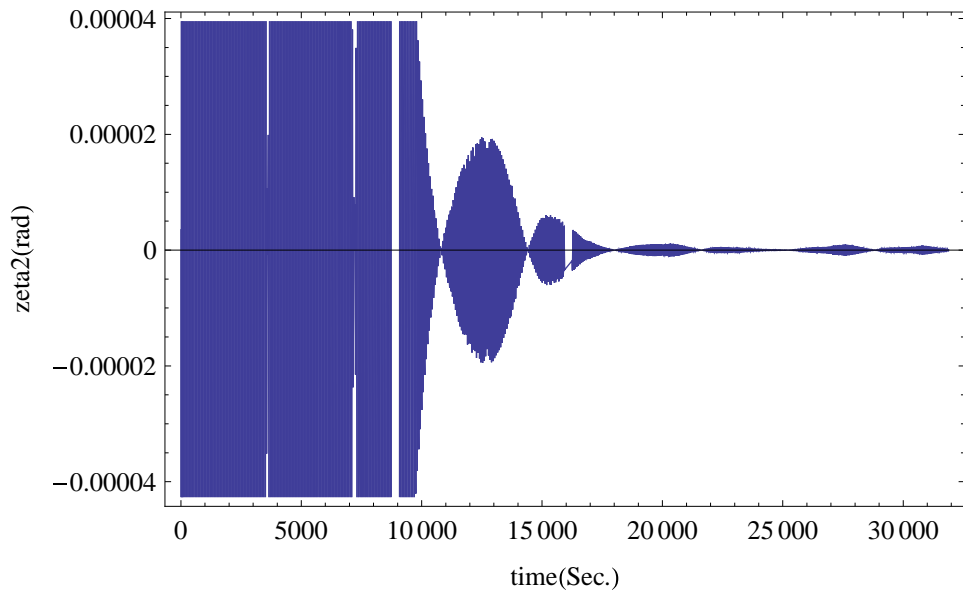


Figure 7.25: Pendular displacement response  $\zeta_2$  ( $T_n = 4.01$ )

at  $\eta_{P1}$  and  $\eta_{P2}$ 's peaks and bottoms, as can be observed in Figures 7.14 and 7.16.

▷ The torsional motions are the same as Chapters 5 and 6, for the rigid body rolling angel is a stand-alone variable in the MMET system, which is decoupled from other generalised coordinates, and the torsional motions have been discussed in Chapters 5 and 6.

▷ For the pendular motions referenced on plane  $x_0 - O - y_0$ , Figures 7.18 and 7.19 are the pendular responses for  $M_{P1}$  and  $m_1$ , and Figures 7.20 and 7.21 are the pendular responses for  $M_{P2}$  and  $m_2$  over the simulation time  $T_n = 4.01$ .

The pendular motions  $\chi_{P1}$  and  $\chi_{P2}$  for the payloads  $M_{P1}$  and  $M_{P2}$  move with ups and

downs within the range of  $-0.00045$  and  $0.00045$  rad, and the pendular motions  $\chi_1$  and  $\chi_2$  for the discrete mass points  $m_1$  and  $m_2$  move within  $-0.000045$  and  $0.000045$  rad.

▷ Similarly, for the pendular motions referenced on plane  $z_0 - O - y_0$ , Figures 7.22 and 7.23 are the pendular responses for payload  $M_{P1}$  and mass point  $m_1$ , and Figures 7.24 and 7.25 are the pendular responses for payload  $M_{P2}$  and mass point  $m_2$ . The pendular motions  $\zeta_{P1}$  and  $\zeta_{P2}$  move within the range  $-0.00045$  and  $0.00045$  rad and with reducing oscillations for payloads  $M_{P1}$  and  $M_{P2}$ , and the pendular motions  $\zeta_1$  and  $\zeta_2$  go within a range of  $-0.000045$  and  $0.000045$  rad for mass points  $m_1$  and  $m_2$ .

Figures 7.18 to 7.25 are the pendular elastic angular displacement on plane  $x_0 - O - y_0$  and plane  $z_0 - O - y_0$ , respectively, which indicate that the convergent pendular elastic behaviours are also observed with reducing amplitude of oscillation and approaching to zero. By involving the tether's mass and mass moment of inertia, their amplitude and shape are smaller and different from massless flexible MMET system's response.

## 7.8 Conclusions

A MDOF discretised flexible MMET system with an arbitrary choice of  $N = 10$  mass points on elliptical orbit has been discussed in this chapter, in which, which includes not only axial and torsional elasticity, but also the pendular elasticity as well.

As there were two parts of the pendular elasticity, referenced on the plane  $x_0 - O - y_0$  and the plane  $z_0 - O - y_0$ ,  $\chi_i$  and  $\zeta_i$  were selected as the generalised coordinates for the two parts of motions related to pendular elasticity, respectively. By using Lagrange's equations, a  $N = 10$  flexible MMET system has been built, then, in order to handle the numerical simulation time-consuming difficulties on the current computational system, a flexible MMET system with  $N = 2$  mass points has been proposed to reduce the number of the nonlinear ordinary differential equations, which can balance the numerical performance and the MDOF discretisation scheme for the MMET system, as shown in Appendix I.

Table 7.4: Figures for spin-up  $\psi$  in Chapters 5,6 and 7

Tether Type	Figure No. ( $T_n = 400.01$ )	Figure No. ( $T_n = 4.01$ )
Axial Elastic	5.4	5.5
Axial and Torsional Elastic	6.3	6.4
Flexible	7.5	7.6

To summarise, the numerical results in Chapters 5, 6 and 7 are listed in Tables 7.4 to 7.13.

Table 7.5: Figures for R in Chapters 5,6 and 7

Tether Type	Figure No. ( $T_n = 400.01$ )	Figure No. ( $T_n = 4.01$ )
Axial Elastic	5.6	5.7
Axial and Torsional Elastic	6.7	6.8
Flexible	7.7	7.8

Table 7.6: Figures for  $\theta$  in Chapters 5,6 and 7

Tether Type	Figure No. ( $T_n = 400.01$ )	Figure No. ( $T_n = 4.01$ )
Axial Elastic	5.9	5.8
Axial and Torsional Elastic	6.6	6.5
Flexible	7.10	7.9

Table 7.7: Figures for  $\alpha$  in Chapters 5,6 and 7

Tether Type	Figure No. ( $T_n = 400.01$ )	Figure No. ( $T_n = 4.01$ )
Axial Elastic	5.11	5.10
Axial and Torsional Elastic	6.10	6.9
Flexible	7.12	7.11

Table 7.8: Figures for  $\gamma$  in Chapters 5,6 and 7

Tether Type	Figure No. ( $T_n = 400.01$ )	Figure No. ( $T_n = 4.01$ )
Axial Elastic	-	5.12
Axial and Torsional Elastic	-	6.11
Flexible	-	7.13

Table 7.9: Figures for  $\eta_1$  and  $\eta_{P1}$  in Chapters 5,6 and 7

Tether Type	Figure No. ( $T_n = 400.01$ )	Figure No. ( $T_n = 4.01$ )
Axial Elastic	5.14	5.13
Axial and Torsional Elastic	6.13	6.12
Flexible	7.15	7.14

Table 7.10: Figures for  $\eta_2$  and  $\eta_{P2}$  Chapters 5,6 and 7

Tether Type	Figure No. ( $T_n = 400.01$ )	Figure No. ( $T_n = 4.01$ )
Axial Elastic	5.17	5.16
Axial and Torsional Elastic	6.15	6.14
Flexible	7.15	7.16

Table 7.11: Torsional elastic motions figures for Chapters 6 and 7

Tether Type	Figure No. ( $T_n = 400.01$ )	Figure No. ( $T_n = 4.01$ )
$\varphi_{P1}$	6.16	-
$\varphi_1$	6.17	-
$\varphi_{P2}$	6.18	-
$\varphi_2$	6.19	-

- Table 7.4 gives the spin-up  $\psi$  plots for the MMET tether systems with discrete mass points, with the given parameters in Appendix C. The  $\psi$  results in Chapters 5 and 6 are with same range -0.325 to 0.325 rad, the  $\psi$  results in Chapter 7 are with smaller

Table 7.12: Figures for pendular elasticity in Chapter 7 - plane  $x_0 - O - y_0$

Tether Type	Figure No. ( $T_n = 400.01$ )	Figure No. ( $T_n = 4.01$ )
$\chi_{P1}$	-	7.20
$\chi_1$	-	7.19
$\chi_{P2}$	-	7.20
$\chi_2$	-	7.21

Table 7.13: Figures for pendular elasticity in Chapter 7 - plane  $z_0 - O - y_0$

Tether Type	Figure No. ( $T_n = 400.01$ )	Figure No. ( $T_n = 4.01$ )
$\zeta_{P1}$	-	7.24
$\zeta_1$	-	7.23
$\zeta_{P2}$	-	7.24
$\zeta_2$	-	7.25

range  $-0.32$  and  $0.32$  rad, which indicate that

- ▷ Including different quantity of mass moments of inertia, the MMET system's spin-up response in Chapter 7 is different from the spin-up responses in Chapters 5 and 6.
- ▷ The MMET system's axial and pendular elastic motions are coupled to each other, and the torsional elastic motion is decoupled from them.
- Table 7.5 is for the tether's position generalised coordinate  $R$ , which determines the distance from the Earth  $E$  to the MMET system's COM. In this case, given  $e = 0.2$ ,  $r_p = 6.89 \times 10^6$  metre and then  $r_a = 1.0335 \times 10^7$  metre, it goes within the range of  $r_p$  to  $r_a$ .
- Table 7.6 is for the true anomaly  $\theta$ , which is in a linear up-changing trend from 0 to 2500 rad coupling range of 0 to 0.5 rad fluctuation spread, over the number of cycles of period  $T_n = 400.01$ , together with the position generalised coordinate  $R$ , which state the tether systems go around the Earth in an elliptical orbit.
- Table 7.7 is for the out-of-plane angle  $\alpha$  with same initial conditions, the  $\alpha$  curve in Chapter 7 is with smaller range  $-0.6$  to  $0.6$  rad than  $\alpha$  curves in Chapters 5 and 6, which state that the out-of-plane angle  $\alpha$ 's motion can be effected by tether's axial and pendular elastic motions.
- Table 7.8 is for the rigid rolling angle  $\gamma$ , which keep moving up in a linear way over the full simulation time, it is a stand-alone generalised coordinate to the MMET system's generalised coordinates.

- Tables 7.9 and 7.10 are the figure list for the axial elastic motions for the MMET systems with  $N = 2$  discrete mass points, in which,

- ▷ The numerical results for  $\eta_2$  and  $\eta_{p2}$  are positive and the results for  $\eta_1$  and  $\eta_{p1}$  are negative, which indicate that the axial motions in the two tether subspans are moving in an opposite direction with same local relative direction definition.

- ▷ Also, this different axial motions validate that the MMET tether system is a symmetrical system with respect to the MMET system COM.

- ▷ The axial elastic motions can be effected by the pendular elastic motions by including more mass moments of inertia.

- Table 7.11 are the list for the torsional elastic motions in Chapters 6 and 7, whose motion is independent of the MMET systems' other motions.

- Tables 7.12 and 7.13 are the list for the pendular elastic motions referenced on plane  $x_0 - O - y_0$  and plane  $z_0 - O - y_0$ , which indicate that,

- ▷ The pendular elasticity for two tether subspans, referenced on the same plane ( $x_0 - O - y_0$  or  $z_0 - O - y_0$ ), are with same behaviours to the other.

- ▷ The pendular elasticity for the same tether subspan, referenced on the different planes ( $x_0 - O - y_0$  and  $z_0 - O - y_0$ ), are with similar curve shapes but slightly smaller amplitudes.

- ▷ The pendular elastic motions can be effected by the axial elastic motions.

- ▷ The numerical simulation results have shown the convergence of the pendular elastic behaviours, which are approaching to zero during given simulation time.

All subsequent analysis for control applications will henceforth include axial, torsional and pendular elasticity within the MMET system.

With unsuitable parameter settings, such as too much masses difference between payloads and tether subspans, too big or small stiffness, or damping coefficients, the numerical simulations cannot be carried out to the end of the full simulation time, and integration error occurs. Currently, this MMET model cannot generate a loop in the tether subspans; this could be investigated in further studies.

## Chapter 8

---

# Fuzzy Logic Control for MMET Spin-up

---

### 8.1 Introduction

Fuzzy logic theory was first proposed by Zadeh in 1965 [188], and was based on the concept of fuzzy sets. Over recent years, fuzzy logic control (FLC) has been used in a wide variety of applications in engineering, such as: in aircraft/spacecraft; in automated highway systems; in autonomous vehicles; in washing machines; in process control; in robotics control; in decision-support systems; and in portfolio selection. Practically speaking, it is not always possible to obtain a precise mathematical model for nonlinear, complex or ill-defined systems. For example, in a complex industrial system, a skilled human operator can learn from his own experience by observing the inputs and outputs of a process and adjusting the inputs to obtain the desired outputs.

It is difficult to process the modelling for a complex system and the control system development, and even if a relatively accurate model of a dynamic system can be developed, it is often too complex to use for controller development, especially for many conventional control design procedures which require restrictive assumptions for the plant.

It is necessary to know system's mathematical model or to make some experiments for tuning conventional proportional-integral-derivative (PID) parameters. However, it is known that conventional PID controllers do not generally work well for nonlinear systems, and particularly for complex and vague systems which have no precise mathematical models. When compared to the conventional controller, the main advantage of fuzzy logic is that no mathematical modelling is required. Since the controller rules are based on the knowledge of the system behaviour and the experience of the control engineer, the FLC requires less complex mathematical modelling than the classical controller does.

Conventional control methods provide a different way of approaching the construction of nonlinear MMET systems, such as feedback-linearisation control and PID control, even when a reasonably good model of the plant is available which satisfies the necessary assumptions. According to the previous chapters 4 to 7, the MMET system's nonlinear behaviours can hardly be controlled by the conventional controllers, which can offer quite a poor solution to the MMET spin-up control problem.

The FLC is a practical alternative for a variety of challenging control applications since it can provide a convenient method for constructing nonlinear controllers via the use of heuristic information. The heuristic information may come from an operator, which acts as a 'human-in-the-loop' controller and from which experiential data is obtained.

Generally, in the FLC design methodology, the human operator needs to write down a set of rules which establish how to control the process. This is called the rule-base and thenceforth a fuzzy controller can emulate the decision-making process of the human by following the rule-base. In other cases, the heuristic information may come from a control engineer who has performed extensive mathematical modelling, analysis, and development of control algorithms for a given process. Again, such expertise is loaded into the fuzzy controller to automate the reasoning processes and actions of the expert. Regardless of where the heuristic control knowledge comes from, fuzzy control provides a user-friendly formalism which can be used for representing and implementing the ideas which can help to achieve high-performance control [189] [190] [221] [222].

Basically, the fuzzy controller block diagram is given in Figure 8.1, and is taken from Passino [190] [221] [222], which shows the architecture of a fuzzy controller in a closed-loop control system. The plant outputs are denoted by  $y(t)$ , its inputs are denoted by  $u(t)$ , the reference input to the fuzzy controller is denoted by  $r(t)$ , and the error between  $y(t)$  and  $r(t)$  is denoted by  $e(t)$ . Generally, the fuzzy controller gathers plant output data  $y(t)$ , compares it to the reference input  $r(t)$ , and then decides what the plant input  $u(t)$  should be in order to ensure that the performance objectives will be required.

As shown in Figure 8.1, the fuzzy controller has four main components:

- A 'rule-base' or a set of 'IF-THEN' rules, which contains a fuzzy logic quantification of the expert's linguistic description of how to achieve good control;
- An 'inference mechanism', which emulates the expert's decision making in the interpretation and application of knowledge about how best to control the plant. A set of such 'IF-THEN' rules is loaded into the rule-base, and an inference strategy is chosen.

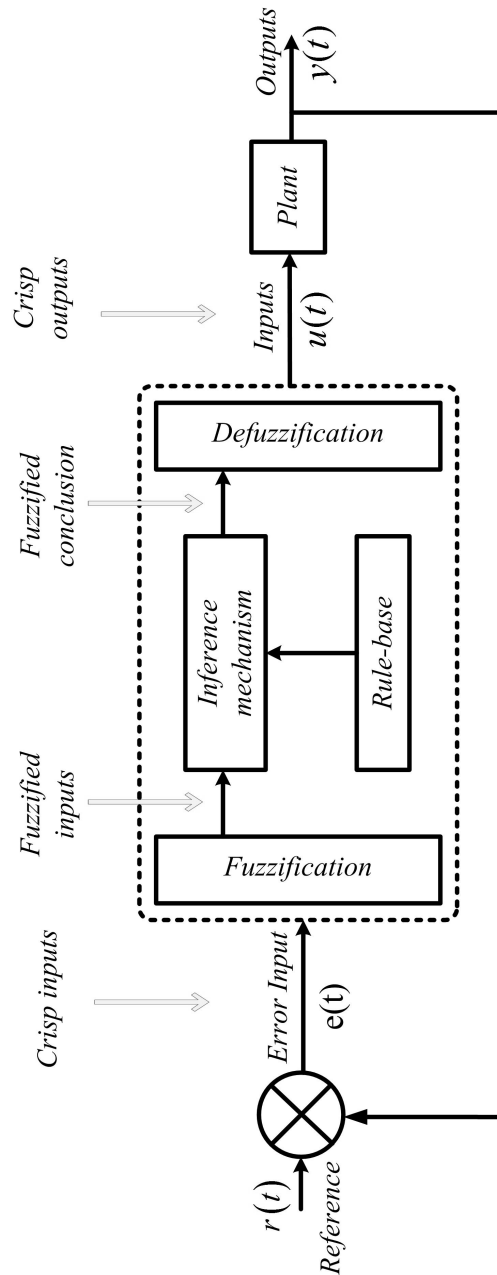


Figure 8.1: Fuzzy logic controller architecture, cited from [190] [221] [222]

Thenceforth the system is ready to be tested to see if the closed-loop specifications are needed;

- A ‘fuzzification’ interface, which converts ‘crisp’ inputs into ‘fuzzy’ information that the inference mechanism can be interpreted and compared to the rules in the rule-base;
- A ‘defuzzification’ interface, converts the conclusions by the inference mechanism into crisp(actual) inputs for the plant.

Briefly, fuzzy control system can be designed in the following steps:

- ⟨1⟩ Choosing the fuzzy controller inputs and outputs;

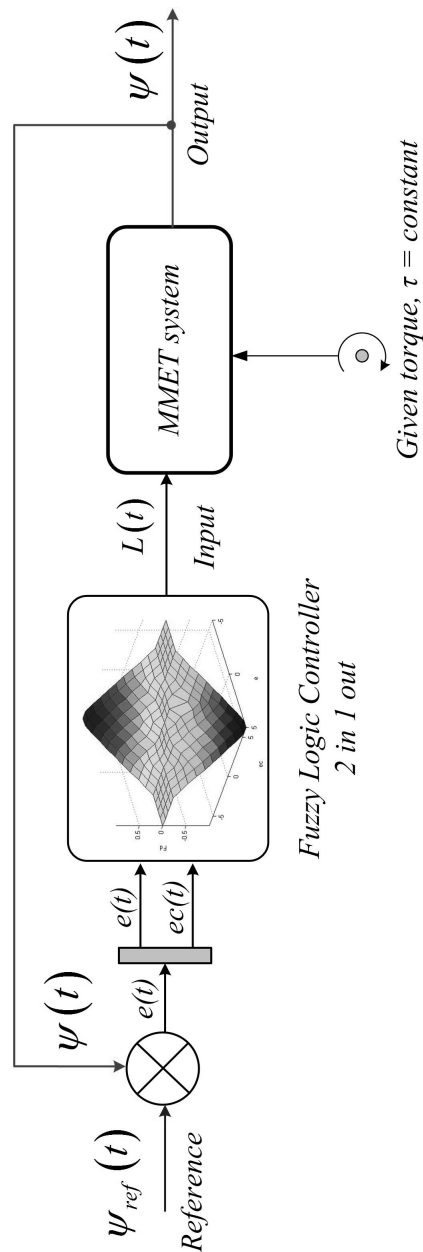


Figure 8.2: The FLC control loop for the MMET spin-up [221] [222]

- (2) Choosing the preprocessing that is needed for the controller inputs and possibly postprocessing that is needed for the outputs;
- (3) Designing each of the four components of the fuzzy controller, as shown in Figure 8.1, which including fuzzification, inference mechanism, rule-base and defuzzification;

## 8.2 Control Objective

The primary objective of this fuzzy logic control design is to develop a FLC controller that makes the MMET spin-up performance -  $\psi(t)$  and  $\dot{\psi}(t)$  - move to its desired position as

quickly as possible, with little or no endpoint oscillation. The MMET system with axial, torsional and pendular elasticity has complex, nonlinear dynamical flexible behaviour, as shown in chapter 7, and the behaviour's characteristics will change as the parameters are changed, such as when the payload has been transferred from the tether. A 2-in-1-out FLC for MMET system spin-up will be discussed in this chapter, whose structure is given in Figure 8.2 [221] [222].

### 8.3 Linguistic Descriptions

Suppose that the human expert shown in Figure 8.3 provides a description of how best to control the plant in some natural language (e.g. English). The linguistic description provided by the expert can generally be broken into several parts. There will be 'linguistic variables' which describe each of the time varying fuzzy controller inputs and outputs, the linguistic description will be loaded into the fuzzy controller, for the MMET system FLC, and is indicated in Table 8.1.

As shown in Figure 8.2, the plant is the MMET modelling with axial, torsional and pendular elasticity, which is explored in chapter 7. The plant outputs are denoted by  $\Psi(t)$ , its inputs are denoted by  $L(t)$ , the reference input to the fuzzy controller is denoted by  $\Psi_{Ref}(t)$ , and the error between  $\Psi(t)$  and  $\Psi_{Ref}(t)$  is denoted by  $e(t)$ . Generally, the 'crisp' error and change-in-error are denoted  $e(t)$  and  $ec(t)$ , the fuzzified error and change-in-error are denoted by E and EC. The FLC gathers plant output data  $\Psi(t)$ , compares it to the reference input  $\Psi_{Ref}(t)$ , and then decides what the plant input  $L(t)$  should be to generate that the MMET spin-up performance objectives will be required.

Table 8.1: Inputs and output linguistic description

Input-1	'error'	$e(t)$
Input-2	'change-in-error'	$ec(t)$
Output-1	'length'	$L(t)$

### 8.4 Inputs and Outputs

Consider a FLC with human-in-the-loop, whose responsibility is to control the MMET system, as shown in Figure 8.2. There are two inputs and one output in this FLC, and it can be referred to as a '2-in-1-out' FLC, in which the error and change-in-error between the spin-up angular velocity  $\dot{\psi}(t)$  and the spin-up angular acceleration  $\ddot{\psi}(t)$  with the reference signals  $\dot{\psi}_{Ref}(t)$  and  $\ddot{\psi}_{Ref}(t)$  are selected as the inputs, as given in equations (8.4.1) and (8.4.2).

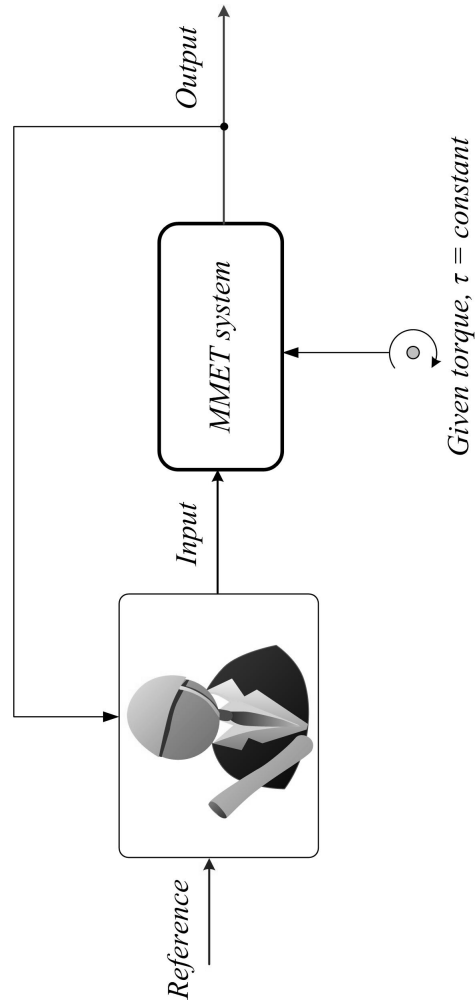


Figure 8.3: The Human control loop for the MMET spin-up

Meanwhile, the tether subspan length  $L(t)$  is the output from the FLC and the input to the MMET system. For the MMET spin-up control, only the tether length  $L(t)$  is allowed as the input control signal, as given in Table 8.1. More about the FLC work process will be discussed in section 8.6.

$$e(t) = \| \dot{\psi}(t) - \dot{\psi}_{Ref}(t) \| \quad (8.4.1)$$

$$ec(t) = \| \ddot{\psi}(t) - \ddot{\psi}_{Ref}(t) \| \quad (8.4.2)$$

Once the fuzzy controller inputs and outputs are chosen, the next step is to determine what the reference inputs are. For the MMET system, the choice of the reference inputs are  $\dot{\psi}_{Ref}(t) = 0$  and  $\ddot{\psi}_{Ref}(t) = 0$ , then equations (8.4.3) and (8.4.4), where  $\| * \|$  is the normalisation operation, which will be discussed in section 8.5.1.

$$e(t) = \| \dot{\psi}(t) \| \quad (8.4.3)$$

$$ec(t) = \| \ddot{\psi}(t) \| \quad (8.4.4)$$

## 8.5 Fuzzification

A process of fuzzification converts its numeric or crisp inputs ( $e(t)$  and  $ec(t)$ ) to input fuzzified inputs (E and EC), so they will be used by the fuzzy inference system. The fuzzified inputs are used to quantify the information in the rule-base, and the inference mechanism operates on fuzzy sets (E and EC) to produce output fuzzy sets (U). Basically, the fuzzy set is a different representation for the crisp numbers, in this context, and it has utilised the scaling gains or factors to perform the fuzzification process, as given in equations (8.5.1) and (8.5.2), where E and EC are the fuzzified input values,  $e(t)$  and  $ec(t)$  are the crisp input values,  $K_i = \{K_e, K_{ec}\}$  is the scaling factor as defined in equation(8.5.6). Equations (8.5.1) and (8.5.2) are the fuzzification for  $e(t)$  and  $ec(t)$ , in which,  $e(t)$  and  $ec(t)$  are the normalised inputs by the normalisation process given in section 8.5.1.

$$E = K_e \times e(t) \quad (8.5.1)$$

$$EC = K_{ec} \times ec(t) \quad (8.5.2)$$

### 8.5.1 Normalisation

Fuzzification is an actual normalisation process which decomposes the system inputs into the fuzzy sets. That is, it is used to map variables from practical value range  $[x_{min}, x_{max}]$  to fuzzy value range  $[-1, 1]$ , as shown in Figures 8.4, 8.5 and 8.6. Briefly, in the FLC normalisation designing process for the MMET system, there are 3 steps for the normalisation process:

⟨1⟩ Scale factor generation, as shown in Figure 8.4. This step is to calculate the scale factor according to the input range  $[x_{min}, x_{max}]$  of the raw data  $x_i$ , as given in equation (8.5.3);

$$\text{norm-}x_i|_{[0,1]} = \frac{x_i - x_{min}}{x_{max} - x_{min}} \quad (8.5.3)$$

⟨2⟩ Scale operation, as shown in Figure 8.5, all the input data are scaled to the range of [lower, upper], which are  $[-1, 1]$  in this case, as given in equation (8.5.4);

$$\text{norm-}x_i|_{\text{scaled}} = (\text{upper} - \text{lower}) \times \text{norm-}x_i|_{[0,1]} \quad (8.5.4)$$

(3) Shift operation, as shown in Figure 8.6, the data are shifted to the new range [lower, upper], as given in equation (8.5.5);

$$\text{norm\_}x_i|_{[\text{lower},\text{upper}]} = \text{lower} + \text{norm\_}x_i|_{\text{scaled}} \quad (8.5.5)$$

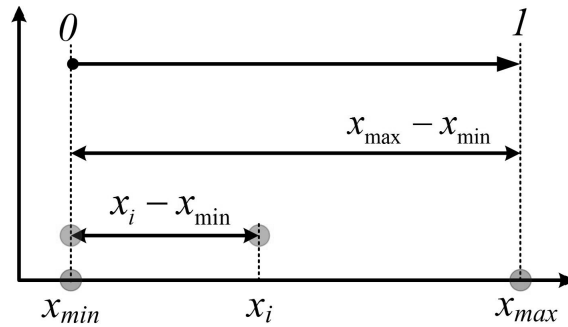


Figure 8.4: Normalisation step 1: scale factor generation

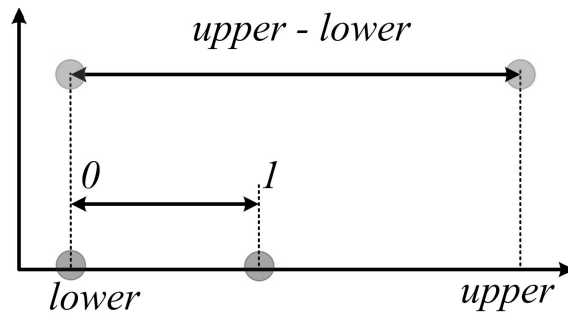


Figure 8.5: Normalisation step 2: scale operation

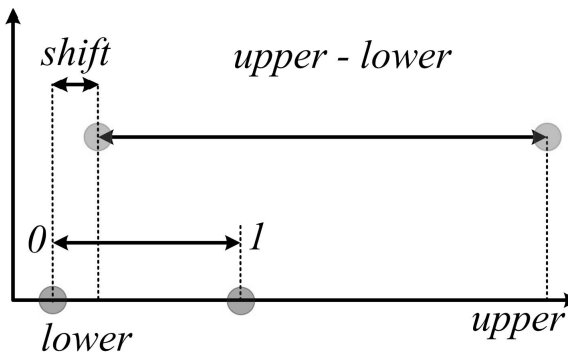


Figure 8.6: Normalisation step 3: shift operation

The scale factor  $K_i$  can be defined in equation (8.5.6), which can be generated from the input data source  $x_i$ , and the max and min values of the input data are denoted by  $x_{\max}$  and  $x_{\min}$ . For the MMET spin-up control FLC, the scale factors for  $e(t)$  and  $ec(t)$  are denoted by  $K_e$  and  $K_{ec}$ , and are given in equations (8.5.7) and (8.5.8).

$$K_i = \frac{x_i - x_{\min}}{x_i (x_{\max} - x_{\min})} \quad (8.5.6)$$

In Figure 8.4, the data range  $[x_{\min}, x_{\max}]$  comes from the practical inputs  $\dot{\psi}$  and  $\ddot{\psi}$  of the FLC for the MMET system spin-up control, the outputs of the normalisation are  $e(t)$  and  $ec(t)$ .

$$K_e = \frac{e_i(t) - e_{\min}(t)}{e_i(t) (e_{\max}(t) - e_{\min}(t))} \quad (8.5.7)$$

$$K_{ec} = \frac{ec_i(t) - ec_{\min}(t)}{ec_i(t) (ec_{\max}(t) - ec_{\min}(t))} \quad (8.5.8)$$

## 8.5.2 Membership functions

A membership function (MF) is a curve which defines how each point in the input space is mapped to a membership value between 0 and 1. The function itself can be an arbitrary curve whose shape can be defined as a function that suits us from the point of view of simplicity, convenience, speed, and efficiency. The MF for the MMET system is a Gaussian combination membership function, which is given in equation (8.5.9) [191] and in Figure 8.7, the  $c$  defines the position of the MF curve, and the  $\sigma$  defines the scale of the MF curve. The inputs of error(E) and change-in-error (EC) and the fuzzified control signal output (U) are interpreted from this fuzzy set, and the appropriate degree of membership is obtained.

$$\mu(x) = \exp\left(-\frac{(x-c)^2}{2\sigma^2}\right) \quad (8.5.9)$$

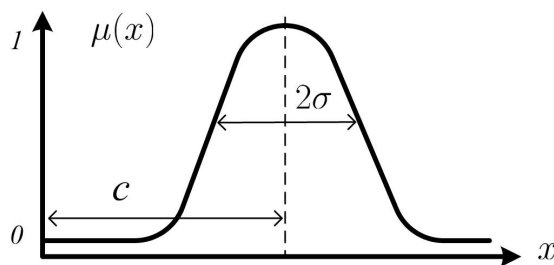


Figure 8.7: Gaussian combination membership function definition

The process of fuzzification allows the system inputs and outputs to be expressed in linguistic terms such that rules can be applied in a simple manner to express the complicated system. In the FLC for the MMET system, there are 9 values of linguistic variables in the fuzzy sets:

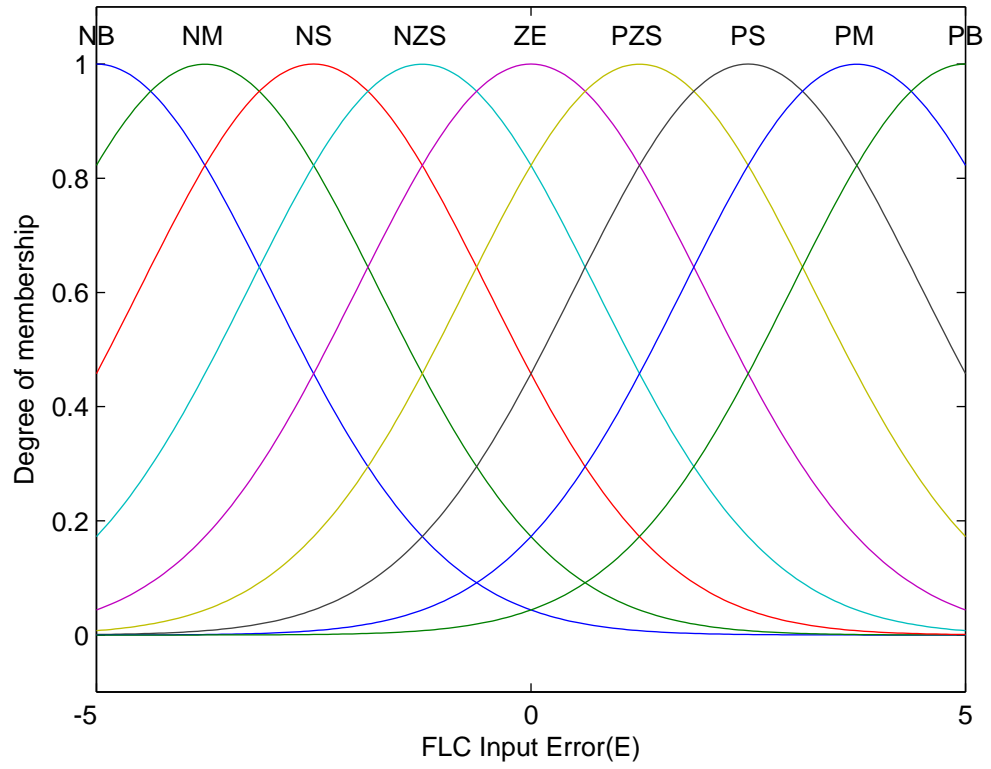


Figure 8.8: The membership function for E

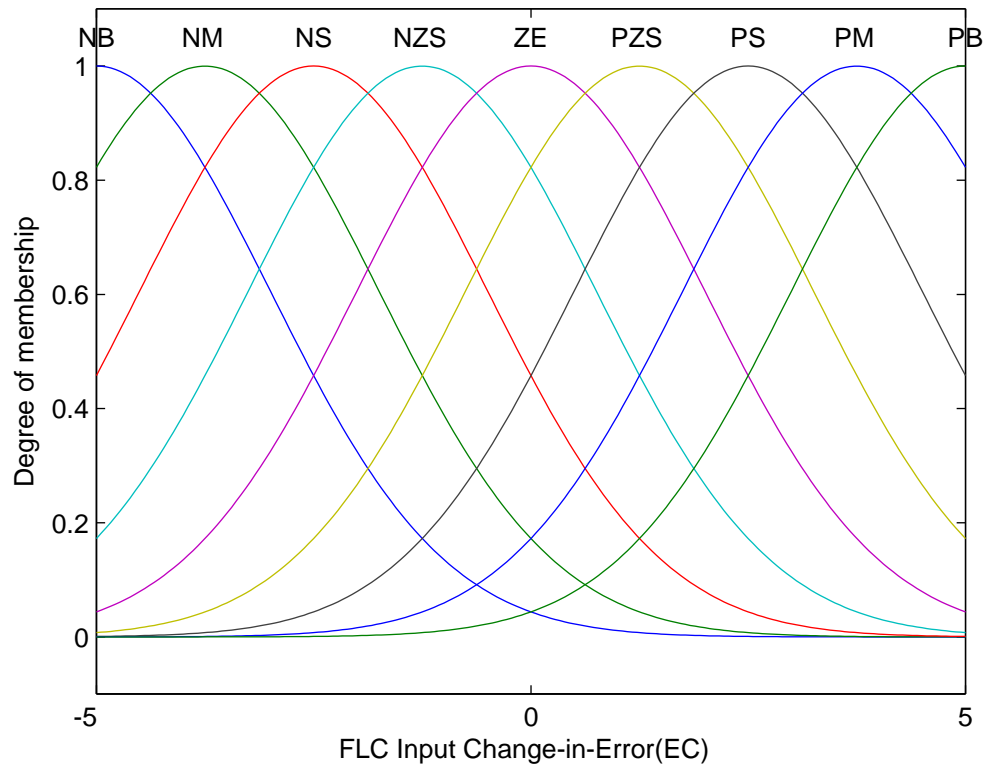


Figure 8.9: The membership function for EC

⟨1⟩ For 2 inputs of E and EC, which are: ⟨ NB , NM , NS , NZS , ZE , PZS , PS , PM , PB ⟩ or ⟨ -5 , -4 , -3 , -2 , 0 , 2 , 3 , 4 , 5 ⟩.

⟨2⟩ For 1 output of U are ⟨ NB , NM , NS , NZS , ZE , PZS , PS , PM , PB ⟩ or ⟨ -2 , -1.5 , -1 , -0.5 , 0 , 0.5 , 1 , 1.5 , 2 ⟩.

The fuzzy linguistic values are also listed in Appendix M. When applied in the numerical calculation, the mapping process are shown in Figures 8.8, 8.9 and 8.13.

## 8.6 Rule-base and Inference Mechanisms

The FLC ‘IF-THEN’ rule base is then applied to describe the expert’s knowledge, the 2-in-1-out FLC rule-base for the spin-up of the MMET system is characterised by a set of linguistic description rules based on conceptual expertise which arises from typical human situational experience. In particular, for the MMET spin-up control, the rule-base is given in Table 8.2, with two inputs and nine linguistic values for each of those, there are at most  $9^2 = 81$  possible rules as following list:

- ⟨1⟩ IF **E** = **NB**, AND **EC** = **NB**, THEN **U** = **NB**;
- ⟨2⟩ IF **E** = **NB**, AND **EC** = **NM**, THEN **U** = **NM**;
- ⟨3⟩ IF **E** = **NB**, AND **EC** = **NS**, THEN **U** = **NS**;
- ⋮
- ⟨81⟩ IF **E** = **PB**, AND **EC** = **PB**, THEN **U** = **NB**;

Table 8.2: The ‘2-in-1-out’ FLC rule table for MMET system

<b>U</b>		<b>EC</b>								
		<b>NB</b>	<b>NM</b>	<b>NS</b>	<b>NZS</b>	<b>ZE</b>	<b>PZS</b>	<b>PS</b>	<b>PM</b>	<b>PB</b>
<b>E</b>	<b>NB</b>	NB	NM	NS	NZS	PZS	PZS	PS	PM	PB
	<b>NM</b>	NM	NM	NZS	NZS	PZS	PZS	PZS	PM	PM
	<b>NS</b>	NS	NS	NZS	NZS	PZS	PZS	PZS	PS	PS
	<b>NZS</b>	NZS	NZS	NZS	NZS	ZE	PZS	PZS	PZS	PZS
	<b>ZE</b>	PZS	PZS	PZS	ZE	ZE	ZE	PZS	PZS	PZS
	<b>PZS</b>	PZS	PZS	PZS	PZS	ZE	NZS	NZS	NZS	NZS
	<b>PS</b>	PS	PS	PZS	PZS	PZS	NZS	NZS	NS	NS
	<b>PM</b>	PM	PM	PS	PZS	PZS	NZS	NS	NM	NM
	<b>PB</b>	PB	PM	PS	PZS	PZS	NZS	NS	NM	NB

The full rule-base is also given in Figure 8.10 as a rule-base 3D plot, which defines the relationship between 2 FLC inputs of the Error (E) and the Change-in-Error (EC) with 1

FLC output(U). Table 8.2 is also the 2-in-1-out FLC rule-base table which can drive the FLC inference mechanism, and this came from the previous experience gained from examining dynamic simulations for tether length changes during angular velocity control. Briefly, the main linguistic control rules are:

- ⟨1⟩ the larger the angular velocity input, the shorter the length tether output; Conversely, the smaller the angular velocity input, the longer the tether length output.
- ⟨2⟩ the larger the angular acceleration, the longer the tether length output; Otherwise, the smaller the angular acceleration, the shorter the tether length output.

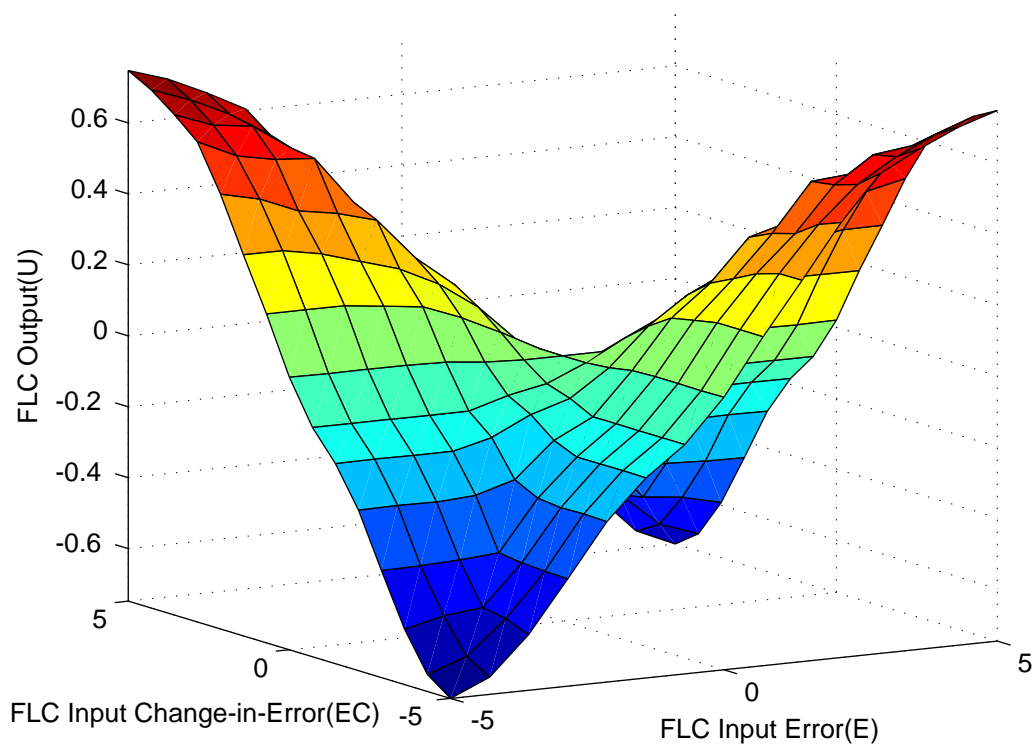


Figure 8.10: The control surface of the fuzzy controller for MMET spin-up

Fuzzy inference is the process of formulating the mapping from a given input to an output using fuzzy logic. The mapping then provides a basis from which decisions can be made, or patterns can be discerned. The process of fuzzy inference involves all of the pieces that are described in the previous sections: Membership Functions; Logical Operations; and ‘IF-THEN’ Rules. Mamdani’s fuzzy inference method [193] [194] [195] [191] is the most commonly witnessed fuzzy methodology, it was among the first control systems built using fuzzy set theory. It was proposed in 1975 by Mamdani as an attempt to control a steam engine and boiler combination by synthesizing a set of linguistic control rules obtained from experienced human operators. Mamdani’s effort was based on Zadeh’s research [196] on

fuzzy algorithms for complex systems and decision processes in 1973. The Fuzzy Inference System (FIS) of Mamdani-type inference for the 2-in-1-out FLC is shown Figure 8.11.

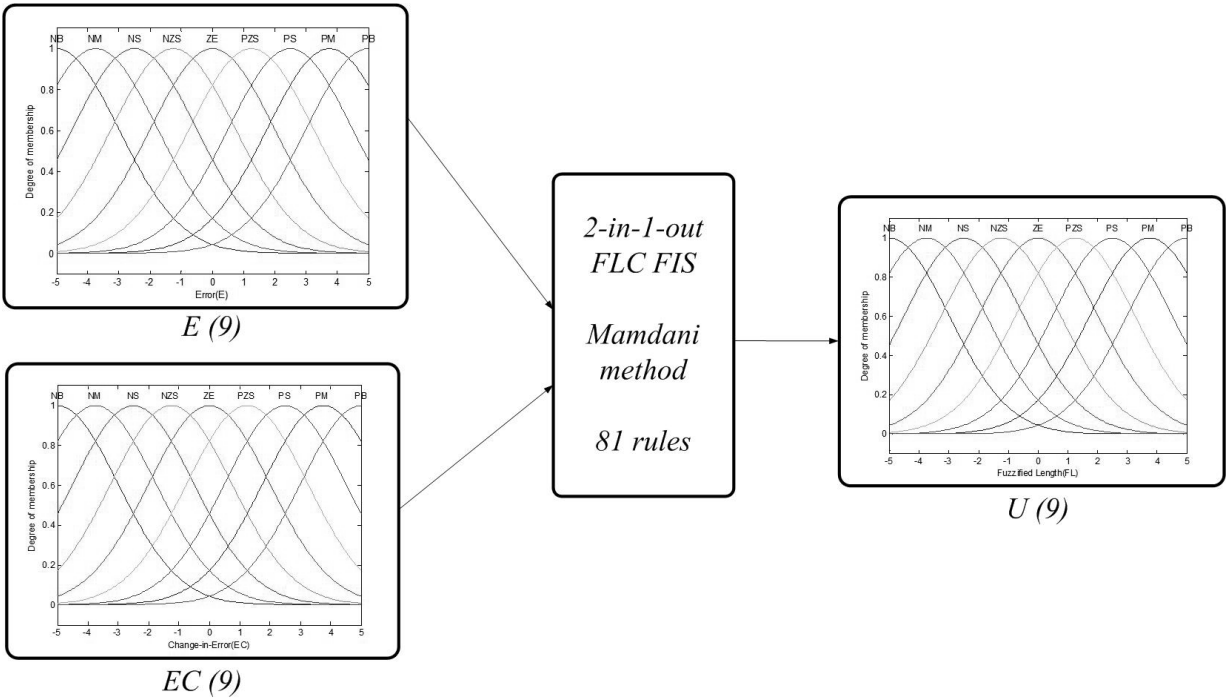


Figure 8.11: The fuzzy inference system for MMET system spin-up

As shown in Figure 8.12, because output is based on the operation of all of the rules in the FIS, the rules need to be combined in a certain manner in order to make a decision. Aggregation is the process by which the fuzzy sets which represent the outputs of each rule are combined into a single fuzzy set before the defuzzification step. The input of the aggregation process is the list of truncated output functions returned by the implication process for each rule, the output of the aggregation process is one fuzzy set for each output variable.

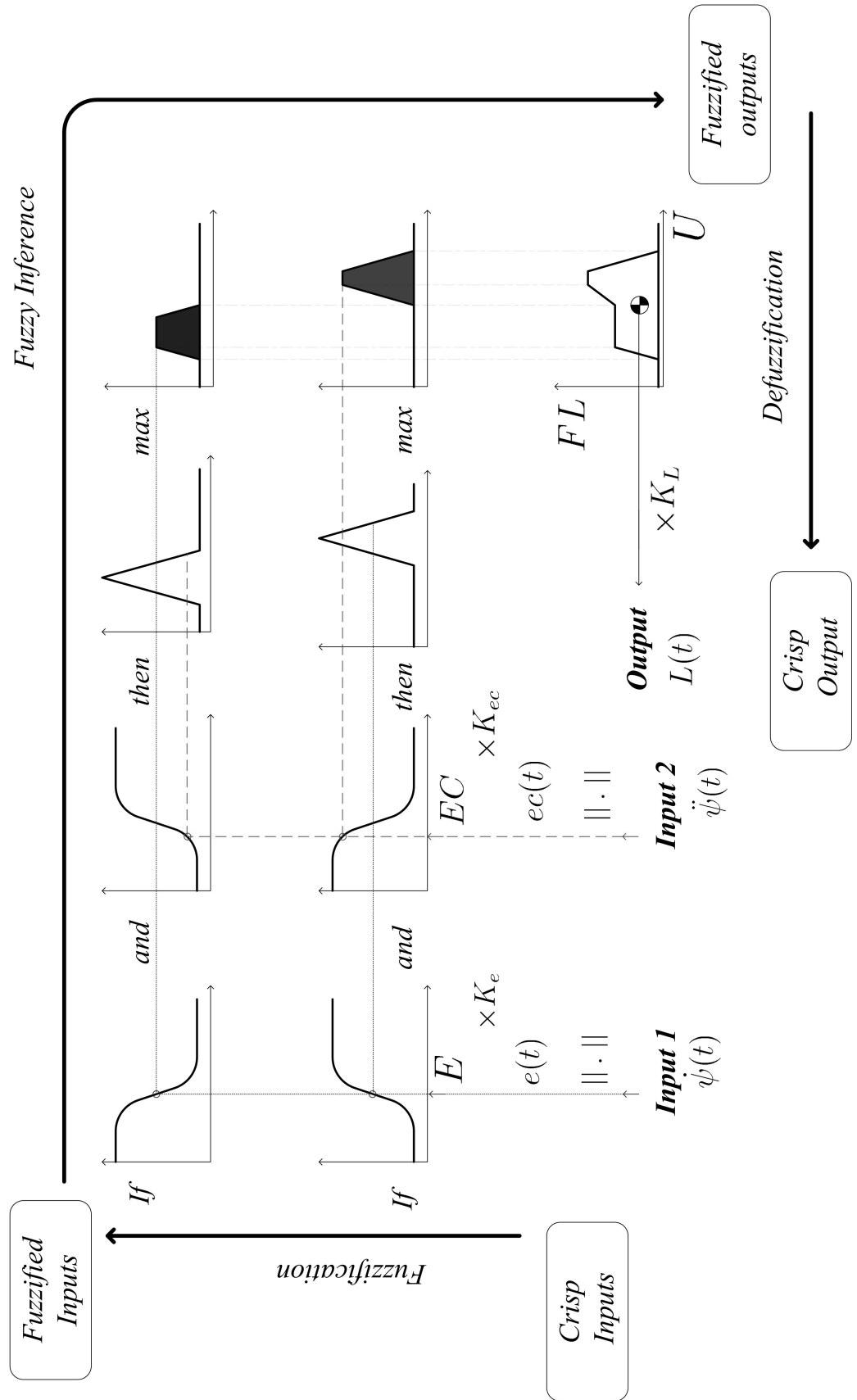


Figure 8.12: The fuzzy logic controller work process [190] [191] [192]

## 8.7 Defuzzification

Defuzzification is the process of producing a quantifiable result, typically a fuzzy system will have a number of rules which transform a number of variables into a fuzzy result. The result is described in terms of membership in fuzzy sets. Defuzzification is the opposite process of fuzzification and is used to map fuzzified variables to practical crisp variables. There are many different methods of defuzzification available [190] [191] [192], for the Mamdani-style inference, it can be choosed centroid with gain  $K_L$  as the defuzzification method, as shown in Figure 8.12.

Defuzzification is the opposite process of fuzzification and is used to map fuzzified variables to practical crisp variables. Similar to the discussion in section 8.5, in this context the scaling gain or factor has been decided upon to perform the defuzzification process, as given in equation (8.7.1), where  $L(t)$  is the crisp tether length to control the MMET spin-up performance,  $U$  is the fuzzy conclusion from FIS,  $FL$  is the membership function output for  $U$ , and  $K_L$  is the scaling gain. The max-min reasoning and the centre of gravity (COG) defuzzification method are utilised in this FLC, which are frequently used in the FLC design [190] [191], as shown in Figure 8.12.

$$L(t) = K_L \times \mu(U) = K_L \times FL \quad (8.7.1)$$

## 8.8 Simulations and Discussions

Numerical results are obtained using a specially devised co-simulation toolkit of MATLAB and MATHEMATICA functions in an integrated program to provide a new toolbox, known henceforth as ‘SMATLINK’, which integrates control in MATLAB/SIMULINK with MMET modelling in MATHEMATICA. The velocity and acceleration of  $\psi(t)$  are selected as  $e(t)$  and  $ec(t)$  feedback signals for the MMET spin-up control. Figure 8.14 shows the control loop for the simulation process, and unless stated otherwise all the results are generated using the parameters for the MMET systems and the controllers, as in Appendix C.

- ▷ The solid lines are the  $\psi(t)$  outputs with FLC, the dot lines are the  $\psi(t)$  outputs without any control effects, as shown in Figures 8.15 to 8.20, the angular displacement, angular velocity and acceleration responses of the MMET spin-up  $\psi(t)$  are indicated, which showing the FLC method has an effect on the spin-up control for the MMET

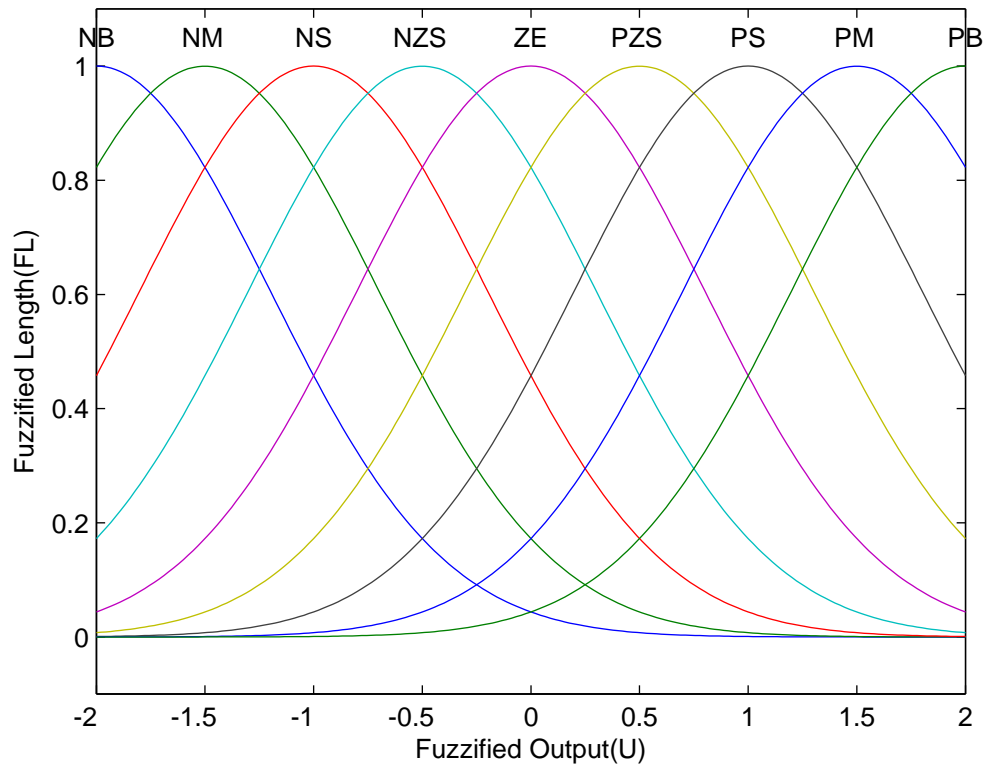


Figure 8.13: The membership function for U

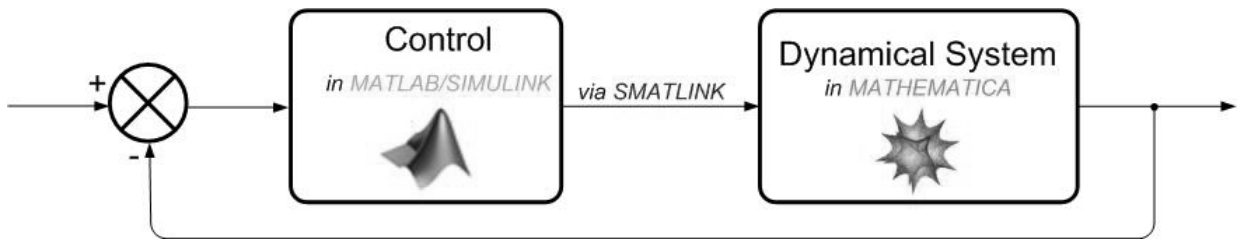


Figure 8.14: MMET spin-up control simulation loop

system with the given initial conditions. The controller spin-up output  $\psi(t)$ ,  $\dot{\psi}(t)$  and  $\ddot{\psi}(t)$  are all closer to the reference signals, which are the dash data in the Figures.

▷ Figures 8.15 and 8.16 are the spin-up angular displacement responses in simulation time  $T_n = 4.01$  and  $T_n = 400.01$ , which show the FLC controlled  $\psi$  output is approaching to a stable status with reducing amplitude.

▷ Figures 8.17 and 8.18 are the response plots for the angular velocity  $\dot{\psi}$ , Figures 8.19 and 8.20 are the angular acceleration response plots for the  $\ddot{\psi}$  in simulation time  $T_n = 4.01$  and  $T_n = 400.01$ , with similar convergent behaviours.

▷ The phase plots in Figures 8.21 and 8.22 are shown as limit cycles, whose shape describes the stable behaviour of the spin-up coordinate  $\psi(t)$  in simulation time  $T_n = 4.01$  and  $T_n = 400.01$ , and it is clear that the FLC controlled MMET system corrob-

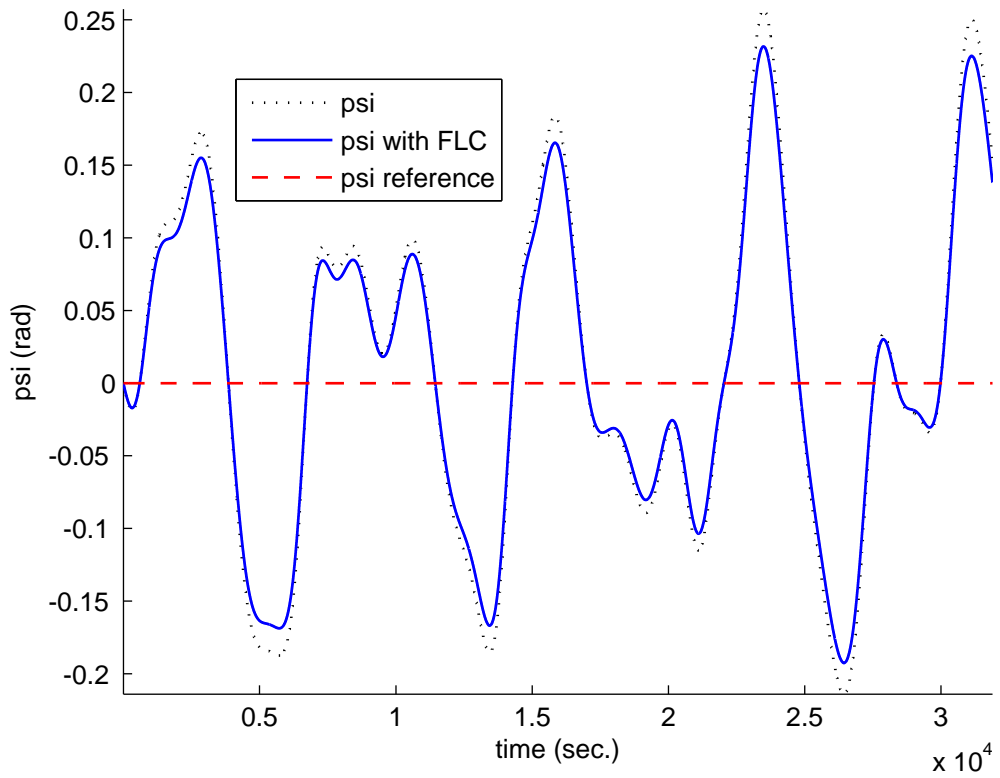


Figure 8.15: The angular displacement  $\psi$  for MMET spin-up response ( $T_n = 4.01$ )

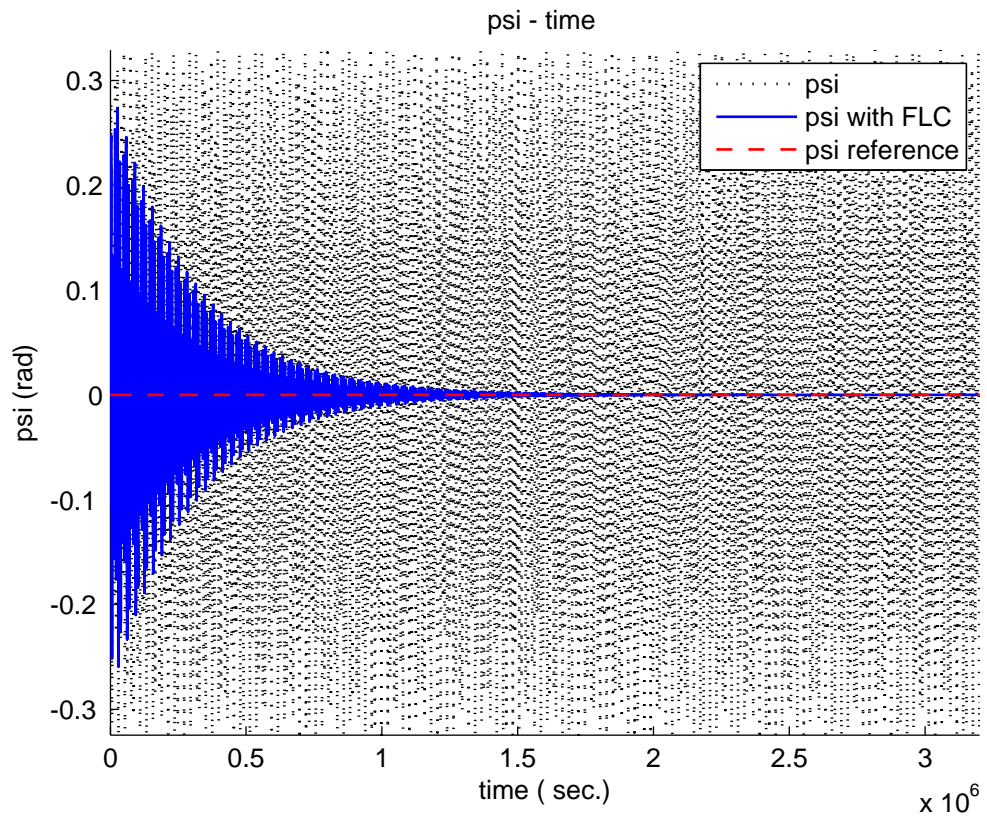


Figure 8.16: The angular displacement  $\psi$  for MMET spin-up response ( $T_n = 400.01$ )

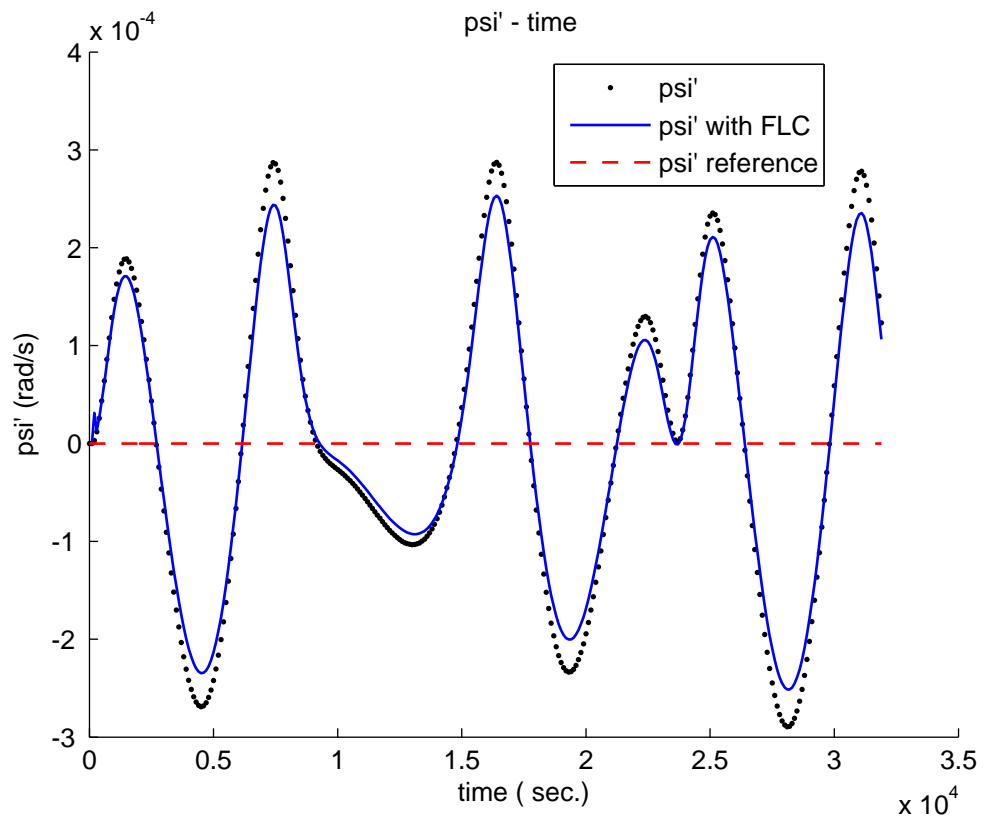


Figure 8.17: The angular velocity  $\psi$  for MMET spin-up response ( $T_n = 4.01$ )

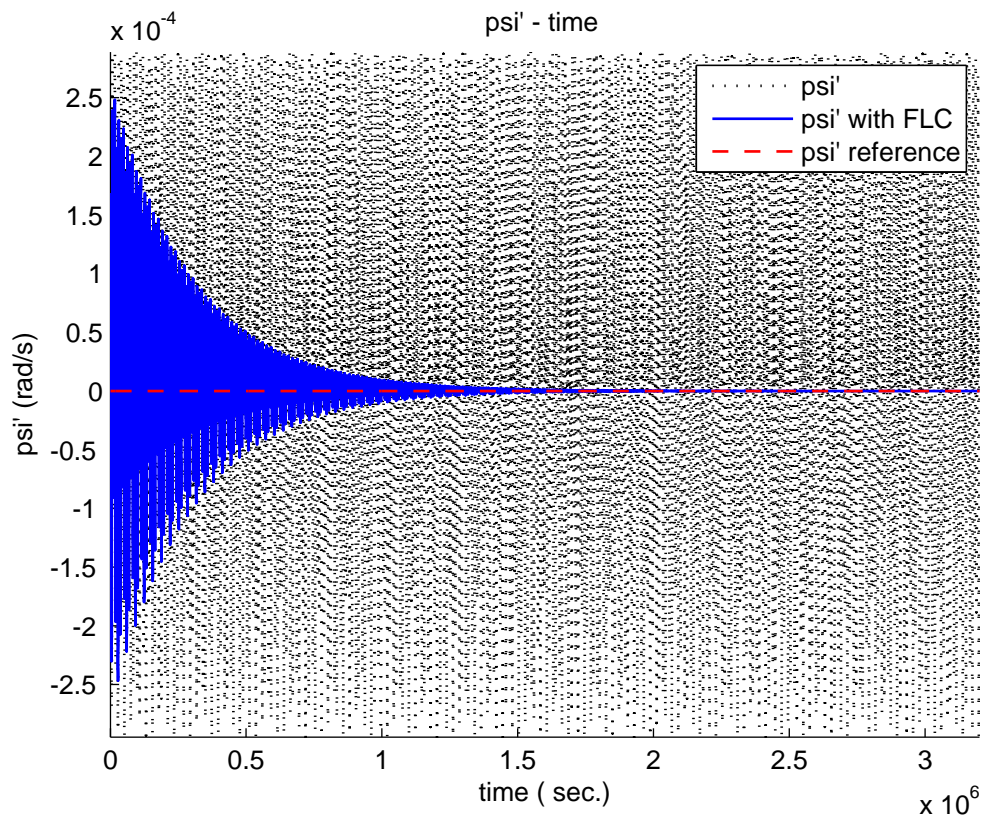


Figure 8.18: The angular velocity  $\psi$  for MMET spin-up response ( $T_n = 400.01$ )

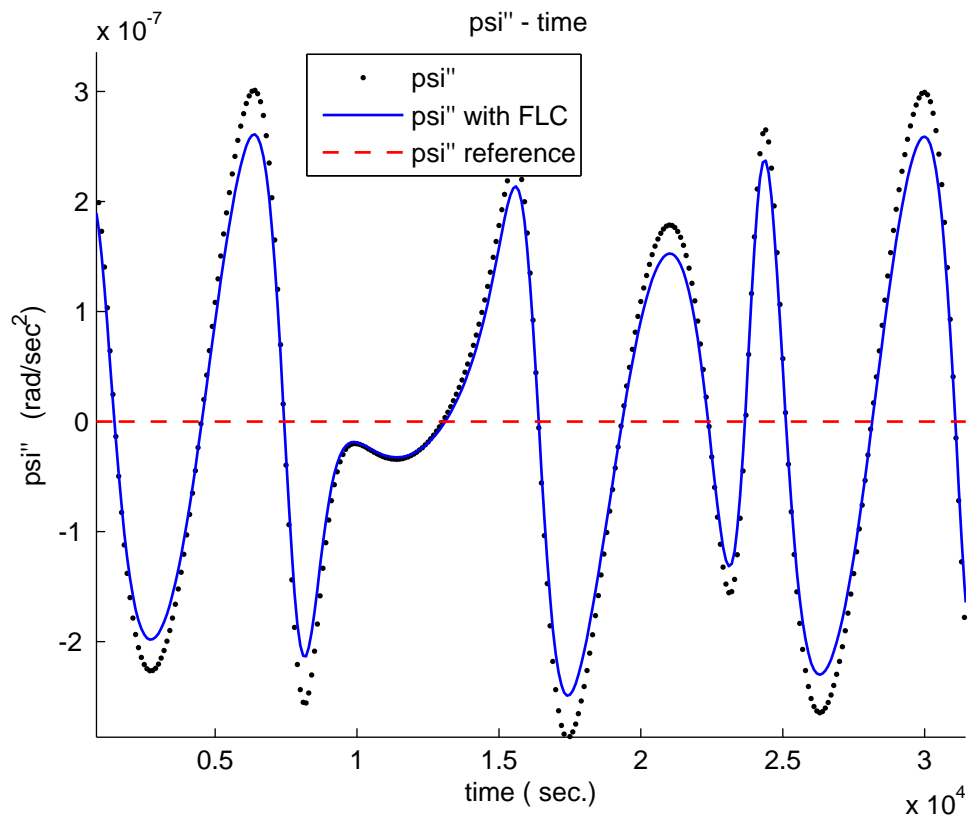


Figure 8.19: The angular acceleration  $\psi$  for MMET spin-up response ( $T_n = 4.01$ )

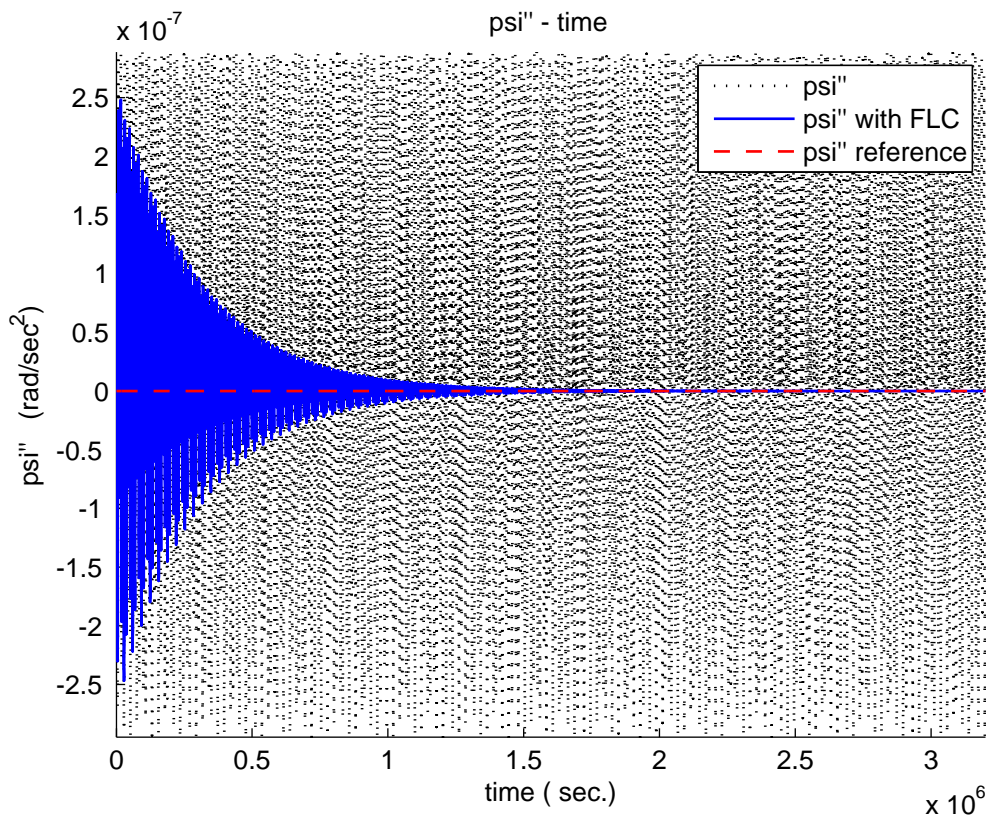


Figure 8.20: The angular acceleration  $\psi$  for MMET spin-up response ( $T_n = 400.01$ )

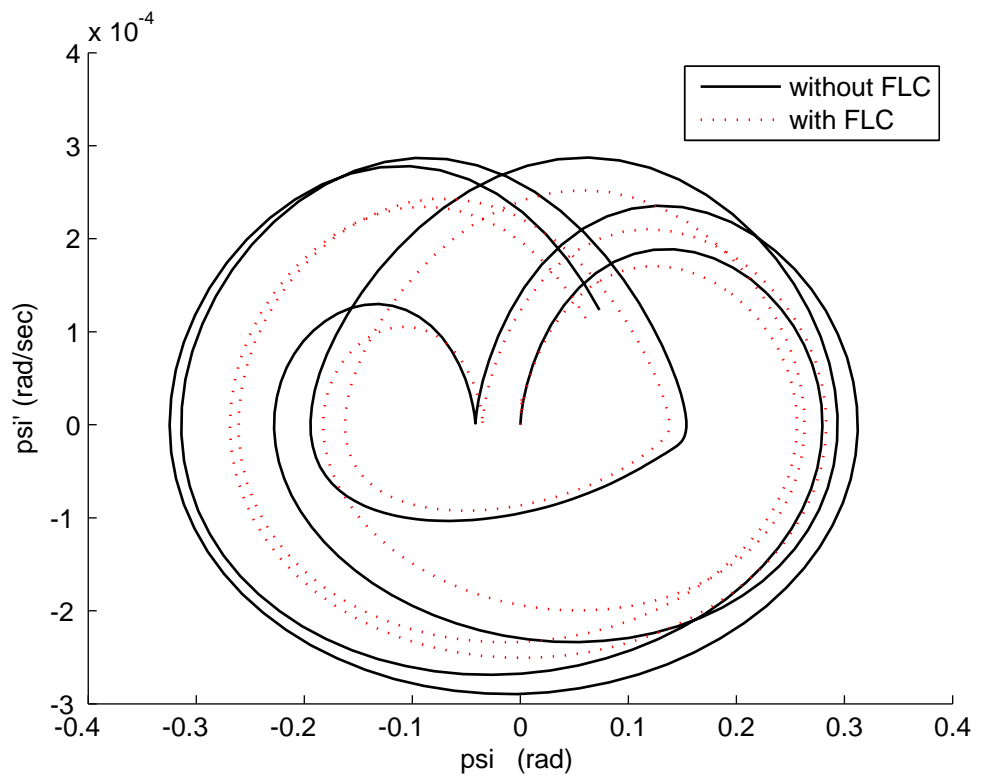


Figure 8.21: The MMET spin-up phase portrait ( $T_n = 4.01$ )

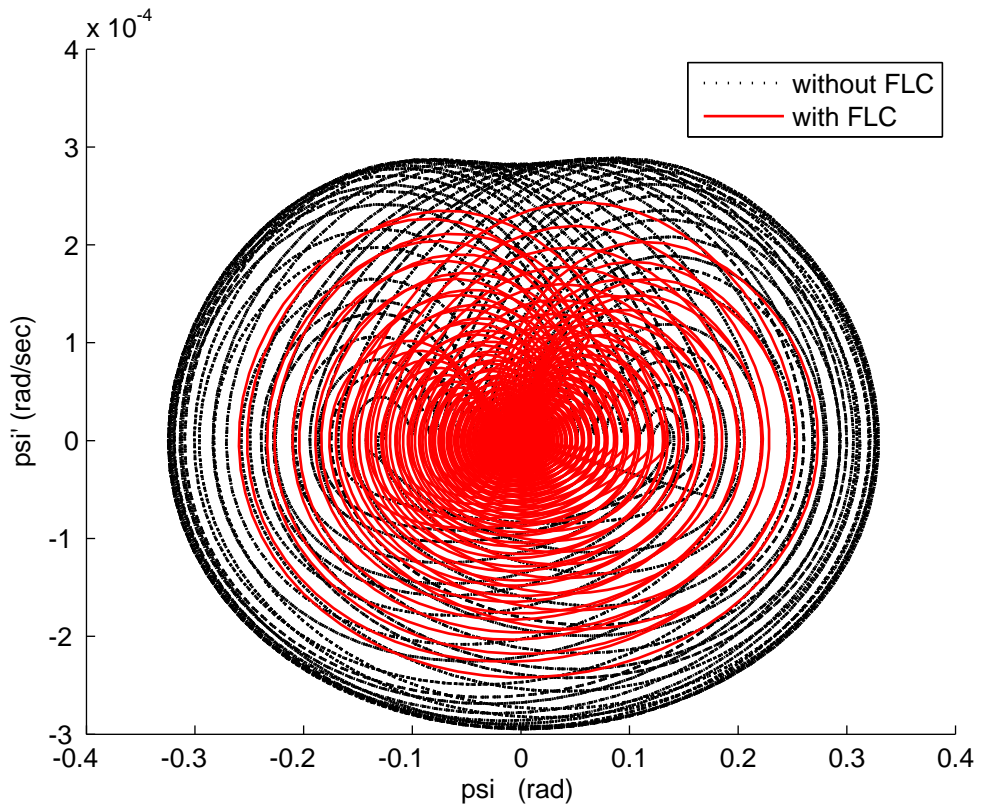


Figure 8.22: The MMET spin-up phase portrait ( $T_n = 400.01$ )

rates interpretation of steady-state.

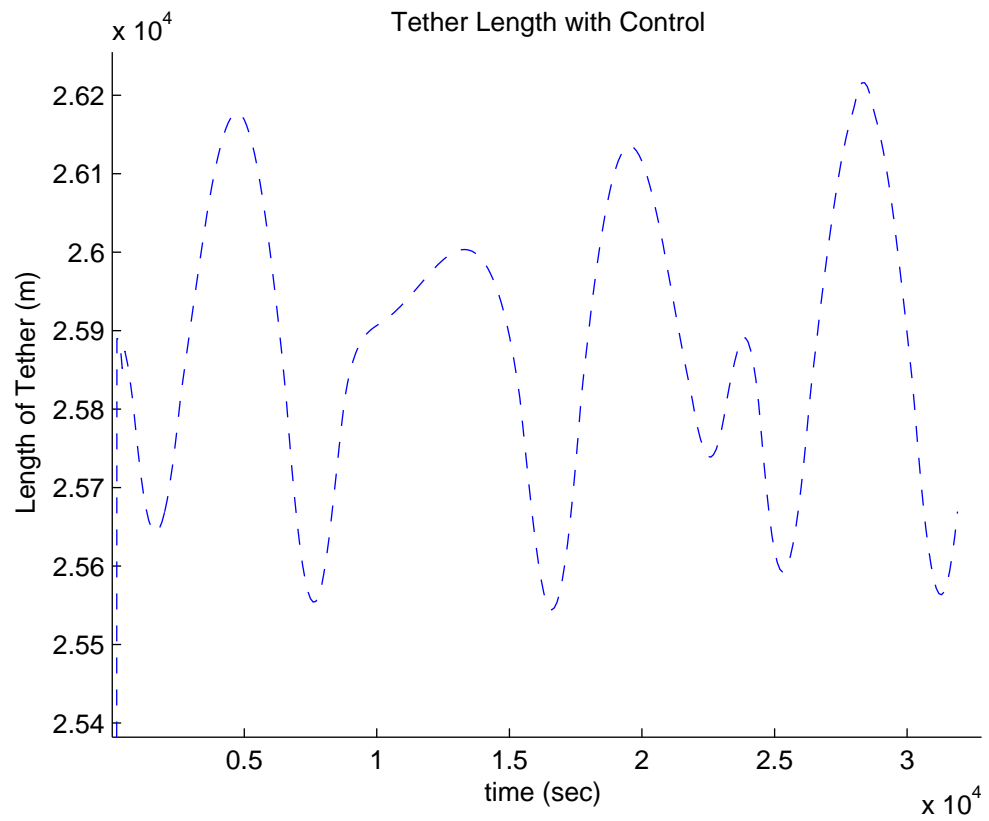


Figure 8.23: The FLC controlled tether subspan length for the MMET spin-up ( $T_n = 4.01$ )

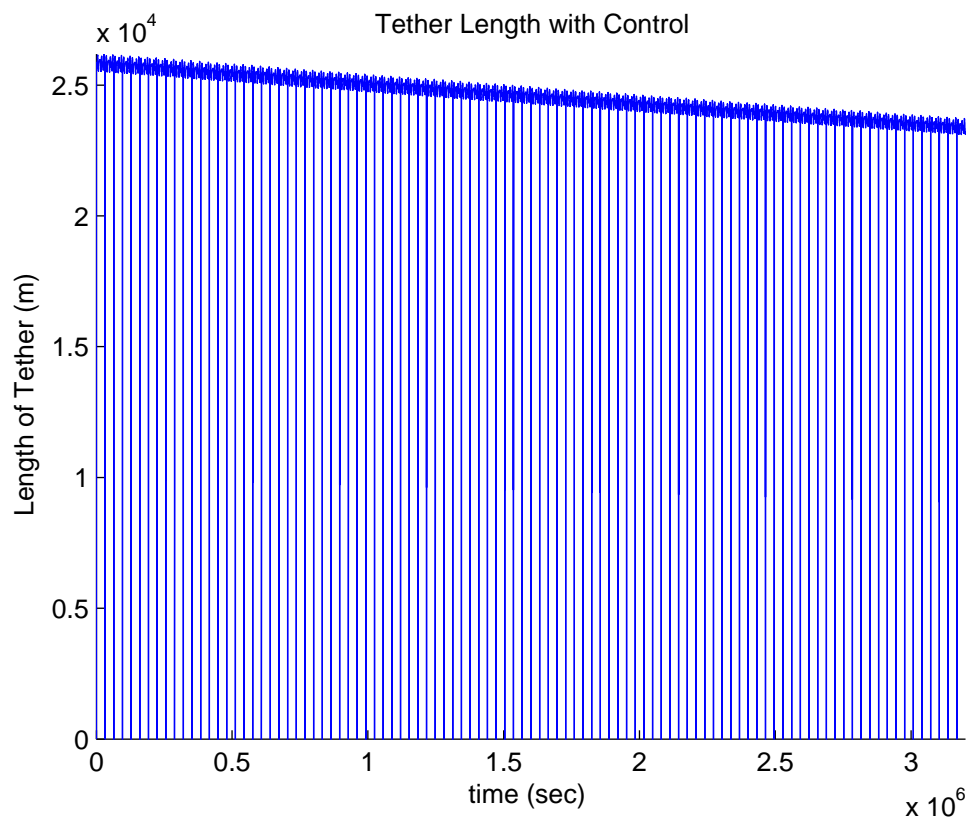


Figure 8.24: The FLC controlled tether subspan length for the MMET spin-up ( $T_n = 400.01$ )

▷ Figures 8.23 and 8.24 show the tether subspan length variation for the MMET spin-up control in simulation time  $T_n = 4.01$  and  $T_n = 400.0$ , which are generated by the FLC controlled MMET system.

► The figures for the axial, torsional and pendular elastic motions are attached in Appendix J.

## 8.9 Conclusions

The fuzzy logic control is a practical alternative which can be used for a variety of challenging control applications since it can provide a convenient method for constructing nonlinear controllers via the use of heuristic information. Because of the nonlinear dynamics and their complexity, the MMET system's spin-up control problem was decided upon to be used to investigate a fuzzy logic based controller in order to maintain the desired length and length rate of the tether. In this chapter, a '2-in-1-out' fuzzy logic controller has been discussed and then applied in the MMET system spin-up control.

Numerical results are obtained using SMATLINK, which integrates control in MATLAB with MMET modelling in MATHEMATICA. More information about SMATLINK is given in Appendix L. The velocity and acceleration of  $\psi(t)$  are selected as  $e(t)$  and  $ec(t)$  feedback signals for the MMET spin-up control.

The simulations show the robustness and usefulness which can be achieved from the fuzzy logic control for the MMET spin-up behaviour, and the stability of the MMET system spin-up response for certain combinations of the tether length and the length rate are observed in simulation time  $T_n = 4.01$  and  $T_n = 400.0$ .

- ▷ The FLC controlled spin-up motions are changing with a reducing oscillation down to a stable status, which expressed the FLC's effects on the spin-up and satisfied the control objective.
- ▷ The axial elastic motions are moving stably with the smaller amplitudes.
- ▷ The torsional elastic motions can not be effected by tether length control strategy.
- ▷ The pendular elastic motions decline with convergent reaction with reducing oscillation, then to a zero status in the end.

## Chapter 9

---

# Hybrid Fuzzy Sliding Mode Control for Spin-up of the MMET

---

### 9.1 Introduction

Variable structure control (VSC) with sliding mode was introduced in the early 1950s by Emelyanov, and subsequently published in the 1960s [197]; it was further developed by several other researchers [198] [199] [200] [201] [202]. Sliding mode control (SMC) has been recognised as a robust and efficient control method for complex, high order or nonlinear dynamical systems. The major advantage of sliding mode control is its low sensitivity to a system's parameter changes under various uncertainty conditions. Another advantage is that it can decouple system motion into independent partial components of lower dimension, which reduces the complexity of the system control and feedback design. However, a major drawback of traditional SMC is its propensity for chattering, which is generally disadvantageous within control systems [203] [204] [205] [206].

It has been widely recognised that fuzzy logic control is an effective control method for various diverse applications, being a model free, universal approximation theorem, and being rule-based, as discussed in chapter 8, where the fuzzy logic control rule-base is generally based on practical human experience. However, the intrinsic linguistic format expression required to construct the FLC rule-base makes it difficult to guarantee the stability and robustness of the control system, and the huge amount of fuzzy rules required for a high-order system makes the analysis complex [207] [200] [208] [209] [210].

The involvement of FLC in the design of a fuzzy sliding mode control (FSMC) based controller can be harnessed to help to avoid the chattering problem. In recent years, a lot of

literature has been generated in the area of FSMC, and this has also covered the chattering phenomenon. The smooth control feature of fuzzy logic can be helpful in overcoming the disadvantages of chattering. This is why it can be useful to combine FLC with SMC to create the FSMC [200] [209] [211] [212] [213] [214] [215] [216] [217] [218] [219] [220].

A hybrid fuzzy sliding mode control method is proposed and applied into the tether subspan length, changing for the spin-up control of the MMET system. This hybrid fuzzy sliding mode control is defined as F $\alpha$ SMC [221] [222], which involves a skyhook surface sliding mode control (SkyhookSMC) method which is applied here to control the tether subspan length for spin-up control of the discretised flexible MMET system, as discussed in chapter 7.

## 9.2 Ideal Skyhook Damping

A widely known (and used) control scheme for controlling the vibration of a vehicle body is skyhook damping, presented by D.C. Karnopp et al. in 1974 [223]. The term ‘skyhook’ is derived from the point that there is a passive or semi-active damper which has hooked the vehicle body to an imaginary stationary reference frame - ideal ‘sky’, the damper is ‘skyhook damper’, as shown in Figure 9.1, which can then reduce vertical vibrations due to all kinds of road disturbance.  $m$  is the vehicle suspension mass,  $k$  is the tyre stiffness,  $q$  is the displacement of road profile disturbance.

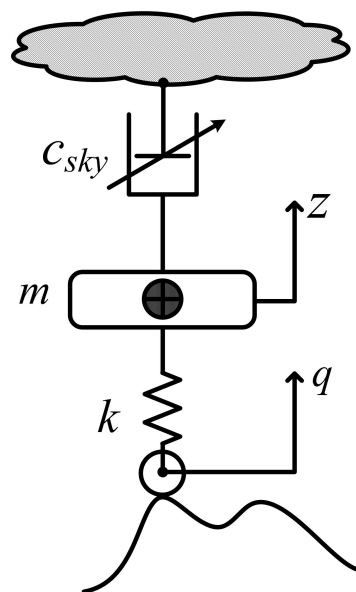


Figure 9.1: Ideal skyhook damper definition, adopted from [223]

Skyhook control can reduce the resonant peak of the sprung mass quite significantly and thus achieves a good ride quality in the vehicle suspension system. Equation (9.2.1) gives

the ideal skyhook control force for the vehicle suspension system, where  $c_{sky}$  is the damping coefficient,  $z$  is the vehicle body displacement.

$$f_{skyhook} = \begin{cases} -c_{sky}\dot{z} & \dot{z} \geq 0 \\ 0 & \dot{z} < 0 \end{cases} \quad (9.2.1)$$

By borrowing the idea of skyhook damping in section 9.2, the SkyhookSMC is introduced to reduce the sliding chattering phenomenon [221] [222].

### 9.3 Skyhook Surface Definition for Sliding Mode Control

Sliding mode control is fundamentally a consequence of discontinuous control. The real motion near the surface can be seen as the superposition of a ‘slow’ movement, along the surface, and the ‘fast’ movement, perpendicular to this surface, is the chattering phenomenon. The chattering phenomenon is an acknowledged drawback of sliding mode control, and is usually caused by unmodelled system dynamics. In traditional SMC design, a signum function is conventionally applied but this can lead to chattering in practice [200] [225].

Therefore, a skyhook surface sliding mode controller (SkyhookSMC) [221] [222] is introduced here to reduce the chattering phenomenon. The objective of the SkyhookSMC is to consider the nonlinear tether system as the controlled plant, and therefore as defined by the general state-space in equation (9.3.1) [200] [224].

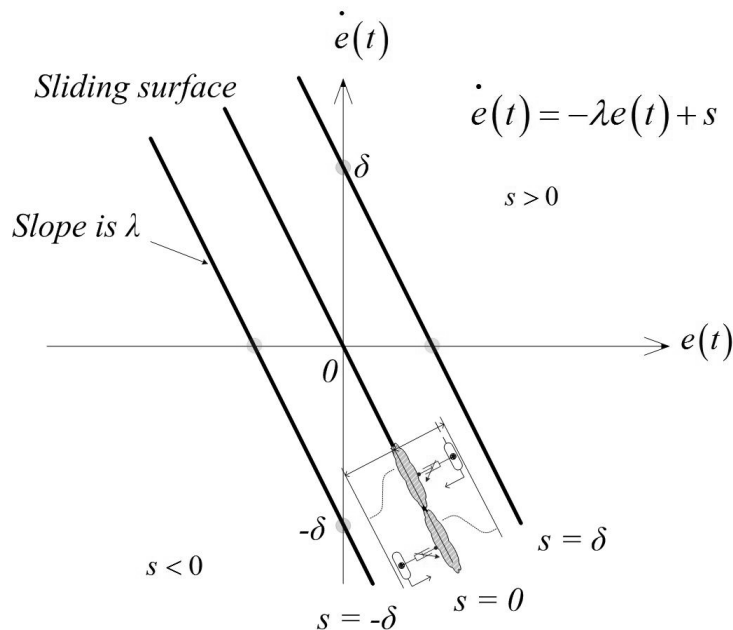


Figure 9.2: Sliding surface definition with skyhook surface [200] [221] [222] [224]

$$\begin{cases} \dot{x} = F(x, u, t) \\ y = H(x, u, t) \end{cases} \quad (9.3.1)$$

where,

$x \in \mathbb{R}^n$  is the state vector;

$n$  is the order of the nonlinear system, for the MMET system is a second-order system,  $n = 2$ ;

$u \in \mathbb{R}^m$  is the input vector,

$m$  is the number of inputs;  $F()$  and  $H()$  are the analytic functions.

$$s(e(t), t) = \left( \frac{d}{dt} + \lambda \right)^{n-1} e(t) \quad (9.3.2)$$

where,

$s(e(t), t)$  is the sliding surface of the hyperplane, as given in equation 9.3.2 and shown in Figure 9.2, which defines by the position error  $e(t)$  and velocity error  $\dot{e}(t)$  in equation (9.3.3);

$\lambda$  is a positive constant that defines the slope of the sliding surface;

$$s = \dot{e}(t) + \lambda e(t) \quad (9.3.3)$$

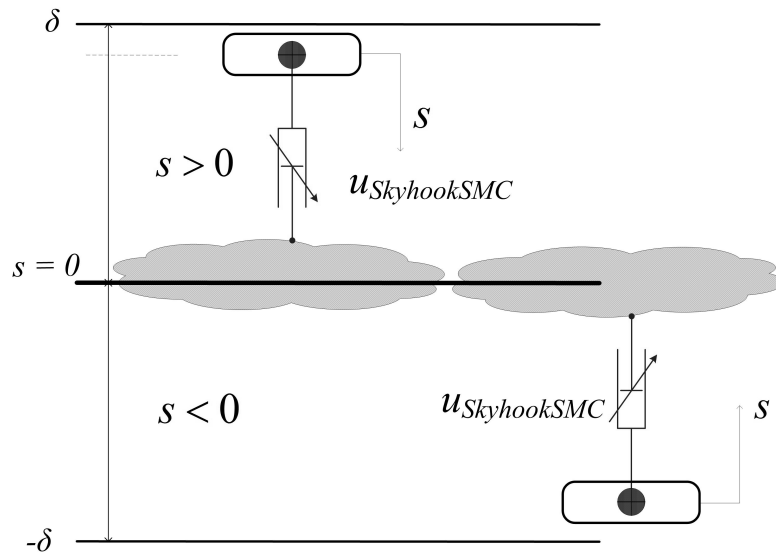


Figure 9.3: The sliding skyhook surface generation

From equations (9.3.2) and (9.3.3), the second-order tracking problem is replaced by a first-order stabilisation problem, in which the scalar  $s$  is kept at zero by means of a governing

condition. Therefore, the second-order system behaves like a first-order system, with time constant  $\lambda$ , and the trajectory will slide along  $s = 0$  to the origin, thus  $s = 0$  is also called the sliding surface or ideal slide mode.

$$V(s) = \frac{1}{2}s^2 \quad (9.3.4)$$

$$\dot{V}(s) = s\dot{s} = \lambda^2 e(t)\dot{e}(t) + \lambda (\dot{e}^2(t) + e(t)\ddot{e}(t)) + \dot{e}(t)\ddot{e}(t) < 0 \quad (9.3.5)$$

Obtained from the use of the Lyapunov stability theorem, the Lyapunov function is given in equation (9.3.4), and it states that the origin is a globally asymptotically stable equilibrium point for the control system. Equation (9.3.4) is positive definite and its time derivative is given in inequality (9.3.5), to satisfy the negative definite condition, that the system should satisfy the inequality in (9.3.5).

As shown in Figures 9.3 and 9.4, a soft switching control law is designed for the major sliding surface switching activity in equation 9.3.6, in which the sliding surface ( $s = 0$ ) is taken as the ideal stationary ‘sky’ in the SkyhookSMC.

$$u_{\text{SkyhookSMC}} = \begin{cases} -c_{\text{sky}} \tanh\left(\frac{s}{\delta}\right) & s\dot{s} > 0 \\ 0 & s\dot{s} \leq 0 \end{cases} \quad (9.3.6)$$

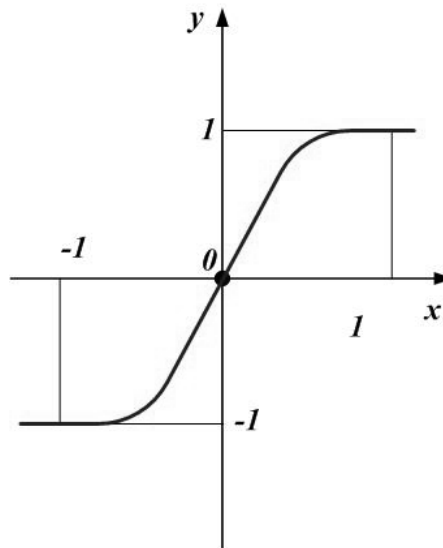


Figure 9.4: Tanh function definition

$$\tanh(x) = \frac{\sinh(x)}{\cosh(x)} = \frac{e^x - e^{-x}}{e^x + e^{-x}} \quad (9.3.7)$$

where,  $\tanh$  is the hyperbolic tangent function, as given in equation (9.3.7) and its graph over the domain  $[-1,1]$  is given in Figure 9.4.  $c_{\text{sky}}$  is an assumed positive damping ratio for the switching control law.

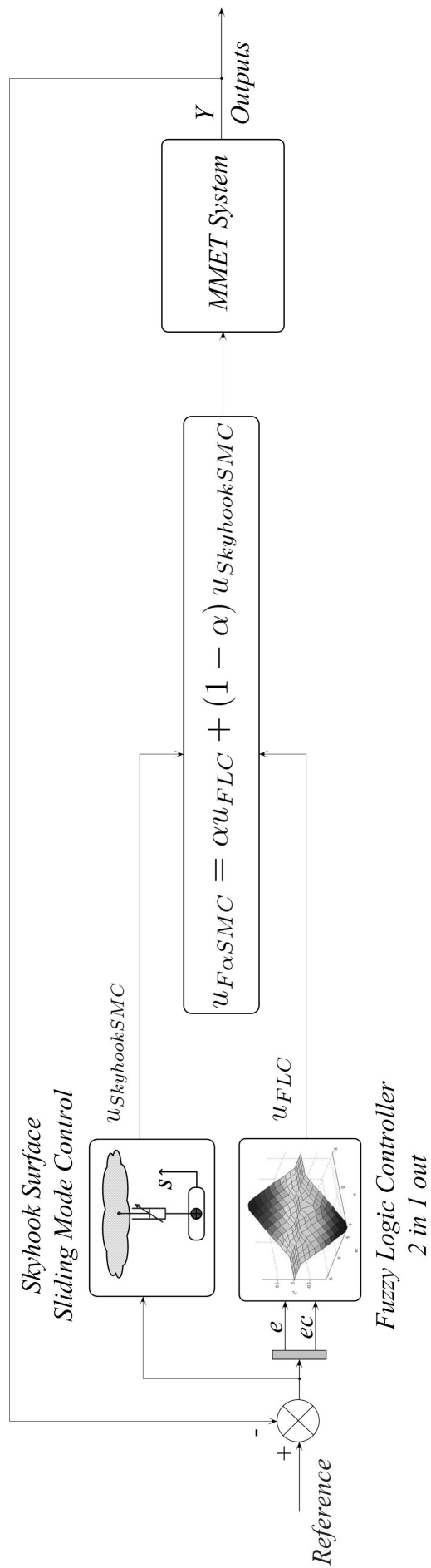


Figure 9.5: The  $F\alpha SMC$  control strategy definition

This law needs to be chosen in such a way that the existence and the reachability of the sliding-mode are both guaranteed, therefore a special boundary layer around the sliding surface is introduced to solve the chattering problem [224], noting that  $\delta$  is an assumed positive constant which defines the thickness of the sliding mode boundary layer.

## 9.4 Hybrid Fuzzy Sliding Mode Control Design

To make the necessary enhancement to the FSMC method, a hybrid control law is introduced here to combine fuzzy logic control with a SkyhookSMC control law, which is named  $F\alpha$ SMC [221] [222]. The hybrid control effects of FLC and SkyhookSMC are combined in equation (9.4.1), the flow diagram of the  $F\alpha$ SMC approach is given in Figure 9.5, the FLC designing process for the MMET spin-up is given in chapter 8.

$$u_{F\alpha SMC} = \alpha u_{FLC} + (1 - \alpha) u_{SkyhookSMC} \quad (9.4.1)$$

where  $\alpha$  is a proportionality factor, included to balance the weight of the fuzzy logic control to that of the SkyhookSMC control. Clearly,  $\alpha = 0$  represents the SkyhookSMC control, and  $\alpha = 1$  represents fuzzy logic control,  $\alpha \in [0,1]$ . The  $u_{FLC}$  design is given in equation (8.7.1), and  $u_{SkyhookSMC}$  is given in equation (9.3.6).

## 9.5 Simulations and Discussions

It is easy to switch the controller between the SkyhookSMC and the FLC modes when a proper value of  $\alpha$  is selected ( $0 < \alpha < 1$ ), and the hybrid fuzzy sliding mode controller is generated, by combining FLC with a soft continuous switching SkyhookSMC law based on equation (9.3.6). All the control methods have an effect on the spin-up of the MMET system from the given initial conditions.

The  $F\alpha$ SMC hybrid fuzzy sliding mode control system parameters require a judicious choice of the FLC scaling gains of  $\{K_e, K_{ec}\}$  for fuzzification,  $K_u$  is the defuzzification gain factor which is used to map the control force to the range that actuators can generate practically.

Similarly, the SkyhookSMC damping coefficient  $c_0$  is required to expand the normalised controller output force into a practical range. The thickness of the sliding mode boundary layer is given by  $\delta$ , and the slope of the sliding surface  $\lambda$ . In this simulation, the  $F\alpha$ SMC is used, with  $\alpha = 0.5$  to balance the control weight between the FLC and the SkyhookSMC

modes. Different values of  $\alpha = \{0.0, 0.5, 1.0\}$  can be used for {SkyhookSMC,  $F\alpha$ SMC, FLC} control of the MMET system, respectively.

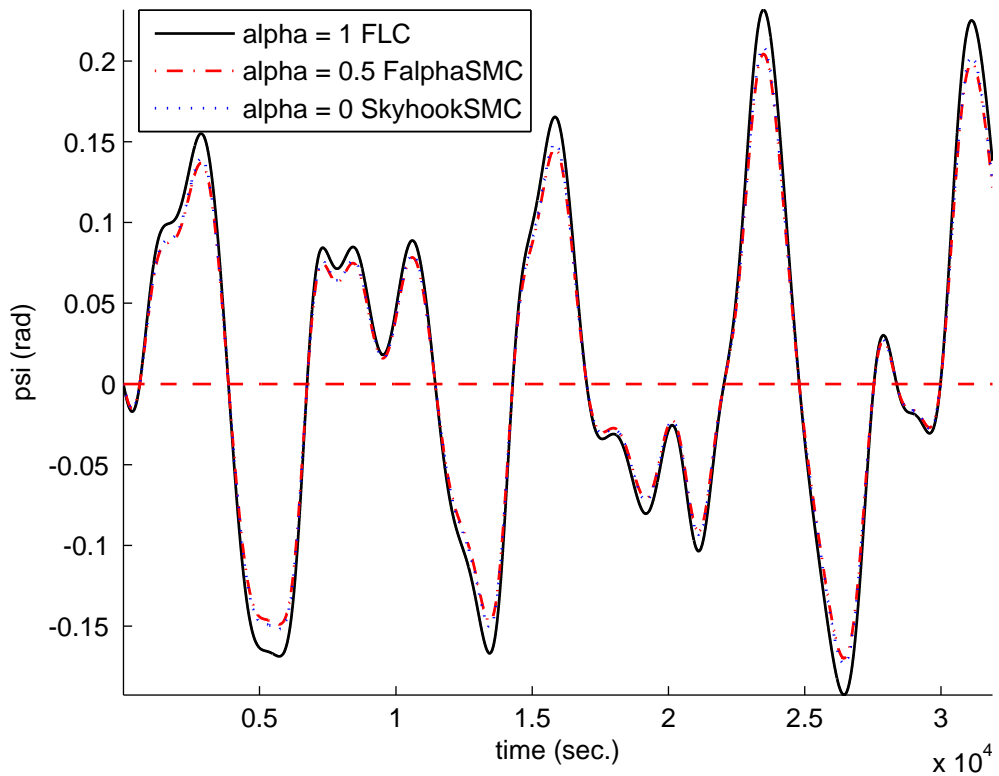


Figure 9.6: The MMET spin-up displacement of  $\psi$ , with different values of  $\alpha$  ( $T_n = 4.01$ )

- ▷ With the given initial conditions in Appendix C, Figures 9.6 to 9.8 and Figures 9.9 to 9.11 giving the MMET system's spin-up behaviour by the time responses of the displacement  $\psi$  and velocity  $\dot{\psi}$  with different values of  $\alpha$ .
- ▷ To compare the spin-up displacement plots' difference for the three controllers clearly, Figures 9.7 and 9.8 express the FLC, SkyhookSMC and  $F\alpha$ SMC controlled spin-up displacement plots in simulation time  $T_n = 400.01$ , which indicate that the FLC's spin-up displacement is bigger than the other two controllers.
- ▷ Figure 9.9 is the spin-up velocity response for the SkyhookSMC,  $F\alpha$ SMC and FLC controlled MMET system in simulation time  $T_n = 4.01$ , Figures 9.10 and 9.11 are the spin-up velocity in simulation time  $T_n = 400.01$ .
- ▷ Figure 9.6 is the spin-up displacement response for the SkyhookSMC,  $F\alpha$ SMC and FLC controlled MMET system in simulation time  $T_n = 4.01$ , which shows the SkyhookSMC and  $F\alpha$ SMC controlled spin-up displacement plots are close to each other, and both of them are smaller than FLC controlled spin-up displacement plot.

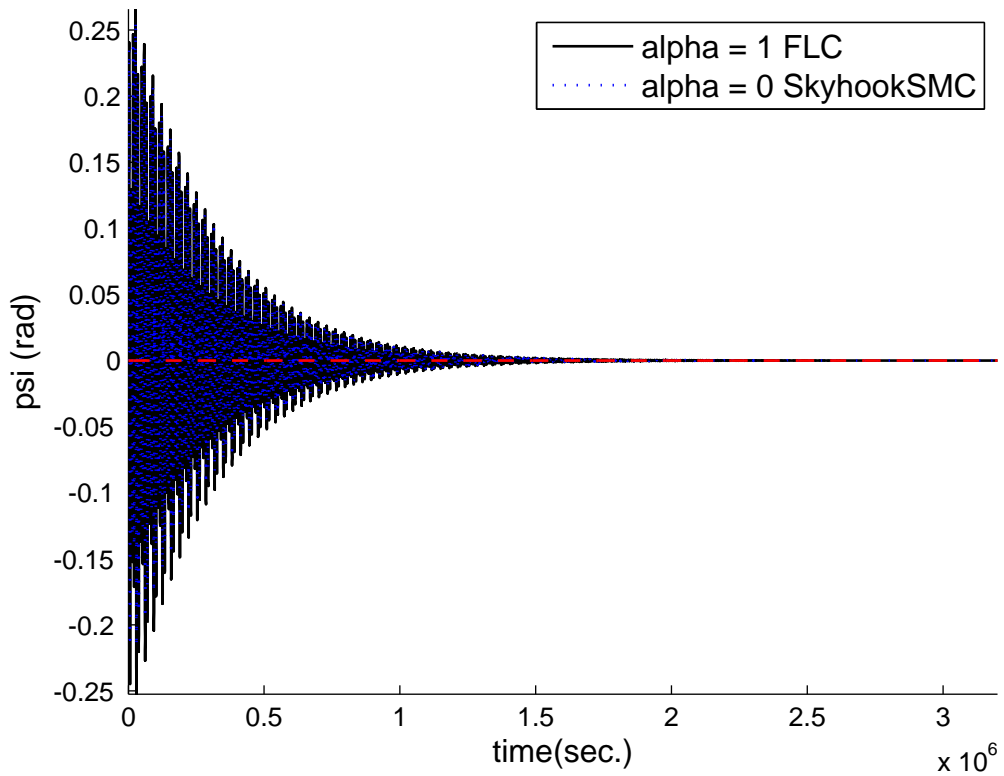


Figure 9.7: The MMET spin-up displacement of  $\psi$ , with different values of  $\alpha$  ( $T_n = 400.01$ ), FLC vs. SkyhookSMC

Furthermore, together with Figures 8.15 and 8.16, the control effects by FLC, SkyhookSMC and  $F\alpha$ SMC can be directly observed. These results indicate that all the control methods have effects on the spin-up of the MMET system. The SkyhookSMC control provides better control effects than for the MMET spin-up the FLC; and  $F\alpha$ SMC stays in between the two control methods above by setting the factor  $\alpha = 0.5$  in between the  $\alpha = 0.0$  and  $\alpha = 1.0$ .

▷ Figure 9.12 is the phase portrait in simulation time  $T_n = 4.01$  and Figure 9.13 is the same phase portrait in simulation time  $T_n = 400.01$ . The phase plane plots with different values of  $\alpha$  are shown as limit cycles, whose behaviour for the spin-up coordinate  $\psi$  clearly corroborates interpretations of steady-state with the  $F\alpha$ SMC control method for the MMET system.

▷ In Figures 9.14 and 9.15, the MMET spin-up error phase plane plots with different  $\alpha$  are given, and these show that all the control methods offer limit cycles. The FLC caused generally faster response behaviour than the two other control methods for the spin-up coordinate  $\psi$ , in simulation time  $T_n = 4.01$  and  $T_n = 400.01$ .

▷ Figure 9.16 is the controlled tether length plots by three control methods in simula-

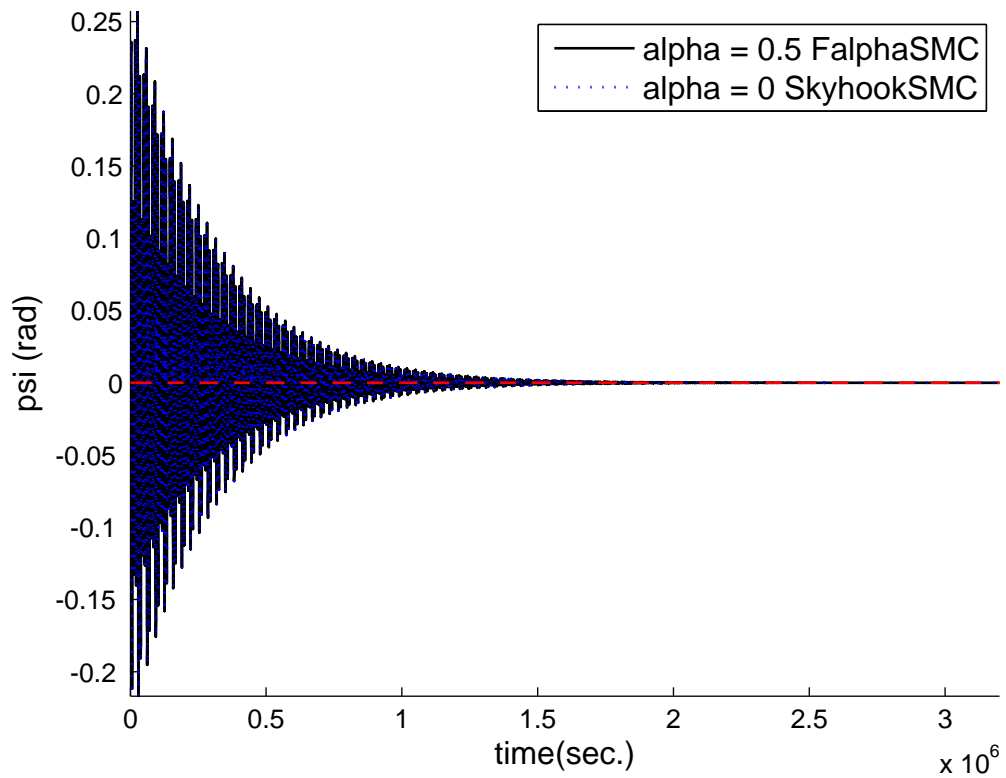


Figure 9.8: The MMET spin-up displacement of  $\psi$ , with different values of  $\alpha$  ( $T_n = 400.01$ ),  $F\alpha$ SMC vs. SkyhookSMC

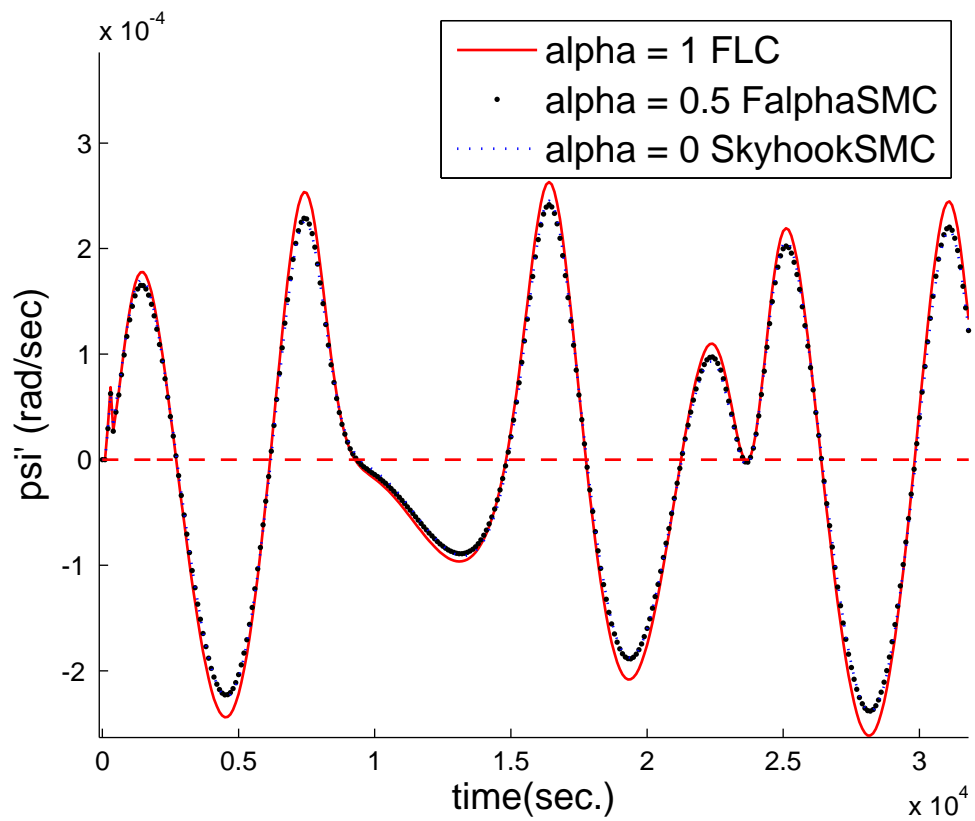


Figure 9.9: The MMET spin-up velocity of  $\psi$ , with different values of  $\alpha$  ( $T_n = 4.01$ )

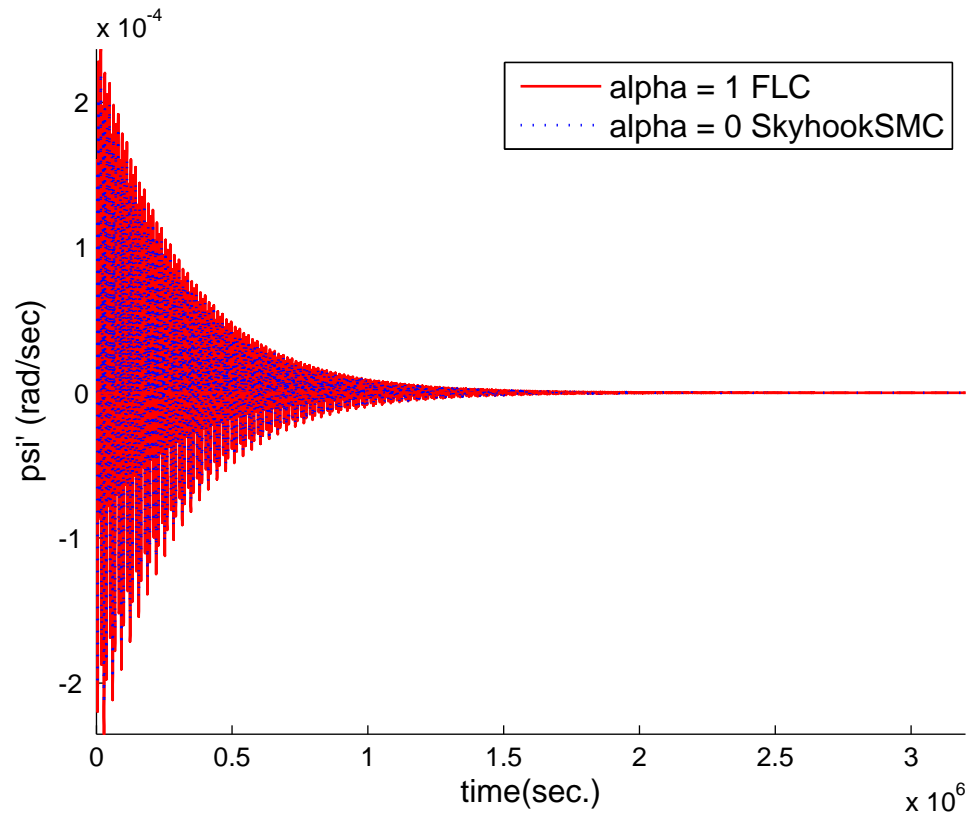


Figure 9.10: The MMET spin-up velocity of  $\psi$ , with different values of  $\alpha$  ( $T_n = 400.01$ ), FLC vs. SkyhookSMC

tion time  $T_n = 4.01$ , in which the FLC controlled tether length is longer than the two others. SkyhookSMC generated the shortest controlled tether length among the three of them. In the longer simulation time, all the tether length responses are given in Figure 9.17, which is related to Figure 8.24.

▷ Figures 9.18 and 9.20 show the plots for the Lyapunov function and their derivative in simulation time  $T_n = 4.01$ , which indicate the effect of  $F\alpha$ SMC control for different values of  $\alpha$ . SkyhookSMC has higher energy activities than the two other control methods, and FLC has the lower associated energy around  $V' = 0$ , with the  $F\alpha$ SMC's energy in the middle of the three.  $F\alpha$ SMC can balance the control effects of FLC and SkyhookSMC for stable MMET 9-DOF spin-up outputs and associated energy activities. Similarly, Figures 9.19 and 9.21 are the the Lyapunov functions and their derivative functions in simulation time  $T_n = 400.01$ .

► The figures for the axial, torsional and pendular elastic motions are attached in Appendix K.

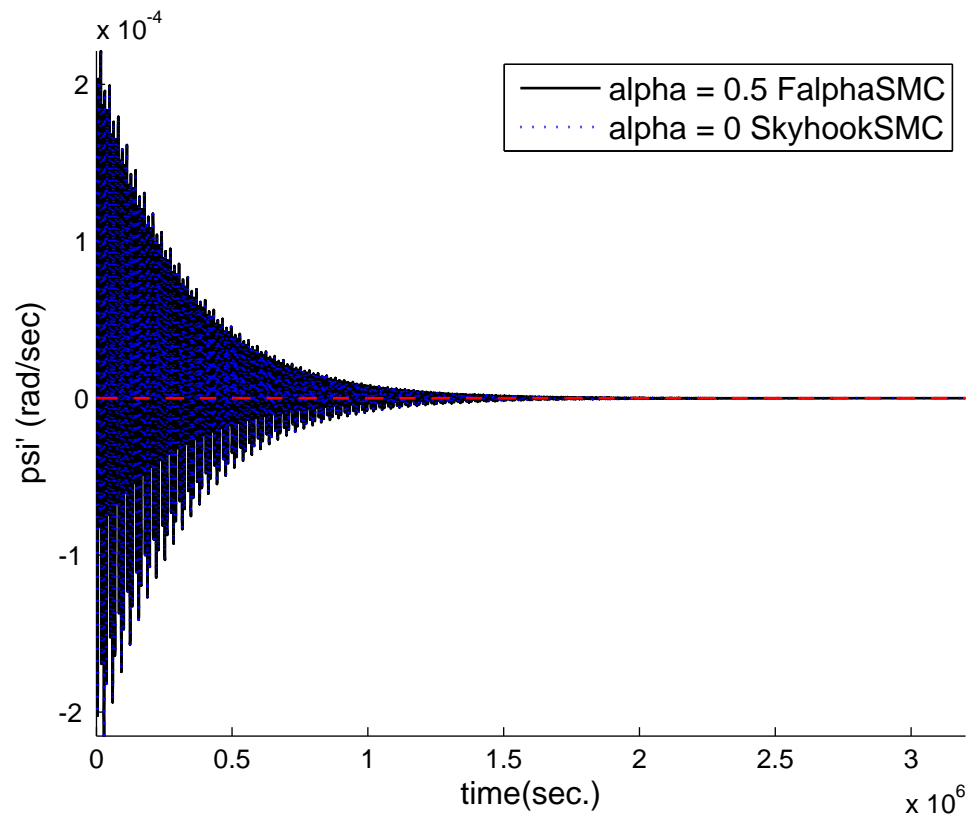


Figure 9.11: The MMET spin-up velocity of  $\psi$ , with different values of  $\alpha$  ( $T_n = 400.01$ ), F $\alpha$ SMC vs. SkyhookSMC

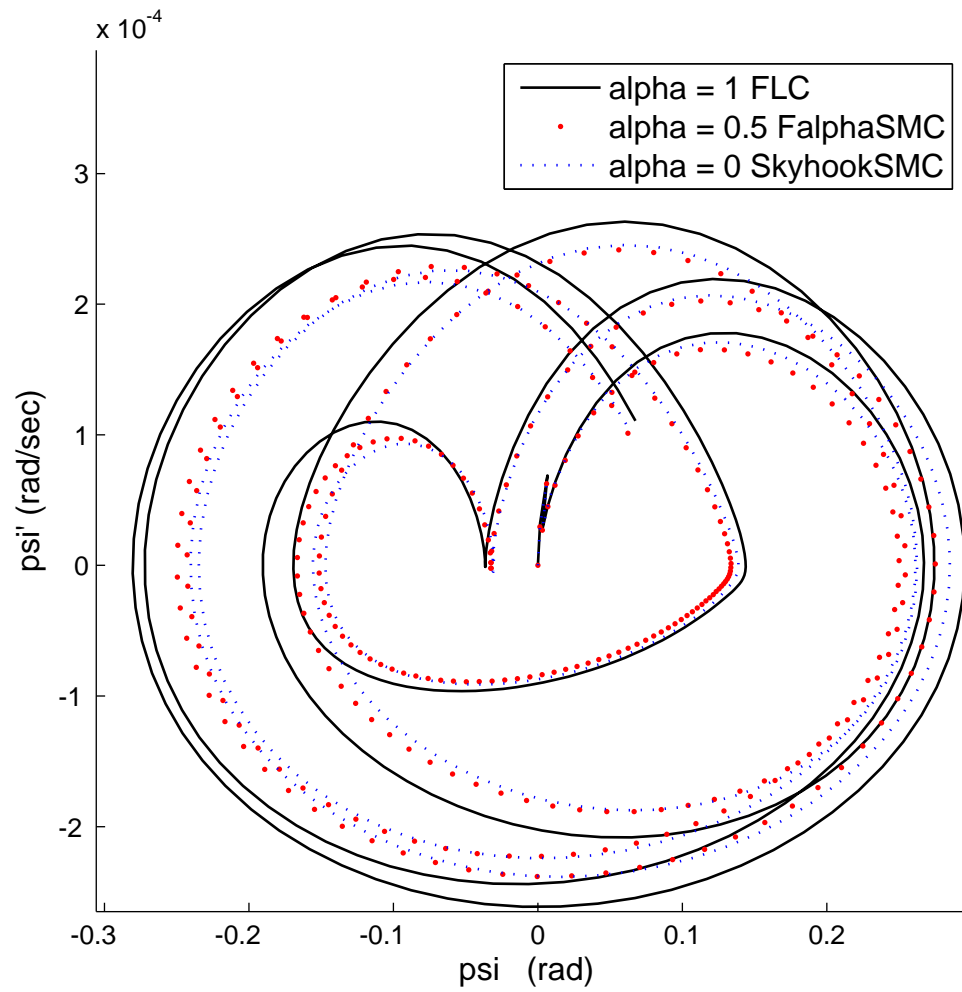


Figure 9.12: The MMET spin-up phase plane portrait with different values of  $\alpha$  ( $T_n = 4.01$ )

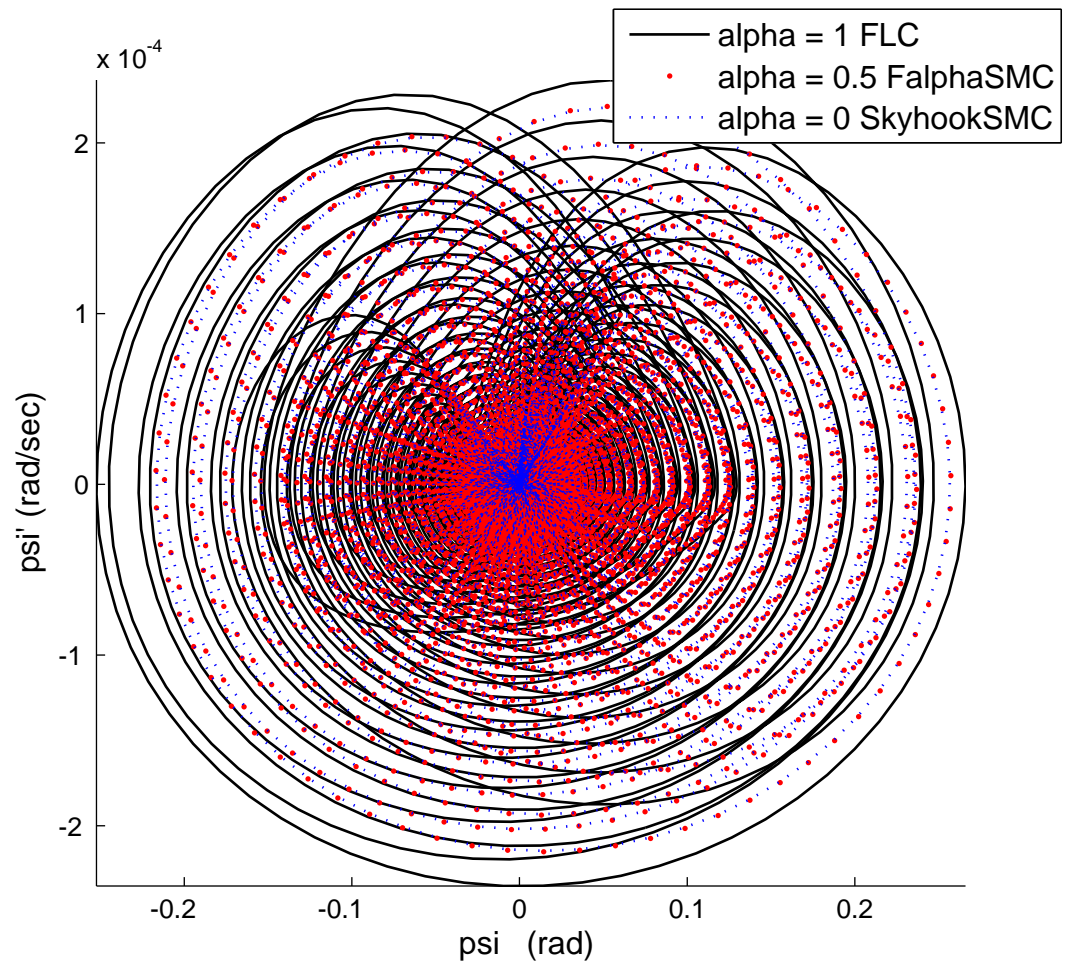


Figure 9.13: The MMET spin-up phase plane portrait with different values of  $\alpha$  ( $T_n = 400.01$ )

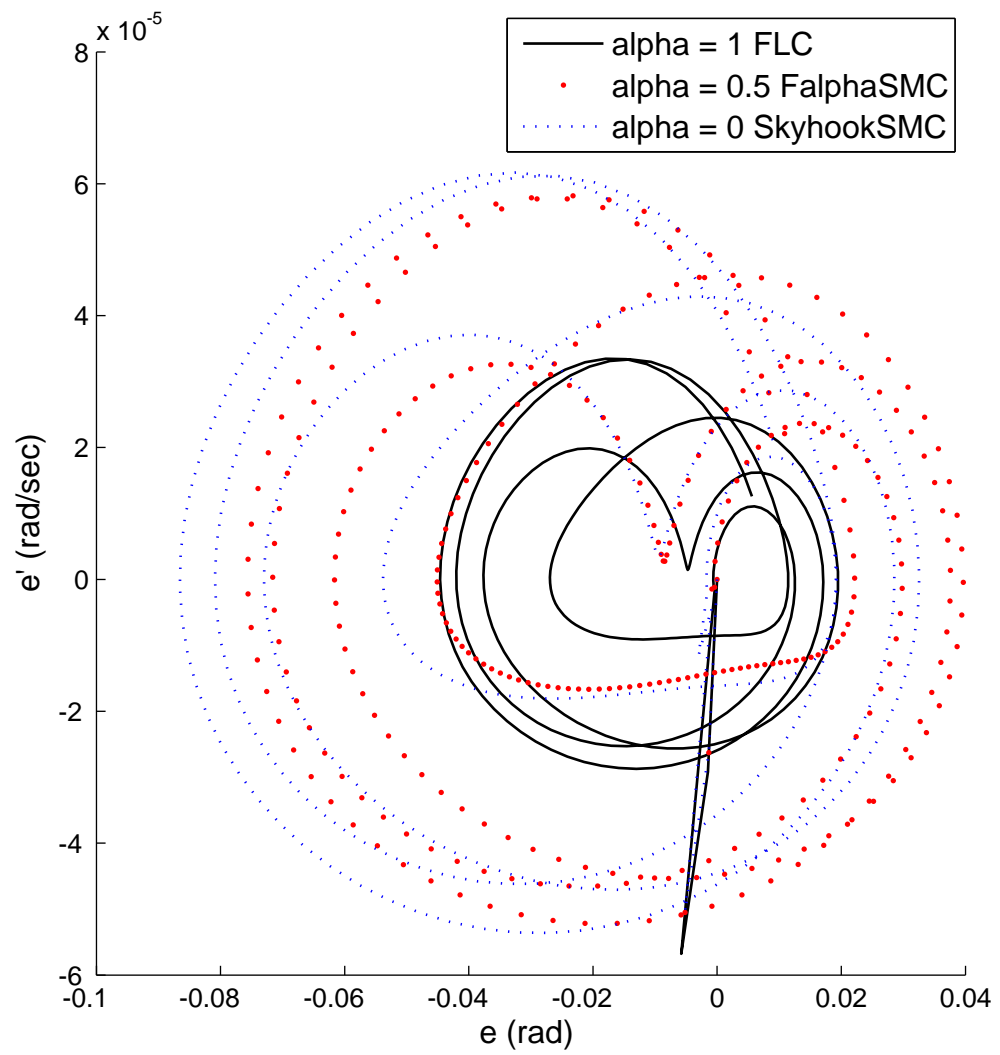


Figure 9.14: The MMET spin-up error phase plane portrait with different values of  $\alpha$  ( $T_n = 4.01$ )

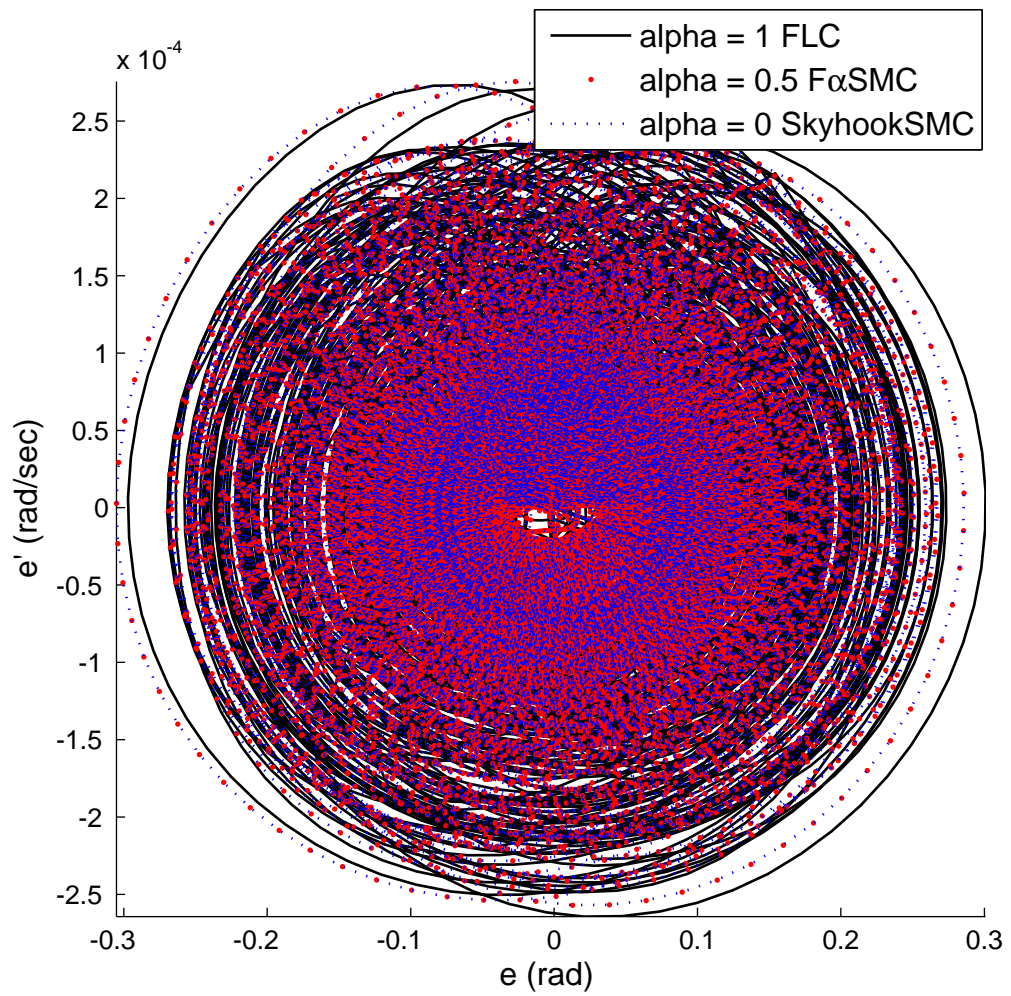


Figure 9.15: The MMET spin-up error phase plane portrait with different values of  $\alpha$  ( $T_n = 400.01$ )

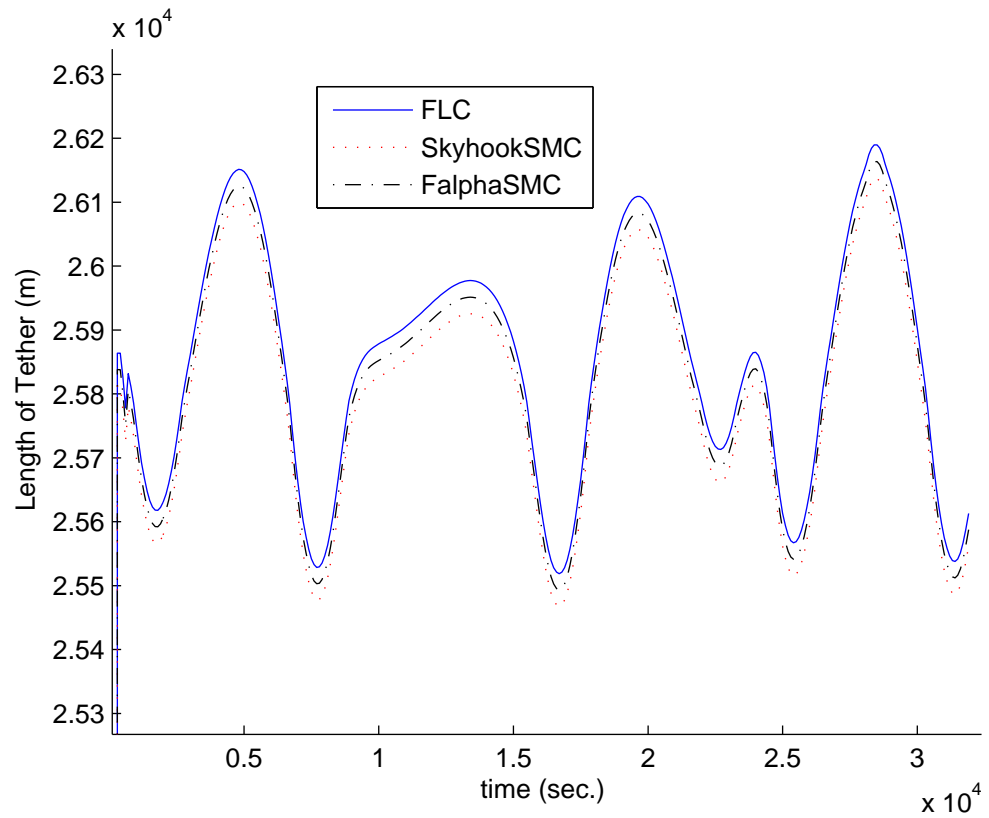


Figure 9.16: Tether length with control ( $T_n = 4.01$ )

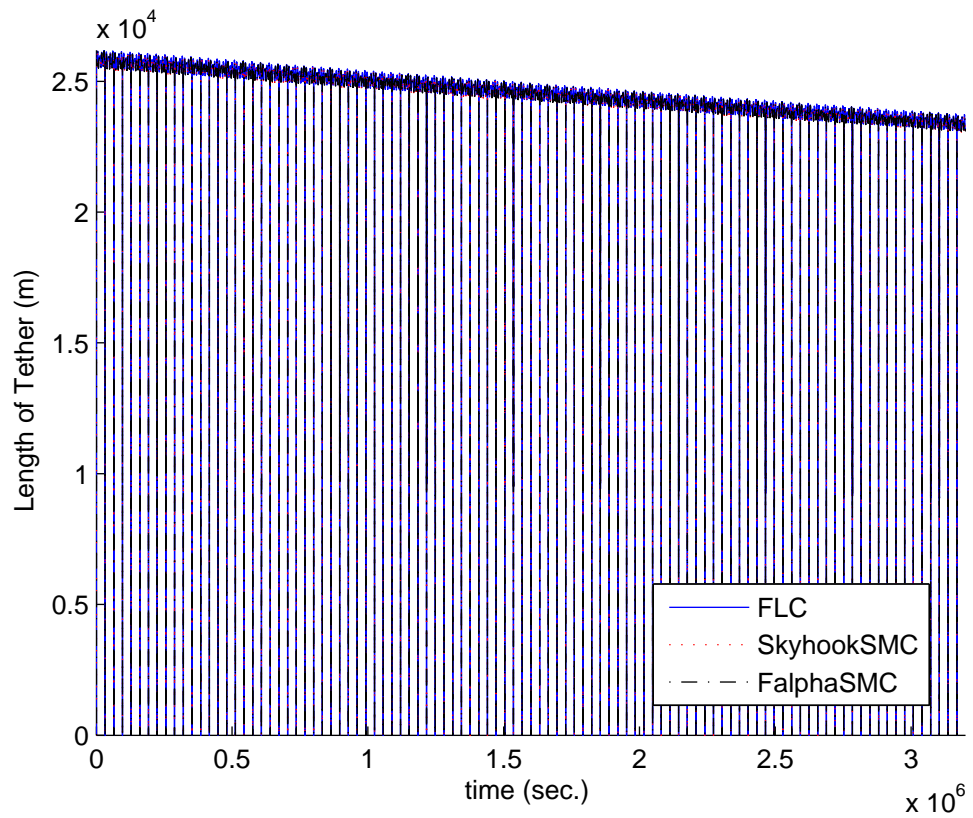


Figure 9.17: Tether length with control ( $T_n = 400.01$ )

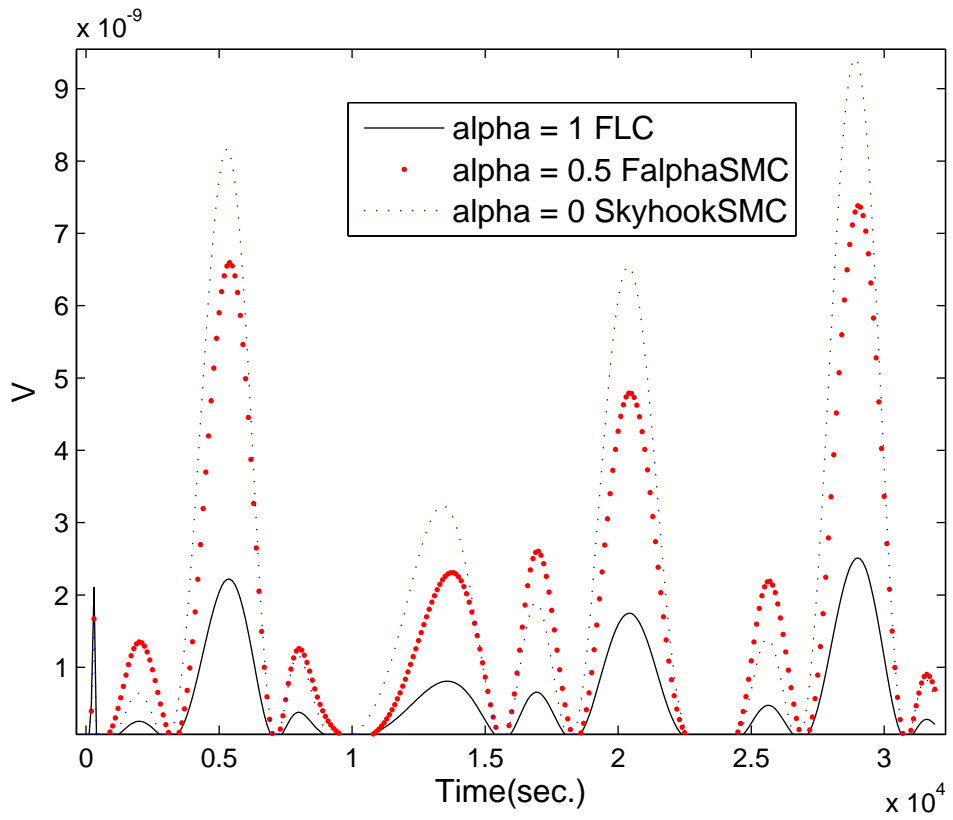


Figure 9.18: The Lyapunov function for the MMET spin-up control ( $T_n = 4.01$ )

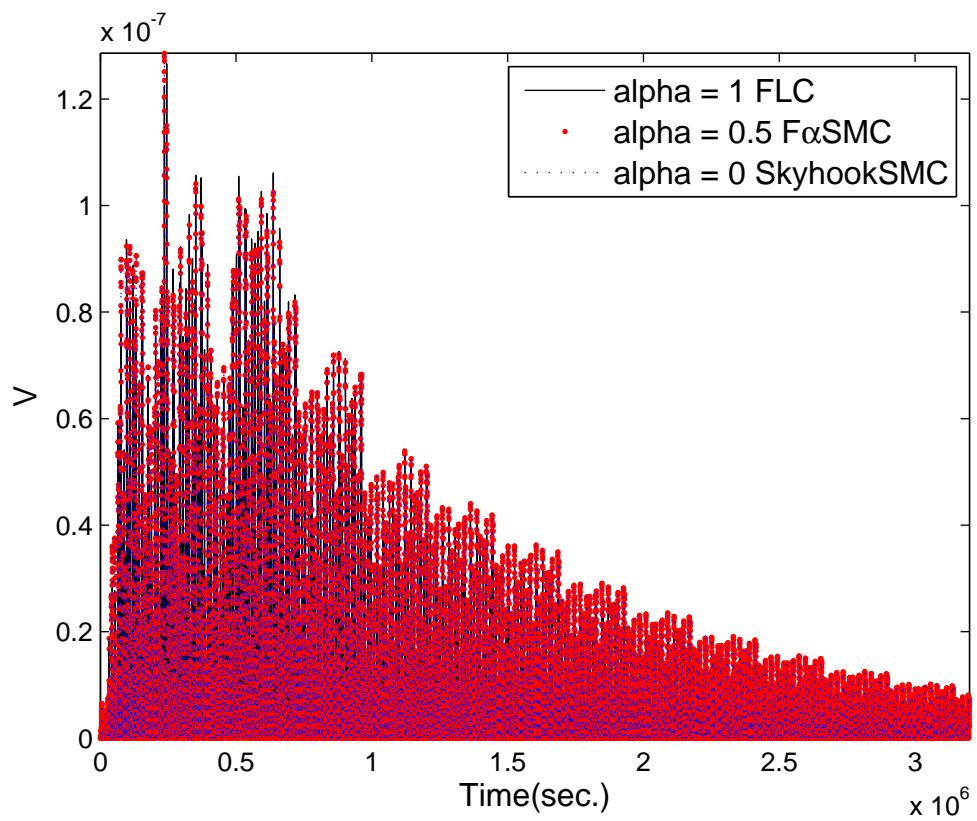


Figure 9.19: The Lyapunov function for the MMET spin-up control ( $T_n = 400.01$ )

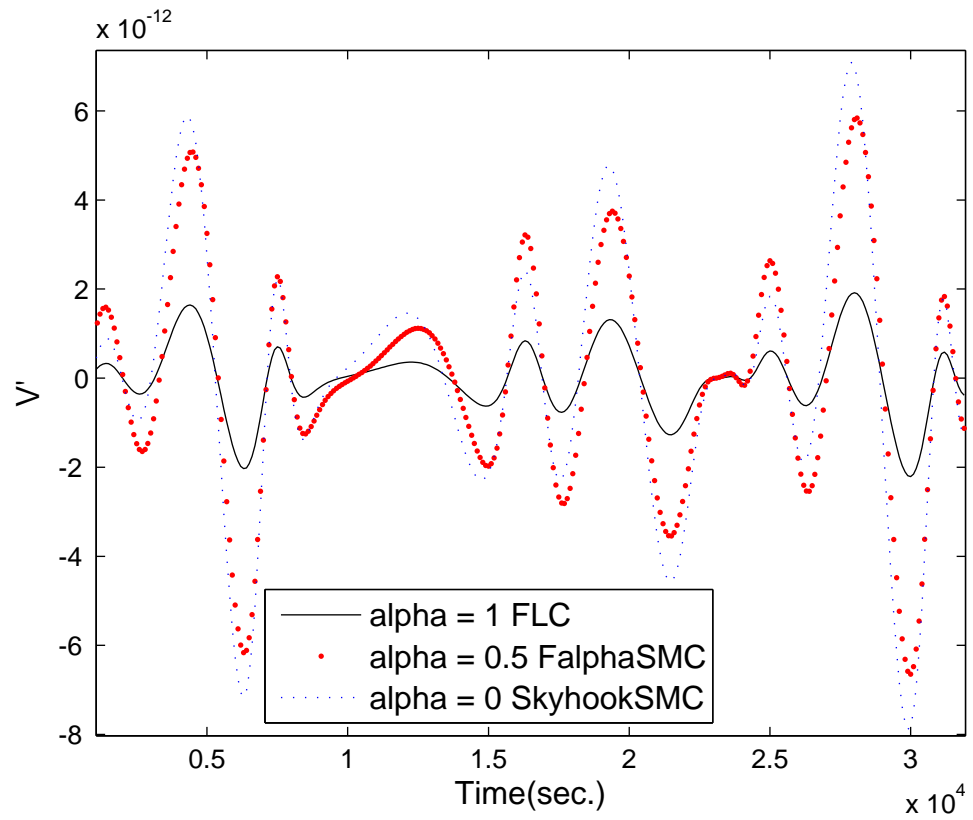


Figure 9.20: The time derivative of the Lyapunov function for the MMET spin-up control ( $T_n = 4.01$ )

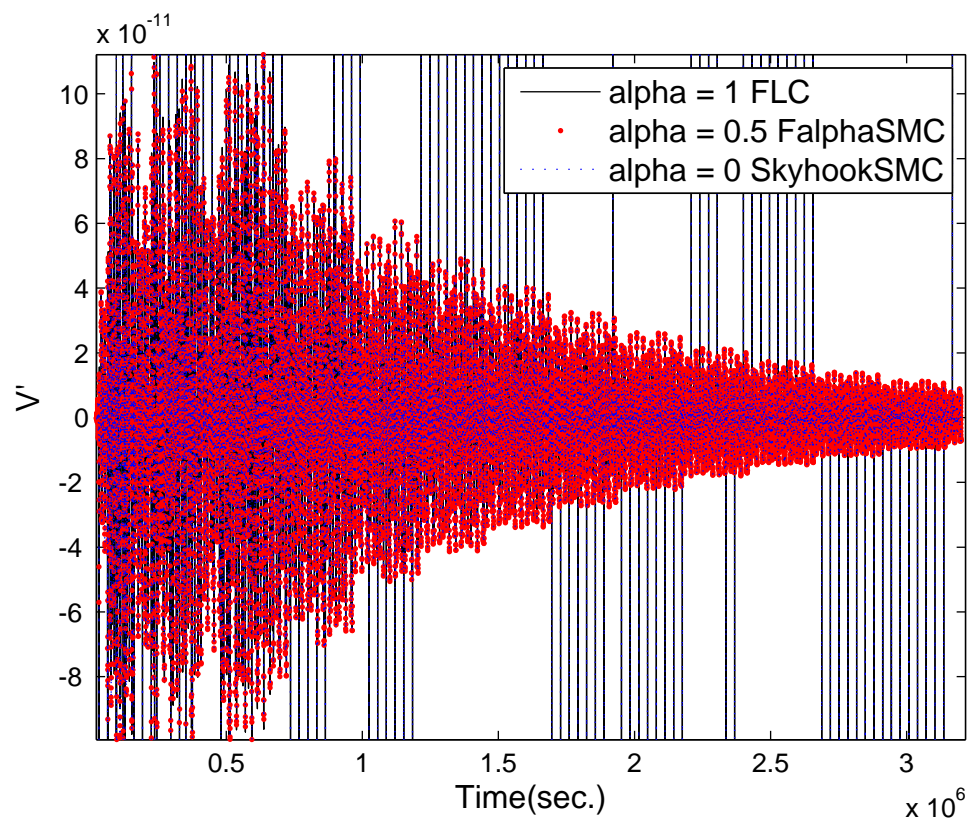


Figure 9.21: The time derivative of the Lyapunov function for the MMET spin-up control ( $T_n = 400.01$ )

## 9.6 Conclusions

A specialised hybrid control law, named  $F\alpha$ SMC, has been proposed and discussed in this chapter. This combines fuzzy logic control with a SkyhookSMC control law together in equation (9.4.1), then it is applied for the control of motorised space tether spin-up coupled with an flexible oscillation phenomenon.

The FLC is given in chapter 8, and for the SkyhookSMC, by borrowing the idea of skyhook damping, it reduces the sliding chattering phenomenon, in which a soft switching control law is presented for the major sliding surface switching activity, as shown in equation 9.3.6.

The simulations with given initial condition data have been devised in a connecting programme between control code written in MATLAB and dynamics simulation code constructed within MATHEMATICA.

- ▷ The results state the control effects for FLC,  $F\alpha$ SMC and FLC, which lead to stable spin-up behaviour with torsional and pendular motions. It is concluded that there is an enhanced level of spin-up control for the MMET system using the specialised hybrid controller.
- ▷ With the weight factor  $\alpha$ , it can balance the weight of the fuzzy logic control to that of the SkyhookSMC control. There is an observed difference for each of the elastic behaviours in the MMET system involving these MMET systems with different controllers - FLC,  $F\alpha$ SMC and SkyhookSMC, in which the control effects of  $F\alpha$ SMC and SkyhookSMC are better than FLC.
- ▷ The  $F\alpha$ SMC controlled spin-up motions are reducing down with oscillation to a stable status, which state the control effects on the spin-up and reached the control objective.
- ▷ The axial elastic motions are moving stably with the smaller amplitudes.
- ▷ The torsional elastic motions can not be effected by tether length control strategy, for it is decoupling to other generalised coordinates.
- ▷ The pendular elastic motions decline with convergent reaction with reducing oscillation, then reach to a zero status in the end.

# Chapter 10

---

## Conclusions and Future Work

---

### 10.1 Work Summary

Space tethers are typically very long structures ranging in length from a few hundred metres to many kilometres, with a relatively small diameter. Space tethers can be applied to swing spacecraft from one orbit to another, or even from one planet to another, without using rocket propellant. Generally speaking, there are two general categories of tethers: ⟨1⟩ momentum exchange tethers, which provide a mechanical connection which enables the transfer of energy and momentum from one object to the other; ⟨2⟩ electrodynamic tethers, which interact with the Earth's magnetosphere to generate power or provide propulsion for space objects connected with them. Space tethers can be used for a diverse range of applications, which include formation flying, safety tethers, artificial gravity generation, probe towing, and aerobraking.

This thesis has discussed various dynamical models for a series of MMET systems, and has proposed two control methods for the discretised flexible MMET system spin-up in the presence of disturbances and parameter conditions. This chapter summarises the models and results, and indicates further research paths which might be of future interest.

Figure 10.1 indicates the MMET systems modelling road-map, helps to organise the structure of this thesis, in which a series of elastic MMET systems are defined, based on this road-map, in Chapters 3 to 7. As shown in Figure 10.1, this thesis addresses some of the models for momentum exchange tethers by using the Lagrangian procedure with proper environmental conditions.

- *Chapter 1*: This chapter introduces the basic concept of space tether, space tether missions and applications, and thesis's structure is also presented in the end.

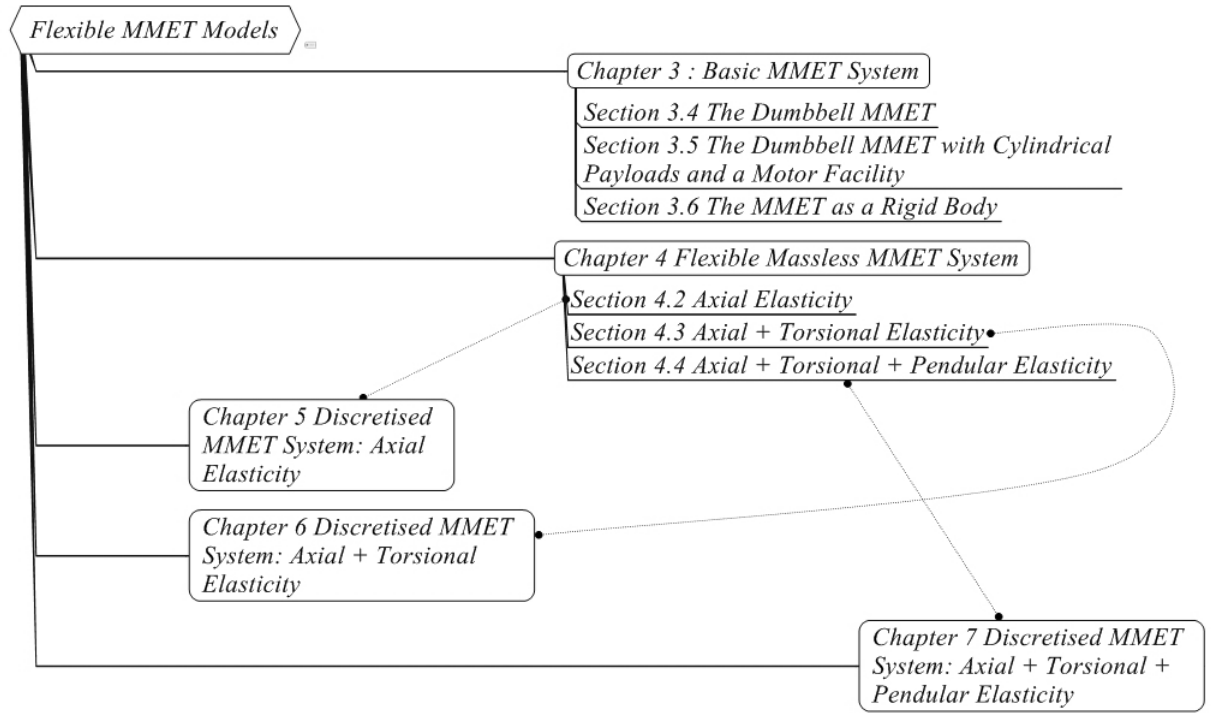


Figure 10.1: Thesis structure for flexible MMET models

- *Chapter 2*: With the aim of establishing useful sources from fundamental researches in the literature available, and highlighting the previous control methods developed, this chapter attempts to provide a useful contextualised source of references for further space tether control studies, which includes five of the following space tether related research topics: ⟨1⟩ tether deployment and retrieval; ⟨2⟩ trajectory generation and orbit control; ⟨3⟩ tether attitude and motion control; ⟨4⟩ tether vibration control and dynamical simulations; ⟨5⟩ space tether dynamical models.
- *Chapter 3*: The dumbbell tether, the basic conceptual schematic of the MMET, the dumbbell MMET system, the dumbbell MMET with cylindrical payloads and a motor facility, and the rigid MMET system;

▷ There are two generalised coordinate systems which are defined; all the MMET system models are modelled within these two coordinate systems. The first one is an Earth centred global coordinate system -  $\{X, Y, Z\}$ ; the second one is the relative rotating coordinate system -  $\{x_0, y_0, z_0\}$ . The centre of the Earth is denoted by  $E(E_x, E_y, E_z)$ , which is defined as the origin of the  $\{X, Y, Z\}$  system, where,  $E_x, E_y, E_z$  are set to  $(0, 0, 0)$ , which is  $E(0, 0, 0)$ .

- ▷ The dumbbell tether system consists of two end masses,  $M_1$  and  $M_2$ , connected by the tether subspans, where the distance from the dumbbell tether's base point to each end mass is denoted by  $L_1$  and  $L_2$ . The dumbbell tether subspans are assumed to be massless relative to the masses of the two end bodies, as shown in Figure 3.2.
- ▷ The concept of the motorised momentum exchange tether and its following research aspects are introduced, as shown in Figure 3.12.
- ▷ As shown in Figure 3.14, the dumbbell MMET system consists of two end masses,  $M_1$  and  $M_2$ , connected by a massless tether with the same length of subspans from the tether's centre of mass  $M_0$  (or  $M_M$ ) to each end mass, denoted by  $L$ .
- ▷ Based on the massless dumbbell MMET modelling, the dumbbell MMET with cylindrical payloads and a motor facility is proposed, in which the payload mass moment of inertias, the motor facility mass moment of inertias, and the torque plane, are included in the model, as shown in Figure 3.14.
- ▷ The tether-tube mass moments of inertia and a tether discretisation methodology are utilised in the rigid body MMET system modelling process, as shown in Figure 3.25.
- *Chapter 4:* the massless elastic MMET system is investigated, in which, there is no appreciable mass in the tether subspans;
  - ▷ A dynamical modelling analysis for a flexible massless MMET system, which implies that there is no mass for the tether subspans, the use of the word 'flexible' means that this MMET system model only contains axial, torsional and pendular elasticity. The models for axial, torsional and pendular elasticity are given in sections 4.2, 4.3 and 4.4, respectively.
  - ▷ The assumptions for the massless elasticity modelling process are provided, which numbered as A1 to A7 in section 4.1.

▷ Three ‘reference’ planes are proposed to describe the torsional and pendular elastic motions, as given in Figures 4.1 and 4.2, which include three orthogonal reference planes:  $x_0 - O - y_0$ ,  $x_0 - O - z_0$  and  $z_0 - O - y_0$ .

▷ The modelling for the torsional elasticity is referenced onto the plane  $x_0 - O - z_0$ , the pendular motion of the tether is referenced onto two orthogonal planes:  $x_0 - O - y_0$  and  $z_0 - O - y_0$ .

▷ There are seven rotational generalised coordinates ( $\psi$ ,  $\psi_x$ ,  $\theta$ ,  $\alpha$ ,  $\alpha_x$ ,  $\gamma$ ,  $\gamma_x$ ) and two translational coordinates ( $L_x$ ,  $R$ ) which were chosen as the generalised coordinates for the flexible massless MMET system, in which the rigid body generalised coordinates ( $\psi$ ,  $\theta$ ,  $\alpha$ ,  $\gamma$ ,  $R$ ) are not duplicating any of the motions of the elastic generalised coordinates ( $\psi_x$ ,  $\alpha_x$ ,  $\gamma_x$ ,  $L_x$ ).

- *Chapters 5, 6 and 7*: These chapters have discussed MMET systems with axial, torsional and pendular elasticity, sequentially;

▷ As opposed to the assumptions A1 to A7 in section 4.1, the assumptions for the discretised MMET modelling are proposed as B1 to B8, in section 5.1.

▷ The modelling for the discretised axially elastic MMET system was undertaken by the Lagrangian process in Chapter 5, as shown in Figure 5.1. With an arbitrary choice of  $N = 10$  mass points, the generalised coordinates  $\eta_i$  ( $i = 1$  to 10) define relative axial motion of the 10 discretised mass points,  $\eta_{P1}$  and  $\eta_{P2}$  are the generalised relative axial coordinates for the mass payloads  $M_{P1}$  and  $M_{P2}$ .

▷ The discretised MMET system which involves both axial and torsional elasticity is proposed in Chapter 6, as shown in Figure 6.1. All the torsional ‘spring-damper’ groups are defined on the reference plane  $x_0 - O - z_0$  as shown in Figure 4.19. With 10 discretised mass points, the generalised relative torsional coordinates  $\varphi_i$  ( $i = 1$  to 10) define the relative torsional motion of the 10 discretised mass points.  $\varphi_{P1}$  and  $\varphi_{P2}$  are the generalised relative torsional coordinates for

the mass payloads  $M_{p1}$  and  $M_{p2}$ .

▷ Based on the MMET modelling in the previous chapters, a discretised flexible MMET system is investigated by involving pendular elasticity in this chapter. As shown in Figures 7.1 and 7.2, there are two parts of the pendular elasticity, which are defined on the plane  $x_0 - O - y_0$  and the plane  $z_0 - O - y_0$ , respectively. In the case of this modelling, the generalised coordinates  $\chi_i$  describe the motions for mass points  $m_i$  ( $i = 1, \dots, 10$ ) of the pendular elasticity on the plane  $x_0 - O - y_0$ . The generalised coordinates  $\zeta_i$  describe the behaviours for mass points  $m_i$  ( $i = 1, \dots, 10$ ) of the pendular elasticity on the plane  $z_0 - O - y_0$ .

▷ To deal with the numerical time-consuming simulation difficulties, we have reduced the discretisation scheme right down to  $N = 2$ , then used Lagrange's equations to derive a reduced set of nonlinear governing equations for the simplified axial, torsional and pendular elastic MMET systems, as discussed in Appendices G, H and I, respectively. Then, based on the simplified MMET systems, the numerical results are generated for the simulations and discussions.

• *Chapters 8 and 9:* A '2-in-1-out' FLC and a F $\alpha$ SMC control methods have been investigated and designed for the discretised flexible MMET system's spin-up behaviour control;

▷ FLC is a practical alternative for a variety of challenging control applications. For the nonlinear dynamics and complex MMET system's spin-up control problem, we investigated a fuzzy logic based controller to maintain the desired length and length rate of the tether in Chapter 8.

▷ In Chapter 8, the velocity and acceleration of  $\psi$  are selected as  $e$  and  $ec$  feedback signals for the MMET spin-up control. The simulation shows the robustness and usefulness which can be achieved from the fuzzy logic control for the MMET spin-up behaviour; the stability of the MMET system spin-up response for certain combinations of the tether length and the length rate are observed.

▷ In Chapter 9, a hybrid fuzzy sliding mode control method is proposed and applied into the tether subspan length changes for the spin-up control of the MMET

system, which involved a skyhook surface sliding mode control (SkyhookSMC) method, which is applied here to control the tether subspan length for spin-up control of the discretised flexible MMET system.

## 10.2 Conclusions

- *Chapter 3:* The numerical results are given in section 3.2.6, section 3.4.6, section 3.5.9 and section 3.6.9, which provide stable and accurate numerical behaviours including the spin-up performance, and also indicate their connections to each other. Meanwhile, the numerical results have been taken as the reference for following MMET model development. The results show the MMET systems' periodic spin-up behaviour on orbit, with zero initial conditions as listed in Appendix C. For the rigid body motion control, the MMET models provided in Chapter 3 are good choices for their highly efficient computation.

- *Chapter 4:* Using the parameters in Appendix C, the numerical results for the selected generalised coordinates in section 4.2.2, section 4.3.2 and section 4.4.2 expressed the periodic motions on orbit, with reducing amplitude of axial, torsional and pendular elastic oscillation for three massless MMET models in sections 4.2, 4.3 and 4.4, respectively, whose similar spin-up behaviours and rigid body behaviours are also noted, and the stable MMET system rigid body motions are observed.

The dynamical modelling process in this context has shown that by including axial, torsional and pendular elasticity, the flexible MMET model proposed a significant bearing on overall performance, involving the tether-tube mass by using a discretisation methodology.

- *Chapter 5:* The numerical results are given in section 5.9, in which periodic behaviour, including the spin-up and the axial elastic performance for this MMET model, are obtained.

Compared with section 4.4.2, when involving the tether's mass and mass moment of inertia, the amplitudes and shapes for the spin-up and the axial elastic behaviours are different, with the same parameter settings as in Appendix C.

- *Chapter 6:* The numerical simulations have shown the convergence of the torsional elastic behaviour by the torsional elastic angular displacement, which is approaching to zero during full simulation time, and the amplitude and shape are slightly different

from massless MMET system's behaviours, by involving the tether's mass and mass moment of inertia.

Together with Chapters 5 and 6, Chapter 7, the numerical simulations have expressed the reducing flexible behaviour, which are approaching to zero during full simulation time, and the amplitudes and shapes are different from massless flexible MMET system's behaviours by involving the tether-tube mass and mass moment of inertia, which means, the initial values for numerical parameters, related to mass and mass moments of inertia, take sensitive effects on the results.

- *Chapter 8*: The simulations show the robustness and usefulness which can be achieved from the fuzzy logic control for the MMET spin-up behaviour, and the stability of the MMET system spin-up response for certain combinations of the tether length and the length rate were observed in simulation time  $T_n = 4.01$  and  $T_n = 400.0$ , and the flexible behaviours showed a similar convergent reaction with reducing oscillation.

- *Chapters 8 and 9*: The skyhook surface sliding mode control can reduce the resonant peak of the sprung mass quite significantly and thus can achieve a good ride quality. By borrowing the idea of skyhook damping in section 9.2, the SkyhookSMC is introduced in order to reduce the sliding chattering phenomenon. As shown in Figure 9.3, a soft switching control law is designed for the major sliding surface switching activity in equation 9.3.6.

A simulation with a given initial condition data has been devised in a connecting programme between control code written in MATLAB and dynamics simulation code constructed within MATHEMATICA, both in Chapters 8 and 9.

- *Chapter 9*: The results state the control effects for FLC, F $\alpha$ SMC and FLC, which led to stable spin-up behaviour with torsional and pendular motions. It is concluded that there is an enhanced level of spin-up control for the MMET system which uses the specialised hybrid controller.

The hybrid control effects of FLC and SkyhookSMC are combined in equation (9.4.1), the flow diagram of the F $\alpha$ SMC approach is given in Figure 9.5, the FLC designing process for the MMET spin-up is given in Chapter 8, in which,  $\alpha$  is a proportionality factor, included to balance the weight of the fuzzy logic control to that of the hyperbolic tangent control. Clearly,  $\alpha = 0$  represents the SkyhookSMC control, and  $\alpha = 1$  represents fuzzy logic control,  $\alpha \in [0,1]$ .

The  $F\alpha$ SMC hybrid fuzzy sliding mode control system parameters require a judicious choice of the FLC scaling gains of  $\{K_e, K_{ec}\}$  for fuzzification,  $K_u$  is the defuzzification gain factor which is used to map the control force to the range that actuators can generate practically. It is easy to switch the controller between the SkyhookSMC and the FLC modes when a proper value of  $\alpha$  is selected ( $0 < \alpha < 1$ ).

The SkyhookSMC leads to better control effects than the FLC for the MMET spin-up, and  $F\alpha$ SMC stays in between the two control methods above by setting the factor  $\alpha = 0.5$  in between the  $\alpha = 0.0$  and  $\alpha = 1.0$ .  $F\alpha$ SMC can balance the control effects of FLC and SkyhookSMC for stable MMET system spin-up outputs and associated energy activities.

Lyapunov function analysis shows the effect of  $F\alpha$ SMC control for different values of  $\alpha$ . SkyhookSMC has higher energy activities than the two other control methods, and FLC has the lower associated energy around  $V' = 0$ , with the  $F\alpha$ SMC's energy in the middle of the three, as shown in Figures 9.18 and 9.20.

- The two research objectives for this thesis are fully achieved. *Firstly*, as discussed in Chapter 3 to Chapter 7, a series of new dynamical models for motorised momentum exchange tethers have been proposed. *Secondly*, a fuzzy logic control and a hybrid fuzzy sliding mode control for a flexible MMET system spin-up have been discussed, and the effectiveness of both of the FLC and  $F\alpha$ SMC control systems has been investigated through numerical simulation by SMATLINK. The numerical results have shown that the MMET system's spin-up behaviour are fully controllable by both of the FLC and the  $F\alpha$ SMC. The Lyapunov stability theory was used to show the global asymptotic stability of the spin-up phase of the MMET system, subjected to either control law.

### 10.3 Future Work

- The parameter settings for the F $\alpha$ SMC need further consideration because the current simulation results come from manual parameter tests. In order to enhance the parameter selection process and validation, some computational intelligence (CI) optimisation tools, such as genetic algorithms (GA) and artificial neural networks (ANN), could be applied into the parameter selection for the FLC, SMC and F $\alpha$ SMC. This would give some useful reference sets for parameter settings. A GA case has already been used as an optimisation tool for parameter selection of the MMET system when applied to payload transfer from low Earth orbit to geostationary Earth orbit, and the GA's optimisation ability has, in that case, been reasonably demonstrated [70].
- The reliability of the control strategies for tether's rigid body motions, coupling with the flexible motions, should be more focused, for formation flying, aeroassisted orbital maneuvering, orbit transfer and other applications.

---

# References

---

- [1] M.L. Cosmo, E.C. Lorenzini, (1997), “Tethers in Space Handbook (Third Edition)”, NASA Marshall Space Flight Center.
- [2] M.P. Cartmell, and D.J. McKenzie, (2007), “A Review of Space Tether Research”, Progress in Aerospace Sciences, Volume 44, Issue 1, January 2008, Pages 1-21.
- [3] H. Curtis, (2004), “Orbital Mechanics for Engineering Students”, Elsevier Science Aerospace Engineering Series, Butterworth-Heinemann, ISBN: 0-7506-6169-0.
- [4] T. Logsdon , (1997), “Orbital Mechanics: Theory and Applications”, John Wiley and Sons, Inc., ISBN: 978-0-471-14636-0.
- [5] A.E. Roy, D. Clarke, (2003), “Astronomy: Principles and Practice, Fourth Edition”, Taylor and Francis, ISBN: 978-0750309172.
- [6] W. Jacoby, P.L. Smilde, (2009), “Gravity Interpretation Fundamentals and Application of Gravity Inversion and Geological Interpretation”, Springer, ISBN: 978-3-540-85328-2.
- [7] G.A. Gurzadyan, (1996), “Theory of Interplanetary Flights”, Taylor and Francis, ISBN: 978-2884490740.
- [8] D. Boccaletti, G. Pucacco, (2008), “Theory of Orbits”, Springer, ISBN: 3540589635.
- [9] H.J. De Blij, P.O. Muller, R.S. Williams (Jr.), (2004), “Physical Geography: the Global Environment (Edition: 3) ”, Oxford University Press, USA, ISBN-13: 978-0195160222.
- [10] M.J. Sidi, (1997), “Spacecraft Dynamics and Control: A Practical Engineering Approach”, Cambridge Aerospace Series, Cambridge University Press, Cambridge.
- [11] C.D. Ghilani, P.R. Wolf, (2005), “ Elementary Surveying: an Introduction to Geomatics”, Prentice Hall, ISBN: 9780131481893.

- [12] J.A. Angelo, (2003), “Space Technology”, Greenwood Publishing Group, ISBN: 9781573563352.
- [13] M.V. Pelt, (2009), “Space Tethers and Space Elevators”, Springer, Praxis Publishing, ISBN: 978-0-387-76555-6.
- [14] L. Meirovitch, (2004), “Methods of Analytical Dynamics”, Dover Publications, ISBN-13: 978-0486432397.
- [15] M.J. Sidi, (2000), “Spacecraft Dynamics and Control: A Practical Engineering Approach”, Cambridge University Press, ISBN-13: 9780521787802.
- [16] D.F. Dickinson, W.C. Straka, (1990), “Tethered Satellite Antenna Arrays for Passive Radar Systems”, Aerospace Applications Conference, Vail, CO, USA, Page 117-125.
- [17] J.A. Carroll and J.C. Oldson, (1995), “Tethers for Small Satellite Applications”, AIAA/USU Small Satellite Conference, Logan, Utah.
- [18] S. Price, (2000), “Audacious and Outrageous: Space Elevators”, NASA Science News.
- [19] Y. Artsutanov, (1960), “To the Cosmos By Electric Train”, Young Person’s Pravda.
- [20] V.V. Beletsky, E.M. Levin, (1993), “Dynamics of Space Tether Systems (Advances in the Astronautical Sciences)”, American Astronautical Society, ISBN-13: 978-0877033707.
- [21] B.C. Edwards, E.A. Westling, (2003), “the Space Elevator: A Revolutionary Earth-to-Space Transportation System”, Spageo Inc, ISBN-13: 978-0972604505.
- [22] M.J. Laine, B. Fawcett, T. Nugent, (2006), “Liftport: the Space Elevator—Opening Space to Everyone”, Meisha Merlin Publishing Inc., ISBN-13: 978-1592221097 .
- [23] J.D. Isaacs, A.C. Vine, H. Bradner, and G.E. Bachus, (1966), “Satellite Elongation into a True Sky-Hook”, Science 11 February, Volume 151. Number 3711, Page 682-683.
- [24] P. Ragan, B. Edwards, (2006), “Leaving the Planet by Space Elevator”, Lulu.com, ISBN-13: 978-1430300069.
- [25] G. Colombo, E. M. Gaposchkin, M. D. Grossi and G. C. Weiffenbach, (1974), “the Sky-hook : A Shuttle-Borne tool for Low-Orbital-Altitude Research”, Meccanica, Volume 10, Number 1, Page 3-20.

- [26] J. Pearson, (1975), “the Orbital Tower: a Spacecraft Launcher using the Earth’s Rotational Energy”, *Acta Astronautica*, Volume 2, Page 785-799.
- [27] H.P. Moravec, (1977), “A Non-Synchronous Orbital Skyhook”, *Journal of the Astronautical Sciences*, Volume 25, Number 4, Page 307-322.
- [28] J. Pearson, (1979), “Anchored Lunar Satellites for Cislunar Transportation and Communication”, *the Journal of the Astronautical Sciences*, Volume 26, Number 1, Page 39-62.
- [29] G. Tiesenhausen, (1984), *Tether in Space: Birth and Growth of A New Avenue to Space Utilization*, NASA, TM-82571, February.
- [30] J.A. Carroll, (1985), “Guidebook for Analysis of Tether Applications”, NASA contractor report - NASA CR-178904.
- [31] J.A. Carroll, (1986), “Tether Applications in Space Transportation”, *Acta Astronautica* Volume 13, Issue 4, April 1986, Pages 165-174.
- [32] L. Johnson, B. Gilchrist, R.D. Estes, and E. Lorenzini, (1999), “Overview of Future NASA Tether Applications”, *Advances in Space Research*, Volume 24, Number 8, Page 1055-1063.
- [33] J.A. Carroll, (2002), “Space Transport Development using Orbital Debris”, Technical report, Tether Applications Inc.
- [34] H. Klinkrad, (2006), “Space debris: models and risk analysis”, Springer, ISBN-13: 978-3540254485.
- [35] D. Darling, (2002), “the Complete Book of Spaceflight: from Apollo 1 to Zero Gravity”, John Wiley and Sons, ISBN: 978-0-471-05649-2.
- [36] NASA, (1966), “Gemini 11”, NSSDC ID: 1966-081A, <http://nssdc.gsfc.nasa.gov>.
- [37] T. Furniss, D. Shayler, M.D. Shayler, (2007), “Praxis Manned Spaceflight Log 1961-2006”, Springer, Praxis Publishing, UK, ISBN: 978-0-387-34175-0.
- [38] N. Kawashima, S. Sasaki, K.I. Oyama, K. Hirao, T. Obayashi, W.J. Raitt, A.B. White, P.R. Williamson, P.M. Banks, W.F. Sharp, (1988), “Results from a Tethered Rocket Experiment (CHARGE-2)”, *Advances in Space Research*, Volume 8, Issue 1, Page 197-201.

- [39] B. N. Maehlum, J. Troim, N. C. Maynard, W. F. Denig, M. Friedrich, K. M. Torkar, (1988), “Studies of the Electrical Charging of the Tethered Electron Accelerator Mother-Daughter Pocket Maimik”, *Geophysical Research Letters*, 15(7), 725-728.
- [40] W.F. Denig, B.N. Maehlum, K. Svenes, (1989), “A Review of the Maimik Rocket Experiment”, *Space Tethers for Science in the Space Station Era*, Venice, 4-8 October, Volume II, Page 443-457.
- [41] R.J. Nemzek, and J.R. Winckler, (1989), “Immediate and Delayed High-Energy Electrons Due to Echo 7 Accelerator Operation”, *Space Tethers for Science in the Space Station Era*, Venice, 4-8 October, Volume II, Page 466-490.
- [42] A.H. James, (1993), “Wave Results from OEDIPUS”, *Advances in Space Research*, Volume 13, Issue 10, October , Pages 5-13.
- [43] E.M. Levin, (2007), “Dynamic Analysis of Space Tether Missions”, *American Astronautical Society*, ISBN-13: 978-0877035374.
- [44] P. Prikryl, H. G. James, D. J. Knudsen, (1999), “OEDIPUS-C Topside Sounding of an Auroral E Region”, *Advances in Space Research*, Volume 24, Issue 8, Pages 1065-1068.
- [45] C. Bonifazi, G. Manarini<sup>1</sup>, J. Sabbagh, F. Svelto, D. C. Thompson, B. E. Gilchrist, P. M. Banks, and M. Dobrowolny, (1993), “Tethered-satellite System (TSS) : Preliminary Results on the Active Experiment Core Equipment”, *Il Nuovo Cimento C*, Volume 16, Number 5, 515-538.
- [46] M. Malerba, (1993), “the First Mission of the Tethered Statellite”, *Il Nuovo Cimento C*, Volume 16, Number 5, 485-494.
- [47] R.S. Ryan, D.K. Mowery, D.D. Tomlin, (1993), “the Dynamic Phenomena of a Tethered Satellite - NASA’s First Tethered Satellite Mission (TSS-1)”, *NASA technical paper*, NAS 1.60:3347, <http://nla.gov.au/nla.cat-vn4066740>.
- [48] S. Bergamaschi, F. Bonon, P. Merlina, M. Morana, (1993), “Theoretical and Experimental Investigation of TSS-1 Dynamics”, *44th International Astronautical Congress*, Graz, Austria, 16-22 October.
- [49] M. Dobrowolny, N. H. Stone, (1994), “A Technical Overview of TSS-1: the First Tethered-Satellite System Mission”, *Il Nuovo Cimento C*, Volume 17, Number 1, January.

- [50] V. Agüero, P. M. Banks, B. Gilchrist, I. Linscott, W. J. Raitt, D. Thompson, V. Tolat, A. B. White, S. Williams, P. R. Williamson and SETS Team, (1994), “the Shuttle Electrodynamic Tether System (SETS) on TSS-1”, *Il Nuovo Cimento C*, Volume 17, Number 1, Page 49-65.
- [51] George C. Marshall Space Flight Center, (1996), “Tethered Satellite System Reflight (TSS-1R) Post-Flight Engineering Performance Report”, George C. Marshall Space Flight Center.
- [52] N.H. Stone, W.J. Raitt, K.H. Wright, Jr., (1999), “the TSS-1R Electrodynamic Tether Experiment: Scientific and Technological Results”, *Advances in Space Research* Volume 24, Issue 8, Page 1037-1045.
- [53] W.J. Barnds, S. Coffey, M. Davis, B. Kelm, and W. Purdy, (1997), “TiPS: Results of a Tethered Satellite Experiment”, the Joint AASI/AIAA Astrodynamics Conference, Sun Valley, Idaho, August.
- [54] E. Heide, M. Kruijff, (2001), “Tethers and Debris Mitigation ”, *Acta Astronautica*, Volume 48, Issues 5-12, March-June, Pages 503-516.
- [55] S. Koss, (1997), “Tether Deployment Mechanism for the Advanced Tether Experiment (ATEX)”, 7th European Space Mechanism and Tribology Symposium, Noordwijk, the Netherlands, page 175-182.
- [56] R. Osiander, M.A.G. Darrin, J. Champion, (2005), “MEMS and Microstructures in Aerospace Applications”, CRC Press, ISBN-13: 978-0824726379.
- [57] J.A. Vaughn, L. Curtis, B.E. Gilchrist, S.G. Bilén, E.C. Lorenzini, (2004), “Review of the ProSEDS Electrodynamic Tether Mission Development”, 40th AIAA/ASME/SAE/ASEE Joint Propulsion Conference and Exhibit, 11 - 14 July, Fort Lauderdale, Florida, AIAA 2004-3501.
- [58] R. Hoyt, J. Slostad, R. Twiggs, (2003), “the Multi-Application Survivable Tether (MAST) Experiment”, AIAA-2003-5219.
- [59] S. Dueck, N. Gadhok, M. Kinsner, J. Kraut, T. Tessier, W. Kinsner, (2003), “YES2 DHS: a Space Tether Control Subsystem”, Volume: 2, Page 1287-1292.
- [60] P. Williams, A. Hyslop, M. Stelzer, and M. Kruijff, (2009), “YES2 Optimal Trajectories in Presence of Eccentricity and Aerodynamic Drag”. *Acta Astronautica* Volume 64, Issues 7-8, April-May 2009, Page 745-769.

- [61] H.A. Fujii, T. Watanabe, H. Kojima, K. Oyama, T. Kusagaya, Y. Yamagiwa, H. Ohtsu, M. Cho, S. Sasaki, K. Tanaka, J. Williams, B. Rubin, C.L. Johnson, G. Khazanov, J.R. Sanmartin, J. Lebreton, E. Heide, M. Kruijff, F. Pascal, and P.M. Trivailo, (2009), "Sounding Rocket Experiment of Bare Electrodynamic Tether System" . *Acta Astronautica*, Volume 64, Issues 2-3, January-February, Page 313-324.
- [62] S.W. Ziegler, M.P. Cartmell, (2001), "Using Motorised Tethers for Payload Orbital Transfer", *Journal of Spacecraft and Rockets*, Volume 38, Number 6, Page 904-913.
- [63] M.P. Cartmell, S.W. Ziegler, R. Khanin and D.I.M. Forehand, (2003), "Multiple scales analyses of the dynamics of weakly nonlinear mechanical systems", *Transactions of ASME, Applied Mechanics Reviews*, 56 (5), Page 455-492.
- [64] M.J. Eiden, M.P. Cartmell, (2003), "Overcoming the Challenges: Tether Systems Roadmap for Space Transportation Applications", *AIAA/ICAS International Air and Space Symposium and Exposition*, 14-17 July, Dayton Convention Center, Dayton, Ohio.
- [65] S.W. Ziegler, (2003), "the Rigid-body Dynamics of Tethers in Space", PhD Dissertation, Department of Mechanical Engineering, University of Glasgow.
- [66] K.F. Sorensen, (2001), "Conceptual Design and Analysis of an MXER Tether Boost Station", 37th AIAA/ASME/SAE/ASEE Joint Propulsion Conference and Exhibit, Salt Lake City, UT, USA, July 8-11, AIAA-2001-3915 .
- [67] M.P. Cartmell, (1998), "Generating Velocity Increments by Means of a Spinning Motorised Tether", 34th AIAA/ASME/SAE/ASEE Joint Propulsion Conference and Exhibit, Cleveland Conference Centre, Cleveland, Ohio, USA, AIAA-98-3739.
- [68] M.P. Cartmell, S.W. Ziegler, (2001), "Experimental Scale Model Testing of a Motorised Momentum Exchange Propulsion Tether", 37th AIAA/ASME/SEA/ASEE Joint Propulsion Conference and Exhibit, July 8-11, Salt Lake City, Utah, USA, AIAA 2001-3914.
- [69] M.P. Cartmell, S.W. Ziegler, D.S. Neill, (2003), "On the Performance Prediction and Scale Modelling of A Motorised Momentum Exchange Propulsion Tether", 20th Symposium Space nuclear power and propulsion; Space technology and applications international forum 2003, 2-5 February, University of New Mexico, Albuquerque, New Mexico, USA.

- [70] Y. Chen, M.P. Cartmell, (2007), "Multi-objective Optimisation On Motorised Momentum Exchange Tether for Payload Orbital Transfer", IEEE Congress on Evolutionary Computation, Publication Date: 25-28 September, Page 987-993.
- [71] Y. Chen, M.P. Cartmell, (2007), "Dynamical Modelling of the Motorised Momentum Exchange Tether Incorporating Axial Elastic Effects", Advanced Problems in Mechanics, 20-28 June, Russian Academy of Sciences, St Petersburg, Russia.
- [72] M. Pasca, E.C. Lorenzini, (1997), "Two Analytical Models for the Analysis of A Tethered Satellite System in Atmosphere", *Meccanica*, Volume 32, Number 4, Page 263-277.
- [73] R.L. Forward, R.P. Hoyt, C. Uphoff, (1998), "Application of the Terminator Tether Electrodynamic Drag Technology to the Deorbit of Constellation Spacecraft", AIAA/ASME/SAE/ASEE Joint Propulsion Conference and Exhibit, 34th, Cleveland, OH, 13-15 July, AIAA-1998-3491.
- [74] R.L. Forward, R.P. Hoyt, C. Uphoff, (2000) "the Terminator Tether: Autonomous Deorbit of LEO Spacecraft for Space Debris Mitigation", 10-13 January.
- [75] L. Iess, (2001), "Space Tethers: an overview", 7th Spacecraft Charging and Technology Conference, ESTEC Conference Centre Noordwijk, the Netherlands, 23-27 April.
- [76] L. Iess, C. Bruno, and C. Ulivieri, (2002), "Satellite De-Orbiting by Means of Electrodynamic Tethers Part II: System Configuration and Performance", *Acta Astronautica*, Volume 50, Number 7, Page 407-16.
- [77] J. Pearson, J. Carroll, E. Levin, P. Hausgen, (2003), "Overview of the Electrodynamic Delivery Express (EDDE)", 39th AIAA/ASME/SAE/ASEE Joint Propulsion Conference and Exhibit, Huntsville, AL, 20-23 July, AIAA 2003-4790.
- [78] S.G. Tragesser, and H. San, (2003), "Orbital Maneuvering with Electrodynamic Tethers", *Journal of Guidance, Control, and Dynamics* Volume 26, Number 5, Page 805-810.
- [79] J. Pearson, E. Levin, J.A. Carroll, J.C. Oldson, "Orbital Maneuvering with Spinning Electrodynamic Tethers", AIAA Paper 2004-5715, 2nd International Energy Conversion Engineering Conference, 16-19 August, Providence, Rhode Island.

- [80] R. Hoyt, J. Buller, (2005), "Analysis of the Interaction of Space Tethers with Catalogued Space Objects ", AIAA-2005-4430, 41st AIAA/ASME/SAE/ASEE Joint Propulsion Conference and Exhibit, Tucson, Arizona, July 10-13.
- [81] J. Pelaez, Y. N. Andres, (2005), "Dynamic Stability of Electrodynamic Tethers in Inclined Elliptical Orbits", *Journal of Guidance, Control, and Dynamics*, Volume 28, Number 4, Page 611-622.
- [82] K.K. Mankala, S.K. Agrawal, (2005), "Equilibrium to Equilibrium Maneuvers of Rigid Electrodynamic Tethers", *Journal of Guidance, Control and Dynamics*, Volume 28, Number 3, Page 541-545.
- [83] A.E. Zakrzhevskii, A.V. Pirozhenko, (2007), "Motion Parameters of An Electrodynamic Tether in Orbit", *International Applied Mechanics*, Volume 43, Number 3, Page 335-343.
- [84] M.S. Bitzer, C.D. Hall, (2007), "Optimal Electrodynamic Tether Phasing Maneuvers", Space Grant Consortium Student Conference, Hampton, Virginia, 15 August.
- [85] K. Sorensen, (2003), "Momentum Exchange Electrodynamic Reboost (MXER) Tether", Technical Report, National Aeronautics and Space Administration, Marshall Space Flight Center Huntsville, Alabama 35812, May 2005, FS-2005-05-61-MSFC, Pub 8-40407.
- [86] A.K. Misra, V.J. Modi, (1982), "Dynamics and Control of Tether Connected Two-Body Systems - A Brief Review", 33rd International Astronautical Federation, International Astronautical Congress, Paris, France, 27 September - 2 October, Pages 219-236.
- [87] A.K. Misra, V.J. Modi, (1986), "A Survey On the Dynamics and Control of Tethered Satellite Systems", NASA/AIAA/PSN International Conference on Tethers, Arlington, VA, 17-19 September.
- [88] K.D. Kumar, (2006), "Review of Dynamics and Control of Nonelectrodynamic Tethered Satellite Systems", *Journal of Spacecraft and Rockets*, Volume 43, Number 4, Pages 705-720.
- [89] D.D. Tomlin, G.C. Faile, K.B. Hayashida, C.L. Frost, C.Y. Wagner, M.L. Mitchell, J.A. Vaughn, and M.J. Galuska, (1997), "Space Tethers: Design Criteria", Technical Report, NASA Center: Marshall Space Flight Center, Alabama, NASA Technical Memorandum 108537.

- [90] R.P. Hoyt, R.L. Forward, (2000), "Cislunar Tether Transport System", 38th Aerospace Sciences Meeting and Exhibit, 10-13 January, Reno, Nevada, AIAA 00-0329.
- [91] R.P. Hoyt, (2001), "Moon and Mars Orbiting Spinning Tether Transport System Architecture Study", Final Report on NASA Institute for Advanced Concepts Contract 07600-034.
- [92] K.D. Kumar, (2001), "Payload Deployment By Reusable Launch Vehicle using Tether", Journal of Spacecraft and Rockets: Engineering Notes, Volume 38, Number 2, Page 291-294.
- [93] P. Williams, C. Blanksby, P. Trivailo, (2003), "Tethered Planetary Capture: Controlled Maneuvers", Acta Astronautica Volume 53, Issues 4-10, August-November, Pages 681-708.
- [94] P. Williams, Sherrin Yeo, C. Blanksby, (2003), "Heating and Modeling Effects in Tethered Aerocapture Missions", Journal of Guidance, Control, and Dynamics, Volume 26, Number 4, Page 643-654.
- [95] P. Williams, C. Blanksby, and P. Trivailo, (2004), "Tethered Planetary Capture Maneuvers", Journal of Spacecraft and Rockets, Volume 41, Number 4, Page 603-613.
- [96] P. Williams, C. Blanksby, and P. Trivailo, (2004), "Libration Control of Flexible Tethers using Electromagnetic Forces and Movable Attachment", Journal of Guidance, Control, and Dynamics, Volume 27, Number 5, Page 882-897.
- [97] P. Williams, C. Blanksby, (2004), "Prolonged Payload Rendezvous using A Tether Actuator Mass", Journal of Spacecraft and Rockets, Volume 41, Number 5, Page 889-892.
- [98] P. Williams, C. Blanksby, P. Trivailo, and H. A. Fujii, (2005), "In-plane Payload Capture using Tethers", Acta Astronautica, Volume 57, Issue 10, November, Pages 772-787.
- [99] P. Williams, (2005), "Optimal Orbit Transfer With Electrodynamic Tether", Journal of Guidance, Control, and Dynamics, Volume 28, Number 2, Pages 369-372.
- [100] P. Williams, (2006), "Dynamics and Control of Spinning Tethers for Rendezvous in Elliptic Orbits", Journal of Vibration and Control, Volume 12, Issue 7, Pages 737-771.
- [101] P. Williams, P. Trivailo, (2006), "Cable-Supported Sliding Payload Deployment From A Circling Fixed-Wing Aircraft", Journal of Aircraft, Volume 43, Number 5, Pages 1567-1570.

- [102] V. J. Modi, A. K. Misra, (1979), "On the Deployment Dynamics of Tether Connected Two-Body Systems", *Acta Astronautica*, Volume 6, Issue 9, September 1979, Page 1183-1197.
- [103] S. Bergamaschi, F. Bonon, P. Merlina, M. Morana, (1994), "Theoretical and experimental investigation of TSS-1 dynamics", *Acta Astronautica*, Volume 34, Page 69-82.
- [104] F.L. Chernousko, (1995), "Dynamics of Retrieval of a Space Tethered System", *Journal of Applied Mathematics and Mechanics*, Volume 59, Number 2, Pages 165-173.
- [105] J. Pelaez, (1995), "On the Dynamics of the Deployment of a Tether from An Orbiter I. Basic Equations", *Acta Astronautica*, Volume 36, Issue 2, Pages 113-122.
- [106] J. Pelaez, (1995), "On the Dynamics of the Deployment of a Tether from an Orbiter- Part II. Exponential Deployment", *Acta Astronautica*, Volume 36, Number 6, September 1995 , Pages 313-335.
- [107] R. Licata, (1997), "Tethered System Deployment Controls By Feedback Fuzzy Logic", *Acta Astronautica*, Volume 40, Number 9, Pages 619-634.
- [108] J.T Carter, M. Greene, (1988), " Deployment and Retrieval Simulation of a Single Tether Satellitesystem", *Proceedings of the Twentieth Southeastern Symposium*, Charlotte, NC, USA, 20-22 March, Page 657-660.
- [109] K. Kumar, S. Pradeep, (1998), "Strategies for Three Dimensional Deployment of Tethered Satellites", *Mechanics Research Communications*, Volume 25, Number 5, September, Pages 543-550.
- [110] H. Gläüßel, F. Zimmermann, S. Brückner, U.M. Schöttle, S. Rudolph, (2004), "Adaptive Neural Control of the Deployment Procedure for Tether-Assisted Re-Entry", *Aerospace Science and Technology*, Volume 8, Issue 1, Pages 73-81.
- [111] A. Djebli, M. Pascal, L. Bakkali, (1999), "Laws of Deployment/Retrieval in Tether Connected Satellites Systems", *Acta Astronautica*, Volume 45, Number 2, July 1999 , Pages 61-73.
- [112] A. Djebli, L. Bakkali, M. Pascal, (2002), "On Fast Retrieval Laws for Tethered Satellite Systems", *Acta Astronautica*, Volume 50, Issue 8, Pages 461-470.
- [113] M.E. Campbell, J.P. How, S. Grocott, D.W. Miller, (1999), "On-Orbit Closed-Loop Control Results for the Middeck Active Control Experiment", *Journal of Guidance, Control, and Dynamics*, Volume 22, Number 2, Pages 267-277.

- [114] B. Barkow, (2003), “Controlled deployment of a tethered satellite system”, PAMM, Volume 2, Issue 1, Pages 224-225.
- [115] B. Barkow, A. Steindl, H. Troger, G. Wiedermann, (2003), “Various Methods of Controlling the Deployment of a Tethered Satellite”, Journal of Vibration and Control, Volume 9, Number 1-2, Pages 187-208.
- [116] B. Barkow, A. Steindl, H. Troger, (2005), “A Targeting Strategy for the Deployment of a Tethered Satellite System”, Journal of Applied Mathematics, 70:626-644.
- [117] A.K. Misra, V.J. Modi, (1982), “Deployment and Retrieval of Shuttle Supported Tethered Satellites”, Journal of Guidance and Control, Volume 5, Number 3, Pages 278-285.
- [118] D.P. Jin, H.Y. Hu, (2003), “Optimal Control of Deployment of A Tethered Subsatellite”, Nonlinear Dynamics, Volume 31, Number 3, Pages 257–274.
- [119] A. Steindl, W. Steiner, H. Troger, (2005), “Optimal Control of Retrieval of A Tethered Subsatellite”, IUTAM Symposium on Chaotic Dynamics and Control of Systems and Processes in Mechanics, Pages 441-450.
- [120] L.C. Evans, (1998), “Partial Differential Equations”, Providence, Rhode Island: American Mathematical Society, ISBN 0-8218-0772-2.
- [121] P. Williams, (2006), “Optimal Deployment/Retrieval of a Tethered Formation Spinning in the Orbital Plane”, Journal of Spacecraft and Rockets, Volume 43, Number 3, Pages 638-650.
- [122] P. Mantri, (2007), “Deployment Dynamics of Space Tether Systems”, PhD thesis, North Carolina State University.
- [123] M. Nohmi, D.N. Nenchev, M. Uchiyama, (1996), “Trajectory Planning and Feedforward Control of A Tethered Robot System”, Proceedings of the IEEE/RSJ International Conference on Intelligent Robots and Systems, Osaka, Japan, Volume 3, Pages 1530–1535.
- [124] Y. Cao, V.J. Modi, C.W. Silva, M. Chu, Y. Chen, A.K. Misra, (2003), “Trajectory Tracking Experiments using A Novel Manipulator”, Acta Astronautica, Volume 52, Number 7, April 2003, Pages 523-540.
- [125] M.B. Milam, (2003), “Real-Time Optimal Trajectory Generation for Constrained Dynamical Systems”, PhD thesis, California Institute of Technology, Pasadena, California.

- [126] D.A. Padgett, (2006), “Nullcline Analysis as a Tethered Satellite Mission Design tool”, Master thesis, North Carolina State University.
- [127] S. Sharma, E.A. Kulczycki, A. Elfes, (2007), “Trajectory Generation and Path Planning for Autonomous Aerobots”, IEEE International Conference on Robotics and Automation, Rome, Italy, 10-14 April.
- [128] M. Kim, (2005), “Continuous Low-Thrust Trajectory Optimization: Techniques and Applications”, PhD thesis, Virginia Polytechnic Institute and State University.
- [129] K. M. Aaron, M. K. Heun, K. T. Nock, (2002), “A Method for Balloon Trajectory Control”, *Advances in Space Research*, Volume 30, Issue 5, 2002, Pages 1227-1232.
- [130] Y. Sakamoto, T. Yasaka, (2003), “Methods for the Orbit Determination of A Tethered Satellite System By A Single Ground Station”, *Memoirs of the Faculty of Engineering, Kyushu University*, 63(3):185-202.
- [131] N. Takeichi, M.C. Natori, N. Okuizumi, K. Higuchi, (2004), “Periodic Solutions and Controls of Tethered Systems in Elliptic Orbits”, *Journal of Vibration and Control*, 10(10):1393-1413.
- [132] L. Anselmo, C. Pardini, (2005), “the Survivability of Space Tether Systems in Orbit Around the Earth”, *Acta Astronautica*, Volume 56, Issue 3, February, Pages 391-396.
- [133] V.J. Modi, A.K. Misra, (1975), “Dynamics of an Array Formed by Three Neutrally Buoyant Cylindrical Cantilevers Subjected to Tensile Follower Forces”, *Journal of Sound and Vibration*, Volume 42, Issue 2, Pages 209-217.
- [134] P.M. Bainum, V.K. Kumar, (1980) “Optimal Control of the Shuttle-Tethered-Subsatellite System”, *Acta Astronautica*, Volume 7, Issue 12, Pages 1333-1348.
- [135] V.J. Modi, D. Xu, A.K. Misra, G. ChangFu, (1982), “On the Control of the Space Shuttle Based Tethered Systems”, *Acta Astronautica*, Volume 9, Issue 6-7, Pages 437-443.
- [136] A.K. Misra, Z. Amier, V.J. Modi, (1988), “Attitude Dynamics of Three-Body Tethered Systems”, *Acta Astronautica*, Volume 17, Issue 10, Pages 1059-1068.
- [137] V.J. Modi, (1990), “Spacecraft attitude dynamics: Evolution and current challenges”, *Acta Astronautica*, Volume 21, Issue 10, Pages 689-718.

- [138] R.N. Lea, J. Villarreal, Y. Jani, C. Copeland, (1992), "Tether Operations using Fuzzy Logic Based Length Control", IEEE International Conference on Fuzzy Systems, San Diego, CA, USA, 8-12 March, Pages 1335-1342.
- [139] V.J. Modi, P.K. Lakshmanan, (1992), "On the Control of Tethered Satellite Systems", Acta Astronautica, Volume 26, Issue 6, Pages 411-423.
- [140] V.J. Modi, R.P. Pidgeon, (1994), "Dynamics and control of a flexible tethered system with offset", Acta Astronautica, Volume 32, Issue 4, Pages 255-265.
- [141] M. Grassi, A. Moccia, S. Vetrella, (1994), "Tethered System Attitude Control After Attachment Point Blocking", Acta Astronautica, Volume 32, Issue 5, Pages 355-362.
- [142] M. Grassi, M.L. Cosmo, (1995), "Attitude Dynamics of the Small Expendable-tether Deployment System", Acta Astronautica, Volume 36, Issue 3, Pages 141-148.
- [143] V.J. Modi, S. Pradhan, A. K. Misra, (1995), "Off-Set Control of the Tethered Systems using A Graph Theoretic Approach", Acta Astronautica, Volume 35, Issue 6, Pages 373-384.
- [144] V.J. Modi, (1995), "On the Semi-passive Attitude Control and Propulsion of Space Vehicles using Solar Radiation Pressure", Acta Astronautica, Volume 35, Issues 2-3, January-February, Pages 231-246.
- [145] V. J. Modi, S. Pradhan, M. Chu, G. Tyc, A. K. Misra, (1996), "Experimental Investigation of the Dynamics of Spinning Tethered Bodies", Acta Astronautica, Volume 39, Issue 7, Pages 487-495.
- [146] M. Pasca, E.C. Lorenzini, (1997), "Two Analytical Models for the Analysis of a Tethered Satellite System in Atmosphere", Meccanica, Volume 32, Number 4, Pages 263-277.
- [147] S. Pradhan, V.J. Modi, A.K. Misra, (1999), "Tether-Platform Coupled Control", Acta Astronautica, Volume 44, Issue 5, Pages 243-256.
- [148] V.J. Modi, S. Pradhan, A.K. Misra, (1997), "Controlled Dynamics of Flexible Orbiting Tethered Systems: Analysis and Experiments", Journal of Vibration and Control, Volume 3, Number 4, Pages 459-497.
- [149] S. Yu, (2000), "Tethered Satellite System Analysis (1) - Two Dimensional Case and Regular Dynamics", Acta Astronautica, Volume 47, Issue 12, Pages 849-858.

- [150] J. F. Goulet, C. W. de Silva, V. J. Modi, A. K. Misra, (2001), "Hierarchical Control of a Space-Based Deployable Manipulator using Fuzzy Logic", *Journal of Guidance, Control, and Dynamics*, Volume 24, Number 2, Pages 395-405.
- [151] K. D. Kumar, K. Kumar, (2001), "Attitude Maneuver of Dual Tethered Satellite Platforms Through Tether Offset Change", *Journal of Spacecraft and Rockets*, Volume 38, Number 2, Pages 237-242.
- [152] M. Kim, C. Hall, (2004), "Control of a Rotating Variable-Length Tethered System", *Journal of Guidance, Control, and Dynamics*, Volume 27, Number 5, Pages 849-858.
- [153] M. Lovera, A. Astolfi, (2004) "Spacecraft Attitude Control using Magnetic Actuators", *Automatica*, Volume 40, Issue 8, Pages 1405-1414.
- [154] V.J. Modi, J. Zhang, C.W. Silva, (2005), "Intelligent Hierarchical Modal Control of a Novel Manipulator With Slewing and Deployable Links", *Acta Astronautica*, Volume 57, Issue 10, Pages 761-771.
- [155] P. Guan, X. Liu, J. Liu, (2005), "Adaptive Fuzzy Sliding Mode Control for Flexible Satellite", *Engineering Applications of Artificial Intelligence*, Volume 18, Issue 4, Pages 451-459.
- [156] X. Zhou, J. Li, H. Baoyin, V. Zakirov, (2006), "Equilibrium Control of Electrodynamic Tethered Satellite Systems in Inclined Orbits", *Journal of Guidance, Control, and Dynamics*, Volume 29, Number 6, Pages 1451-1454.
- [157] M. Kim, C. Hall, (2004), "Dynamics and Control of Rotating Tethered Satellite Systems", *Journal of Spacecraft and Rockets*, Volume 44, Number 3, Pages 649-659.
- [158] O. Mori, S. Matunaga, (2007), "Formation and Attitude Control for Rotational Tethered Satellite Clusters", *Journal of Spacecraft and Rockets*, Volume 44, Number 1, Pages 211-220.
- [159] S. Chung, J.E. Slotine, D.W. Miller, (2007). "Nonlinear Model Reduction and Decentralized Control of Tethered Formation Flight by Oscillation Synchronization", *Journal of Guidance, Control, and Dynamics*, Volume 30, Number 2, Pages 390-400.
- [160] S. Chung, D.W. Miller, (2008), "Propellant-Free Control of Tethered Formation Flight, Part 1: Linear Control and Experimentation", *Journal of Guidance, Control, and Dynamics*, Volume 31, Number 3, Pages 571-584.

- [161] S. Chung, J.E. Slotine, D.W. Miller, (2008), "Propellant-free Control of Tethered Formation Flight, part 2: Nonlinear underactuated control", *Journal of Guidance, Control, and Dynamics*, Volume 31, Number 5, Pages 1437-1446.
- [162] A.K. Misra, (2008), "Dynamics and Control of Tethered Satellite Systems", *Acta Astronautica*, Volume 63, Number 11-12, Pages 1169-1177.
- [163] C. Tschann, V.J. Modi, A. Soudack, (1971), "Planar Librations of Gravity-Oriented Satellites using Analog Simulation", *Mathematics and Computers in Simulation*, Volume 13, Number 3, Pages 124-130.
- [164] K.W. Lips, V.J. Modi, (1978), "Transient Attitude Dynamics of Satellites With Deploying Flexible Appendages", *Acta Astronautica*, Volume 5, Number 10, Pages 797-815.
- [165] A.K. Misra, D.M. Xu, V.J. Modi, (1986), "On Vibrations of Orbiting Tethers", *Acta Astronautica*, Volume 3, Number 10, Pages 587-597.
- [166] J.T. Carter, M. Greene, (1992), "Simulation of Single Tether Systems", *Simulation*, Volume 58, Number 1, Pages 42-48.
- [167] S. Kalantzis, V. J. Modi, S. Pradhan, A.K. Misra, (1998), "Dynamics and Control of Multibody Tethered Systems", *Acta Astronautica*, Volume 42, Number 9, Pages 503-517.
- [168] F. Dignath, W. Schiehlen, (2000), "Control of the Vibrations of a Tethered Satellite System", *Journal of Applied Mathematics and Mechanics*, Volume 64, Number 5, Pages 715-722.
- [169] M.J. Leamy, A.K. Noor, (2001), "Dynamic Simulation of a Tethered Satellite System using Finite Elements and Fuzzy Sets", *Computer Methods in Applied Mechanics and Engineering*, Volume 190, Number 37-38, Pages 4847-4870.
- [170] P. Williams, (2005), "Spacecraft Rendezvous on Small Relative Inclination Orbits using Tethers", *Journal of Spacecraft and Rockets*, Volume 42, Number 6, Pages 1047-1060.
- [171] M. Krupa, W. Poth, M. Schagerl, A. Steindl, W. Steiner, H. Troger\*, and G. Wiedermann, (2006), "Modelling, Dynamics and Control of Tethered Satellite Systems", *Nonlinear Dynamics*, Volume 43, Number 1-2, Pages 73-96.

- [172] P. Williams, Daniel Sgarioto, P. Trivailo, (2006), “Optimal Control of an Aircraft-towed Flexible Cable System”, *Journal of Guidance, Control, and Dynamics*, Volume 29, Number 2, Pages 401-410.
- [173] P. Williams, (2006), “Libration Control of Tethered Satellites in Elliptical Orbits”, *Journal of Spacecraft and Rockets*, Volume 43, Number 2, Pages 476-479.
- [174] J. Valverde, J. L. Escalona, J. Domínguez, A. R. Champneys, (2006), “Stability and Bifurcation Analysis of a Spinning Space Tether”, *Journal of Nonlinear Science*, Volume 16, Number 5, Pages 507-542.
- [175] P. Williams, P. Trivailo, (2007), “Dynamics of Circularly Towed Aerial Cable Systems, Part I: Optimal Configurations and Their Stability”, *Journal of Guidance, Control, and Dynamics*, Volume 30, Number 3, Pages 753-765.
- [176] P. Williams, P. Trivailo, (2007), “Dynamics of Circularly Towed Aerial Cable Systems, part 2: Transitional flight and deployment control”, *Journal of Guidance, Control, and Dynamics*, Volume 30, Number 3, Pages 766-779.
- [177] S.G. Bilén, (1994), “Space-borne Tethers”, *IEEE Potentials*, Volume: 13, Issue: 3, Pages 47-50.
- [178] W.D. Kelly, (1984), “Delivery and Disposal of A Space Shuttle External Tank to Low-Earth Orbit”, *Journal of Astronaut Science*, Volume: 32, Issue: 3, Pages 343-350.
- [179] A.B. DeCou, (1989), “Tether Static Shape for Rotating Multimass, Multitether, Spacecraft for “triangle” Michelson Interferometer”, *Journal of Guidance*, Volume: 12, Number: 2, Pages 273-275.
- [180] K. Kumar, R. Kumar and A.K. Misra, (1992), “Effects of Deployment Rates and Librations on Tethered Payload Raising”, *Journal of Guidance, Control, and Dynamics*, Volume: 15, Number: 5, Pages 1230-1235.
- [181] F.R. Vigneron, A.M. Jablonski, R. Chandrashaker, J.L. Bergmans, B.A. McClure and G. Tyc, (1997), “Comparison of Analytical Modelling of OEDIPUS Tethers with Data from Tether Laboratory”, *Journal of Guidance, Control, and Dynamics*, Volume: 20, Number: 3, Pages 471-478.
- [182] K. Kumar, K.D. Kumar, (2000), “Tethered Dual Spacecraft Configuration: a Solution to Attitude Control Problems”, *Aerospace Science Technology*, Volume: 4, Pages 495-505.

- [183] A.P. Mazzoleni, J.H. Hoffman, (2001) "Nonplanar Spin-up Dynamics of the ASTOR Tethered Satellite System", In: Proceedings of the AAS/AIAA Space Flight Mechanics Meeting, 2001, AAS[AAS 01-193].
- [184] A.P. Mazzoleni, J.H. Hoffman, (2003), "End-body Dynamics of Artificial Gravity Generating Tethered Satellite System during Non-planar Spin-up with Elastic Effects Included", Advances In The Astronautical Sciences, Volume: 116, Part 1, Pages 579-694.
- [185] E. Mouterde, M.P. Cartmell and Y. Wang, (2004), Computational Simulation of Feedback Linearised Control of a Motorised Momentum Exchange Tether on a Circular Earth Orbit, by invited paper for Keynote Address in the Computational Methods in Nonlinear Dynamics, Symposium of the sixth World Congress on Computational Mechanics, September 5-10, Beijing, China.
- [186] L. Debnath, (2005), "Nonlinear Partial Differential Equations for Scientists and Engineers", 2nd edition, Birkhauser, ISBN: 978-0817643232.
- [187] L.E. Goodman, W.H. Warner, (2003), "Dynamics", Dover Publications Inc., ISBN-13: 978-0486420066.
- [188] L.A. Zadeh, (1965) "Fuzzy Sets", Information and Control, Volume 8, Number 3, Pages 338-353.
- [189] R. Burns, (2001) "Advanced Control Engineering", Butterworth-Heinemann, Oxford.
- [190] K.M. Passino, S. Yurkovich, (1998), "Fuzzy Control", Addison Wesley Longman, Menlo Park, CA.
- [191] MathWorks, (2009), "Fuzzy Logic Toolbox<sup>TM</sup> User's Guide", the MathWorks, Inc. 3 Apple Hill Drive Natick, MA 01760-2098.
- [192] W.V. Leekwijck, E.E. Kerre, (1999), "Defuzzification: Criteria and Classification", Fuzzy Sets and Systems, Volume 108, Issue 2, Pages 159-178.
- [193] E.H. Mamdani, S. Assilian, (1975), "an Experiment in Linguistic Synthesis with a Fuzzy Logic Controller", International Journal of Man-Machine Studies, Volume 7, Number 1, Pages 1-13.
- [194] E.H. Mamdani, (1976), "Advances in the Linguistic Synthesis of Fuzzy Controllers", International Journal of Man-Machine Studies, Volume 8, Number 1, Pages 669-678.

- [195] E.H. Mamdani, (1977), "Applications of Fuzzy Logic to Approximate Reasoning using Linguistic Synthesis", IEEE Transactions on Computers, Volume 26, Number 12, Pages 1182-1191.
- [196] L.A. Zadeh, (1973), "Outline of a New Approach to the Analysis of Complex Systems and Decision Processes", IEEE Transactions on Systems, Man, and Cybernetics, Volume 3, Number 1, Pages 28-44.
- [197] S. V. Emelyanov, (1967), "Variable Structure Control Systems (in Russian)", Moscow: Nauka.
- [198] Y. Itkis, (1976), "Control Systems of Variable Structure", New York: Wiley.
- [199] V. A. Utkin, (1978), "Sliding Modes and Their Application in Variable Structure Systems", Moscow: Nauka (in Russian) (also Moscow: Mir, 1978, in English).
- [200] J.J.E. Slotine, W.P. Li, (1991), "Applied Nonlinear Control", Prentice-Hall International.
- [201] J.Y. Hung, W. Gao, J.C. Hung (1993), "Variable Structure Control : A Survey", IEEE Transactions on Industrial Electronics, Volume 40, Number 1, February, Pages 2-22.
- [202] S. G. Tzafestas ,G. G. Rigatos, (1999), "A Simple Robust Sliding Mode Fuzzy Logic Controller of the Diagonal Type", Journal of Intelligent and Robotic Systems, Volume 26, Numbers 3-4 , Pages 353-388.
- [203] A. Ishigame, T. Furukawa, S. Kawamoto, T. Taniguchi, (1991), "Sliding Mode Controller Design Based on Fuzzy Inference for Non-Linear System", International Conference on Industrial Electronics, Control and Instrumentation, Kobe, Japan, 28 October - 1 November, Volume 3, Pages 2096-2101.
- [204] A. Ishigame, T. Furukawa, S. Kawamoto, T. Taniguchi, (1993), "Sliding Mode Controller Design Based on Fuzzy Inference for Nonlinear Systems", IEEE Trans. Industrial Electronics, 40(1), 64-70.
- [205] C. Kung, W. Kao, (1998) "GA-based Grey Fuzzy Dynamic Sliding Mode Controller Design", the 1998 IEEE International Conference on Fuzzy Systems Proceedings, IEEE World Congress on Computational Intelligence, Anchorage, AK, USA Volume 1, Pages 583-588.

- [206] K.D. Young, Ümit Özgüner, (1999), "Sliding Mode: Control Engineering in Practice", Proceedings of the American Control Conference, San Diego, California, June, Pages 150-162.
- [207] C.C. Lee, (1990), "Fuzzy Logic in Control Systems: Fuzzy Logic Controller–Part I and II", IEEE Transactions on Systems, Man, and Cybernetics, Volume 20, Number 2, Pages 404-435.
- [208] S.W. Kim, M. Park, (1996), "A Multirule-Base Controller using the Robust Property of a Fuzzy Controller and its Design Method", IEEE Transactions Fuzzy Systems, Volume 4, Pages 315-327.
- [209] B. O'Dell, (1997), "Fuzzy Sliding Mode Control: A Critical Review", Oklahoma State University, Advanced Control Laboratory, Technical Report ACL-97-001.
- [210] C. Lin, C. Hsu, (2004), "Adaptive Fuzzy Sliding-Mode Control for Induction Servomotor Systems", IEEE Transactions on Energy Conversion, Volume 19, Number 2, Pages 362-368.
- [211] K. C. Ng, Y. Li, D. J. Murray-smith, K. C. Sharman, (1995), "Genetic Algorithm Applied to Fuzzy Sliding Mode Controller Design", First International Conference on Genetic Algorithms in Engineering Systems: Innovations and Applications, GALESIA, 12-14 September, Pages 220-225.
- [212] J. C. Lo and Y. H. Kuo, (1998), "Decoupled fuzzy sliding-mode control", IEEE Transactions Fuzzy Systems Volume 6, Pages 426-435.
- [213] B. J. Choi, S. W. Kwak, and B. K. Kim, (1999), "Design of a Single-Input Fuzzy Logic Controller and its Properties", Fuzzy Sets and Systems, Volume 106, Pages 299-308.
- [214] C. Kung, T. Chen, L. Kung, (2005), "Modified Adaptive Fuzzy Sliding Mode Controller for Uncertain Nonlinear Systems", IEICE Transactions Fundamentals, Volume E88-A, Number 5, Pages 1328-1334.
- [215] J. Wang, A.B. Rad, P.T. Chan, (2001), "Indirect Adaptive Fuzzy Sliding Mode Control: Part I: fuzzy switching", Fuzzy Sets and Systems, Volume 122, Issue 1, Pages 21-30.
- [216] C.H. Wang, H.L. Liu and T.C. Lin, (2002), "Direct Adaptive Fuzzy-Neural Control with State Observer and Supervisory Controller for Unknown Nonlinear Dynamical Systems", the IEEE Transactions on Fuzzy Systems, Volume 10, Pages 39-49.

- [217] H.T. Yau, C.L. Chen, (2006), “Chattering-free Fuzzy Sliding-Mode Control Strategy for Uncertain Chaotic Systems”, *Chaos, Solitons and Fractals*, Volume 30, Pages 709-718.
- [218] I. Eksin, M. Güzelkaya, S. Tokat, (2002), “Self-Tuning Mechanism for Sliding Surface Slope Adjustment in Fuzzy Sliding Mode Controllers”, *Proceedings of the Institution of Mechanical Engineers, Part I: Journal of Systems and Control Engineering*, Volume 216, Number 5, Pages 393-406.
- [219] E. Iglesias, Y. García, M. Sanjuan, O. Camacho, C. Smith, “Fuzzy Surface-Based Sliding Mode Control”, *ISA Transactions*, Volume 46, Issue 1, Pages 73-83.
- [220] M. Roopaeia, M. Zolghadrib, S. Meshksarc, (2009), “Enhanced Adaptive Fuzzy Sliding Mode Control for Uncertain Nonlinear Systems”, *Communications in Nonlinear Science and Numerical Simulation*, Volume 14, Issues 9-10, Pages 3670-3681.
- [221] Y. Chen, M.P. Cartmell, (2009), “Hybrid Sliding Mode Control for Motorised Space Tether Spin-up when Coupled with Axial Oscillation”, *Proceedings of XXXVII Summer School and Advanced Problems in Mechanics Conference*, June 30-July 5, St Petersburg, Russia, Pages 137-151.
- [222] Y. Chen, M.P. Cartmell, (2009), “Hybrid Fuzzy And Sliding-Mode Control for Motorised Tether Spin-Up When Coupled With Axial Vibration”, *7th International Conference on Modern Practice in Stress and Vibration Analysis*, 8-10 September 2009, New Hall, Cambridge, UK.
- [223] D.C. Karnopp, M.J. Crosby, R.A. Harwood, (1974), “Vibration Control using Semi-Active Force Generators”, *Journals of Engineering for Industry, Transactions of the ASME*, 94:619-626.
- [224] J.J. E. Slotine, (1982), “Tracking Control of Nonlinear Systems using Sliding Surfaces With Application to Robot Manipulations”, *PhD Dissertation*, Laboratory for Information and Decision Systems, Massachusetts Institute of Technology.
- [225] Wilfrid Perruquetti, Jean Pierre Barbot, (2002), “Sliding Mode Control in Engineering”, *CRC Press*, ISBN-13: 978-0824706715.

# Appendices

## Appendix A

---

### Partial Derivatives for Equation 3.5.11

---

The partial derivatives of equations (3.5.11) with respect to the selected generalised coordinates  $\psi$ ,  $\theta$ ,  $\alpha$ ,  $\gamma$ ,  $R$  and  $L$  are given in equations (A.0.1) to (A.0.6).

$$\left\{ \begin{array}{l} \frac{\partial x}{\partial \psi} = -L \cos \alpha \sin (\theta + \psi) \\ \frac{\partial y}{\partial \psi} = L \cos \alpha \cos (\theta + \psi) \\ \frac{\partial z}{\partial \psi} = 0 \end{array} \right. \quad (\text{A.0.1})$$

$$\left\{ \begin{array}{l} \frac{\partial x}{\partial \theta} = -L \cos \alpha \sin (\theta + \psi) \\ \frac{\partial y}{\partial \theta} = L \cos \alpha \cos (\theta + \psi) \\ \frac{\partial z}{\partial \theta} = 0 \end{array} \right. \quad (\text{A.0.2})$$

$$\left\{ \begin{array}{l} \frac{\partial x}{\partial \alpha} = -L \sin \alpha \cos (\theta + \psi) \\ \frac{\partial y}{\partial \alpha} = -L \sin \alpha \sin (\theta + \psi) \\ \frac{\partial z}{\partial \alpha} = L \cos \alpha \end{array} \right. \quad (\text{A.0.3})$$

$$\left\{ \begin{array}{l} \frac{\partial x}{\partial \gamma} = 0 \\ \frac{\partial y}{\partial \gamma} = 0 \\ \frac{\partial z}{\partial \gamma} = 0 \end{array} \right. \quad (\text{A.0.4})$$

$$\left\{ \begin{array}{l} \frac{\partial x}{\partial R} = 0 \\ \frac{\partial y}{\partial R} = 0 \\ \frac{\partial z}{\partial R} = 0 \end{array} \right. \quad (\text{A.0.5})$$

$$\left\{ \begin{array}{l} \frac{\partial x}{\partial L} = \cos \alpha \cos (\theta + \psi) \\ \frac{\partial y}{\partial L} = \cos \alpha \sin (\theta + \psi) \\ \frac{\partial z}{\partial L} = \sin \alpha \end{array} \right. \quad (\text{A.0.6})$$

According to equation (3.5.10), the generalised forces for the selected generalised coordinates of this solid massless MMET system can be stated in equations (A.0.7) to (A.0.12).

$$Q_{\psi} = F_x \frac{\partial x}{\partial \psi} + F_y \frac{\partial y}{\partial \psi} + F_z \frac{\partial z}{\partial \psi} \quad (\text{A.0.7})$$

$$Q_{\theta} = F_x \frac{\partial x}{\partial \theta} + F_y \frac{\partial y}{\partial \theta} + F_z \frac{\partial z}{\partial \theta} \quad (\text{A.0.8})$$

$$Q_{\alpha} = F_x \frac{\partial x}{\partial \alpha} + F_y \frac{\partial y}{\partial \alpha} + F_z \frac{\partial z}{\partial \alpha} \quad (\text{A.0.9})$$

$$Q_R = F_x \frac{\partial x}{\partial R} + F_y \frac{\partial y}{\partial R} + F_z \frac{\partial z}{\partial R} \quad (\text{A.0.10})$$

$$Q_{\gamma} = F_x \frac{\partial x}{\partial \gamma} + F_y \frac{\partial y}{\partial \gamma} + F_z \frac{\partial z}{\partial \gamma} \quad (\text{A.0.11})$$

$$Q_L = F_x \frac{\partial x}{\partial L} + F_y \frac{\partial y}{\partial L} + F_z \frac{\partial z}{\partial L} \quad (\text{A.0.12})$$

## Appendix B

---

### Partial Derivatives for Equation 3.5.12

---

Then, the partial derivatives of the Cartesian components  $x$ ,  $y$  and  $z$  in equations (A.0.1) to (A.0.6) can also be stated as in equations (B.0.1) to (B.0.6).

$$\left\{ \begin{array}{l} \frac{\partial x}{\partial \psi} = -L \cos \alpha \sin \psi \\ \frac{\partial y}{\partial \psi} = L \cos \alpha \cos \psi \\ \frac{\partial z}{\partial \psi} = 0 \end{array} \right. \quad (\text{B.0.1})$$

$$\left\{ \begin{array}{l} \frac{\partial x}{\partial \theta} = 0 \\ \frac{\partial y}{\partial \theta} = 0 \\ \frac{\partial z}{\partial \theta} = 0 \end{array} \right. \quad (\text{B.0.2})$$

$$\left\{ \begin{array}{l} \frac{\partial x}{\partial \alpha} = -L \sin \alpha \cos \psi \\ \frac{\partial y}{\partial \alpha} = -L \sin \alpha \sin \psi \\ \frac{\partial z}{\partial \alpha} = L \cos \alpha \end{array} \right. \quad (\text{B.0.3})$$

$$\left\{ \begin{array}{l} \frac{\partial x}{\partial \gamma} = 0 \\ \frac{\partial y}{\partial \gamma} = 0 \\ \frac{\partial z}{\partial \gamma} = 0 \end{array} \right. \quad (\text{B.0.4})$$

$$\left\{ \begin{array}{l} \frac{\partial x}{\partial R} = 0 \\ \frac{\partial y}{\partial R} = 0 \\ \frac{\partial z}{\partial R} = 0 \end{array} \right. \quad (\text{B.0.5})$$

$$\left\{ \begin{array}{l} \frac{\partial x}{\partial L} = \cos \alpha \cos \psi \\ \frac{\partial y}{\partial L} = \cos \alpha \sin \psi \\ \frac{\partial z}{\partial L} = \sin \alpha \end{array} \right. \quad (\text{B.0.6})$$

## Appendix C

# Simulation Parameter Settings

Table C.1: MMET system parameters

Symbol	Parameter	Value	Unit
$\mu$	gravitational constant	$3.9877848 \times 10^{14}$	$\text{m}^3\text{s}^{-2}$
$M_P$	propulsion tether payload mass	10000	Kg
$M_M$	mass of motor facility	5000	Kg
$r_{\text{Tinner}}$	radius of tether inner tube	0.08	m
$r_{\text{Touter}}$	radius of tether outer tube	0.1	m
$r_M$	radius of motor facility	0.5	m
$r_P$	radius of payload	0.5	m
$r_{\text{per}}$	periapsis distance	$6.890 \times 10^6$	m
$r_{\text{apo}}$	apoapsis distance	$1.0335 \times 10^7$	m
$L_0$	static length tether sub-span	50000	m
$A$	undeformed tether tube cross-sectional area	$1.13097 \times 10^{-2}$	$\text{m}^2$
$\rho$	tether density	970	$\text{kg}/\text{m}^3$
$e$	circular orbit with eccentricity	0.2	
$\tau$	motor torque	$2.5 \times 10^6$	Nm
$c_0$	tether sub-span axial damping coefficient	$2 \times 10^6$	Ns/m
$k_0$	tether sub-span axial stiffness	$2 \times 10^7$	N/m
$c_{t0}$	tether sub-span torsional damping coefficient	$2 \times 10^6$	Ns/m
$k_{t0}$	tether sub-span torsional stiffness	$2 \times 10^7$	N/m
$c_{l0}$	tether sub-span pendular damping coefficient	$2 \times 10^6$	Ns/m
$k_{l0}$	tether sub-span pendular stiffness	$2 \times 10^7$	N/m
$K_e$	FLC scaling gains for $e$	1	
$K_{ec}$	FLC scaling gains for $ec$	1	
$K_u$	FLC scaling gains for $u$	21000	
$\alpha$	F $\alpha$ SMC switching factor	{0, 0.5, 1}	

Table C.2: MMET system parameters - (Continued)

Symbol	Parameter	Value	Unit
$c_{sky}$	SkyhookSMC damping coefficient	-3000	
$\delta$	thickness of the sliding mode boundary layer	0.8	
$\lambda$	slope of the sliding surface	0.0014	
$A$	Tether tube cross-sectional area		$m^2$
$N$	Number of mass points	10,2	
$\epsilon$	Factor for the mass point mass moment of inertia	10,2	
$n$	Number of massless points	20	
$\rho$	Tether density	970	$kg/m^3$
$L_x$	Dynamic length of propulsion tether		$m$
$L$	Length of propulsion tether branch	$L_x + L_0$	$m$
$I_p$	Mass moment of inertia of the payload		$kgm^2$
$I_T$	Mass moment of inertia of the tether		$kgm^2$
$I_M$	Mass moment of inertia of the motor		$kgm^2$
$h_p$	Height of the cylinder payload	0.5	$m$
$h_M$	Height of cylinder the motor facility	0.5	$m$
$T_n$	The number for periodic cycles	4.01 or 400.01	
$t$	Simulation time	equation (1.1.11)	$s$
$g$	Acceleration of gravity	9.81	$m/s^2$
$T$	The period of orbit		$s$

Table C.3: MMET system parameters - (Continued)

Symbol	Parameter	Value	Unit
$\psi(0)$	Initial value of $\psi$	0.0 or 0.001	rad
$\dot{\psi}(0)$	Initial value of $\dot{\psi}$	0.0 or 0.001	rad/s
$\eta_1(0)$	Initial value of $\eta_1$	0.0	m
$\eta_2(0)$	Initial value of $\eta_2$	0.0	m
$\eta_{P1}(0)$	Initial value of $\eta_{P1}$	0.0	m
$\eta_{P2}(0)$	Initial value of $\eta_{P2}$	0.0	m
$\varphi_1(0)$	Initial value of $\varphi_1$	0.0 or 0.001	rad
$\varphi_2(0)$	Initial value of $\varphi_2$	0.0 or 0.001	rad
$\varphi_{P1}(0)$	Initial value of $\varphi_{P1}$	0.0 or 0.001	rad
$\varphi_{P2}(0)$	Initial value of $\varphi_{P2}$	0.0 or 0.001	rad
$\chi_1(0)$	Initial value of $\chi_1$	0.0	rad
$\chi_2(0)$	Initial value of $\chi_2$	0.0	rad
$\chi_{P1}(0)$	Initial value of $\chi_{P1}$	0.0	rad
$\chi_{P2}(0)$	Initial value of $\chi_{P2}$	0.0	rad
$\zeta_1(0)$	Initial value of $\zeta_1$	0.0	rad
$\zeta_2(0)$	Initial value of $\zeta_2$	0.0	rad
$\zeta_{P1}(0)$	Initial value of $\zeta_{P1}$	0.0	rad
$\zeta_{P2}(0)$	Initial value of $\zeta_{P2}$	0.0	rad
$\theta(0)$	Initial value of $\theta$	0.0 or 0.001	rad
$\dot{\theta}(0)$	Initial value of $\dot{\theta}$	(C.0.1)	rad/s
$\alpha(0)$	Initial value of $\alpha$	0.0 or 0.001	rad
$\dot{\alpha}(0)$	Initial value of $\dot{\alpha}$	0.0 or 0.001	rad/s
$\alpha_x(0)$	Initial value of $\alpha_x$	0.0 or 0.001	rad
$\dot{\alpha}_x(0)$	Initial value of $\dot{\alpha}_x$	0.0 or 0.001	rad/s
$\gamma(0)$	Initial value of $\gamma$	0.0 or 0.001	rad
$\dot{\gamma}(0)$	Initial value of $\dot{\gamma}$	0.0 or 0.001	rad/s
$\gamma_x(0)$	Initial value of $\gamma_x$	0.0 or 0.001	rad
$\dot{\gamma}_x(0)$	Initial value of $\dot{\gamma}_x$	0.0 or 0.001	rad/s
$L_x(0)$	Initial value of $L_x$	0.0	m
$\dot{L}_x(0)$	Initial value of $\dot{L}_x$	0.0	m/s

$$\dot{\theta} = \sqrt{\frac{\mu(1 + e \cos \theta)}{R^3}} \quad (\text{C.0.1})$$

## Appendix D

---

# Lagrange Equation Components for Section 4.2

---

### D.1 Potential Energy

The potential energy for the axially elastic massless MMET system is provided in equation (D.1.1), in which the strain energy stores in the assumed spring elements defined in equation (D.1.2). The damping in each group elastic element is assumed to be classical linear viscous in form and is expressed by equation (D.1.3).

$$\begin{aligned} u &= -\frac{\mu M_1}{R_1} - \frac{\mu M_2}{R_2} - \frac{\mu M_M}{R} + 2SE_{0|axial} \\ &= -\frac{\mu M_1}{\sqrt{L^2 + R^2 + 2LR \cos \alpha \cos \psi}} - \frac{\mu M_2}{\sqrt{L^2 + R^2 - 2LR \cos \alpha \cos \psi}} \\ &\quad - \frac{\mu M_M}{R} + 2SE_{0|axial} \end{aligned} \quad (D.1.1)$$

Where, the  $SE_{0|axial}$  term is the strain energy of each massless tether subspan with axial elasticity, as stated in equation (D.1.2). That is, for the symmetrical double-ended MMET system, the total strain energy is  $2SE_{0|axial}$ , as shown in equation (D.1.1). The  $CE_{0|axial}$  quantity is an assumed dissipation function based on Rayleigh damping and is stated in equation (D.1.3).

$$SE_{0|axial} = \frac{1}{2} k_{eq} L_x^2 \quad (D.1.2)$$

$$CE_{0|axial} = \frac{1}{2} c_{eq} \dot{L}_x^2 \quad (D.1.3)$$

For the serial ‘spring-damper’ group, it is assumed,  $k_0 = k_1 = k_2 = \dots = k_{n+1}$ ,  $c_0 = c_1 = c_2 = \dots = c_{n+1}$ , where the  $k_0$  and  $c_0$  are the default stiffness and damping coefficient values when they are applied in the numerical calculation. Equations (4.2.2) and (4.2.3) for the equivalent spring and damper can be transformed into equations (D.1.4) and (D.1.5).

$$k_{eq} = \frac{k_0}{n + 1} \quad (D.1.4)$$

$$c_{eq} = \frac{c_0}{n + 1} \quad (D.1.5)$$

## D.2 Kinetic Energy

As the payload and motor facility masses are connected by axially elastic massless tether subspans, the kinetic energy of the system is provided by equation (D.2.1), where  $(x_0, y_0, z_0)$  is given in equation (3.2.4),  $(x_1, y_1, z_1)$  is given in equation (3.4.3), and  $(x_2, y_2, z_2)$  is given in equation (3.4.4).

$$\begin{aligned} T = & \frac{1}{2}M_{P1} (\dot{x}_{P1}^2 + \dot{y}_{P1}^2 + \dot{z}_{P1}^2) + \frac{1}{2}M_{P2} (\dot{x}_{P2}^2 + \dot{y}_{P2}^2 + \dot{z}_{P2}^2) + \frac{1}{2}M_M (\dot{x}_0^2 + \dot{y}_0^2 + \dot{z}_0^2) + \\ & \frac{1}{2} [I_{z_{P1}} + I_{z_{P2}} + I_{z_M}] (\dot{\psi} + \dot{\theta})^2 + \\ & \frac{1}{2} [I_{x_{P1}} + I_{x_{P2}} + I_{x_M}] \dot{\alpha}^2 + \\ & \frac{1}{2} [I_{y_{P1}} + I_{y_{P2}} + I_{y_M}] \dot{\gamma}^2 \end{aligned} \quad (D.2.1)$$

## D.3 Generalised Coordinates

In the case of this modelling, it has been decided to represent the system dynamics by means of four angular coordinates  $(\psi, \theta, \alpha, \gamma)$  and two translational coordinates  $(R, L_x)$ , in which, the selection of  $\psi, \theta, \alpha, R$  and  $\gamma$  are the same generalised coordinates as discussed in section 3.6.8, Table 3.5.  $L_x$  is the generalised coordinate for axially elastic motion.

## D.4 Generalised Forces

According to the previous discussion in section 3.5.7, the generalised force generated by the motor on the system needs to be derived, from the principle of virtual work, and is defined in equation (3.5.8).

As stated in equation (4.2.1),  $L_0$  is the static tether length, and  $L_x$  is the axially elastic length along the tether subspans, then the virtual displacements in equation (3.5.12) can be re-stated as equation (D.4.1).

$$\begin{cases} x = (L_0 + L_x) \cos \alpha \cos \psi \\ y = (L_0 + L_x) \cos \alpha \sin \psi \\ z = (L_0 + L_x) \sin \alpha \end{cases} \quad (\text{D.4.1})$$

Considering the virtual work done by all non-conservative forces through a virtual displacement, according to equation (3.5.9) and equation (3.5.10), the virtual work of the axial effect generalised coordinate  $L_x$  is given in equation (D.4.2), and the generalised force of  $L_x$  leads to equation (D.4.3), whose derivation process is similar to that of equation (A.0.12). The generalised forces for coordinates  $\psi$ ,  $\theta$ ,  $\alpha$ ,  $\gamma$ , and  $R$  are the same as in equations (3.5.13) to (3.5.17).

$$\delta W_{L_x} = Q_{L_x}(t) \delta L_x \quad (\text{D.4.2})$$

$$Q_{L_x}(t) = F_x \frac{\partial x}{\partial L_x} + F_y \frac{\partial y}{\partial L_x} + F_z \frac{\partial z}{\partial L_x} - c_{eq} \dot{L}_x \quad (\text{D.4.3})$$

Where,  $F_x$ ,  $F_y$  and  $F_z$  are the Cartesian components of  $F$ , which have been discussed for equation (3.5.5).

$$\begin{cases} \frac{\partial x}{\partial L_x} = \cos \alpha \cos \psi \\ \frac{\partial y}{\partial L_x} = \cos \alpha \sin \psi \\ \frac{\partial z}{\partial L_x} = \sin \alpha \end{cases} \quad (\text{D.4.4})$$

According to equation (D.4.4), equation (D.4.3) can be transformed into equation (D.4.5).

$$Q_{L_x} = -c_{eq} \dot{L}_x \quad (\text{D.4.5})$$

## Appendix E

---

# Lagrange Equation Components for Section 4.3

---

### E.1 Potential Energy

In this axially and torsionally elastic massless MMET system, the axial and torsional elastic potential energy is stored as the strain energy in the elastic elements - the axial and torsional ‘spring-damper’ groups. The strain energy terms for the tether axial and torsional elasticity are given in equation (D.1.2) and (E.1.1), in which it is assumed  $k_{t0} = k_{t1} = k_{t2} = \dots = k_{tn}$ , where the  $k_{t0}$  is the default stiffness value when applied in the numerical simulation.

The damper in each group elastic element is assumed to be classical linear viscous, which is stated in equation (E.1.2), similarly, it is assumed  $c_{t0} = c_{t1} = c_{t2} = \dots = c_{tn}$ , where the  $c_{t0}$  is the default damping coefficient value for the numerical simulation.

Based on the  $k_{t0}$  and  $c_{t0}$  settings, equations (4.3.1) and (4.3.2) can be re-written as (E.1.3) and (E.1.4).

$$SE_{0|torsional} = \frac{1}{2}k_{teq}\gamma_x^2 \quad (E.1.1)$$

$$CE_{0|torsional} = \frac{1}{2}c_{teq}\dot{\gamma}_x^2 \quad (E.1.2)$$

Where,

$$k_{teq} = \frac{k_{t0}}{n+1} \quad (E.1.3)$$

$$c_{teq} = \frac{c_{t0}}{n+1} \quad (E.1.4)$$

The tether's potential energy is given in equation (E.1.5), and  $\mu$  is the product of the universal gravitational constant  $G$  with the Earth's Mass.

$$\begin{aligned} U &= -\frac{\mu M_1}{R_1} - \frac{\mu M_2}{R_2} - \frac{\mu M_M}{R} + 2SE \\ &= -\frac{\mu M_1}{\sqrt{L^2 + R^2 + 2LR \cos \alpha \cos \psi}} - \frac{\mu M_2}{\sqrt{L^2 + R^2 - 2LR \cos \alpha \cos \psi}} \end{aligned} \quad (\text{E.1.5})$$

$$-\frac{\mu M_M}{R} + 2SE$$

where,

$$SE = SE_{0|axial} + SE_{0|torsional} \quad (\text{E.1.6})$$

Equation (E.1.6) gives the strain energy of this axially and torsionally elastic massless MMET system, in which for the symmetrical double-ended MMET system, the total strain energy is  $2SE$ , as provided by equation (E.1.6).

The  $SE_{0|axial}$  term is the axially elastic strain energy of each tether subspan and is defined in equation (D.1.2). The  $SE_{0|torsional}$  term is the torsionally elastic strain energy of each tether subspan and is defined in equation (E.1.1).

The  $CE_{0|axial}$  term is an assumed dissipation function of the axial elasticity modelling, based on Rayleigh damping and defined in equation (D.1.3). The  $CE_{0|torsional}$  term is an assumed dissipation function of the torsional elasticity modelling, based on the Rayleigh damping as expressed in equation (E.1.2).

## E.2 Kinetic Energy

The kinetic energy of this MMET system is given in equation (E.2.1), where  $(x_0, y_0, z_0)$ ,  $(x_1, y_1, z_1)$  and  $(x_2, y_2, z_2)$  are the same as are given in section D.2, and  $L$  is given in equation (4.2.1). The mass moments of inertia for the two cylindrical payloads and the motor facility are declared in section 3.5.1 and 3.5.2.

$$\begin{aligned}
T = & \frac{1}{2}M_{P1} (\dot{x}_{P1}^2 + \dot{y}_{P1}^2 + \dot{z}_{P1}^2) + \frac{1}{2}M_{P2} (\dot{x}_{P2}^2 + \dot{y}_{P2}^2 + \dot{z}_{P2}^2) + \frac{1}{2}M_M (\dot{x}_0^2 + \dot{y}_0^2 + \dot{z}_0^2) + \\
& \frac{1}{2} [I_{z_{P1}} + I_{z_{P2}} + I_{z_M}] (\dot{\psi} + \dot{\theta})^2 + \frac{1}{2} [I_{x_{P1}} + I_{x_{P2}} + I_{x_M}] \dot{\alpha}^2 + \\
& \frac{1}{2} [I_{y_{P1}} + I_{y_{P2}} + I_{y_M}] \dot{\gamma}^2 + \frac{1}{2} [I_{y_{P1}} + I_{y_{P2}}] \dot{\gamma}_x^2
\end{aligned} \tag{E.2.1}$$

### E.3 Generalised Coordinates

In the case of this modelling, it has been decided to represent the system dynamics by means of five angular coordinates ( $\psi$ ,  $\theta$ ,  $\alpha$ ,  $\gamma$ ,  $\gamma_x$ ) and two translational coordinates ( $R$ ,  $L_x$ ), in which the  $\psi$ ,  $\theta$ ,  $\alpha$ ,  $\gamma$ ,  $R$  and  $L_x$  are the same generalised coordinates as discussed in section D.3, and  $\gamma_x$  is the generalised coordinate for motion accommodating torsional elasticity.

### E.4 Generalised Forces

The virtual work for the torsional effect generalised coordinate  $\gamma_x$  is derived in equation (E.4.1), and the generalised force of  $\gamma_x$  is expressed in equation (E.4.2). The generalised forces for coordinates  $\psi$ ,  $\theta$ ,  $\alpha$ ,  $R$  and  $L_x$  are reported in equations (3.5.13) to (3.5.17) and (D.4.5).

$$\delta W_{\gamma_x} = Q_{\gamma_x} (t) \delta \gamma_x \tag{E.4.1}$$

where,

$$Q_{\gamma_x} (t) = F_x \frac{\partial x}{\partial \gamma_x} + F_y \frac{\partial y}{\partial \gamma_x} + F_z \frac{\partial z}{\partial \gamma_x} - c_{teq} \dot{\gamma}_x \tag{E.4.2}$$

The quantity  $\gamma_x$  states the torsional effect for this MMET system. The generalised force of  $\gamma_x$  can also be reformed as equation (E.4.4) by substituting equation (E.4.3) into equation (E.4.2).

$$\left\{ \begin{array}{l} \frac{\partial x}{\partial \gamma_x} = 0 \\ \frac{\partial y}{\partial \gamma_x} = 0 \\ \frac{\partial z}{\partial \gamma_x} = 0 \end{array} \right. \tag{E.4.3}$$

$$Q_{\gamma_x} = -c_{teq} \dot{\gamma}_x \quad (\text{E.4.4})$$

## Appendix F

---

# Lagrange Equation Components for Section 4.4

---

### F.1 Generalised Coordinates

In order to describe the kinematic behaviour of the flexible massless MMET system, there are seven rotational generalised coordinates ( $\psi$ ,  $\psi_x$ ,  $\theta$ ,  $\alpha$ ,  $\alpha_x$ ,  $\gamma$ ,  $\gamma_x$ ) and two translational coordinates ( $L_x$ ,  $R$ ) as shown in Figure 4.33. Note that, the rigid body generalised coordinates ( $\psi$ ,  $\theta$ ,  $\alpha$ ,  $\gamma$ ,  $R$ ) are not duplicating any of the motions of the elastic generalised coordinates ( $\psi_x$ ,  $\alpha_x$ ,  $\gamma_x$ ,  $L_x$ ).

The coordinates  $\psi$ ,  $\theta$ ,  $\alpha$ ,  $\gamma$ ,  $R$ ,  $L_x$  and  $\gamma_x$  are the same generalised coordinates as given section E.3, and  $\psi_x$  is the generalised coordinate required for showing the effects of the equivalent motion of the pendular elasticity on the plane  $x_0 - O - y_0$ , as shown in Figure 4.32.  $\alpha_x$  is the generalised coordinate relating to the equivalent motion of the pendular elasticity on the plane  $z_0 - O - y_0$ , as shown in Figure 4.34.

### F.2 Kinetic Energy

As the payloads ( $M_{P1}$ ,  $M_{P2}$ ) and motor facility ( $M_M$ ) masses are connected by flexible massless tether subspans, the kinetic energy of this MMET system is given in equation (F.2.1).

$$\begin{aligned}
T = & \frac{1}{2}M_{P1} (\dot{x}_1^2 + \dot{y}_1^2 + \dot{z}_1^2) + \frac{1}{2}M_{P2} (\dot{x}_2^2 + \dot{y}_2^2 + \dot{z}_2^2) + \\
& \frac{1}{2}M_M (\dot{x}_0^2 + \dot{y}_0^2 + \dot{z}_0^2) + \frac{1}{2} (M_{P1} + M_{P2}) \dot{L}_x^2 + \\
& \frac{1}{2} [I_{zP1} + I_{zP2} + I_{zM}] (\dot{\psi} + \dot{\theta})^2 + \frac{1}{2} [I_{xP1} + I_{xP2} + I_{xM}] \dot{\alpha}^2 + \\
& \frac{1}{2} [I_{yP1} + I_{yP2} + I_{yM}] \dot{\gamma}^2 + \frac{1}{2} [I_{yP1} + I_{yP2}] \dot{\gamma}_x^2 + \\
& \frac{1}{2} [I_{zP1} + I_{zP2} + (M_{P1} + M_{P2}) L^2] \dot{\psi}_x^2 + \\
& \frac{1}{2} [I_{xP1} + I_{xP2} + (M_{P1} + M_{P2}) L^2] \dot{\alpha}_x^2
\end{aligned} \tag{F.2.1}$$

### F.3 Potential Energy

The gravitational potential energy is obtained by implementing Newton's gravitational law, and is stated in equation (F.3.1), where  $\mu$  is the product of the universal gravitational constant  $G$  with the Earth's Mass.

$$\begin{aligned}
U = & -\frac{\mu M_1}{R_1} - \frac{\mu M_2}{R_2} - \frac{\mu M_M}{R} + 2SE \\
= & -\frac{\mu M_1}{\sqrt{L^2 + R^2 + 2LR \cos \alpha \cos \psi}} - \frac{\mu M_2}{\sqrt{L^2 + R^2 - 2LR \cos \alpha \cos \psi}} \\
& -\frac{\mu M_M}{R} + 2SE
\end{aligned} \tag{F.3.1}$$

Where, equation (F.3.2) gives the strain energy along each tether subspan, so, for the symmetrical double-ended MMET system, the total strain energy is  $2SE$ , as obtained in equation (F.3.1).

As has been noted, equations (D.1.2), (E.1.1) and (F.3.3) express the strain energy relating to the axial, torsional and pendular elasticity, respectively. Equations (D.1.3), (E.1.2) and (F.3.4) defined the assumed dissipation function based on Rayleigh damping for including axial, torsional and pendular elastic effects, correspondingly.

$$SE = SE_0|_{axial} + SE_0|_{torsional} + SE_0|_{pendular} \quad (F.3.2)$$

$$SE_0|_{pendular} = \frac{1}{2}k_{leq} (\psi_x^2 + \alpha_x^2) \quad (F.3.3)$$

$$CE_0|_{pendular} = \frac{1}{2}c_{leq} (\dot{\psi}_x^2 + \dot{\alpha}_x^2) \quad (F.3.4)$$

## F.4 Generalised Forces

The virtual work for the pendular effect generalised coordinates  $\psi_x$  and  $\alpha_x$  is given in equations (F.4.1) and (F.4.2), in which the generalised forces for  $\psi_x$  and  $\alpha_x$  are reported in equations (F.4.3) and (F.4.4). The generalised forces for coordinates  $\psi$ ,  $\theta$ ,  $\alpha$ ,  $\gamma$ ,  $R$ ,  $L_x$  and  $\gamma_x$  are the same as stated in section E.3.

$$\delta W_{\psi_x} = Q_{\psi_x}(t) \delta \psi_x \quad (F.4.1)$$

$$\delta W_{\alpha_x} = Q_{\alpha_x}(t) \delta \alpha_x \quad (F.4.2)$$

$$Q_{\psi_x} = F_x \frac{\partial x}{\partial \psi_x} + F_y \frac{\partial y}{\partial \psi_x} + F_z \frac{\partial z}{\partial \psi_x} - c_{leq} \dot{\psi}_x = -c_{leq} \dot{\psi}_x \quad (F.4.3)$$

$$Q_{\alpha_x} = F_x \frac{\partial x}{\partial \alpha_x} + F_y \frac{\partial y}{\partial \alpha_x} + F_z \frac{\partial z}{\partial \alpha_x} - c_{leq} \dot{\alpha}_x = -c_{leq} \dot{\alpha}_x \quad (F.4.4)$$

By substituting equations (F.4.5) and (F.4.6) into equations (F.4.3) and (F.4.4), the generalised forces for  $\psi_x$  and  $\alpha_x$  can then be simplified into equations (F.4.7) and (F.4.8).

$$\left\{ \begin{array}{l} \frac{\partial x}{\partial \psi_x} = 0 \\ \frac{\partial y}{\partial \psi_x} = 0 \\ \frac{\partial z}{\partial \psi_x} = 0 \end{array} \right. \quad (F.4.5)$$

$$\left\{ \begin{array}{l} \frac{\partial x}{\partial \alpha_x} = 0 \\ \frac{\partial y}{\partial \alpha_x} = 0 \\ \frac{\partial z}{\partial \alpha_x} = 0 \end{array} \right. \quad (\text{F.4.6})$$

$$Q_{\psi_x} = -c_{\text{leq}} \dot{\psi}_x \quad (\text{F.4.7})$$

$$Q_{\alpha_x} = -c_{\text{leq}} \dot{\alpha}_x \quad (\text{F.4.8})$$

## Appendix G

---

# Dynamical Modelling for Axial Elastic MMET System with Two Discretised Mass Points

---

In this chapter, a simplified MMET system by following the same discretisation scheme is proposed with  $N = 2$  discretised mass points. As shown in Figure G.1, the axial elastic MMET system with 2 discretised mass points for two tether subspans, in which the generalised coordinates  $\eta_i$  ( $i = 1$  to 2) are for the 2 discretised mass points.  $\eta_{P1}$  and  $\eta_{P2}$  are the generalised coordinates for the mass payloads  $M_{P1}$  and  $M_{P2}$ , the Cartesian coordinate for the motor facility  $M_0$  is given in section 5.2, and Figure G.1 is a simplified case for Figure 5.1.

### G.1 The Cartesian Coordinates for Payloads $M_{P1}$ and $M_{P2}$

The Cartesian coordinates for the payloads  $M_{P1}$  and  $M_{P2}$  are given in equations (G.1.1) and (G.1.2).

$$\begin{cases} x_1 = x_0 + (\eta_{P1} + \eta_1 + L_0) \cos \alpha \cos (\theta + \psi) \\ y_1 = y_0 + (\eta_{P1} + \eta_1 + L_0) \cos \alpha \sin (\theta + \psi) \\ z_1 = (\eta_{P1} + \eta_1 + L_0) \sin \alpha \end{cases} \quad (\text{G.1.1})$$

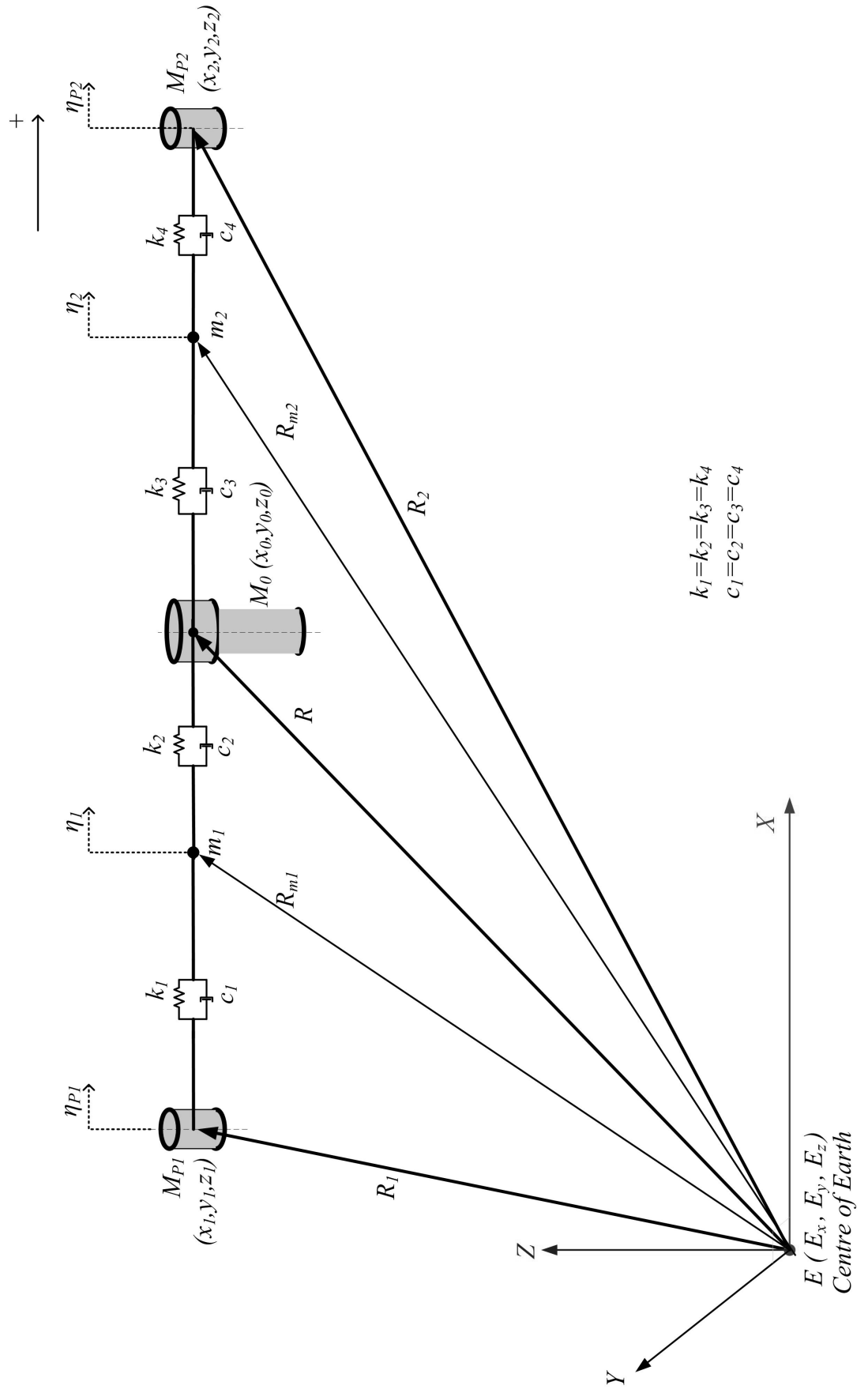


Figure G.1: Axial elastic MMET tether with 2 mass points

$$\begin{cases} x_2 = x_0 - (\eta_2 + \eta_{P2} + L_0) \cos \alpha \cos (\theta + \psi) \\ y_2 = y_0 - (\eta_2 + \eta_{P2} + L_0) \cos \alpha \sin (\theta + \psi) \\ z_2 = -(\eta_2 + \eta_{P2} + L_0) \sin \alpha \end{cases} \quad (\text{G.1.2})$$

## G.2 The Cartesian Coordinates for Mass Points $m_1$ to $m_2$

The Cartesian coordinates for the discretised mass points  $m_1$  to  $m_2$  are given in equations (G.2.1) and (G.2.2).

$$\begin{cases} x_{m_1} = x_0 + \left( \eta_1 + \frac{L_0}{2} \right) \cos \alpha \cos (\theta + \psi) \\ y_{m_1} = y_0 + \left( \eta_1 + \frac{L_0}{2} \right) \cos \alpha \sin (\theta + \psi) \\ z_{m_1} = \left( \eta_1 + \frac{L_0}{2} \right) \sin \alpha \end{cases} \quad (\text{G.2.1})$$

$$\begin{cases} x_{m_2} = x_0 - \left( \eta_2 + \frac{L_0}{2} \right) \cos \alpha \cos (\theta + \psi) \\ y_{m_2} = y_0 - \left( \eta_2 + \frac{L_0}{2} \right) \cos \alpha \sin (\theta + \psi) \\ z_{m_2} = - \left( \eta_2 + \frac{L_0}{2} \right) \sin \alpha \end{cases} \quad (\text{G.2.2})$$

Similarly, the distance from Earth  $E(0, 0, 0)$  to each of the discretised mass point is represented by  $R_{m_i}$ , as given in equation (5.3.11).

## G.3 Potential Energy

The tether's potential energy is given in equation (G.3.1), where  $\mu$  is the product of the universal gravitational constant  $G$  with the Earth's mass.

$$U = -\frac{\mu M_{P1}}{R_1} - \frac{\mu M_{P2}}{R_2} - \frac{\mu M_0}{R} - \frac{\mu m_1}{R_{m_1}} - \frac{\mu m_2}{R_{m_2}} + SE|_{axial} \quad (\text{G.3.1})$$

Where, the  $SE|_{axial}$  term is a strain energy of the axial elasticity, as stated in equation (G.3.2) with the assumption  $k_0 = k_1 = k_2 = k_3 = k_4$ , where  $k_0$  is the default stiffness value.

$$SE|_{axial} = \frac{1}{2} k_0 \left( (\eta_{P1} - \eta_1)^2 + \eta_1^2 + \eta_2^2 + (\eta_2 - \eta_{P2})^2 \right) \quad (\text{G.3.2})$$

The  $CE|_{axial}$  term is an assumed dissipation function, as given in equation (G.3.3) with the assumption  $c_0 = c_1 = c_2 = c_3 = c_4$ , where the  $c_0$  is the default damping coefficient value.

$$CE|_{\text{axial}} = \frac{1}{2}c_0 ((\dot{\eta}_{P1} - \dot{\eta}_1)^2 + \dot{\eta}_1^2 + \dot{\eta}_2^2 + (\dot{\eta}_2 - \dot{\eta}_{P2})^2) \quad (\text{G.3.3})$$

## G.4 Kinetic Energy

The kinetic energy of this MMET system with 2 discretised mass points is stated in equation (G.4.1).

$$\begin{aligned} T = & \frac{1}{2}M_{P1} (\dot{x}_1^2 + \dot{y}_1^2 + \dot{z}_1^2) + \frac{1}{2}M_{P2} (\dot{x}_2^2 + \dot{y}_2^2 + \dot{z}_2^2) + \frac{1}{2}M_0 (\dot{x}_0^2 + \dot{y}_0^2 + \dot{z}_0^2) + \\ & \left[ \frac{1}{2}m_1 (\dot{x}_{m_1}^2 + \dot{y}_{m_1}^2 + \dot{z}_{m_1}^2) + \frac{1}{2}m_2 (\dot{x}_{m_2}^2 + \dot{y}_{m_2}^2 + \dot{z}_{m_2}^2) \right] + \\ & \left[ \frac{1}{2}I_{z_{P1}} + \frac{1}{2}I_{z_{P2}} + I_{z_T} + \frac{1}{2}I_{z_M} \right] (\dot{\psi} + \dot{\theta})^2 + \\ & \left[ \frac{1}{2}I_{x_{P1}} + \frac{1}{2}I_{x_{P2}} + I_{x_T} + \frac{1}{2}I_{x_M} \right] \dot{\alpha}^2 + \\ & \left[ \frac{1}{2}I_{y_{P1}} + \frac{1}{2}I_{y_{P2}} + I_{y_T} + \frac{1}{2}I_{y_M} \right] \dot{\gamma}^2 \end{aligned} \quad (\text{G.4.1})$$

## G.5 Governing Equations of Motion

In the case of this model, the selected generalised coordinates are four angular coordinates ( $\psi$ ,  $\theta$ ,  $\alpha$ ,  $\gamma$ ) and five translational coordinates ( $R$ ,  $\eta_1$ ,  $\eta_{P1}$ ,  $\eta_2$  and  $\eta_{P2}$ ), in which the generalised coordinates  $\eta_1$ ,  $\eta_{P1}$ ,  $\eta_2$  and  $\eta_{P2}$  are to express the equivalent behaviour due to its axial elasticity. The generalised coordinates  $q_i$  and the generalised forces  $Q_i$  ( $i = 1 - 9$ ) are a reduced set of those quoted for the case of  $N = 10$ .

Lagrange's equations are used to generate the governing equations of motion, the full equations are to be found in the path CD-ROM/axial/N2/, as listed in Table 5.2.

## Appendix H

---

# Dynamical Modelling for Axial and Torsional Elastic MMET System with Two Discretised Mass Points

---

Based on the axial elastic MMET system in Appendix G, in this chapter, a simplified axial and torsional MMET system with two discretised mass points is proposed.

As shown in Figure H.1, the torsional generalised coordinates  $\varphi_1$  and  $\varphi_2$  are for the 2 discretised mass points  $m_1$  and  $m_2$ ,  $\varphi_{P1}$  and  $\varphi_{P2}$  are the torsional generalised coordinates for the mass payloads  $M_{P1}$  and  $M_{P2}$ , the Cartesian coordinates for the motor facility  $M_0$ , payloads  $M_{P1}$  and  $M_{P2}$  are given by equations (3.2.4), (G.1.1) and (G.1.2), and the Cartesian coordinates for mass points  $m_1$  to  $m_2$  are given by equations (G.2.1) and (G.2.2).

For the axial elasticity modelling process is same as it has been discussed in Appendix G, so it will not be discussed in this appendix.

### H.1 Potential Energy

The tether's potential energy is given in equation (H.1), where  $\mu$  is the product of the universal gravitational constant  $G$  with the Earth's mass. The distance from Earth  $E(0, 0, 0)$  to each of the discretised mass point is represented by  $R_{m_i}$ , as given in equation (5.3.11).

$$U = -\frac{\mu M_{P1}}{R_1} - \frac{\mu M_{P2}}{R_2} - \frac{\mu M_0}{R} - \frac{\mu m_1}{R_{m_1}} - \frac{\mu m_2}{R_{m_2}} + SE|_{axial} + SE|_{torsional} \quad (H.1.1)$$

Where, the  $SE|_{axial}$  and  $SE|_{torsional}$  are the strain energy terms for axial and torsional elasticity, as stated in equation (G.3.2) and (H.1.2) with the assumption  $k_0 = k_1 = k_2$  and  $k_{t0} = k_{t1} = k_{t2}$ , where  $k_0$  and  $k_{t0}$  are the default axial and torsional stiffness values.

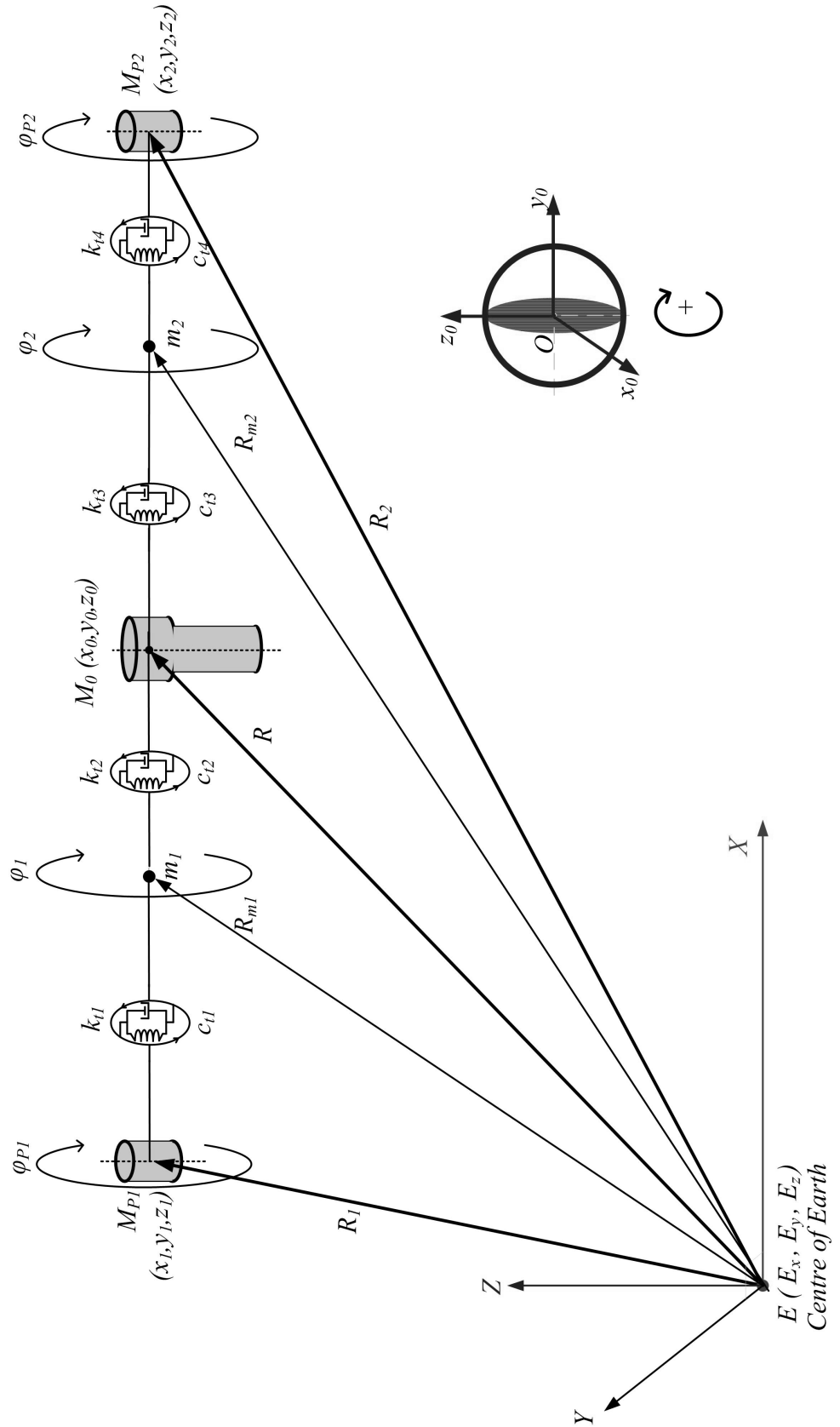


Figure H.1: Axial and torsional elastic MMET tether with 2 mass points

$$SE|_{\text{torsional}} = \frac{1}{2}k_{t0} ((\varphi_{P1} - \varphi_1)^2 + \varphi_1^2 + \varphi_2^2 + (\varphi_2 - \varphi_{P2})^2) \quad (\text{H.1.2})$$

The  $CE|_{\text{torsional}}$  term is an assumed torsional dissipation function, as given in equation

(H.1.3), with the assumption of  $c_{t0} = c_{t1} = c_{t2}$ , where the  $c_{t0}$  is the default torsional damping coefficient value.

$$CE|_{\text{torsional}} = \frac{1}{2}c_{t0} ((\dot{\varphi}_{P1} - \dot{\varphi}_1)^2 + \dot{\varphi}_1^2 + \dot{\varphi}_2^2 + (\dot{\varphi}_2 - \dot{\varphi}_{P2})^2) \quad (\text{H.1.3})$$

## H.2 Kinetic Energy

The kinetic energy of the MMET system with 2 discretised mass points is stated in equation (H.2.1).

$$\begin{aligned} T = & \frac{1}{2}M_{P1} (\dot{x}_1^2 + \dot{y}_1^2 + \dot{z}_1^2) + \frac{1}{2}M_{P2} (\dot{x}_2^2 + \dot{y}_2^2 + \dot{z}_2^2) + \frac{1}{2}M_0 (\dot{x}_0^2 + \dot{y}_0^2 + \dot{z}_0^2) + \\ & \left[ \frac{1}{2}m_1 (\dot{x}_{m1}^2 + \dot{y}_{m1}^2 + \dot{z}_{m1}^2) + \frac{1}{2}m_2 (\dot{x}_{m2}^2 + \dot{y}_{m2}^2 + \dot{z}_{m2}^2) \right] + \\ & \left[ \frac{1}{2}I_{zP1} + \frac{1}{2}I_{zP2} + I_{zT} + \frac{1}{2}I_{zM} \right] (\dot{\psi} + \dot{\theta})^2 + \\ & \left[ \frac{1}{2}I_{xP1} + \frac{1}{2}I_{xP2} + I_{xT} + \frac{1}{2}I_{xM} \right] \dot{\alpha}^2 + \\ & \left[ \frac{1}{2}I_{yP1} + \frac{1}{2}I_{yP2} + I_{yT} + \frac{1}{2}I_{yM} \right] \dot{\gamma}^2 + \\ & \left[ \frac{1}{2}I_{yP1} \dot{\varphi}_{P1}^2 + \frac{1}{2}I_{yP2} \dot{\varphi}_{P2}^2 + \frac{1}{2}I_{ym1} \dot{\varphi}_1^2 + \frac{1}{2}I_{ym2} \dot{\varphi}_2^2 \right] \end{aligned} \quad (\text{H.2.1})$$

## H.3 Governing Equations of Motion

In the case of this model, the selected generalised coordinates are eight angular coordinates ( $\psi$ ,  $\theta$ ,  $\alpha$ ,  $\gamma$ ,  $\varphi_1$ ,  $\varphi_{P1}$ ,  $\varphi_2$  and  $\varphi_{P2}$ ) and five translational coordinates ( $R$ ,  $\eta_1$ ,  $\eta_{P1}$ ,  $\eta_2$  and  $\eta_{P2}$ ), in which the generalised coordinate  $\varphi_1$ ,  $\varphi_{P1}$ ,  $\varphi_2$  and  $\varphi_{P2}$  are to express the torsional behaviours due to the torsional elasticity.

Lagrange's equations are used to generate the governing equations of motions, the full equations are to be found in the path CD-ROM/axial-torsional/N2/, as listed in Table 6.2

## Appendix I

---

# Dynamical Modelling for Axial, Torsional and Pendular Elastic MMET System with Two Discretised Mass Points

---

In this chapter, based on the axial and torsional elastic MMET system in Appendix H, a simplified flexible MMET system with two discretised mass points is introduced by following the same discretisation scheme as mentioned in Chapter 7. Again, the word ‘flexible’ means that this MMET system is incorporating axial, torsional and pendular elasticity, and the ‘pendular’ elasticity means a set of  $N = 2$  coupled pendulums with  $N$  equals the number of elements between each mass element in each of the tether sub-span.

As shown in Figure I.1, the pendular generalised coordinates  $\chi_1$  and  $\chi_2$  are for the 2 discretised mass points  $m_1$  and  $m_2$ .

$\chi_{P1}$  and  $\chi_{P2}$  are the pendular generalised coordinates for the mass payloads  $M_{P1}$  and  $M_{P2}$ , referenced on plane  $x_0 - O - y_0$ , it is a simplified MMET system of the original MMET system as given Figure 7.1.

As shown in Figure I.2, the pendular generalised coordinates  $\zeta_1$  and  $\zeta_2$  are for the 2 discretised mass points  $m_1$  and  $m_2$ .

$\zeta_{P1}$  and  $\zeta_{P2}$  are the pendular generalised coordinates for the mass payloads  $M_{P1}$  and  $M_{P2}$ , referenced on plane  $z_0 - O - y_0$ , it is a simplified MMET system of the original MMET system as given Figure 7.2.

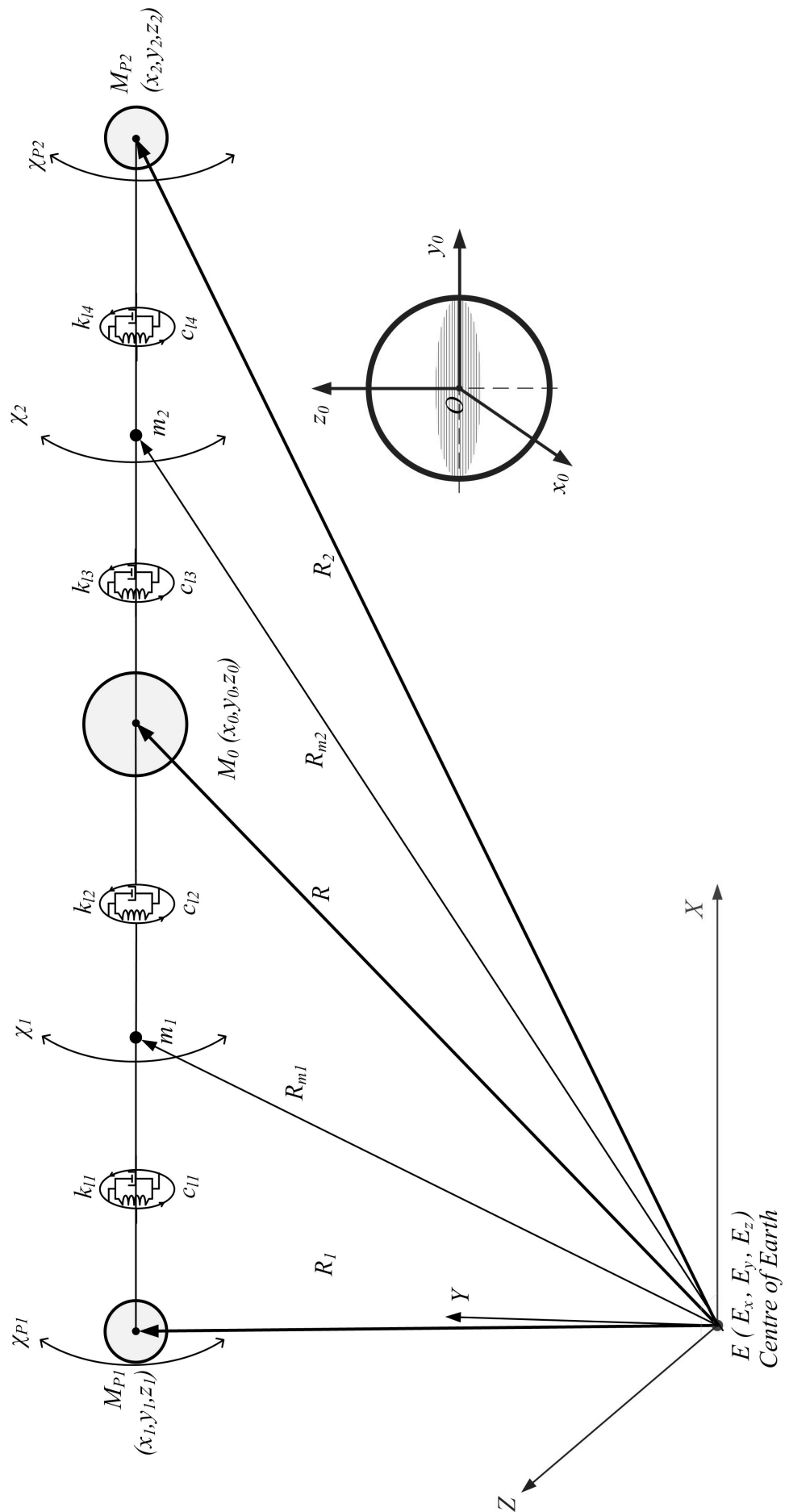


Figure I.1: Pendular elastic MMET tether with 2 discretised mass points -  $x_0 - O - y_0$

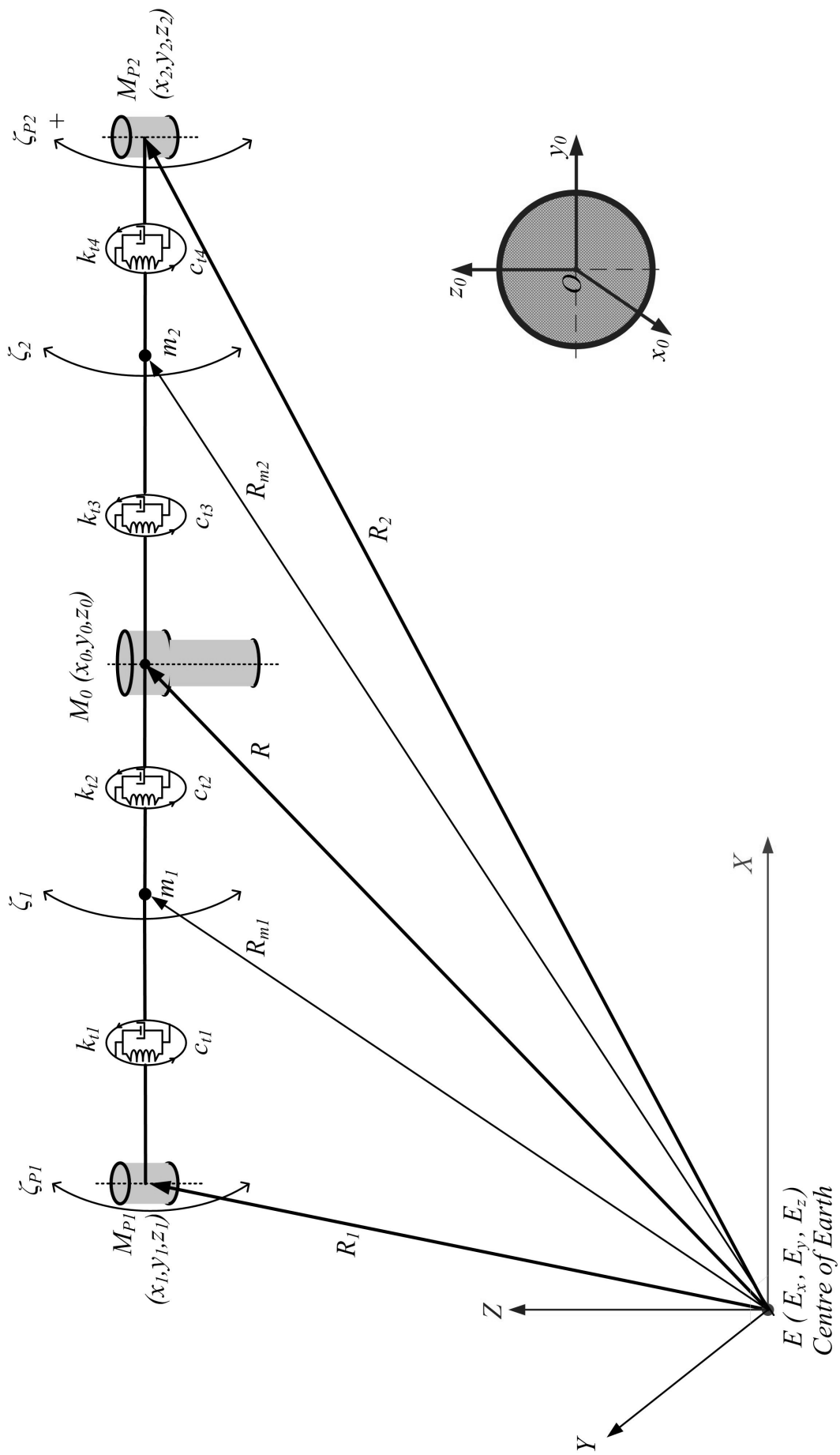


Figure I.2: **Pendular elastic MMET tether with 2 discretised mass points -  $z_0 - O - y_0$**

## I.1 Potential Energy

The tether's potential energy is given in equation (I.1.1), where  $\mu$  is the product of the universal gravitational constant  $G$  with the Earth's mass. The Cartesian coordinates for the motor facility  $M_0$ , payloads  $M_{P1}$  and  $M_{P2}$  are given by equations (3.2.4), (G.1.1) and (G.1.2), and the Cartesian coordinates for mass points  $m_1$  to  $m_2$  are given by equations (G.2.1) and (G.2.2). The distance from Earth  $E(0, 0, 0)$  to each of the discretised mass point is represented by  $R_{m_i}$ , as given in equation (5.3.11).

$$U = -\frac{\mu M_{P1}}{R_1} - \frac{\mu M_{P2}}{R_2} - \frac{\mu M_0}{R} - \frac{\mu m_1}{R_{m_1}} - \frac{\mu m_2}{R_{m_2}} + SE|_{axial} + SE|_{torsional} + SE|_{pendular} \quad (I.1.1)$$

Where, the  $SE|_{axial}$ ,  $SE|_{torsional}$  and  $SE|_{pendular}$  are the strain energy terms of axial, torsional and pendular elasticity, as stated in equation (G.3.2), (H.1.2) and (I.1.2) with the assumption  $k_0 = k_1 = k_2$ ,  $k_{t0} = k_{t1} = k_{t2}$  and  $k_{l0} = k_{l1} = k_{l2}$ , where  $k_0$ ,  $k_{t0}$  and  $k_{l0}$  are the default axial, torsional and pendular stiffness values.

$$SE|_{pendular} = \frac{1}{2}k_{l0} ((\chi_{P1} - \chi_1)^2 + \chi_1^2 + \chi_2^2 + (\chi_2 - \chi_{P2})^2) + \frac{1}{2}k_{l0} ((\zeta_{P1} - \zeta_1)^2 + \zeta_1^2 + \zeta_2^2 + (\zeta_2 - \zeta_{P2})^2) \quad (I.1.2)$$

The  $CE|_{pendular}$  term is an assumed torsional dissipation function, as given in equation (I.1.3), with the assumption  $c_{l0} = c_{l1} = c_{l2}$ , where the  $c_{l0}$  is the default torsional damping coefficient value.

$$CE|_{pendular} = \frac{1}{2}c_{l0} ((\dot{\chi}_{P1} - \dot{\chi}_1)^2 + \dot{\chi}_1^2 + \dot{\chi}_2^2 + (\dot{\chi}_2 - \dot{\chi}_{P2})^2) + \frac{1}{2}c_{l0} ((\dot{\zeta}_{P1} - \dot{\zeta}_1)^2 + \dot{\zeta}_1^2 + \dot{\zeta}_2^2 + (\dot{\zeta}_2 - \dot{\zeta}_{P2})^2) \quad (I.1.3)$$

## I.2 Kinetic Energy

The kinetic energy of the MMET system with 2 discretised mass points is stated in equation (I.2.1).

$$\begin{aligned}
T = & \frac{1}{2}M_{P1} (\dot{x}_1^2 + \dot{y}_1^2 + \dot{z}_1^2) + \frac{1}{2}M_{P2} (\dot{x}_2^2 + \dot{y}_2^2 + \dot{z}_2^2) + \frac{1}{2}M_0 (\dot{x}_0^2 + \dot{y}_0^2 + \dot{z}_0^2) + \\
& \left[ \frac{1}{2}m_1 (\dot{x}_{m_1}^2 + \dot{y}_{m_1}^2 + \dot{z}_{m_1}^2) + \frac{1}{2}m_2 (\dot{x}_{m_2}^2 + \dot{y}_{m_2}^2 + \dot{z}_{m_2}^2) \right] + \\
& \left[ \frac{1}{2}I_{z_{P1}} + \frac{1}{2}I_{z_{P2}} + I_{z_T} + \frac{1}{2}I_{z_M} \right] (\dot{\psi} + \dot{\theta})^2 + \\
& \left[ \frac{1}{2}I_{x_{P1}} + \frac{1}{2}I_{x_{P2}} + I_{x_T} + \frac{1}{2}I_{x_M} \right] \dot{\alpha}^2 + \left[ \frac{1}{2}I_{y_{P1}} + \frac{1}{2}I_{y_{P2}} + I_{y_T} + \frac{1}{2}I_{y_M} \right] \dot{\gamma}^2 + \\
& \left[ \frac{1}{2}I_{y_{P1}} \dot{\phi}_{P1}^2 + \frac{1}{2}I_{y_{P2}} \dot{\phi}_{P2}^2 + \frac{1}{2}I_{y_{m1}} \dot{\phi}_1^2 + \frac{1}{2}I_{y_{m2}} \dot{\phi}_2^2 \right] + \\
& \left[ \frac{1}{2} (I_{z_{P1}} + M_{P1}x_1^2) \dot{\chi}_{P1}^2 + \frac{1}{2} (I_{z_{m1}} + m_1x_{m1}^2) \dot{\chi}_1^2 + \right. \\
& \left. \frac{1}{2} (I_{z_{m2}} + m_2x_{m2}^2) \dot{\chi}_2^2 + \frac{1}{2} (I_{z_{P2}} + M_{P2}x_2^2) \dot{\chi}_{P2}^2 \right] + \\
& \left[ \frac{1}{2} (I_{x_{P1}} + M_{P1}x_1^2) \dot{\zeta}_{P1}^2 + \frac{1}{2} (I_{x_{m1}} + m_1x_1^2) \dot{\zeta}_{m1}^2 + \right. \\
& \left. \frac{1}{2} (I_{x_{m2}} + m_2x_{m2}^2) \dot{\zeta}_{m2}^2 + \frac{1}{2} (I_{x_{P2}} + M_{P2}x_2^2) \dot{\zeta}_{P2}^2 \right]
\end{aligned} \tag{I.2.1}$$

### I.3 Governing Equations of Motion

Besides the rigid body, axial and torsional elastic generalised coordinates as discussed in Appendix H, in this section:

- ▷ The generalised coordinates  $\chi_1$ ,  $\chi_{P1}$ ,  $\chi_2$  and  $\chi_{P2}$  are selected for the torsional behaviours, referenced on plane  $x_0 - O - y_0$ .
- ▷ The generalised coordinates  $\zeta_1$ ,  $\zeta_{P1}$ ,  $\zeta_2$  and  $\zeta_{P2}$  are selected for the torsional behaviours, referenced on plane  $z_0 - O - y_0$ .

Lagrange's equations are used to generate the governing equations of motions, the full equations are to be found in the path CD-ROM/axial-torsional-pendular/N2/, as listed in Table 7.3

## Appendix J

# Elastic Motion Figures for Chapter 8

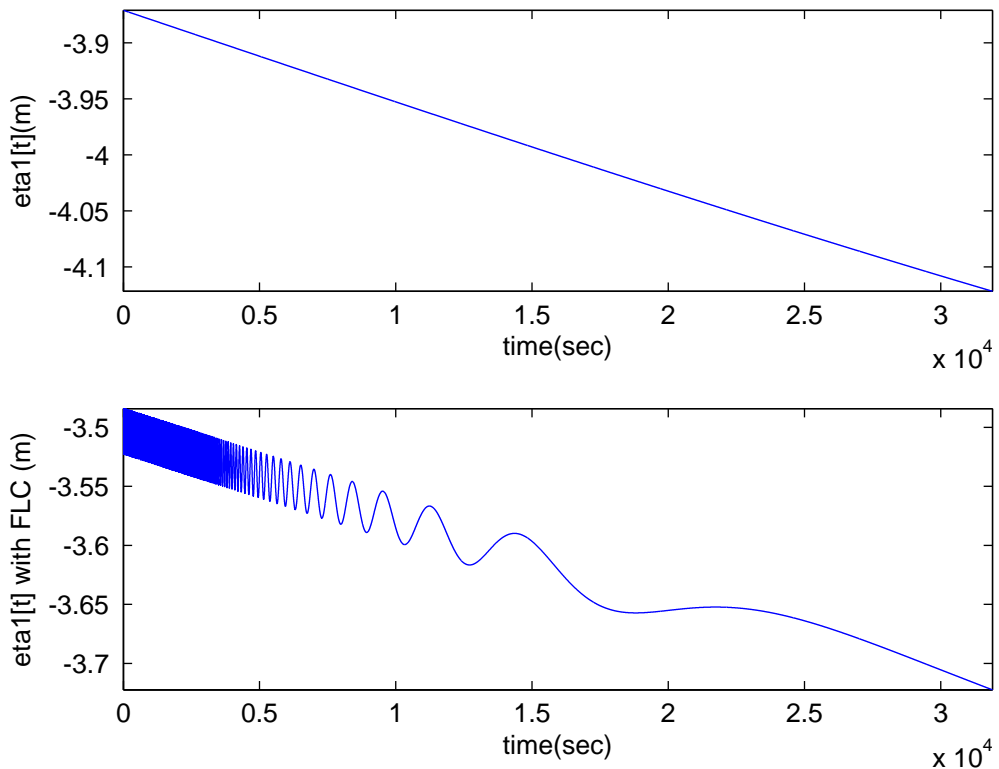


Figure J.1: Axial elastic behaviour with FLC -  $\eta_1(T_n = 4.01)$

▷ Figures J.1 and J.2 state the FLC controlled axial elastic behaviour for the discretised mass point  $m_1$  over a short simulation time (number of periodic cycles,  $T_n = 4.01$ ) and long simulation time (number of periodic cycles,  $T_n = 400.01$ ), respectively. In the beginning ( $0$  to  $2.5 \times 10^4$  seconds), the controlled axial elastic motion is changing with a reducing frequency oscillations within the range  $-3.0$  to  $-4.0$  rad.

▷ Figures J.3 and J.4 are the axial elastic responses for the payload  $M_{P1}$  over a simu-

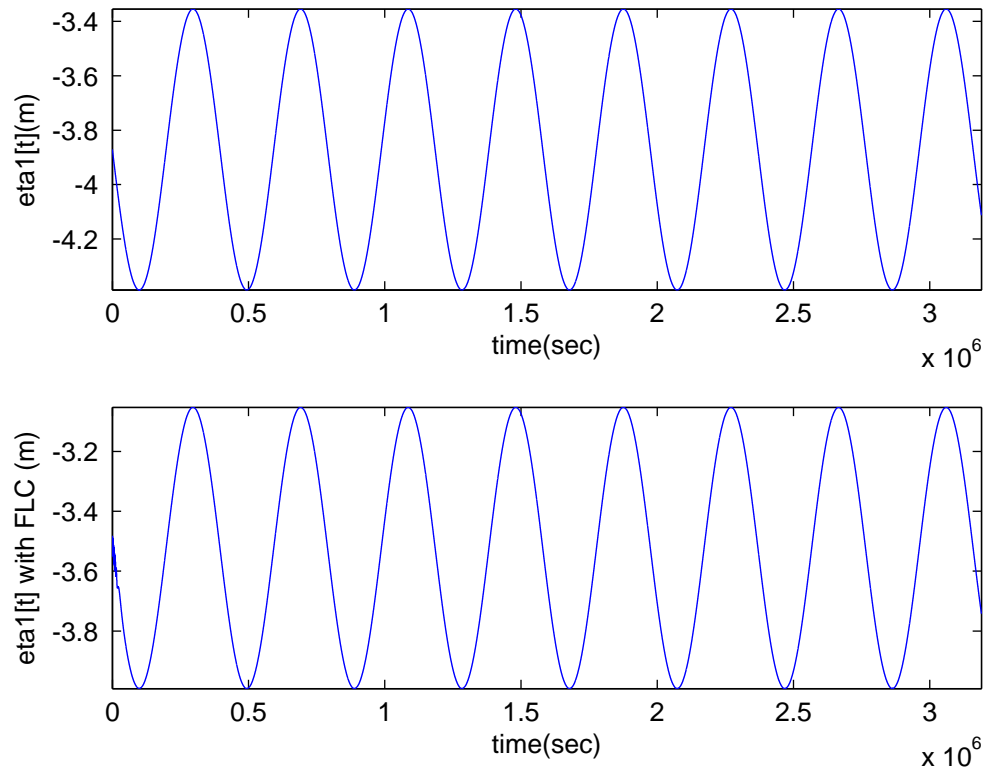


Figure J.2: Axial elastic behaviour with FLC -  $\eta_1(T_n = 400.01)$

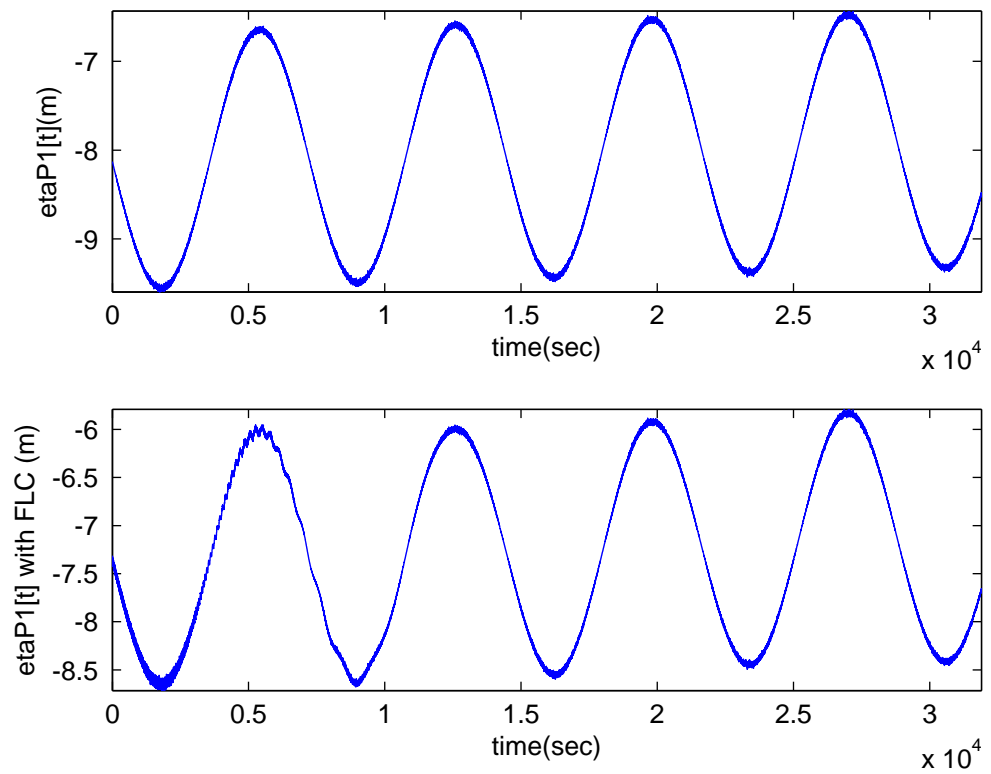


Figure J.3: Axial elastic behaviour with FLC -  $\eta_{P1}(T_n = 4.01)$

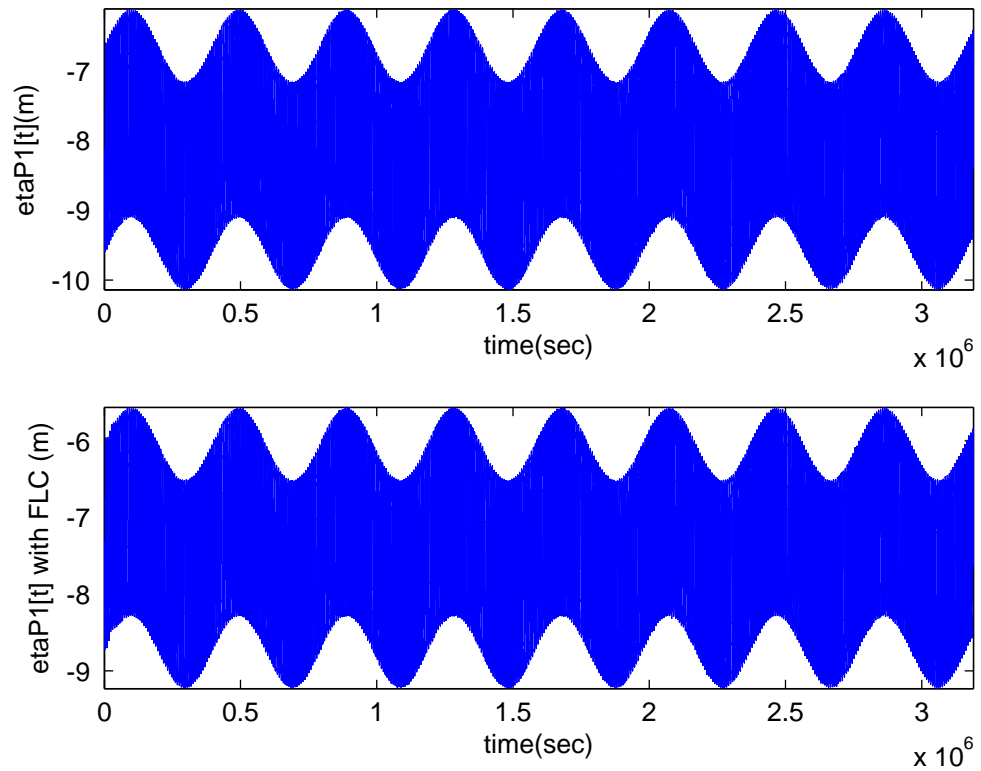


Figure J.4: Axial elastic behaviour with FLC -  $\eta_{P1}(T_n = 400.01)$

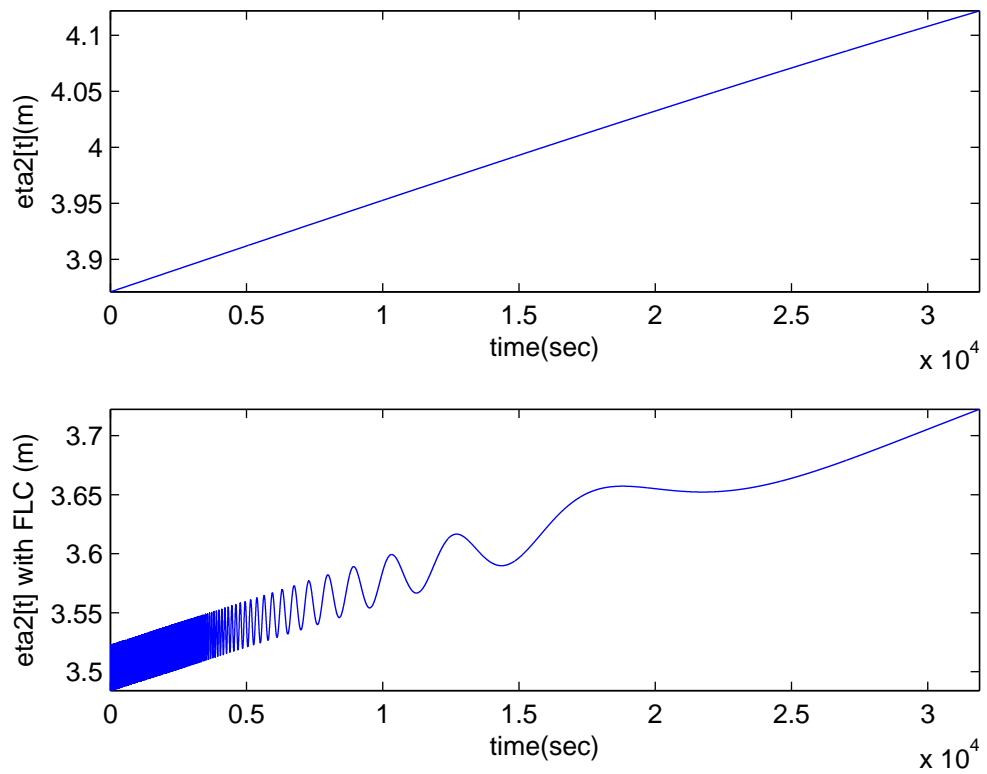


Figure J.5: Axial elastic behaviour with FLC -  $\eta_2(T_n = 4.01)$

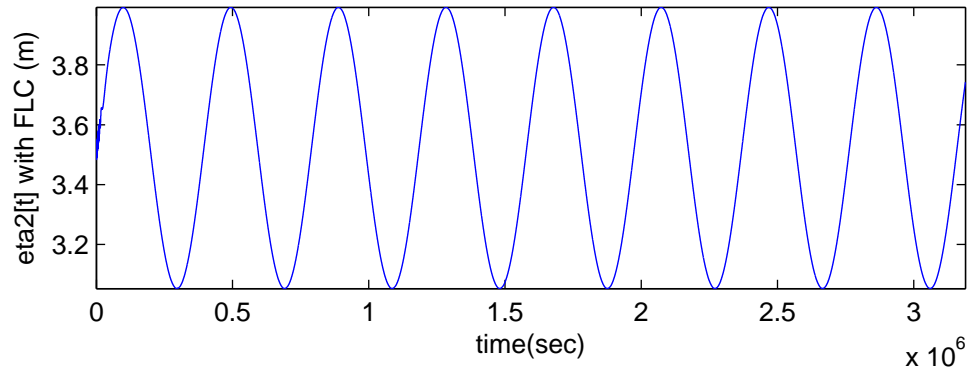
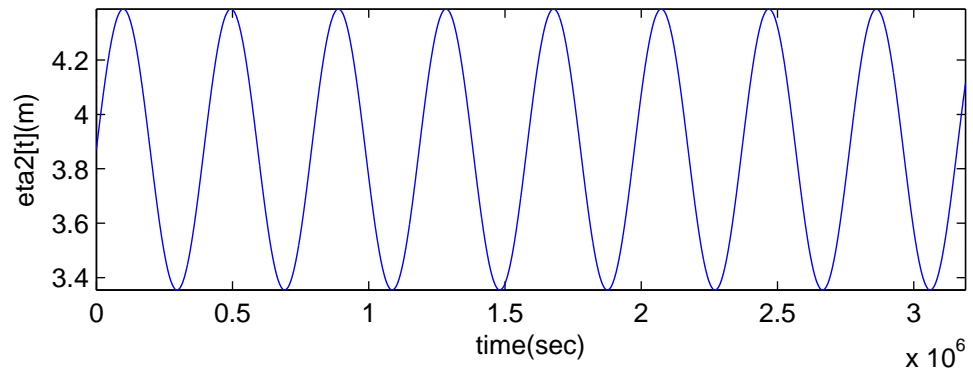


Figure J.6: Axial elastic behaviour with FLC -  $\eta_2$  ( $T_n = 400.01$ )

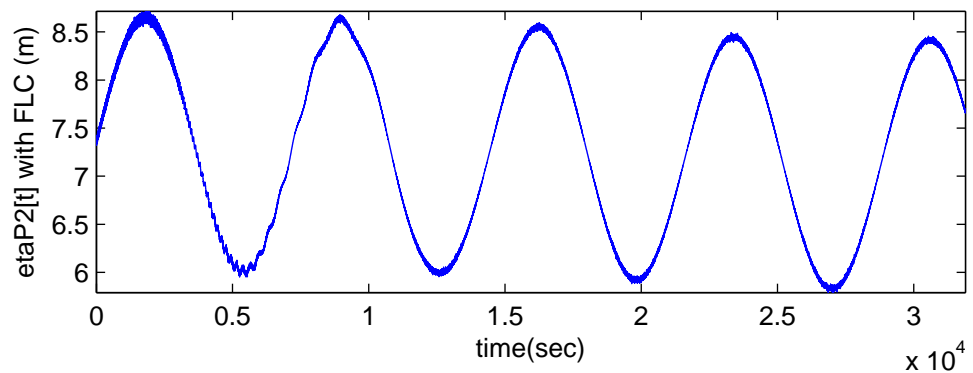
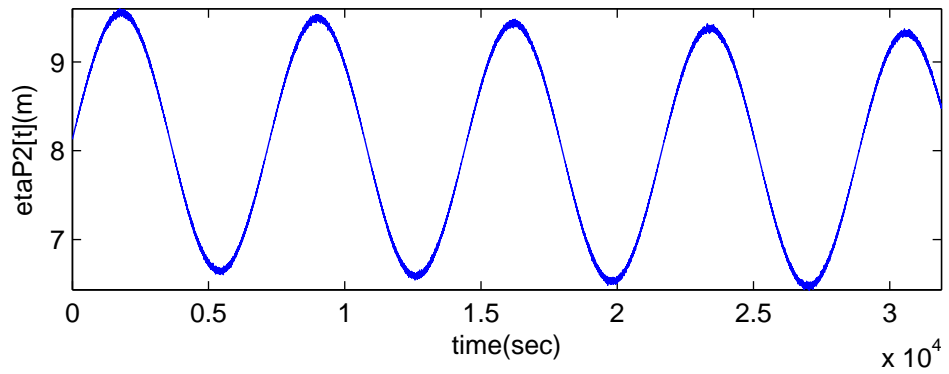


Figure J.7: Axial elastic behaviour with FLC -  $\eta_{P2}$  ( $T_n = 4.01$ )

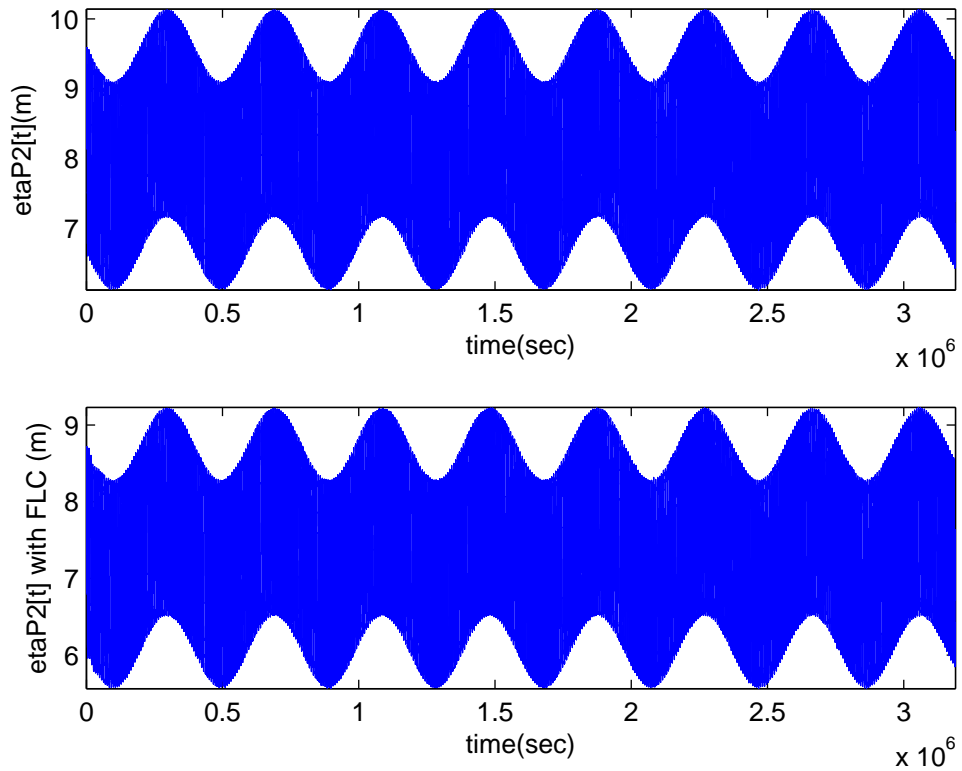


Figure J.8: Axial elastic behaviour with FLC -  $\eta_{P2}(T_n = 400.01)$

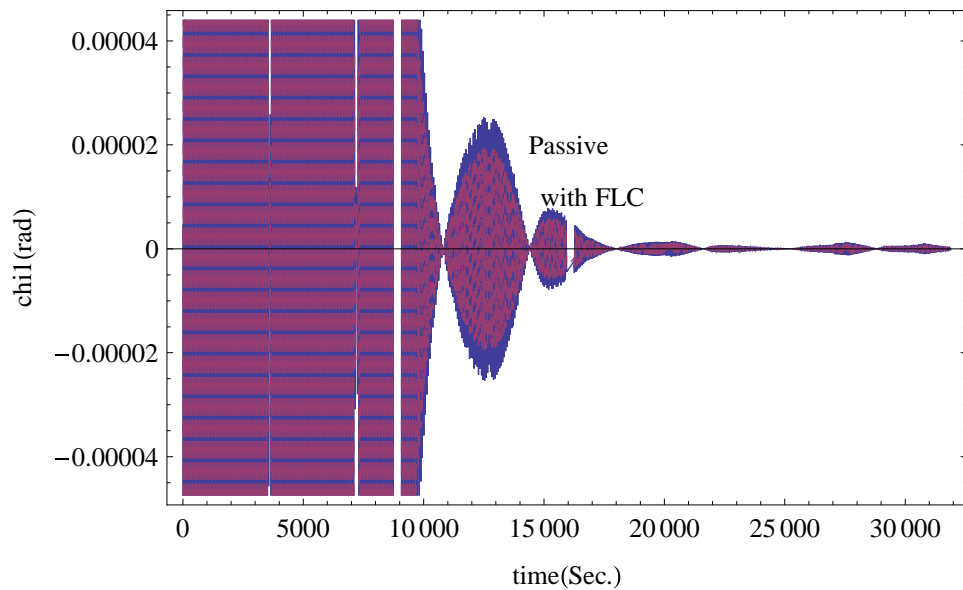


Figure J.9: Pendular elastic behaviour with FLC -  $\chi_1(T_n = 4.01)$

lation time  $T_n = 4.01$  and  $400.01$ , which are moving with a higher frequency than the axial elastic behaviour for the discretised mass point  $m_1$  with the range  $-5.0$  to  $-9.5$  rad

▷ Figures J.5 and J.6 are the axial elastic motions for the discretised mass point  $m_2$  with the range  $3.0$  to  $4.0$  rad, Figures J.7 and J.8 are the axial elastic motions for the payload  $M_{P2}$  with the range  $5.0$  to  $9.5$  rad, which are in the symmetrical location with

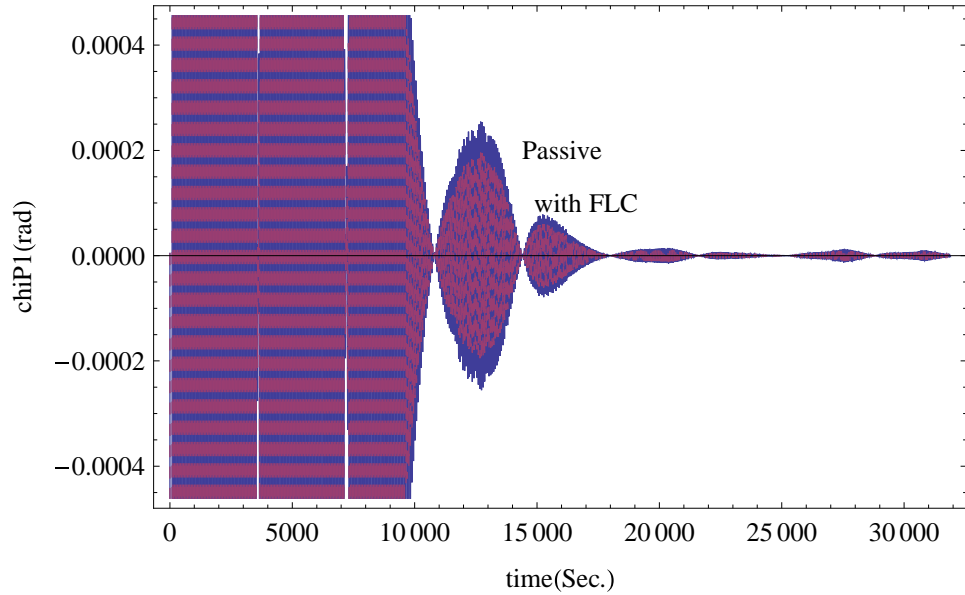


Figure J.10: Pendular elastic behaviour with FLC -  $\chi_{P1}(T_n = 4.01)$

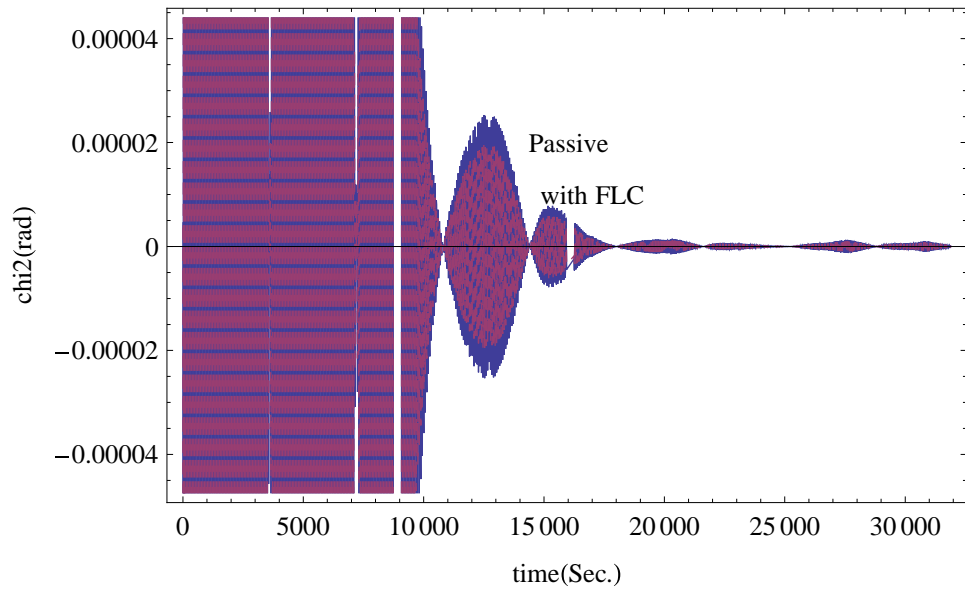


Figure J.11: Pendular elastic behaviour with FLC -  $\chi_2 (T_n = 400.01)$

respect to the MMET system COM.

▷ Reference on plane  $x_0 - O - y_0$ , Figures J.9 and J.10 are the pendular elastic motions for the discretised mass point  $m_1$  within  $-0.000045$  to  $0.000045$  rad and payload  $M_{P1}$  within  $-0.00045$  to  $0.00045$  rad.

▷ Meanwhile, Figures J.11 and J.12 are for the pendular elastic motions for the discretised mass point  $m_2$  and payload  $M_{P2}$ , in the symmetrical location with respect to the MMET system COM, reference on plane  $x_0 - O - y_0$ .

▷ Reference on plane  $z_0 - O - y_0$ , Figures J.13 and J.14 are the pendular elastic motions for the discretised mass point  $m_1$  within  $-0.00004$  to  $0.00004$  rad and payload

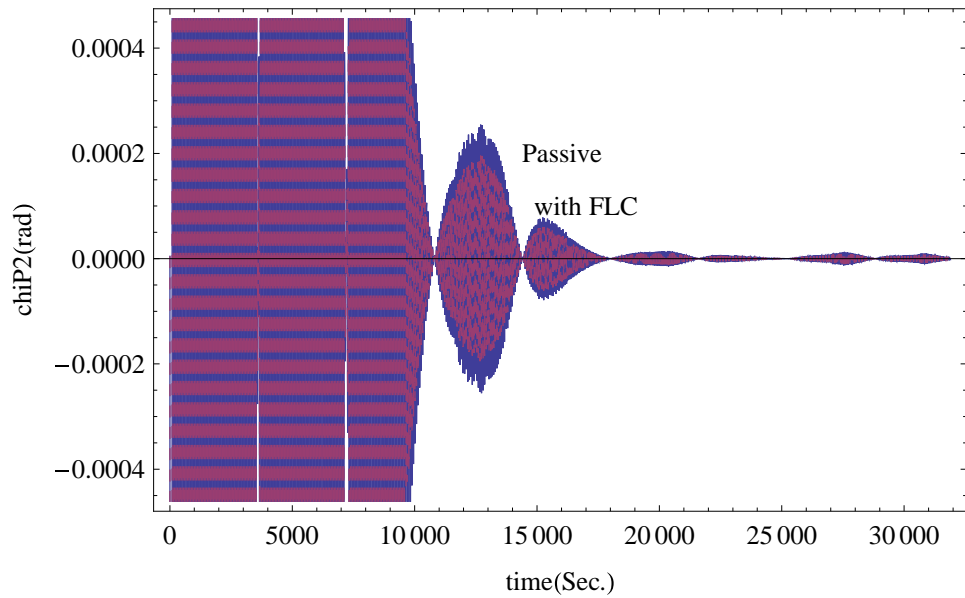


Figure J.12: Pendular elastic behaviour with FLC -  $\chi_{P2}(T_n = 4.01)$

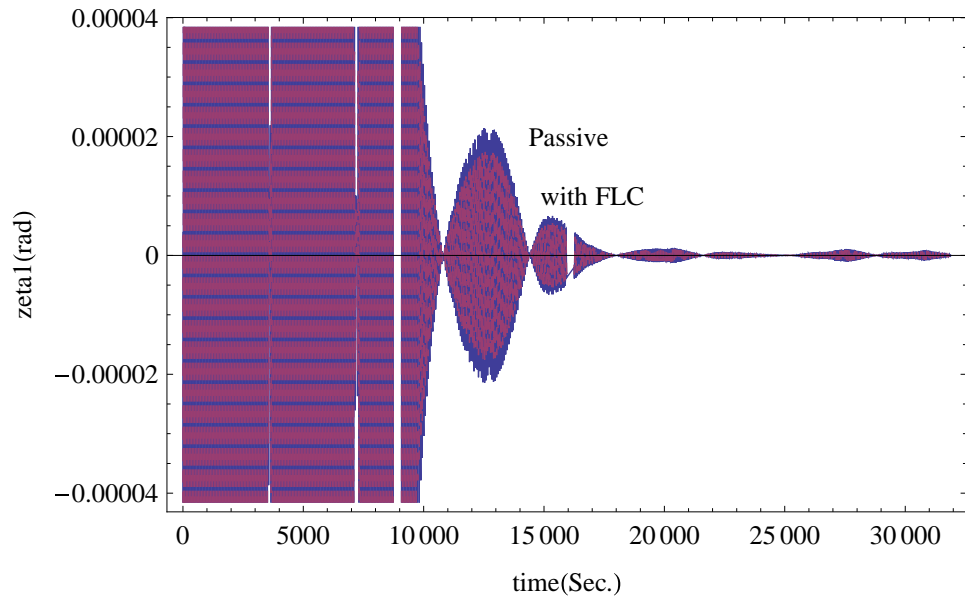


Figure J.13: Pendular elastic behaviour with FLC -  $\zeta_1(T_n = 4.01)$

$M_{P1}$  within  $-0.0004$  to  $0.0004$  rad.

▷ Symmetrically, Figures J.15 and J.16 are for the pendular elastic motions for the discretised mass point  $m_2$  and payload  $M_{P2}$ , reference on plane  $z_0 - O - y_0$ .

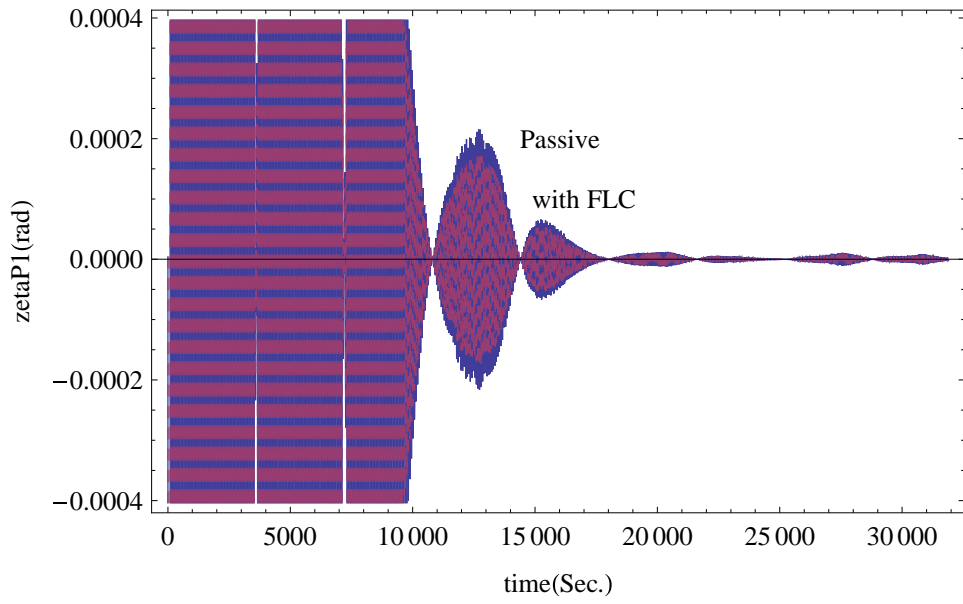


Figure J.14: Pendular elastic behaviour with FLC -  $\zeta_{P1}(T_n = 4.01)$

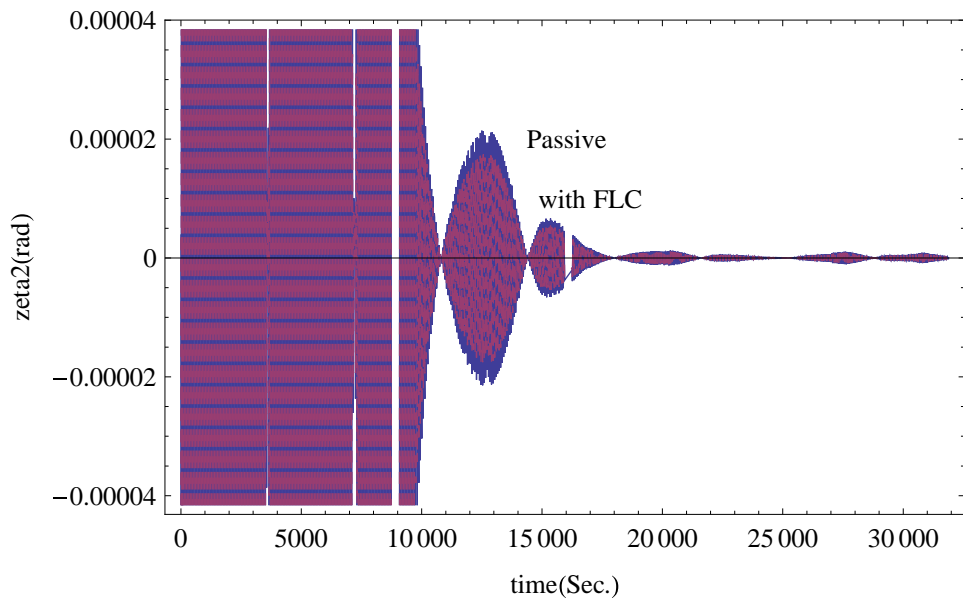


Figure J.15: Pendular elastic behaviour with FLC -  $\zeta_2(T_n = 400.01)$

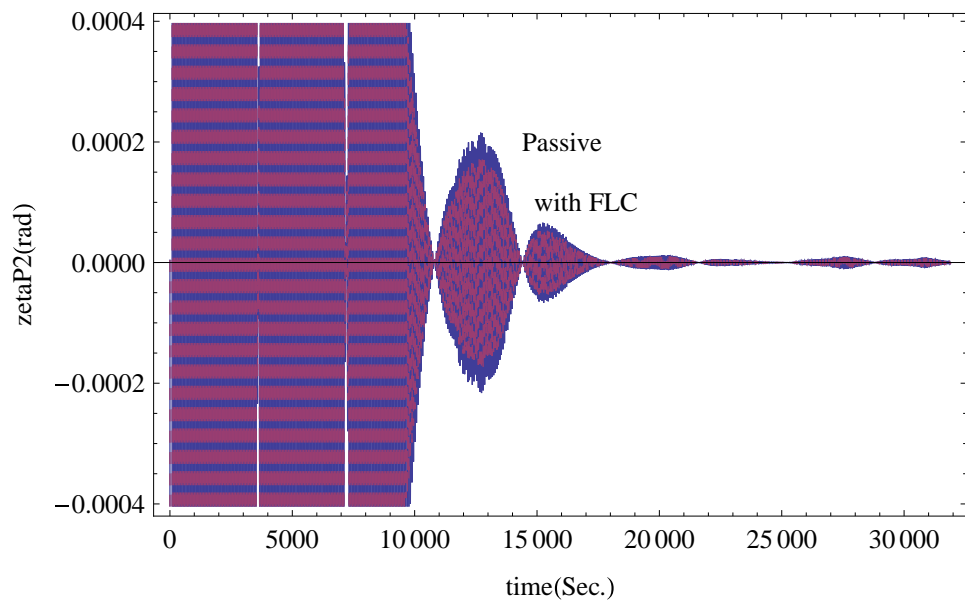


Figure J.16: Pendular elastic behaviour with FLC -  $\zeta_{p2}(T_n = 4.01)$

## Appendix K

---

# Elastic Motion Figures for Chapter 9

---

▷ Figures K.1 to K.4 are the axial elastic motions for the discretised points  $m_1$  and  $m_2$  over the simulation time  $T_n = 4.01$  and  $400.01$ , in which the F $\alpha$ SMC and SkyhookSMC controlled MMET system's axial elastic motions are with similar oscillation frequencies to each other, and smaller amplitudes than the axially elastic behaviour in the MMET system with the FLC.

Also, the  $m_1$  and  $m_2$  are in the symmetrical position with respect to the MMET COM, in the beginning part of the figures, the FLC controlled axial elastic motion start with shorter reducing frequency oscillation than the other controllers', and all of the three controlled MMET system axial elastic outputs are changing with similar periodic behaviours in the later simulation time.

▷ Figures K.5 to K.8 are the axial elastic motions for the payloads  $M_{p1}$  and  $M_{p2}$  over the simulation time  $T_n = 4.01$  and  $400.01$  with larger amplitudes than the  $m_1$  and  $m_2$ 's. The F $\alpha$ SMC controlled  $\eta_1$ ,  $\eta_2$ ,  $\eta_{p1}$ , and  $\eta_{p2}$ , their responses are slightly larger than SkyhookSMC, and FLC has the max amplitude of the three controllers.

As can be seen from Figures K.5 and K.7, the  $M_{p1}$  and  $M_{p2}$ 's responses are the high frequency oscillations carried by the periodic wave, in which the F $\alpha$ SMC and SkyhookSMC controlled MMET system's outputs are with slightly longer obvious high frequency oscillations than the FLC's output. And then, as shown in Figures K.6 and K.8, all the controlled outputs stays in a stable periodic waves, whose active frequencies are higher than the axial elastic motions for  $m_1$  and  $m_2$ .

▷ Figures K.9 and K.10 are the pendular elastic motions for discretised mass point  $m_1$  referenced on plane  $x_0 - O - y_0$ , by comparing the control effects of FLC, F $\alpha$ SMC

and SkyhookSMC, which indicate the  $\chi_1$  responses amplitude: FLC > F $\alpha$ SMC > SkyhookSMC.

▷ Similarly, Figures K.11 and K.12 are the responses for the discretised mass point  $m_2$ 's pendular elastic motion on plane  $x_0 - O - y_0$ , the F $\alpha$ SMC's plot  $\chi_2$  is slightly larger than SkyhookSMC's plot.

▷ Figures K.13 to K.16 compare the pendular elastic behaviours for the payloads  $M_{P1}$  and  $M_{P2}$  with three controllers, which state the  $\chi_{P1}$  and  $\chi_{P2}$  responses amplitude: FLC > F $\alpha$ SMC > SkyhookSMC, referenced on both planes  $x_0 - O - y_0$ .

▷ Figures K.17 to K.20 are the pendular elastic behaviours  $\zeta_1$  and  $\zeta_2$  for the discretised mass points  $m_1$  and  $m_2$ , referenced on the plane  $z_0 - O - y_0$  with three controllers.

▷ Figures K.21 to K.24 are the pendular elastic behaviours  $\zeta_{P1}$  and  $\zeta_{P2}$  or the payloads  $M_{P1}$  and  $M_{P2}$  referenced on the plane  $z_0 - O - y_0$ . All the pendular behaviours are with the appearance of stable oscillation performance and reducing to a zero status.

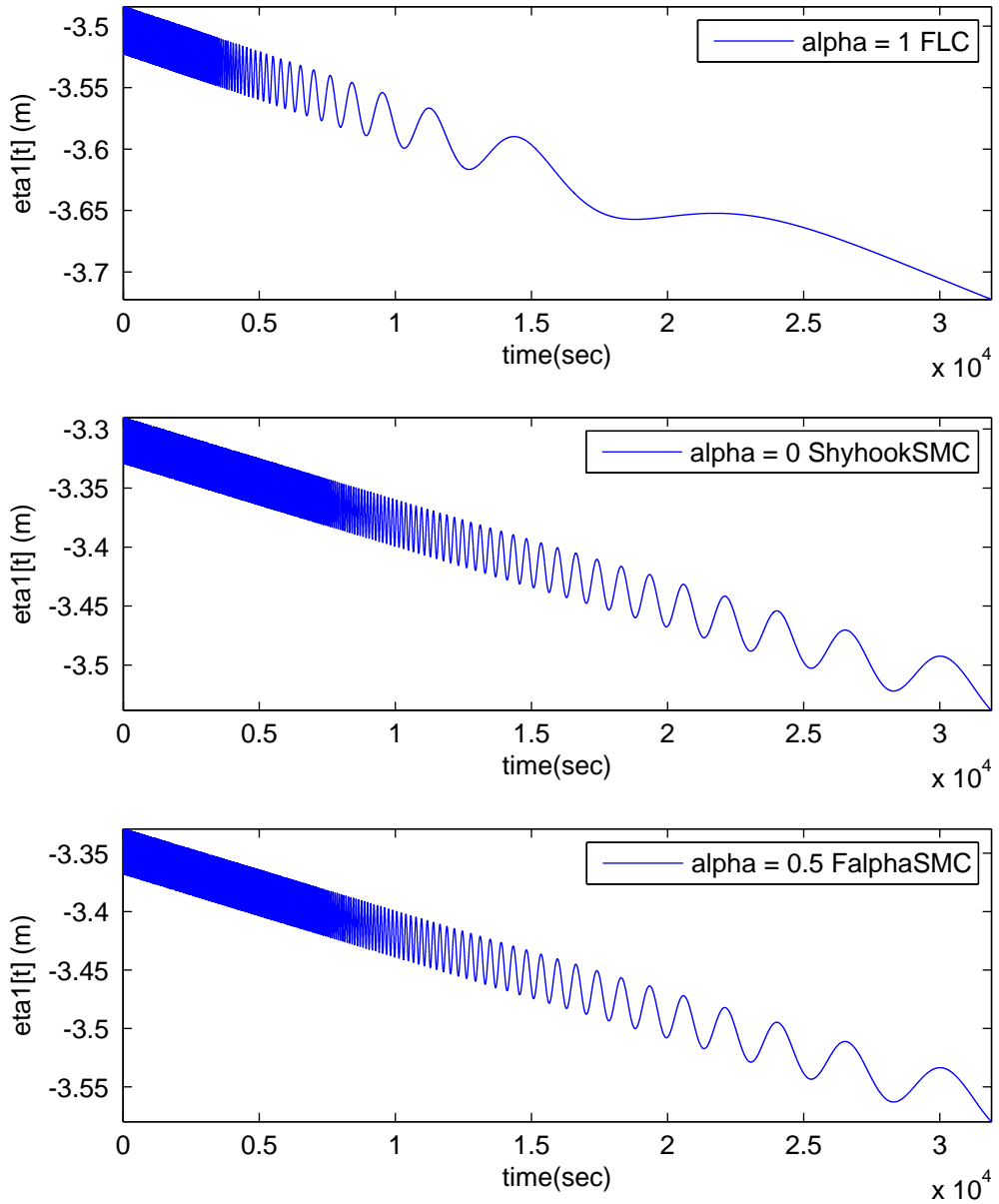


Figure K.1: Axial elastic behaviour with control -  $\eta_1(T_n = 4.01)$

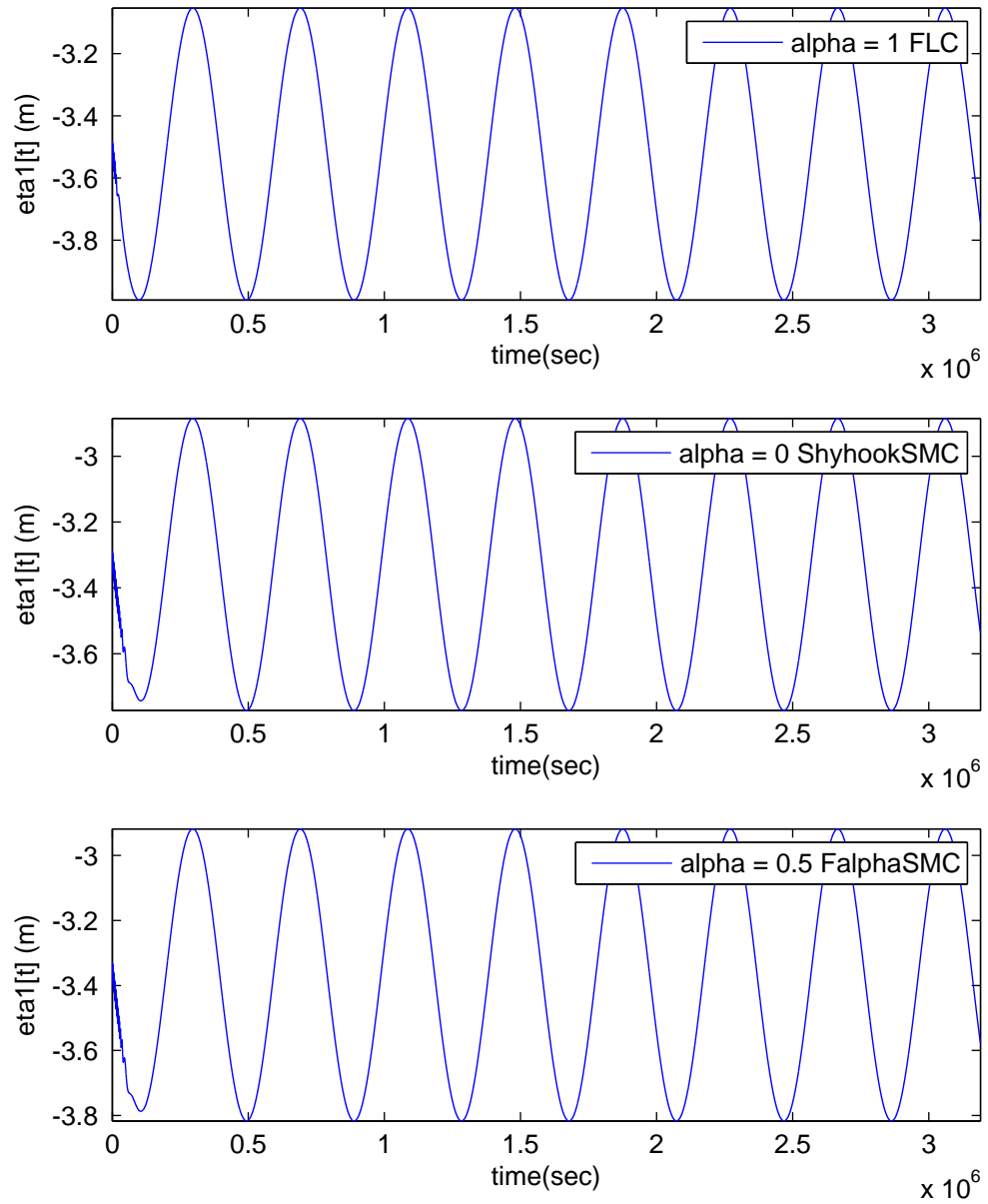


Figure K.2: Axial elastic behaviour with control -  $\eta_1(T_n = 400.01)$

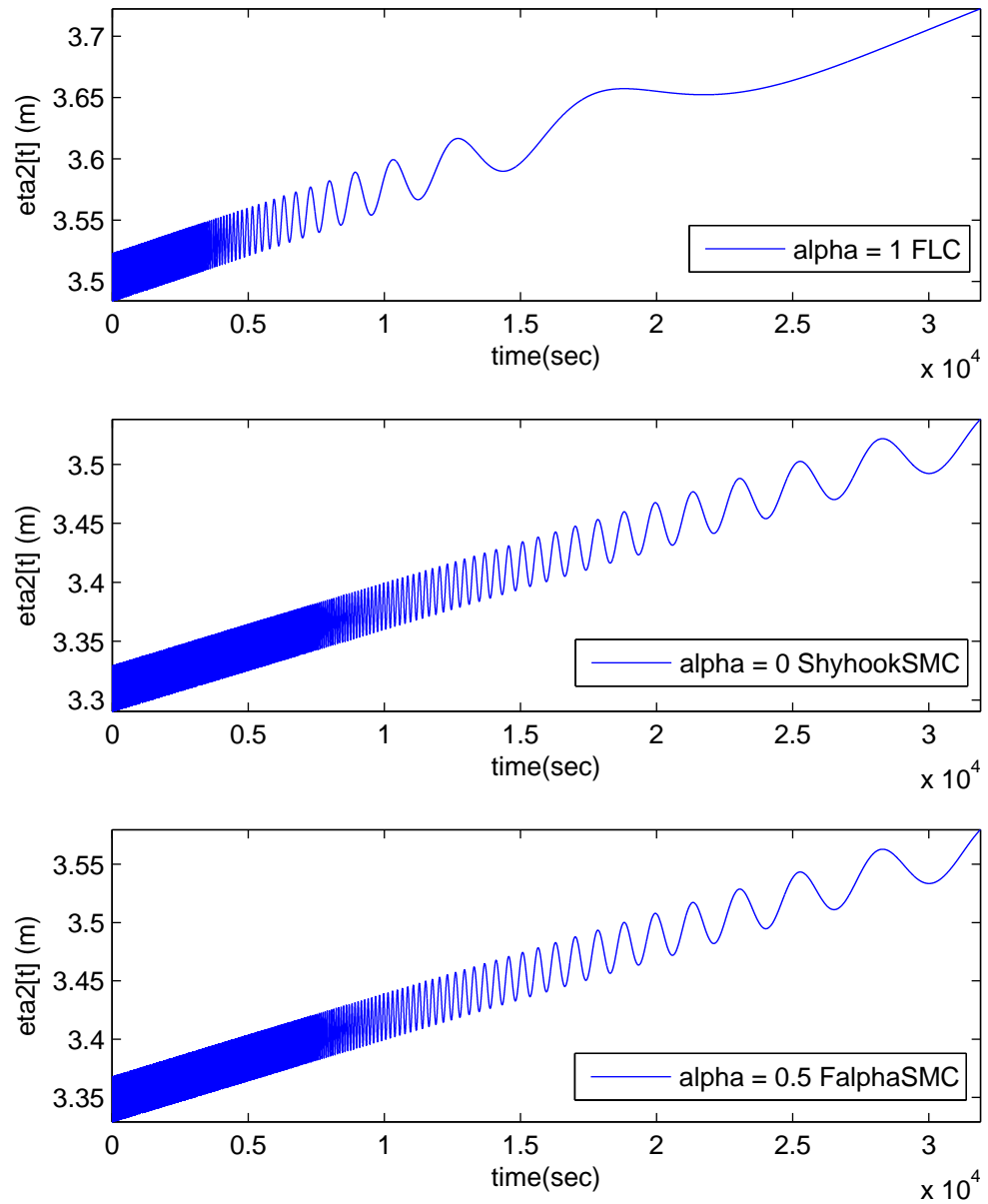


Figure K.3: Axial elastic behaviour with control -  $\eta_2(T_n = 4.01)$

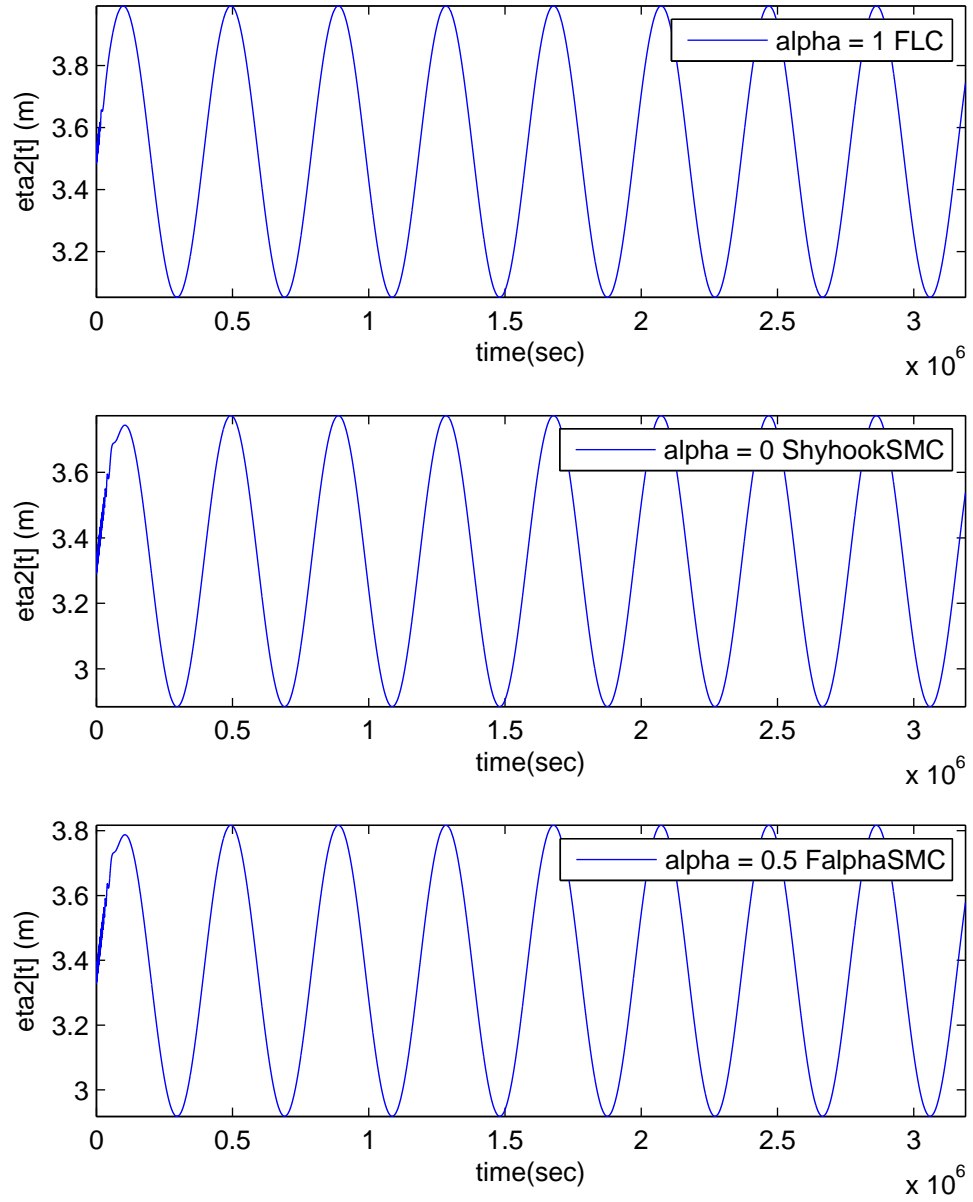


Figure K.4: Axial elastic behaviour with control -  $\eta_2(T_n = 400.01)$

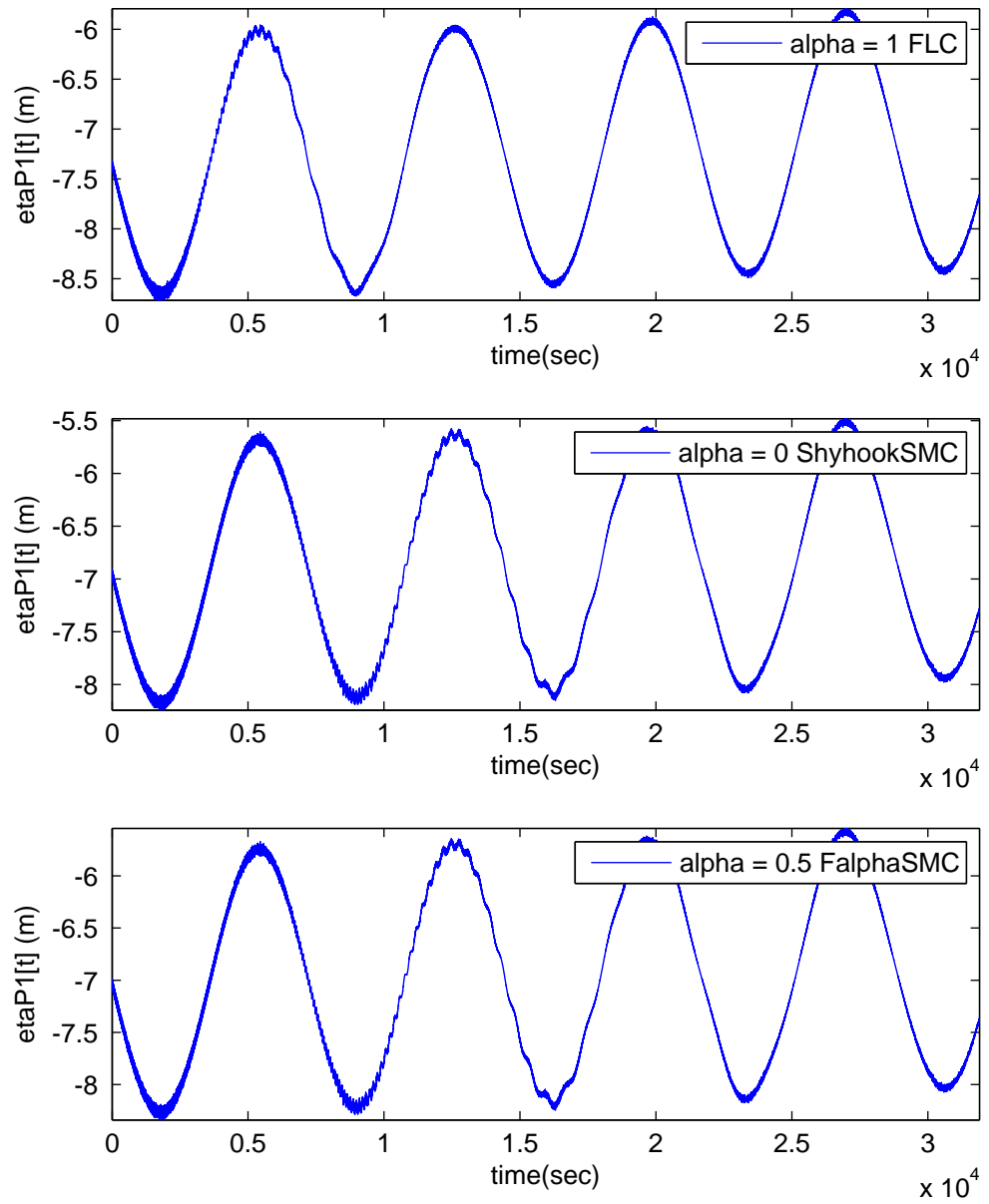


Figure K.5: Axial elastic behaviour with control -  $\eta_{P1}$  ( $T_n = 4.01$ )

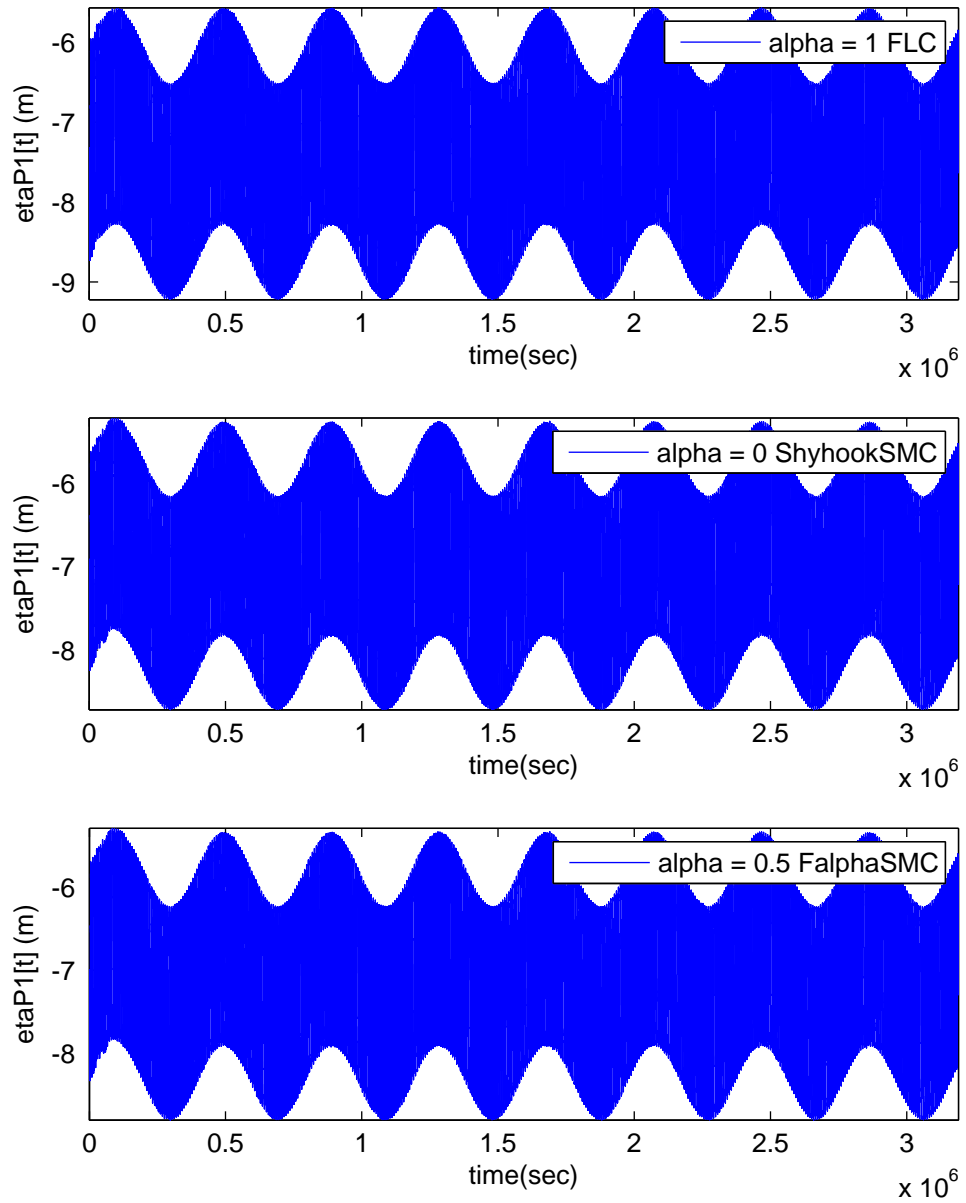


Figure K.6: Axial elastic behaviour with control -  $\eta_{P1}$  ( $T_n = 400.01$ )

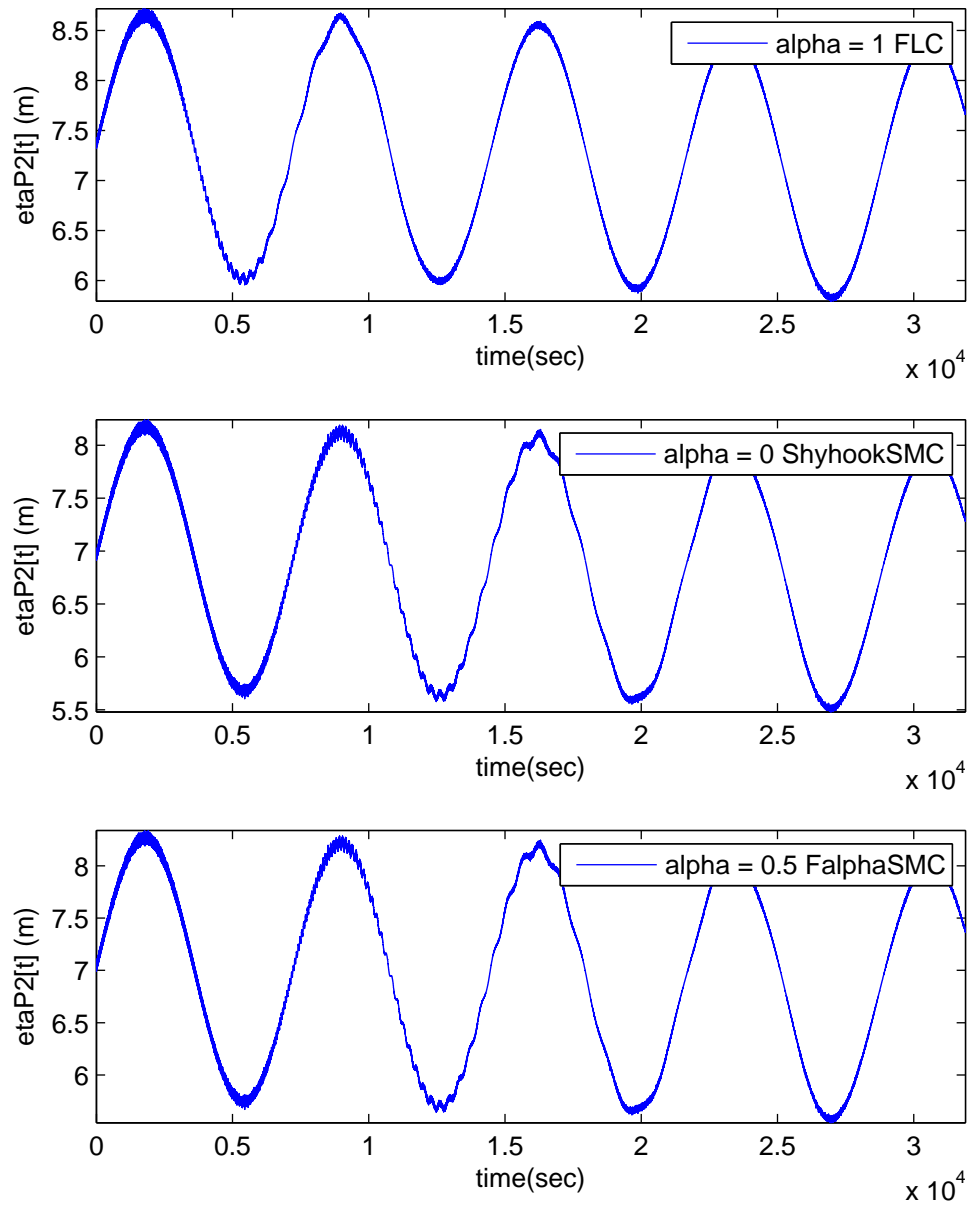


Figure K.7: Axial elastic behaviour with control -  $\eta_{P2}$  ( $T_n = 4.01$ )

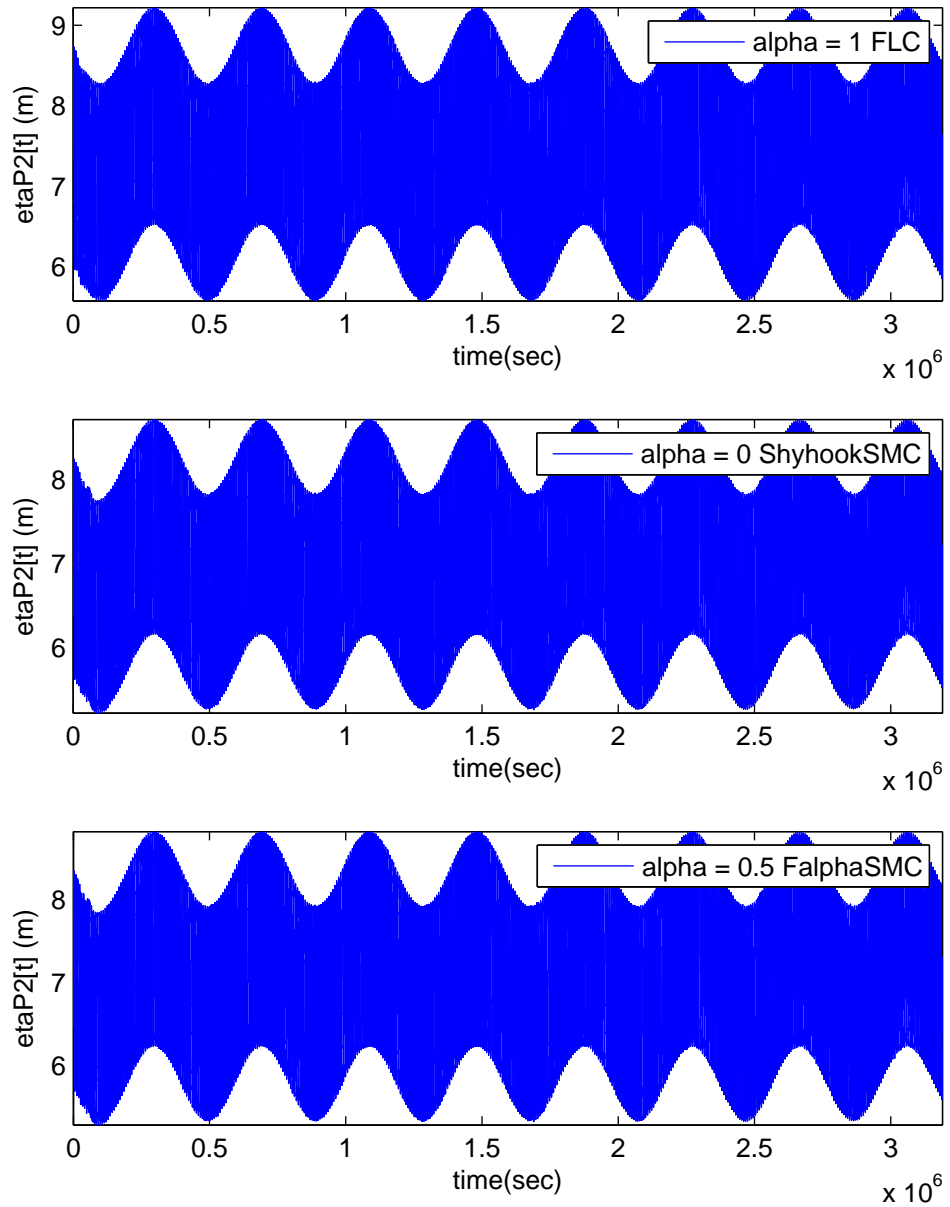


Figure K.8: Axial elastic behaviour with control -  $\eta_{P2}$  ( $T_n = 400.01$ )

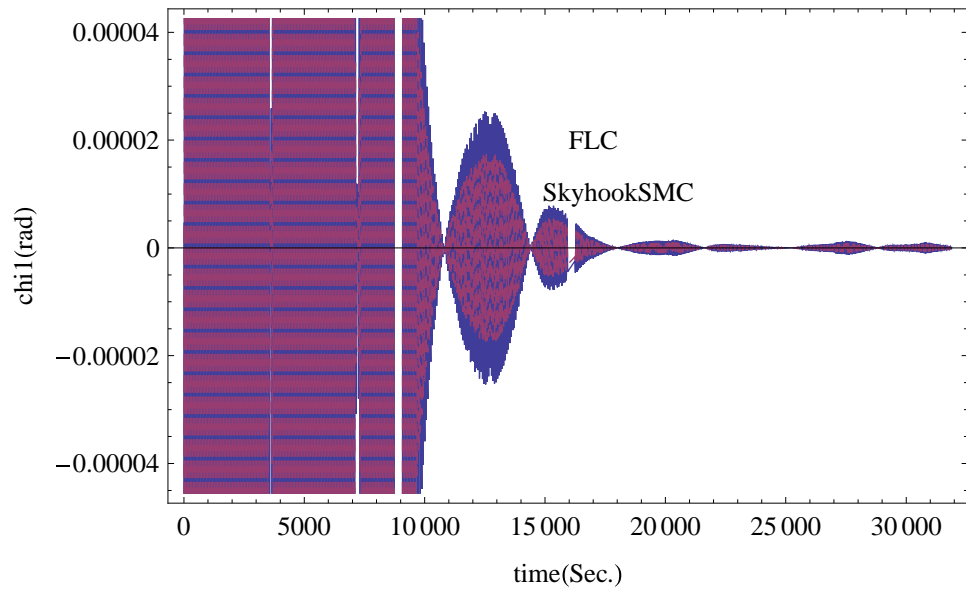


Figure K.9: Torsional elastic behaviour with control -  $\chi_1$ , FLC vs. SkyhookSMC ( $T_n = 4.01$ )

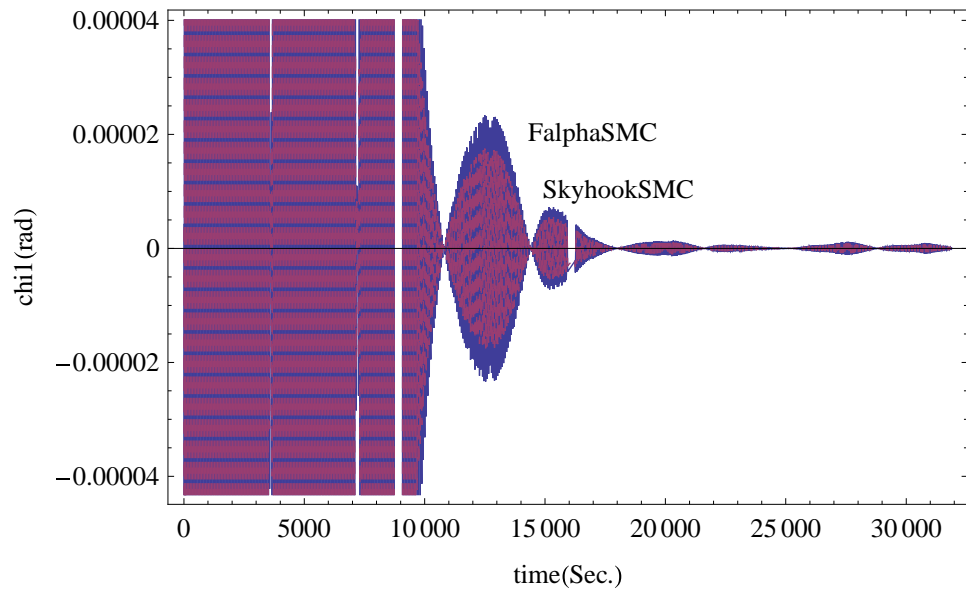


Figure K.10: Torsional elastic behaviour with control -  $\chi_1$ , FalphaSMC vs. SkyhookSMC ( $T_n = 4.01$ )

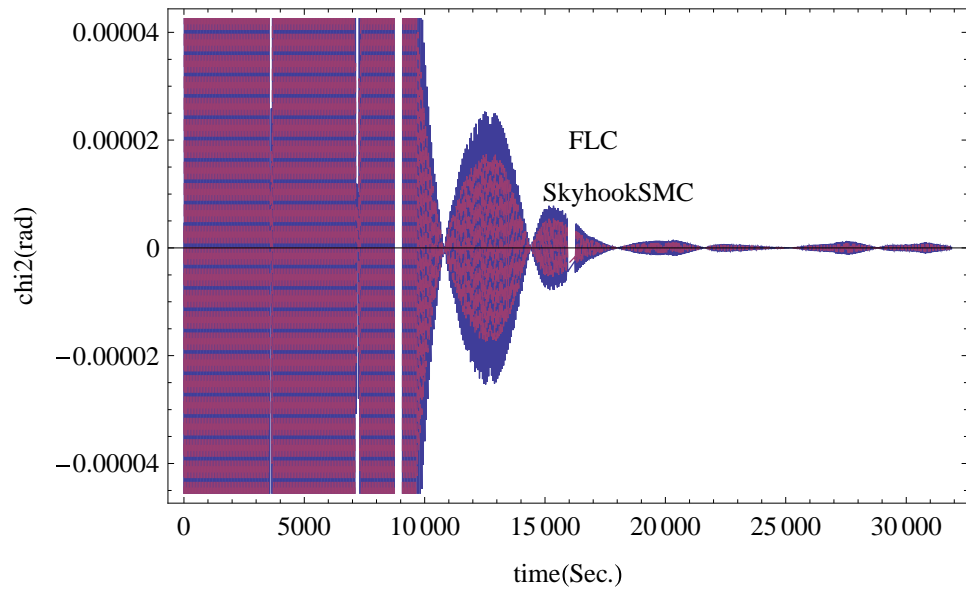


Figure K.11: Torsional elastic behaviour with control -  $\chi_2$ , FLC vs. SkyhookSMC ( $T_n = 4.01$ )

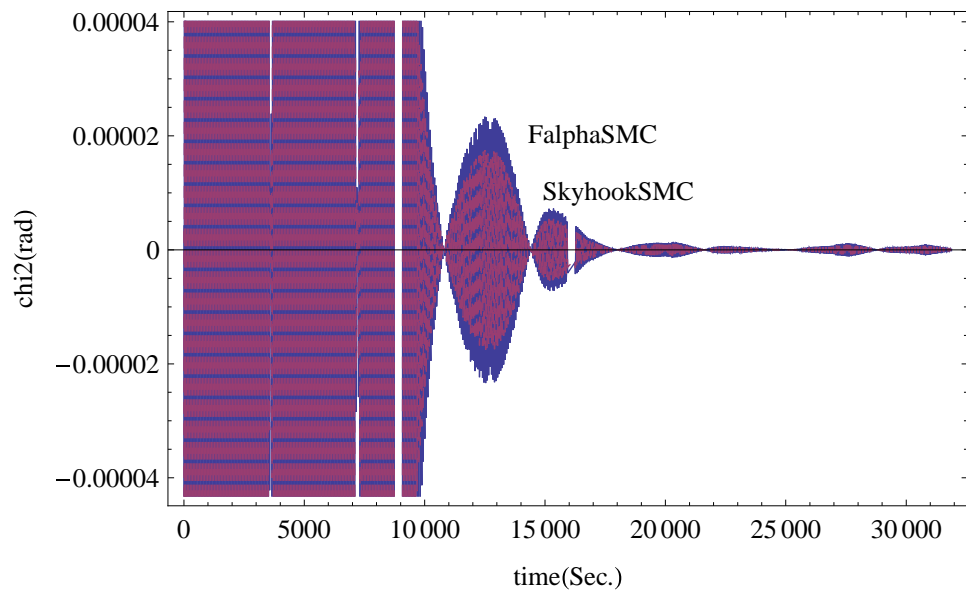


Figure K.12: Torsional elastic behaviour with control -  $\chi_2$ , FalphaSMC vs. SkyhookSMC ( $T_n = 4.01$ )

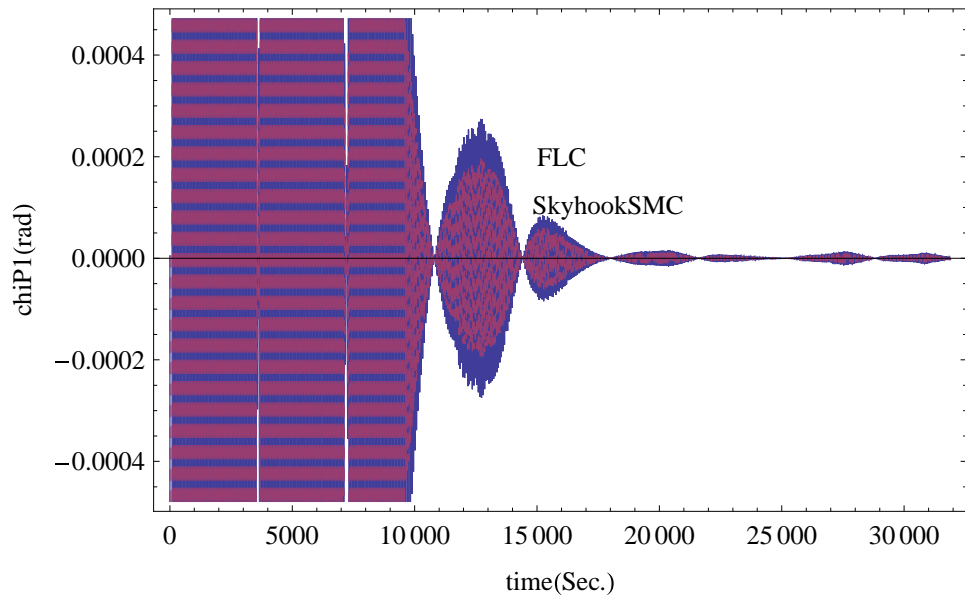


Figure K.13: Torsional elastic behaviour with control -  $\chi_{P1}$ , FLC vs. SkyhookSMC ( $T_n = 4.01$ )

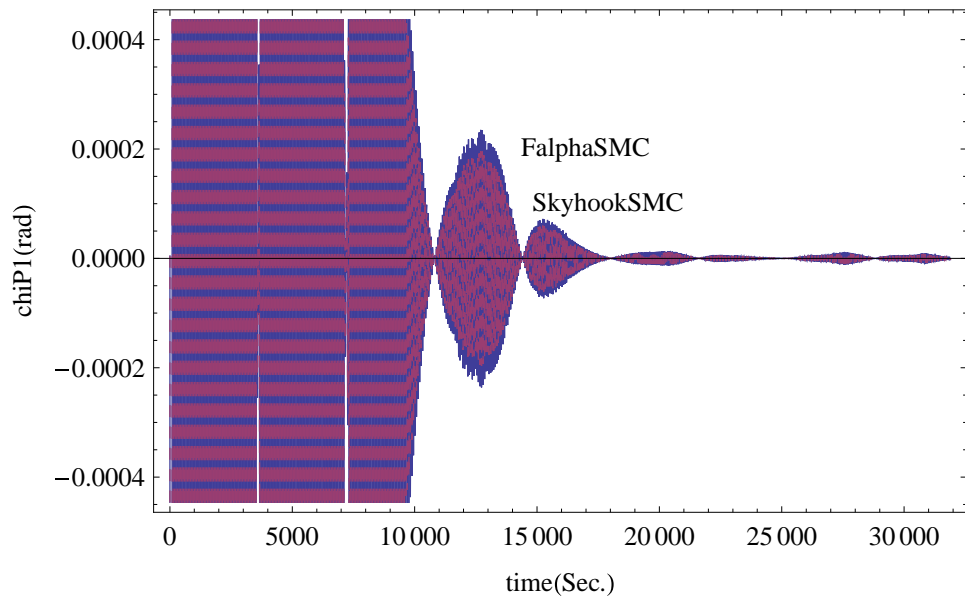


Figure K.14: Torsional elastic behaviour with control -  $\chi_{P1}$ , FalphaSMC vs. SkyhookSMC ( $T_n = 4.01$ )

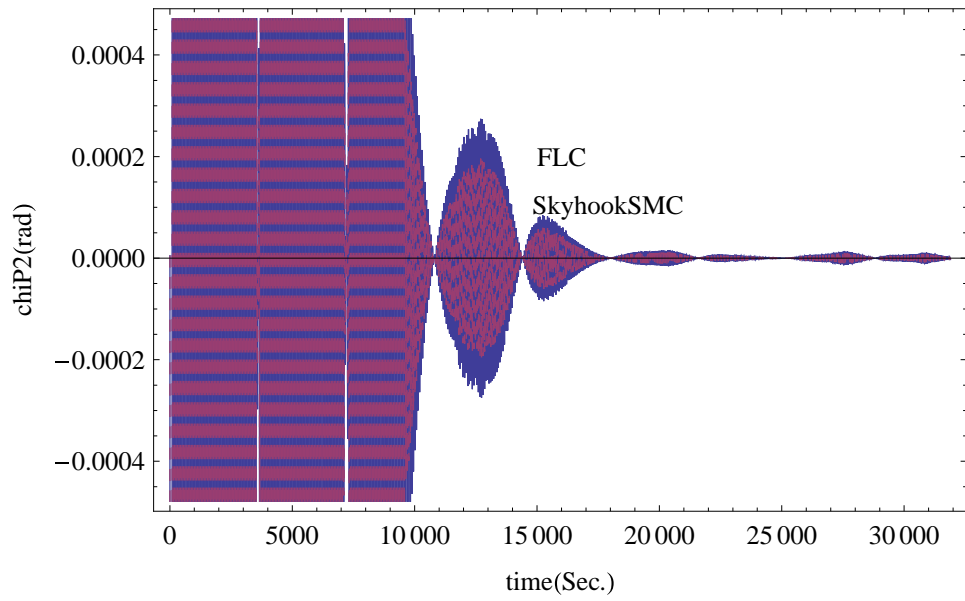


Figure K.15: Torsional elastic behaviour with control -  $\chi_{P2}$ , FLC vs. SkyhookSMC ( $T_n = 4.01$ )

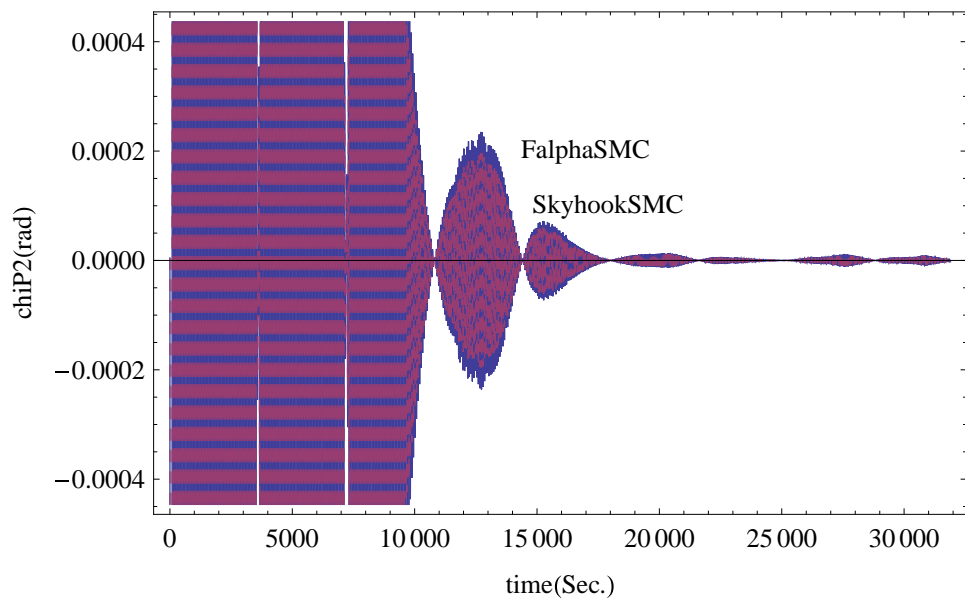


Figure K.16: Torsional elastic behaviour with control -  $\chi_{P2}$ , FalphaSMC vs. SkyhookSMC ( $T_n = 4.01$ )

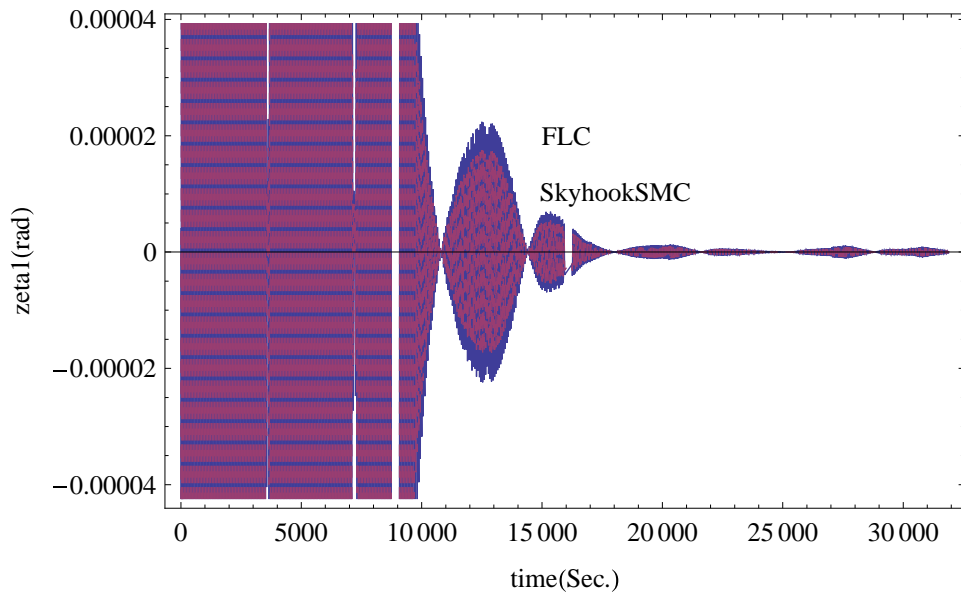


Figure K.17: Torsional elastic behaviour with control -  $\zeta_1$ , FLC vs. SkyhookSMC ( $T_n = 4.01$ )

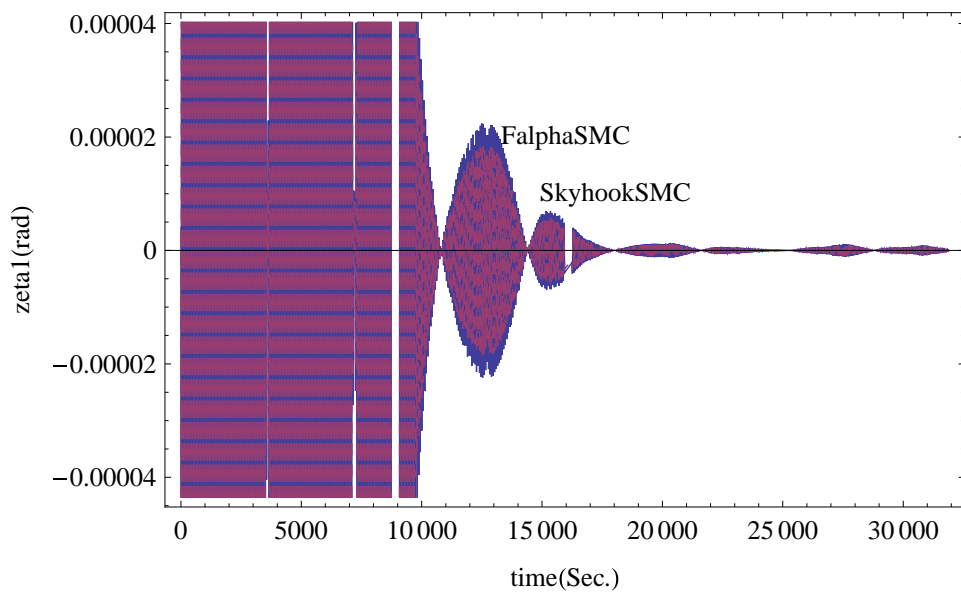


Figure K.18: Torsional elastic behaviour with control -  $\zeta_1$ , FalphaSMC vs. SkyhookSMC ( $T_n = 4.01$ )

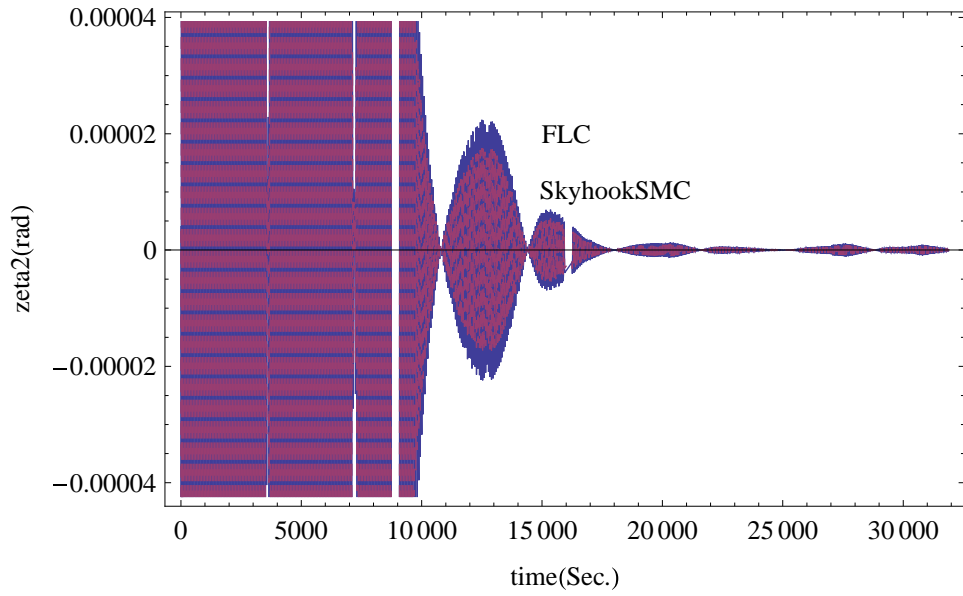


Figure K.19: Torsional elastic behaviour with control -  $\zeta_2$ , FLC vs. SkyhookSMC ( $T_n = 4.01$ )

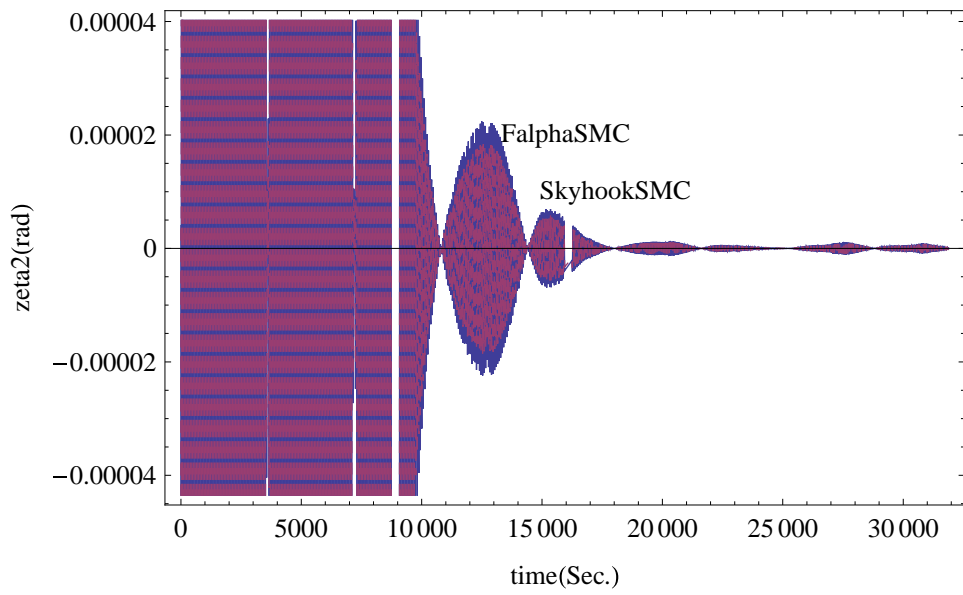


Figure K.20: Torsional elastic behaviour with control -  $\zeta_2$ , FalphaSMC vs. SkyhookSMC ( $T_n = 4.01$ )

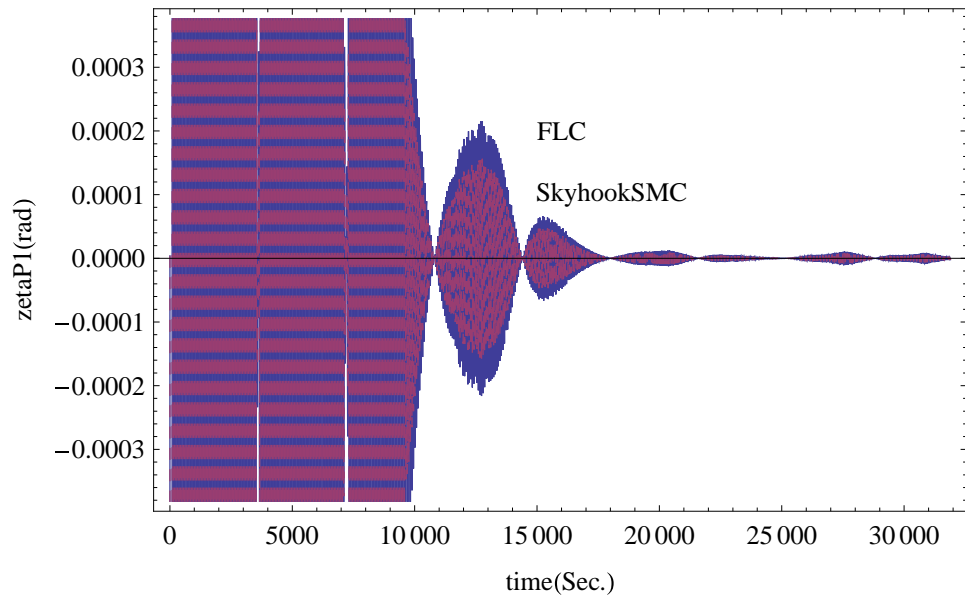


Figure K.21: Torsional elastic behaviour with control -  $\zeta_{P1}$ , FLC vs. SkyhookSMC ( $T_n = 4.01$ )

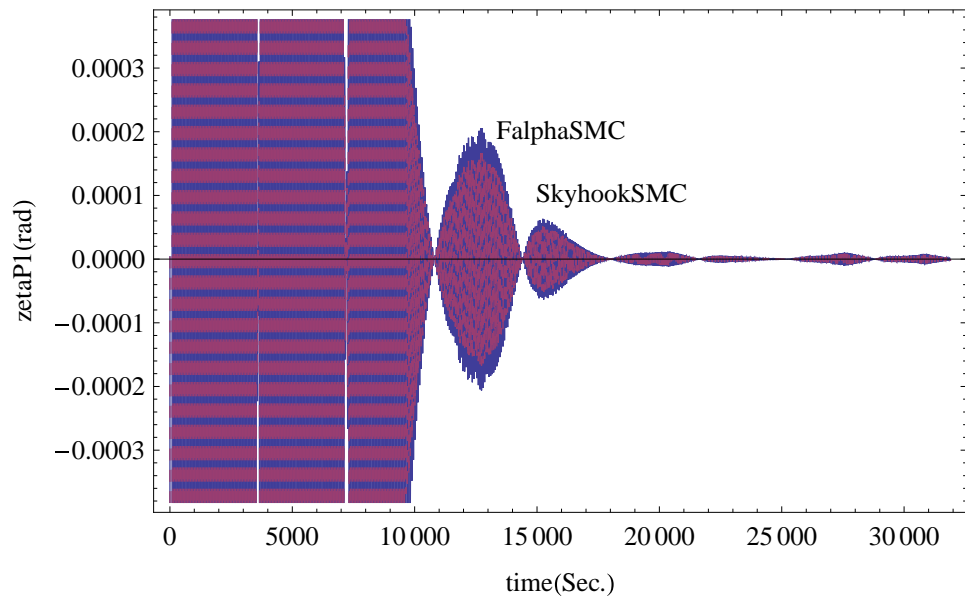


Figure K.22: Torsional elastic behaviour with control -  $\zeta_{P1}$ , FalphaSMC vs. SkyhookSMC ( $T_n = 4.01$ )

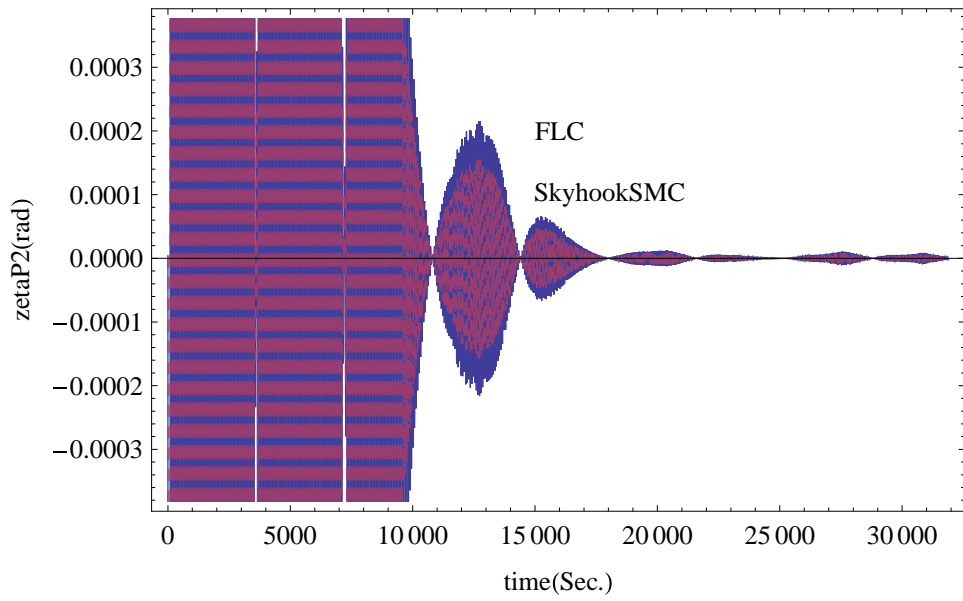


Figure K.23: Torsional elastic behaviour with control -  $\zeta_{p2}$ , FLC vs. SkyhookSMC ( $T_n = 4.01$ )

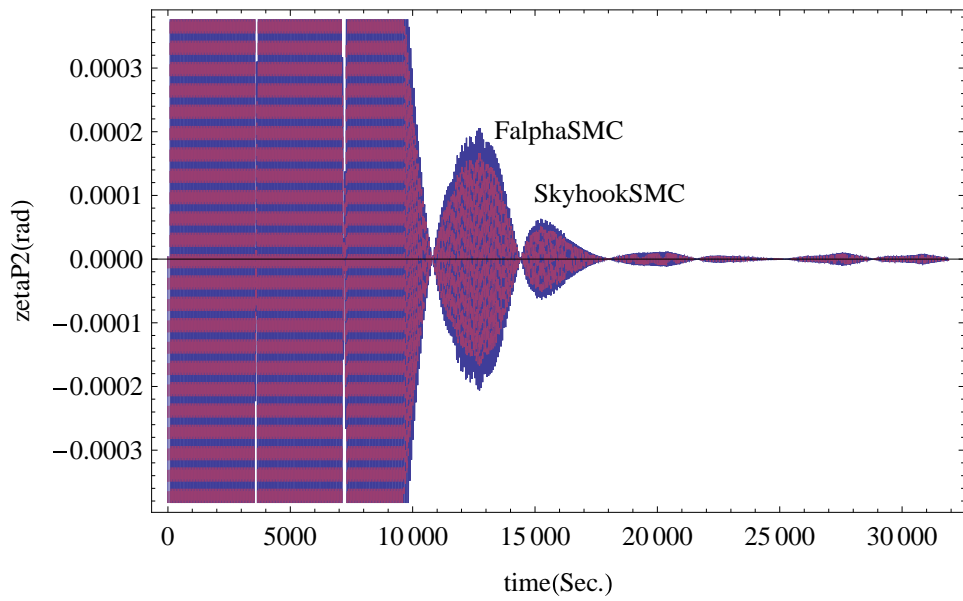


Figure K.24: Torsional elastic behaviour with control -  $\zeta_{p2}$ , FalphaSMC vs. SkyhookSMC ( $T_n = 4.01$ )

## Appendix L

---

# SMATLINK - How to integrate MATLAB with MATHEMATICA

---

### L.1 Introduction

Simple MATLAB and MATHEMATICA link laboratory toolbox (SMATLINK) is a toolbox to connect MATLAB and MATHEMATICA, it allows easy data exchange and manipulation, implementation of existing MATLAB or MATHEMATICA codes. There are two parts in SMATLINK package:

⟨1⟩ SMATLINK::matlabcall

▷ This part can do ‘MATLAB call MATHEMATICA’, in which, MATLAB is the Front-End and MATHEMATICA is the Calculating Engine, as shown in Figure L.1.

⟨2⟩ SMATLINK :: mathematicacall

▷ This part can do ‘MATHEMATICA call MATLAB’, in which, Mathematica is the Front-End and MATLAB is the Calculating Engine, as shown in Figure L.2.

### L.2 Why SMATLINK

The main reasons to use SMATLINK are:

⟨1⟩ Mobilise mathematical and computational resources;

⟨2⟩ Access leverage from limited mathematical and computational resources;

⟨3⟩ Economise the mathematical and computational resource requirements;

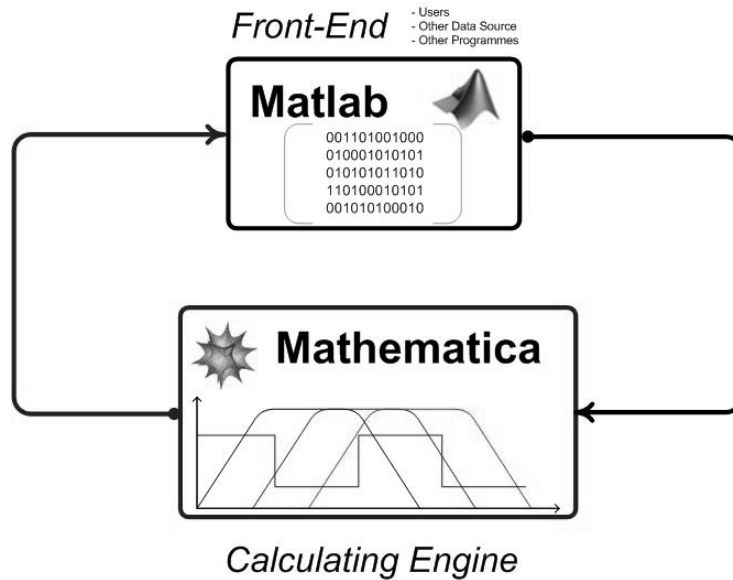


Figure L.1: SMATLINK::matlabcall work loop

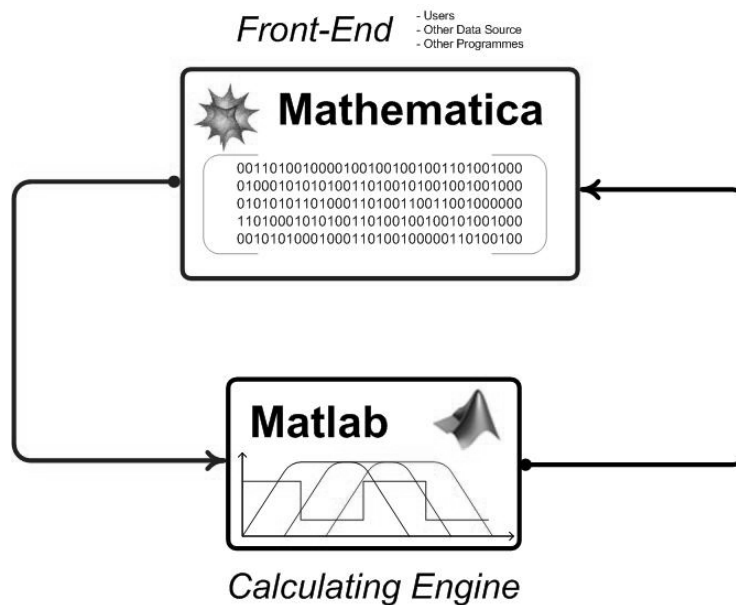


Figure L.2: SMATLINK::mathematicacall work loop

### L.3 MMET spin-up control co-simulation

As mentioned in sections 8.8 and 9.5, the numerical simulations for the MMET system spin-up control are obtained by using the toolkit of SMATLINK, which can integrate control in MATLAB/SIMULINK with the MMET model in MATHEMATICA. Figure L.3 shows the overall work loop for this simulations, in which the MATLAB/SIMULINK is the front-end to accept user's inputs and parameter settings, and control the 'master' timing for all the simulation process. On the other hand, MATHEMATICA represents the dynamical models for the MMET systems, which is waiting for the control signals from MATLAB/SIMULINK via SMATLINK, and generate the MMET systems' feedback then

send the feedback signals back to MATLAB/SIMULINK via SMATLINK. Figure L.5 presents the co-simulation timing control process, in which, the MATLAB controller is the ‘master’ timer, the MATHEMATICA MMET model is waiting for the control signals from MATLAB, it solves the controlled dynamical equations for the MMET system by NDSover[] with proper parameters, then the results has been sent back to MATLAB via SMATLINK.

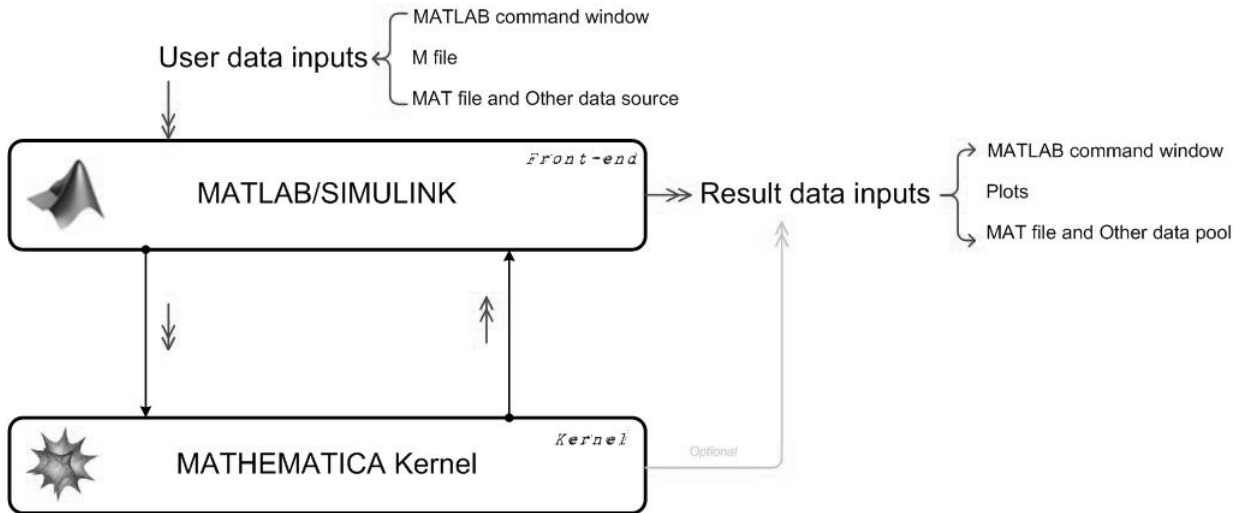


Figure L.3: The MMET system spin-up control co-simulation via SMATLINK

A simple case is given in Figure L.4, which shows how to call a MATHEMATICA function from MATLAB command window.

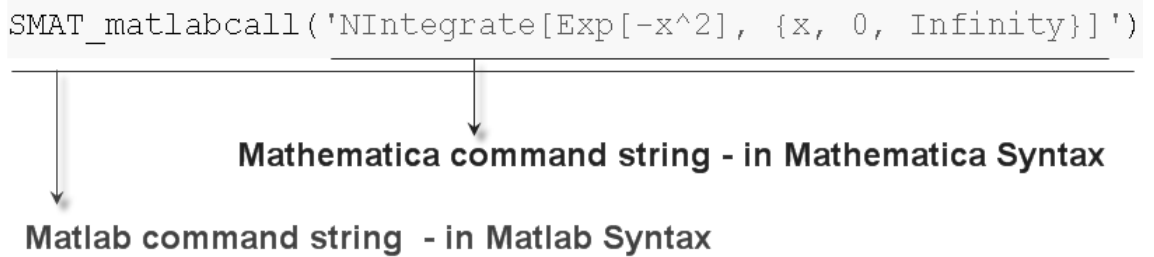


Figure L.4: How to call MATHEMATICA function from MATLAB

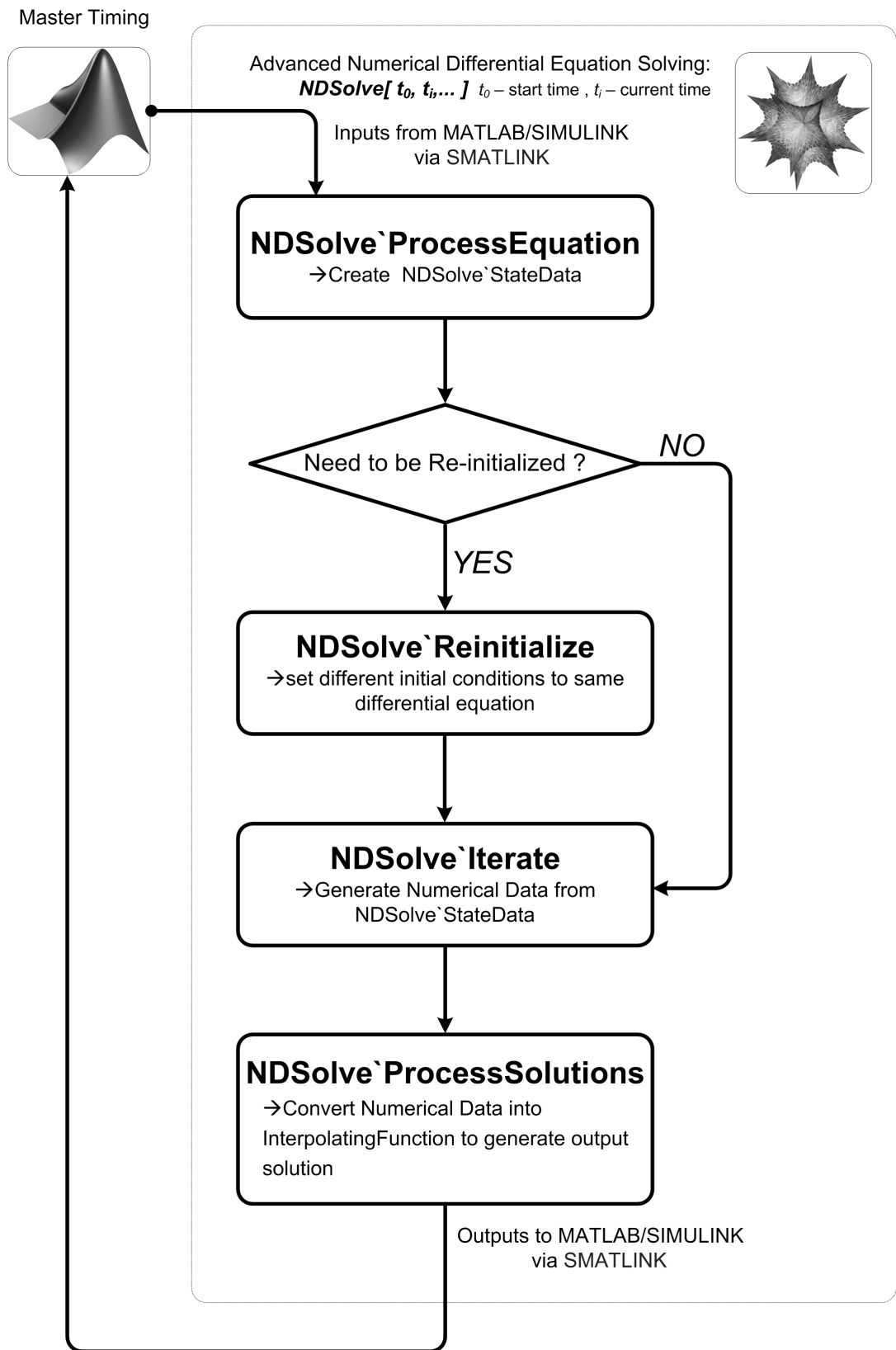


Figure L.5: SMATLINK timing control

## Appendix M

---

# Fuzzy Logic Control Terminology

---

Table M.1: Fuzzy Linguistic Values

Fuzzy Linguistic Value	Description	E	EC	U
NB	Negative Big	-5	-5	-2
NM	Negative Middle	-4	-4	-1.5
NS	Negative Small	-3	-3	-1
NZS	Negative Zero Small	-2	-2	-0.5
ZE	Zero	0	0	0
PZS	Positive Zero Small	2	2	0.5
PS	Positive Small	3	3	1
PM	Positive Middle	4	4	1.5
PB	Positive Big	5	5	2